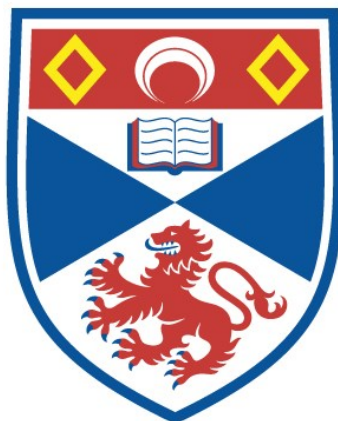


# Design and synthesis of triazine-based blue and oriented TADF emitters for high-efficiency OLEDs

Ettore Crovini

A thesis submitted for the degree of PhD  
at the  
University of St Andrews



2023

Full metadata for this item is available in  
St Andrews Research Repository  
at:

<https://research-repository.st-andrews.ac.uk/>

Identifier to use to cite or link to this thesis:

DOI: <https://doi.org/10.17630/sta/400>

This item is protected by original copyright

## **Candidate's declaration**

I, Ettore Crovini, do hereby certify that this thesis, submitted for the degree of PhD, which is approximately 45,555 words in length, has been written by me, and that it is the record of work carried out by me, or principally by myself in collaboration with others as acknowledged, and that it has not been submitted in any previous application for any degree. I confirm that any appendices included in my thesis contain only material permitted by the 'Assessment of Postgraduate Research Students' policy.

I was admitted as a research student at the University of St Andrews in October 2018.

I received funding from an organisation or institution and have acknowledged the funder(s) in the full text of my thesis.

Date 07/01/23

Signature of candidate

## **Supervisor's declaration**

I hereby certify that the candidate has fulfilled the conditions of the Resolution and Regulations appropriate for the degree of PhD in the University of St Andrews and that the candidate is qualified to submit this thesis in application for that degree. I confirm that any appendices included in the thesis contain only material permitted by the 'Assessment of Postgraduate Research Students' policy.

Date 07/01/23

Signature of supervisor

## **Permission for publication**

In submitting this thesis to the University of St Andrews we understand that we are giving permission for it to be made available for use in accordance with the regulations of the University Library for the time being in force, subject to any copyright vested in the work not being affected

thereby. We also understand, unless exempt by an award of an embargo as requested below, that the title and the abstract will be published, and that a copy of the work may be made and supplied to any bona fide library or research worker, that this thesis will be electronically accessible for personal or research use and that the library has the right to migrate this thesis into new electronic forms as required to ensure continued access to the thesis.

I, Ettore Crovini, have obtained, or am in the process of obtaining, third-party copyright permissions that are required or have requested the appropriate embargo below.

The following is an agreed request by candidate and supervisor regarding the publication of this thesis:

### **Printed copy**

Embargo on all of print copy for a period of 1 year on the following ground(s):

- Publication would preclude future publication

### **Supporting statement for printed embargo request**

Not all the material in this thesis has been published at the current stage.

### **Electronic copy**

Embargo on all of electronic copy for a period of 1 year on the following ground(s):

- Publication would preclude future publication

### **Supporting statement for electronic embargo request**

Not all the material in this thesis has been published at the current stage.

### **Title and Abstract**

- I agree to the title and abstract being published.

Date 07/01/23

Signature of candidate

Date 07/01/23

Signature of supervisor

## **Underpinning Research Data or Digital Outputs**

### **Candidate's declaration**

I, Ettore Crovini, understand that by declaring that I have original research data or digital outputs, I should make every effort in meeting the University's and research funders' requirements on the deposit and sharing of research data or research digital outputs.

Date 07/01/23

Signature of candidate

### **Permission for publication of underpinning research data or digital outputs**

We understand that for any original research data or digital outputs which are deposited, we are giving permission for them to be made available for use in accordance with the requirements of the University and research funders, for the time being in force.

We also understand that the title and the description will be published, and that the underpinning research data or digital outputs will be electronically accessible for use in accordance with the license specified at the point of deposit, unless exempt by award of an embargo as requested below.

The following is an agreed request by candidate and supervisor regarding the publication of underpinning research data or digital outputs:

Embargo on all of electronic files for a period of 1 year on the following ground(s):

- Publication would preclude future publication

### **Supporting statement for embargo request**

Not all the material in this thesis has been published at the current stage.

Date 07/01/23

Signature of candidate

Date 07/01/23

Signature of supervisor

### **Funding**

This work was supported by the EU Horizon 2020 Grant Agreement No. 812872 (TADFlife).

## **Abstract**

This thesis focuses on the design, synthesis, characterization and OLED fabrication and testing of TADF emitters, with a particular emphasis on trying to achieve high horizontal orientation of their TDM.

**Chapter 1** explains the basic concepts behind light-matter interaction, photoluminescence, and electroluminescence, focusing on TADF materials and their use in OLEDs. An in-depth explanation of the outcoupling effect will be given, with a discussion of several literature-known strategies to achieve optimal orientation of the emitter in the OLED stack.

**Chapter 2** focuses on a highly oriented TADF emitter, **ICzTRZ**. The theoretical and optoelectronic properties and TDM orientation of the material were studied, with its most interesting feature being the nearly completely horizontal orientation of the TDM in the film. OLED performance is then discussed.

**Chapter 3** describes a study to try and enhance the efficiency of **ICzTRZ** by adopting a twin-emitter design strategy, with **DICzTRZ**. Due to its high molecular weight, we hypothesize that **DICzTRZ** could also maintain horizontal orientation in solution-processed films.

**Chapter 4** concludes the work on the **ICz** family, with a study on how the horizontal orientation of **ICzTRZ** derivatives changes when the position and the number of *tert*-butyl groups on the material are modified.

In **Chapter 5**, the knowledge gathered from the previous study on the **ICz** series is applied to the known randomly oriented emitter **DMAC-TRZ**, to try in achieving horizontal orientation of the material and therefore generate an improvement in the device efficiency.

**Chapter 6** continues the work on **DMAC-TRZ** by investigating the effect that a heteroaromatic bridge has on the photophysics of the emitter.

**Chapter 7** summarizes and compares the results from **Chapters 2-6**. A discussion of the future work and outlooks of these projects is also presented.



## Acknowledgments

Firstly, thank you to my high school science teacher, Prof. Zoppi, who almost failed me in chemistry and had me follow extra classes to improve, which made me appreciate the subject. To Prof. Timothy Noël, for hosting me in his lab in Eindhoven for my master's thesis project, which made me decide to pursue a Ph. D. and a final thanks to my supervisor Prof. Eli Zysman-Colman, for giving me the position and providing constant support, and guidance.

Another set of thanks goes to all my co-workers and collaborators that helped me with many projects. In no particular order, thanks to Fabian, Zhen, Celine, Bilal, Prakhar, Minh, Francesco, Francisco, Kleitos, Larissa, Rama, Yoshimasa, Tomas, Ronald, Olive, Stefan, Paloma, Shiv, and Nidhi. Also, to Prof. Ifor Samuel, Prof. Andy Monkman, Prof. Hironori Kaji, Prof. Stefan Bräse, Prof. Wolfgang Brütting, Prof. Malte Gather, Prof. Anna Painelli, and Dr. Cristina Sissa.

Thanks to all members of the Marie-Curie ITN TADFLife, in particular my old uni classmate Francesco that ended up in the same project by chance and was responsible for much-appreciated wastes of time during meetings, to Kleitos and Larissa for making my stay at Durham such an enjoyable experience, and to Bilal and Prakhar for doing the same in Augsburg. Also, thanks to all other members of the ITN, both ESR and PIs.

On a more personal note, I would like to thank my family for giving me the possibility to undertake the Ph. D. and supporting me throughout this journey, including Green for being the cutest, chunky cat ever. A special thanks to my home friends, Melissa, Francesca, Letizia, Rob, and Erik, your constant chats and pretending to be interested while I complained about projects kept me going, and COVID times would have been much harder without our Skype calls and silly online games.

A very big thanks go to all the friends I made in St Andrews during this journey, in particular the wine Friday crew, present and past, Dave, Nidhi, Oil, Tim, Callum, Jess, Lea, Maire, Francis, Fabian, Tabea, Julius, Jasmin 1, and Jasmin 2. The time spent with you guys was truly amazing, and maybe even worth skipping dinner a few times for a few more rounds of Moldova. And finally, the biggest thanks goes to Megan for putting up with me (and *vice versa*) for the past 3 years, making them a truly special time in my life.

## List of Abbreviations

The molecular structure of the emitters (**Figure 201**), host materials (**Figure 202**), and OLED relevant materials (**Figure 203**) discussed in this thesis is provided in the **Appendix**.

<b>Abbreviations</b>	<b>Expansion</b>
<b>2-MeTHF</b>	2-methyltetrahydrofuran
<i>a</i>	Anisotropy factor
<b>A</b>	Acceptor
<b>a.u.</b>	Arbitrary units
<b>BCPO</b>	Bis-4-( <i>N</i> -carbazolyl)phenyl)phenylphosphine oxide
<b>CBP</b>	4,4'-Bis( <i>N</i> -carbazolyl)-1,1'-biphenyl
<b>CE</b>	Current efficiency
<b>CIE</b>	Commision Internationale de L'Éclairage
<b>CT</b>	Charge transfer
<b>CT-LE</b>	Mixed charge transfer-locally excited
<b>CV</b>	Cyclic voltammetry
<b>Cz</b>	9 <i>H</i> -Carbazole
<b>CzSi</b>	9-(4- <i>tert</i> -Butylphenyl)-3,6-bis(triphenylsilyl)-9 <i>H</i> -carbazole
<b>D</b>	Donor
<b>DCM</b>	Dichloromethane
<b>DET</b>	Dexter energy transfer
<b>DF</b>	Delayed fluorescence
<b>DFT</b>	Density functional theory
<b>DMA</b>	Dimethylacetamide
<b>DMAC</b>	9,9-Dimethyl-9,10-dihydroacridine

<b>DMF</b>	<i>N,N</i> -Dimethylformamide
<b>DPA</b>	Diphenylamine
<b>DPEPO</b>	Bis[2-(diphenylphosphino)phenyl]ether oxide
<b>DPV</b>	Differential pulse voltammetry
<b>DSC</b>	Differential scanning calorimetry
<b>EA</b>	Elemental Analysis
<b>EBL</b>	Electron blocking layer
<b>EML</b>	Emissive layer
<b>E<sup>ox</sup></b>	Oxidation potential
<b>E<sup>red</sup></b>	Reduction potential
<b>EQE</b>	External quantum efficiency
<b>EQE<sub>100</sub></b>	External quantum efficiency at 100 cd m <sup>-2</sup>
<b>EQE<sub>1000</sub></b>	External quantum efficiency at 1,000 cd m <sup>-2</sup>
<b>ETL</b>	Electron transporting layer
<b><i>f</i></b>	Oscillator Strength
<b>F</b>	Fluorescence
<b>FC</b>	Franck Condon
<b>Fc/Fc<sup>+</sup></b>	Ferrocene/Ferrocenium couple
<b>FOLED</b>	Fluorescent OLED
<b>FRET</b>	Förster resonant energy transfer
<b>FWHM</b>	Full width at half maxima
<b>HAT-CN</b>	1,4,5,8,9,11-Hexaazatriphenylenehexacarbonitrile
<b>HBL</b>	Hole blocking layer
<b>Hex</b>	<i>n</i> -Hexane

<b>HF</b>	Hartree Fock
<b>HLCT</b>	Hybrid local charge transfer
<b>HOMO</b>	Highest occupied molecular orbital
<b>HRMS</b>	High resolution mass spectrometry
<b>HTL</b>	Hole transporting layer
<b>IC</b>	Internal conversion
<b>ICz</b>	Indolo[3,2- <i>b</i> ]carbazole
<b>IRF</b>	Instrument response factor
<b>IQE</b>	Internal quantum efficiency
<b>ISC</b>	Intersystem crossing
<b>ITO</b>	Indium tin oxide
$k_{nr}$	Non-radiative rate constant
$k_{nr}^S$	Singlet Non-radiative rate constant
$k_{nr}^T$	Triplet Non-radiative rate constant
$k_{ISC}$	Intersystem crossing rate constant
$k_{RISC}$	Reverse Intersystem crossing rate constant
$k_r^S$	Fluorescence Radiative rate constant
<b>L</b>	Luminance or brightness
<b>LE</b>	Locally excited
<b>LiQ</b>	Lithium quinolin-8-olate
<b>L</b>	Luminance or brightness
<b>LUMO</b>	Lowest unoccupied molecular orbital
<b>MC</b>	Metal-Centered
<b>mCBP</b>	3,3'-Di(9 <i>H</i> -carbazol-9-yl)-1,1'-biphenyl

<b>mCBPCN</b>	3,3'-Di(carbazol-9-yl)-5-cyano-1,1'-biphenyl
<b>mCP</b>	1,3-Bis( <i>N</i> -carbazolyl)benzene
<b>MeCyHex</b>	Methyl Cyclohexane
<b>MO</b>	Molecular orbital
<b>NMR</b>	Nuclear magnetic resonance
<b>NPB</b>	<i>N,N'</i> -Di(1-naphthyl)- <i>N,N'</i> -diphenyl-(1,1'-biphenyl)-4,4'-diamine
<b>NRD</b>	Non-radiative decay
<b>OLED</b>	Organic light-emitting diode
<b>PE</b>	Power efficacy
<b>PEDOT:PSS</b>	Poly(3,4-ethylenedioxythiophene) polystyrene sulfonate
<b>PF</b>	Prompt fluorescence
<b>PhCzBCz</b>	9-(2-(9-phenyl-9H-carbazol-3-yl)phenyl)-9H-3,9'-bicarbazole)
<b>Phos</b>	Phosphorescence
<b>PL</b>	Photoluminescence
<b>PMMA</b>	Polymethyl methacrylate
<b>PhOLED</b>	Phosphorescent organic light emitting diode
<b>PPCz</b>	3,6-Bis(diphenylphosphinyl)-9-phenyl-Carbazole
<b>PPF</b>	2,8-bis(diphenylphosphoryl)dibenzo[b,d]furan
<b>PTZ</b>	Phenothiazine
<b>PXZ</b>	Phenoxazine
<b>PVK</b>	Poly(9-vinylcarbazole)
<b>r<sup>2</sup></b>	Linear correlation coefficient
<b>RIC</b>	Reverse internal conversion
<b>RISC</b>	Reverse intersystem crossing

<b>RMSD</b>	Root mean square deviation
<b>RO<sub>n</sub></b>	Roll-off at $n \text{ cd m}^{-2}$
<b>RTP</b>	Room temperature phosphorescence
<b>S</b>	Orientation order parameter
<b>S<sub>0</sub></b>	Singlet ground state
<b>S<sub>1</sub></b>	Lowest singlet excited state
<b>S<sub>n+1</sub></b>	Higher lying singlet excited state
<b>SCE</b>	Saturated calomel electrode
<b>SOC</b>	Spin orbit coupling
<b>t<sub>n</sub></b>	Device's lifetime
<b>T<sub>1</sub></b>	Lowest triplet excited state
<b>T<sub>n+1</sub></b>	Higher lying triplet excited state
<b>T2T</b>	2,4,6-tris(biphenyl-3-yl)-1,3,5-triazine
<b>TADF</b>	Thermally activated delayed fluorescence
<b>TAPC</b>	4,4'-Cyclohexylidenebis[ <i>N,N</i> -bis(4-methylphenyl)benzenamine]
<b>TCTA</b>	Tris(4-carbazoyl-9-ylphenyl)amine
<b>T<sub>d</sub></b>	Decomposition temperature
<b>TDA-DFT</b>	Tamm-Dancoff approximation
<b>TDM</b>	Transition dipole moment
<b>TE</b>	Transverse Electric
<b>T<sub>g</sub></b>	Glass transition temperature
<b>TGA</b>	Thermogravimetric analysis
<b>THF</b>	Tetrahydrofuran
<b>T<sub>m</sub></b>	Melting temperature

<b>TM</b>	Transverse Magnetic
<b>TmPyPB</b>	1,3,5-Tris( <i>m</i> -pyrid-3-yl-phenyl)benzene
<b>TPBi</b>	1,3,5-Tris(1-phenyl-1 <i>H</i> -benzo[d]imidazol-2-yl)benzene
<b>TPQ</b>	Triplet polaron quenching
<b>TRZ</b>	2,4,6-Triphenyl-1,3,5-triazine
<b>TSP01</b>	Diphenyl[4-(triphenylsilyl)phenyl]phosphine oxide
<b>TTA</b>	Triplet-triplet annihilation
<b>V<sub>on</sub></b>	Turn on voltage
<b>wt%</b>	Weight percent
<b>E<sub>gap</sub></b>	Energy gap between HOMO and LUMO
<b>ΔE<sub>ST</sub></b>	Energy difference between lowest singlet and triplet excited state
<b>ε</b>	Molar extinction coefficient
<b>Φ<sub>DF</sub></b>	Delayed fluorescence quantum yield
<b>Φ<sub>PF</sub></b>	Prompt fluorescence quantum yield
<b>Φ<sub>PL</sub></b>	Photoluminescence quantum yield
<b>θ</b>	Fraction of horizontal dipoles
<b>λ<sub>PL</sub></b>	Photoluminescence emission maximum
<b>λ<sub>abs</sub></b>	Absorption maximum
<b>λ<sub>exc</sub></b>	Excitation wavelength
<b>λ<sub>EL</sub></b>	Electroluminescence emission maximum
<b>η<sub>out</sub></b>	Outcoupling efficiency
<b>τ<sub>d</sub></b>	Delayed fluorescence lifetime
<b>τ<sub>p</sub></b>	Prompt fluorescence lifetime

---

## Table of contents

Motivation and objectives .....	19
<b>Chapter 1: Fundamental principles and theory behind Thermally Activated Delayed Fluorescence (TADF) OLEDs.....</b>	<b>23</b>
<b>1.1 - Light-matter interactions .....</b>	<b>23</b>
<b>1.2 - Photoluminescence .....</b>	<b>26</b>
<b>1.3 - Electroluminescence.....</b>	<b>31</b>
<b>1.4 - Structure and Mechanism of an OLED device.....</b>	<b>32</b>
<b>1.5 - Parameters of an OLED device.....</b>	<b>33</b>
<b>1.6 - Development of OLEDs .....</b>	<b>36</b>
<b>1.6.1 - Generation 1 OLEDs: Fluorescence .....</b>	<b>36</b>
<b>1.6.2 - Generation 2 OLEDs: Phosphorescence .....</b>	<b>37</b>
<b>1.6.3 - Generation 2.5 OLEDs: Triplet-Triplet Annihilation.....</b>	<b>39</b>
<b>1.6.4 - Generation 3 OLEDs: Thermally Activated Delayed Fluorescence .....</b>	<b>41</b>
<b>1.6.5 - Mechanism of TADF emitters .....</b>	<b>41</b>
<b>1.6.6 - Design of TADF emitters .....</b>	<b>44</b>
<b>1.6.7 - Host materials for TADF molecules .....</b>	<b>50</b>
<b>1.7 – Theoretical calculations .....</b>	<b>52</b>
<b>1.7.1 – DFT calculations.....</b>	<b>52</b>
<b>1.7.2 – Hybrid functionals and Basis sets .....</b>	<b>55</b>
<b>1.7.3 – TD and TDA calculations.....</b>	<b>56</b>
<b>1.8 - Transition Dipole Moment orientation of the emissive molecule.....</b>	<b>59</b>
<b>1.8.1 - Light outcoupling .....</b>	<b>59</b>
<b>1.8.2 - Transition Dipole Moment orientation.....</b>	<b>62</b>
<b>1.8.3 - Measuring the orientation of the Transition Dipole Moment .....</b>	<b>64</b>
<b>1.8.4 - Currently used strategies to improve the orientation of the emitter .....</b>	<b>65</b>
<b>1.8.5 - Molecular weight, thickness, and aspect ratio effect.....</b>	<b>66</b>
<b>1.9 - Conclusions .....</b>	<b>68</b>
<b>Chapter 2 - Di-functionalized Indolocarbazole-Triazine based materials as a design for highly horizontally oriented TADF emitters .....</b>	<b>70</b>



2.1 – Attributions .....	70
2.2 – Introduction .....	70
2.3 - Results and discussion .....	74
2.3.1 – Synthesis .....	74
2.3.2 - Theoretical calculations .....	75
2.3.3 - Optoelectronic properties .....	78
2.3.4 - Orientation measurements .....	90
2.3.5 - OLED devices .....	92
2.4 – Conclusions .....	94
<b>Chapter 3 - Twin-emitter design strategy to try in achieving horizontal orientation in solution-processed films. ....</b>	<b>96</b>
3.1 – Attributions .....	96
3.2 - Introduction .....	96
3.3 - Results and discussion .....	104
3.3.1 - Synthesis .....	104
3.3.2 - Theoretical calculations .....	104
3.3.3 - Optoelectronic characterization .....	108
3.3.4 - Orientation measurements .....	121
3.3.5 - OLED devices .....	122
3.4 - Conclusions .....	125
<b>Chapter 4 - Effect of different tert-butyl group substitution on the orientation of ICzTRZ. ....</b>	<b>127</b>
4.1 - Attributions .....	127
4.2 - Introduction .....	127
4.3 - Results and discussion .....	134
4.3.1 – Synthesis .....	134
4.3.2 - Theoretical calculations .....	135
4.3.3 - Orientation measurements .....	138
4.3.4 - Effect of the glass transition temperature .....	142
4.3.5 - Molecular weight (MW), thickness ( $z_E$ ) and emitter/host length ratio ( $x_E/x_H$ ) .....	143
4.4 – Conclusions .....	145

<b>Chapter 5 – Acridine modification to achieve horizontal orientation and long-lived and efficient TADF-OLEDs.</b>	147
<b>5.1 - Attributions</b>	147
<b>5.2 - Introduction</b>	147
<b>5.3 - Results and discussion</b>	154
<b>5.3.1 - Synthesis</b>	154
<b>5.3.2 - Theoretical calculations</b>	155
<b>5.3.3 - Optoelectronics properties</b>	158
<b>5.3.4 - Orientation measurements</b>	180
<b>5.3.5 - OLED devices</b>	182
<b>5.4 - Conclusions</b>	187
<b>Chapter 6 - The effect of an heteroaromatic bridge and the role of dihedral angle in a novel and efficient TADF emitter</b>	219
<b>6.1 - Attributions</b>	219
<b>6.2 - Introduction</b>	219
<b>6.3 – Results and discussion</b>	223
<b>6.3.1 - Synthesis and crystal structure</b>	223
<b>6.3.2 - Theoretical calculations</b>	224
<b>6.3.3 - Optoelectronic characterization</b>	231
<b>6.4 – Conclusions</b>	245
<b>6.5 - Compound characterization</b>	246
<b>Chapter 7 - Conclusions and future outlooks</b>	254
<b>Experimental section</b>	260
<b>Appendix</b>	266
<b>References</b>	268

## Motivation and objectives

Organic light-emitting diodes (OLEDs) are now considered the most promising technology for next-generation displays, thanks to advantages like efficient and light-weight devices, capability of achieving true-black color, and possibility to fabricate transparent and flexible devices.<sup>1,2</sup> Such devices are composed of a multi-layer structure where the light-emission results from the electroluminescence of the emitter.

Fluorescent emitters were first used in an OLED by Tang and Van Slyke in 1987,<sup>3</sup> and even if the device only presented an efficiency of c.a. 1%, it was operated at a relatively low driving voltage of under 10 V and presented a long lifetime of c.a. 100 h, sparking the interest in OLEDs. The electroluminescence in the OLED is generated by the radiative decay of excitons, which are bound states, formed by the combination of electrons and holes, generated when the current is applied to the device. Being electrons and hole fermions, their combination will lead to 25% of excitons in a singlet state and 75% of excitons in a triplet state, due to spin statistics. Thus, the first generation of OLED devices, employing fluorescent molecules (FOLED) never managed to achieve particularly high efficiencies, as the internal quantum efficiency (IQE) of the OLED would have never surpassed 25%, since only the singlet excitons can radiatively decay in these systems.

In 1998, the first example of a phosphorescent OLED (PhOLED) was presented by Baldo *et al.*<sup>4</sup> Most PhOLEDs contain Pt or Ir complexes as emitters, and efficiencies above 30% have been reported in several examples.<sup>5-7</sup> In phosphorescent complexes, the 75% of the excitons that are generated in a triplet state can decay radiatively thanks to the large degree of spin-orbit coupling (SOC). SOC is an intrinsic property of every atom, and is directly proportional to the atomic number of the element to the power of four.<sup>8</sup> This makes heavy metal complexes' triplet excitons able to decay radiatively. However, while green and red PhOLEDs have achieved excellent results and are the current technology used by industry, blue PhOLEDs suffer from stability issues. A disadvantage of Ir complexes is the presence of thermally accessible <sup>3</sup>MC (metal-centered) excited states, which lead to an increase in non-radiative decay and photochemical decomposition of the complexes *via* deligation.<sup>9-11</sup> The stability problem of blue metal complexes is leading the industry towards metal-free alternatives, which would also solve problems related to the scarcity of the metals currently employed, and would avoid the problem of possible environmental contamination.<sup>12</sup>

A third way to improve upon the IQE of OLEDs is to employ triplet-triplet annihilation (TTA) materials. TTA was observed for the first time in 1963 in pyrene,<sup>13</sup> and coined P-type fluorescence. The mechanism of TTA is based on a bimolecular energy transfer process between two triplet excitons, generating a new high-energy singlet exciton, which can then decay radiatively. This strategy allows to partially use the 75% of excitons in the triplet state as half of them will be upconverted to singlet excitons, while the other half will be down-converted to a ground state singlet exciton, meaning that up to an extra 37.5% of the excitons will contribute to the device emission, pushing the IQE to a theoretical maximum of 62.5%.

A fourth way to harvest all 100% of excitons is represented by thermally activated delayed fluorescence (TADF) molecules, also known as E-type fluorescence as it was originally observed in Eosin-Y.<sup>14-16</sup> Adachi and co-workers first employed a purely organic TADF material in an OLED in 2011,<sup>17</sup> achieving an EQE<sub>max</sub> of 5.3%. The following year this efficiency was greatly surpassed,<sup>18</sup> with the first report of a highly efficient green TADF OLED, with EQE<sub>max</sub> of 19.3%. TADF molecules present a small enough energy gap between the S<sub>1</sub> and T<sub>1</sub> states,  $\Delta E_{ST}$ , to allow the triplet excitons to upconvert into singlet excitons through a process called reverse inter-system-crossing (RISC), allowing for a theoretical 100% IQE. TADF is now considered the most promising way to harvest triplet excitons.<sup>19</sup>

To achieve white light and a full-color OLED display, all three primary colors (red, green, and blue) will need to be present in the device. As previously stated, heavy-metal phosphorescent complexes are commercially employed for the green and the red layer of the devices but blue phosphorescent complexes suffer from stability problems.<sup>20</sup> Current commercially available blue-OLEDs use TTA materials, which presents the aforementioned limitation in terms of a maximum IQE of 62.5%. The possibility of harvesting 100% of the formed excitons, makes TADF materials the most attractive replacement for the blue OLED materials. Realizing blue TADF OLEDs comes with its own set of challenges, the main one being obtaining a stable device able to achieve the deep-blue color required by industry standards. These standards are what's required for OLED phones and ultra-high definition (HD) TV, which are already commercialized by companies like Samsung, LG and Apple.<sup>21</sup>

The emitter able to achieve the desired deep-blue color would have a high band-gap ( $E_{gap}$ , energy difference between the frontier molecular orbitals of the material) and a high triplet state energy. The

application of current to the device is what generates charges (holes in the anode and electrons in the cathode) and they then “hop” toward each other *via* sequential electron transfer. The recombination of these charges, the formation of exciton, and the electroluminescence process will happen in the “central” emitting layer of the OLED device. This means that the energy barriers that the charges have to overcome in order to travel towards each other are the highest occupied molecular orbital (HOMO) and the lowest unoccupied molecular orbital (LUMO) levels of the different layers for holes and electrons respectively. Consequently, a large band gap material will make it harder for the charge to be injected in the emitting layer, as both the emitting layer and the adjacent layers will have more extremes HOMO and LUMO values, requiring the device to be run at higher voltages, leading to lower lifetimes and higher power consumption. These problems mark the need for an efficient and stable deep-blue emitter.

The emitting layer of an OLED is most commonly composed of the emitter dispersed in a host material to prevent undesired quenching of the triplet excitons at elevated concentrations as well as aggregation phenomena.<sup>22</sup> This is where the high energy triplet level of the emitter introduces the challenge of finding an appropriate host material. A good host material will need to have a triplet energy level higher than that of the emitter. This is to prevent undesired Dexter energy transfer from the emitter to the host material, which would lower the efficiency of the device. However, there aren't many host materials that possess high enough triplet energy levels for deep-blue materials ( $T_1$  level above 3.0 eV), and most of them, like the widely used DPEPO, are not stable, which reduces the device lifetime.<sup>22</sup>

Not all the light that is generated from the emitter will be able to escape the device. The aforementioned multilayer structure of the device, where every layer has a different refractive index, will lead the light generated to be completely or partially refracted at the interface between layers. This is known as the light outcoupling efficiency ( $\eta_{out}$ ) and highly reduces the amount of light exiting the device, lowering the external quantum efficiency (EQE) to around 25%.

$$EQE = IQE \eta_{out} \quad (1)$$

Since the emitter generates light perpendicularly to its transition dipole moment, one of the most effective strategies to improve upon the EQE is to create a layer where the transition dipole moment

of the emitter is oriented horizontally (parallel to the plane of the film), maximizing the fraction of light exiting the device, thus leading to superior efficiencies. If the transition dipole moment of the emitter will not present a preferential orientation but will be randomly organized, the orientation will be called isotropic, and it will negatively impact the amount of light able to escape to the device. The worst case is when the transition dipole moments is vertically oriented (perpendicular to the plane of the film), as in this case the majority of the light will be emitted pointing inwards, drastically affecting the EQE of the device.

In our recent review<sup>23</sup> we discovered several parameters that seem to influence the orientation of the emitter in the emissive layer. A meta-analysis of the literature was carried out and the published emitters were divided into two different classes, those with molecular weight (MW) below or above 600 g mol<sup>-1</sup>. For the lighter emitters, the glass transition temperature ( $T_g$ ) and the MW of the host were found to be the main discriminants for highly oriented materials. For the heavier emitters, the MW was the most influential parameter, but the geometry of the molecule also came into play.

The work presented in this thesis focuses on the modeling, synthesis, characterization, and device fabrication of novel blue TADF emitters, with a particular emphasis on achieving high horizontal orientation to maximize the efficiency of the OLEDs.

## Chapter 1: Fundamental principles and theory behind Thermally Activated Delayed Fluorescence (TADF) OLEDs

### 1.1 - Light-matter interactions

Whenever we discuss photophysics of any kind we are discussing interactions between light and matter. When light hits a material there are several types of interactions that can happen:

**Transmission:** phenomena during which the light moves through a material without interacting with it. It can be quantified by the transmittance which is defined as the ratio of the transmitted radiant power ( $P_\lambda$ ) and the incident power ( $P_\lambda^0$ ).<sup>24-26</sup>

$$T = \frac{P_\lambda}{P_\lambda^0} \quad (2)$$

**Refraction:** change in the direction of a wave passing from one media to another or from a gradual change in the medium (**Figure 1**).<sup>27</sup> Light refraction follows Snell's law, which states that, for a given pair of media, the ratio of the sines of the angle of incidence ( $\theta_i$ ) and of the angle of refraction ( $\theta_r$ ) is equal to the ratio of the phase velocities ( $v_{p1}$ ,  $v_{p2}$ ) and the ration of the refraction indexes of the two media ( $n_1$ ,  $n_2$ ):

$$\frac{\sin\theta_i}{\sin\theta_r} = \frac{v_{p1}}{v_{p2}} = \frac{n_2}{n_1} \quad (3)$$

A wave will travel through different materials at different speeds, but the frequency ( $\nu$ ) will not change. Since the wavelength of a wave is defined as:

$$\lambda = \frac{v_p}{\nu} \quad (4)$$

refraction also becomes a wavelength-dependent phenomenon, since if the speed decreases the wavelength will do too. For light refraction, the refractive index of the material ( $n$ ) is more commonly used, which is defined as:

$$n = \frac{c}{\nu} \quad (5)$$

Where  $c$  is the speed of light under vacuum. Air has a refractive index of 1, while glass and most organic media have a refractive index of 1.5.

**Reflection:** change in the wavefront direction at an interface between two media where it returns to the medium from which it originated (**Figure 1**). Reflection of light can occur when light travels between two media with different refractive indexes. The angle of incidence after which value light undergoes total internal reflection is called the critical angle.

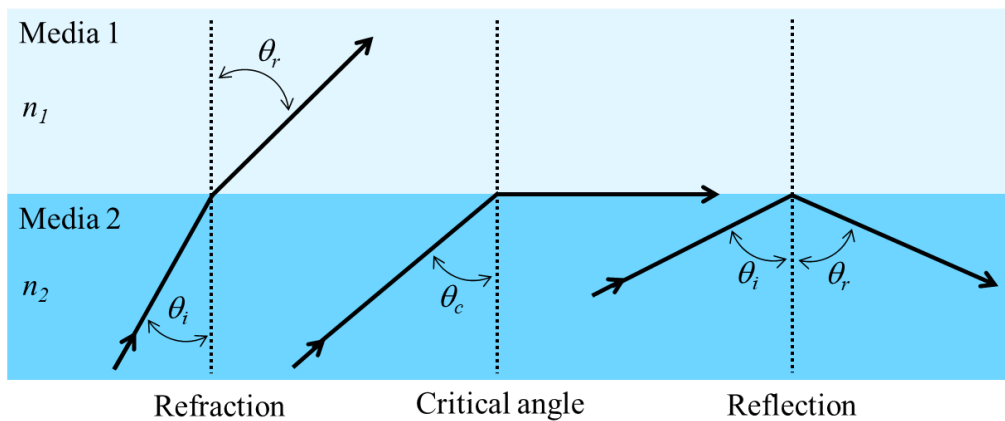


**Figure 1.** Different types of light-refraction between two media.

**Diffraction:** the process by which a beam of light or another system of waves is spread out as a result of passing through a narrow aperture or across an edge, typically accompanied by interference between the waveforms produced.

**Scattering:** a particular type of reflection where the light bounces off a series of particles existing in the media through which is propagating.

**Absorption:** absorption of the electromagnetic radiation by the material, transforming the electromagnetic energy of the photon into internal energy.



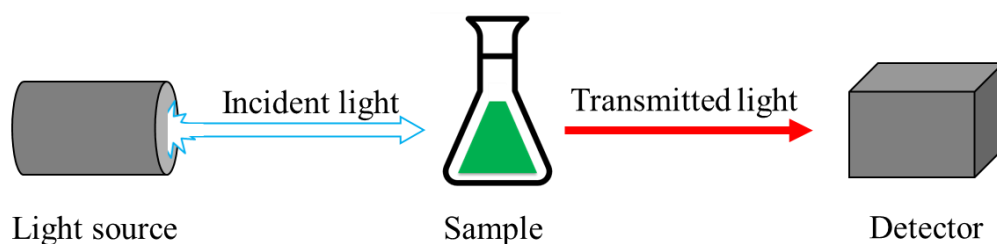


**Figure 2.** Schematic representation of absorption spectroscopy

Absorption can be quantified through absorption spectroscopy (**Figure 2**). A beam of white light is shined on the sample, some of the light will be absorbed by it, and the rest will be transmitted to the detector. The spectrophotometer then measures the transmittance ( $T$ ) which is the ratio of the intensities of the light hitting the detector and of the light hitting the sample. From that, we can obtain the absorbance value ( $A$ ), equal to the negative log of the transmittance. We can also express absorbance in terms of the Beer-Lambert Law, where  $\epsilon$  is the molar absorptivity coefficient,  $C$  is the molarity of the sample, and  $l$  is the path length of the light (usually set to 1 cm in most spectrophotometers).

$$T = \frac{I}{I_0} \quad (6)$$

$$A = -\log T \quad (7)$$

$$A = -\epsilon C l \quad (8)$$

## 1.2 - Photoluminescence

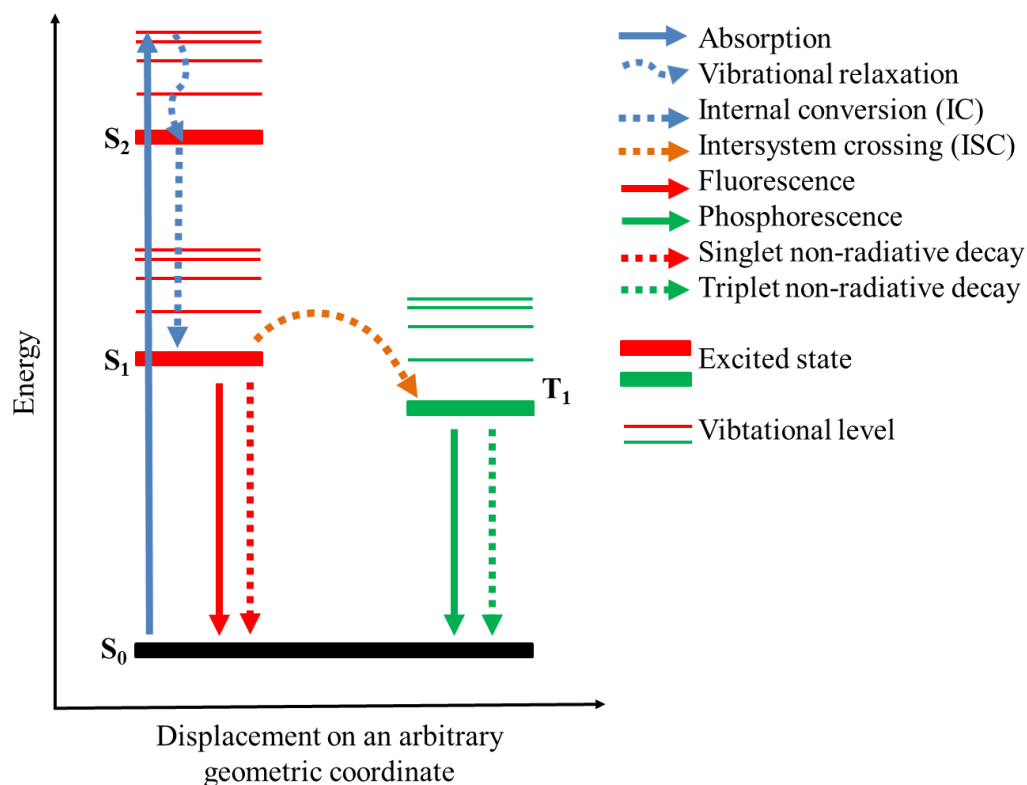


**Figure 3.** Photophysical pathways for a general photoexcited molecule.

The process of light generation from the radiative decay of an exciton is called photoluminescence (**Figure 3**). When a molecule absorbs a photon of sufficient energy, one of the electrons in the ground state ( $S_0$ ) is excited to a higher energy electronic level ( $S_n$ , with  $n > 0$ ). The resulting excited state can then return to the ground state *via* radiative decay (fluorescence), which will generate light, or non-radiative decay, where the energy will be lost as heat. As fluorescence happens without a change in the spin of the states involved, it is defined as a spin-allowed process. Despite what excited state is accessed after the excitation, radiative decay will very likely occur from the lowest excited state ( $S_1$ ) as internal conversion from higher excited states (for example  $S_2$ ) to  $S_1$  will happen faster than all other processes ( $10^{-14}$ – $10^{-11}$  s for internal conversion against  $10^{-9}$ – $10^{-7}$  s for fluorescence), making the emission spectra independent from the excitation wavelength. This is known as Kasha's rule.<sup>28</sup>

Alternatively, a third case is represented by the exciton passing from  $S_1$  (excited singlet state) to  $T_1$  (excited triplet state) through intersystem crossing (ISC). Commonly, for organic molecules, relaxation from the triplet state to the ground state is generally non-emissive, due to the spin-

forbidden nature of the  $T_1 \rightarrow S_0$  transition. This makes the radiative decay incredibly slow and cryogenic conditions are needed to suppress non-radiative pathways, allowing phosphorescence. Compounds can achieve emission from the triplet state thanks to the spin-orbit coupling (SOC). In this type of compound, the orbital angular momentum quantum number ( $n$ ) and the spin quantum number ( $l$ ) can mix, allowing to overcome the spin-forbidden nature of the process. As a first approximation, we can consider that only the  $S_1$  and  $T_1$  states are involved in ISC, this is defined as first-order mixing. The first-order mixing coefficient ( $\lambda$ ) between  $S_1$  and  $T_1$  will then be inversely proportional to the energy gap between them ( $\Delta E_{ST}$ ) and directly proportional to the spin-orbital interaction ( $H_{SO}$ ).

$$\lambda = \frac{H_{SO}}{\Delta E_{ST}} \quad (9)$$

The spin-orbit coupling constant ( $\zeta$ ), which is an intrinsic property of every element, is directly proportional to  $Z^4$  (atomic number), leading heavier atoms to promote more SOC. For example, employing heavy metal complexes will result in larger spin-orbit coupling interactions, thus allowing the triplet state to relax radiatively (phosphorescence). More importantly, the SOC will be maximized if the two states involved in the transition have different orbital types. This is known as El-Sayed's rule<sup>8</sup> and thus provides a route for formally spin-forbidden transitions to happen. For example, an ISC transition between  $^1\pi\pi^* \rightarrow ^3n\pi^*$  will be faster than an ISC transition between  $^1\pi\pi^* \rightarrow ^3\pi\pi^*$ .

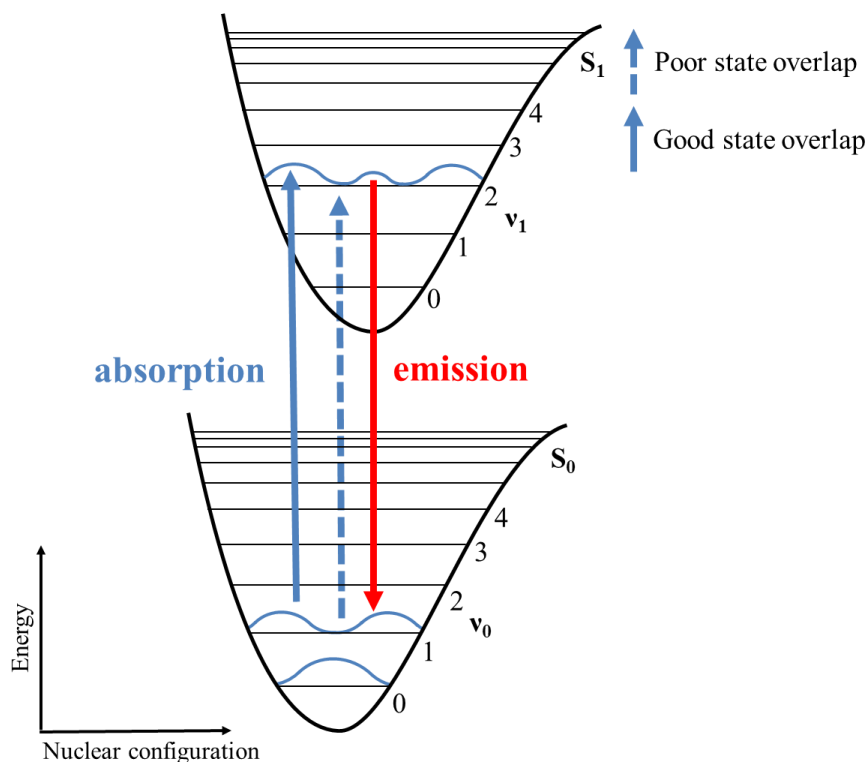


**Figure 4.** Different states and vibrational modes involved in an absorption/emission process.

The intensity of the absorption/emission will be a function of the oscillator strength, which defines the probability of the transition to happen. This probability is directly proportional to the electronic and vibrational overlap of the two states involved in the transition. As shown in **Figure 4**, within every electronic state there are different vibrational modes, each of different energy. The degree of overlap in a transition can be defined with the Frank-Condon factor:

$$f_{n,m} \propto |\langle N_n | N_m \rangle|^2 \quad (10)$$

This is known as the Frank-Condon principles, and it states that the probability, and therefore intensity, of a transition (either absorption or emission) will be directly proportional to the overlap of the wavefunction of the two vibronic states involved ( $N_n$  and  $N_m$  represent the wavefunction of the initial and final vibronic state, respectively). This equation shows the overlap integral between the ground state and the excited state involved in the transitions. Greater overlap will lead to an increased probability for the transition to happen and to a greater absorption/emission intensity. If we look at **Figure 4**, the dotted light-blue arrow represents a transition that is not very likely to happen due to

the poor overlap between the two vibrational modes, while the thick light-blue arrow represents an absorption that goes from a maximum in the lowest vibrational mode of  $S_0$  to a maximum in the second vibrational mode of  $S_1$ , making it much more likely to happen and with a higher intensity.

The probability of the transition to happen is also dependent on the transition dipole moment (TDM), which can be expressed as:

$$TDM = \mu_{fi} = \langle \varphi_i | \mu | \varphi_f \rangle \quad (11)$$

Where  $\varphi_i$  and  $\varphi_f$  represent the initial ground state and the finishing electronic excited state and  $\mu$  is the electronic transition dipole operator. This equation can be further expanded to the product of 3 different terms (each term must be  $\neq 0$  for the transition to happen):

$$\langle \varphi_i | \mu | \varphi_f \rangle = \int \chi_i \chi_f dQ \int S_i S_f d\tau_e \int \phi_i \mu \phi_f \tau_e \quad (12)$$

(1)                      (2)                      (3)

**(1) Nuclear wave function operator:** the first term depends on the overlap of nuclear configuration and expresses if the molecule changes its nuclear configuration during the transition. For absorption, this term will be near zero as this transition happens too quickly ( $10^{-15}$  s) for the nuclei to have time to re-arrange. This operator becomes more prominent for emission spectroscopy as the excited state has a sufficiently long lifetime for the geometry to change.

**(2) Electronic spin:** this term represents the spin-selection rule. For a transition to be spin-allowed, it must happen without a change in the spin multiplicity ( $S_1 \rightarrow S_0$  is allowed,  $T_1 \rightarrow S_0$  is forbidden). Term 2 will be equal to zero for spin-forbidden transitions.

**(3) Electronic transition dipole moment:** for an electronic transition to be orbitally allowed, it needs to happen with a change in the orbital's symmetry and therefore a change in the orbital quantum number  $l$ , this is the Laporte selection rule.<sup>29</sup> In a molecule a spin-allowed absorption is allowed if there is a change in the angular momentum of the orbitals involved in the transition.

The efficiency of a photoluminescence process can be quantified by measuring the photoluminescence quantum yield ( $\Phi_{PL}$ ) of the material, which is defined as the ratio between the radiative decay constant ( $k_r$ ) and the sum of the radiative and non-radiative decay constant ( $k_{nr}$ ).

$$\Phi_{PL} = \frac{k_r}{k_r + \sum k_{nr}} \quad (13)$$

Therefore, to maximize the amount of light generated and thus its efficiency, a fast radiative decay constant and a slow non-radiative decay constant are required. Both radiative and non-radiative pathways will be affected by the energy gap between the ground state and the excited state. This is called the energy gap law. This comes as a direct consequence of Fermi's Golden Rule:

$$k_{fi} \propto |\mu_{fi}|^2 \quad (14)$$

This implies that for radiative transitions ( $f$  and  $i$  indicate the final point and the initial point of the transition, respectively), the rate is directly proportional to the square of the transition dipole moment of that transition. This means that as the energy gap between the ground and excited-state state decreases, the  $\Phi_{PL}$  also decreases. This will affect the rate of both radiative and non-radiative processes:

$k_{nr}$ : the Energy Gap Law for non-radiative transitions states that  $k_{nr}$  is inversely proportional to the energy gap between the ground and excited state,<sup>30</sup> meaning that transitions of higher energy will have higher  $\Phi_{PL}$ .

$k_r$ : the Energy Gap Law for radiative transitions states that  $k_r$  is directly proportional to the cube of the frequency of the emission,<sup>31</sup> and as the frequency is directly proportional to the energy, thus higher energy emission will lead to higher  $\Phi_{PL}$ .

As stated before, emission from a singlet state will happen predominately from the lowest electronic excited state (Kasha's rule). Since the transition dipole moment is responsible for the probability of

a transition, which is defined by the oscillator strength of that transition, the Fermi Golden Rule links  $k_r$  to the oscillator strength, making molecule with higher  $f$  for the  $S_1 \rightarrow S_0$  transition more efficient.

### 1.3 - Electroluminescence

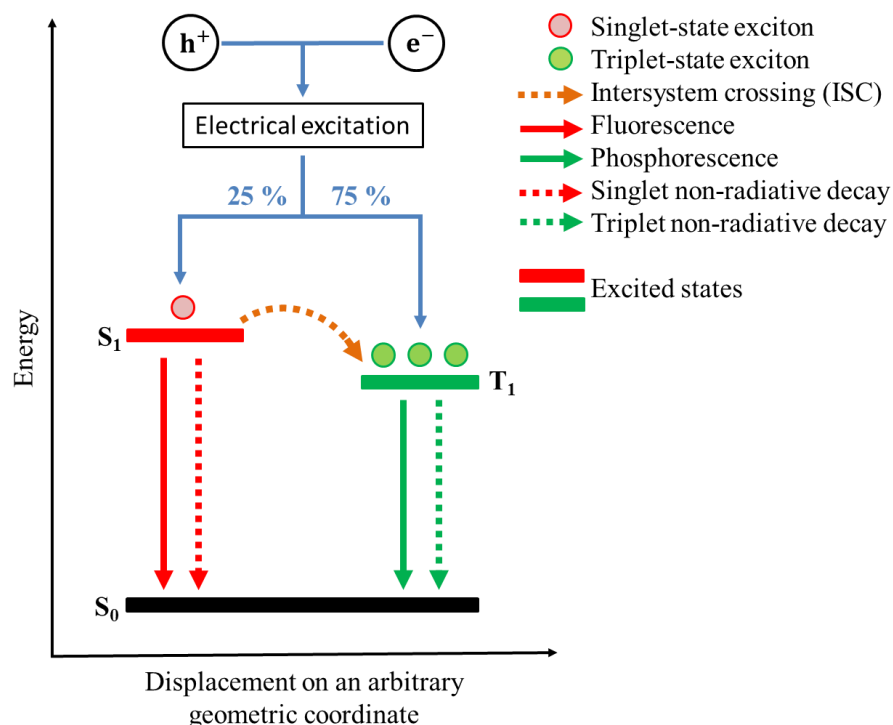


**Figure 5.** Photophysical pathways for a general electrically-excited molecule.

Light generation can also be achieved *via* electrical excitation, which is called electroluminescence (**Figure 5**). A voltage is applied across a medium, which will inject electrons (that will form radical anions) and at the same time holes (radical cations) will be generated as electrons exit from the anode. The combination of holes and electrons will lead to the formation of an exciton. Holes and electrons are species that possess half-integer spin (fermions), and the combination of these species will lead to the formation of both singlet excited states ( $S=0$ , with a total spin multiplicity of  $2S+1=1$ ) and triplet excited states ( $S=1$ , with a total spin multiplicity  $2S+1=3$ ). While in photoluminescence the singlet excited state is populated first, electroluminescence provides a possibility to directly populate triplet states. The formed excitons can then undergo the different photophysical processes previously explained. Singlet excitons can decay radiatively (fluorescence), non-radiatively (heat generation), and undergo ISC, however triplet excitons will not generally generate light (phosphorescence) without the use of heavy atoms (SOC) or cryogenic conditions. Electroluminescence is the process used in OLEDs to generate light.

## 1.4 - Structure and Mechanism of an OLED device

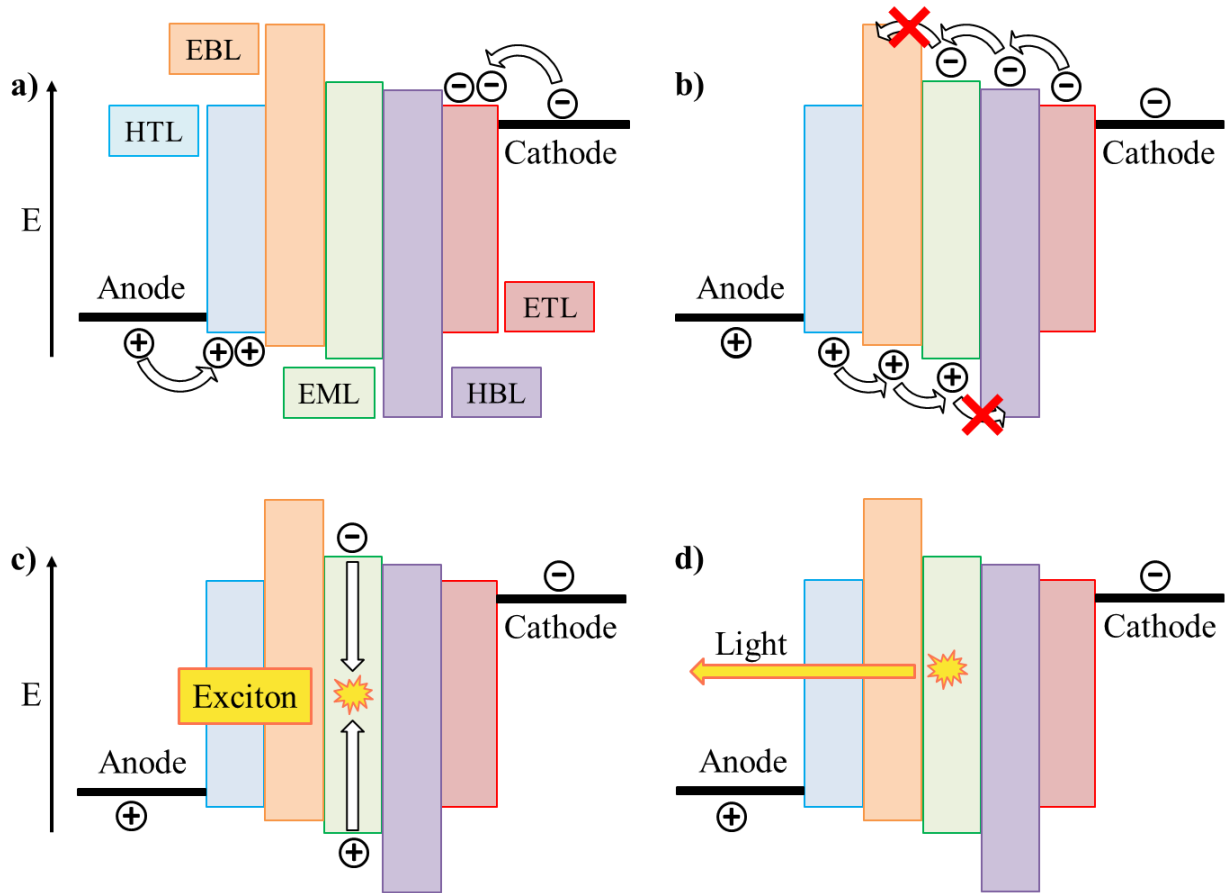


**Figure 6.** Mechanism of OLEDs. **a)** carrier injection; **b)** carrier transport; **c)** exciton formation; **d)** exciton decay.

An OLED is composed of a metallic cathode, an Electron-Transporting-Layer (ETL), an Emissive-Layer (EML), a Hole-Transporting Layer (HTL), a semi-transparent anode, generally indium tin oxide (ITO) and a substrate, which is usually glass. Hole blocking layers (HBL) and Electron blocking layers (EBL) can be furtherly added around the emissive layer to improve the efficiency of the exciton formation process.

The generation of light in an OLED stack can be divided into 4 steps (**Figure 6**):

**Carrier Injection:** the current passing through the device from the cathode to the anode will insert electrons in the LUMO of the ETL (negative carriers) while at the same time, it will generate holes in the HOMO of the HTL (positive carriers).



**Carrier transport:** the injected carriers travel toward each other *via* sequential electron transfer. This happens at the interface layers and requires an energy input high enough to surpass the activation energy barrier. HBL and EBL are made of materials having a very low energy HOMO or high energy LUMO level respectively. This makes the charge transport from the EML to them energetically unfavorable, thus stopping it.

**Exciton formation:** Holes and electrons combine inside the EML and generate excitons.

**Exciton decay:** The newly formed exciton can now decay through radiative or non-radiative pathways. Radiative decay is what generates the lighting in the device.

### 1.5 - Parameters of an OLED device

The efficiency of the EML can be expressed by the Internal Quantum Efficiency (IQE):

$$IQE = \gamma \eta_r \Phi_{PL} \quad (15)$$

$\gamma$  represents the charge carrier balance of electrons and holes which express the fraction of generated electrons and holes that can recombine in EML to generate an exciton ( $\gamma$  is usually considered to be 1, indicating the efficiency of hole-electron recombination).  $\eta_r$  is the radiative exciton fraction and takes into account the multiplicity of possible spins. Due to spin-statistic, 25% of the excitons will be in a singlet state and 75% in a triplet state. The final factor of the equation is the previously discussed  $\Phi_{PL}$ . The presence of several layers, with different refractive indexes, causes not all the light that is generated in the EML will be able to leave the device, due to refraction phenomena at the media interface.  $\eta_{out}$  is called the outcoupling factor and considers the amount of light that manages to exit the device. The overall efficiency of an OLED device can be quantified by the External Quantum Efficiency (EQE) of the device.

$$EQE = IQE \eta_{out} \quad (1)$$

The amount of light generated by an OLED is called luminous flux and is measured in lumens (lm). This value can be also measured in relation to the solid angle (angle at the centre of a sphere subtended

by a part of the surface equal in area to the square of the radius) in the form of a candela, equal to one lumen per steradian ( $1 \text{ cd} = 1 \text{ lm sr}^{-1}$ , steradian is the unit of measure of the solid angle in the SI). From these units we can measure the power efficacy (PE) and the current efficiency (CE) of the device. PE is measured in lumens per Watt ( $\text{lm W}^{-1}$ ) and indicates the amount of light that is generated by a certain amount of electrical power. CE is measured in candela per ampere ( $\text{cd A}^{-1}$ ) and describes the efficiency with which the charge is transferred into the OLED system, and thus creates light in the device. The luminance, or brightness, of the OLED (L) can be quantified in  $\text{cd m}^{-2}$ , and it's defined as the amount of luminous flux arriving in the solid viewing angle.<sup>21</sup> The voltage at which the device reaches a brightness of  $1 \text{ cd m}^{-2}$  is defined as the turn on voltage of the device. The lifetime of the device is defined in a number of ways, from  $t_{95}$  (the time it takes the device's predefined luminance to decrease by 5%) to  $t_{50}$  (the time it takes the device's predefined luminance to decrease by 50%). The predefined luminance is normally taken as  $1000 \text{ cd m}^{-2}$ . Specifically for blue, OLED devices for industrial application require a  $t_{95}$  of around 5000 hours.<sup>20</sup>

The EQE value that is most often reported, the  $\text{EQE}_{\text{max}}$ , is usually taken at very low brightness values, meaning that a very low current is run through the device. With increasing current, and brightness, the EQE of the OLED typically decreases, this is known as efficiency roll-off (RO), and since many OLED applications require a very high level of brightness (for example, large area OLEDs for general illuminations will require at least  $5000 \text{ cd m}^{-2}$ ),<sup>32</sup> producing devices with improved RO is highly desirable.<sup>33</sup> The decrease of the EQE in a device is caused by exciton-quenching phenomena, which are all dependent on the concentration of excitons. Therefore, at higher brightness (meaning at higher current density) the device efficiency drops because the higher voltage given to the device increases the number of excitons formed and so the likelihood of exciton quenching. For this reason, the  $\text{EQE}_{\text{max}}$  value doesn't give much information about the stability of the device. EQE values taken at  $100 \text{ cd m}^{-2}$  and  $1000 \text{ cd m}^{-2}$  are more useful for this, as they show us how the device behaves under more relevant operational conditions. The decrease in the efficiency with higher current density and luminescence is defined as efficiency roll-off ( $\text{RO}_{100}$  and  $\text{RO}_{1000}$ ):

$$\text{RO}_n = \frac{\text{EQE}_{\text{max}} - \text{EQE}_n}{\text{EQE}_{\text{max}}} \quad (16)$$

The color of an OLED display can be defined with the Commission International de l'Éclairage (CIE) 1931 diagram (**Figure 7**). Coordinates are assigned to each color and are reported as points on a diagram representing all colors perceivable by the human eye. To achieve a full-color display and white lighting, the three primary colors need to be present in the display, red, green, and blue, which coordinates are established as (0.71, 0.29) for red, (0.17, 0.80) for green, and (0.13, 0.05) for blue.<sup>34</sup> These industry standards values have been most recently revised for HD-TV, and are known as BT.2020.

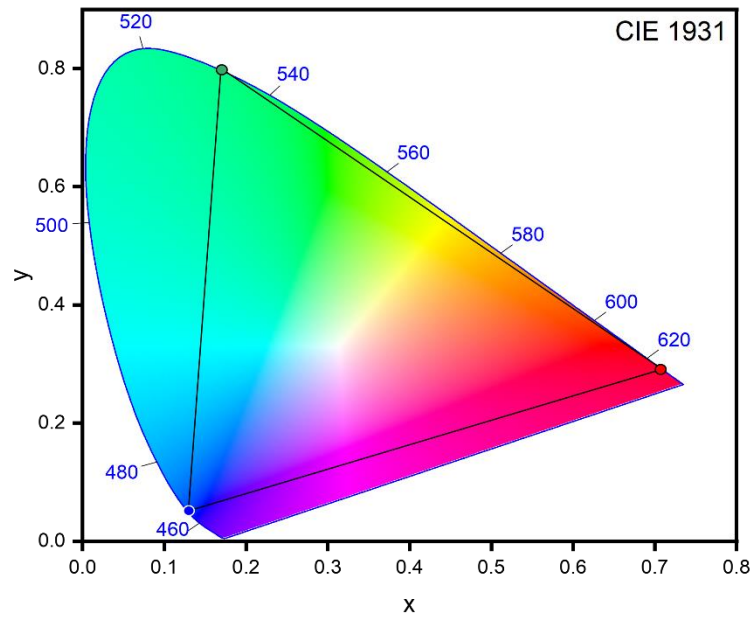


**Figure 7.** CIE diagram (BT 2020 standards for red, green, and blue are highlighted as circles of the respective color).

## 1.6 - Development of OLEDs

Several classes of OLEDs, with different exciton harvesting strategies, have been developed during the years. We can distinguish four different generations:

### 1.6.1 - Generation 1 OLEDs: Fluorescence

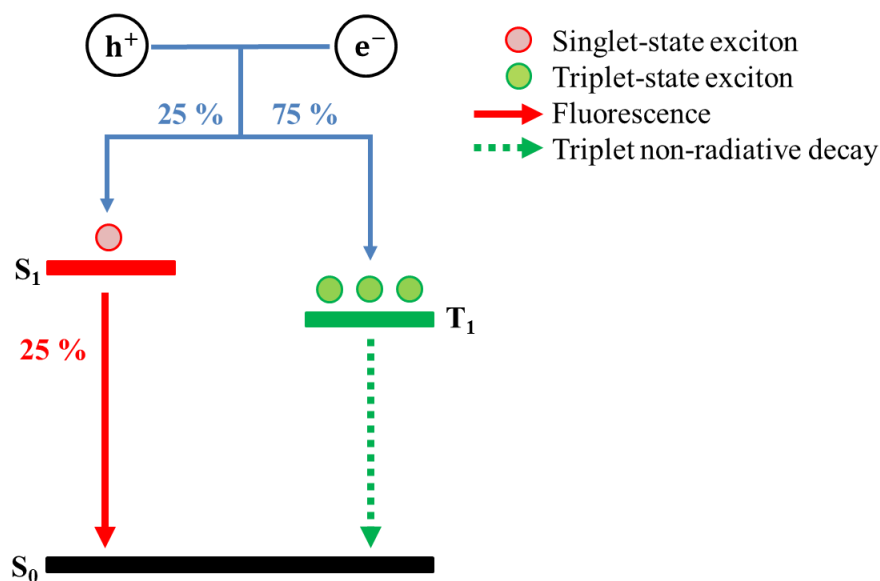


**Figure 8.** Simplified mechanism of a Generation 1 emitter.

Tang and Van Slyke demonstrated in 1987<sup>3</sup> that an OLED could operate at relatively low voltage by using a fluorescent emitter in a two-layer device. ITO was used as the anode, tris(8-hydroxyquinolato) aluminum(III) (Alq3) was used as the EML, 4,4'-cyclohexylidenebis[*N,N*-bis(4-methyl phenyl)benzenamine] (TAPC) was used as the HTL and magnesium was employed as the cathode. While this first example presented very low EQE (c.a. 1%) the low driving voltage of under 10 V and the long lifetime of c.a. 100 h showed the potential of OLEDs.

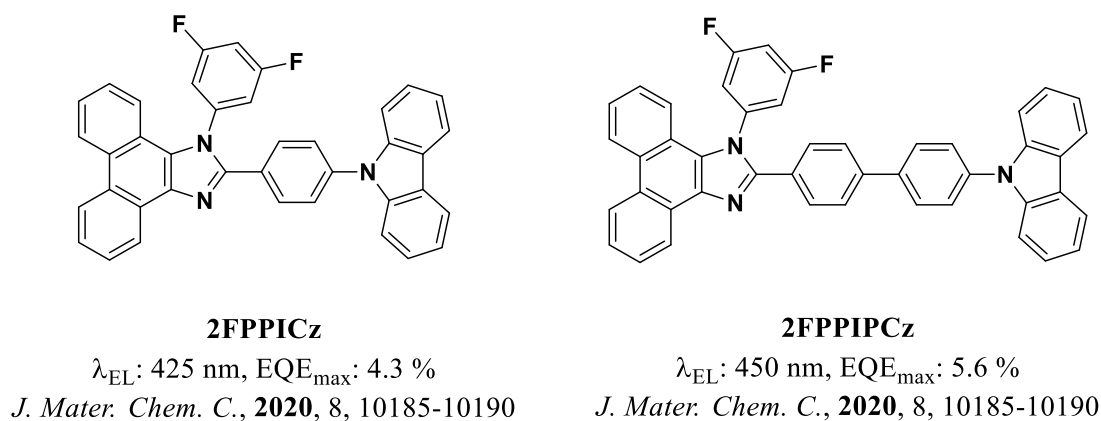


**Figure 9.** Chemical structures of **2FPPICz** and **2FPPIPCz**.

As previously explained, the combination of holes and electrons will lead to the formation of 25% of the excitons in a singlet state and 75% of excitons in a triplet state (**Figure 8**). The main drawback of fluorescent emitters is that only the singlet state excitons will be able to decay radiatively, making the IQE of the emitting layer unable to surpass 25%. Despite this disadvantage, fluorescent materials are still being investigated as exemplified in a recent study by Xin *et al* for deep-blue OLEDs that achieved an EQE<sub>max</sub> of 4.3% and 5.6% at  $\lambda_{EL}$  of 425 nm and 450 nm using the emitters **2FPPICz** and **2FPPIPCz**, respectively (**Figure 9**).<sup>35</sup>

### 1.6.2 - Generation 2 OLEDs: Phosphorescence

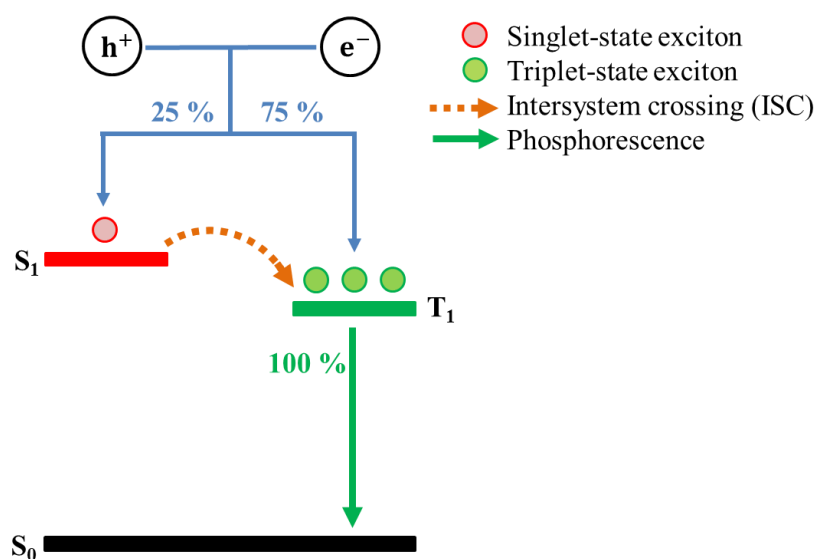


**Figure 10.** Simplified mechanism of a Generation 2 emitter.

Employing heavy-metal complexes allows harvesting of the triplet excitons thanks to the spin-orbit coupling from the heavy atom (**Figure 10**). Baldo *et al.* reported the first example of a phosphorescent OLED (PhOLED) in 1998<sup>4</sup>, by doping an Alq<sub>3</sub>-based device with a different concentration of PtOEP, a well-studied red-emitting phosphorescent dye. The devices showed phosphorescence and an EQE of 4% for the 6 wt% doped devices, becoming the highest performing red device of the time. Pt and Ir based complexes are the main materials used in PhOLED reaching high EQE of above 30%.<sup>36–41</sup>

PhOLED with EQE<sub>max</sub> above 31% have been reported for all three primary colors (**Figure 11**) but despite these important results, employing heavy-metal complexes makes PhOLED an environmentally non-friendly strategy due to the scarcity and high toxicity of the metals employed. Moreover, while current red and green devices are phosphorescent, blue devices of this category are not stable enough and are not able to retain a good color purity during use. Thus, there remains a need for purely organic alternatives that address these weaknesses.

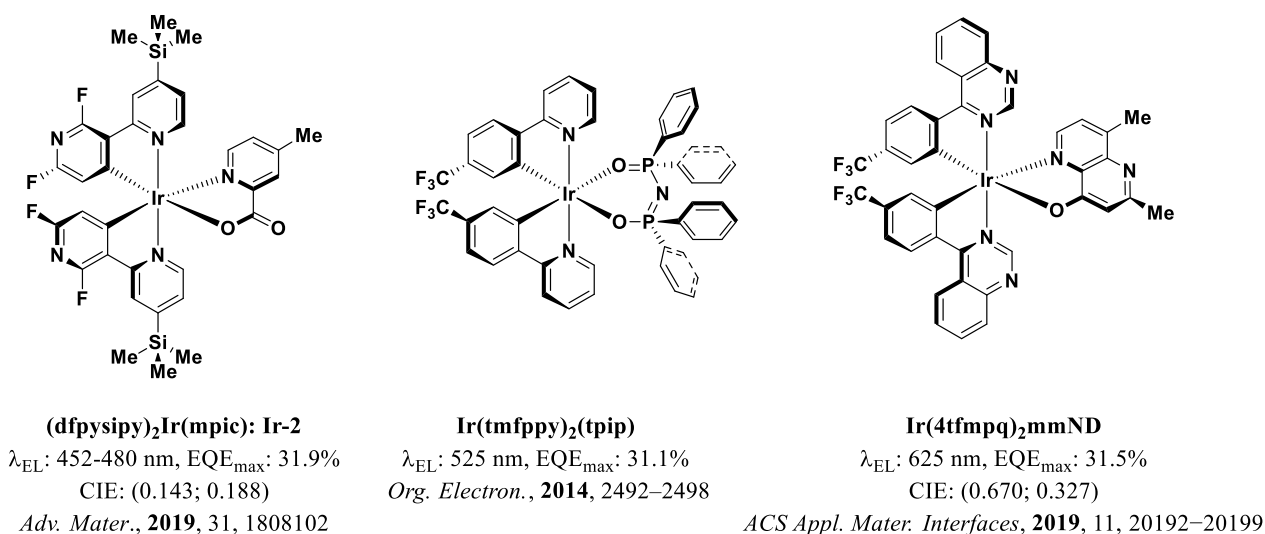


**Figure 11.** Chemical structure of phosphorescent complexes used in state-of-the-art blue (**Ir-2**), green (**Ir(tmfpPy)<sub>2</sub>(tpip)**), and red (**Ir(4tfmpq)<sub>2</sub>mmND**) PhOLEDs.

### 1.6.3 - Generation 2.5 OLEDs: Triplet-Triplet Annihilation

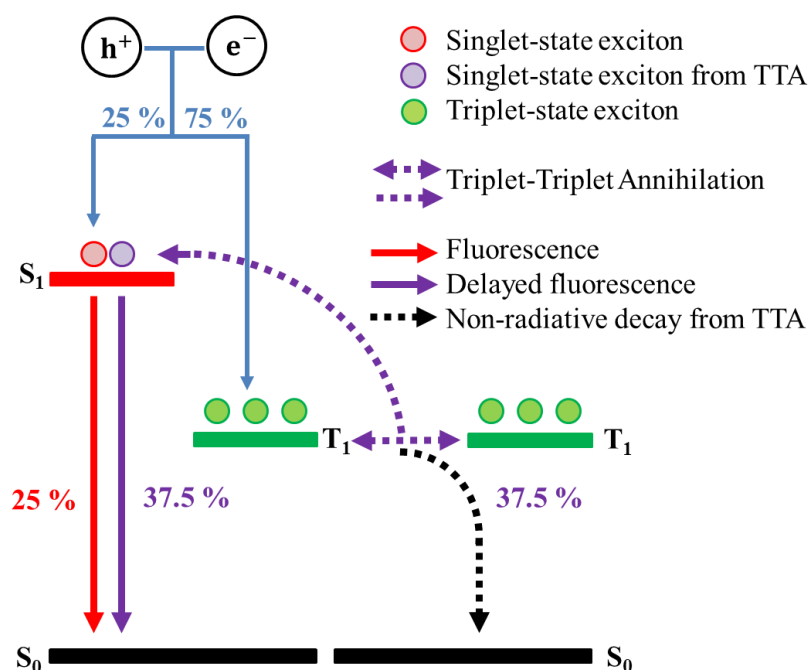
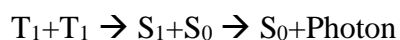


**Figure 12.** Simplified mechanism of a Generation 2.5 emitter.

Triplet-Triplet annihilation (TTA) was recognised in 1963 in pyrene,<sup>13</sup> and thus named P-type delayed fluorescence. When a triplet exciton is sufficiently long-lived, it can undergo a bimolecular energy transfer process with another triplet exciton, generating a new high-energy singlet exciton. This newly formed singlet exciton can then decay radiatively, through delayed fluorescence. The simplified process of TTA can be written as:



The thermodynamic requirement is that the sum of the energy of the two triplets needs to be higher than the energy of the singlet. Since two  $T_1$  excitons are needed to generate a single  $S_1$  exciton, TTA represents another strategy to overcome the 25% maximum IQE of fluorescent emitters. The initial electrical excitation will lead to the usual 25% singlet excitons, which will decay through prompt fluorescence and 75% triplet excitons. Those triplet excitons will then undergo TTA, leading to half of them being upconverted to singlet excitons, which will then decay through delayed fluorescence, while the other half will become ground state singlet excitons, meaning that an extra 37.5% of excitons will be able to decay radiatively, pushing the possible maximum IQE to 62.5% (**Figure 12**).

Anthracene and pyrene have been widely used in TTA materials thanks to their good stability and low  $T_1$  levels, suitable to achieve deep-blue TTA emission. Hu *et al.* published the anthracene based material **BD3**,<sup>42</sup> which presented a high  $EQE_{max}$  of 12% and deep-blue CIE color coordinates of (0.15, 0.06). The pyrene material developed by Chou *et al.*<sup>43</sup> (**Figure 13**) presented a slightly lower  $EQE_{max}$  of 10.2% and CIE coordinates of (0.14, 0.14), but also a positive efficiency roll-off, due to the large TTA contribution. Kuchta *et al.* later reported a device that achieved an  $EQE_{max}$  of 14% at CIE coordinates of (0.22; 0.19) using a host:guest system comprising **p-TPB-2Cz**, and **m-TPB-2Cz** (**Figure 13**).<sup>44</sup> Current commercial blue OLEDs use TTA emitters.<sup>45,46</sup>

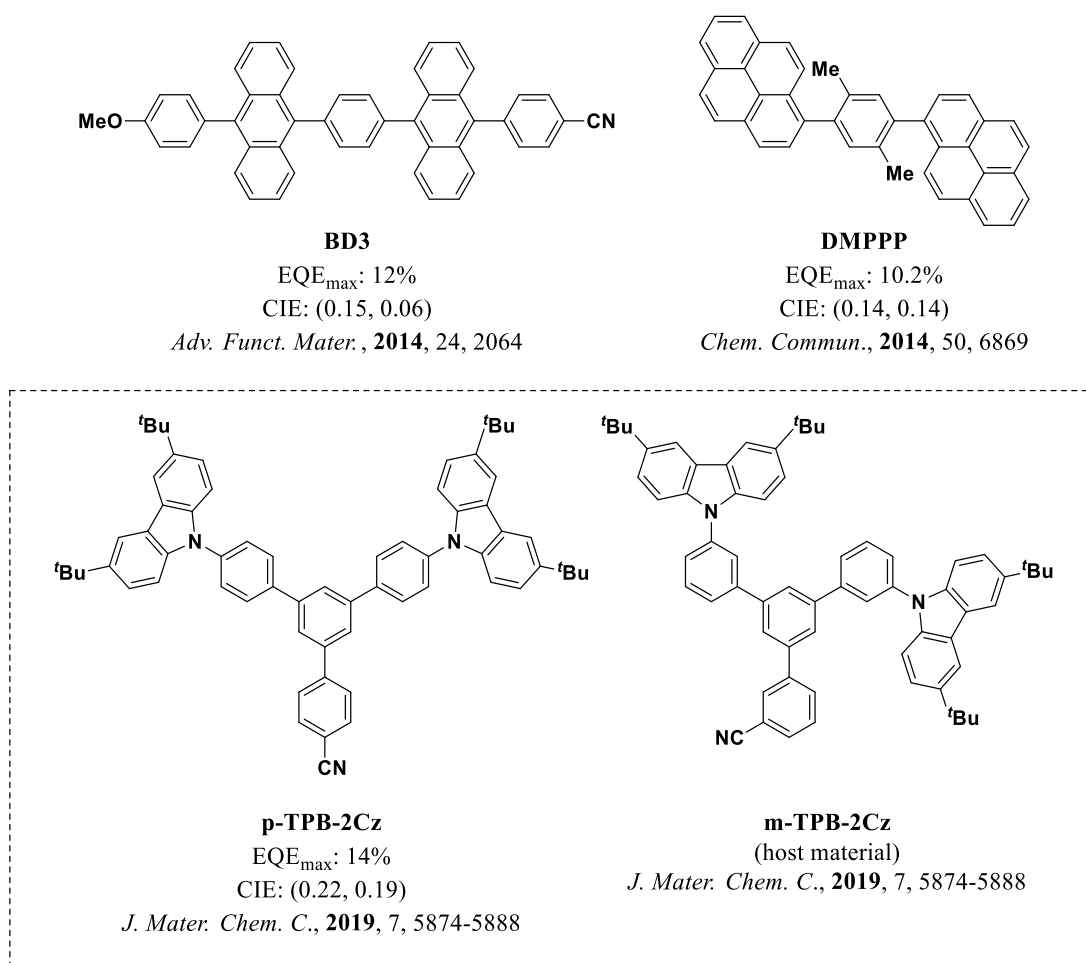


**Figure 13.** Chemical structure of the discussed TTA materials.



### 1.6.4 - Generation 3 OLEDs: Thermally Activated Delayed Fluorescence

The most attractive replacement emitter materials for OLEDs are based on thermally activated delayed fluorescence (TADF) molecules.<sup>18</sup> Delayed fluorescence had been previously observed in Eosin-Y, and named at the time E-type fluorescence, and in several other reports.<sup>14-16</sup> In 2012, Adachi reported the first example of highly efficient green OLED, with an IQE of 93% and maximum external quantum efficiency,  $\text{EQE}_{\text{max}}$ , of 19.3%, employing a purely organic TADF emitter, 4CzIPN.<sup>18</sup> TADF compounds possess an energy difference between the  $S_1$  and  $T_1$  states ( $\Delta E_{ST}$ ) sufficiently small that with the thermal energy present at room temperature the triplet excitons can be converted into singlet excitons through a process called reverse intersystem crossing (RISC). This would allow the device to achieve a theoretical 100% IQE. TADF is now considered the most promising way to harvest triplet excitons.<sup>19</sup>

### 1.6.5 - Mechanism of TADF emitters

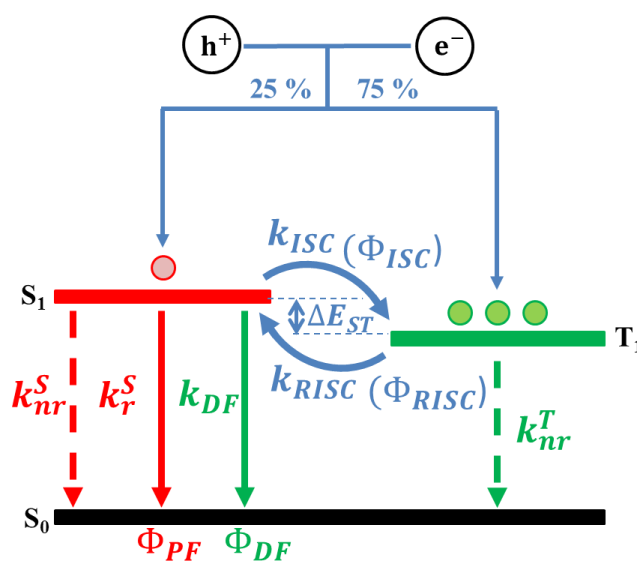


**Figure 14.** Different radiative and non-radiative decay pathways of a TADF molecule.

Light generated in a TADF molecule will consist of a prompt fluorescence, generated from the decay of excitons in the singlet state, and a delayed fluorescence, from the decay of excitons that are converted from the triplet to the singlet state, through RISC (**Figure 14**). A fast  $k_{RISC}$  is needed to lower the residence time of the triplet exciton and prevent unwanted non-radiative pathways.<sup>47-49</sup> The constant of reverse intersystem crossing ( $k_{RISC}$ ) needs to be maximized to be much faster than the non-radiative decay constant of the triplet states ( $k_{nr}^T$ ), which can be achieved by minimizing the  $\Delta E_{ST}$  as shown in the following formula.

$$k_{RISC} = A \exp\left(-\frac{\Delta E_{ST}}{k_B T}\right) \quad (17)$$

The thermally activated character of the delayed fluorescence is also shown in the formula, making RISC an endothermic process. The energy of the singlet and triplet excited state can be obtained from the orbital energy ( $E$ ), the electron repulsion energy ( $K$ ), and the electron exchange energy ( $J$ ). The  $\Delta E_{ST}$  is directly proportional to the electron exchange energy.

$$E_{S1} = E + K + J \quad (18)$$

$$E_{T1} = E + K - J \quad (19)$$

$$\Delta E_{ST} = E_{S1} - E_{T1} = 2J \quad (20)$$

$$J = \iint \phi_H(1)\phi_L(1)\left(\frac{e^2}{r_1 - r_2}\right)\phi_L(2)\phi_H(2)dr_1dr_2 \quad (21)$$

$J$  is obtained from the overlap integrals of the HOMO and the LUMO where  $\phi_H$  and  $\phi_L$  are the HOMO and LUMO wavefunctions, respectively,  $(e^2/r_1-r_2)$  is the Coulombic interaction operator, and digits 1 and 2 indicate two electrons that occupy the HOMO and the LUMO. To decrease  $J$  value and consequently the  $\Delta E_{ST}$  the overlap between the FMOs needs to be minimized and the  $r_1-r_2$  distance needs to be increased. Creating a structure with separated electron-donating (D) and electron-accepting (A) moiety can reduce the overlap between HOMO and LUMO. This results in a charge-transfer (CT) type molecule where the HOMO is localized primarily on the donor and the LUMO on the acceptor. Locally excited (LE) states, where there is a strong overlap between the HOMO and the LUMO, are also present and they are thought to play an important role in the TADF mechanism.<sup>50,51</sup>

The ISC and RISC processes in purely organic materials are spin-forbidden processes. As previously stated, we can assume an approximation, defined as first order mixing, where we consider that the mixing happens only between the  $S_1$  and  $T_1$  states.

However, by considering only  $S_1$  and  $T_1$ , the first order mixing ignores the involvement of intermediate triplet states. These states can be accessed via a process called reverse internal conversion (RIC), which can be activated thermally and via vibrationally induced SOC.<sup>52</sup> If both  $S_1$  and  $T_1$  states would be CT in nature ( $^1CT$  and  $^3CT$ , respectively), according to El Sayed's rule,  $k_{RISC}$  will be extremely slow, even if the material presented a very small  $\Delta E_{ST}$ . If such a molecule possessed an intermediate triplet state with LE character ( $^3LE$ ), triplet excitons could populate such state via RIC, before being converted in singlet excitons via RISC, increasing the efficiency of the TADF mechanism. The vibrational coupling between  $T_1$  and higher lying triplets ( $T_{1+n}$ ) works best when they are very close in energy.

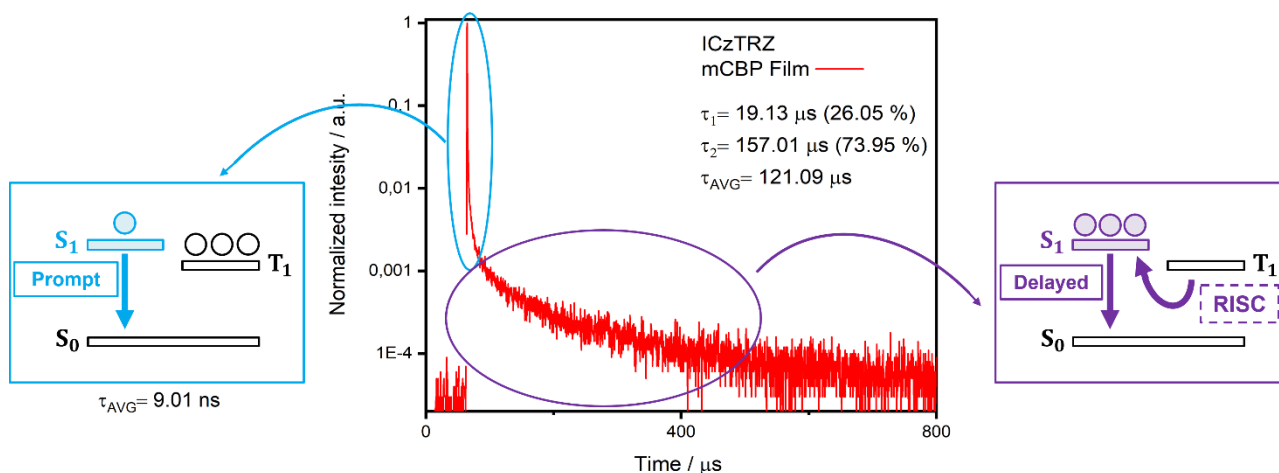


**Figure 15.** schematic representation of a typical time-resolved photoluminescence measurement of a TADF molecule.

The prompt and delayed fluorescence can be experimentally identified by carrying out a measurement of time-resolved photoluminescence (**Figure 15**). The lifetimes of the two phenomena can then be extracted by fitting such measurement. Prompt fluorescence usually decays in the nanoseconds time range, while delayed fluorescence can decay in the micro to milliseconds time range.

### 1.6.6 - Design of TADF emitters

TADF emitters are most commonly a Donor-Acceptor (D-A) system, where the communication between the two moieties is restricted. The electron-rich part of the material, the donor, is where the HOMO will be localized and the LUMO will be localized on the electron-poor part of the molecule, the acceptor. The lower the communication between donor and acceptor is, the lower the  $\Delta E_{ST}$ . However, some degree of communication between the two moieties must be maintained since if they are completely isolated from each other the TADF mechanism will be impossible. The respective strength will also influence the HOMO and LUMO levels of the material, and thus the emission color of the emitter. Some of the more commonly used moieties can be found in **Figure 16**.

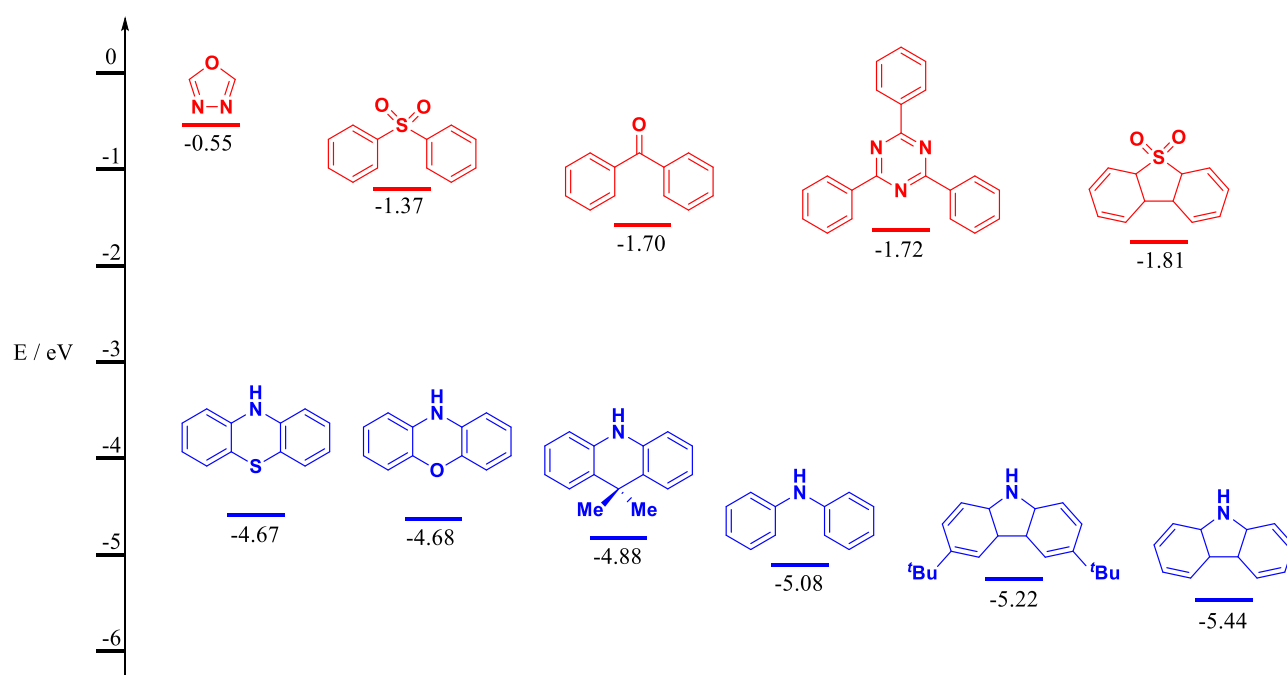


**Figure 16.** Chemical structures and HOMO (blue line) and LUMO (red line) levels of commonly used Donor (blue) and Acceptor (red) moieties.<sup>53</sup>

Several strategies have been utilized over the years to tune the separation of the HOMO and LUMO of a molecule:

**Physical separation of Donor and Acceptor:** it's possible to increase the separation between the donor and the acceptor by inserting an aromatic bridge in between them.<sup>54</sup> In this work by Zhang *et al.* the insertion of a phenyl ring between the D/A units of anthraquinone-based emitters (**Figure 17**) brought a greater separation between the HOMO and the LUMO, inducing a decrease of the  $\Delta E_{ST}$ ,

while also improving the radiative decay constant of the singlet states ( $k_r^S$ ) of the molecule, thus leading to improved photophysical properties of the red emitter.<sup>55</sup>

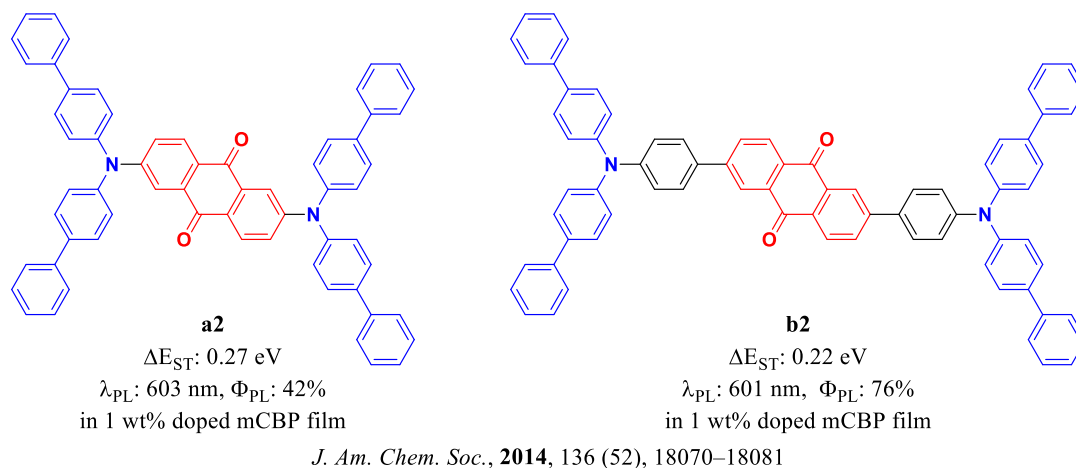
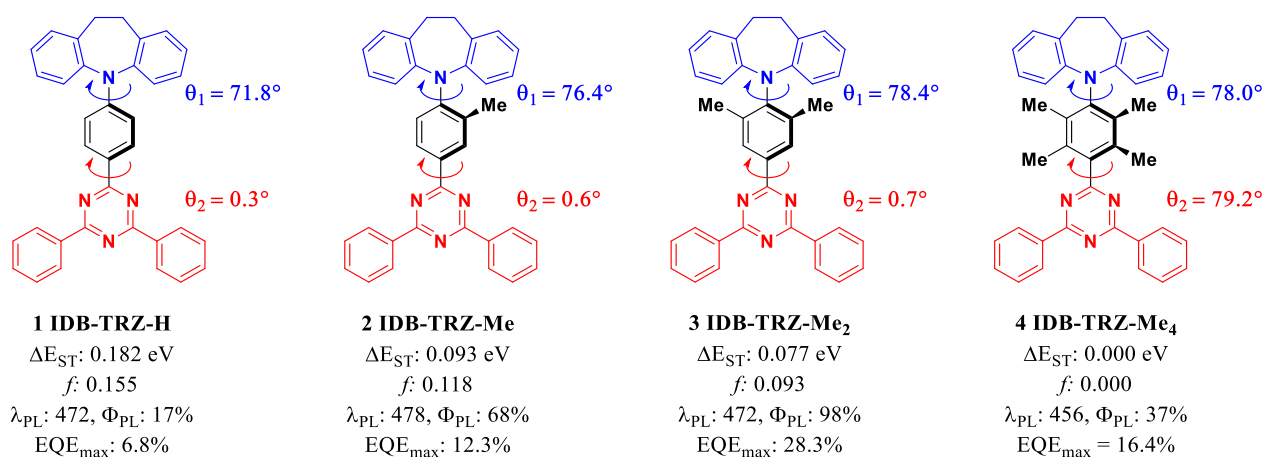


**Figure 17.** Effect of the insertion of a phenyl bridge between donor and acceptor.<sup>55</sup>

**Increasing the dihedral angle between Donor and Acceptor:** Cui *et al.*<sup>56</sup> and Huang<sup>57</sup> each demonstrated that increasing the dihedral angle of the Donor-Bridge bond and Bridge-Acceptor bond can lead to a reduced overlap between the FMOs, thus decreasing the  $\Delta E_{ST}$  of the emitter. In this work from Wang<sup>58</sup> *et al.*, a series of dibenzoazepine (donor moiety) and diphenyl-triazine (acceptor moiety) based TADF emitters (**Figure 18**) with an increasing number of methyl groups on the phenylene bridge was investigated. The bulkier nature of the methyl group compared to the hydrogen pushes the D-Bridge and A-Bridge bonds closer to 90°. For compounds **1** to **4**, there is a progressive decrease in the  $\Delta E_{ST}$  of the molecule with an increase in the two dihedral angles, and an increase in the  $\Phi_{PL}$  of materials **1** to **3**, due to the suppression of non-radiative decay. The fabricated OLEDs present an increase in the  $EQE_{max}$  going from **1** to **3** while the device of molecule **4** shows a lower efficiency. This is because limiting the overlap between the HOMO and the LUMO will have a negative effect on the oscillator strength of the emitter, making the chance of radiative relaxation smaller, thus lowering the  $\Phi_{PL}$  of the material.



*Adv. Opt. Mater.*, **2019**, 1901150, 1–7

**Figure 18.** Molecular structure and properties of the **IDB-TRZ** series of emitters.<sup>58</sup>

**Modification of the aromatic bridge:** creating a more twisted structure will lead to greater structural relaxation, and to a broader emission spectrum, which means lower efficiencies and worse color purity. A way to avoid these problems is to use a heteroaromatic bridge instead of the usual phenyl, leading to a more planar structure while at the same time retaining good TADF properties. This strategy was employed by Dos Santos *et al.* to improve the efficiency of **pDTCz-DPS** (Figure 19).<sup>59,60</sup> The introduction of a heteroaromatic bridge creates a more planar structure and leads to higher EQEs. The materials presented by Rajamalli *et al.*,<sup>59</sup> **pDTCz-2DPyS**, and **pDTCz-3DPyS**, presented good  $\Phi_{PL}$  values of 62 % and 61%, respectively and were employed in OLEDs that showed  $EQE_{max}$  of 13% and 12%, respectively (vs  $EQE_{max}$  of 4.7% for the reference emitter **pDTCz-DPS**). The OLEDs also presented blue emission at  $\lambda_{EL}$  of 466 nm and 452 nm for the devices with **pDTCz-2DPyS**, and **pDTCz-3DPy**, respectively. Dos Santos *et al.*<sup>60</sup> furtherly expanded the series by introducing the TADF emitters **pDTCz-DPzS**, and **pDTCz-DPmS**. The addition of another nitrogen atom on the phenyl bridge led to an improvement of  $\Phi_{PL}$  to 68% and 73%, which translated to a higher  $EQE_{max}$  of 18% and 14% for the devices with **pDTCz-DPzS**, and **pDTCz-DPmS**, respectively. The OLED with **pDTCz-DPmS** was also able to achieve blue emission spectra with  $\lambda_{EL}$  of 461 nm, while the device with **pDTCz-DPzS** presented a red-shifted  $\lambda_{EL}$  of 522 nm.

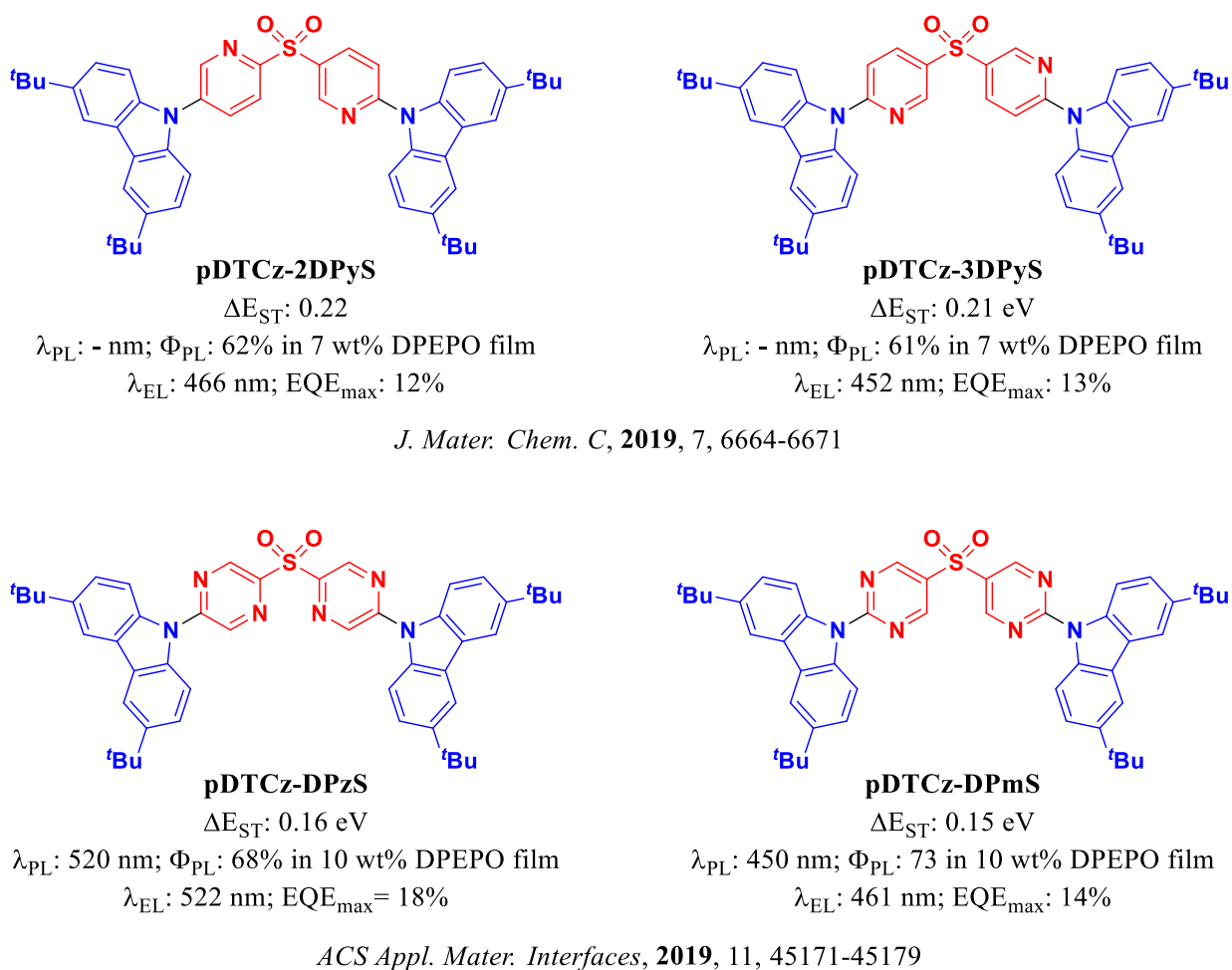


**Figure 19.** Molecular structure and properties of the **pDTCz** series of emitters.<sup>59,60</sup>

An in-depth literature analysis of the structures related to the projects discussed in this thesis (**Figure 24**) will be provided at the beginning of each experimental chapter. The donor moieties used are indolo[3,2-b]carbazole (**ICz**) and 9,9-dimethyl-9,10-dihydroacridine (**DMAC**). Indolocarbazole refers to a large family of compounds composed of two anelated carbazole rings. These compounds present a large, planar, and conjugated structure, high morphological and thermal stability<sup>61,62</sup>, and have been extensively applied in optoelectronics, both as host and as emitters.<sup>63,64</sup> Specifically, the indolo[3,2-b]carbazole used in our work has been employed in the design of several blue emitters that achieved high horizontal orientation of their TDMs in evaporated films.<sup>65–68</sup> **ICz** can be synthesized *via* a one-step reaction, starting from di(1H-indol-3-yl)methane and trimetoxymethane in acid conditions (**Figure 20**).<sup>67</sup> The acid condition would cleave a methanol molecule from the trimetoxymethane, allowing one of the double bonds on the di(1H-indol-3-yl)methane to attach to electrophilic carbon. The resulting carbocation, stabilized by resonance, would then undergo a Wagner-Meerwein rearrangement. This process is a [1,2] carbocation rearrangement in which the

alkyl group migrates between two adjacent carbons.<sup>69,70</sup> An acid-catalysed, electrophilic ring closure will then follow and after the loss of formaldehyde, the aromaticity of the system will be restored.

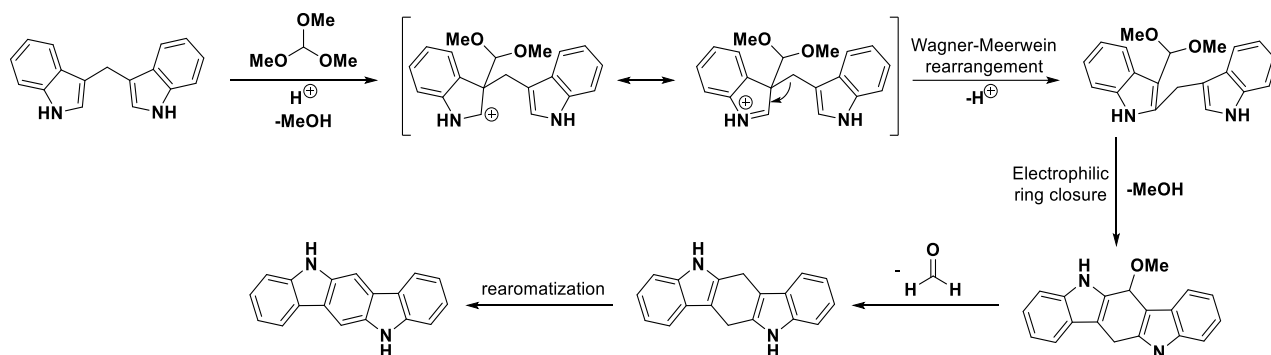


**Figure 20.** Mechanism of indolo[3,2-b]carbazole 's synthesis.

Another indolocarbazole derivative that will be discussed in this thesis is the 2,8-di-*tert*-butyl-5,11-dihydroindolo[3,2-b]carbazole, which presents two *tert*-butyl groups in positions 2 and 8. The synthesis of this material (**Figure 21**)<sup>71</sup> starts with a Wolff-Kishner reaction between 4-*tert*-butylphenyl)hydrazine monohydrochloride and cyclohexane-1,4-dione with sodium acetate in a water and ethanol solution, to achieve the hydrazone compounds, which was then converted into the desired product *via* an acid-induced cyclization.

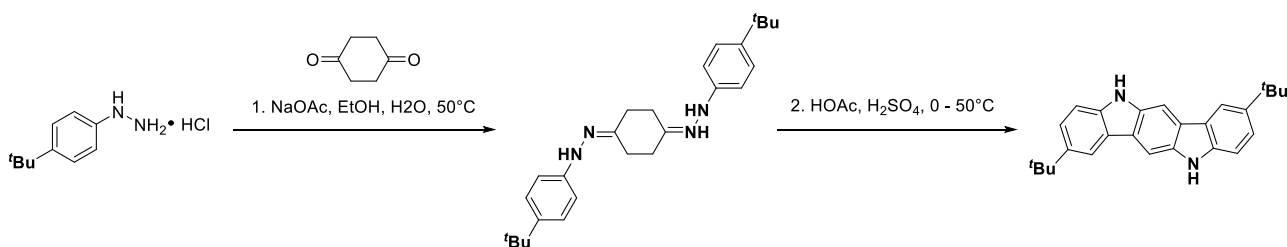


**Figure 21.** 2,8-di-*tert*-butyl-5,11-dihydroindolo[3,2-b]carbazole.

**DMAC** is a relatively stronger electron-donor than **ICz** (HOMO levels of -5.13 eV and -5.18 for **DMAC** and **ICz** respectively), **DMAC** has been employed primarily in green and blue TADF emitters,<sup>72–75</sup> and also as a host material.<sup>76</sup> It can be synthesized *via* a three-step process (**Figure 22**).<sup>77</sup> The first step is an Ullmann coupling between methyl anthranilate and iodobenzene, with potassium



carbonate. This is then followed by methylation of the ester with methyl lithium. The final product is then obtained *via* an acid-induced cyclization, with a loss of water.

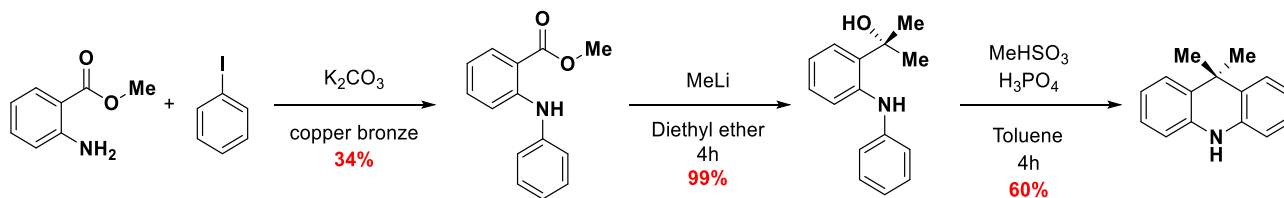


**Figure 22.** Synthesis of **DMAC**.

As shown in many published examples, these donors are typically paired with the acceptor 2,4,6-triphenyl-1,3,5-triazine (**TRZ**),<sup>65,75,78–80</sup> which is one of the most widely used acceptors in emitters and has also been used as a fragment in a few host materials.<sup>81,82</sup> It is most commonly found decorated with phenyl groups in positions 2,4,6-, as this modification both strengthens the electron-withdrawing character of the acceptor and puts the donor and acceptor in a conformation favourable for achieving TADF, since it has been shown in many reports where in the absence of the bridging phenylene group the compound adopts a planar conformation, and therefore possesses high  $\Delta E_{ST}$  and no TADF.<sup>83,84</sup>

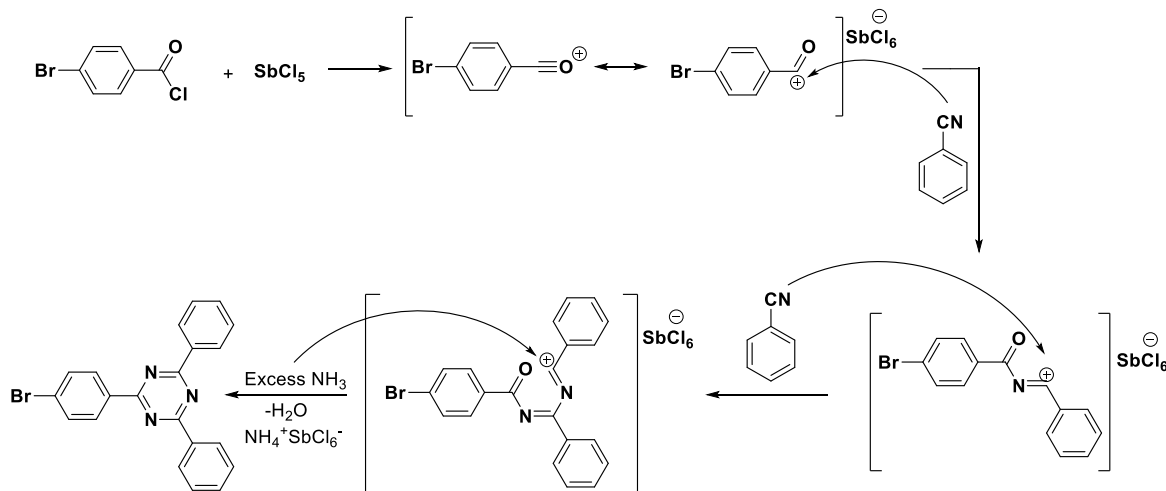


**Figure 23.** Mechanism of 2,4,6-triphenyl-1,3,5-triazine's synthesis

The 2-(4-bromophenyl)-4,6-diphenyl-1,3,5-triazine variant is the one used in the coupling reactions discussed in this thesis. It can be synthesized from 4-Bromobenzoyl chloride and benzonitrile, with

antimony pentachloride (**Figure 23**). Antimony pentachloride is a Lewis acid that will start the reaction by cleaving off the chlorine from the bromo-benzoyl chloride, making it possible for the two equivalents of benzonitrile to attach to the electron poor sites. The resulting salt will then be filtered, washed with dichloromethane and then added to a 35% ammonia solution which will cyclize the structure by forming the 1,3,5-triazine.

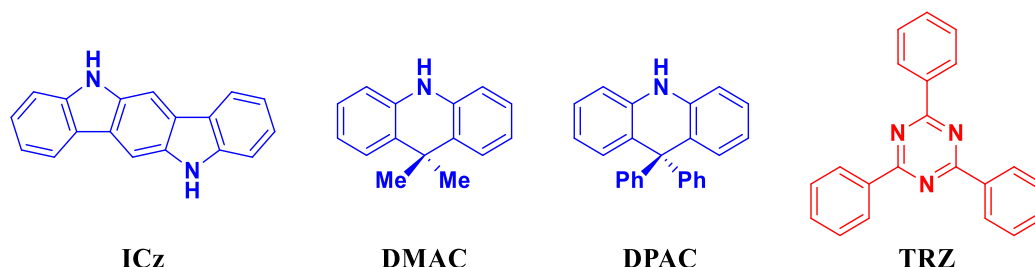


**Figure 24.** Molecular structure of the discussed donors (blue) and acceptor (red).

### 1.6.7 - Host materials for TADF molecules

The TADF mechanism involves triplets excited states, which are significantly longer-lived than singlet excited state. A higher triplet exciton concentration will make them more likely to be quenched through phenomena like triplet-polaron quenching (TPQ) or TTA. A higher concentration of emitter can also lead to an increase in intermolecular interactions like  $\pi$ - $\pi$  stacking and the consequent crystallization that would result in quenching of the emission and decreased device efficiency. Dispersion of the TADF molecule in a host material can help to solve these problems.<sup>22</sup> The host will also influence the photophysical properties of the emitter since the polarity of the matrix can affect CT states through dipole-dipole interaction. The  $\Delta E_{ST}$  values will differ for different hosts.

A good host material needs to present two main characteristics:

**Triplet energy level higher than that of the emitter:** if the host presented a lower or comparable  $T_1$  energy level, the triplet excited state of the emitter could undergo Dexter energy transfer to the host material, quenching the triplet excitons of the guest. Also, this higher-energy triplet state will confine the emitter excitons in the EML, preventing any leakage.

**Overlap of Emission (host) and Absorption (emitter) spectra:** while energy transfer from the emitter to the host is detrimental to the efficiency of the OLED, Dexter energy transfer from the host to the emitter can lead to improved exciton formation and thus, better performance. To optimize the

Dexter energy transfer, the molecular orbitals of the host must interact with the ones of the emitter; a strong overlap between the emission of the host and the absorption of the emitter is also needed.

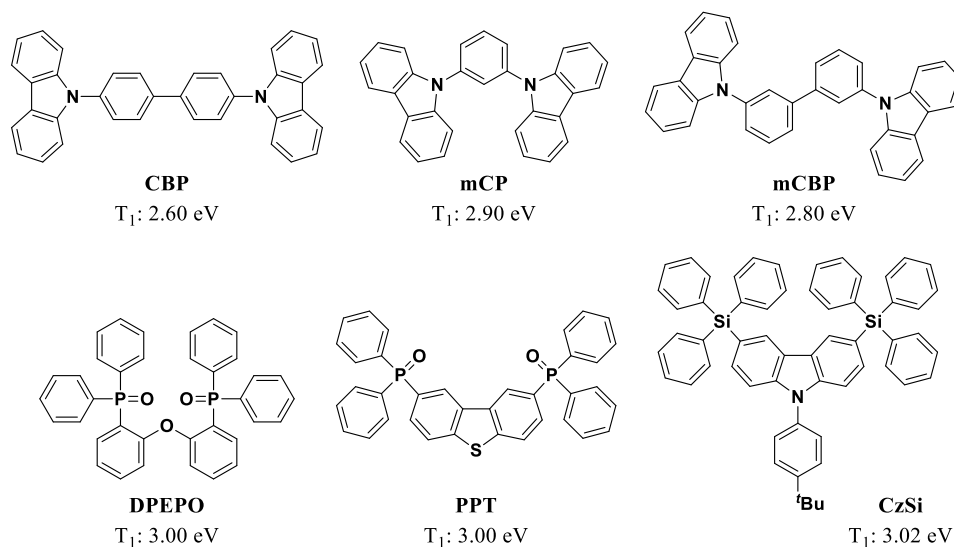


**Figure 25.** Molecular structure of common host material employed in TADF-OLEDs.

In **Figure 25** are reported the most widely used host-materials, due to their low cost, availability, and known photophysical properties. CBP has a low triplet energy level of 2.6 eV,<sup>85</sup> making it a desirable choice for red emitters.<sup>19,55</sup> The main drawback of this host is the possible crystallization during the device operation, due to the material's low molecular weight and symmetrical structure, which shortens the operational lifetime. mCP and mCBP are preferable for green emitters<sup>86–90</sup> (while also used for blue materials<sup>91</sup>), with triplet energies of 2.9 eV and 2.8 eV,<sup>85</sup> respectively. The relatively high triplet energy of mCP makes it a widely used host; however, it presents low thermal and morphological stability.<sup>92</sup> mCBP presents a slightly lower triplet energy than mCP but possesses a higher  $T_g$  and thus higher morphological stability.<sup>85</sup> DPEPO presents a very high triplet energy level of 3.0,<sup>93</sup> making it a possible candidate for blue emitters,<sup>94,95</sup> although it presents some considerable defects like poor stability and charge transport ability that limits its effectiveness. PPT and CzSi have also been used for blue emitters,<sup>18,96</sup> thanks to their high triplet energies of 3.00 and 3.02,<sup>12</sup> respectively. The structure of the host materials used in the following chapters can be found in **Figure 202**.

## 1.7 – Theoretical calculations

### 1.7.1 – DFT calculations

Density Functional Theory (DFT) calculations are an important tool for predicting the optoelectronic properties of a potential TADF molecule. To obtain information on the energy of the system, the time independent Schrodinger equation will need to be solved, which is written as:<sup>1</sup>

$$\hat{H}\Psi = E\Psi \quad (22)$$

Where  $\hat{H}$  is the Hamiltonian of the system,  $E$  is the total energy of the system, and  $\Psi$  is the wavefunction of the system. By assuming that the nuclei are much larger and slower than the electrons (Born-Oppenheimer approximation), the energy of the system can be expanded to be the sum of its three components.<sup>1,2</sup>

$$\hat{H}\Psi = [\hat{T} + \hat{V} + \hat{U}]\Psi \quad (23)$$

Where  $\hat{T}$  is the kinetic energy of electrons,  $\hat{V}$  is the electron-nuclei attraction energy and  $\hat{U}$  is the electron-electron repulsion energy. From here the time independent Schrödinger equation for a  $N$  electron system is rewritten as:

$$\hat{H}\Psi = \left[ \sum_{i=1}^N \left( -\frac{\hbar^2}{2m_i} \nabla_i^2 \right) + \sum_{i=1}^N V(r_i) + \sum_{i<j}^N U(r_i, r_j) \right] \Psi \quad (24)$$

The kinetic energy term can be expressed in function of the Lapacian operator ( $\nabla_i^2$ ), which corresponds to the coordinates of the system's particles. DFT allows the Schrodinger equation to be solved and obtain the energy of the system based on the electron density  $\rho(r)$ .<sup>3</sup> The relationship between the wavefunction of the system and  $\rho(r)$  can be written as:

$$\rho(r) = N \int \dots \int |\Psi(x_1, x_2, \dots, x_N)|^2 dx_2 \dots dx_N \quad (25)$$

The theoretical foothold for DFT came from Pierre Hohenberg and Walter Kohn with the two Hohenberg-Kohn (HK) theorems:<sup>3</sup>

**1<sup>st</sup> HK theorem:** the ground state properties of a many-electron system are uniquely determined by an electron density that depends on only three spatial coordinates.

**2<sup>nd</sup> HK theorem:** for any given density that is different than the ground state density, the calculation of the total energy of the system results in a higher energy than that of the energy computed for the true ground state  $\rho_0$ .

$$E[\rho] \geq E_0[\rho_0] \quad (26)$$

The energy of the ground state can again be expanded to the sum of its components:

$$E_0[\rho_0] = T[\rho_0] + V[\rho_0] + U[\rho_0] \quad (27)$$

Where T is the kinetic energy, V is the electron-nuclei attraction energy, and U is the electron-electron repulsion energy. T and U are universal functionals, meaning that are independent of the system under study and are known as the HK functional ( $F_{HK}$ ), while V is dependent on the system.

$$F_{HK}[\rho_0] = T[\rho_0] + U[\rho_0] \quad (28)$$

$$V[\rho_0] = \int \rho_0(r) V_{ex}(r) dr \quad (29)$$

Where  $V_{ex}$  is the external potential. U can be separated into a Coulomb term ( $J[\rho_0]$ ) and a non-classical term  $E_{ncl}[\rho_0]$ .

$$U[\rho_0] = J[\rho_0] + E_{ncl}[\rho_0] = \frac{1}{2} \int \int \frac{\rho_0(r_1) \rho_0(r_2)}{r_{12}} dr_1 dr_2 + E_{ncl}[\rho_0] \quad (30)$$

In this system,  $T$  would need to be computed in a system of interacting electrons which is not possible. Walter Kohn and Lu Jeu Sham solved this problem by introducing a local effective (fictitious) external potential in which the non-interacting particles move, called  $V_{\text{eff}}(r)$ .<sup>4</sup>

$$V_{\text{eff}}[\rho_0(r)] = \sum_i V_S^i[\rho_0(r)] \quad (31)$$

This leads to a fictitious system, called the Kohn-Sham system, of non-interacting particles that generates the same density as a system of interacting particles. The Schrodinger-like equation of the system will be called the Kohn-Sham equation and can be written as a set of  $N$  one-electron equations.

$$f_i^{KS} \phi_i = \varepsilon_i \phi_i \quad (32)$$

Where  $f_i^{KS}$  is the Kohn-Sham operator and  $\phi_i$  is the Kohn-Sham orbital. The kinetic energy of a Kohn-Sham system can then be expressed as:

$$T[\rho_0] = T_S[\rho_0] + T_c[\rho_0] \quad (33)$$

Equation 29 can then be rewritten as:

$$F_{HK}[\rho_0] = T_S[\rho_0] + T_c[\rho_0] + J[\rho_0] + E_{ncl}[\rho_0] \quad (34)$$

$T_c[\rho(r)]$  and  $E_{ncl}[\rho_0]$  are then combined under the term  $E_{XC}[\rho_0]$ , which is the exchange correlation energy.

$$F_{HK}[\rho_0] = T_S[\rho(r)] + J[\rho(r)] + E_{XC}[\rho(r)] \quad (35)$$

By deriving the  $E_{XC}$  over the electron density  $\rho(r)$ , the exchange correlation potential ( $V_{XC}$ ) can be obtained, which expresses all the many-particles interactions. This can then be used to calculate the effective single particle potential.

$$V_S(r) = V(r) \int \frac{\rho(r_2)}{r_{12}} dr_2 + V_{XC} \quad (36)$$

Where  $V(r)$  is the external potential, the second integral term represents the Hartree term for electron-electron repulsion, and  $\rho(r)$  can be expressed as:

$$\rho(r) = \sum_{i=1}^N |\varphi_i(r)|^2 \quad (37)$$

The DFT problem now becomes solving the Kohn-Sham equation, which is done through a self-consistent method. This is done by guessing an initial  $\rho(r)$ , followed by calculating the  $V_S(r)$  of the system and solving the Kohn-Sham equation. This is then repeated until convergence is reached.<sup>2</sup>

In practical terms, this allows us to establish the lowest energy conformation of the molecule in the selected environment. Several different conditions can be simulated (gas phase, solvent interaction, host material interaction). Following the ground-state optimization, the HOMO and LUMO electron density distributions can be visualized to gain an appreciation of the degree of overlap between the FMOs in the ground state.

### 1.7.2 – Hybrid functionals and Basis sets

Whenever a DFT calculation is performed, a functional and a basis set need to be defined. Functionals are used to introduce a certain amount of Hartree-Fock electron-electron self-interaction in the  $E_{XC}$  term. This can then be rewritten for hybrid functionals as:

$$E_{XC} = aK + (1 - a)E_X^{DFT} + E_C^{DFT} \quad (38)$$

K is the amount of HF electron-exchange introduced,  $E_X^{DFT}$  and  $E_C^{DFT}$  are respectively the exchange energy and the correction energy obtained *via* DFT. Popular hybrid functionals are B3LYP,<sup>5</sup> PBE0<sup>6,7</sup> and MO6-2X<sup>8-10</sup> which respectively contain 20%, 25%, and 54% of HF exchange. Other functionals do exist but PBE0 and MO6-2X are the functionals used in this thesis, further the TADF community focus on these hybrid functionals.

A basis set is a set of functions that is used to treat the partial differential equation of the model as an algebraic equation, which can be efficiently solved by a computer.<sup>11-13</sup> These functions are usually Atom-Centred (AO) Linear Combination of Atomic Orbitals (LCAO). Polarization functions are also added to take into account the change in  $\rho(r)$  caused by neighbouring atoms. The most commonly used basis sets for DFT modelling of TADF materials are the Pople basis set.<sup>7</sup> A generic Pople basis set can be expressed as:

$$X\text{-}YZg$$

Where X is the number of Gaussian functions constituting each core electrons basis functions. Y and Z indicates that the valence orbitals are composed respectively by a linear combination of Y and Z Gaussian functions. g indicates the possible polarization functions, which are atom dependant. For example the basis set 6-31G(d,p) means that this basis set includes 6 gaussian type orbital (GTOs) for the core electrons, a split valence set of 3 plus 1 GTOs, a p and d polarization function for hydrogen and non-hydrogen atoms respectively. This basis set is the one primarily employed within this body of work and is the main one used by the TADF community.

### 1.7.3 – TD and TDA calculations

After the initial optimization, Time Dependant-DFT (TD-DFT) can be used to gain information on the excited states of the material, and thus learn if a material could be a possible TADF molecule. TD-DFT is an expansion of the DFT method, where the system is investigated under the presence of a Time-Dependant potential (electric or magnetic field).<sup>14,15</sup> The foundation of TD-DFT is the Runge-Gross (RG) theorem, which is the time-dependant equivalent of the 1<sup>st</sup> HK theorem.<sup>16</sup> It states that



the properties of a many-electron system can be determined by a time dependant electron density  $\rho(r, t)$  that depends on only three spatial coordinates. A fictitious system of non-interacting electrons ( $V_{eff}(r, t)$ ) under the effect of a fictitious, time dependant external potential  $V_{ext}(r, t)$ , will be introduced, in order to express the properties of the interacting system.<sup>17</sup> The time-dependant density of the non-interacting system ( $\rho_s(r, t)$ ) will be considered equal to the time-dependant density of the interacting system ( $\rho(r, t)$ ). The time-dependant Kohn-Sham equation can then be written:

$$\left[ -\frac{1}{2} \sum_i^N \nabla^2 + V_{eff}(r, t) \right] \phi_i(r, t) = i \frac{\delta}{\delta t} \phi_i(r, t) \quad (39)$$

Where  $\phi_i(r, t)$  are the time-dependant Kohn-Sham orbitals, from which the time dependand density can be obtained:

$$\rho(r, t) = \sum_i^N |\phi_i(r, t)|^2 \quad (40)$$

If the applied, time-dependant, potential is small enough to not completely perturbate the structure of the ground state, the linear-response approximation can be applied,<sup>17</sup> which allow us to obtain the linear electron density response ( $\rho^{(1)}(r, t)$ ):

$$\rho^{(1)}(r, t) = \iint d^3r' dt' \chi(r, t, r', t') V_{eff}^{(1)}(r', t') \quad (41)$$

where  $V_{eff}^{(1)}(r', t')$  is the first-order perturbed effective potential and  $\chi(r, t, r', t')$  is the first-order response function. A Fourier transform can be used to go from the time domain to the frequency domain:<sup>18</sup>

$$\rho^{(1)}(r, \omega) = \int d^3r' dt' \chi(\omega, r, r') V_{eff}^{(1)}(r', \omega) \quad (42)$$

The new first-order response function  $\chi(\omega, r, r')$  can be expressed as:

$$\chi(\omega, r, r') = \sum_{i,a} \left( \frac{\phi_i^*(r) \phi_a(r) \phi_i(r') \phi_a^*(r')}{\omega - (\varepsilon_a - \varepsilon_i)} - \frac{\phi_i(r) \phi_a^*(r) \phi_i^*(r') \phi_a(r')}{\omega + (\varepsilon_a - \varepsilon_i)} \right) \quad (43)$$

Where  $i$  and  $a$  correspond respectively to an occupied and an unoccupied energy level, with  $\varepsilon_i$  and  $\varepsilon_a$  being their energies. The poles of this functions represent the excitation energy ( $\omega$ ). To obtain it, we equation **43** needs to be rewritten as a matrix, known as the TD-DFT equation:<sup>16</sup>

$$\begin{bmatrix} A & B \\ B^* & A^* \end{bmatrix} \begin{bmatrix} X \\ Y \end{bmatrix} = \omega \begin{bmatrix} 1 & 0 \\ 0 & -1 \end{bmatrix} \begin{bmatrix} X \\ Y \end{bmatrix} \quad (44)$$

If the excited state in question exhibits a large degree of Charge Transfer, the matrix term B will tend to zero. The Tamm-Dancoff Approximation (TDA)<sup>19,20</sup> sets this matrix element to zero, and the TD-DFT equation becomes:

$$AX = \omega A \quad (45)$$

This not only makes the calculation more computationally accessible, but also solves the problem of triplet overestimation that is known to happen in TD-DFT.<sup>21</sup> For these reasons, TDA-DFT is used throughout this thesis. From this, the energy values of several singlet and triplet excited states can be obtained, allowing us to calculate the theoretical  $\Delta E_{ST}$  of the molecule, which allows us to establish if a molecule could be a potential TADF material. The TDA-DFT calculation discussed in this thesis are also vertical excitation of the ground state geometry calculations, meaning that they simulate the excitation of the molecule by absorption.

## 1.8 - Transition Dipole Moment orientation of the emissive molecule

### 1.8.1 - Light outcoupling

Due to the presence of many layers of different materials, with different refractive indices, not all the light that is generated in the EML will be able to leave the device. In current state-of-the-art devices, only 20-30% of the light can leave the stack while the remaining photons remain trapped inside the OLED or are lost as heat (**Figure 26**). Three different types of power dissipation can happen in an OLED:

**Substrate mode:** to escape from the device, photons need to cross a refractive-index interface between the substrate and the surrounding medium. Given the lower refractive index of the latter (usually air), light emitted at an angle larger than the substrate-air critical angle is reflected at the interface *via* total internal reflection, remaining trapped in the substrate.

**Waveguided mode:** based on the same principle as the substrate mode, light can be trapped when it is emitted at an angle larger than the anode-substrate critical angle. Differently from the substrate mode, waveguided mode depends on the thickness of the layer and will occur in layers of thicknesses of the same order of magnitude as the wavelength of visible light.

**Evanescent mode:** organic semiconductor hosts electron-plasma oscillations at the interface between the organic layers and the cathode known as Surface-Plasmon-Polariton (SPP) or evanescent mode. Photons traveling too close to this interface can couple to this mode and be dissipated as heat.

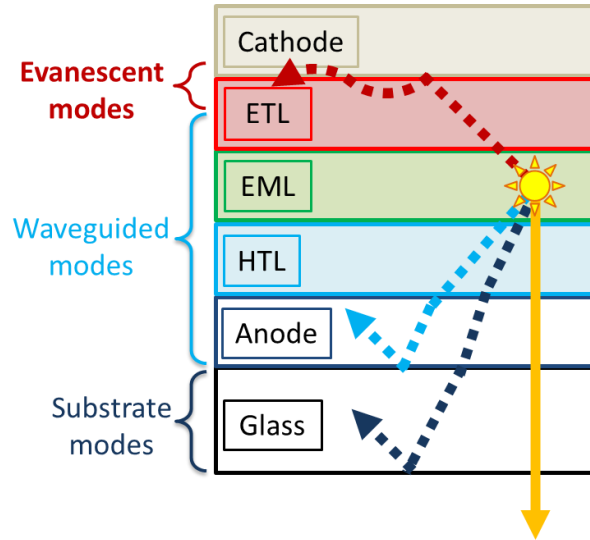


**Figure 26.** Different types of power dissipation in an OLED stack.

As previously stated, the EQE of a device will be impacted by the outcoupling factor  $\eta_{out}$  (**Equation 1**).  $\eta_{out}$  quantifies the amount of light able to escape the device, and can be defined as the ratio of radiated optical power able to escape the device (U) and the total radiated power of the device (F):

$$\eta_{out} = \frac{U}{F} \quad (46)$$

Any emission from a randomly oriented dipole  $p$  can be described as the sum of its different components  $p_x, p_y, p_z$ , averaged over the total emitted dipoles:<sup>23,118–120</sup>

$$\langle p \rangle = \langle p_x + p_y + p_z \rangle \quad (47)$$

The spectral power density (K) is composed of different polarization components, one Transverse Electric (TE) and two Transverse Magnetic (TM), one vertical (TM<sub>v</sub>), and one horizontal (TM<sub>h</sub>). These different polarization components can then be related to  $p$ , the total emitted dipoles, where  $p_x, p_y, p_z$  will be equivalent to the TE<sub>h</sub>, TM<sub>h</sub>, TM<sub>v</sub> components of the emission, respectively. K can then be expressed as:

$$K(\lambda, u, \theta) = [K_{TMh}(\lambda, u) + K_{TEh}(\lambda, u)]\langle \sin^2 \theta \rangle + K_{TMv}(\lambda, u)\langle \cos^2 \theta \rangle \quad (48)$$

where  $\lambda$  is the wavelength of the emission,  $u$  is the direction of the normalized emission, and  $\theta$  is the angle of the individual dipoles with respect to the normal of the film. The film denotes the XY plane, with the normal of the film corresponding to his z-axis.

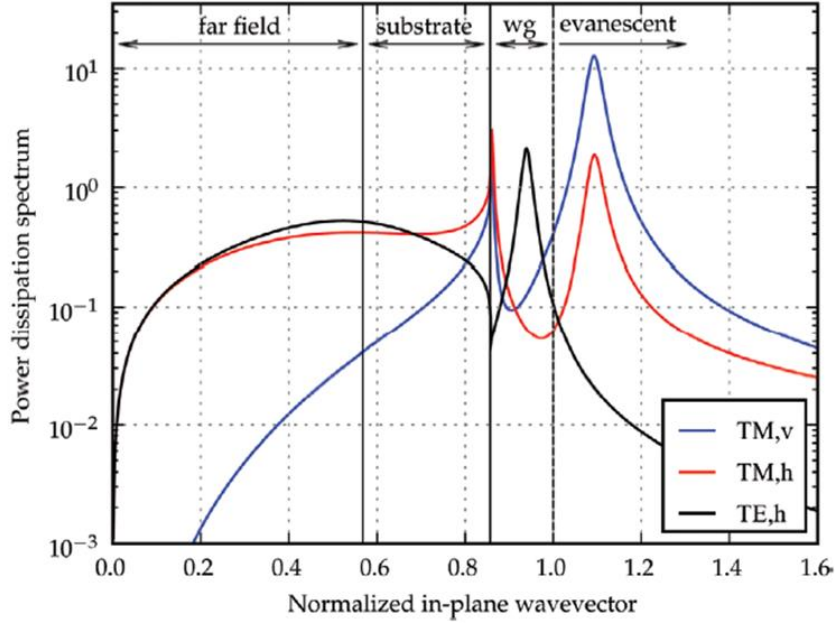


**Figure 27.** Power dissipation spectra of the different polarization component (Transverse Electric (TE,h) and Transverse Magnetic (TM,v and TM,h)) for a red OLED, measured at  $\lambda= 610$  nm. The film denotes the XY plane and it's normalized along his z-axis. Adapted with permission. <sup>121</sup>  
Copyright 2010, Society of Photo-Optical Instrumentation Engineers (SPIE).

By looking at the power dissipation graph (**Figure 27**) it's clear that the different components of K give different contributions to the amount of light able to escape the device (far-field power dissipation). By integrating K over  $u$  and  $\lambda$ , U and F can be obtained:

$$U(\theta) = \int_{\lambda} \int_{u_{crit}(\lambda)}^0 s(\lambda) K(\lambda, u, \theta) du^2 d\lambda \quad (49)$$

$$F(\theta) = \int_{\lambda} \int_{\infty}^0 s(\lambda) K(\lambda, u, \theta) du^2 d\lambda \quad (50)$$

Where  $s(\lambda)$  is the normalized emission spectrum of the emitter and  $u_{\text{crit}}$  is the direction of the normalized emission after which total internal reflection occurs and it's instead trapped in the device. By looking at this equation, the strong dependence of  $\eta_{\text{out}}$  from the orientation of  $p$  can be observed, where the outcoupling factor is maximum for  $\theta$  equal  $90^\circ$  from the normal of the film (z-axis), meaning that the transition dipole moment of the emitter is oriented parallel to the XY plane.

### 1.8.2 - Transition Dipole Moment orientation

A radiative transition in an organic molecule can be described by the vector that identifies the displacement of the electron in the molecule, this vector is called transition dipole moment (TDM). Emitters present more than one radiative transition, in the orientation literature the TDM of the molecule is the one that represents the dipole moment of the main dominant transition. The light coming from this transition will be emitted perpendicularly to the TDM of the molecule, this means that if the TDM is placed parallel to the plane of the device (XY plane) the majority of the radiated light will be perpendicular to the device stack. When the TDM is oriented in this way (**Figure 28**), the molecule is said to be horizontally oriented, which is the best scenario to maximize the amount of light exiting the device. If the TDM of the molecule will be perpendicular to the plane of the device, the molecule will be vertically oriented, which is the worst possible case, since the majority of the emitted light will remain trapped inside the device stack. If the TDM are oriented randomly inside the device, it will be called isotropic oriented.

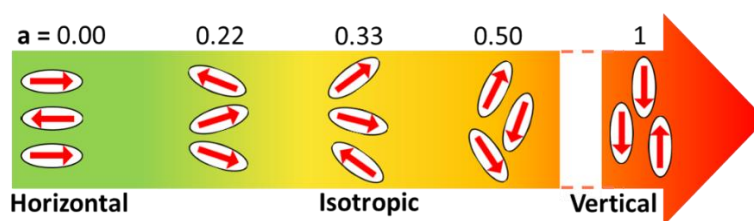


**Figure 28.** Different types of orientation in a thin film layer regarding the anisotropy factor ( $a$ ).

The average orientation of the TDMs can be expressed as a single parameter based on the ratio of the total power radiated by vertical or horizontal dipoles to the total power radiated by all dipoles. Several values are used in the literature:

**Anisotropy factor ( $a$ ):** fraction of total power radiated by vertical dipoles. If all emitters are oriented completely horizontally,  $a = 0$ , while if all are oriented vertically,  $a = 1$ , and for an isotropic orientation  $a = 0.33$ .

$$a = \frac{\sum_{\text{all emitters}} p_z^2}{\sum_{\text{all emitters}} p_x^2 + p_y^2 + p_z^2} \langle \cos^2 \theta \rangle \quad (51)$$

**Fraction of horizontal dipoles ( $\Theta$ ):** ratio of the horizontal components to the total radiated power.  $\Theta=1$  if all emitters are horizontally oriented,  $\Theta=0$  if they are all vertically oriented, and  $\Theta=0.67$  for isotropic orientation.

$$\Theta = \sum_{\text{all emitters}} \frac{p_x^2 + p_y^2}{p_x^2 + p_y^2 + p_z^2} = 1 - a \quad (52)$$

**Orientation order parameter ( $S$ ):**  $S=-0.5$  for a completely horizontally oriented molecule,  $S=1$  for vertical orientation, and  $S=0$  for isotropic orientation.

$$S = \frac{3\langle \cos^2 \theta \rangle - 1}{2} = \frac{3a - 1}{2} \quad (53)$$

### 1.8.3 - Measuring the orientation of the Transition Dipole Moment

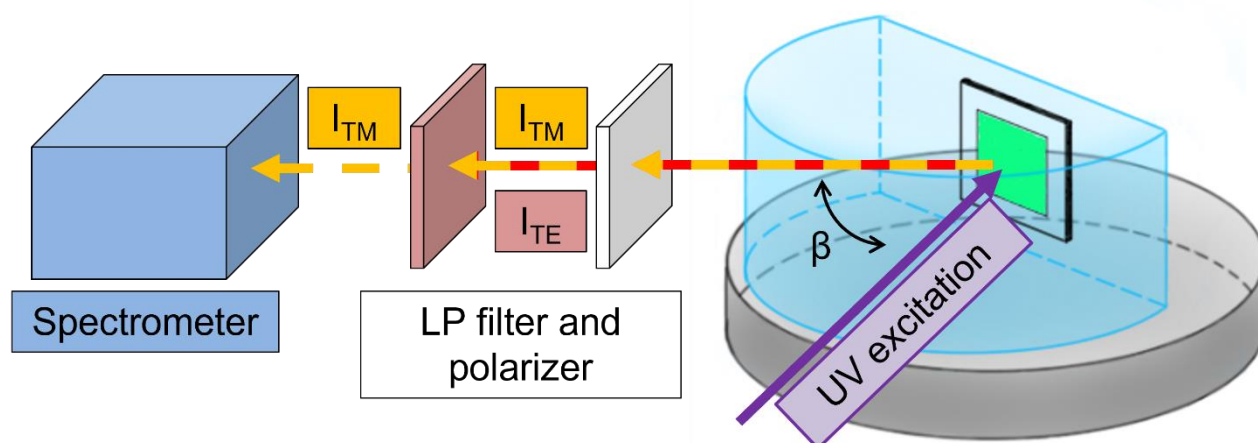


**Figure 29.** Experimental set-up for angle-dependent luminescence spectroscopy.

The current state-of-the-art technology to measure the TDM orientation is angle-dependent luminescence spectroscopy (**Figure 29**). The sample is evaporated under vacuum onto a glass substrate and attached to a fused silica prism using an index matching oil. As previously mentioned, the sample can be described in a Cartesian framework where the z-axis is perpendicular to the plane of the film, which will denote the XY plane. The prism is placed on a rotating stage and the sample is excited with a near-UV laser. The emission spectrum is then recorded at different angles and the emitted light first passes through a Long Pass (LP) filter to remove the excitation source. To enhance the accuracy of the measurement, the TE component of the light is eliminated *via* a polarizer that only transmits TM light. Only the  $TM_h$  and  $TM_v$  components are recorded by the spectrometer and the instrument can then extract the spectral radiant intensity  $I(\beta, \lambda, a)$  as a function of the angle at which the measurement is performed ( $\beta$ ), the emission wavelength ( $\lambda$ ) and the anisotropy factor ( $a$ ).  $a$  is then related to the vertical and horizontal component of the radiant intensity ( $I_{TM_h}$  and  $I_{TM_v}$ ) with the formula:

$$I_{TM}(\beta, \lambda, a) = aI_{TM,v} + (1 - a)I_{TM,h} \quad (54)$$

The ratio between  $I_{TM_h}$  and  $I_{TM_v}$  will give us a good indication of the average orientation of molecules in the film since horizontally oriented molecules will contribute to the emission in the forward direction ( $I_{TM_h}$ ) while vertically oriented molecules will contribute to the emission only at angles



higher than c.a.  $45^\circ$  ( $I_{TMv}$ ). Finally, the measured  $I_{TM}$  is fitted through optical simulations to extract the anisotropy factor.

#### 1.8.4 - Currently used strategies to improve the orientation of the emitter

The design challenge now becomes a matter of creating an emitter that presents preferential horizontal orientation coupled with good TADF properties. Three main strategies are currently accepted in the literature, to effectively improve the horizontal orientation of the molecule:

**Tuning of the molecular shape:** Yokoyama *et al.*<sup>62</sup> showed that longer molecules and the introduction of terminal bulky groups lead to a molecule with a higher degree of horizontal orientation (**Figure 30**). The presence of bulky groups will make the intermolecular and molecule-substrate interactions based solely on weak Van der Waals. Horizontal orientation will become more likely as it's the best way to minimize surface energy. **BSB-Cz** presented near-perfect horizontal orientation while in molecule **9**, the presence of less hindered  $-N(Me)_2$  groups instead of the carbazole, led to the formation of a crystalline phase and vertical orientation. Furthermore, the horizontal orientation of a molecule with bulky terminal groups can be enhanced by increasing its length as demonstrated by **CBP**, which has the same bulky group as **BSB-Cz** but presented isotropic orientation.

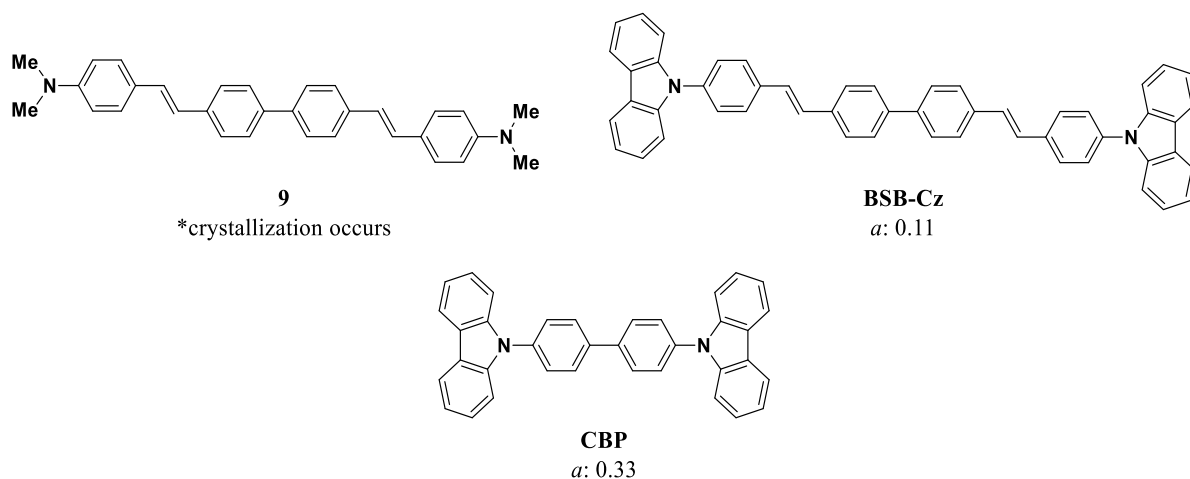


**Figure 30.** Structure of the molecule with different terminal groups and length tested for orientation measurements.<sup>62</sup>

**Film growth kinetics:** evaporating a molecule under a high vacuum has been shown to give better horizontal orientation than what is achievable by solution-processed films. The better results achieved by thermal evaporation are due to a higher packing density, higher stability of the system, and lower tendencies for reorganization by post-process thermal annealing.<sup>122</sup>

**Temperature of the substrate:** cooling the substrate can enhance the horizontal orientation of the emitter. Komino *et al.*<sup>123</sup> were able to achieve perfect alignment of the TDM of the emitter **Cis-BOX2** (**Figure 31**) ( $a = 0$ ) by cooling the substrate to 200 K, while the same molecule, when evaporated onto a substrate at 370 K gave isotropic orientation. Isotropic orientation was also obtained by post-fabrication thermal annealing by heating the horizontal sample to 380 K.

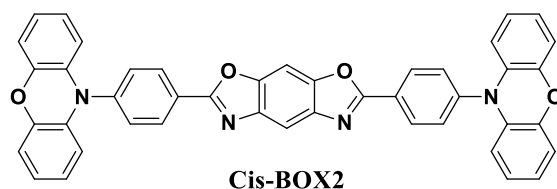


**Figure 31.** Structure of the molecule investigated at different substrate temperatures.<sup>123</sup>

### 1.8.5 - Molecular weight, thickness, and aspect ratio effect

In a recent review article we highlighted the factors that seem to control the orientation of TADF emitters in evaporated films.<sup>23</sup> To do so we started by building a database containing 230 different published host/guest systems (from the combination of 130 different fluorescent and TADF emitters in neat/ doped films).

Besides literature-reported properties, the database was populated by DFT calculated x, y, and z extension of the emitter, and then used to quantify their Linearity (L), and Planarity (P). This was done since, in the literature, molecules are referred to as linear or planar based on their chemical structure with no quantifiable parameter:

$$L = 1 - \left(\frac{y}{x}\right) \quad (55)$$

$$P = 1 - \left(\frac{y}{z}\right) \quad (56)$$

Looking at binary host-guest systems, they were able to identify two classes of emitters based on the Molecular Weight, emitter with  $MW < \text{or} > 600 \text{ g mol}^{-1}$ , since it's the relevant section to this study.

Low molecular weight emitters ( $MW < 600 \text{ g mol}^{-1}$ ) are known to be more affected by diffusion phenomena of the host during film formation. This was reflected by our analysis where we found the only parameter to have a real impact on the orientation to be the glass transition temperature ( $T_g$ ) of the host, where higher  $T_g$  led to lower anisotropy factor values, implying higher horizontal orientation. This is caused by the fact that host materials with higher glass transition temperatures have been shown to block the diffusion mechanism during film deposition.<sup>122</sup> This was mainly derived from the study of **DMAC-TRZ**<sup>68</sup> and **Coumarin 6**<sup>124</sup> by Brütting *et al.* where the emitter was doped in different hosts with different  $T_g$  values (**Figure 32**). Both emitters presented smaller  $a$  values when doped in the host materials with the higher  $T_g$  value.

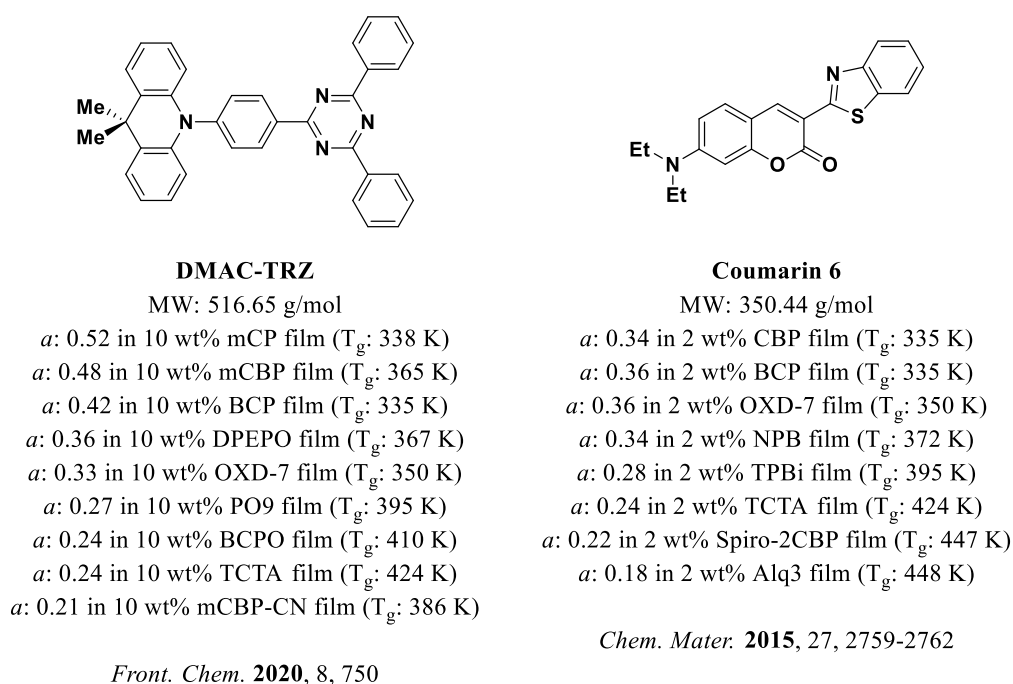


**Figure 32.** Effect of the  $T_g$  of the host on the horizontal orientation of **DMAC-TRZ**<sup>68</sup> and **Coumarin 6**<sup>124</sup> ( $MW < 600 \text{ g mol}^{-1}$ ).

For emitters with  $MW > 600 \text{ g mol}^{-1}$ , the problem of diffusion phenomena during film deposition is already partially solved by the higher weight of the emitters, especially when used in high concentration, leading to the  $T_g$  of the host being less impactful in achieving high horizontal orientation. The values that were found to be the most significant were the MW of the emitter and

their thickness ( $z_E$ ), the MW of the host, and the ratio between the length of the emitter and the length of the host ( $x_E/x_H$ ). The influence of molecular weight and aspect ratio ( $x_E/x_H$ ) is evidenced by the fact that the only emitters able to achieve  $a \leq 0.10$  presented at least one of these characteristics: molecular weight above 700 and/or  $x_E/x_H > 1.3$ . This can be seen in the study by Tanaka *et al.* (**Figure 33**),<sup>125</sup> where the horizontal orientation of the discussed materials is better for the heavier materials. The best results are obtained by **4CzTPN-Ph**, which presents the highest MW (1398 g mol<sup>-1</sup>) and  $x_E/x_H > 1.3$ .

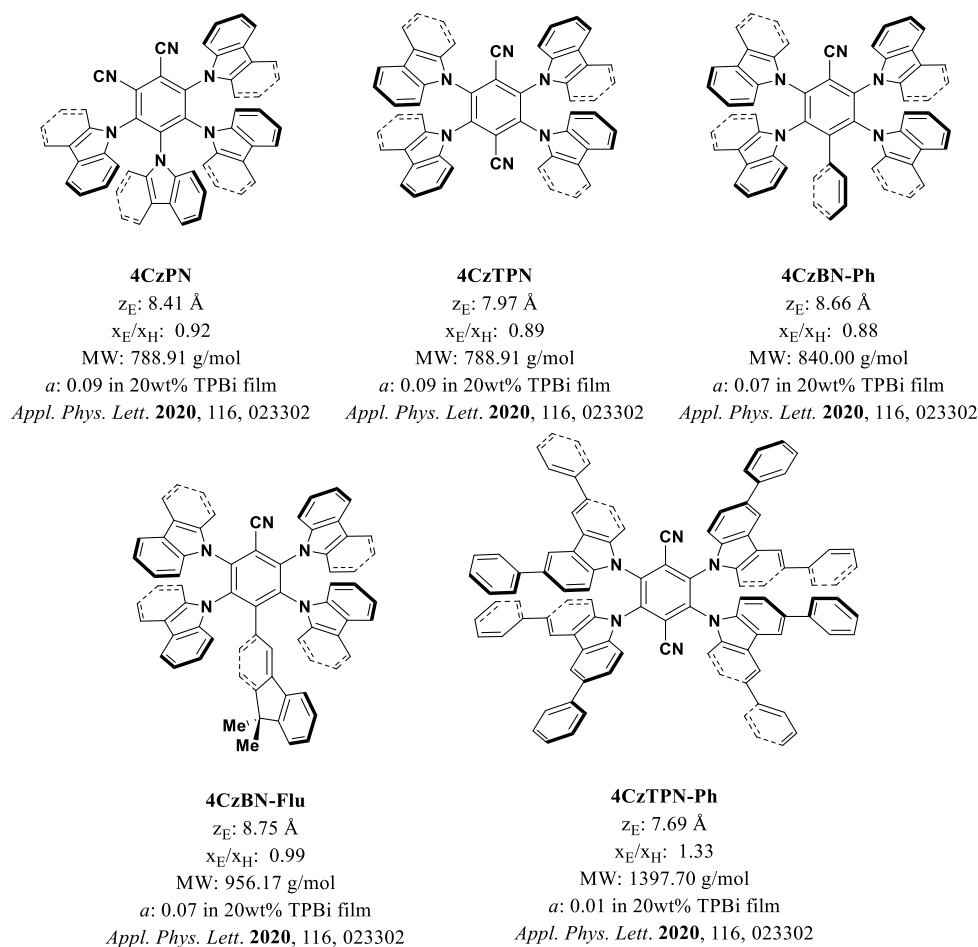


**Figure 33.** Effect of the MW,  $x_E/x_H$ , and  $z_E$  on the horizontal orientation of carbazole-benzonitrile derivatives (MW > 600 g mol<sup>-1</sup>).<sup>125</sup>

## 1.9 - Conclusions

In this chapter, the basic principles behind photo- and electro-luminescence have been discussed and an overview of the different exciton harvesting mechanisms has been provided. Finally, the concept of orientation of the TDM has been discussed and how this factor can lead to enhanced efficiencies in the OLED. The following chapters focus on showcasing novel TADF emitters, with a particular emphasis on their photophysical properties and their orientation behavior in thin films.

- enhanced solubility
- improved orientation
- reduced aggregation



ANISOTROPY FACTOR

MCBP  
0.09



EQE  
22%

- good donor-strength
- excellent charge-transport

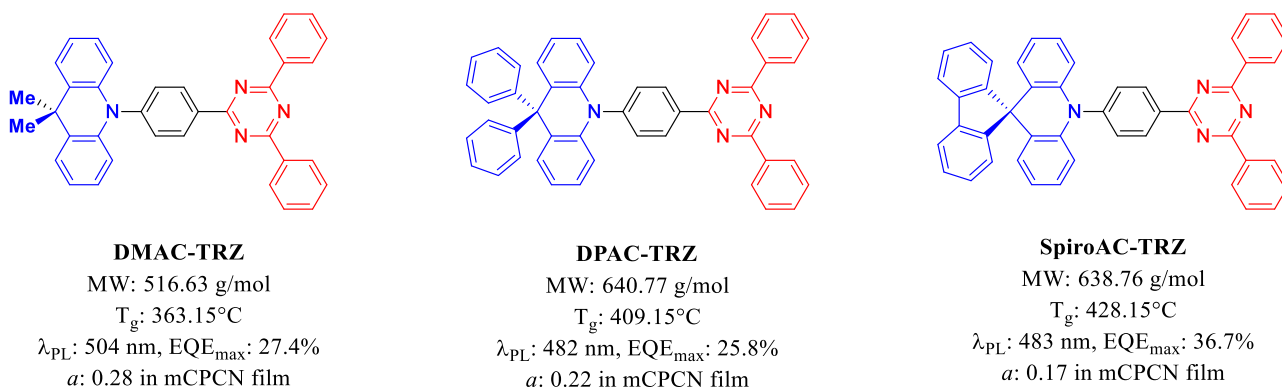


## Chapter 2 - Di-functionalized Indolocarbazole-Triazine based materials as a design for highly horizontally oriented TADF emitters

### 2.1 – Attributions

I am the main author of this text. Unless otherwise stated in the text, I directly carried out the experimental work presented. Of the work presented in this chapter, I performed the theoretical calculations and optoelectronic characterization (CV-DPV, UV-vis, solvatochromism study, and solution and solid state steady-state and time-resolved photoluminescence measurements). I also carried out angle-dependent luminescence spectroscopy to obtain the anisotropy factors, together with Bilal Abbas Naqvi from the Wolfgang Brütting group at the University of Augsburg. The synthesis of the material was done by Dr. Zhen Zhang, from the Stefan Bräse group at the Karlsruhe Institute of Technology (KIT). Devices were fabricated and tested by Dr. Paloma Lay Dos Santos in the Ifor Samuel group at the University of St Andrews. Device simulations were carried out by Prakhar Sahai from the Wolfgang Brütting group. TGA and DSC measurements to study the thermal properties of the materials were performed by Francesco Rodella from the Peter Strohriegl group at the University of Bayreuth. The paper highlighting this work has been published in *Adv. Optical Mater.* **2020**, 2001354, DOI: 10.1002/adom.202001354.

### 2.2 – Introduction



*Adv. Mater.* **2016**, 28, 6976-6983

**Figure 34.** Chemical structure and performances of the discussed acridine-triazine-based emitters.<sup>78</sup>

Many highly horizontally oriented TADF emitters and high performance TADF OLEDs use 2,4,6-triphenyl-1,3,5-triazine as the acceptor group (**Figure 34**). Lyn *et al.* presented three acridine and

triazine-based emitters with an increasing degree of horizontal orientation of their TDM.<sup>78</sup> **DMAC-TRZ**, **DPAC-TRZ**, and **SpiroAC-TRZ** in doped mCPCN films possess  $a$  values, of 0.28, 0.22, and 0.17, respectively. The molecular weight of the emitters ranges between  $\sim 500$  and  $\sim 650$  g mol<sup>-1</sup>, therefore possessing MWs that bridges the distinction previously made (MW < 600 g mol<sup>-1</sup> or MW > 600 g mol<sup>-1</sup>). The trend followed by these emitters seems to follow more closely that of emitters with MW < 600 g mol<sup>-1</sup>, for which a more horizontal orientation of the TDM is correlated to higher  $T_g$  values (**DMAC-TRZ**, **DPAC-TRZ**, and **SpiroAC-TRZ** possess  $T_g$  values of 363.15 °C, 409.15 °C, and 428.15 °C, respectively).

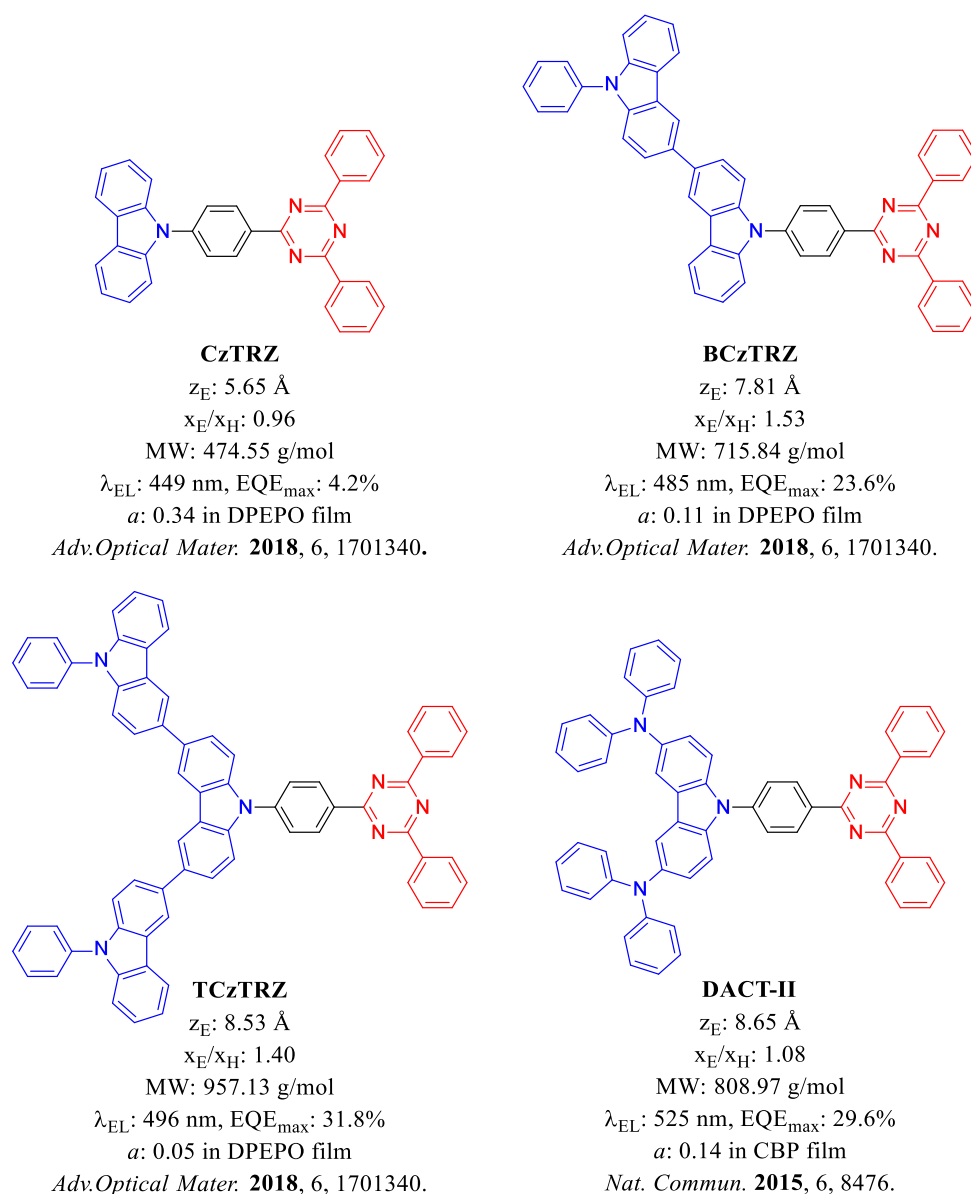


**Figure 35.** Chemical structure and performances of the discussed carbazole-triazine-based emitters.  
126,127

Beyon *et al.*, and Kaji *et al.* reported four carbazole-based emitters **CzTRZ**, **BCzTRZ**, **TCzTRZ**,<sup>126</sup> and **DACT-II**<sup>127</sup> (**Figure 35**). In the first project of Beyon *et al.*, the orientation of the emitters gets progressively more horizontal with more carbazole units added to the material, going from isotropic, with an anisotropy factor ( $a$ ) of 0.34 for **CzTRZ**, to 0.11 for **BCzTRZ** and 0.05 for **TCzTRZ**. More horizontal orientation occurs in compounds with higher molecular weight, and also in materials with  $x_E/x_H$  of 1.53 and 1.40 ( $x_E/x_H > 1.30$  was found to be an essential parameter for  $a < 0.1^{23}$ ). The devices with **TCzTRZ** showed an  $\text{EQE}_{\text{max}}$  of 31.8% at  $\lambda_{\text{EL}}$  of 496 nm, the highest efficiency in the series. **DACT-II** is also preferentially horizontally aligned ( $a = 0.14$ ) but even though its molecular weight is comparable to that of **TCzTRZ**, it does not reach the same anisotropy factor values due to the  $x_E/x_H$  being only 1.08. Devices fabricated with this material still reached excellent efficiencies, with an  $\text{EQE}_{\text{max}}$  of 29.6%.

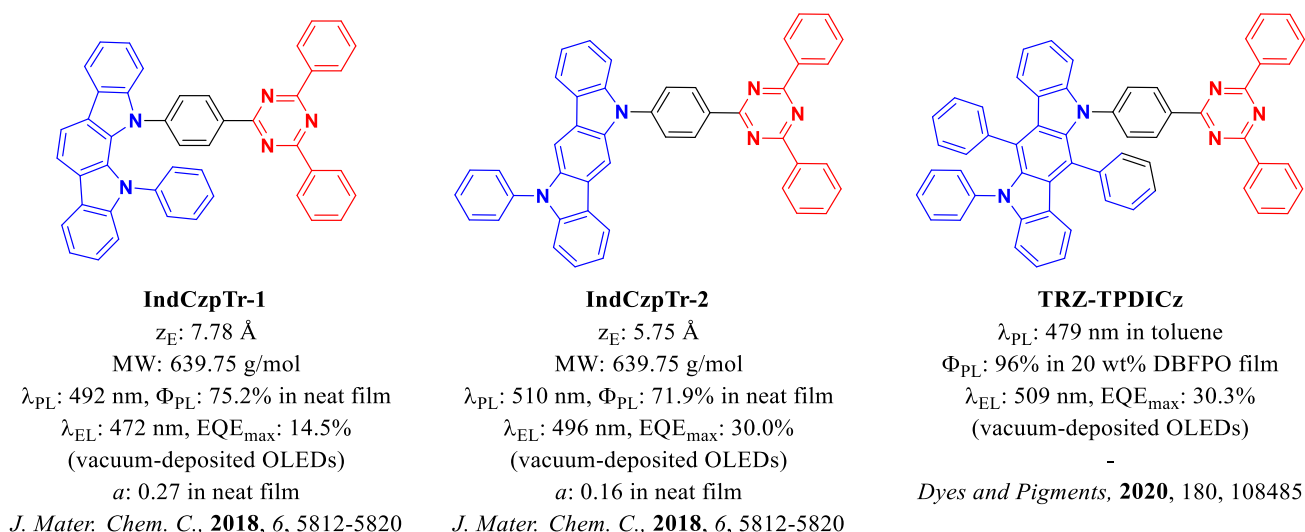


**Figure 36.** Chemical structure and performances of the discussed indolocarbazole-triazine-based emitters.<sup>65,79</sup>

Another donor moiety used in several horizontally oriented compounds leading to high-performing OLEDs is indolo[3,2-b]carbazole (**ICz**). As previously stated (**Chapter 1 – Paragraph 1.6.6 - Design of TADF emitters**) **ICz** has a planar, and conjugated structure, and high morphological and thermal stability.<sup>61,62</sup> Xiang *et al.* reported two emitters incorporating this donor, **IndCzpTr1**, and **IndCzpTr2**<sup>65</sup> (**Figure 36**), which showed high  $\Phi_{\text{PL}}$  of 75.2% and 71.9%, respectively, with  $\tau_d$ , of 25.48  $\mu\text{s}$  and 34.31  $\mu\text{s}$ , respectively, in neat films, the devices produced with these materials reached  $\text{EQE}_{\text{max}}$  values of 14.5% and 30%, respectively. The orientation of the TDM of the two materials was



studied in neat film, showing  $a$  values of 0.27 and 0.16 for **IndCzpTr1** and **IndCzpTr2**, respectively. However, there is insufficient data in the literature on neat films of emitters to identify any specific parameters that controlled the orientation of emitters. A possible theory is that the higher linearity (**Chapter 1 – Paragraph 1.8.5 - Molecular weight, thickness, and aspect ratio effect**) of **IndCzpTr2** improved the horizontal orientation of the material. Very high efficiencies were also achieved by Maeng *et al.* in the device with the emitter **TRZ-TPDICz**,<sup>79</sup> where the addition of the two phenyl groups on the donor increased the donor strength. The material presents near unity  $\Phi_{\text{PL}}$  at 96% in 20 wt% DBFPO film (DBFPO = 2,8-bis(diphenylphosphine oxide) dibenzofuran), which then led to a very high  $\text{EQE}_{\text{max}}$  of 30.3%.

Even though indolocarbazole-based emitters have been showcased in several reports, at the time of investigation indolo[3,2-b]carbazole had never been functionalized with two acceptor moieties. **ICzTRZ** (**Figure 37**) represents the first example of a Acceptor-Donor-Acceptor (A-D-A) type ICz-based TADF emitter. *tert*-Butyl groups were added to the distal phenyl rings for several reasons:

- Enhance the solubility of the material.
- Increase the bulkiness of the material to reduce the possibility of aggregation-caused quenching.
- Increase the molecular weight and thus the likelihood that the transition dipole moment of the material will be horizontally oriented to the plane of the film/device.

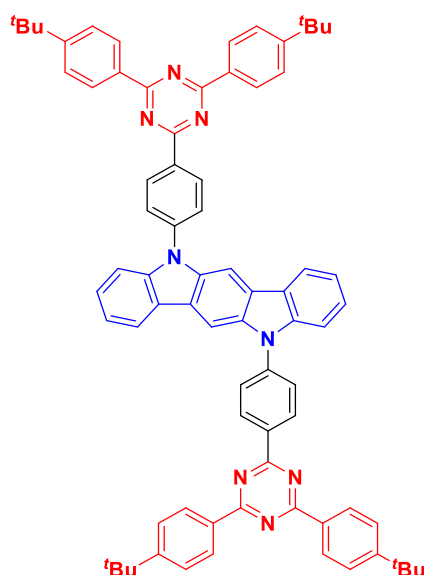
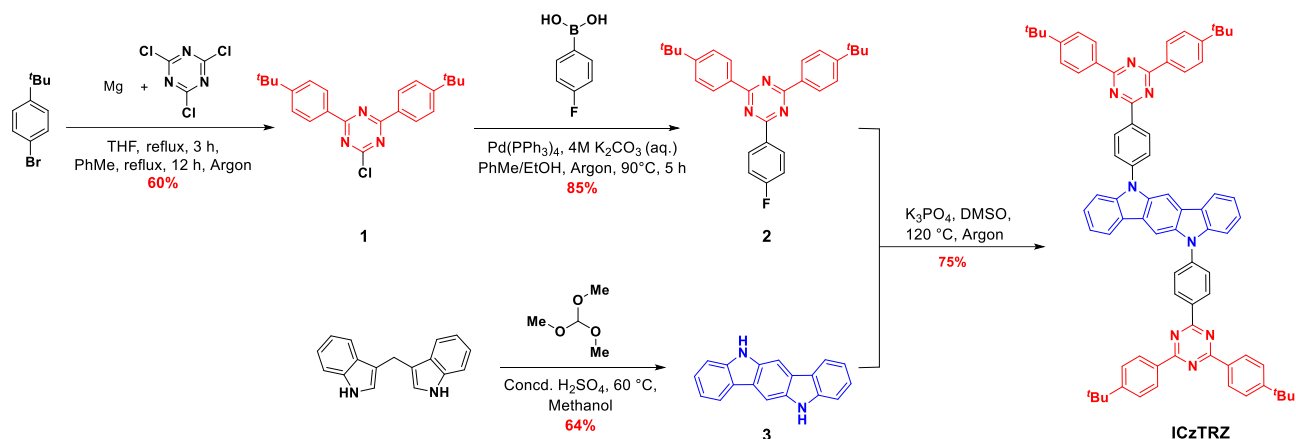


**Figure 37.** Chemical structure of **ICzTRZ**.

## 2.3 - Results and discussion

### 2.3.1 – Synthesis



**Scheme 1.** Synthetic route to ICzTRZ.

The synthesis of the material was performed by Dr. Zhen Zhang, from the Stefan Bräse group at the Karlsruhe Institute of Technology (KIT) (**Chapter 2 – Paragraph 2.1 – Attributions**). ICzTRZ, was obtained *via* a three steps synthesis (**Scheme 1**). The initial triazine precursor (**1**) was synthesized with a Grignard reaction between two equivalents of *tert*-butyl phenyl magnesium bromide and 2,4,6-trichloro-1,3,5-triazine. The final triazine acceptor (**2**) was then obtained by the addition of a 4-fluorophenyl to **1** *via* a Suzuki-Miyaura coupling reaction. An acid-promoted cyclization of 3,3'-diindolylmethane was used to make the Indolocarbazole moiety (**3**), and the target molecule was obtained by coupling **2** to it, with a nucleophilic aromatic substitution, using tripotassium phosphate as the base. The emitter was fully characterized by <sup>1</sup>H NMR, <sup>13</sup>C NMR, melting point determination, high resolution mass spectroscopy, and elemental analysis.<sup>67</sup> Single crystal X-ray diffraction was used to observe the structure of ICzTRZ (**Figure 38**). Both triazines are similarly oriented, with a 46.5° dihedral angle between the ICz donor and adjacent phenyl spacer, before the TRZ acceptor.

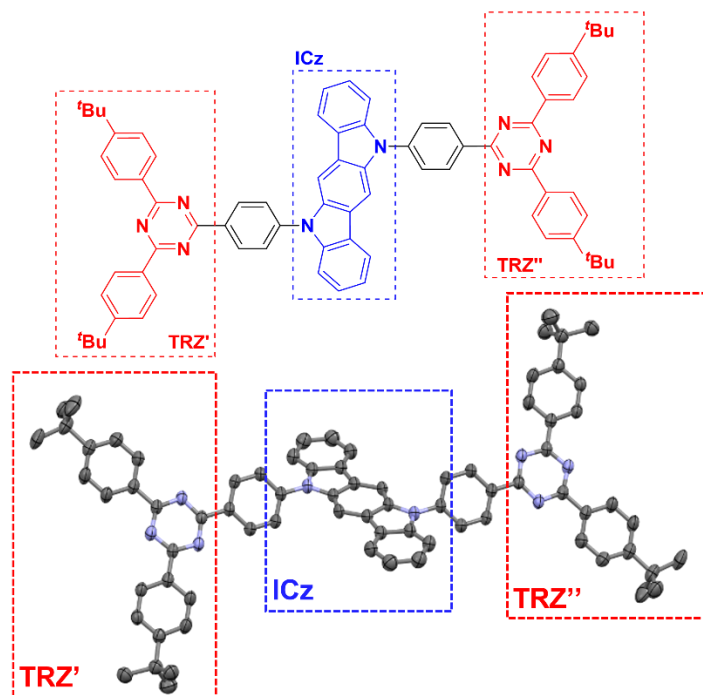


**Figure 38.** Molecular and crystal structure of **ICzTRZ** (hydrogens were omitted for clarity).

### 2.3.2 - Theoretical calculations

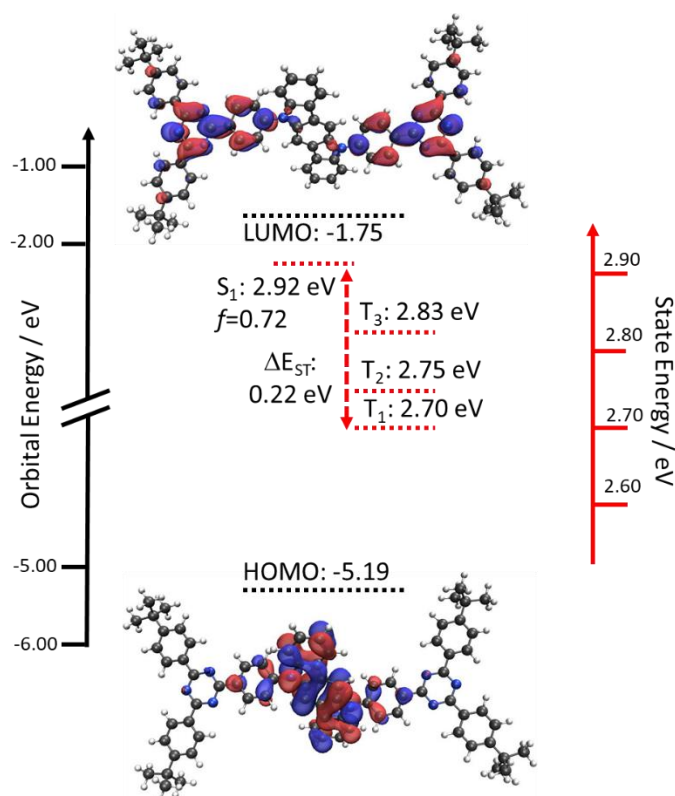


**Figure 39.** HOMO and LUMO electron density distributions and energy levels, excited state energy levels of **ICzTRZ**. (Obtained via DFT and TD-DFT at the PBE0/6-31G(d,p) level, Isovalue for new surfaces: MO=0.02, Density=0.0004).

DFT and TD-DFT calculations at the PBE0/6-031G(d,p)<sup>102,103</sup> level revealed the potential of **ICzTRZ** as a TADF emitter (**Figure 39**). The ground-state geometry optimization was carried out in the gas phase and from the TD-DFT calculations, a  $\Delta E_{ST}$  value of 0.22 eV was obtained, with an  $S_1$  energy of 2.92 eV and a  $T_1$  energy of 2.70 eV. The  $S_1$  state possessed a high oscillator strength ( $f_{osc}$ ) of 0.72, implying that the material's  $S_1 \rightarrow S_0$  transition would have a fast radiative decay and consequently high  $\Phi_{PL}$ . Two intermediate triplet excited states were also predicted to exist between  $S_1$  and  $T_1$ , which could be beneficial to enhance second-order mixing,<sup>52</sup> leading to a more efficient RISC process.<sup>52,128–131</sup> The HOMO, with an energy of -5.19 eV, and LUMO, with an energy of -1.75 eV, are localized on the donor and the acceptor moieties, respectively. The triazine and the central phenylene bridge are coplanar, with a dihedral angle of only 2°. The more significant twist is between the indolocarbazole and the phenylene bridge, with a dihedral angle of 48°. Both results closely match what was observed in the crystal structure. The permanent dipole moment (PDM) and transition dipole moment (TDM) of the material were also obtained, with values of 0.3 Debye and 7.9 Debye, respectively.

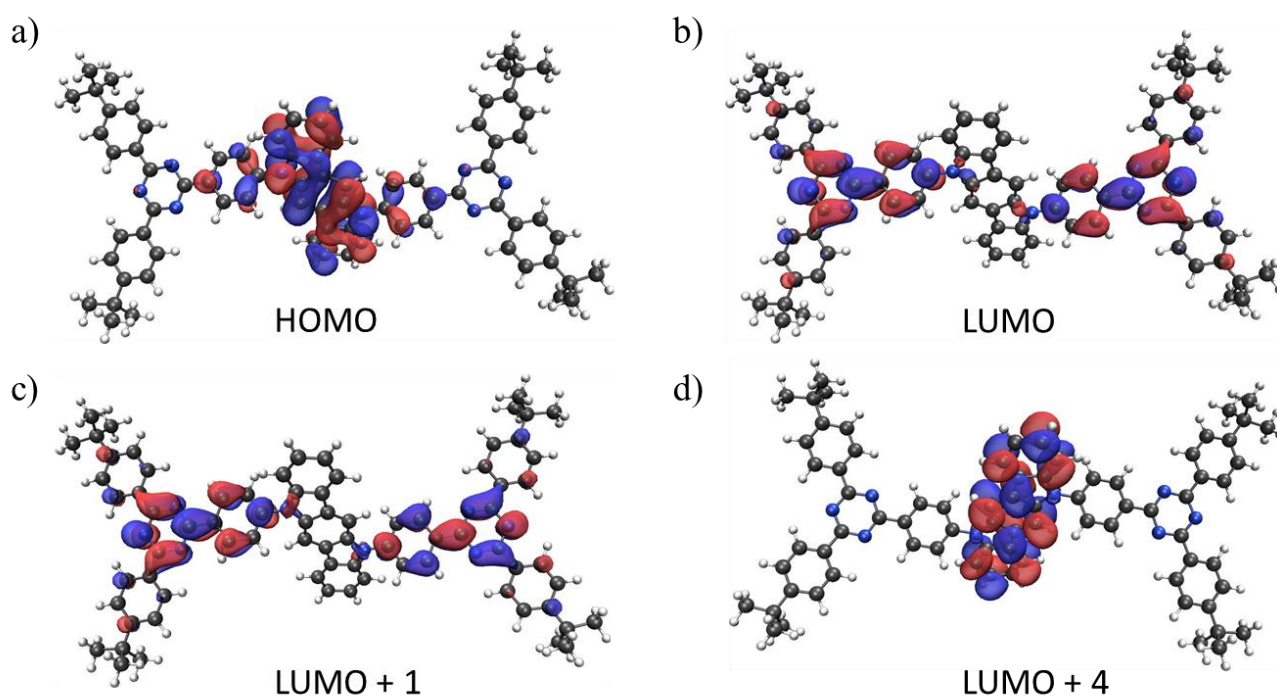


**Figure 40.** Electronic density surfaces of a) HOMO b) LUMO c) LUMO +1 d) LUMO +4. (Isovalue for new surfaces: MO=0.02, Density=0.0004).

**Table 1.** Excited states properties of ICzTRZ.

Excited State <sup>a</sup>	Energy / eV; nm	Nature <sup>b</sup>	Character of the transition
<b>T<sub>1</sub></b>	2.70; 460	(H-2)→(L+1) (5%) <b>H→L (82%)</b> H→(L+5) (5%)	<sup>3</sup> CT
<b>T<sub>2</sub></b>	2.75; 450	(H-2)→L (7%) <b>H→(L+1) (82%)</b> H→(L+6) (3%)	<sup>3</sup> CT
<b>T<sub>3</sub></b>	2.83; 438	<b>H→(L+4) (90%)</b>	<sup>3</sup> LE
<b>S<sub>1</sub></b> ( <i>f</i> =0.72)	2.92; 424	<b>H→L (98%)</b>	<sup>1</sup> CT

<sup>a</sup> (PBE0/6-31G(d,p)); <sup>b</sup> the transitions highlighted in red are the main ones contributing to the excited state character.

The nature of the different transitions from the ground state to the singlet/triplet excited state can be identified (**Table 1**), with  $S_0 \rightarrow T_1$ ,  $S_0 \rightarrow T_2$  and  $S_0 \rightarrow S_1$  transitions being charge-transfer in nature (<sup>3</sup>CT for the two triplet transition and <sup>1</sup>CT for the singlet transition) since a clear displacement of the electron density can be observed, going from the indolocarbazole donor to the triazine acceptor (**Figure 40**). The  $S_0 \rightarrow T_3$  instead is a <sup>3</sup>LE transition on the indolocarbazole. As previously mentioned, the presence of a <sup>3</sup>LE state will make RISC from the <sup>3</sup>LE to the <sup>1</sup>CT state much faster due to enhanced SOC, thus improving the efficiency roll-off of eventual devices.

### 2.3.3 - Optoelectronic properties

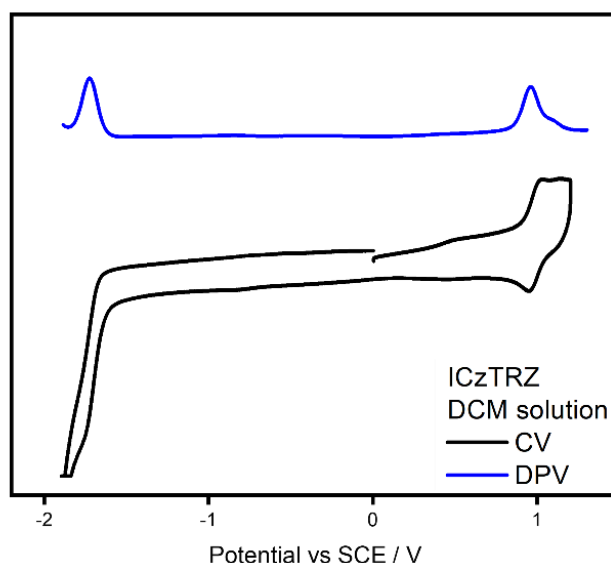


**Figure 41.** Cyclic Voltammetry (CV) and Differential Pulse Voltammetry (DPV) of **ICzTRZ** in DCM.

The electrochemical properties of **ICzTRZ** were studied with CV and DPV in degassed DCM with tetra-*n*-butylammonium hexafluorophosphate as the electrolyte and Fc/Fc<sup>+</sup> as the internal reference (**Figure 41**). **ICzTRZ** shows a reversible oxidation wave with  $E_{ox}$  at 0.96 V (measured from the DPV), a second oxidation wave at 1.14 eV, which are assigned to the oxidations of the indolocarbazole moiety, and an irreversible reduction wave at -1.83 V, assigned to the reduction of the triazine acceptor.<sup>60,132–135</sup> The HOMO and LUMO levels were then calculated to be -5.66 eV and -3.17 eV, respectively (from the DPV corrected vs Fc/Fc<sup>+</sup>). A large difference from what was obtained by DFT can be seen (HOMO of -5.19 eV, and LUMO of -1.75), the reason being that while the theoretical calculations are carried out in a simulated gas phase, electrochemistry measurements are run in a solvent.

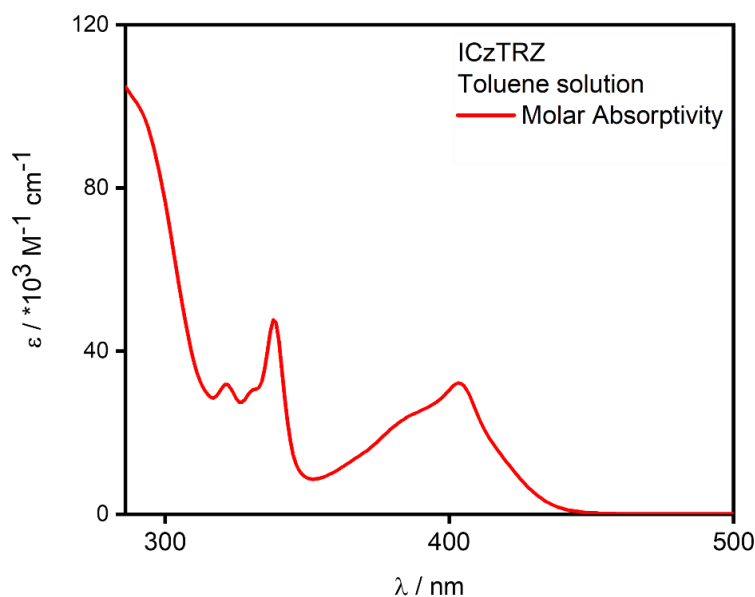


**Figure 42.** UV-vis absorption spectrum of **ICzTRZ** in toluene.

The UV-vis absorption spectrum in toluene (**Figure 42**) coincides with the absorption spectra of other indolocarbazole-based compounds.<sup>65</sup> The nature of the different transitions was assigned using TD-DFT calculations (**Table 2**). The spectrum shows several high-intensity absorption bands from 280 to 350 nm that possess both CT (for the bands at 321 nm, and 331 nm) and LE character (for the band at 340 nm) localized on the indolocarbazole. There are low-intensity bands around 400 nm that are assigned to a CT transition between the **ICz** and the **TRZ** acceptor moieties.

**Table 2.** Properties of the excited states involved in the UV-vis absorption transitions of **ICzTRZ**.

Excited State <sup>a</sup>	Energy / eV; nm	Nature <sup>b</sup>	Character of the transition
<b>S1</b> ( $f_{osc}=0.72$ )	2.92; 424	<b>H→L (98%)</b>	<b><sup>1</sup>CT</b>
<b>S2</b> ( $f_{osc}=0.00$ )	3.01; 412	H→(L+1) (98%)	<sup>1</sup> CT
<b>S3</b> ( $f_{osc}=0.00$ )	3.16; 393	H→(L+2) (98%)	<sup>1</sup> CT
<b>S4</b> ( $f_{osc}=0.00$ )	3.16; 393	H→(L+3) (98%)	<sup>1</sup> CT
<b>S5</b> ( $f_{osc}=0.02$ )	3.41; 363	<b>(H-1)→L (85%)</b> H→(L+2) (13%)	<b><sup>1</sup>CT</b>
<b>S6</b> ( $f_{osc}=0.00$ )	3.46; 358	(H-1)→(L+1) (98%)	<sup>1</sup> CT
<b>S7</b> ( $f_{osc}=0.09$ )	3.52; 352	<b>H→(L+4) (80%)</b> (H-1)→L (13%) (H-1)→(L+14) (3%)	<b><sup>1</sup>LE</b>
<b>S8</b> ( $f_{osc}=0.00$ )	3.68; 337	(H-1)→(L+2) (84%) (H-1)→(L+2) (16%)	<sup>1</sup> CT

<b>S<sub>9</sub></b> ( $f_{osc}=0.00$ )	3.68; 337	(H-1)→(L+3) (84%) (H-1)→(L+2) (16%)	<sup>1</sup> CT
<b>S<sub>10</sub></b> ( $f_{osc}=0.59$ )	3.91; 317	(H-2)→(L+1) (81%) (H-1)→(L+4) (12%)	<sup>1</sup> CT

<sup>a</sup> (PBE0/6-31G(d,p)); <sup>b</sup> the transitions highlighted in red are those involved in the UV transitions.

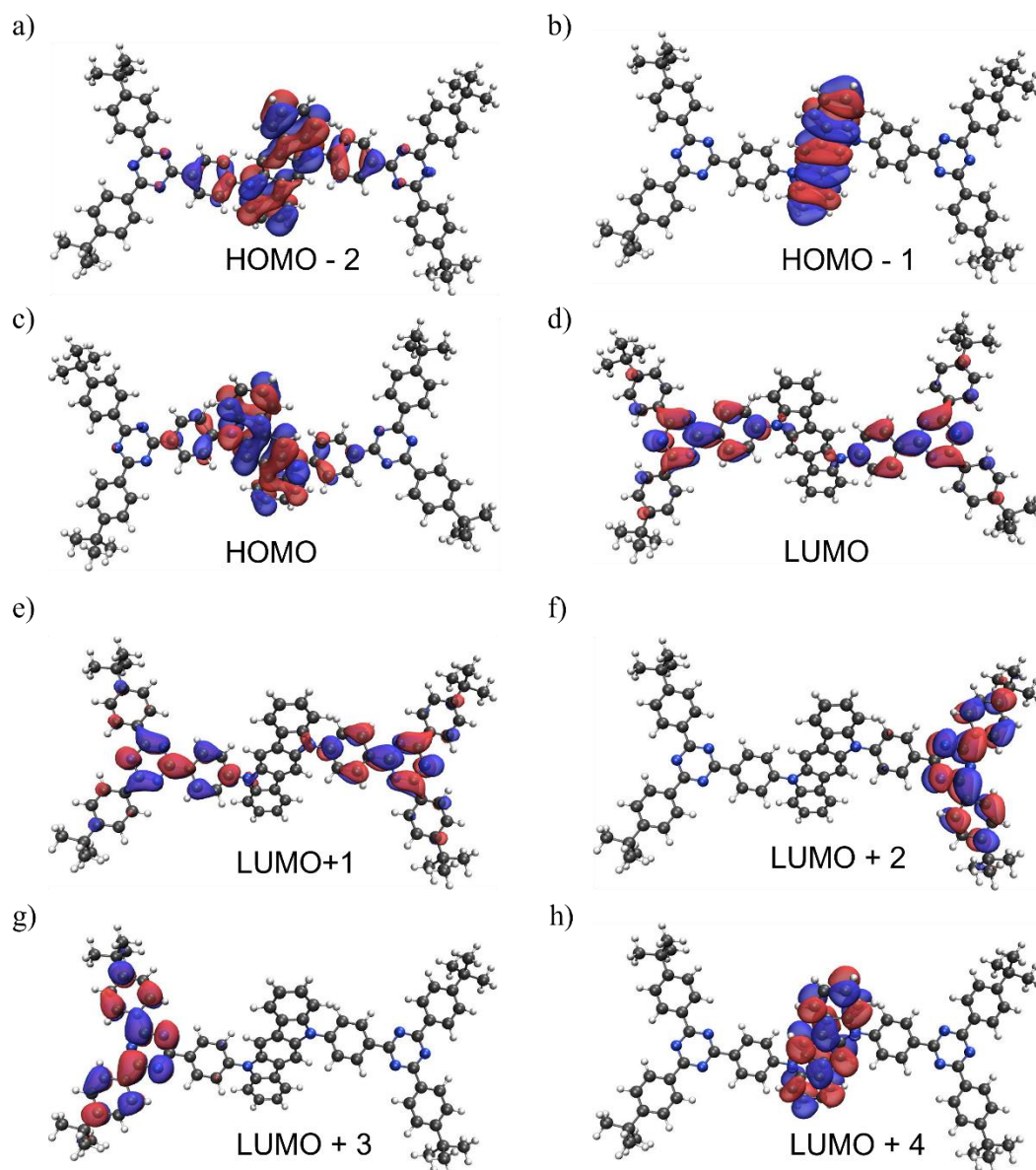


**Figure 43.** Electronic density surfaces of a) HOMO-2 b) HOMO-1 c) HOMO +1 d) LUMO e) LUMO +1 f) LUMO +2 g) LUMO +3 h) LUMO +4. (Isovalue for new surfaces: MO=0.02, Density=0.0004).



Absorption and emission measurements have also been carried out in different solvents to assess the solvatochromism behavior of the material (**Figure 45**). In the ground state, solvent molecules will orient themselves to cancel out the PDM of the material dissolved in it (**Figure 44**). When the material is then photoexcited, the electron density distribution of the material will change, and the solvent will reorganize itself while in the excited state. This will lead to a stabilization of the excited state, lowering its energy, and thus changing the emission color. Larger dipole moments of the excited state and larger dielectric constants of the solvent will lead to higher stabilization of the excited state and a more pronounced redshift of the emission. The absorption wavelength is usually not altered by the solvatochromic effect, as absorption is much faster than the solvent reorganization.<sup>136</sup>

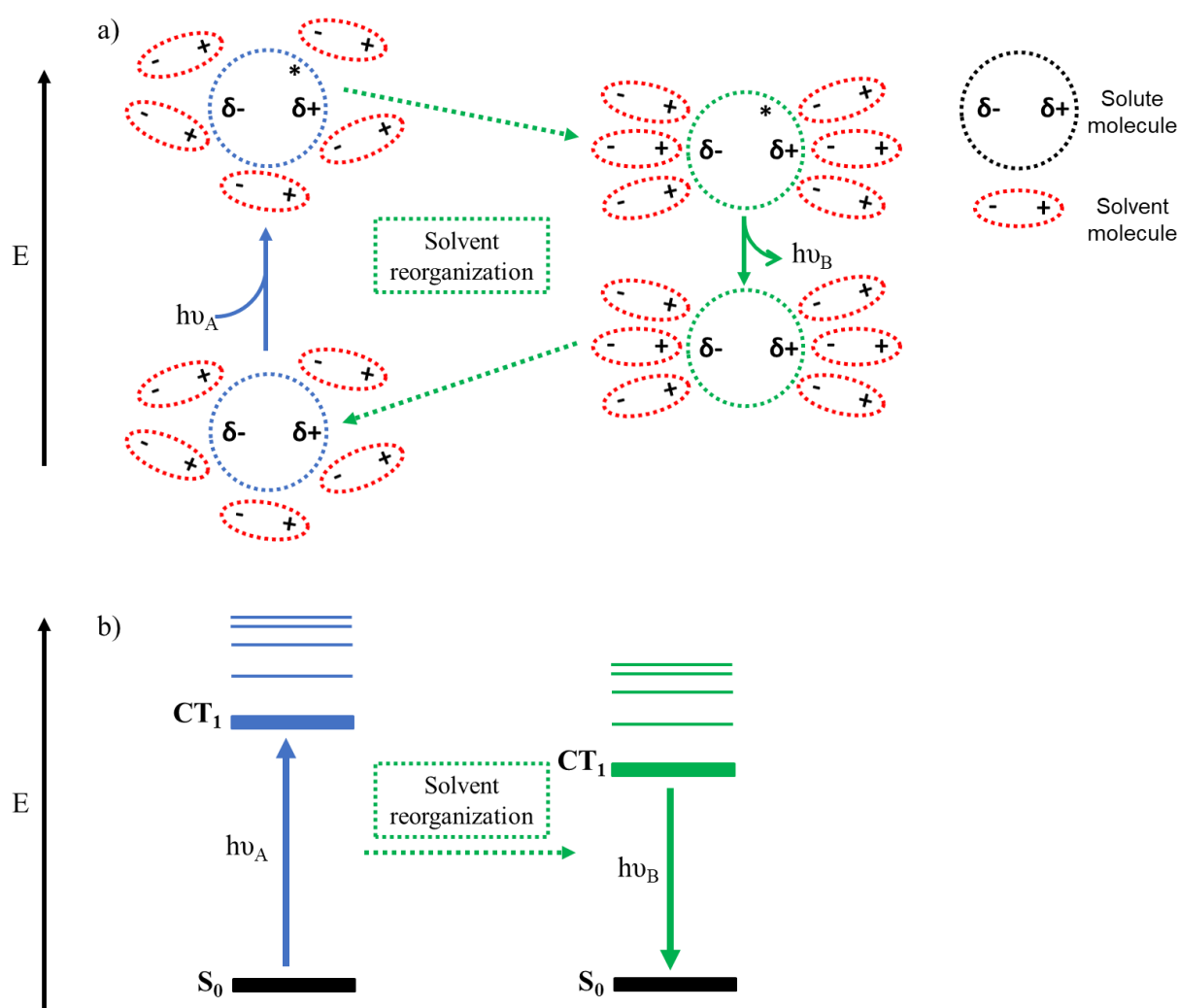


**Figure 44.** a) Schematic representation of the solvent and solute rearrangement, and b) Jablonski diagram of the solvatochromic effect.

As expected, **ICzTRZ** presents no solvatochromism in the absorption spectra. The emission spectra are instead affected by solvent polarity, resulting in a red-shift, and broadening of the emission with increased solvent polarity. This can also be understood by looking at the DFT calculations of **ICzTRZ**, where a large TDM was predicted, which would result in a much stronger interaction with the solvent. The nature of the emission can be discerned by looking at the shape of the emission. The spectra measured in toluene, THF, and DCM are all broad and unstructured, typical of a CT-type transition, while the emission profile in methyl-cyclohexane (the less polar solvent) is structured, thus reflecting the presence of a LE type state.

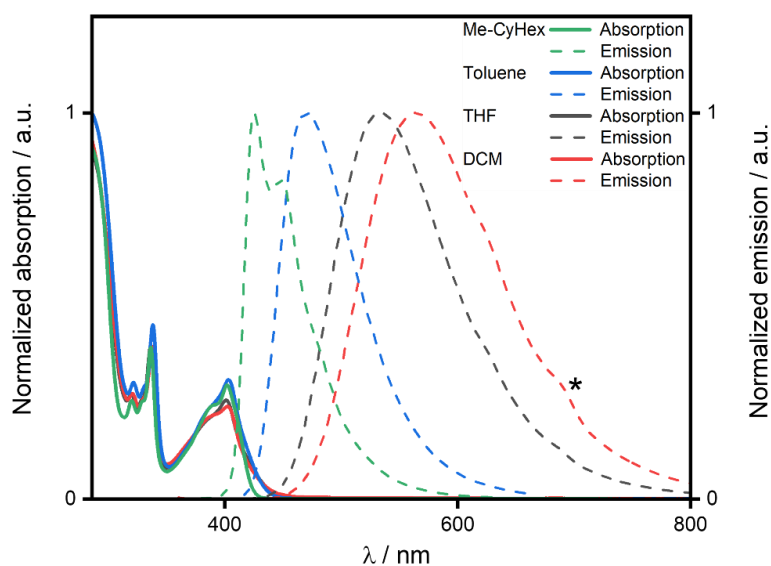


**Figure 45.** Absorption and emission spectra of **ICzTRZ** in different solvents ( $\lambda_{exc}= 340$  nm, \* = second harmonic of the excitation source).

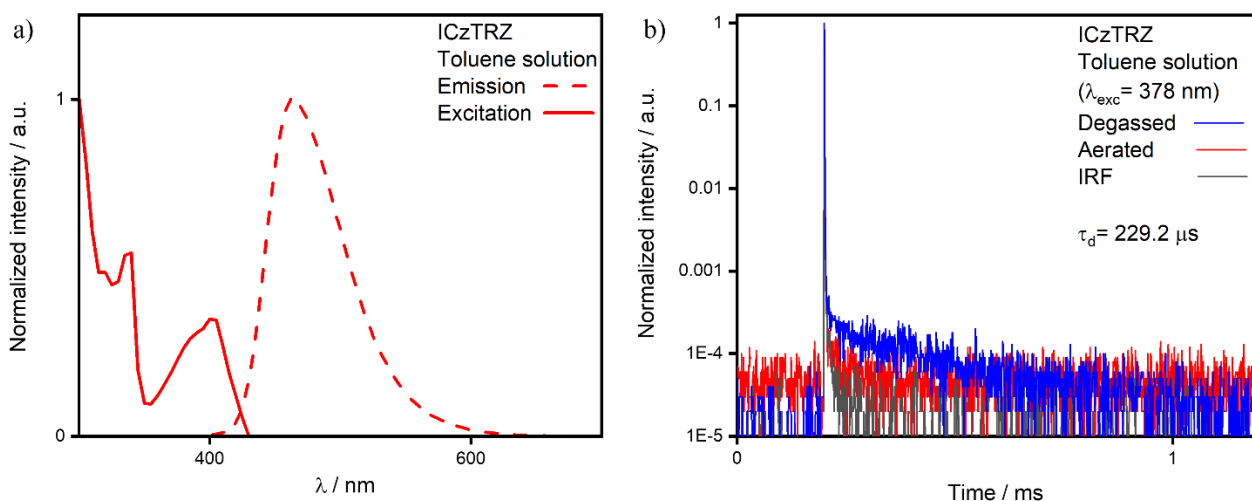


**Figure 46.** a) Emission and excitation spectra of **ICzTRZ** ( $10^{-5}$  M toluene solution,  $\lambda_{\text{exc}} = 340$  nm); b) time-resolved fluorescence decay of degassed and aerated solutions of **ICzTRZ** (Toluene,  $10^{-5}$  M solutions,  $\lambda_{\text{exc}} = 378$  nm, the delayed fluorescence decay was measured by Multi Channel Scaling (MCS)).

The photophysical behavior of the material was studied in  $10^{-5}$  M toluene solution (**Figure 46**). The excitation spectrum was measured, and it closely resembles the previously discussed UV-vis absorption spectrum (**Figure 46a**). **ICzTRZ** in toluene shows blue emission at 462 nm with a  $\Phi_{\text{PL}}$  of 72%, under vacuum, which decreased to 56% after the solution was exposed to air. Time-resolved PL measurements of the solution showed the presence of both prompt and delayed fluorescence, and the lifetimes of the two components can then be extracted *via* exponential fitting of the decay curve. Both fluorescence decays present monoexponential decay kinetics with  $\tau_{\text{p}}$  of 9.0 ns for the prompt fluorescence and  $\tau_{\text{d}}$  of 229.2  $\mu\text{s}$  for the delayed fluorescence. Upon exposure to oxygen, the delayed emission could no longer be detected and coincided with the IRF. The decrease in quantum yield and the disappearance of the delayed component is a result of oxygen quenching the triplet states, giving us proof that triplet states are involved in the photoluminescence of **ICzTRZ**.

Using an iCCD camera the emission profile over different time ranges was measured. Spectral information for the prompt fluorescence and the phosphorescence can then be extracted by selecting the time windows in the nanosecond and in the millisecond time range, respectively. Both prompt fluorescence and phosphorescence are detectable at 77 K where there is not expected to be sufficient thermal energy to promote RISC. From the onset of the two emission spectra, the  $T_1$  energy (coming from the phosphorescence) and  $S_1$  (coming from the fluorescence) can be extracted. The  $\Delta E_{\text{ST}}$  of

**ICzTRZ** in toluene is 0.32 eV, with a triplet energy level of 2.62 eV (421 nm) and a singlet energy level of 2.94 eV (472 nm) (**Figure 47**). The fluorescence spectrum is broad and unstructured, typical for a CT-type state, while the phosphorescence is structured, indicative of emission from a  $^3\text{LE}$  state.

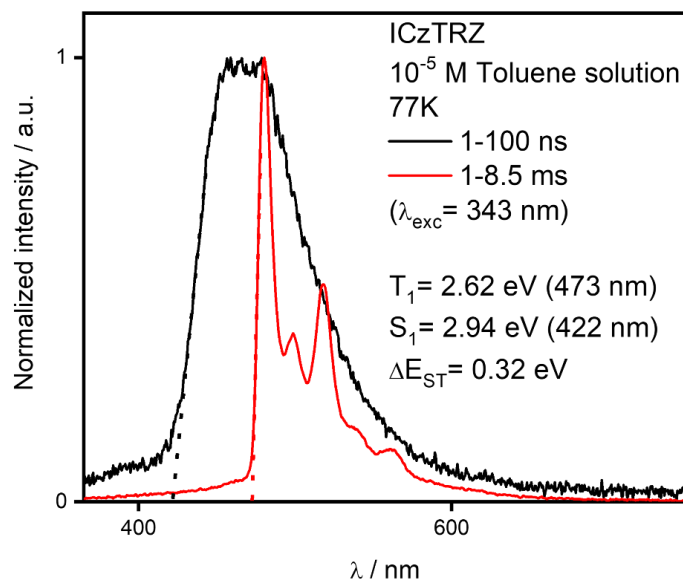


**Figure 47.** Prompt fluorescence and phosphorescence spectra of **ICzTRZ** at 77 K in  $10^{-5}$  M Toluene glass ( $\lambda_{\text{exc}} = 343 \text{ nm}$ , prompt and delayed fluorescence spectra were obtained over the 1–100 ns and 1–8.5 ms time ranges, respectively).

The solid-state photophysical properties of **ICzTRZ** are more relevant to the corresponding electroluminescence in an OLED. **ICzTRZ** was therefore investigated in a host matrix, starting by spin-coating a 10 wt% doped film in PMMA on a quartz substrate to study **ICzTRZ** in a relatively non-polar matrix. The film showed blue emission at  $\lambda_{\text{PL}}$  of 470 nm with a  $\Phi_{\text{PL}}$  of 31% under a  $\text{N}_2$  flow. Transient PL measurements were then carried out. A prompt fluorescence with a biexponential decay kinetics and an average  $\tau_{\text{p}}$  of 11.48 ns [ $\tau_1 = 7.64 \text{ ns}$  (62%),  $\tau_2 = 17.64 \text{ ns}$  (38%)] and a delayed component with a biexponential decay with an average  $\tau_{\text{d}}$  of 252.8  $\mu\text{s}$  [ $\tau_1 = 85.45 \mu\text{s}$  (51%),  $\tau_2 = 427.3 \mu\text{s}$  (49%)] were observed (**Figure 48**). Compared to the toluene data there is a significant increase in the delayed fluorescence lifetime in the PMMA film. Switching from a solution to a solid film also led to a bi-exponential decay instead of the previously observed mono-exponential. This is because in the film there are likely different conformers of the emitter, and this conformational disorder then leads to a range of multiexponential fluorescence decays.<sup>64,137</sup>

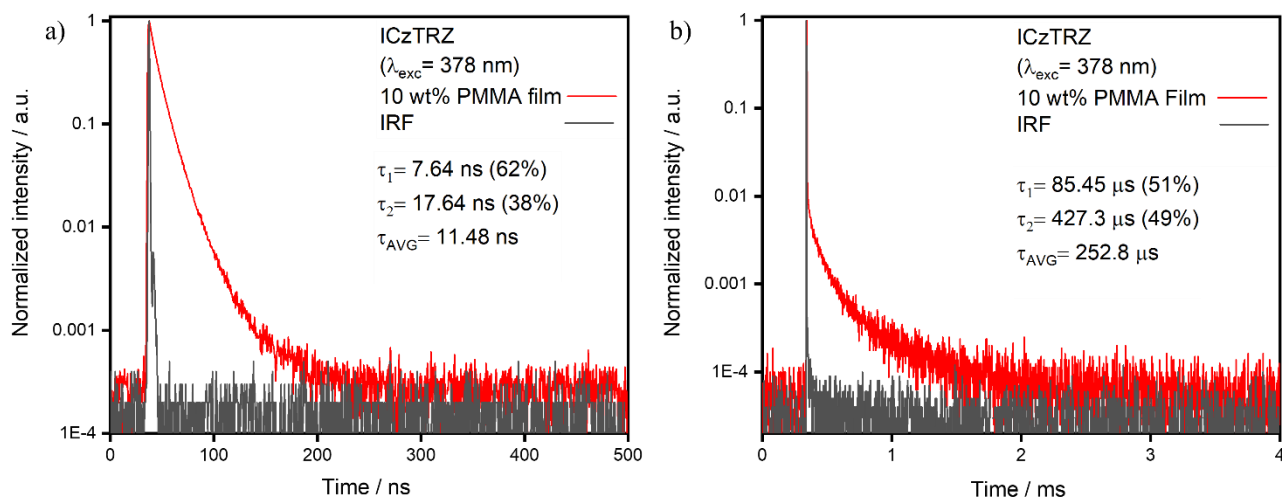


**Figure 48.** Time-resolved decay of **a)** prompt and **b)** delayed fluorescence decay of **ICzTRZ** (10 wt% PMMA film,  $\lambda_{exc} = 378$  nm, the prompt fluorescence decay was measure with TCSPC, the delayed fluorescence decay was measured by MCS).

The iCCD camera was used again to measure the  $\Delta E_{ST}$  in the PMMA film (**Figure 49**). The sample was drop-cast onto a sapphire substrate, as sapphire handles the low temperatures better than quartz. Drop-casting will lead to a greater thickness of the film and consequently, higher brightness, which is needed to compensate for the loss of power of the laser in the set-up that was used. **ICzTRZ** in the PMMA film has  $T_1$  level of 2.64 eV, and  $S_1$  level of 2.57 eV, leading to a  $\Delta E_{ST}$  of 0.11 eV. By comparing these values with the energy levels of the excited states measured in the toluene glass, the effect of the different environment on the singlet can be seen ( $S_1 = 2.94$  eV in toluene), while the triplet energy level stays effectively the same ( $T_1 = 2.62$  eV in toluene). This can be easily explained by looking at the different nature of the states. In both samples, the fluorescence is CT in nature, thus more susceptible to the polarity of the environment. The phosphorescence instead has LE character, which is unaffected by the polarity of the medium.

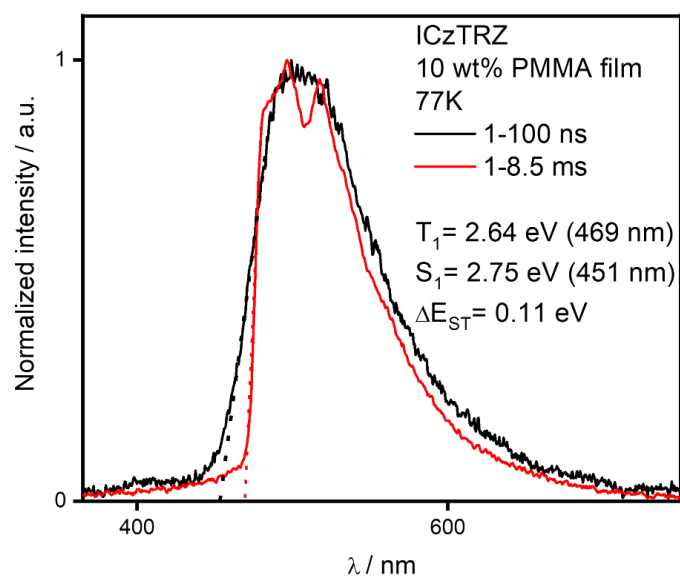


**Figure 49.** Prompt fluorescence and phosphorescence spectra of **ICzTRZ** at 77 K in a drop-cast 10 wt% PMMA film ( $\lambda_{\text{exc}} = 343$  nm, prompt and delayed fluorescence spectra were obtained over the 1–100 ns and 1–8.5 ms time ranges, respectively).

**Table 3.** Host and concentration screen.

Host	Doping concentration / wt%	PLQY N <sub>2</sub> ; Air <sup>a</sup> / %
<b>DPEPO</b>	5	24; 19
	10	35; 32
<b>mCBP</b>	5	72; 59
	10	64; 58
<b>mCP</b>	5	54; 51
	10	52; 49
<b>PPT</b>	5	40; 34
	10	30; 25

<sup>a</sup>  $\lambda_{\text{exc}}=340$  nm.

A host and concentration screen were next carried out to find the optimal conditions for **ICzTRZ** (**Table 3**). The best results were obtained with **mCBP** at a doping concentration of 5 wt%, with a  $\Phi_{\text{PL}}$  of 72% under a N<sub>2</sub> atmosphere, which decreased to 59% when exposed to O<sub>2</sub>.

Time-resolved PL measurements were then carried out in doped 5 wt% film of **ICzTRZ** in **mCBP** (**Figure 50**). A prompt fluorescence with biexponential decay kinetics, and an average  $\tau_p$  of 8.73 ns

$[\tau_1=4.50$  ns (34%),  $\tau_2=10.93$  ns (66%)] and a delayed fluorescence with biexponential decay kinetics and an average  $\tau_d$  of 121.1  $\mu$ s [ $\tau_1=19.13$   $\mu$ s (26%),  $\tau_2=157.0$   $\mu$ s (74%)] were extracted from the emission decay. The multiexponential decay kinetics reflects again the presence of multiple conformers of the **ICzTRZ** emitter in the film. When compared to the **PMMA** doped films, the prompt fluorescence lifetime remains similar while there is a substantial decrease in the delayed fluorescence lifetime. A shorter delayed lifetime is desirable for device application as the triplet states will have less time to undergo undesired quenching pathways. The shorter delayed lifetime in **mCBP** doped films, combined with the higher  $\Phi_{PL}$  shows the promise of **mCBP** as the host material for possible OLEDs applications.

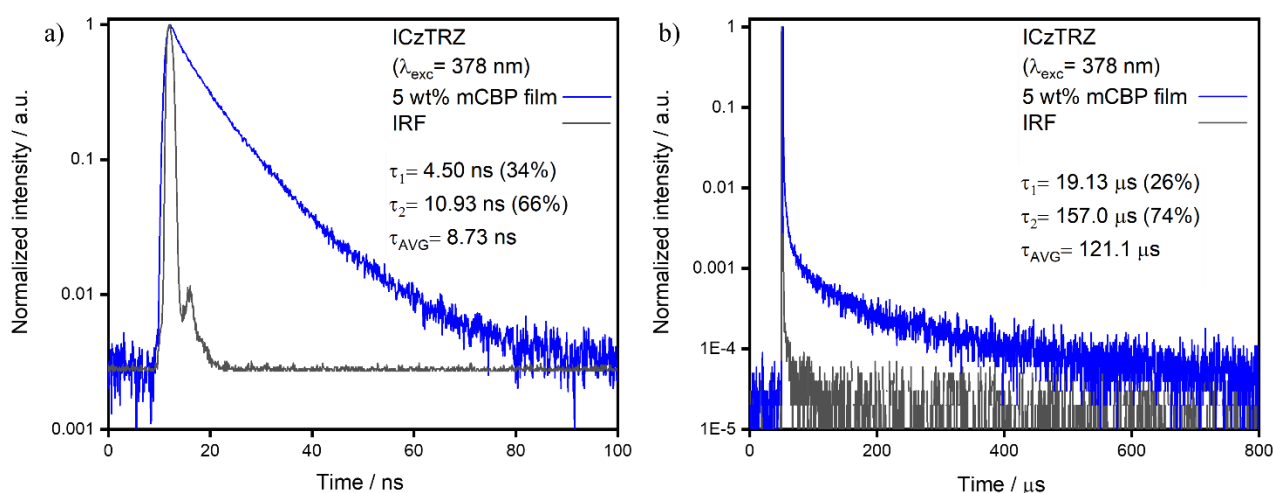


**Figure 50.** Time-resolved decay of **a)** prompt and **b)** delayed fluorescence decay of **ICzTRZ** (5 wt% mCBP film,  $\lambda_{exc} = 378$  nm, the prompt fluorescence decay was measure by TCSPC, the delayed fluorescence decay was measured by MCS).

The  $\Delta E_{ST}$  of the material was then obtained from a 5 wt% drop-casted **mCBP** film, with the iCCD camera (**Figure 51**). **ICzTRZ** in this film possesses a  $T_1$  energy of 2.62 eV and an  $S_1$  energy of 2.85 eV, resulting in a  $\Delta E_{ST}$  of 0.23 eV obtained from the difference in energy of the onset of the prompt and phosphorescence spectra, measured at 77 K. As previously observed, the phosphorescence is structured and was not affected by the change in polarity of the environment, while prompt fluorescence is significantly blue-shifted compared to the PMMA film and is broad and unstructured.

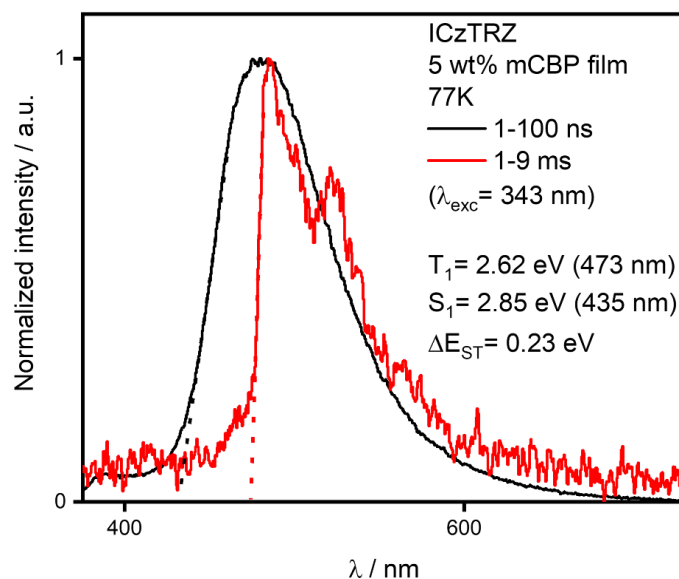


**Figure 51.** Prompt fluorescence and phosphorescence spectra of **ICzTRZ** at 77 K in a drop-casted 5 wt% mCBP film ( $\lambda_{\text{exc}} = 343$  nm, prompt and delayed fluorescence spectra were obtained over the 1–100 ns and 1–9 ms time ranges, respectively).

The temperature dependence of the delayed emission was measured to prove the TADF nature of the emitter (**Figure 52**). The 5 wt% doped film of **ICzTRZ** in mCBP was spin-coated on a sapphire substrate, cooled with liquid nitrogen to 77 K, and then the delayed fluorescence decay was measured at four different temperatures. At 77 K there is a complete disappearance of the delayed component, and its intensity progressively increases with higher temperatures, evidencing the temperature dependence of the RISC process.



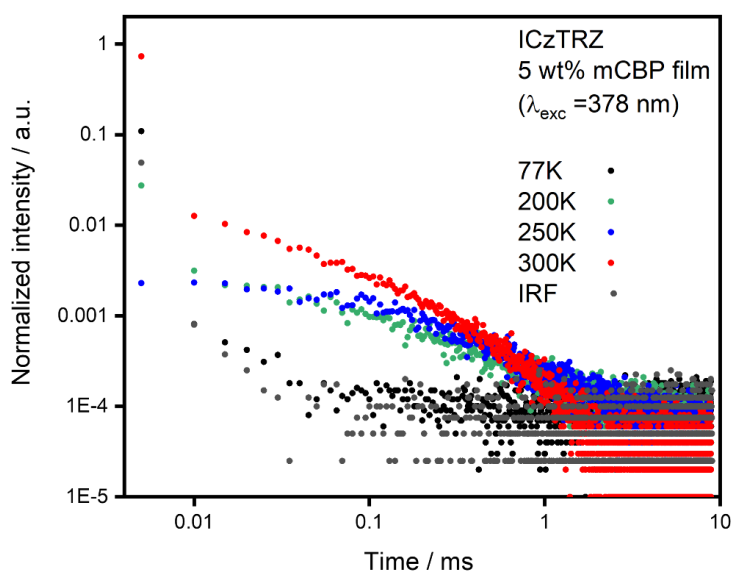


**Figure 52.** Delayed fluorescence decay data measured at different temperatures in spin-coated 5 wt% mCBP film of ICzTRZ ( $\lambda_{\text{exc}} = 378$  nm, all the delayed fluorescence decays were measured by MCS).

**Table 4.** Photophysical properties of ICzTRZ.

Environment	$\lambda_{\text{PL}}$ / nm <sup>a</sup>	$\Phi_{\text{PL}}$ N <sub>2</sub> ; air <sup>b/</sup> %	$\tau_{\text{p}}$ , $\tau_{\text{d}}$ <sup>e/</sup> ns; $\mu\text{s}$	$S_1$ <sup>f</sup> / eV	$T_1$ <sup>g</sup> / eV	$\Delta E_{\text{ST}}$ <sup>h</sup> / eV
Toluene ( $10^{-5}$ M)	462	72; 56 <sup>c</sup>	9.0; 229.2	2.94	2.62	0.32
mCBP 5 wt%	479	70; 59 <sup>d</sup>	8.7; 121.1	2.85	2.62	0.23
PMMA 10 wt%	470	31; 28 <sup>d</sup>	11.5; 252.8	2.75	2.64	0.11

<sup>a</sup> measured at room temperature; <sup>b</sup>  $\lambda_{\text{exc}} = 340$  nm; <sup>c</sup> obtained *via* the optically dilute method, <sup>138</sup> quinine sulfate (0.5 M) in H<sub>2</sub>SO<sub>4</sub> (aq) was used as the reference,  $\Phi_{\text{PL}}$ : 54.6%,  $\lambda_{\text{exc}} = 360$  nm; <sup>139</sup> <sup>d</sup> obtained using an integrating sphere; <sup>e</sup>  $\tau_{\text{p}}$  (prompt lifetime) and  $\tau_{\text{d}}$  (delayed lifetime) were obtained from the transient PL decay of degassed solution/doped film,  $\lambda_{\text{exc}} = 378$  nm; <sup>f</sup>  $S_1$  was obtained from the onset of the prompt emission measured at 77 K; <sup>g</sup>  $T_1$  was obtained from the onset of the phosphorescence spectrum measured at 77 K; <sup>h</sup>  $\Delta E_{\text{ST}} = S_1 - T_1$ .

### 2.3.4 - Orientation measurements

The orientation of the TDM of **ICzTRZ** was measured in the previously mentioned OLED-relevant host materials (**Figure 53**). The  $a$  factor was measured from vacuum-deposited doped films by using polarization- and angle-dependent luminescence spectroscopy, after which the data were analyzed by optical simulation. In all the tested host materials the TDM of **ICzTRZ** presents a nearly completely horizontal orientation with the best results obtained from the doped film in DPEPO with an anisotropy factor of 0.06 (**Table 5**).

**Table 5.** Orientation data of **ICzTRZ** obtained from angle-resolved photoluminescence measurements in different host materials.

Host	Doping / wt%	$a^a$	$\theta_h^b$	$S^c$
mCBP	10	0.09±0.02	0.91	-0.365
mCP	10	0.12±0.01	0.88	-0.32
DPEPO	10	0.06±0.02	0.94	-0.41

<sup>a</sup>anisotropy factor; <sup>b</sup> fraction of horizontal dipole ( $\theta_h = 1-a$ ); <sup>c</sup> orientation order parameter ( $S = (3a-1)/2$ ).

**ICzTRZ**'s excellent horizontal orientation of its TDM is most likely caused by its high MW of 1095.45 g mol<sup>-1</sup> and relatively thin structure with  $z_E$  of 8.69 Å. The effect that different host materials have on the anisotropy factor of the emitter can also be observed (**Table 6**). Host materials able to suppress diffusion phenomena during film deposition seem to have had a positive effect on the orientation of the material, despite **ICzTRZ** being a high MW emitter (MW > 600 g mol<sup>-1</sup>). Hosts with higher MW and  $T_g$  like DPEPO and mCBP yielded the best  $a$  values, while the lighter mCP led to slightly worse orientation. The length ratio between emitter and host is above the observed threshold of  $x_E/x_H > 1.3$ , observed to be needed to achieve  $a < 0.1$ , but it seems that its influence is downplayed by the MW and  $T_g$ 's, as mCP presented the highest  $x_E/x_H$  and the worst  $a$ .

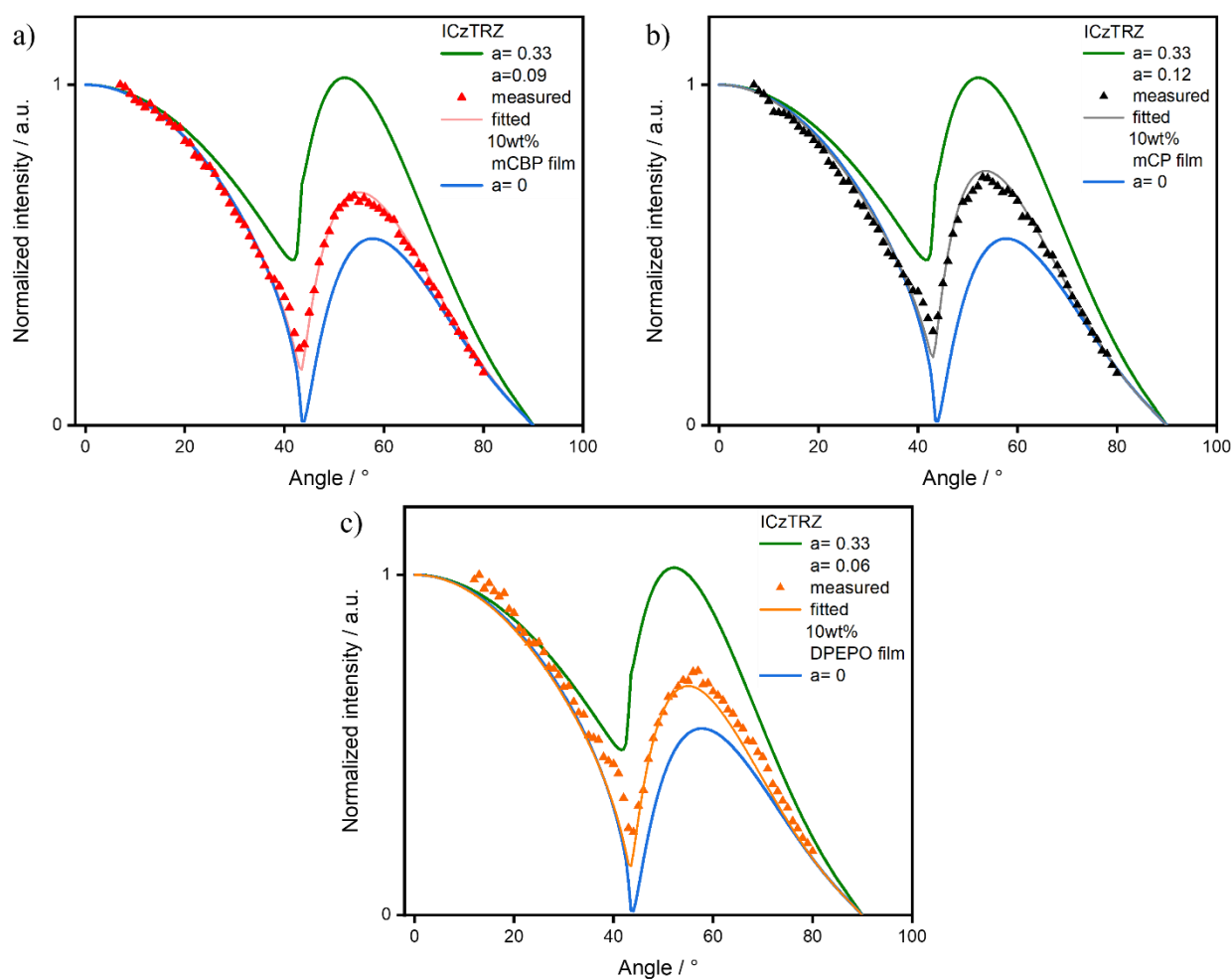


**Figure 53.** Angle-resolved photoluminescence measurement of evaporated films of 10 wt% **ICzTRZ** in a) mCBP, b) mCP, c) DPEPO. The light red/grey/orange lines show a fit using the dipole emission model, yielding the anisotropy factor,  $a$  (data taken at  $\lambda_{PL} = 500$  nm)

**Table 6.** Host materials' properties that influenced the orientation of **ICzTRZ** in evaporated films.

Host	Doping / wt%	$a$	MW	$T_g / ^\circ\text{C}$	$\chi_E/\chi_H$
mCBP	10	$0.09 \pm 0.02$	484.6	92	1.86
mCP	10	$0.12 \pm 0.01$	408.5	65	2.22
DPEPO	10	$0.06 \pm 0.02$	570.56	93	1.88

### 2.3.5 - OLED devices

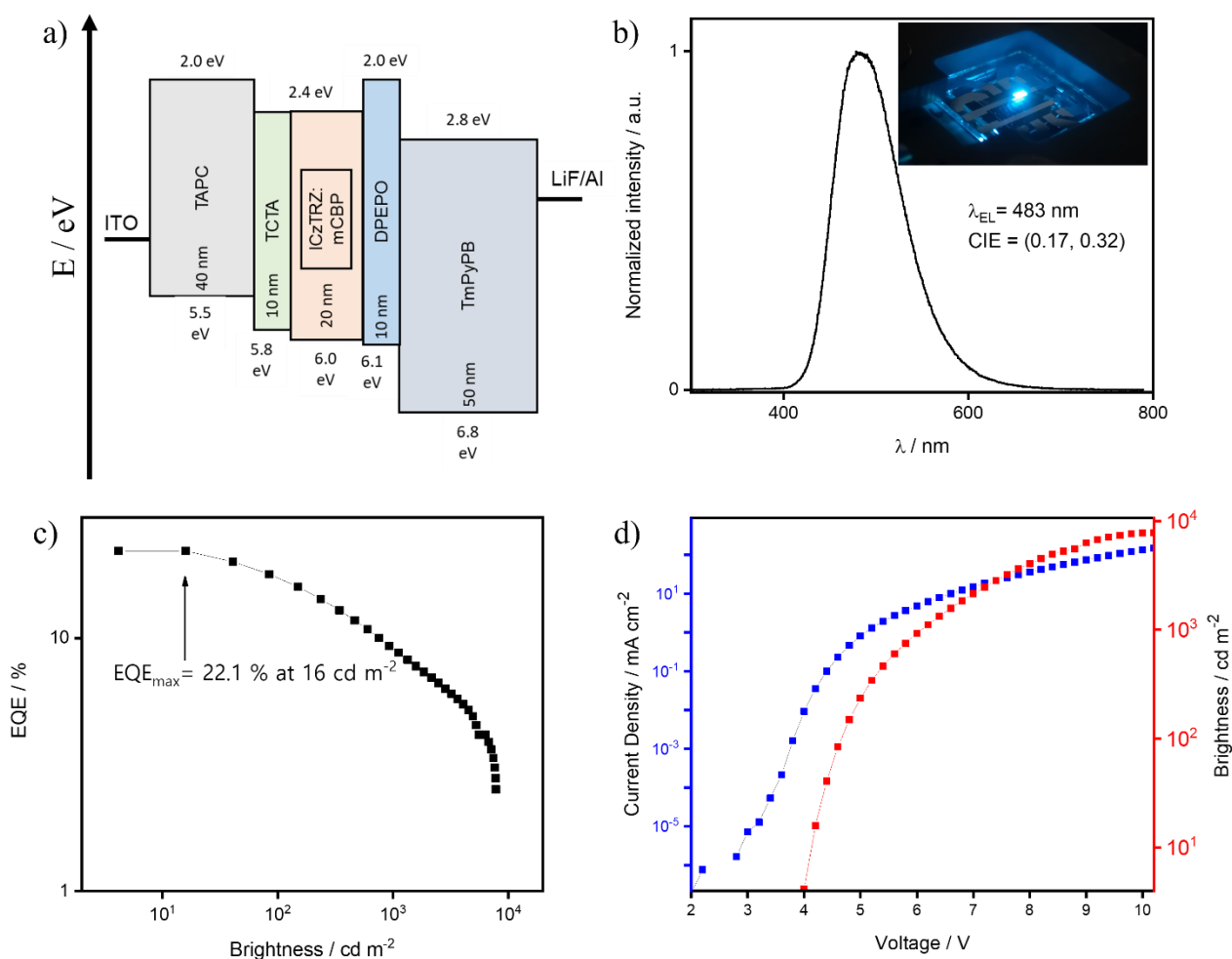


**Figure 54.** ICZTR's OLED device data, **a)** Device stack with HOMO and LUMO energy level of the different materials; **b)** electroluminescence spectra; **c)** external quantum efficiencies (EQE) vs brightness; **d)** current density vs voltage versus brightness curves.

While **DPEPO** was the host material that yielded the highest degree of horizontal orientation, the  $\Phi_{\text{PL}}$  of **ICzTRZ** in it is quite low, at 35%. **mCBP** offered the best compromise between high  $\Phi_{\text{PL}}$  and low  $\alpha$ , and it was then chosen as the host material for the device (**Figure 54**). OLEDs were fabricated and tested by Dr. Paloma Lay Dos Santos in the Ifor Samuel group at the University of St Andrews (**Chapter 2 – Paragraph 2.1 – Attributions**), with the optimized structure ITO/TAPC (40 nm)/TCTA (10 nm)/5 wt% **ICzTRZ:mCBP** (20 nm)/(DPEPO) (10 nm)/TmPyPb (50 nm)/LiF (0.6 nm)/Al (100 nm). ITO is the semitransparent anode, TAPC and TCTA act as hole transport layers, **mCBP** is the host, DPEPO is the hole blocking layer, TmPyPB acts as the electron transport material and LiF modifies the work function of the aluminum cathode.

The device shows (

**Table 7)** an electroluminescence spectrum with a  $\lambda_{EL}$  at 483 nm, corresponding to CIE coordinates of 0.17, 0.32. The  $EQE_{max}$  at  $16 \text{ cd m}^{-2}$  is 22.1%. At luminance values of  $100 \text{ cd m}^{-2}$ , and  $1000 \text{ cd m}^{-2}$  the EQE decreases quite significantly to  $EQE_{100}$  of 17.3%, and  $EQE_{1000}$  of 9.1%. The OLED possesses a low turn-on voltage of  $\sim 3.5 \text{ V}$  and high brightness level of  $7805 \text{ cd/m}^2$ .

$$EQE = \gamma \eta_r \Phi_{PL} \eta_{out} \quad (57)$$

By using the  $EQE_{max}$  value of 22.1% and  $\Phi_{PL}$  of 70%, and assuming that both the charge carrier balance  $\gamma$  and the radiative exciton fraction are 1, the outcoupling efficiency was inferred to be 31%. The high outcoupling value implies that the horizontal orientation of the material is retained in the evaporated EML layer of the device. This was further confirmed by optical simulations of the device EQE (**Figure 55**), carried out by Prakhar Sahai from the Wolfgang Brütting group (**Chapter 2 – Paragraph 2.1 – Attributions**). Using the measured  $\Phi_{PL}$ ,  $a$ , and the optical constant of the given OLED stack, an  $EQE_{max}$  of 21% was predicted, very close to the experimental results. Moreover, for a  $\Phi_{PL}$  of 70%,  $EQE_{max}$  above 20% would only be possible if **ICzTRZ** presented high horizontal orientation in the emissive layer, as otherwise, the efficiency would have been around  $\sim 15\%$ , meaning that the emitter presents high horizontal orientation in the device as well.

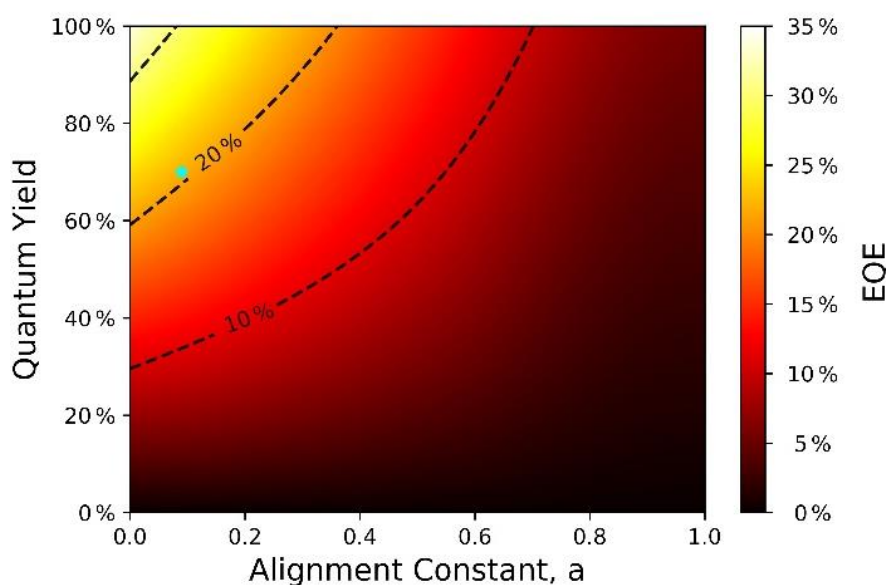


**Figure 55.** Simulated device efficiency of **ICzTRZ**'s OLED device (green dot).

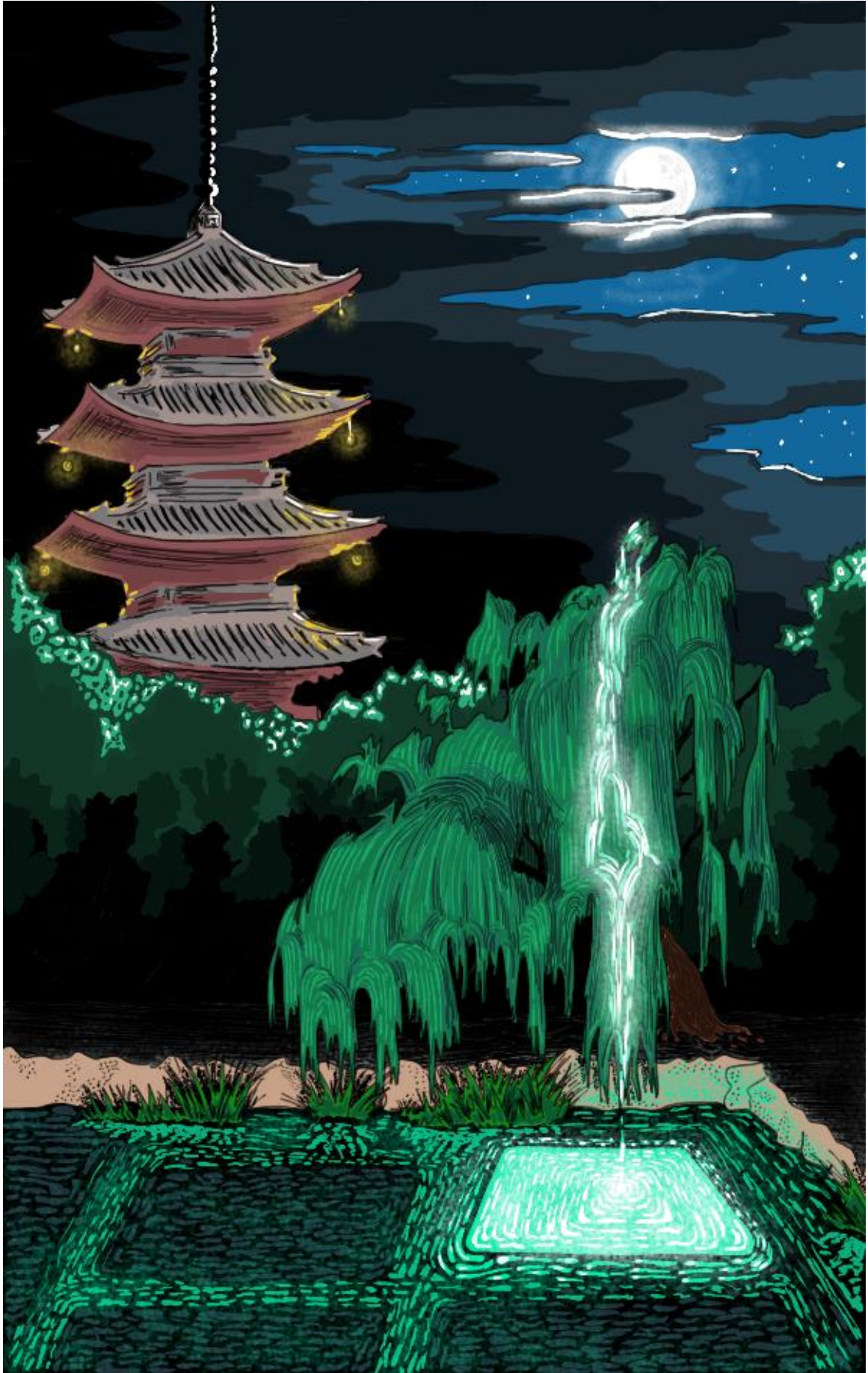
**Table 7.** ICzTRZ's device properties.

Device	V <sub>on</sub> <sup>a</sup> / V	EQE <sub>max</sub> <sup>b</sup> / %	EQE <sub>100</sub> <sup>bc</sup> / %	EQE <sub>1000</sub> <sup>bc</sup> / %	L <sub>max</sub> <sup>d</sup> / cd/m <sup>2</sup>	CIE (x,y)	λ <sub>EL</sub> <sup>f</sup> / nm
ICzTRZ	3.5	22.1	17.3	9.1	7805	0.17, 0.32	483

<sup>a</sup> V<sub>on</sub>= Turn on voltage; <sup>b</sup> EQE= external quantum efficiency; <sup>c</sup> Subscript 100 and 1000 refer to values taken at 100 cd/m<sup>2</sup> and 1000 cd/m<sup>2</sup>; <sup>d</sup> L = luminance; <sup>e</sup> CIE= Internationale de L'Éclairage coordinates; <sup>f</sup> EL= electroluminescence.

## 2.4 – Conclusions

In this study, the first A-D-A type indolocarbazole-based emitter, **ICzTRZ**, was reported. The emitter was fully characterized and in the optimal host material, mCBP, presented a high Φ<sub>PL</sub> of 70% a temperature dependant delayed component, with a lifetime of 121.1 μs. The most interesting feature of **ICzTRZ** is the almost-complete horizontal orientation of its TDM in all three host matrices tested, which then had a positive effect on the efficiency of the fabricated OLEDs. The excellent horizontal orientation of the material is primarily due to its high MW and low molecular thickness, and secondarily to the host materials helping in preventing diffusion phenomena during film deposition. All these positive properties led to a high-performing sky-blue-emitting device with, an EQE<sub>max</sub> of 22.1%, a λ<sub>EL</sub> of 483 nm (CIE coordinates of 0.17, 0.32), and a high luminance value of 7800 cd/m<sup>2</sup>. While the efficiency of **ICzTRZ** didn't manage to surpass that of the current state of the art blue TADF-OLEDs<sup>140</sup>, the horizontal orientation of its transition dipole moment is amongst the best in the literature.<sup>125,126</sup>

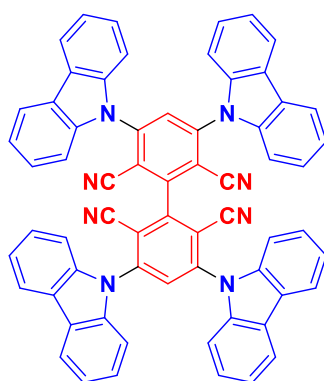


## Chapter 3 - Twin-emitter design strategy to try in achieving horizontal orientation in solution-processed films.

### 3.1 – Attributions

I am the main author of this text. Unless otherwise stated in the text, I directly carried out the experimental work presented. Of the work presented in this section, I performed the theoretical calculations and optoelectronic characterization (CV-DPV, UV-vis, solvatochromism study, and solution and solid state steady-state and time-resolved photoluminescence measurements). The synthesis of the material was done by Dr. Zhen Zhang from the Stefan Bräse group at the Karlsruhe Institute of Technology (KIT). Angle-dependent luminescence spectroscopy to obtain the anisotropy factors, and device simulations, were carried out by Bilal Abbas Naqvi and Prakhar Sahai from the Wolfgang Brütting group at the University of Augsburg. Devices were fabricated and tested by Yoshimasa Wada from the Hironori Kaji group at the University of Kyoto. The paper highlighting this work has been published in *Beilstein J. Org. Chem.*, **2021**, 17, 2894-2905, DOI: [10.3762/bjoc.17.197](https://doi.org/10.3762/bjoc.17.197).

### 3.2 - Introduction



**DDCzIPN**

$\lambda_{\text{PL}}$ : - nm,  $\Phi_{\text{PL}}$ : 91% in toluene  
 $\lambda_{\text{EL}}$ : 497 nm,  $\text{EQE}_{\text{max}}$ : 18.9%  
(vacuum-deposited OLEDs)

-

*Angew. Chem. Int. Ed.*, **2015**, 54, 5201–5204

**Figure 56.** Chemical structure and properties of **DDCzIPN**.<sup>144</sup>



There are several examples in the literature, where the addition of a second emitting unit (twin-emitter design) led to an enhanced molar extinction coefficient of absorption, leading to higher  $\Phi_{\text{PL}}$ .<sup>141–146</sup> Several carbazole-nitrile-based emitters were reported by Lee and coworkers (**Figure 56**), such as **DDCzIPN**,<sup>144</sup> and the **TCzPN** series of emitters.<sup>145</sup> **DDCzIPN** shows an enhanced molar absorptivity of  $3.7 \times 10^5 \text{ M}^{-1} \text{ cm}^{-1}$  (vs  $1.1 \times 10^5 \text{ M}^{-1} \text{ cm}^{-1}$  for **DCzIPN**) and a higher  $\Phi_{\text{PL}}$  of 91% (vs 67% for **DCzIPN**) compared to the single chromophore analog. The improvement was carried over in the fabricated devices, with the OLED with **DDCzIPN** showing a higher  $\text{EQE}_{\text{max}}$  of 18.9% (vs 16.4% for the OLED with **DCzIPN**).

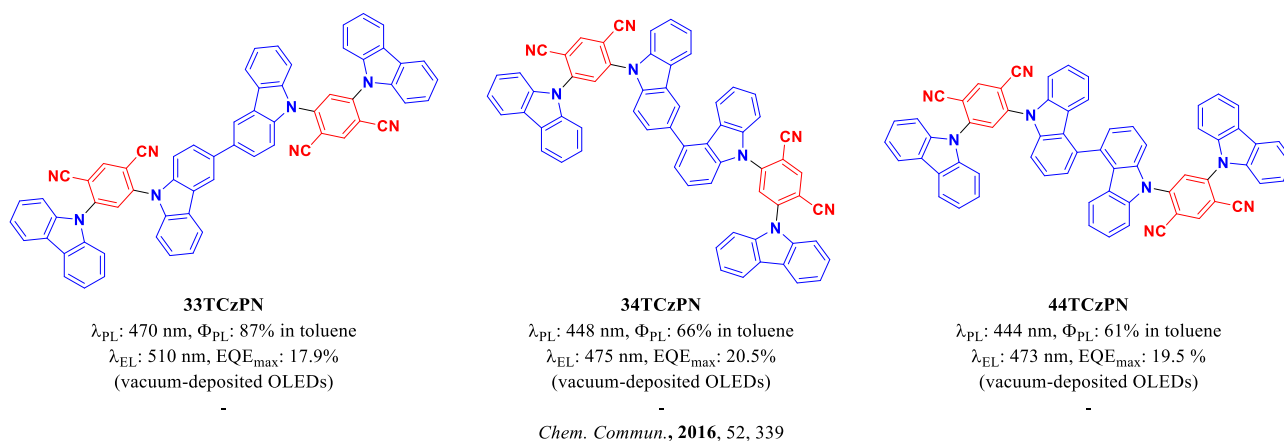
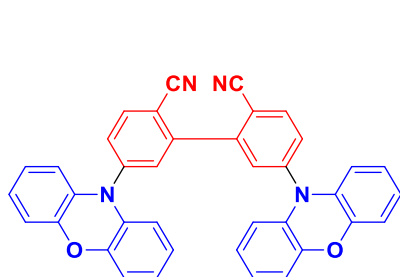


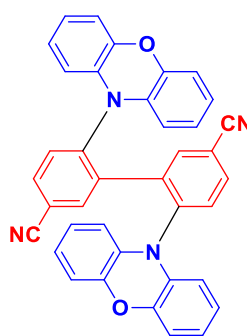
**Figure 57.** Chemical structure and properties of the **TCzPN** series of emitters.<sup>145</sup>

The same group then studied how different connection positions would impact the TADF behavior of the emitters, by developing the three carbazole-nitrile-based emitters **33TCzPN**, **34TCzPN**, and **44TCzPM** (**Figure 57**). The emission color could be tuned depending on the different substitution patterns, with a significant blue-shift in the emission going from **33TCzPN**,  $\lambda_{\text{PL}}$  of 470 nm, to **34TCzPN**, and **44TCzPM**, with  $\lambda_{\text{PL}}$  of 448 nm and 444 nm, respectively. However, this blue shift was accompanied by a decrease in  $\Phi_{\text{PL}}$ , from 87% to 66%, and 61% for **33TCzPN**, **34TCzPN**, and **44TCzPM**, respectively. The electroluminescence spectra behaved similarly to what was observed in the toluene solution, with **33TCzPN** showing green emission at  $\lambda_{\text{EL}}$  of 510 nm, and **34TCzPN**, and **44TCzPM** showing sky-blue emission at  $\lambda_{\text{EL}}$  of 475 nm and 473 nm, respectively. Interestingly, the devices didn't follow the same efficiency trend, with  $\text{EQE}_{\text{max}}$  of 17.9%, 20.5%, and 19.5% for the OLEDs with **33TCzPN**, **34TCzPN**, and **44TCzPM**, respectively. The best efficiency was obtained in the device with **34TCzPN** despite the lower  $\Phi_{\text{PL}}$ . While not explored in the paper, a possible explanation could be in the orientation of the TDM of the material, since the different shapes could lead to more favorable  $x_{\text{E}}$  or  $x_{\text{E}}/x_{\text{H}}$  values.



**2,2'-DPXZ-PN**

$\lambda_{\text{PL}}$ : 532 nm,  $\Phi_{\text{PL}}$ : 67% in 10wt% CBP film  
 $\lambda_{\text{EL}}$ : 524 nm,  $\text{EQE}_{\text{max}}$ : 13.4%  
 (vacuum-deposited OLEDs)



**3,3'-DPXZ-PN**

$\lambda_{\text{PL}}$ : 523 nm,  $\Phi_{\text{PL}}$ : 82% in 10wt% CBP film  
 $\lambda_{\text{EL}}$ : 518 nm,  $\text{EQE}_{\text{max}}$ : 14.9%  
 (vacuum-deposited OLEDs)

*J. Mater. Chem. C.*, **2018**, 6, 11615-11621

**Figure 58.** Chemical structure and properties of the **2,2'-DPXZ-PN** and **3,3'-DPXZ-PN** series of emitters.<sup>146</sup>

Wei *et al.* published two dual-core TADF emitters, **2,2'-DPXZ-PN**, and **3,3'-DPXZ-PN**,<sup>146</sup> (**Figure 58**) where they observed that not only the  $\epsilon$  and  $\Phi_{\text{PL}}$  were improved, but also the thermal stability compared to the single core material, **PXZ-PN**, with decomposition temperatures almost doubled from a  $T_{\text{d}}$  236 °C for **PXZ-PN**, to 481 °C and 402 °C for **2,2'-DPXZ-PN**, and **3,3'-DPXZ-PN**, respectively. The devices fabricated with these materials showed green emission at  $\lambda_{\text{EL}}$  of 524 nm and 518 nm, with corresponding  $\text{EQE}_{\text{max}}$  of 13.4% and 14.9% for **2,2'-DPXZ-PN**, and **3,3'-DPXZ-PN**, respectively.

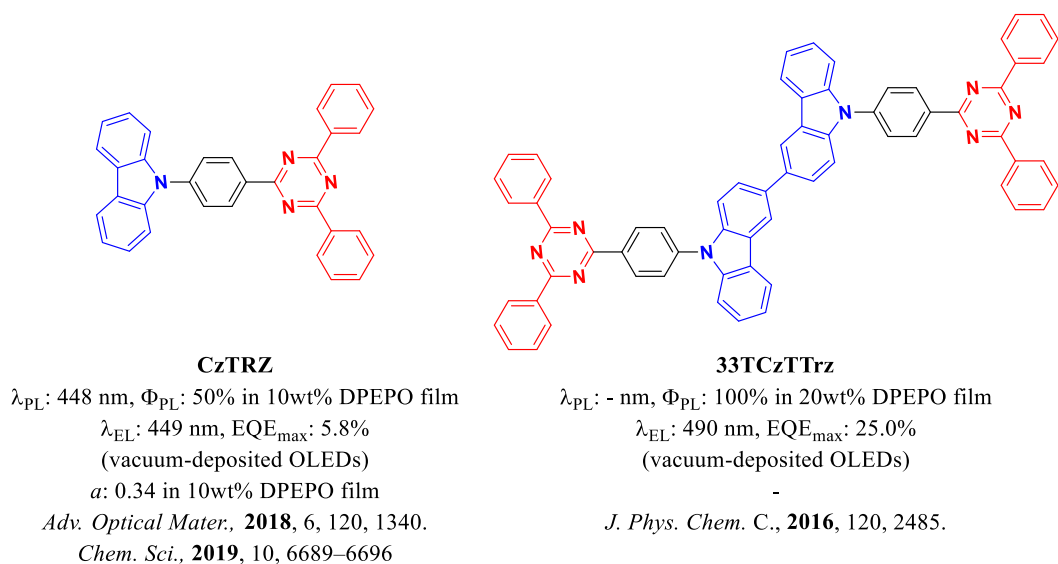


**Figure 59.** Chemical structure and properties of the **CzTRZ** and **33TCzTTrz**.<sup>147</sup>

The dual-emitter design also managed to turn a non-TADF molecule like **CzTRZ**<sup>126,132</sup> where the device showed low efficiency ( $\text{EQE}_{\text{max}}$  of 5.8%) into a much superior TADF emitter, **33TCzTTrz**<sup>147</sup> (**Figure 59**), with a much more efficient OLED with an  $\text{EQE}_{\text{max}}$  of 25.0%. However, a red-shift in the electroluminescence spectrum was observed, with  $\lambda_{\text{EL}}$  going from 449 nm for **CzTRZ** to 490 nm for **33TCzTTrz**.

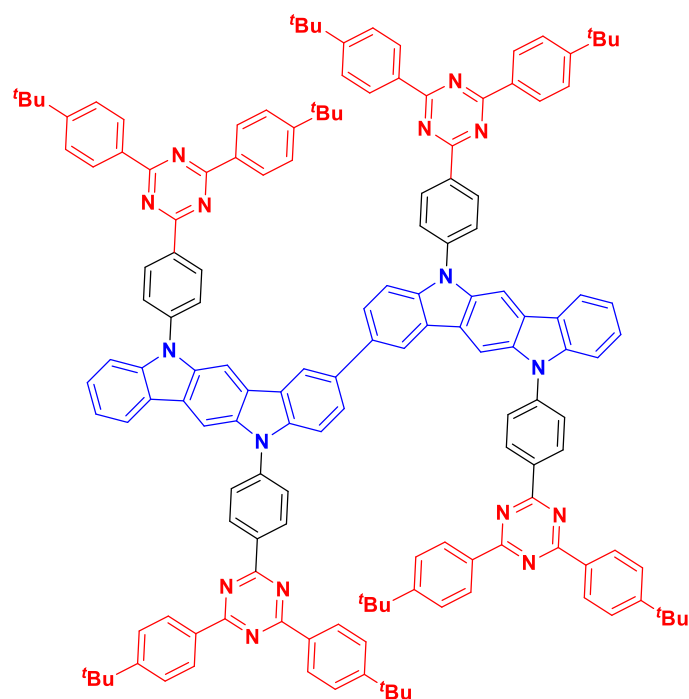


**Figure 60.** Chemical structure of **DICzTRZ**.

The material highlighted in this section, **DICzTRZ (Figure 60)** was designed with the aforementioned twin-emitter strategy in mind, in order to try and further improve the performance of **ICzTRZ**. However, as an already high MW we would be doubled, the evaporation of the material would become impossible leading to the necessity for solution processing of the emitting layer of the device. **ICzTRZ**'s best feature was the almost-total horizontal orientation in evaporated film, but solution-processed films tend to present isotropic orientation<sup>122</sup> due to the molecule being able to rearrange itself thanks to the slower deposition times and a higher degree of freedom of movement. However, it has been previously documented that polymers and other high MW materials can present some degree of horizontal orientation even from a solution-processed film.<sup>148,149</sup> Therefore, besides trying to improve the efficiency of **ICzTRZ**, the twin-emitter design will also allow us to investigate the effect of the higher MW on the orientation of solution-processed films.

Solution processing of the emissive layer in OLED devices can make the fabrication of OLEDs simpler and more cost-efficient to fabricate. Unfortunately, solution-processed devices employing small molecules usually underperform when compared to the vacuum-deposited alternative, as it's easier for them to crystallize during the manufacturing of the layer, thus achieving worse film-morphology.<sup>150–153</sup>

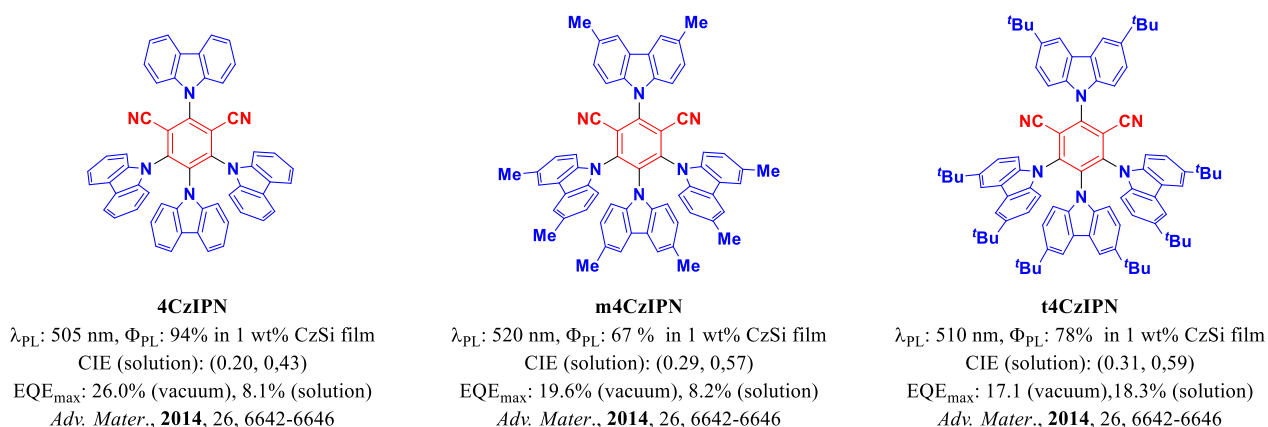


**Figure 61.** Chemical structure and properties of **4CzIPN**, **m4CzIPN**, and **t4CzIPN**.<sup>154</sup>

A good comparison between vacuum-deposited and solution-processed devices was made by Cho *et al.* by comparing the effect that the different manufacturing techniques had on the efficiency of the OLEDs of **4CzIPN**, **m4CzIPN**, and **t4CzIPN (Figure 61)**.<sup>154</sup> CzSi was chosen as the host material as its amorphous nature and high glass transition temperature prevent crystallization during the spin-coating process.<sup>155</sup>  $\Phi_{\text{PL}}$  in CzSi doped film are 94%, 67%, and 78% with  $\lambda_{\text{PL}}$  of 505 nm, 520 nm, and

510 nm for **4CzIPN**, **m4CzIPN**, and **t4CzIPN**, respectively. While the  $\Phi_{\text{PL}}$  results show a decrease in efficiency with the addition of the methyl and *tert*-butyl groups, AFM, which was used to study the morphology of the film, revealed that *tert*-butyl groups led to more stable films by preventing the formation of aggregates in the film. A comparative study between vacuum-deposited and solution-processed devices was then carried out. The  $\text{EQE}_{\text{max}}$  of the OLED with **4CzIPN** drops from 26.0% to 8.1%. Methyl groups had little to no effect on the efficiency of the device with **m4CzIPN**, and the vacuum-deposited counterpart showed much better results, with an  $\text{EQE}_{\text{max}}$  of 19.5% vs the 8.2% obtained for the solution-processed device. The addition of *tert*-butyl groups instead improves massively the results of the solution-processed device, leading to a solution-processed OLED with comparable efficiency to the vacuum-deposited device (17.1% for the vacuum-deposited device and 18.3% for the solution-processed device). As in the doped film, the electroluminescence spectra were red-shifted by the addition of the electron-donating solubilizing groups, with CIE coordinates of (0.20, 0.43), (0.29, 0.57), and (0.31, 0.59) for **4CzIPN**, **m4CzIPN** and **t4CzIPN**, respectively.

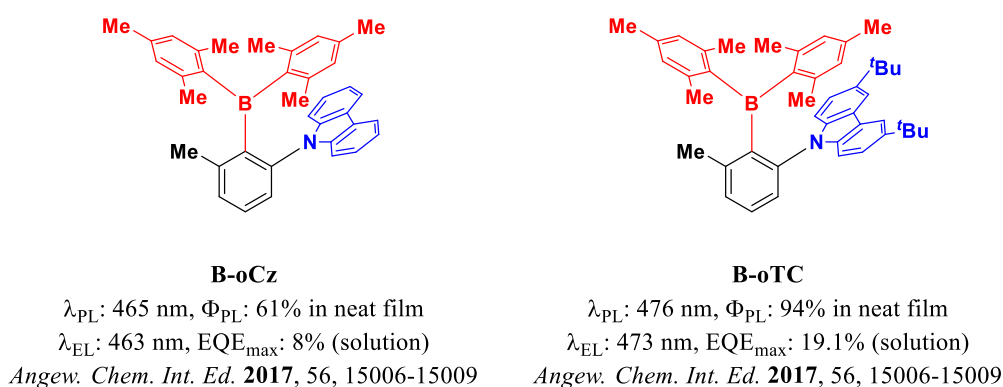


**Figure 62.** Chemical structure and properties of **B-oCz**, and **B-oTC**.<sup>156</sup>

The same strategy of adding solubilizing groups to improve the properties of solution-processed devices was used by Chen *et al.*,<sup>156</sup> who managed to significantly improve the efficiency of charge-transfer type TADF-OLEDs. The two emitters **B-oCz** and **B-oTC** (**Figure 62**) were studied in neat film and presented, respectively,  $\Phi_{\text{PL}}$  values of 61%, and 94% at  $\lambda_{\text{PL}}$  of 465, and 476, clearly showing that the self-quenching at high concentrations is suppressed by the addition of the *tert*-butyl groups. The OLEDs fabricated with these materials followed the same trend, with an efficiency that is improved by the addition of the *tert*-butyl groups, with  $\text{EQE}_{\text{max}}$  values rising from 8.0%, for **B-oCz**, to 19.1%, for **B-oTC**, at  $\lambda_{\text{EL}}$  of 463 nm (CIE: 0.15, 0.17), and 473 nm (CIE: 0.15, 0.26), respectively.

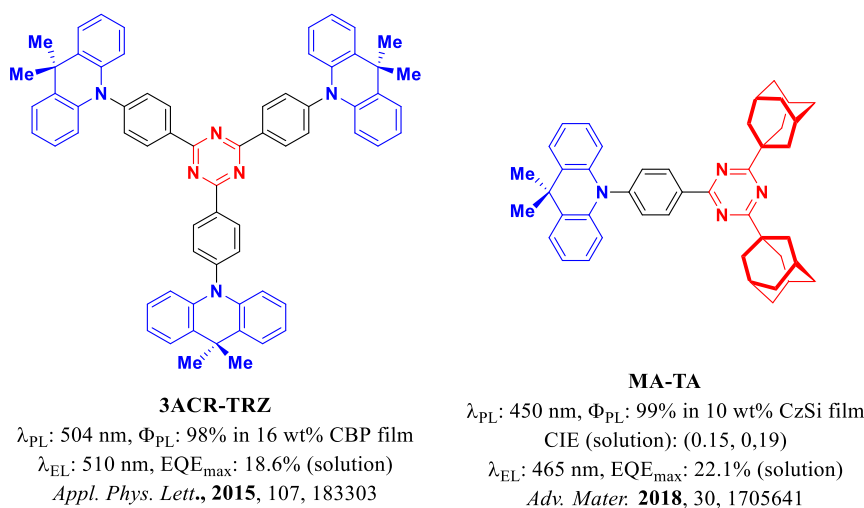


**Figure 63.** Chemical structure and properties of **3ACR-TRZ**, and **MA-TA**.<sup>157</sup>

Acridine-triazine-based emitters, used in efficient solution-processed devices, have been reported by Wada *et al.* (**Figure 63**). The emitter **3ACR-TRZ**<sup>157</sup> showed a near unity  $\Phi_{\text{PL}}$  of 98%, at  $\lambda_{\text{PL}}$  of 504 nm in 16 wt% CBP doped film. The solution-processed OLED achieved a high  $\text{EQE}_{\text{max}}$  of 18.6%, showing a slight red-shift in the emission compared to the PL, with  $\lambda_{\text{EL}}$  of 510 nm. Another example of an acridine-triazine TADF employed in highly efficient solution-processed OLED is **MA-TA**,<sup>73</sup> also reported by Wada *et al.*. The substitution with adamantly allows an improved solubility of the material and achieves a deeper blue color. The material presents a 99%  $\Phi_{\text{PL}}$ , with pure blue emission at 450 nm, in a 10 wt% doped CzSi film. **MA-TA** was then employed in a solution-processed OLED, which retained the pure-blue emission at  $\lambda_{\text{EL}}$  of 465 nm (CIE: 0.15, 0.19), and achieved an  $\text{EQE}_{\text{max}}$  of 22.1%.

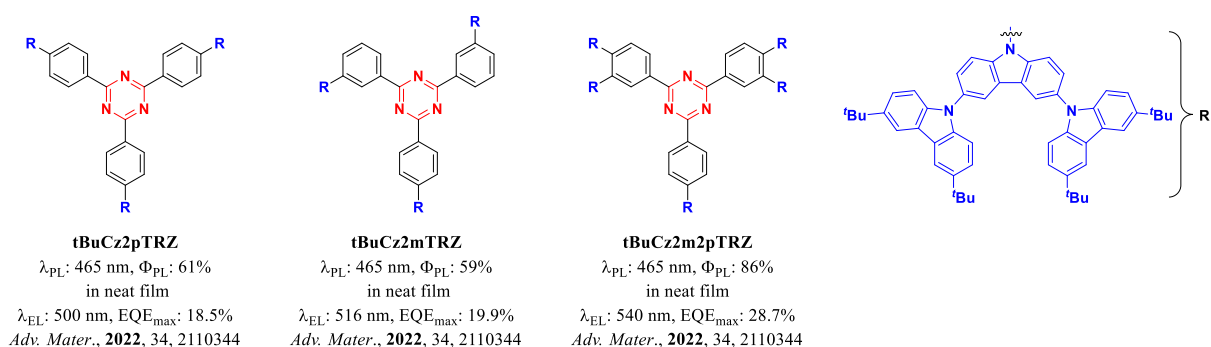


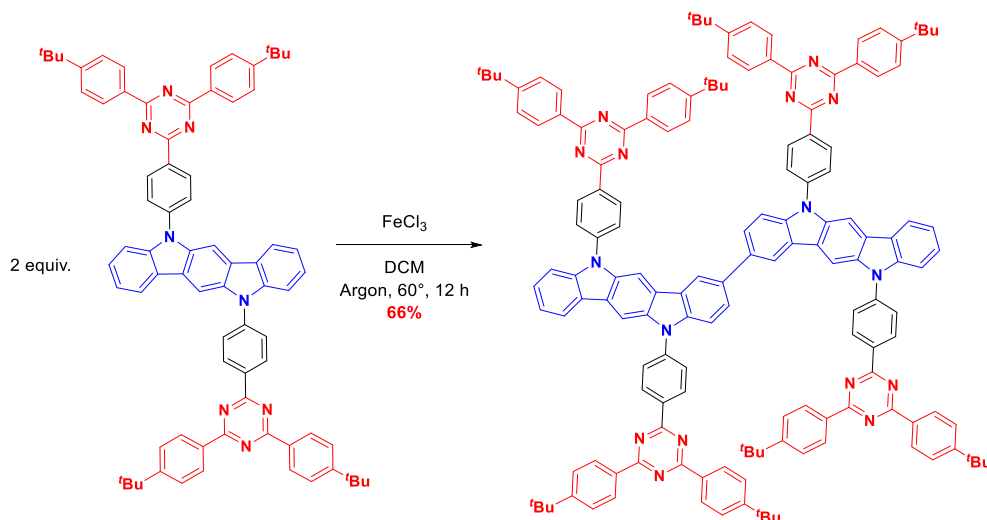
**Figure 64.** Chemical structures and properties of **tBuCz2pTRZ**, **tBuCz2mTRZ**, and **tBuCz2m2pTRZ**.<sup>158</sup>

Dendrimers have been used as a possible solution to avoid crystallization during spin-coating by Sun *et al.*, with three carbazole-triazine-based TADF emitters, **tBuCz2pTRZ**, **tBuCz2mTRZ**, and **tBuCz2m2pTRZ** (Figure 64).<sup>158</sup> Photophysical investigation of these materials in neat film showed emission at  $\lambda_{\text{PL}}$  of 481 nm, 483 nm, and 520 nm, with  $\Phi_{\text{PL}}$  of 61%, 59%, and 86% for **tBuCz2pTRZ**, **tBuCz2mTRZ**, and **tBuCz2m2pTRZ**, respectively. The presence of multiple donor units in **tBuCz2m2pTRZ** led to a much higher density of low-lying excited states, which enhanced the RISC process and also suppressed concentration quenching. The OLEDs fabricated with **tBuCz2pTRZ**, **tBuCz2mTRZ** showed  $\text{EQE}_{\text{max}}$  of 18.5%, and 19.9%, at  $\lambda_{\text{EL}}$  of 500 nm, and 516 nm, respectively. However, the synergic effect of the multiple *tert*-butyl carbazole in **tBuCz2m2pTRZ** led to a solution-processed device with an  $\text{EQE}_{\text{max}}$  of 28.7%, but with a slight red-shift in the emission, to  $\lambda_{\text{EL}}$  of 540 nm was observed.

By taking an overview of these reports, it can be hypothesized that the large molecular structure of **DICzTRZ** might lead to good film morphology, and consequently an efficient solution-processed device. Also, as reported by Sun *et al.*,<sup>158</sup> the dimer design could lead to a higher density of triplet states, thus making for a more efficient RISC process.

### 3.3 - Results and discussion

#### 3.3.1 - Synthesis



**Scheme 2.** Synthetic route to **DICzTRZ**.

The synthesis of the material was done by Dr. Zhen Zhang, from the Stefan Bräse group at the Karlsruhe Institute of Technology (KIT) (**Chapter 3 – Paragraph 3.1 – Attributions**). **DICzTRZ**, was obtained *via* a one-step synthesis, starting from **ICzTRZ** (**Scheme 2**). A solution of **ICzTRZ** in DCM was slowly added to a solution of FeCl<sub>3</sub>, under an Argon flow. The mixture was stirred at 60 °C for 12 h to afford **DICzTRZ** in a yield of 66%. The emitter was fully characterized by <sup>1</sup>H NMR and <sup>13</sup>C NMR spectroscopy, Mp determination, IR spectroscopy, and MS (MALDI-TOF). I tried to grow crystals of the material in order to observe its structure *via* X-ray diffraction but I was unsuccessful.

#### 3.3.2 - Theoretical calculations

The same computational methodologies employed for **ICzTRZ** were used to assess if **DICzTRZ** could be a viable TADF material (**Figure 65**). **DICzTRZ** possesses a higher energy HOMO, at -5.03 eV (vs -5.19 eV for **ICzTRZ**), indicating that the twin emitter design strengthened the donor. The LUMO level of **DICzTRZ** and **ICzTRZ** stays almost unchanged, at -1.76 eV and -1.75 eV, respectively, as the triazine acceptor has been left unmodified. **DICzTRZ** possesses S<sub>1</sub> and T<sub>1</sub> levels of 2.64 eV and 2.83 eV, respectively, resulting in a ΔE<sub>ST</sub> of 0.19 eV, close to the ΔE<sub>ST</sub> of **ICzTRZ**, at 0.22 eV. The PDM and TDM of the molecule were calculated to be 2.09 Debye and 7.60 Debye, respectively. When compared with **ICzTRZ**, the molecule presents a much stronger PDM in the ground state (0.3 Debye for **ICzTRZ**) while the TDM is slightly lower (7.90 Debye for **ICzTRZ**).



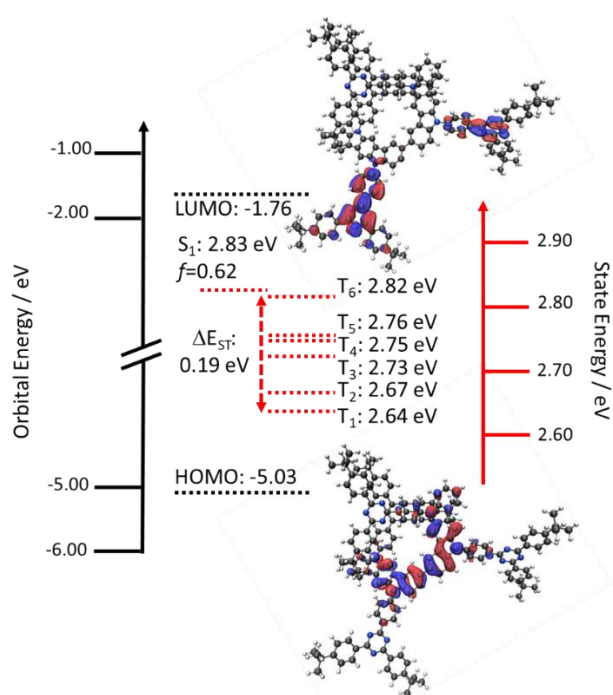


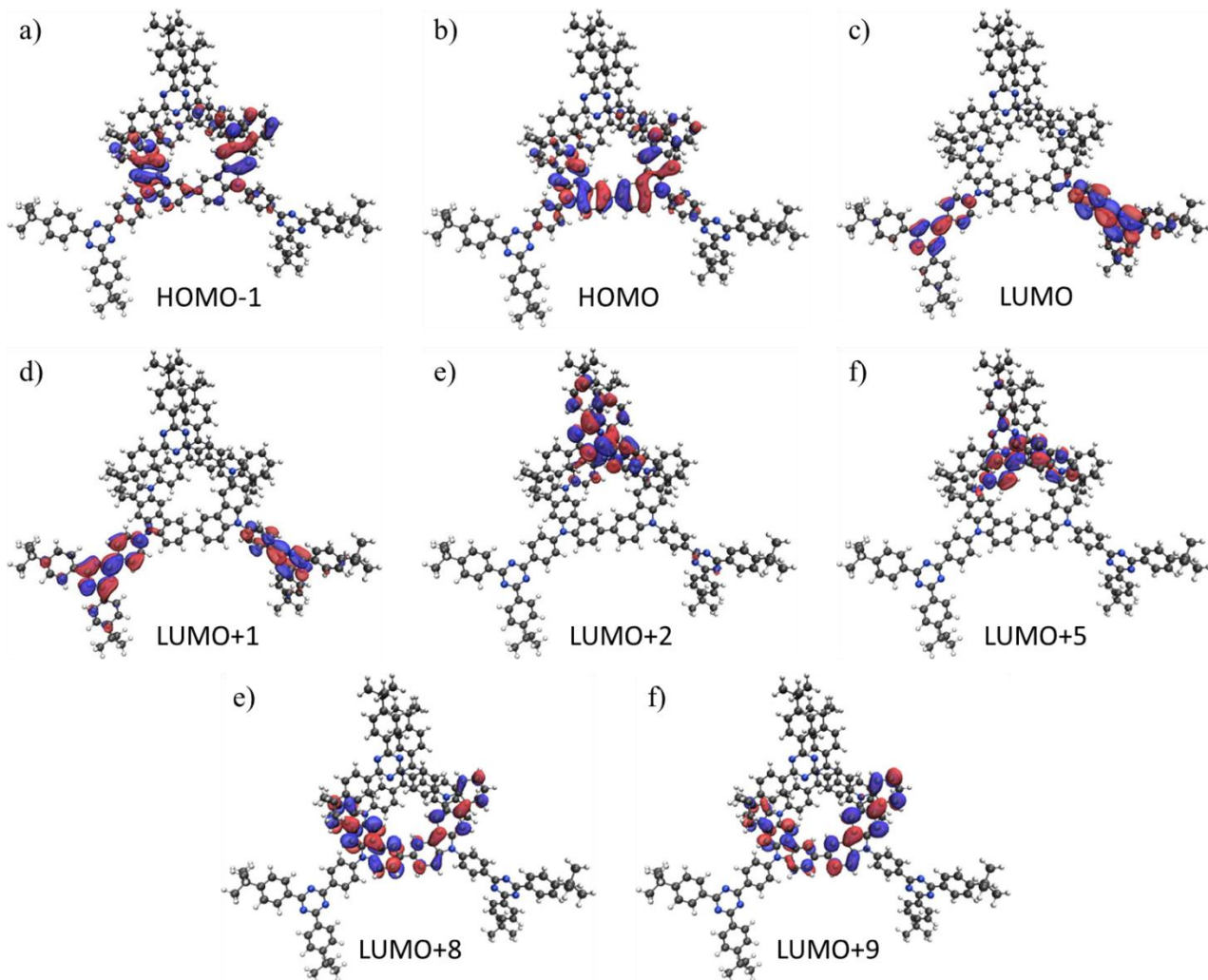
**Figure 65.** HOMO and LUMO electron density distributions and energy levels, excited state energy levels of **DICzTRZ**. (Obtained via DFT and TD-DFT at the PBE0/6-31G(d,p), Isovalue for new surfaces: MO=0.02, Density=0.0004).

The twin emitter design led to an increased number of intermediate triplet states, as reported by Sun *et al.*, which should lead to an enhanced RISC process. The nature of the excited state was then investigated. **DICzTRZ** presents a varied excited state landscape with both CT (T<sub>1</sub>, T<sub>2</sub>, T<sub>5</sub>, and T<sub>6</sub>) and LE (T<sub>3</sub>, and T<sub>4</sub>) triplet states, which as previously mentioned, can be beneficial to reduce the efficiency roll-off of eventual OLEDs.

**Table 8.** Excited states properties of **DICzTRZ**.

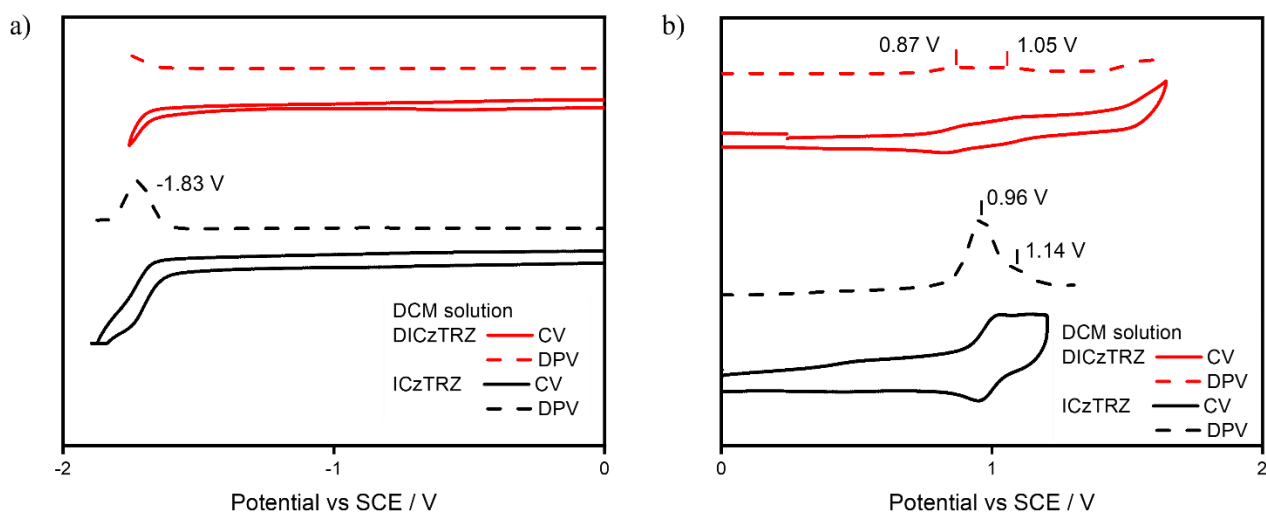
<b>Excited State<sup>a</sup></b>	<b>Energy / eV</b>	<b>Nature<sup>b</sup></b>	<b>Character of the transition</b>
<b>T<sub>1</sub></b>	2.64	<b>H→L (71%)</b> (H-5)→(L+1) (3%) H→(L+10) (2%) (H-1)→(L+1) (12%)	<sup>3</sup> CT
<b>T<sub>2</sub></b>	2.67	<b>H→(L+1) (67%)</b> (H-5)→L (3%) (H-1)→(L+1) (3%) (H-1)→L (16%)	<sup>3</sup> CT
<b>T<sub>3</sub></b>	2.73	<b>H→(L+8) (61%)</b> (H-1)→(L+8) (6%) (H-1)→(L+9) (22%)	<sup>3</sup> LE (DICz)
<b>T<sub>4</sub></b>	2.75	<b>H→(L+9) (43%)</b> (H-1)→(L+2) (2%) H→(L+7) (2%) H→(L+2) (13%) (H-1)→(L+8) (21%)	<sup>3</sup> LE (DICz)
<b>T<sub>5</sub></b>	2.76	<b>H→(L+2) (38%)</b> H→(L+9) (13%) (H-1)→(L+6) (3%) (H-1)→(L+5) (2%) (H-4)→(L+2) (2%) H→(L+5) (2%) (H-1)→(L+8) (5%) H→(L+6) (6%) (H-1)→(L+2) (10%)	<sup>3</sup> CT
<b>T<sub>6</sub></b>	2.82	H→(L+5) (50%) <b>(H-1)→(L+5) (11%)</b> H-1→(L+2) (9%) H→(L+2) (5%) (H-4)→(L+5) (4%)	<sup>3</sup> CT
<b>S1 (f=0.62)</b>	2.83	<b>H→L (88%)</b> (H-1)→(L+1) (7%)	<sup>1</sup> CT

<sup>a</sup> (PBE0/6-31G(d,p)); <sup>b</sup> the transitions highlighted in red are the main ones contributing to the excited state character.



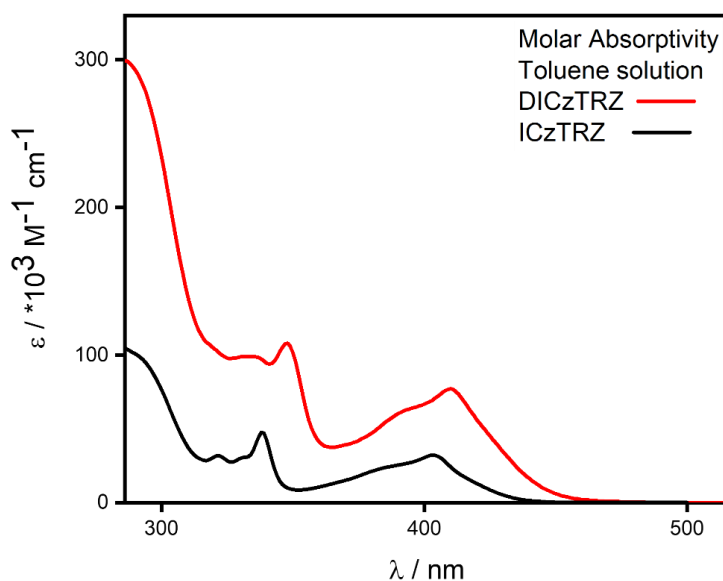
**Figure 66.** Electronic density surfaces of a) HOMO-1, b) HOMO, c) LUMO, d) LUMO+1, e) LUMO+2, f) LUMO+5, LUMO +8 d) LUMO +9. (Isovalue for surfaces: MO=0.02, Density=0.0004).

### 3.3.3 - Optoelectronic characterization



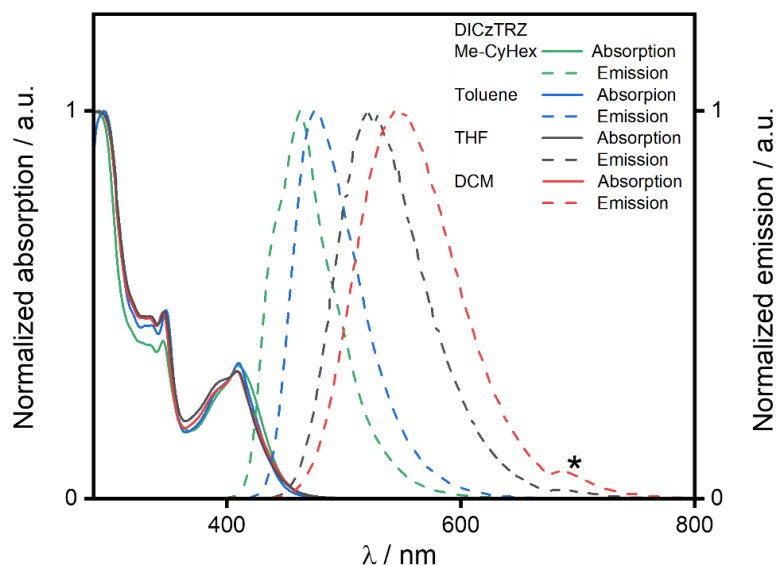
**Figure 67.** Cyclic Voltammetry (CV) and Differential Pulse Voltammetry (DPV) of **DICzTRZ** (red) and **ICzTRZ** (black) in DCM, **a)** reduction scan and **b)** oxidation scan (scan rate = 100 mV/s).

The electrochemical properties of **DICzTRZ** were studied by CV and DPV, with tetra-*n*-butylammonium hexafluorophosphate as the electrolyte and Fc/Fc<sup>+</sup> as the internal reference (**Figure 67**). **DICzTRZ** shows a similar profile to **ICzTRZ**, with two oxidation waves, at 0.87 V, and 1.05 V (obtained from DPV). Unlike **ICzTRZ**, no reduction wave was observed. The HOMO level calculated from the oxidation potential is -5.21 eV, (vs -5.66 eV for **ICzTRZ**), showing that the twin-emitter structure possesses a stronger donor, as predicted by DFT. Both compounds also present a second oxidation wave that is more prominent and cathodically shifted in **DICzTRZ** at 1.05 V compared to 1.14 V for **ICzTRZ**.



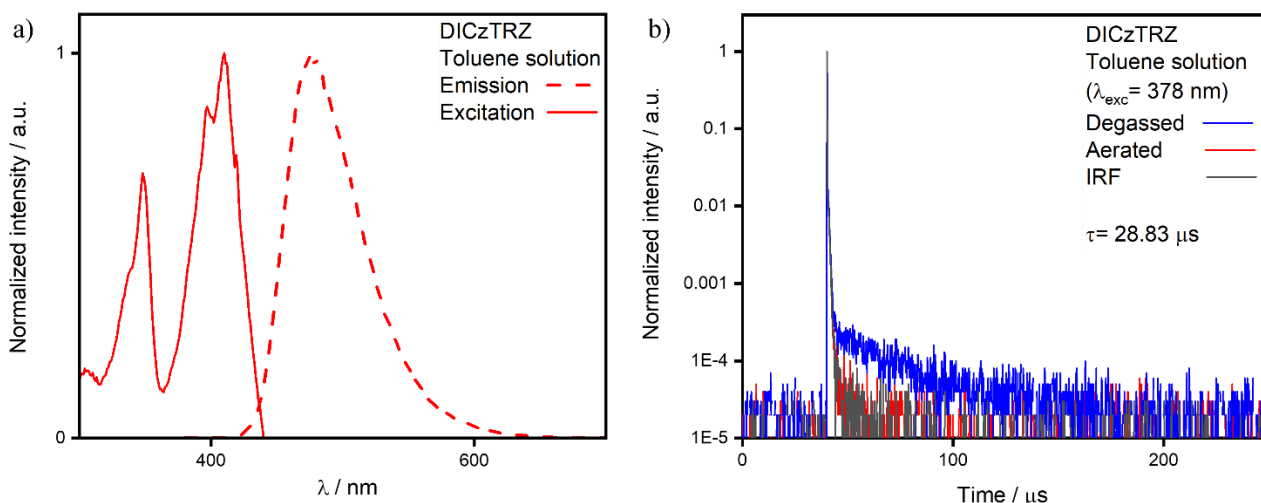
**Figure 68.** UV-vis absorption spectra of **DICzTRZ** (red) and **ICzTRZ** (black) in toluene.

The UV-vis absorption of **DICzTRZ** (**Figure 68**) closely resembles that of **ICzTRZ** and other published indolocarbazoles materials.<sup>65</sup> The addition of a secondary emitting unit slightly red-shifted the absorption spectrum of **DICzTRZ**, and as expected from what is reported in the literature,<sup>141–146</sup> the molar absorptivity of the dimer is much higher than the monomer **ICzTRZ**, with  $\epsilon$  of  $31,700 \text{ M}^{-1} \text{ cm}^{-1}$  and  $76,900 \text{ M}^{-1} \text{ cm}^{-1}$  (for the band at around 400 nm) for **DICzTRZ** and **ICzTRZ**, respectively. This is much higher than the expected value, which should be double the molar absorptivity of the monomer. This could be caused by intramolecular electronic interactions between the two indolocarbazole units,<sup>159</sup> which could also be responsible for the slight red-shift of the absorption profile of **DICzTRZ**. Moreover, despite the DFT calculations identifying the transition at 400 nm as CT in nature, their molar absorptivity are high for a CT type band. As the profiles are identical, it was concluded that transitions would have the same characters as those observed from **ICzTRZ**, with the two LE (on the indolocarbazole donor) absorption bands between 330 and 350 nm, and the two lower energy and lower absorptivity CT bands at 390 nm and 410 nm (attempts to undertake the DFT calculations weren't successful due to the large size of the molecule).



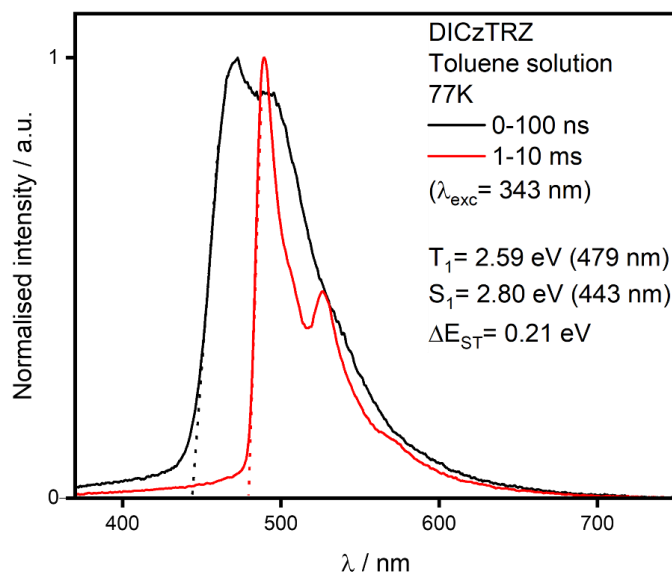
**Figure 69.** Absorption and emission spectra of **DICzTRZ** in different solvents ( $\lambda_{\text{exc}} = 340 \text{ nm}$ , \* = second harmonic of the excitation source).

The absorption spectra of **DICzTRZ** are not affected by the polarity of different solvents as it can be seen by overlapping them (**Figure 69**). The typical redshift of the emission in more polar environments is observed in the PL spectra, characteristic of a CT-type transition, with  $\lambda_{\text{PL}}$  going from 462 nm in methyl-cyclohexane to 548 nm in dichloromethane. The  $E_{\text{gap}}$  level of the material was obtained from the intersection of the normalized absorption and emission spectra in DCM, with a value of 2.71 eV. By then adding it to the HOMO level, obtained from DPV, the LUMO level of the material was calculated to be -2.50 eV. This value is very different from the one obtained from DFT calculations (-1.76 eV), again caused by the different environment that the theoretical calculations are carried out.



**Figure 70.** **a)** Emission and excitation spectra of **DICzTRZ** ( $10^{-5}$  M toluene solution,  $\lambda_{\text{exc}} = 340$  nm); **b)** time-resolved fluorescence decay of degassed and aerated solutions of **DICzTRZ** (Toluene,  $10^{-5}$  M solutions,  $\lambda_{\text{exc}} = 378$  nm, the delayed fluorescence decay was measured by MCS).

The photophysical behavior of **DICzTRZ** was then analyzed, starting in degassed  $10^{-5}$  M toluene solution (**Figure 70**). **DICzTRZ** shows a  $\lambda_{\text{PL}}$  of 477 nm, redshifted compared to **ICzTRZ** ( $\lambda_{\text{PL}}$  of 462 nm) and the excitation spectrum coincides with the UV-vis absorption profile (**Figure 68**). The time-resolved PL decay of **DICzTRZ** under degassed conditions shows prompt and delayed fluorescence lifetimes of 8.94 ns and 28.83  $\mu\text{s}$ , respectively, both showing a monoexponential decay. The solution was aerated, and the complete disappearance of the delayed component was observed, confirming the involvement of triplet states in the PL behavior of **DICzTRZ**. The prompt fluorescence is also affected by oxygen, with a shortening of its lifetime to  $\tau_{\text{p}}$ , of 6.80 ns, showing a small degree of singlet state quenching caused by the oxygen. The prompt component of **DICzTRZ** is comparable to that of **ICzTRZ**, which itself presented a prompt component of 9.0 ns, while the delayed component lifetime of **DICzTRZ** is one order of magnitude shorter than that of **ICzTRZ** (28.83  $\mu\text{s}$  for **DICzTRZ** vs 229.2 ms for **ICzTRZ**). This indicates a much more efficient RISC process for the dimer, which can be attributed to the much higher concentration of intermediate triplet states, caused by the twin emitter design. While the RISC process seems to be improved, the  $\Phi_{\text{PL}}$  of **DICzTRZ** is slightly lower than **ICzTRZ**, with a value of 60% (vs 72% for the monomer) that decreased to 44% when the solution was exposed to oxygen. This was also expected from DFT calculations, as the oscillator strength of the transition to the  $S_1$  state of **DICzTRZ** is lower than that of **ICzTRZ** ( $f$  of 0.62 for **DICzTRZ** vs 0.72 for **ICzTRZ**).

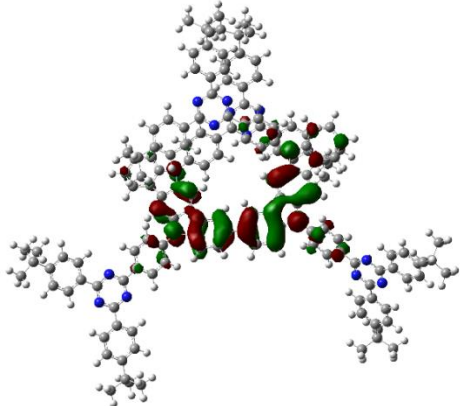
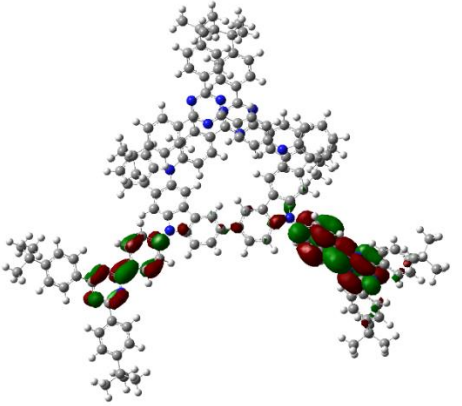
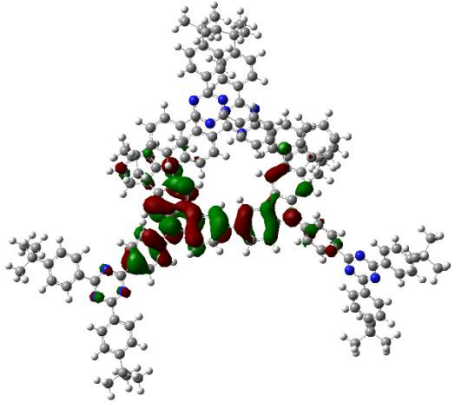
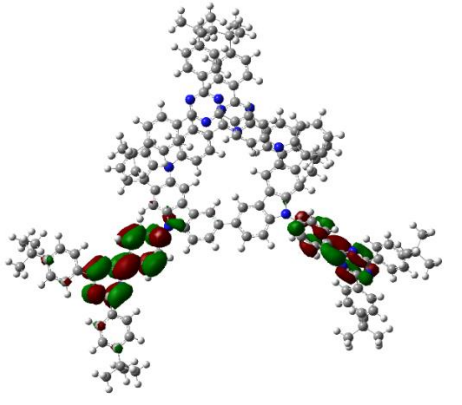
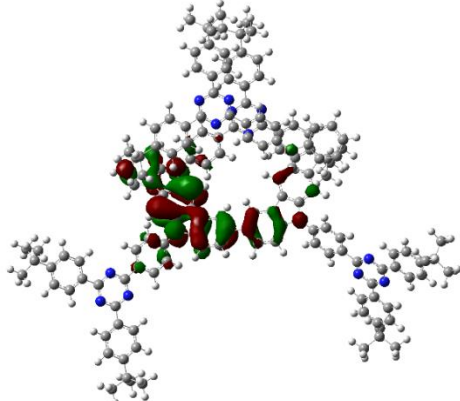
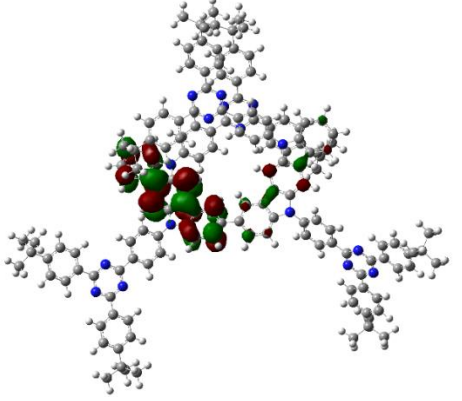


**Figure 71.** Prompt fluorescence and phosphorescence spectra of **DICzTRZ** at 77 K in in  $10^{-5}$  M Toluene glass ( $\lambda_{\text{exc}} = 343$  nm, prompt and delayed fluorescence spectra were obtained over the 0–100 ns and 1–10 ms time ranges, respectively).

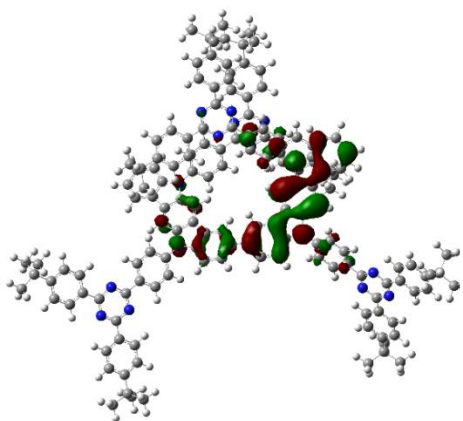
The  $\Delta E_{\text{ST}}$  of **DICzTRZ** was measured with an iCCD camera in toluene glass at 77 K (**Figure 71**), and the value is 0.21 eV, significantly smaller than the 0.32 eV  $\Delta E_{\text{ST}}$  of **ICzTRZ**. **DICzTRZ** and **ICzTRZ** possess comparable  $T_1$  levels at 2.59 eV and 2.62 eV, respectively, while the  $S_1$  level of the dimer is lower in energy at 2.80 eV, vs 2.94 eV in **ICzTRZ**. The smaller  $\Delta E_{\text{ST}}$  of **DICzTRZ** also aligns with the faster delayed fluorescence decay, as the smaller gap between singlet and triplet state should make the RISC process more efficient. The fluorescence spectrum at 77 K has a peculiar shape, with a broad and unstructured peak, typical of a CT type state, but with two well-resolved emission maxima, making it a more likely candidate for a mixed CT-LE type state. The phosphorescence spectrum presents the expected well-defined, sharp peaks typical of LE-type states. From DFT calculations carried out in the gas phase, it is known that the  $T_1$  state is CT in nature. The fact that in the frozen toluene solution the transition has LE character could indicate that we are different conformation of the material than the one predicted by DFT are being looked at, where the  $T_1$  has a CT character.



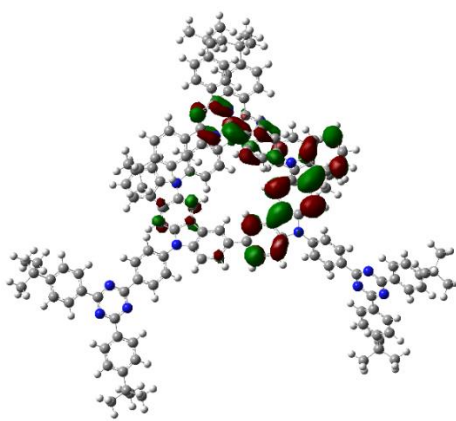
**Table 9.** Electronic density surfaces of NTOs of **DICzTRZ** (Obtained via DFT and TD-DFT at the PBE0/6-31G(d,p), Isovalue for new surfaces: MO=0.02, Density=0.0004).

Excited state	HONTO	LUNTO	Character of the transition
T <sub>1</sub>			CT
T <sub>2</sub>			Mixed LE-CT
T <sub>3</sub>			LE

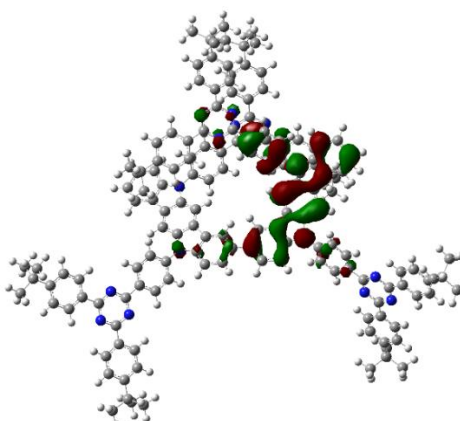
**T<sub>4</sub>**



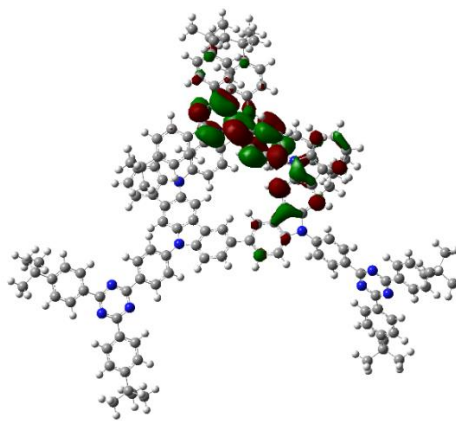
LE



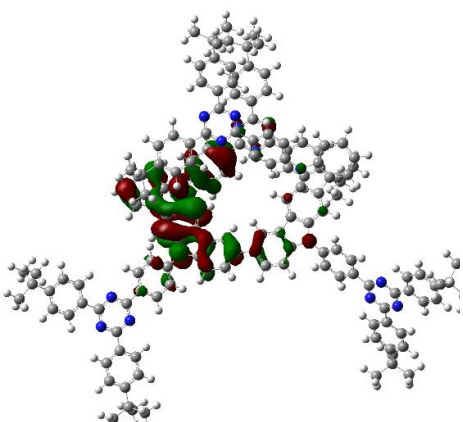
**T<sub>5</sub>**



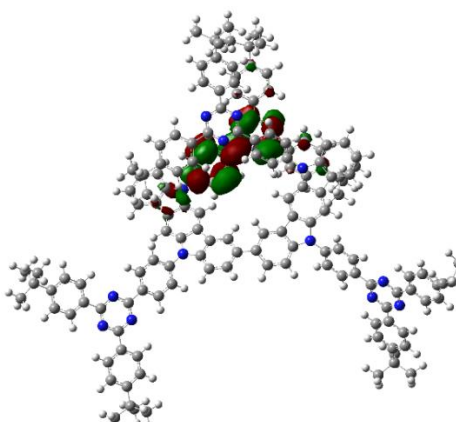
Mixed  
LE-CT



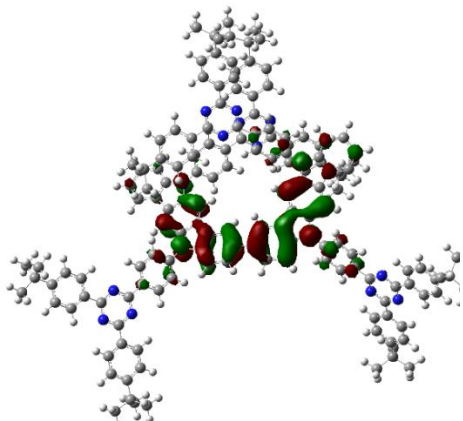
**T<sub>6</sub>**



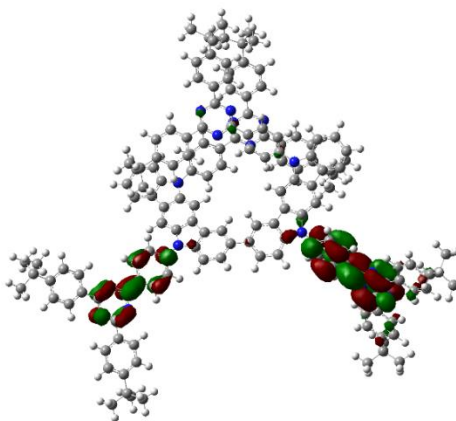
Mixed  
LE-CT



**S<sub>1</sub>**



CT



The nature of the excited state was furtherly characterized by analysing the natural transition orbitals (NTOs) of **DICzTRZ**, which allow us to obtain a more simplified representation of the electronic transition of different excited states (**Table 9**). The HONTO and LUNTO for T<sub>1</sub> show a clear delocalization of electronic density, going from the central indolocarbazole to the adjacent triazine acceptors. T<sub>2</sub> has quite similar behavior to T<sub>1</sub>, but there is a slight overlap of electron density in the left triazines (as shown in the figure) giving some degree of mixed CT/LE character to the S<sub>0</sub>→T<sub>2</sub> transition. T<sub>3</sub> and T<sub>4</sub> present a clear LE character, with both HONTO and LUNTO localized on the donor. The character of each T<sub>5</sub> and T<sub>6</sub> is more difficult to assign as there is a significant overlap of the electron density of the HONTO and the LUNTO, typical of a LE type transition, but there is also communication between the indolocarbazole and triazine moieties, classical of a CT type transition, leading to a mixed CT/LE character. S<sub>1</sub> is similar to T<sub>2</sub>, with a clear movement of electron density from the diindolocarbazole donor to the triazine acceptor, and thus CT type transition.

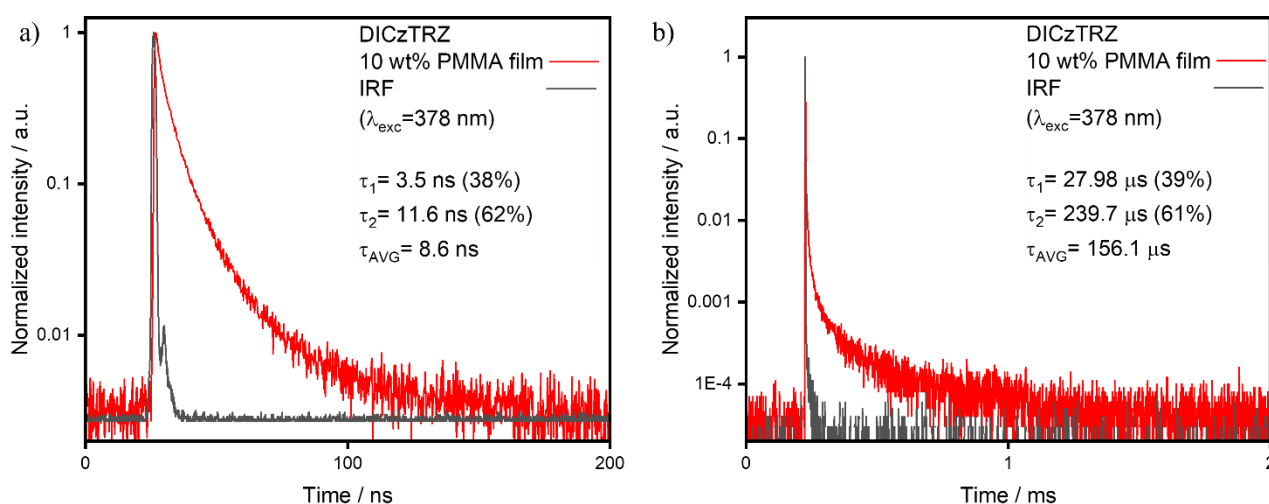


**Figure 72.** Time-resolved decay of **a)** prompt and **b)** delayed fluorescence decay of **DICzTRZ** (10 wt% PMMA film,  $\lambda_{exc}=378$  nm, the prompt fluorescence decay was measure by TCSPC, the delayed fluorescence decay was measured by MCS).

The photophysical properties of **DICzTRZ** were then investigated in a solid matrix. starting with the non-polar host material PMMA at a 10 wt% doping concentration. **DICzTRZ** in the doped PMMA film shows a  $\lambda_{PL}$  of 514 nm and a  $\Phi_{PL}$  of 29% under N<sub>2</sub> atmosphere that decreased to 22% when exposed to air. The TRPL shows prompt and delayed fluorescence (**Figure 72**), with multiexponential decay kinetics and lifetimes with an average  $\tau_p$  of 8.6 ns [ $\tau_1=3.5$  ns (38%),  $\tau_2=11.6$  ns (62%)] and an average  $\tau_d$  of 156.1  $\mu$ s [ $\tau_1=27.98$   $\mu$ s (40%),  $\tau_2=239.7$   $\mu$ s (61%)], respectively. As was observed for

the toluene solution, the prompt fluorescence lifetime of **DICzTRZ** and **ICzTRZ** are quite similar ( $\tau_p = 11.5$  ns for the monomer) while the delayed fluorescence of the dimer is faster ( $\tau_d = 252.8$   $\mu$ s for **ICzTRZ**), indicating an improved RISC process, most likely caused by the higher density of triplet states.

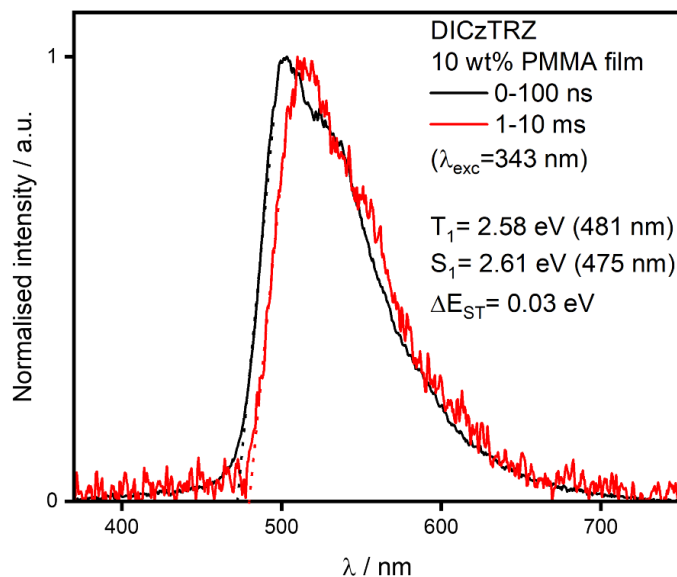


**Figure 73.** Prompt fluorescence and phosphorescence spectra of **DICzTRZ** at 77 K in a drop-cast 10 wt% PMMA film ( $\lambda_{exc} = 343$  nm, prompt and delayed fluorescence spectra were obtained over the 0–100 ns and 1–10 ms time ranges, respectively).

The singlet and triplet energy levels were then extracted, respectively, from the fluorescence and phosphorescence spectra of a drop-cast 10 wt% PMMA film, recorded at 77 K (**Figure 73**).  $S_1$  and  $T_1$  have energies of 2.61 eV and 2.58 eV, respectively, resulting in an extremely small  $\Delta E_{ST}$  of 0.03 eV. The shape of the fluorescence spectrum resembles the one obtained in the toluene solution, which can be attributed to a state of mixed LE-CT character, due to the more resolved emission profile and to the stabilization of the energy level caused by the different environment (from  $S_1$  energy of 2.80 eV in toluene to 2.61 in PMMA). The phosphorescence spectrum in the PMMA film is broader than the one measured in the toluene solution, possibly due to the presence of multiple conformers in the solid-state film.<sup>158</sup> However, typical for an LE-type state, the energy of the triplet state remains almost unaffected by the different environment. When compared to **ICzTRZ**, the dimer's energy level is lower, at 2.58 eV, and the  $\Delta E_{ST}$  is significantly smaller (0.11 eV for **ICzTRZ**), leading to a more efficient RISC process and thus explaining the faster-delayed fluorescence decay.

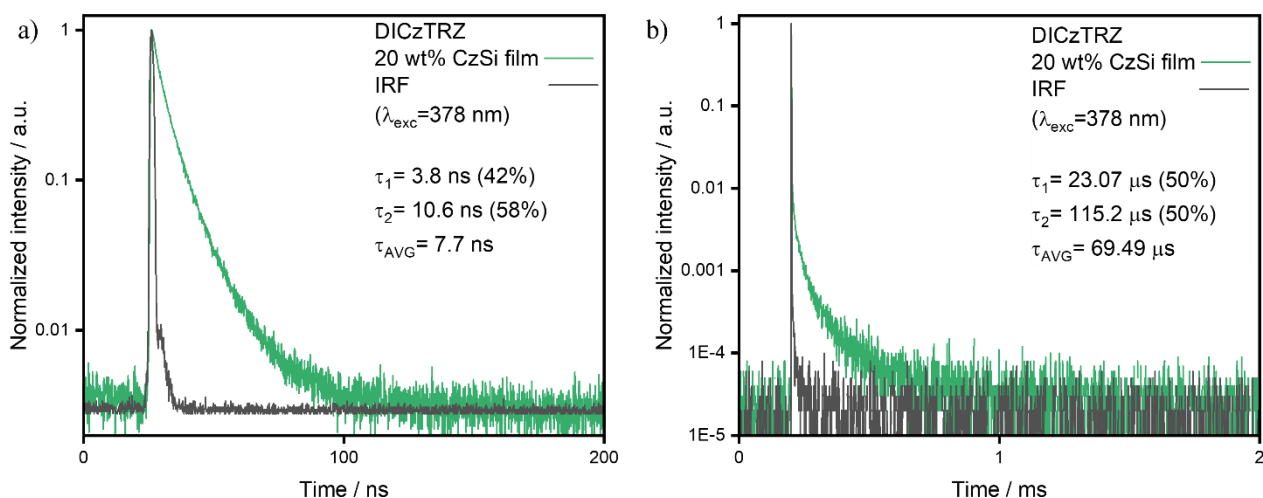


**Figure 74.** Time-resolved decay of **a)** prompt and **b)** delayed fluorescence decay of **DICzTRZ** (20 wt% CzSi film,  $\lambda_{exc}=378$  nm, the prompt fluorescence decay was measured by TCSPC, the delayed fluorescence decay was measured by MCS).

As our goal was to employ **DICzTRZ** in solution-processed devices, CzSi was chosen as the host material since it has been demonstrated to stop crystallization processes during the spin-coating step.<sup>154</sup> In 20 wt% doped film the  $\Phi_{PL}$  of **DICzTRZ** is 57%, the highest amongst the doping concentrations tested, under a  $N_2$  atmosphere. In this matrix, emission maximum of 488 nm was observed, together with prompt and delayed fluorescence (**Figure 74**) with lifetimes of  $\tau_p$  7.7 ns [ $\tau_1=3.8$  ns (42%),  $\tau_2=10.6$  ns (58%)] and  $\tau_d$  of 69.49  $\mu$ s [ $\tau_1=23.07$   $\mu$ s (50%),  $\tau_2=115.2$   $\mu$ s (50%)], respectively. **DICzTRZ** in CzSi shows much better performances than in the PMMA matrix, with a higher  $\Phi_{PL}$  and a shorter delayed lifetime, indicating a much more favorable RISC process. For the sake of comparison, **ICzTRZ** was also doped at a concentration of 20 wt% in CzSi. The results match the previously observed trends, with **ICzTRZ** possessing a higher  $\Phi_{PL}$  of 63%, under  $N_2$ , a similar prompt lifetime of 9.5 ns, and a slower delayed component of 147.3  $\mu$ s (**Figure 75**).

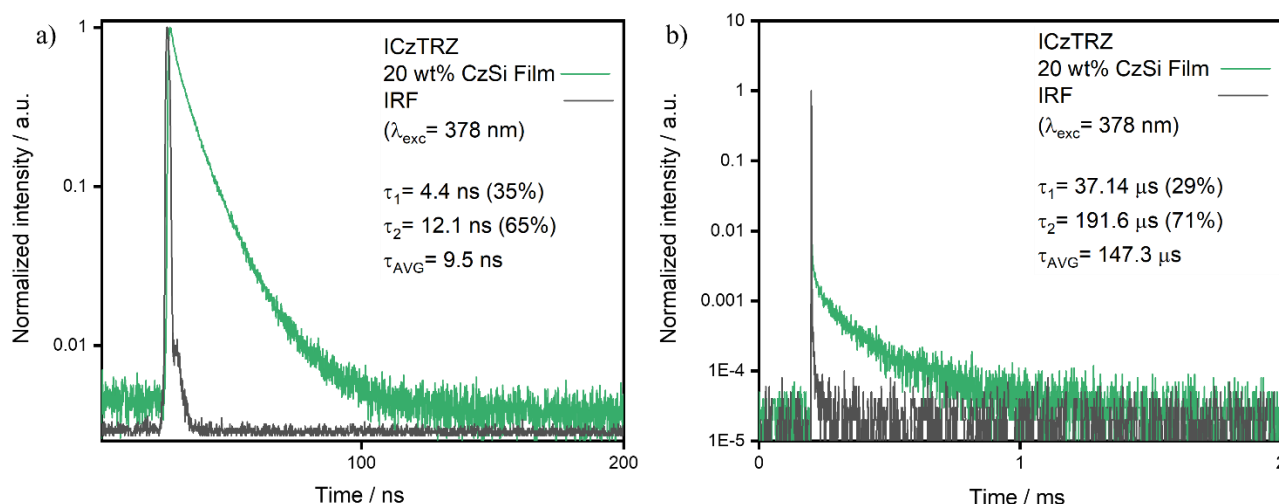


**Figure 75.** Time-resolved decay of **a)** prompt and **b)** delayed fluorescence decay of **ICzTRZ** (20 wt% CzSi film,  $\lambda_{exc} = 378$  nm, the prompt fluorescence decay was measured by TCSPC, the delayed fluorescence decay was measured by MCS).

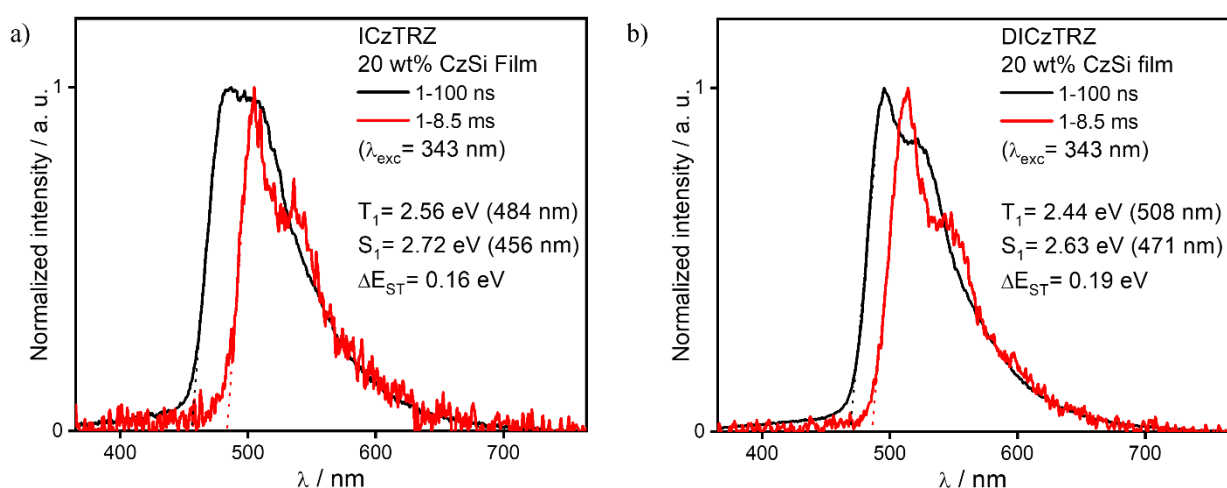


**Figure 76.** Prompt fluorescence and phosphorescence spectra of **a)** **ICzTRZ**, and **b)** **DICzTRZ** at 77 K in a drop-casted 20 wt% CzSi film ( $\lambda_{exc} = 343$  nm, prompt and delayed fluorescence spectra were obtained over the 1-100 ns and 1-8.5 ms time ranges, respectively).

The  $\Delta E_{ST}$  of **ICzTRZ** and **DICzTRZ** in a 20 wt% drop-cast CzSi film was obtained with the aid of an iCCD camera, where similar values of 0.16 eV and 0.19 eV for the monomer and dimer, respectively, were recorded (**Figure 76**). The mixed LE and CT character of **DICzTRZ**  $S_1$  state can be seen due to the much more resolved structure of its fluorescence spectrum. **ICzTRZ** shows a more unstructured fluorescence spectrum, but it is possible to observe two poorly resolved bands in the

emission spectrum in the CzSi matrix. The phosphorescence spectrum of both materials has the typical shape of an LE-type emission. Both **ICzTRZ** and **DICzTRZ** in the CzSi film possess a singlet energy comparable to the PMMA one, with 2.72 eV/2.75 eV (CzSi/PMMA) for **ICzTRZ**, and 2.63/2.61 eV for **DICzTRZ**. The triplet energy level is interestingly quite affected by the polarity of the host, with energies of 2.56 eV and 2.44 eV for **ICzTRZ**, and **DICzTRZ**, respectively.

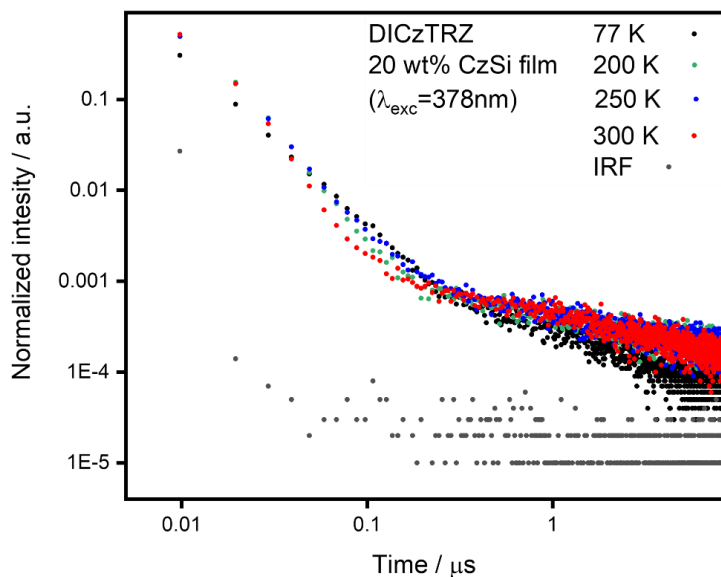


**Figure 77.** Delayed fluorescence decay data measured at different temperatures in spin-coated 20 wt% CzSi film of **DICzTRZ** ( $\lambda_{\text{exc}} = 378 \text{ nm}$ , all the delayed fluorescence decays were measured by MCS).

To conclude the solid-state PL study of **DICzTRZ**, the temperature-dependent time-resolved PL decays were measured showing the classic increase in the intensity of the delayed emission at higher temperatures, providing evidence for the TADF nature of the emitter (**Figure 77**). The intensity variation is much less pronounced than that observed in **ICzTRZ**, and even at 77 K a delayed fluorescence decay can be spotted. This means that 77 K is not a low enough temperature to suppress the RISC process in **DICzTRZ**, due to the more efficient RISC process observed in the dimer.<sup>158</sup>

**Table 10.** Photophysical properties of **ICzTRZ** and **DICzTRZ**.

Material	Environment	$\lambda_{\text{PL}}$ / $\Phi_{\text{PL}}$ $\text{N}_2$ ;	$\tau_p, \tau_d$ $^e/$ ns;	$S_f$ $^f/$ eV	$T_1$ $^g$ / $\Delta E_{\text{ST}}$ $^h/$ eV
		$\text{nm}^a$	$\mu\text{s}$		eV

<b>ICzTRZ</b>	Toluene ( $10^{-5}$ M)	462	72; 56 <sup>c</sup>	9.0; 229.2	2.94	2.62	0.32
	CzSi 20 wt%	475	63; 50 <sup>d</sup>	9.5; 147.3	2.72	2.56	0.16
	PMMA 10 wt% <sup>67</sup>	470	31; 28 <sup>d</sup>	115; 252.8	2.75	2.64	0.11
<b>DICzTRZ</b>	Toluene ( $10^{-5}$ M)	477	60; 44 <sup>c</sup>	8.9; 28.83	2.80	2.59	0.21
	CzSi 20 wt%	488	57; 42 <sup>d</sup>	7.7; 69.49	2.63	2.44	0.19
	PMMA 10 wt%	514	29; 22 <sup>d</sup>	8.6; 156.1	2.61	2.58	0.03

<sup>a</sup> measured at room temperature; <sup>b</sup>  $\lambda_{\text{exc}} = 340$  nm; <sup>c</sup> obtained via the optically dilute method, <sup>138</sup> quinine sulfate (0.5 M) in H<sub>2</sub>SO<sub>4</sub> (aq) was used as the reference,  $\Phi_{\text{PL}}: 54.6\%$ ,  $\lambda_{\text{exc}} = 360$  nm; <sup>139</sup> <sup>d</sup> obtained *via* integrating sphere; <sup>e</sup>  $\tau_p$  (prompt lifetime) and  $\tau_d$  (delayed lifetime) were obtained from the transient PL decay of degassed solution/doped film,  $\lambda_{\text{exc}} = 378$  nm; <sup>f</sup> S<sub>1</sub> was obtained from the onset of the prompt emission measured at 77 K; <sup>g</sup> T<sub>1</sub> was obtained from the onset of the phosphorescence spectrum measured at 77 K; <sup>h</sup>  $\Delta E_{\text{ST}} = S_1 - T_1$ .



### 3.3.4 - Orientation measurements

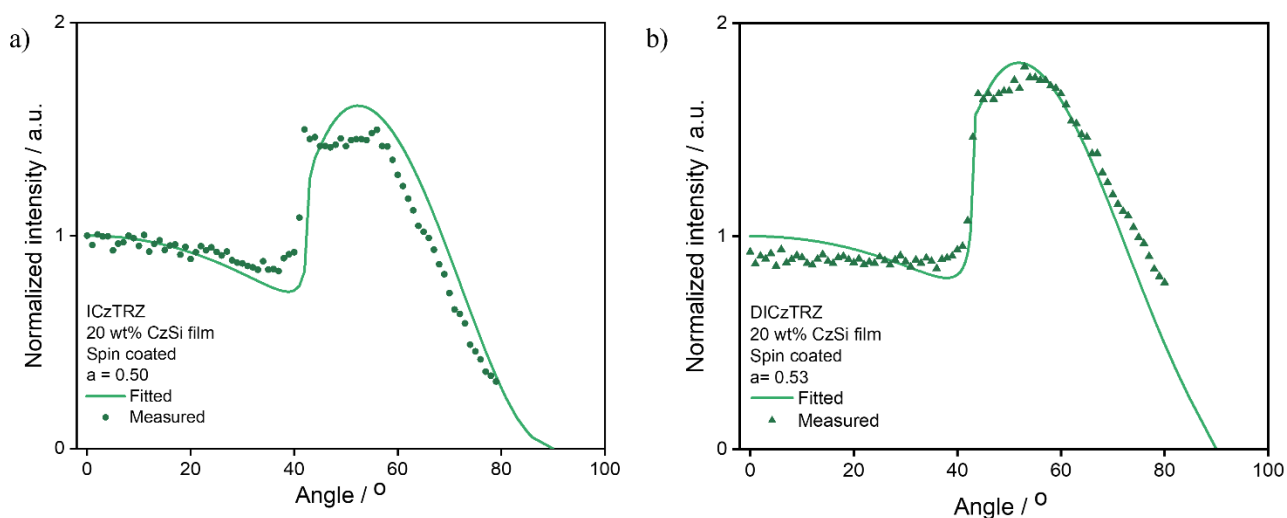


**Figure 78.** Angle-resolved photoluminescence measurement of 20 wt% spin-coated films of **a)** **ICzTRZ** (dots), and **b)** **DICzTRZ** (triangles), in CzSi. The light green lines show a fit using the dipole emission model, yielding the anisotropy factor,  $a$  (data taken at  $\lambda = 420$  nm).

Polarization and angle-resolved PL spectroscopy was performed by collaborators (**Chapter 3 – Paragraph 3.1 – Attributions**) to assess whether the high molecular weight of **DICzTRZ** would lead to horizontal orientation even from solution-processed films. As a comparison, the measurement was also carried out with **ICzTRZ** in the same host and doping concentration. After analysing the data *via* optical simulation, the anisotropy factors were calculated to be  $a = 0.53$ , and  $a = 0.50$  for **DICzTRZ** and **ICzTRZ**, respectively (**Figure 78**), meaning that the material has a vertically oriented TDM, and thus having most of their emitted light trapped inside the film.

The result can be attributed to the different processing techniques, further reinforcing the concept that vacuum deposition creates a non-equilibrium situation at the surface where the film is growing, which is essential to achieve high degrees of horizontal orientation.<sup>160</sup> Solution processing allows the emitter a higher degree of freedom, allowing them to freely rotate and reach a more or less isotropic situation before the solvent has fully evaporated, thus locking the orientation of the molecules. Interestingly, **DICzTRZ** and **ICzTRZ** do not have isotropically oriented TDMs but they are vertical, leading us to believe that CzSi must have an influence on the orientation of the emitter, even if towards an unfavorable result.

### 3.3.5 - OLED devices

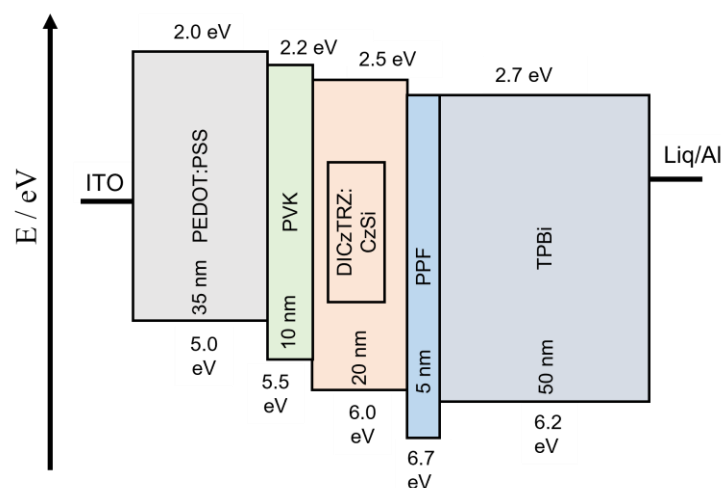


**Figure 79.** OLED device stack with **DICzTRZ** showing HOMO and LUMO energy level of the different materials.

The **DICzTRZ** OLED (**Figure 79**) were fabricated and tested by Yoshimasa Wada from the Hironori Kaji group at the University of Kyoto (**Chapter 3 – Paragraph 3.1 – Attributions**), with the device structure: ITO (50 nm)/PEDOT:PSS (35 nm)/PVK (10 nm)/x wt% emitter: CzSi (20 nm)/PPF (5 nm)/TPBi (50 nm)/Liq (1 nm)/Al (80 nm), where x is 20 or 30. ITO is the semitransparent anode, PEDOT:PSS is the hole transport layer, PVK is the electron blocking layer,<sup>161</sup> CzSi is the host, PPF is the hole-blocking layer,<sup>162</sup> TPBi is the electron transport layer, and LiF modifies the work function of the aluminum cathode. The same device was also fabricated with **ICzTRZ**, to compare their properties (**Figure 81**).

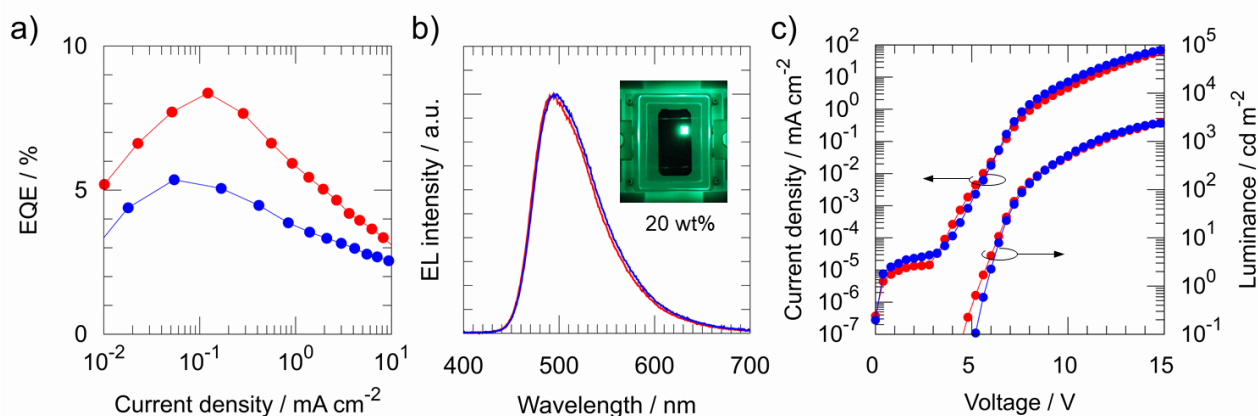


**Figure 80.** Device performances of 20 wt% (red) and 30 wt% (blue) **DICzTRZ** OLED devices, **a)** EQE vs current density **b)** EL spectra and **c)** current density vs voltage vs luminance.

The best results were obtained with 20 wt% emitter doped devices (**Table 11**). Due to the vertical orientation of **DICzTRZ** in the solution-processed films, the OLED device achieved only an  $\text{EQE}_{\text{max}}$  of 8.4%, with sky-blue emission at  $\lambda_{\text{EL}}$  of 494 nm (CIE coordinates of 0.22, 0.47) at  $10 \text{ cd m}^{-2}$  (**Figure 80**). **ICzTRZ**'s slightly higher  $\Phi_{\text{PL}}$  translates to a higher  $\text{EQE}_{\text{max}}$  of 11.6% and blue-shifted emission with  $\lambda_{\text{EL}}$  of 485 nm (CIE coordinates of 0.19, 0.37).

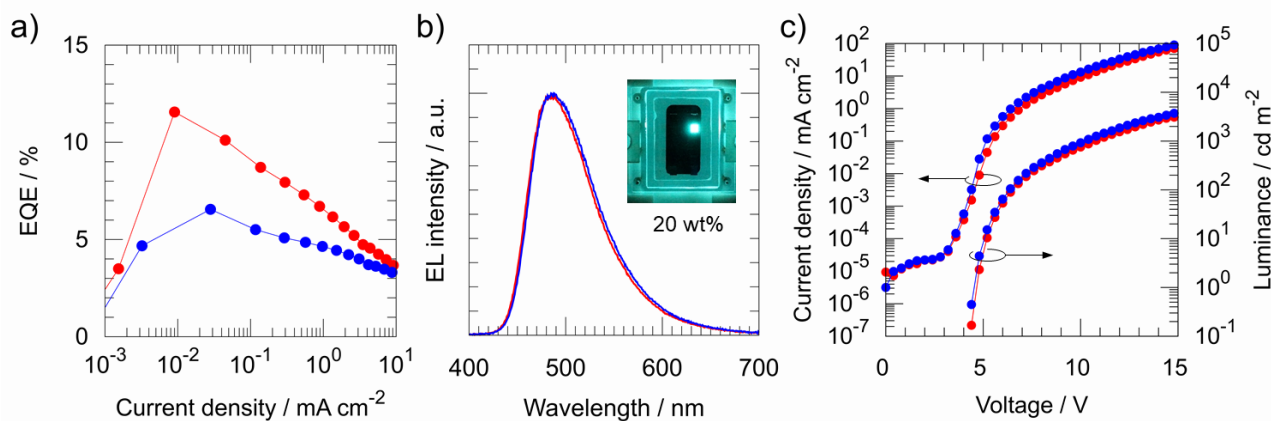


**Figure 81.** Device performances of 20 wt% (red) and 30 wt% (blue) **ICzTRZ** OLED devices, a) EQE vs current density b) EL spectra and c) current density vs voltage vs luminance.

**Table 11.** **ICzTRZ**'s and **DICzTRZ**'s device properties.

Emitter	Concentration / %	$\text{EQE}_{\text{max}}$ / %	$\lambda_{\text{EL}}$ / nm <sup>a</sup>	CIE (x, y)
<b>ICzTRZ</b>	20	11.6	485	(0.19, 0.37)
	30	6.6	485	(0.20, 0.39)
<b>DICzTRZ</b>	20	8.4	494	(0.22, 0.47)
	30	5.4	498	(0.22, 0.49)

<sup>a</sup> Determined from EL spectrum at  $1 \text{ mA cm}^{-2}$ .

Simulations of the efficiencies of the devices were then carried out (**Figure 82**). By using the measured parameters  $\lambda_{\text{PL}}$ ,  $a$ , and the optical constants of the different materials in the OLED stack, **DICzTRZ** device was predicted to have an  $\text{EQE}_{\text{max}}$  of around 9-10%, in very good agreement with the experimental results. The simulation carried out on the OLED with **ICzTRZ** is also in good agreement with the experimental results, with an expected  $\text{EQE}_{\text{max}}$  of around 11%. Further simulations were carried out assuming a theoretical anisotropy factor of c.a. 0.1 for a theoretically

evaporated device using **ICzTRZ**. This was believed to be a fair assumption given the previous excellent result of **ICzTRZ**, in combination with the good host properties of CzSi (High molecular weight of 816.21 g mol<sup>-1</sup>, and high T<sub>g</sub> of 131°C).

With this theoretical anisotropy factor and the measured properties of **ICzTRZ**, the device was expected to have an EQE<sub>max</sub> of about 22%, similar to what was obtained from the mCBP evaporated device discussed in **Chapter 2**. Both simulation and experimental results enforce that, for this class of molecules, thermal evaporation is the superior fabrication technique.

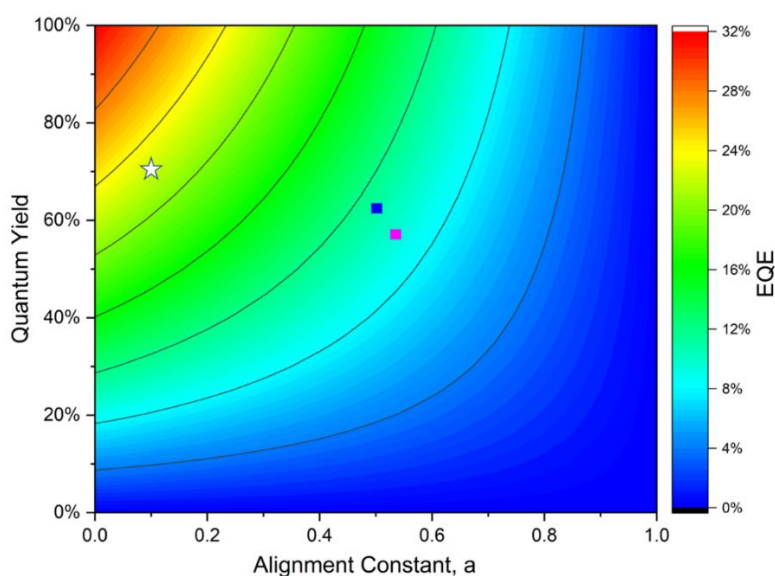
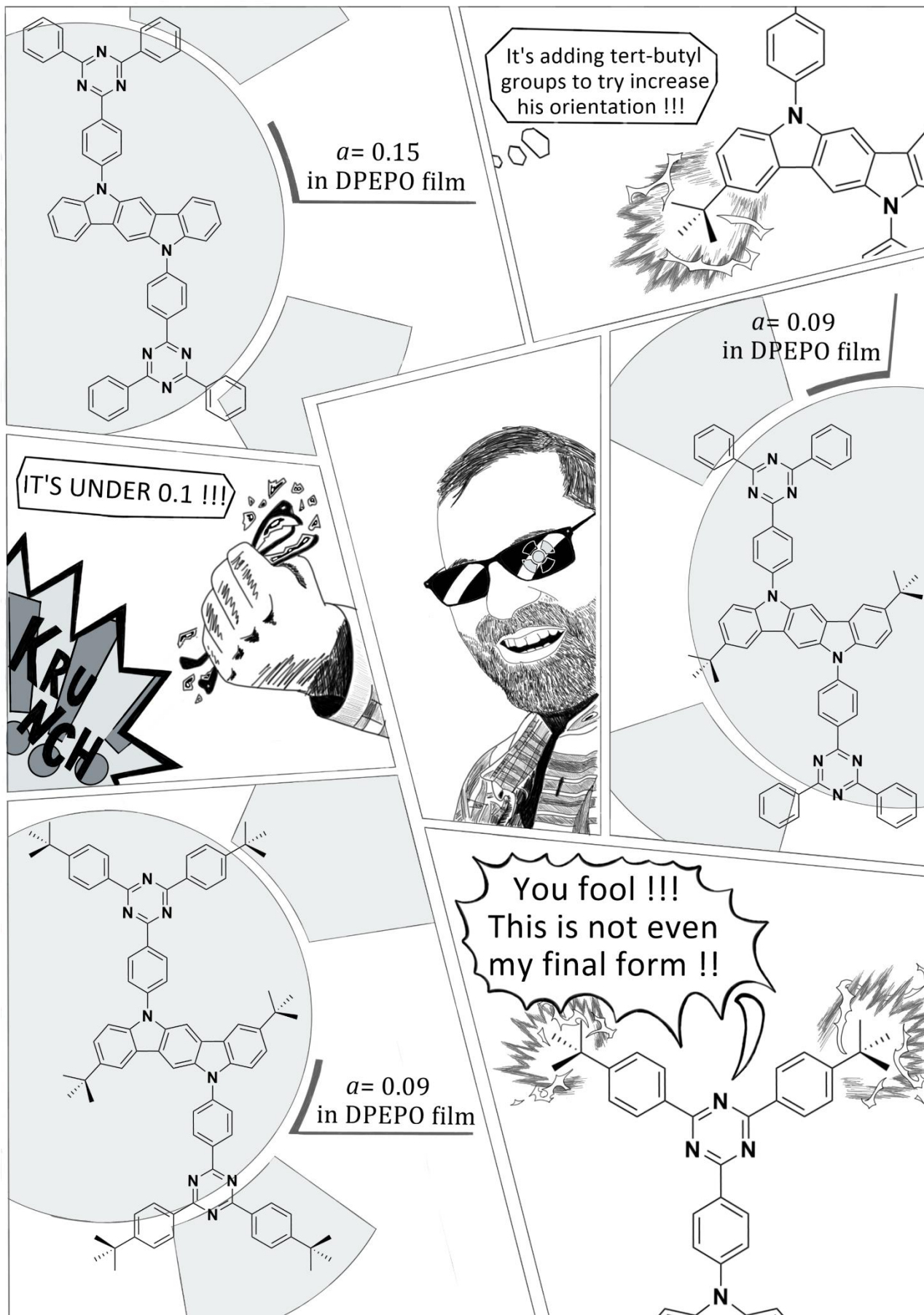


**Figure 82.** Device efficiency simulation of the fabricated OLEDs depicting the variation in EQE with varied PL Quantum Yield (vertical axis) and anisotropy factor (horizontal axis). The predicted EQEs are indicated with pink and blue rectangular marks for the **DICzTRZ** and **ICzTRZ** solution-processed OLEDs, respectively. The white star shows the predicted EQE for an evaporated **ICzTRZ** OLED with the orientation and  $\Phi_{\text{PL}}$  taken from Ref.<sup>6</sup>

### 3.4 - Conclusions

By applying a twin emitter design to **ICzTRZ**, the novel TADF emitter **DICzTRZ** was presented, hypothesizing that its increased size would enable the emitter to retain the high horizontal orientation of its TDM, just like **ICzTRZ**, even in solution-processed films. The twin emitter design led to a much higher density of triplet states, and thus a more efficient RISC process, as evidenced by the faster-delayed component of the material. An increase in the molar extinction coefficient, a slight red-shift in the emission, and an unfortunate lowering of the photoluminescence quantum yield of the material were observed. The best results were obtained in the 20 wt% doped film of **DICzTRZ** in CzSi, with blue emission at  $\lambda_{\text{PL}}$  of 488 nm and  $\Phi_{\text{PL}}$  of 57.1%. Unfortunately, the TDM of **DICzTRZ** is preferentially vertically oriented, which coupled with the lower  $\Phi_{\text{PL}}$  compared to **ICzTRZ** led to underperforming devices, with a low  $\text{EQE}_{\text{max}}$  of 8.4%. While the results were not optimal, this study further demonstrates that vacuum deposition is the superior technique to achieve high horizontal orientation of the TDM of emitters.



## Chapter 4 - Effect of different tert-butyl group substitution on the orientation of ICzTRZ.

### 4.1 - Attributions

I am the main author of this text. Unless otherwise stated in the text, I directly carried out the experimental work presented. Of the work presented in this chapter, I performed the theoretical calculations and orientation data analysis. I am a co-author of the review from Tenopala *et al.*<sup>23</sup> from which originated the idea of this project. The synthesis of the materials was done by Dr. Zhen Zhang from the Stefan Bräse group at Karlsruhe Institute of Technology (KIT). Angle-dependent luminescence spectroscopy to obtain the anisotropy factors of the materials was performed by Bilal Abbas Naqvi, Prakhar Sahay, and Minh Bình Nguyễn from the Wolfgang Brütting group at the University of Augsburg. TGA and DSC measurements were performed by Francesco Rodella and Daniel Wagner from the Peter Strohriegel group at the University of Bayreuth. The paper highlighting this work is currently being written.

### 4.2 - Introduction

The connection between high device efficiency and high horizontal orientation of the TDM of the emitter employed is now well established in the OLED emitter field of research, chapters 1 and 2 were prime examples of this correlation.<sup>67,68,122,163</sup> However, the factors that control the orientation of the TDM of the emitters in the thin film layer have still not been fully elucidated. Tenopala *et al.* classified the emitters employed in binary host/guest systems into two classes, based on their MW, low MW emitters (below 600 g mol<sup>-1</sup>) and high MW (above 600 g mol<sup>-1</sup>).<sup>23</sup> The horizontal orientation of the first class of emitters was found to be more dependent on the T<sub>g</sub> of the host materials. Higher T<sub>g</sub> values were found to be correlated with an improvement in the orientation of the TDM of the emitter by suppressing diffusion phenomena during film deposition. The degree of horizontal orientation of the second class of emitters was observed to be affected by the MW of the emitter where heavier emitters presented more horizontally oriented TDMs, the thickness of the emitter, z<sub>E</sub>, where thinner molecules would present more horizontally oriented TDMs, and the ratio between the length of the emitter and the length of the host, x<sub>E</sub>/x<sub>H</sub>, where most materials that showed a < 0.1 presented x<sub>E</sub>/x<sub>H</sub> > 1.3. The orientation of the TDM of many previously reported emitters can be explained with this model.

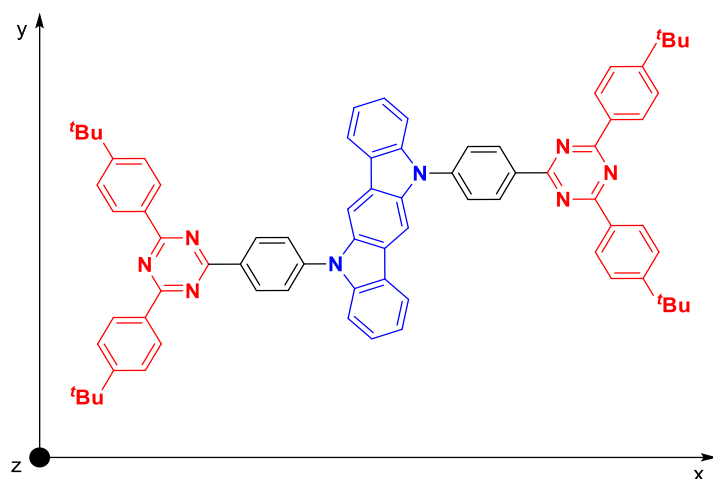
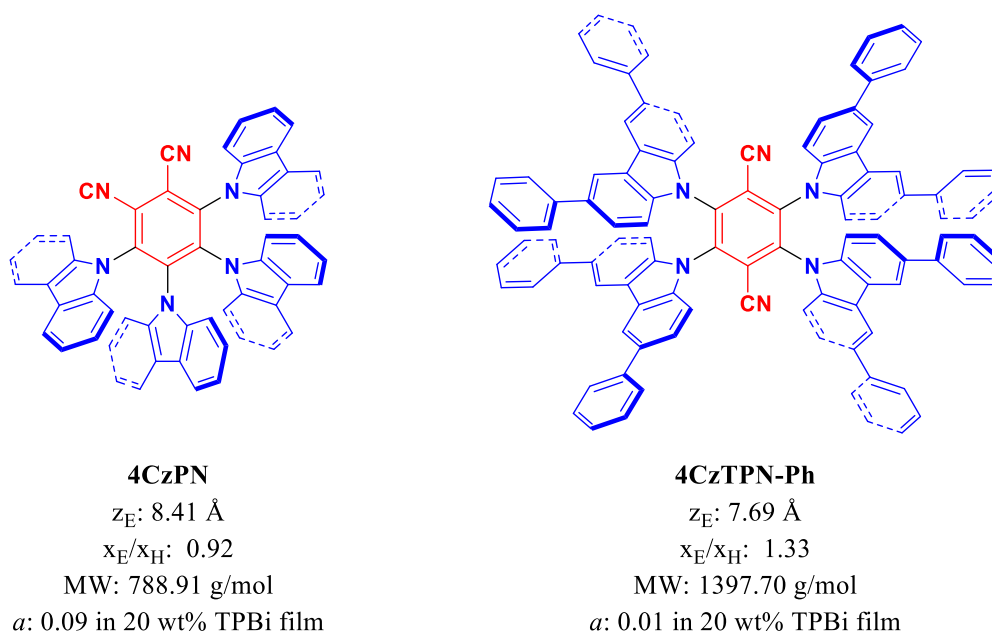


**Figure 83.** Approximate representation of the x, y, and z axis used to calculate the dimension of the emitters discussed in this chapter.

The previously mentioned example from Tanaka *et al.*<sup>125</sup> perfectly shows the effect of molecular weight and  $x_E/x_H$ . The anisotropy factor decreases with increasing MW, and  $x_E/x_H > 1.3$ . The heaviest material, **4CzTPN-Ph**, showed the most horizontal orientation of its TDM in the series. The thickness of the material could also be of help in achieving a more horizontal orientation, with **4CzTPN-Ph** possessing a lower  $z_E$  value of 7.69 Å vs 8.41 Å in **4CzPN**.

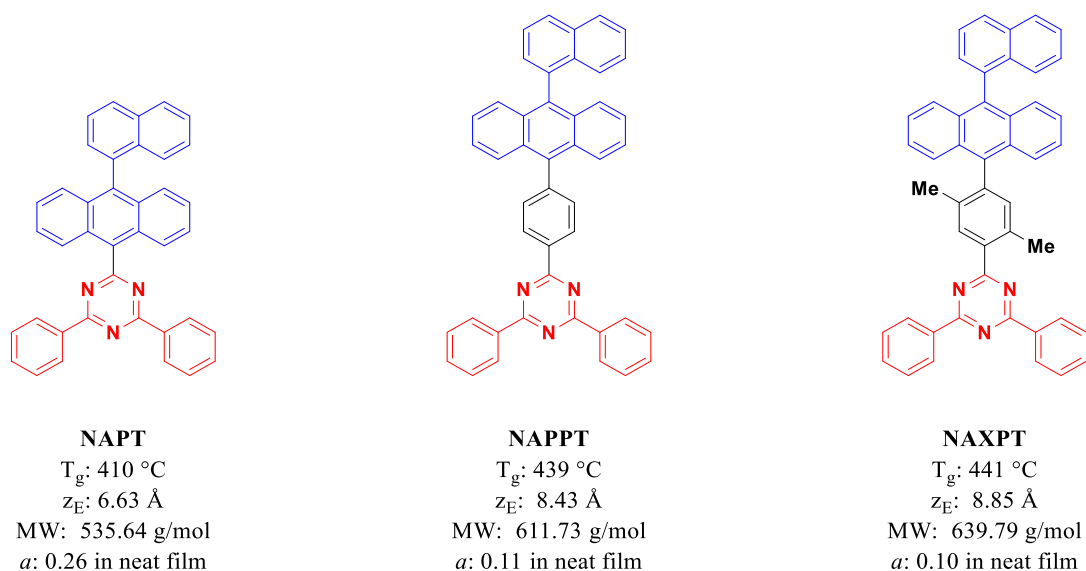


*Appl. Phys. Lett.* **2020**, 116, 023302

**Figure 84.** Effect of the MW,  $x_E/x_H$ , and  $z_E$  on the TDM horizontal orientation of **4CzPN** and **4CzTPN-Ph**.<sup>125</sup>



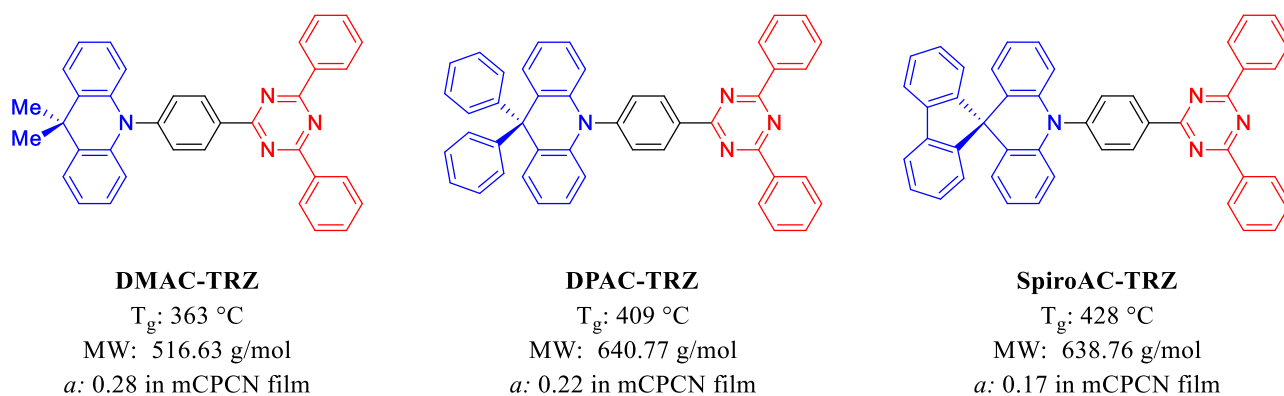
Kim *et al.* showed how the inclusion of a phenyl ring between the donor and the acceptor could improve the horizontal orientation of a molecule (**Figure 85**).<sup>164</sup> An improvement in the horizontal orientation of the TDM of the materials can be seen, going from the lightest, an isotropic emitter **NAPT** (MW= 535.64 g mol<sup>-1</sup>) with an *a* value of 0.26 to the heavier materials **NAPPT** (MW= 611.73 g mol<sup>-1</sup>), and **NAXPT** (MW= 639.79 g mol<sup>-1</sup>), with *a* values of 0.11 and 0.10, respectively. The thickness of the materials seems to be inversely correlated with the degree of horizontal orientation of the TDM, with the thinner materials showing more vertical orientation of their TDM. However, the *T<sub>g</sub>* of the material seems to be more correlated with the orientation of the TDM, since a more horizontal orientation is observed with higher *T<sub>g</sub>* materials (**NAPT**, **NAPPT**, and **NAXPT** possess *T<sub>g</sub>* values of 410 °C, 439 °C, and 441 °C, respectively). While in a host/guest system the higher *T<sub>g</sub>* of the host prevents diffusion phenomena,<sup>122</sup> in this case, a non-doped environment was employed, thus it is possible that the higher glass transition temperature of the emitter, in tandem with the higher MW, were responsible for the lower *a* values.



*Chem. Commun.*, **2016**, 52, 10956-10959

**Figure 85.** Effect of the *T<sub>g</sub>*, *z<sub>E</sub>*, and MW on the TDM horizontal orientation of **NAPT**, **NAPPT**, and **NAXPT**.<sup>164</sup>

In the example from Lin *et al.*,<sup>78</sup> where they reported two variations of **DMAC-TRZ** where they replaced the methyl groups for bigger phenyl and fluorene substituents on the acridine in the emitters **DPAC-TRZ**, and **SpiroAC-TRZ**, respectively, the materials follow the trend of low MW emitters, where a more horizontal orientation of the TDM was correlated with higher *T<sub>g</sub>* values (**Figure 86**).



*Adv. Mater.* **2016**, 28, 6976-6983

**Figure 86.** Effect of the MW, and  $T_g$  on the TDM horizontal orientation of **DMAC-TRZ**, **DPAC-TRZ**, and **SpiroAC-TRZ**.<sup>78</sup>

Several other spiro-acridine derivatives have been investigated (**Figure 87**). **TSpiroS-TRZ**<sup>165</sup> has an anthracene moiety attached to the acridine donor, which is then followed by a thioxanthene.<sup>166</sup> **motmTrSac**<sup>166</sup> has the same molecular structure of **SpiroAC-TRZ** but with the addition of several methyl groups. The emitters present similar  $a$  factors of 0.10 and 0.12 for **TSpiroS-TRZ**, and **motmTrSac**, respectively, both showcasing another instance where high MW emitters led to highly horizontally oriented TDMs.

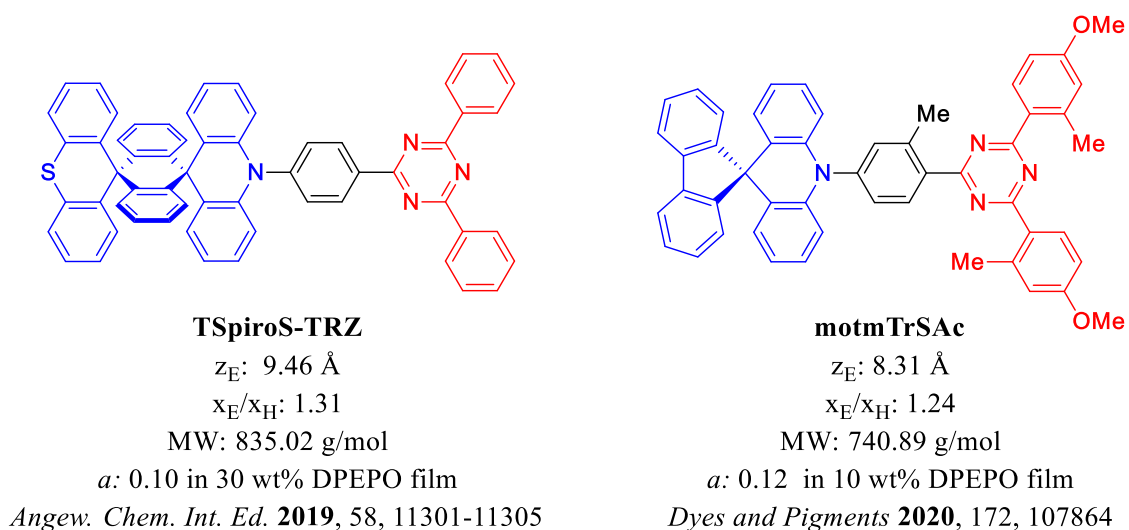


**Figure 87.** Effect of the MW,  $x_E/x_H$ , and  $z_E$  on the TDM horizontal orientation of **TSpiroS-TRZ**,<sup>165</sup> **motmTrSac**.<sup>166</sup>

An A-D-D-A emitter using a spiro-attached acridine was used in two studies, with the emitters **TZ-SBA**,<sup>167</sup> by Liu *et al.*, and **SBA-2DPS**, by Zeng *et al.*<sup>168</sup> (**Figure 88**), which possess  $a$  values of 0.14

and 0.12, respectively. This strategy of effectively doubling the molecule leads to favourable properties like higher MW, and  $x_E/x_H$  factor above 1.3, therefore enhancing the horizontal orientation from isotropic to horizontal [DMAC-TRZ ( $a= 0.36$  in 10 wt% DPEPO)<sup>68</sup> for TZ-SBA ( $a= 0.14$  in 20 wt% DPEPO), and DMAC-1DPS ( $a= 0.41$  in 30 wt% DPEPO) for SBA-2DPS ( $a= 0.13$  in 30 wt% DPEPO)].

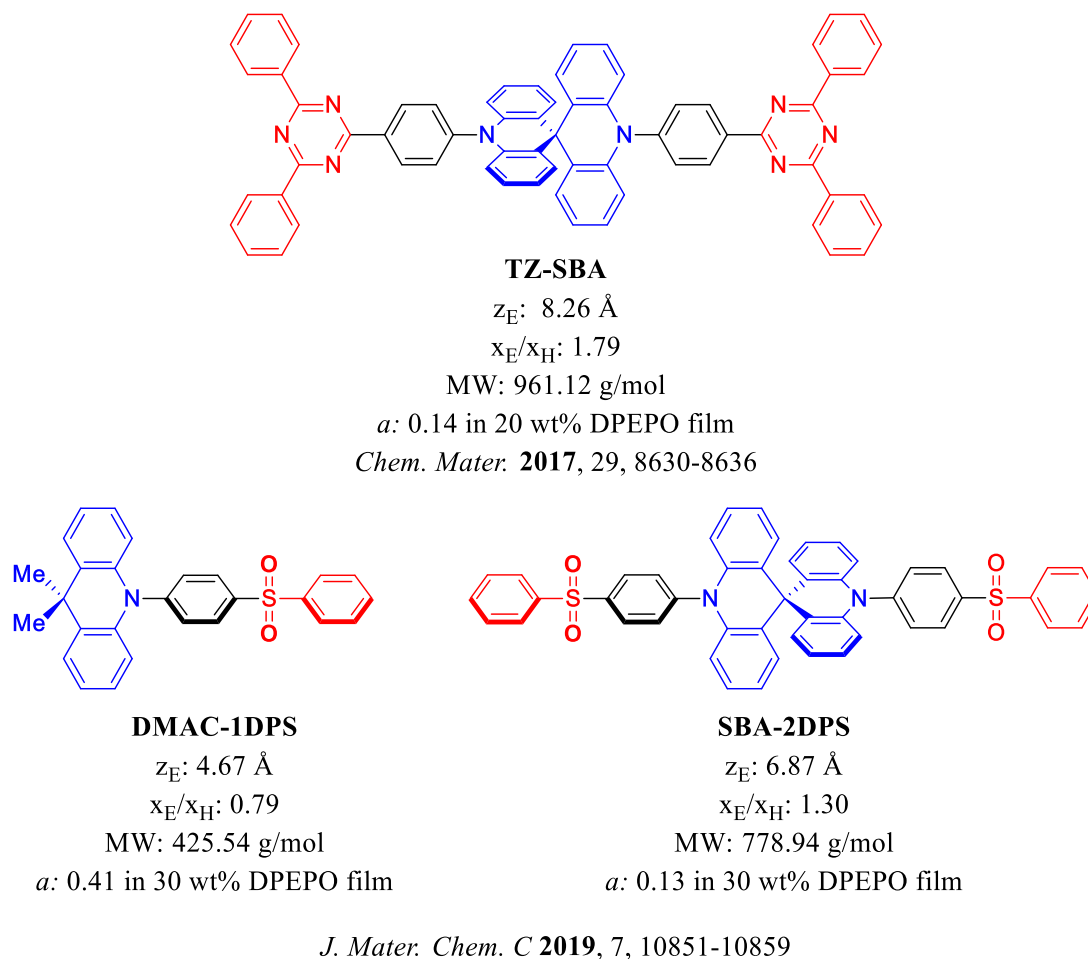
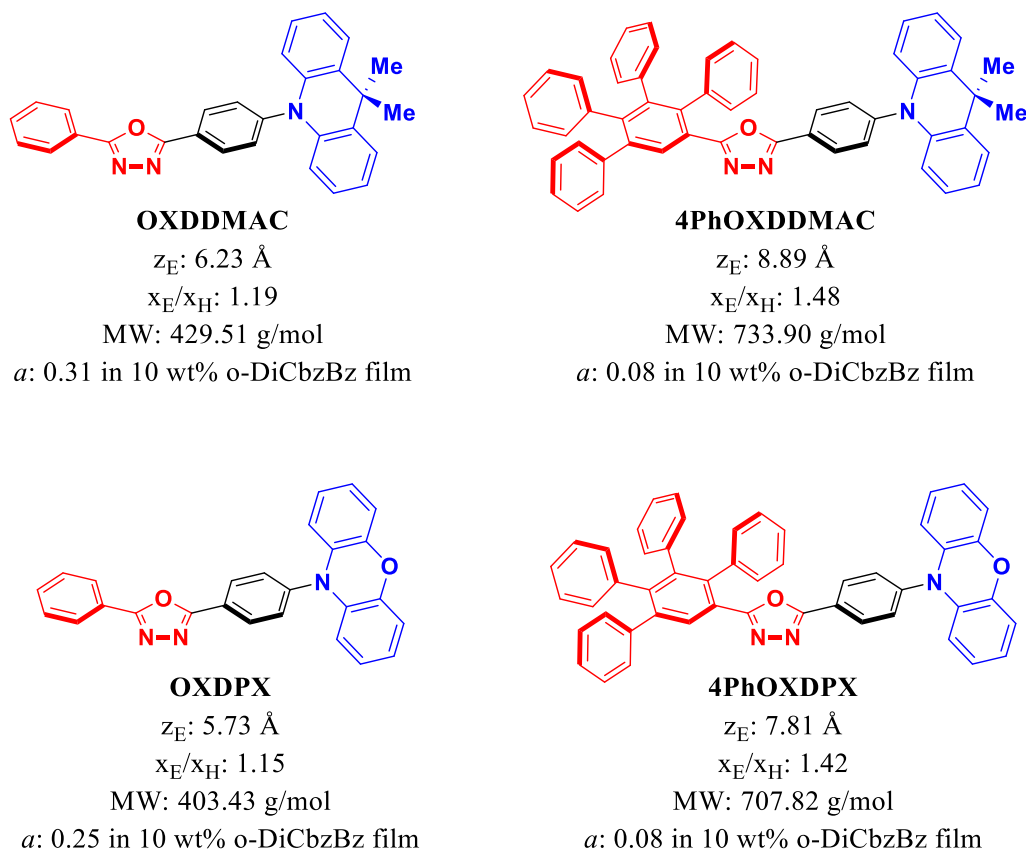


**Figure 88.** Effect of the MW,  $x_E/x_H$ , and  $z_E$  on the horizontal orientation of **TZ-SBA**,<sup>167</sup> **DMAC-1DPS**, and **SBA-2DPS**.<sup>168</sup>

The effect of the MW and  $x_E/x_H$  is very evident in the example from Lee *et al.*,<sup>169</sup> where the addition of four phenyl groups on a light MW emitter correlated with a change in the orientation from isotropic to horizontal (**Figure 89**). The two light emitters **OXDDMAC**, and **OXDPX**, with MWs of 429.51 g mol<sup>-1</sup>, and 403.43, respectively, possess  $a$  values of 0.31 and 0.25, respectively. With the addition of the four extra aromatic rings in the materials **4PhOXDDMAC**, and **4PhOXDPX** the MW increases to 733.90 g mol<sup>-1</sup>, and 707.82 g mol<sup>-1</sup>, respectively, and the  $a$  factor decreases to 0.08 for both emitters. **OXDDMAC**, and **OXDPX** also present larger  $x_E/x_H$  values of 1.19, and 1.15, respectively,

while for **4PhOXDDMAC**, and **4PhOXDPX**  $x_E/x_H$  surpasses the 1.3 threshold, at 1.42, and 1.48, respectively.



*ACS Appl. Mater. Interfaces*, **2018**, 10, 43842-43849

**Figure 89.** Effect of the MW,  $x_E/x_H$ , and  $z_E$  on the horizontal orientation of **OXD** series of emitters.<sup>169</sup>

**ICzTRZ** possesses one of the smallest  $a$  values reported in the literature ( $a$  of 0.06 in vacuum-deposited 10 wt% DPEPO film), thanks to its high MW of 1095.45 g mol<sup>-1</sup>, thin structure with a  $z_E$  of 8.69 Å, and helped by the use of high  $T_g$  hosts, such as DPEPO and mCBPCN. These results perfectly follow the trends elucidated by Tenopala *et al.*<sup>23</sup> as previously explained (**Chapter 2-Paragraph 2.2.4 - Orientation measurements**) and to further corroborate these trends, in this Chapter three new emitters, **ICzTRZ-0**, **d'Bu-ICzTRZ-0**, and **d'Bu-ICzTRZ** are presented. The goal of the project was to study the effect that different positions and different number of *tert*-butyl groups have on the orientation of the TDM of the materials. **ICzTRZ** contains two *tert*-butyl groups on each triazine acceptor, **ICzTRZ-0** possesses no *tert*-butyl groups, while **d'Bu-ICzTRZ-0** has 2 *tert*-butyl

groups on the indolocarbazole donor, and **d<sup>t</sup>Bu-ICzTRZ** possesses two *tert*-butyl groups on both the indolocarbazole donor and triazine acceptor. The *tert*-butyl groups on **ICzTRZ** also improve the solubility of the material, thus the removal of such groups led to some of the material being insoluble in all the solvents that were tested, making it impossible to carry out most of the previously discussed optoelectronic characterization, leading this study to focus on the theoretical properties and orientation measurements (carried out on evaporated film) of the materials.

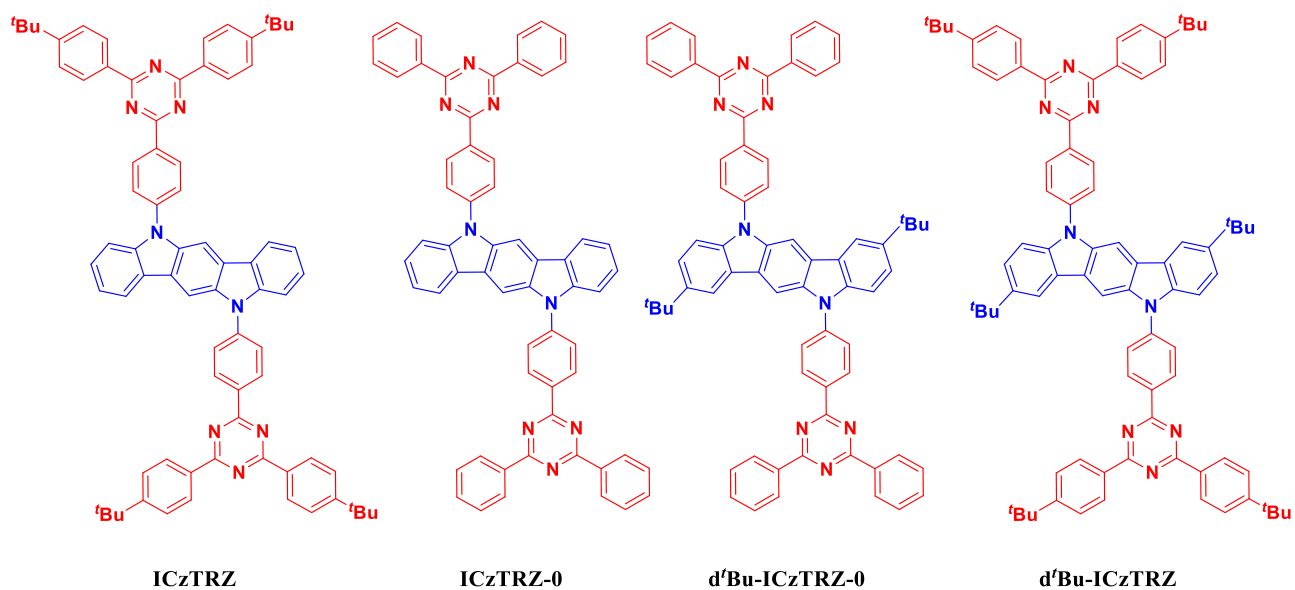
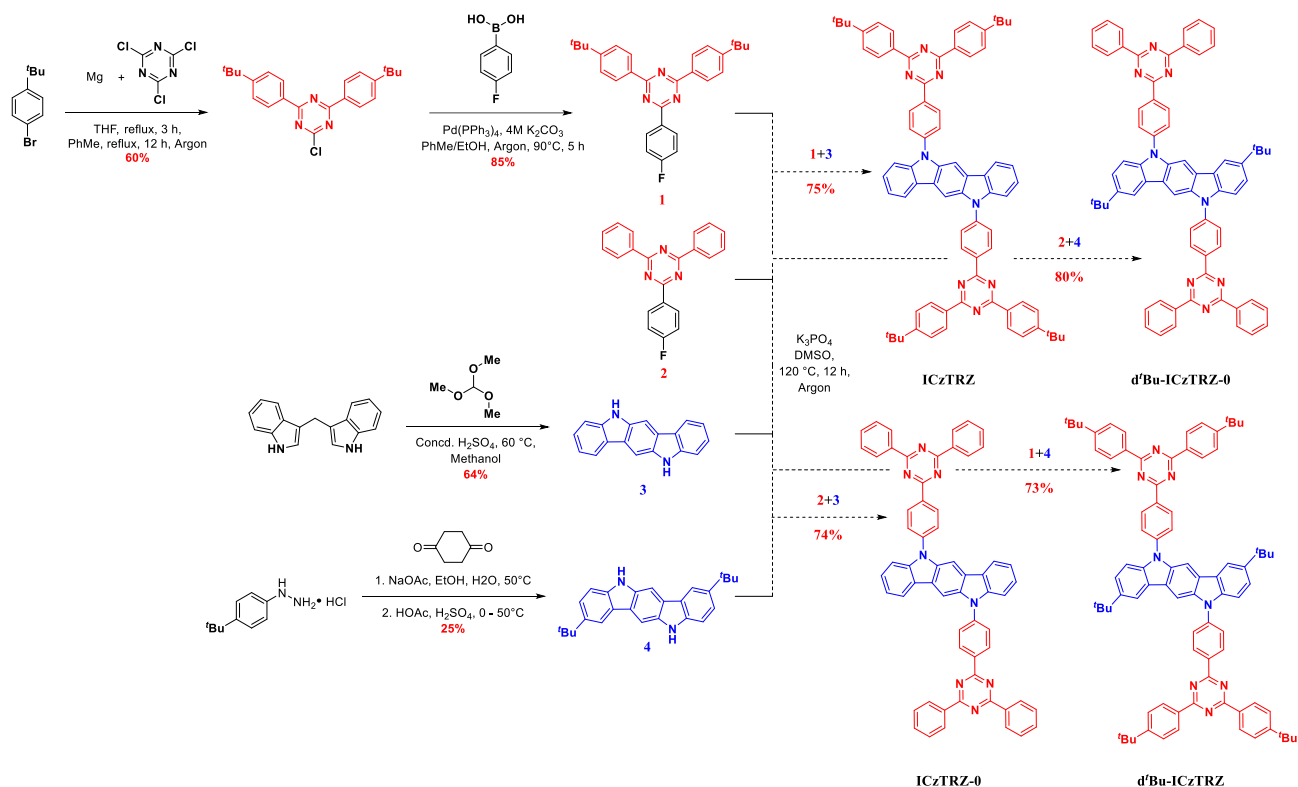


**Figure 90.** Chemical structure of **ICzTRZ** and the three novel emitters discussed in this chapter.

## 4.3 - Results and discussion

### 4.3.1 – Synthesis



**Scheme 3.** Synthetic route to ICzTRZ, ICzTRZ-0, d'Bu-ICzTRZ-0, and d'BuICzTRZ.

The synthesis of the materials was done by Dr. Zhen Zhang, from the Stefan Bräse group at the Karlsruhe Institute of Technology (KIT) (**Chapter 4 – Paragraph 4.1 – Attributions**). The four indolocarbazole-based materials were prepared as shown in **Scheme 3**. The *tert*-butyl-triphenyl-triazine (**1**) and indolocarbazole (**3**) were synthesized as explained in **Chaper 2 – Paragraph 2.3.1**. Compound **1** was obtained starting with a Grignard reaction between two equivalents of *tert*-butylphenyl magnesium bromide and 2,4,6-trichloro-1,3,5-triazine to obtain the precursor triazine, which was then converted to the desired *tert*-butyl-triazine acceptor *via* a Suzuki-Miyaura reaction with 4-fluorophenyl boronic acid. The fluoro-triphenyl triazine (**2**) was used as purchased. The indolocarbazole (**3**) was synthesized *via* an acid-promoted cyclization of 3,3-diindolylmethane. The *tert*-butyl-indolocarbazole (**4**) was obtained via a reaction of 4-*tert*-butylphenyl)hydrazine monohydrochloride and cyclohexane-1,4-dione and sodium acetate in a water and ethanol solution. All emitters were obtained using the same nucleophilic aromatic substitution reaction between different combinations of donor and acceptor (**1+3** for ICzTRZ, **2+3** for ICzTRZ-0, **2+4** for d'BuICzTRZ-0, and **1+4** for d'BuICzTRZ). Due to the extremely poor solubility of these materials

a full  $^1\text{H}$  NMR and  $^{13}\text{C}$  NMR characterization of the materials was impossible. The emitters were also fully characterized by Mp determination, HRMS, and IR spectroscopy.

### 4.3.2 - Theoretical calculations

The HOMO and LUMO for **ICzTRZ** were predicted to be -5.19 eV and -1.75 eV, respectively. **ICzTRZ-0** shows a low weakening of the donor character of the molecule, which was expected due to the absence of the electron-donating *tert*-butyl groups attached to the triazine acceptor with HOMO and LUMO levels that both stabilized to -5.25 eV and -1.86 eV. The greater change is observed on the LUMO, since the presence of *tert*-butyl groups on the acceptor would destabilize the LUMO more significantly. **d'Bu-ICzTRZ-0** shows stronger donor character, caused by the insertion of the electron-donating *tert*-butyl groups directly on the ICZ donor, while the LUMO level is nearly identical to that of **ICzTRZ-0** at -1.84 eV since the acceptor moiety is the same. The presence of *tert*-butyl groups on both the donor and acceptor, in **d'Bu-ICzTRZ** results in destabilized HOMO and LUMO levels of -5.09 eV, and -1.73 eV, respectively.

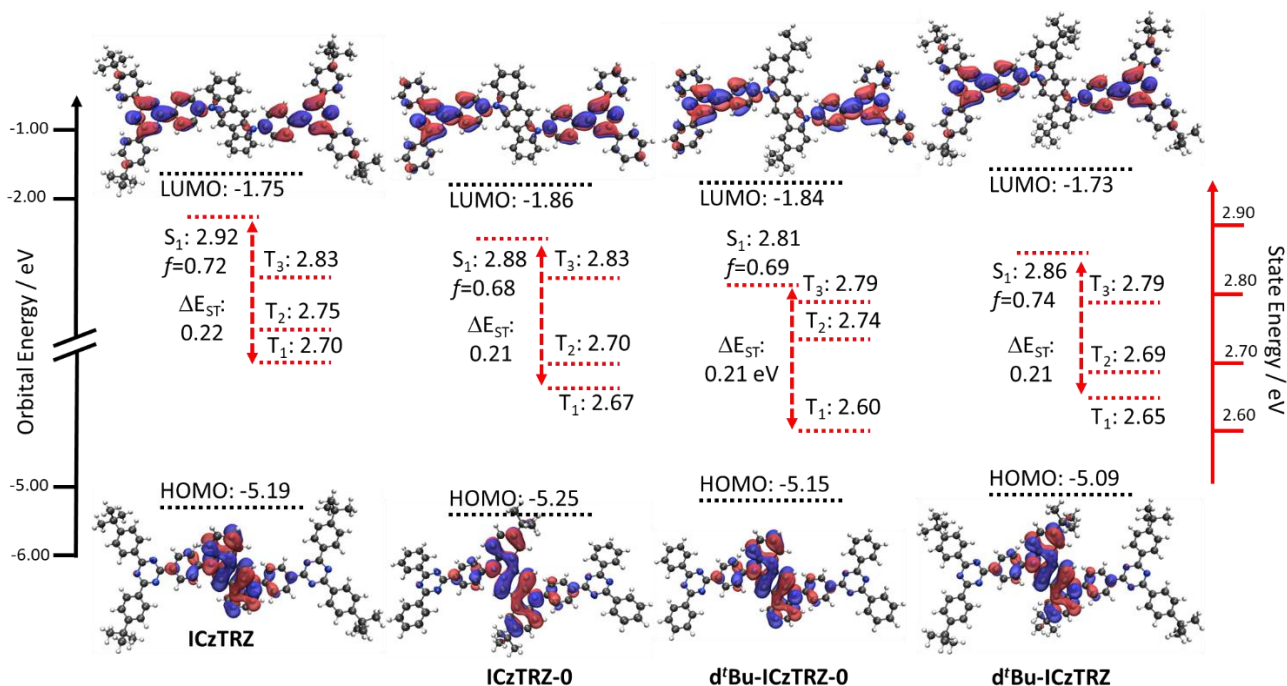


**Figure 91.** HOMO and LUMO electron density distributions and energy levels, excited state energy levels of **ICzTRZ**, **ICzTRZ-0**, **d'Bu-ICzTRZ-0**, and **d'Bu-ICzTRZ** (Obtained via DFT and TD-DFT at the PBE0/6-31G(d,p), Isovalue for new surfaces: MO=0.02, Density=0.0004).

**Table 12.** Excited states properties of ICzTRZ, ICzTRZ-0, d'Bu-ICzTRZ-0, and d'Bu-ICzTRZ (PBE0/6-31G(d,p)).

Excited State <sup>a</sup>	Energy / eV; nm	Nature <sup>b</sup>	Character of the transition
<b>ICzTRZ</b>			
<b>T<sub>1</sub></b>	2.70; 459	(H-2)→(L+1) (5%) <b>H→L (82%)</b> H→(L+5) (5%)	<sup>3</sup> CT
<b>T<sub>2</sub></b>	2.75; 451	(H-2)→L (7%) <b>H→(L+1) (82%)</b> H→(L+6) (3%)	<sup>3</sup> CT
<b>T<sub>3</sub></b>	2.83; 438	<b>H→(L+4) (90%)</b>	<sup>3</sup> LE
<b>S<sub>1</sub> (f=0.72)</b>	2.92; 425	<b>H→L (98%)</b>	<sup>1</sup> CT
<b>ICzTRZ-0</b>			
<b>T<sub>1</sub></b>	2.67; 464	(H-2)→(L+1) (5%) <b>H→L (84%)</b> H→(L+5) (3%)	<sup>3</sup> CT
<b>T<sub>2</sub></b>	2.70; 459	(H-2)→L (6%) <b>H→(L+1) (83%)</b> H→(L+6) (2%)	<sup>3</sup> CT
<b>T<sub>3</sub></b>	2.83; 438	<b>H→(L+4) (91%)</b>	<sup>3</sup> LE
<b>S<sub>1</sub> (f=0.68)</b>	2.88; 430	<b>H→L (97%)</b>	<sup>1</sup> CT
<b>d'Bu-ICzTRZ-0</b>			
<b>T<sub>1</sub></b>	2.60; 477	(H-2)→(L+1) (5%) <b>H→L (85%)</b> H→(L+5) (3%)	<sup>3</sup> CT
<b>T<sub>2</sub></b>	2.74; 452	(H-2)→L (6%) <b>H→(L+1) (84%)</b> H→(L+6) (2%)	<sup>3</sup> CT
<b>T<sub>3</sub></b>	2.79; 444	<b>H→(L+4) (93%)</b>	<sup>3</sup> LE
<b>S<sub>1</sub> (f=0.69)</b>	2.81; 441	<b>H→L (97%)</b>	<sup>1</sup> CT
<b>d'Bu-ICzTRZ</b>			
<b>T<sub>1</sub></b>	2.65; 468	(H-2)→(L+1) (5%) <b>H→L (83%)</b> H→(L+5) (5%)	<sup>3</sup> CT



<b>T<sub>2</sub></b>	2.69; 461	(H-2)→L (6%) <b>H→(L+1) (83%)</b> H→(L+6) (3%)	<sup>3</sup> CT
<b>T<sub>3</sub></b>	2.79; 444	<b>H→(L+4) (93%)</b>	<sup>3</sup> LE
<b>S<sub>1</sub> (f=0.74)</b>	2.86; 434	<b>H→L (97%)</b>	<sup>1</sup> CT

<sup>a</sup> (PBE0/6-31G(d,p)); <sup>b</sup> the transitions highlighted in red are the main ones contributing to the excited state character.

All materials possess a very similar excited state landscape, with almost identical  $\Delta E_{ST}$  values of 0.22 eV for **ICzTRZ**, and 0.21 eV for each of **ICzTRZ-0**, **d'Bu-ICzTRZ-0** and **d'Bu-ICzTRZ**. They all have three closely lying triplet excited states, which could be beneficial to the RISC process,<sup>52,128–131</sup> where T<sub>1</sub> and T<sub>2</sub> present a clear CT character involving a transition between the **ICz** donor and the **TRZ** acceptors, while T<sub>3</sub> shows a LE character localized on the indolocarbazole. All S<sub>1</sub> states present high oscillator strength (*f*), with values of 0.72, 0.68, 0.69, and 0.74 for **ICzTRZ**, **ICzTRZ-0**, **d'Bu-ICzTRZ-0**, and **d'Bu-ICzTRZ**, respectively and all show CT character, with the transition going from the indolocarbazole donor to one of the two triazine acceptors. Going from **ICzTRZ** to **ICzTRZ-0**, the removal of the *tert*-butyl groups increases the strength of the acceptor, thus stabilizing the excited states, with S<sub>1</sub> and T<sub>1</sub> energies going from 2.92 eV and 2.70 eV to 2.88 eV and 2.67 eV, respectively. Adding the *tert*-butyl back, but on the donor in **d'Bu-ICzTRZ-0**, lowers the energies even more to 2.81 eV for S<sub>1</sub> and 2.60 eV for T<sub>1</sub>, explained by the even stronger donor character of the material. Adding two more *tert*-butyl groups on the triazines in **d'Bu-ICzTRZ**, destabilizes the acceptor, and raises the excited state energies, at S<sub>1</sub> and T<sub>1</sub> levels of 2.86 eV and 2.65 eV.

### 4.3.3 - Orientation measurements

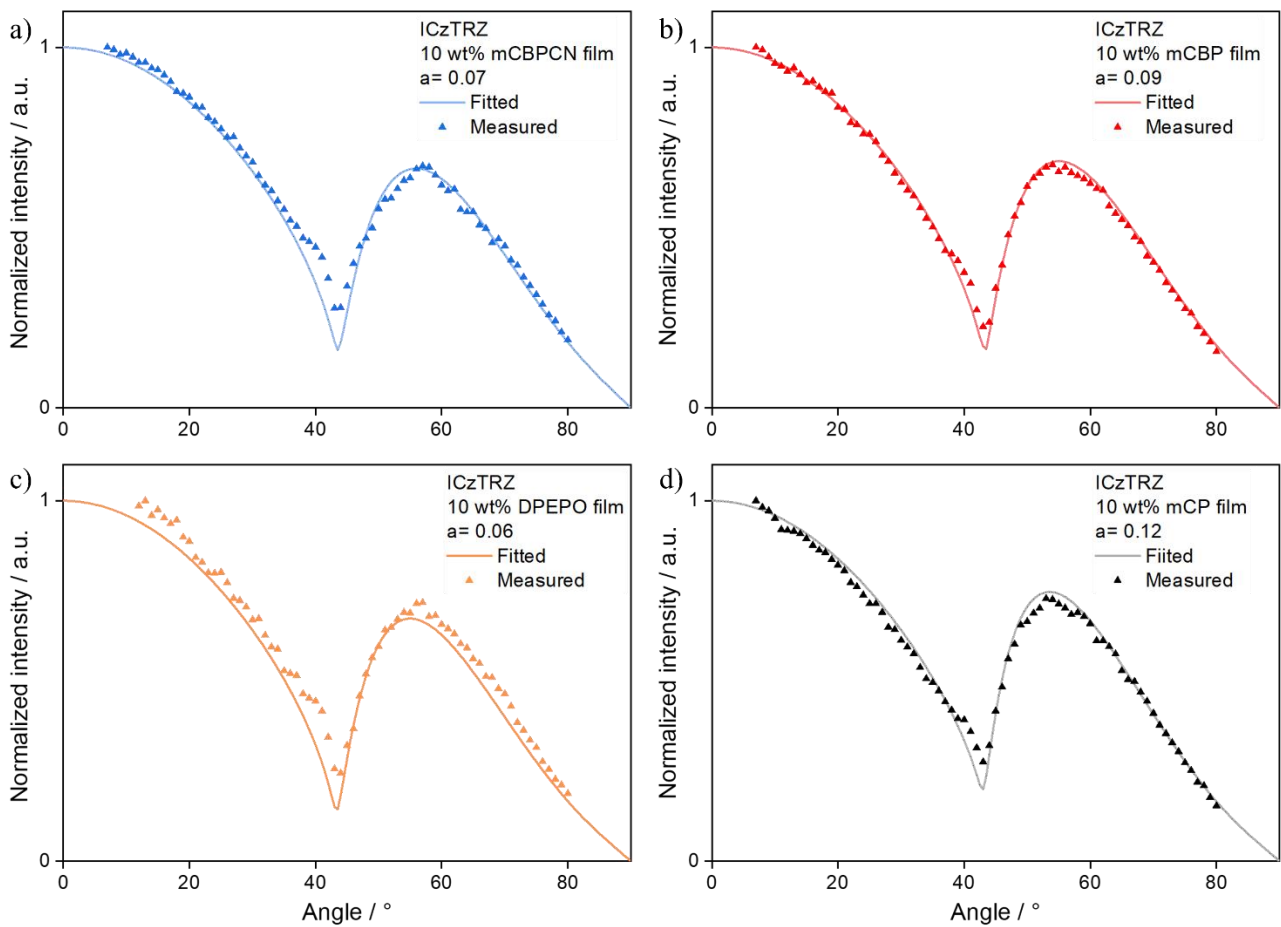


**Figure 92.** Angle-resolved photoluminescence measurement of evaporated films of 10 wt% ICzTRZ in **a)** mCBP-CN, **b)** mCBP, **c)** DPEPO, **d)** mCP. The light continuous lines show a fit using the dipole emission model, yielding the anisotropy factor,  $a$  (data taken at  $\lambda_{PL} = 500$  nm).

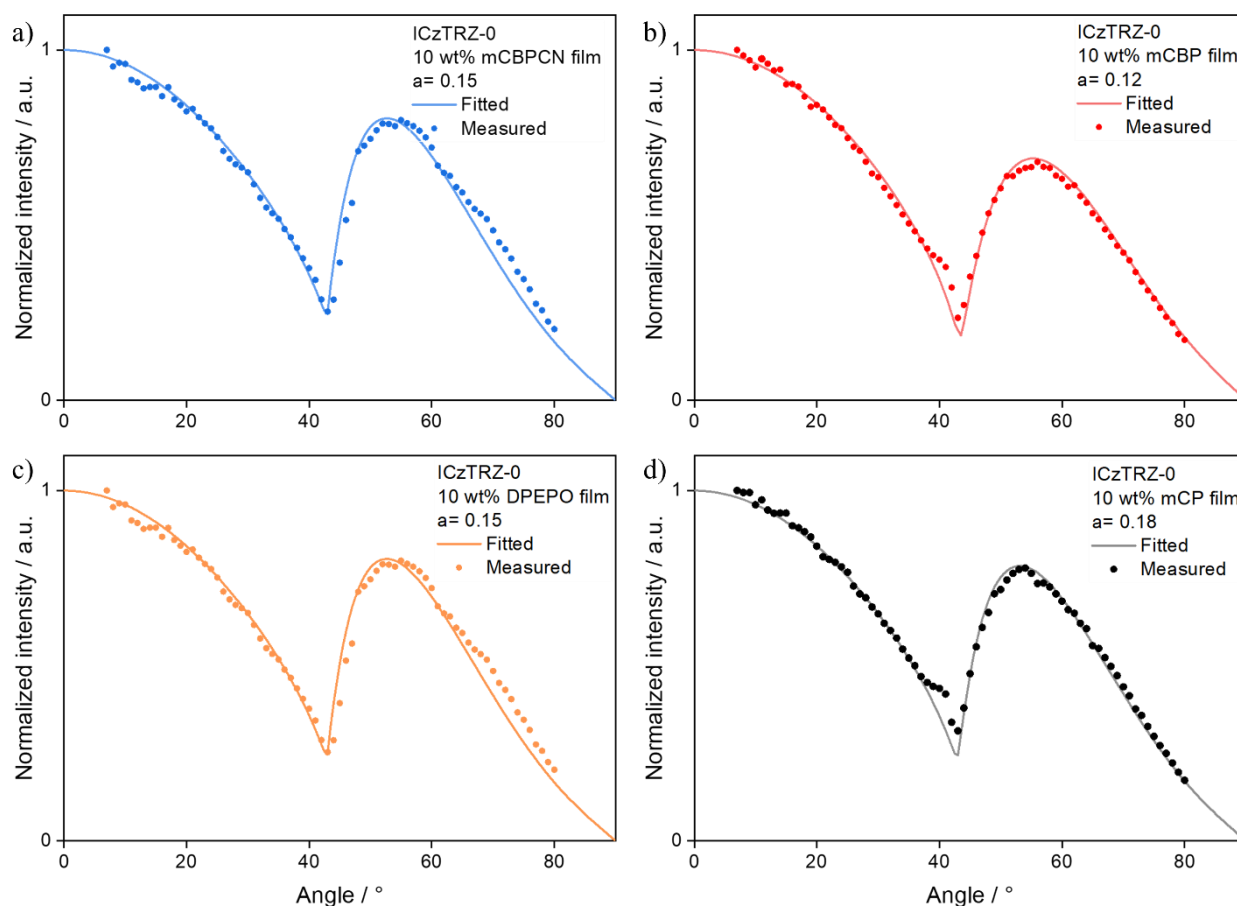


**Figure 93.** Angle-resolved photoluminescence measurement of evaporated films of 10 wt% **ICzTRZ-0** in **a)** mCBP-CN, **b)** mCBP, **c)** DPEPO, **d)** mCP. The light continuous lines show a fit using the dipole emission model, yielding the anisotropy factor,  $a$  (data taken at  $\lambda = 480$  nm).

Angle-dependent luminescence spectroscopy to obtain the anisotropy factors of the materials was performed by Bilal Abbas Naqvi, Prakhar Sahay, and Minh Bình Nguyễn from the Wolfgang Brütting group at the University of Augsburg (**Chapter 4 – Paragraph 4.1 – Attributions**). Each of these emitters possesses a TDM that is mainly horizontally oriented in 10 wt% evaporated films, regardless of the nature of the host matrix (**Table 13**, and **Figure 96**). **ICzTRZ** possesses the smallest anisotropy factor of the series, with  $a$  values of 0.07, 0.09, 0.06, and 0.12 for doped film in mCBPCN, mCBP, DPEPO, and mCP, respectively. The derivative with no *tert*-butyl groups shows the largest  $a$  values of 0.15, 0.12, 0.15, and 0.18 for doped film in mCBP-CN, mCBP, DPEPO, and mCP, respectively. Both **d'Bu-ICzTRZ-0**, and **d'Bu-ICzTRZ** possess nearly identical  $a$  values of 0.09, 0.10, 0.09, and 0.11 (0.10 for **d'Bu-ICzTRZ**) for doped film in mCBPCN, mCBP, DPEPO, and mCP, respectively. Several parameters were then taken into consideration to try and understand the trends observed in these data and what is controlling the orientation of the TDM in this family of emitters.

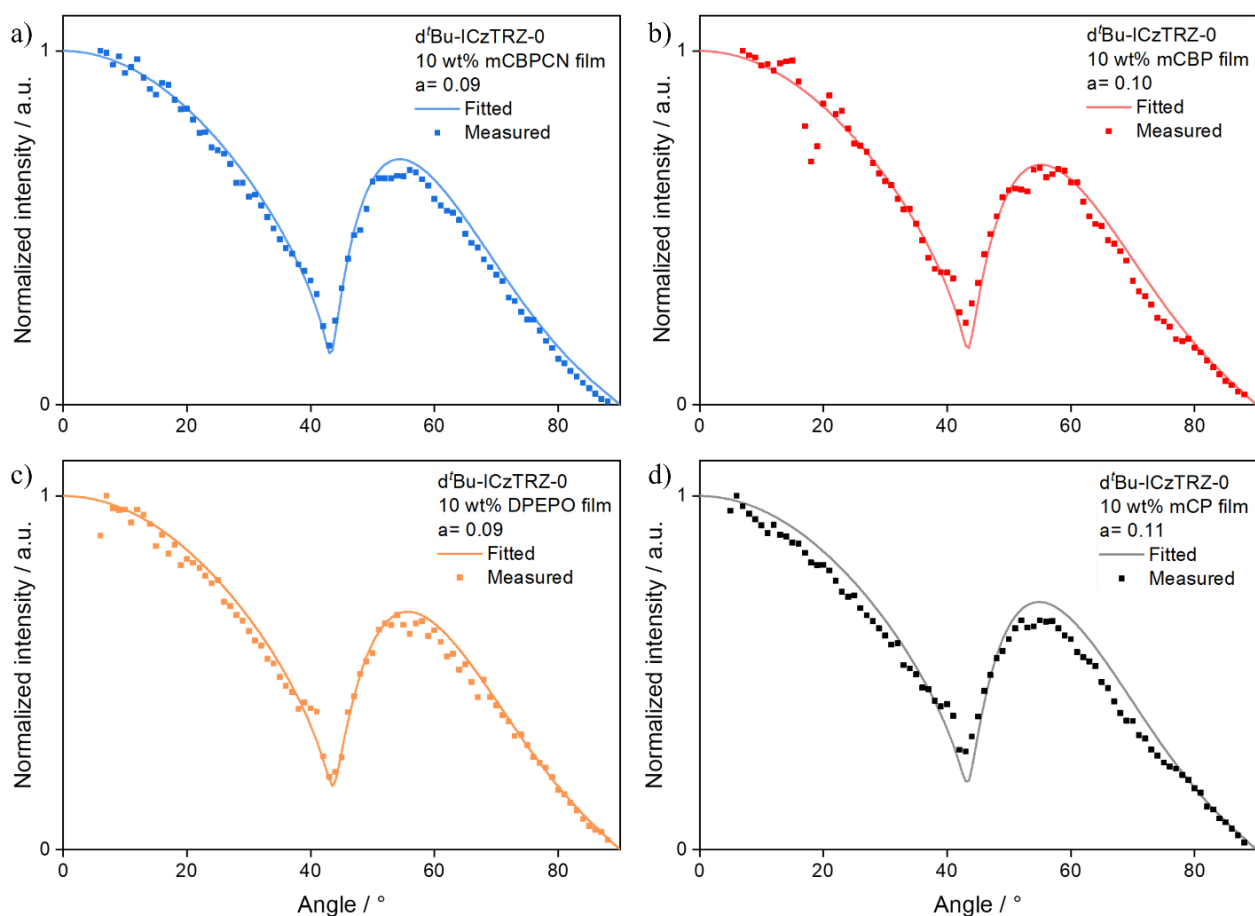


**Figure 94.** Angle-resolved photoluminescence measurement of evaporated films of 10 wt% **d<sup>t</sup>Bu-ICzTRZ-0** in **a)** mCBP-CN, **b)** mCBP, **c)** DPEPO, **d)** mCP. The light continuous lines show a fit using the dipole emission model, yielding the anisotropy factor,  $a$  (data taken at  $\lambda = 490$  nm).

**Table 13.** Orientation data of **ICzTRZ**, **ICzTRZ-0**, **d<sup>t</sup>Bu-ICzTRZ-0**, and **d<sup>t</sup>Bu-ICzTRZ** obtained from angle-resolved photoluminescence measurements in different host materials.

$a$	Doping / wt%	mCBPCN	mCBP	DPEPO	mCP
<b>ICzTRZ</b>	10	0.07	0.09	0.06	0.12
<b>ICzTRZ-0</b>	10	0.15	0.12	0.15	0.18
<b>d<sup>t</sup>Bu-ICzTRZ-0</b>	10	0.09	0.10	0.09	0.11
<b>d<sup>t</sup>Bu-ICzTRZ</b>	10	0.09	0.10	0.09	0.10

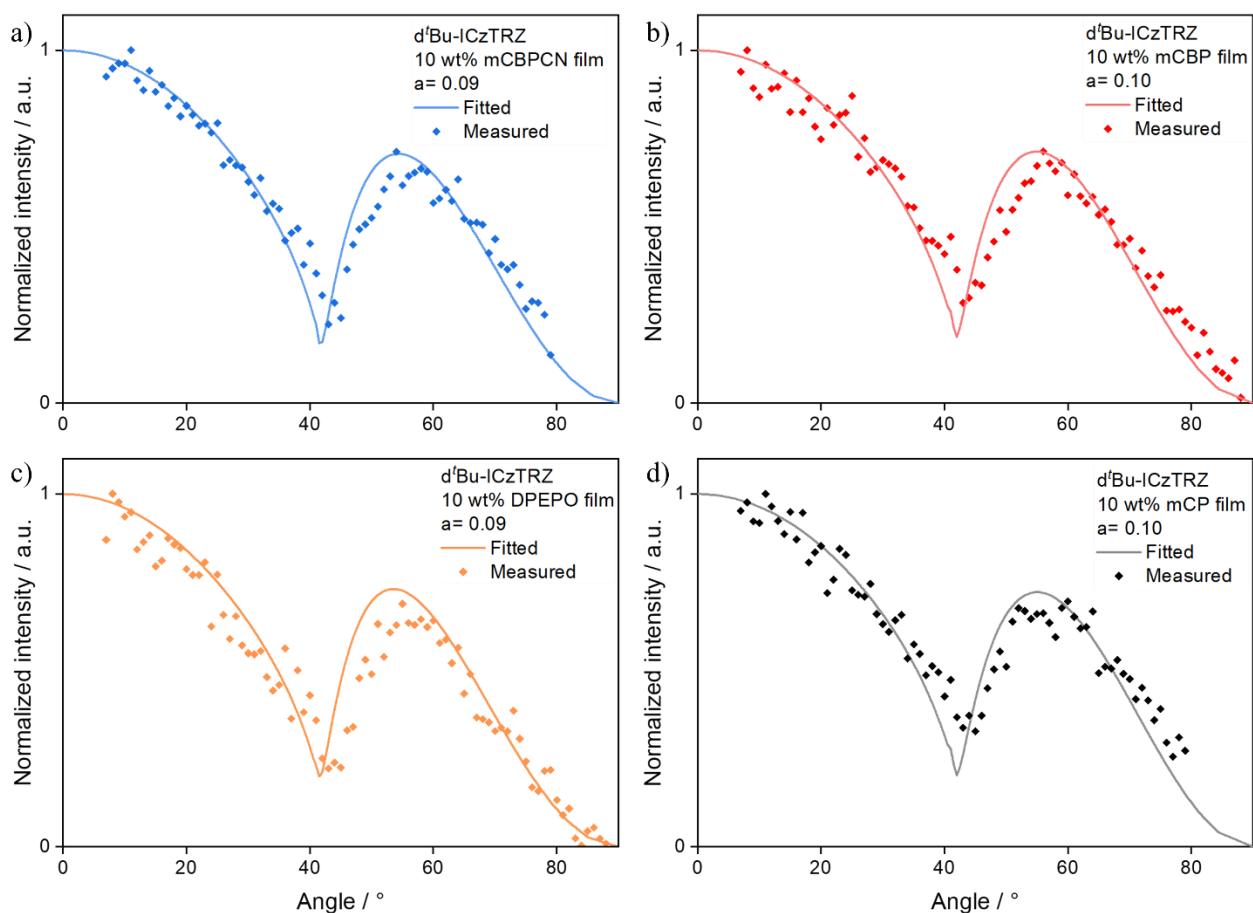


**Figure 95.** Angle-resolved photoluminescence measurement of evaporated films of 10 wt% **d'Bu-ICzTRZ** in **a)** mCBP-CN, **b)** mCBP, **c)** DPEPO, **d)** mCP. The light continuous lines show a fit using the dipole emission model, yielding the anisotropy factor,  $a$  (data taken at  $\lambda = 520$  nm).

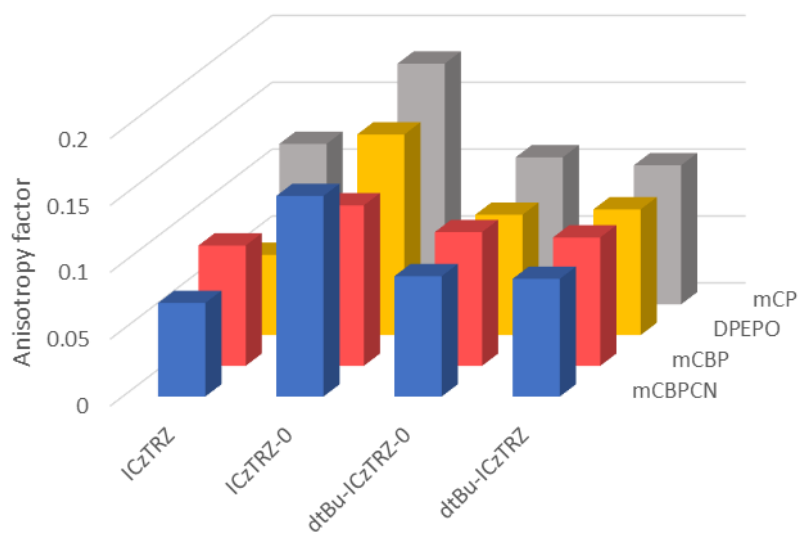


**Figure 96.** 3D plot of the orientation data of **ICzTRZ**, **ICzTRZ-0**, **d'Bu-ICzTRZ-0**, and **d'Bu-ICzTRZ** obtained from angle-resolved photoluminescence measurements in different host materials.

#### 4.3.4 - Effect of the glass transition temperature

**Table 14.** Glass transition temperature of the emitters and the host materials discussed in this study.

Emitters		Hosts	
Molecule	T <sub>g</sub> / °C	Molecule	T <sub>g</sub> / °C
<b>ICzTRZ</b>	253	<b>mCBP-CN</b>	113
<b>ICzTRZ-0</b>	Undetermined	<b>mCBP</b>	92
<b>d'Bu-ICzTRZ-0</b>	227	<b>DPEPO</b>	93
<b>d'Bu-ICzTRZ</b>	264	<b>mCP</b>	65

The first parameter that was considered was the glass transition temperature ( $T_g$ ) of the materials (**Table 14**). TGA and DSC measurements were performed by Francesco Rodella and Daniel Wagner from the Peter Strohriegl group at the University of Bayreuth (**Chapter 4 – Paragraph 4.1 – Attributions**). No  $T_g$  could be determined for **ICzTRZ-0** as no glass transition was observed for this material, while **ICzTRZ**, **d'Bu-ICzTRZ-0**, and **d'Bu-ICzTRZ** present  $T_g$  values of 253°C, 227°C, and 264°C, respectively. It appears that there is no correlation between the  $T_g$  of the emitters and the  $a$  values. This is in line with what was described by Tenopala *et al.*,<sup>23</sup> since these emitters present a MW much higher than 600 g mol<sup>-1</sup>, so the  $T_g$  will have little effect on the  $a$  value as the high MW weight will be enough to stop diffusion phenomena during film deposition. On the other hand, the  $T_g$  of the host materials is correlated with smaller  $a$  values of the doped films. This was already observed in **ICzTRZ**,<sup>68</sup> and it continues to be the case for the rest of the series, with smaller  $a$  values obtained in films with higher  $T_g$  host materials like DPEPO ( $T_g$  of 93 °C) and mCBPCN ( $T_g$  of 113 °C). There is only one value that does not follow this trend, and it is for **ICzTRZ-0** in the 10 wt% doped mCBP film, with  $a$  of 0.12, which represents the best result for **ICzTRZ-0** even if mCBP presents a lower  $T_g$ .

#### 4.3.5 - Molecular weight (MW), thickness ( $z_E$ ) and emitter/host length ratio ( $x_E/x_H$ )

**Table 15.** Molecular weight and calculated properties of **ICzTRZ**, **ICzTRZ-0**, **d<sup>t</sup>Bu-ICzTRZ-0**, and **d<sup>t</sup>Bu-ICzTRZ** (PBE0/6-31G(d,p)).

Emitter	MW /g mol	$x_E^a / \text{Å}$	$y_E^b / \text{Å}$	$z_E^c / \text{Å}$	$L^d$	$P^e$
<b>ICzTRZ</b>	1095.45	31.03	17.05	8.69	0.45	0.49
<b>ICzTRZ-0</b>	871.02	28.12	12.30	6.64	0.56	0.46
<b>d<sup>t</sup>Bu-ICzTRZ-0</b>	983.24	28.11	16.62	7.56	0.41	0.55
<b>d<sup>t</sup>Bu-ICzTRZ</b>	1207.67	31.14	16.87	10.51	0.46	0.38

<sup>a</sup> extension of the emitter along the x axis, also defined as molecular length; <sup>b</sup> extension of the emitter along the y axis; <sup>c</sup> extension of the emitter along the z axis, also defined as molecular thickness; <sup>d</sup> Linearity,  $1-(y_E/x_E)$ ; <sup>e</sup> Planarity,  $1-(y_E/z_E)$ .

All the emitters reported in this study belong to the class with  $MW > 600 \text{ g mol}^{-1}$ , which means that the parameter that should mostly affect their orientation in the evaporated film are the MW, molecular thickness ( $z_E$ ), and the ratio between the length of the emitter and the length of the host ( $x_E/x_H$ ).

**ICzTRZ**'s MW is the second highest in the series, at  $1095.45 \text{ g mol}^{-1}$ , **ICzTRZ-0** is the lightest, at  $871.02 \text{ g mol}^{-1}$ , followed by **d<sup>t</sup>Bu-ICzTRZ-0** at  $983.24 \text{ g mol}^{-1}$ , and finally, **d<sup>t</sup>Bu-ICzTRZ** is the heaviest material in the series at  $1207.67 \text{ g mol}^{-1}$ . The lowest  $a$  value is obtained with **ICzTRZ**, the second heaviest emitter, while the heaviest material, **d<sup>t</sup>Bu-ICzTRZ**, possesses a nearly identical  $a$  value to the much lighter **d<sup>t</sup>Bu-ICzTRZ-0**, meaning that MW alone can't account for the results obtained. **ICzTRZ-0** instead follows this trend perfectly, being the lightest and possessing the least horizontally oriented TDM of the series.

Taking now the thickness of the materials into consideration, **ICzTRZ** present a  $z_E$  value of 8.69, the second highest in the series. The absence of *tert*-butyl groups makes **ICzTRZ-0** the thinnest material, with  $z_E$  of 6.64. The presence of *tert*-butyl groups on the **ICz** leads to a  $z_E$  value of 7.65 for **d<sup>t</sup>Bu-ICzTRZ-0**, and the further addition of the *tert*-butyl groups on the triazines acceptor raises the thickness of **d<sup>t</sup>Bu-ICzTRZ** to 10.51, the highest in the series. It becomes more apparent now why

**ICzTRZ** prevailed on **d'Bu-ICzTRZ** despite the lower MW, as the thinner materials are more prone to better horizontal orientate their TDMs. The same effect can be seen in **d'Bu-ICzTRZ-0**, where the even thinner structure makes up for the smaller MW than **d'Bu-ICzTRZ** yet both compounds show almost identical  $a$  values. **ICzTRZ-0**'s  $z_E$ , however, is not able to compensate in terms of influence on the  $a$  value for the much lower MW, leading to higher anisotropy factor values.

Finally, the length ratio was considered (**Table 16**). As previously mentioned, to achieve an anisotropy factor below 0.1, the  $x_E/x_H$  value needs to be greater than 1.3. All the emitters present  $x_E/x_H > 1.3$ , making it this parameter less impactful on discriminating the differences in  $a$  values amongst the four compounds.

**Table 16.** Ratio between the length of the emitter and the length of the different host materials used (PBE0/6-31G(d,p)).

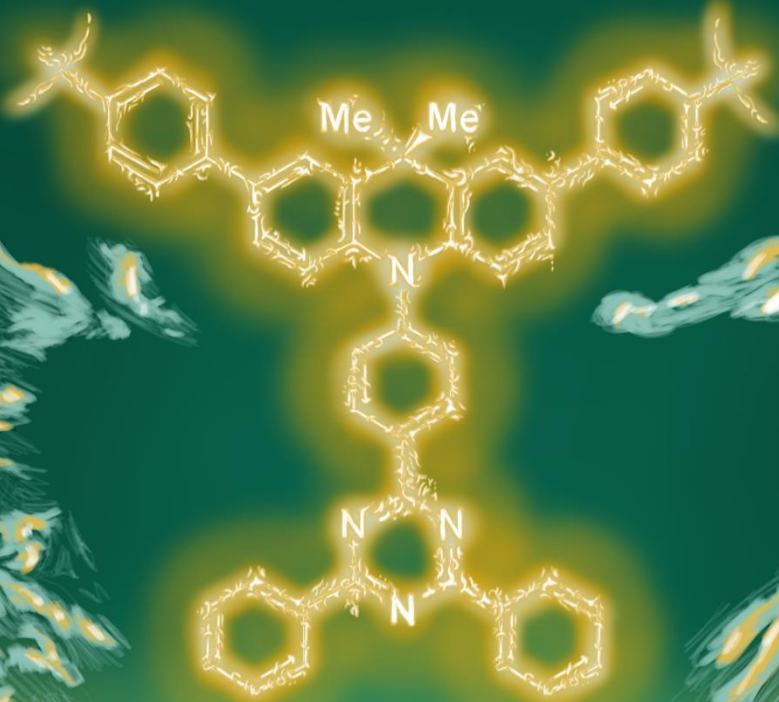
$x_E/x_H$	mCBP-CN	mCBP	DPEPO	mCP
<b>ICzTRZ</b>	1.72	1.86	1.88	2.22
<b>ICzTRZ-0</b>	1.56	1.68	1.70	2.01
<b>d'Bu-ICzTRZ-0</b>	1.56	1.68	1.70	2.01
<b>d'Bu-ICzTRZ</b>	1.73	1.86	1.89	2.23



#### 4.4 – Conclusions

In this study three new materials, **ICzTRZ-0**, **d'Bu-ICzTRZ-0**, and **d'Bu-ICzTRZ** were reported, based on the previously published and discussed **ICzTRZ**.<sup>67,68</sup> A full theoretical study was carried out, showing their potential as TADF emitters, even though due to solubility issues, it wasn't possible to prove this claim. However, a full investigation on the orientation of the materials in evaporated films was carried out in order to study the effect that a different number and position of *tert*-butyl groups have on the anisotropy factor. The results were then analysed by using the model provided by Teonopala *et al.*<sup>23</sup> in their recent review. All the materials possess very horizontally orientated TDMs and the trends in *a* values fit perfectly with the trends presented in the review article, with MW and the thickness of the emitter being the major factors influencing the orientation of the material. A clear continuation of this project will be the study of the optoelectronic properties of these new materials by carrying out measurements on evaporated film of the materials, which wasn't feasible at the time, due to a lack of material.

# ELDEN RISC



**10 / 10**  
5 NOVEL  
EMITTERS

**10 / 10**  
STUDY OF  
DIFFERENT  
SUBSTITUENTS

**10 / 10**  
EFFICIENT  
DEVICES

PS5 | PS4 | XBOX ONE | XBOX SERIES X|S | PC DIGITAL

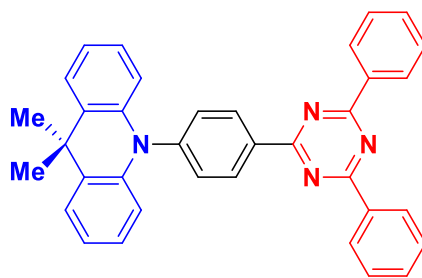
## Chapter 5 – Acridine modification to achieve horizontal orientation and long-lived and efficient TADF-OLEDs.

### 5.1 - Attributions

I am the main author of this text. Unless otherwise stated in the text, I directly carried out the experimental work presented. Of the work presented in this chapter, I designed and synthesized the materials, conducted the theoretical calculations and optoelectronic characterization (CV-DPV, UV-vis, solvatochromism study, and solution state steady-state and time-resolved photoluminescence measurements). The solid-state photophysical properties of the materials were investigated by me and Kleitos Stavrou from the group of Prof. Andrew Monkman at the University of Durham. Kleitos Stavrou also undertook the fabrication of the devices, and I then measured their properties. Angle-dependent luminescence spectroscopy to obtain the anisotropy factors of the materials was performed by Prakhar Sahay and Minh Bình Nguyễn from the group of Prof. Wolfgang Brütting at the University of Augsburg. The paper highlighting this work is currently being written.

### 5.2 - Introduction

**DMAC** is a widely used donor group for TADF emitter design is **DMAC**. The combination of **DMAC** and triphenyl-triazine has been explored in many reports and the archetype of this family of emitters is **DMAC-TRZ**, first reported by Tsai *et al.*<sup>72</sup> This compound has a very small  $\Delta E_{ST}$  of 0.046 eV in mCBPCN film, caused by the orthogonal conformation of donor and acceptor. **DMAC-TRZ** emits sky-blue light at a  $\lambda_{PL}$  of 495 nm, with a high  $\Phi_{PL}$  of 90% and was employed in efficient devices with  $EQE_{max}$  of 26.5%, at a  $\lambda_{EL}$  of 500 nm. **DMAC-TRZ** also exhibits very low concentration quenching, with the neat film of the material showing a  $\Phi_{PL}$  of 83%. The non-doped device showed an  $EQE_{max}$  of 20.0%.<sup>72</sup> Both the doped and non-doped devices were among the highest performing device at the time of their publication, and due to these good properties and simple design, **DMAC-TRZ** has been investigated extensively as the emitter in several computational and photophysical studies.<sup>68,170,171</sup>



### DMAC-TRZ

$\Delta E_{ST}$ : 0.046 eV

$\lambda_{PL}$ : 495 nm;  $\Phi_{PL}$  : 90% in 8 wt% mCPCN film

$\lambda_{PL}$ : 500 nm;  $\Phi_{PL}$  : 83% in neat film

$\lambda_{EL}$ : 500 nm;  $EQE_{max}$ : 26.5% (doped)

$\lambda_{EL}$ : 510 nm;  $EQE_{max}$ : 20.0% (neat)

*Chem. Commun.*, **2015**, 51, 13662-13665

**Figure 97.** Chemical structure and properties of **DMAC-TRZ** in its first report.<sup>72</sup>

Kaji and co-workers reported two modified structures of **DMAC-TRZ** incorporating adamantane in **MA-TA**,<sup>73</sup> and **a-DMAC-TRZ**<sup>172</sup> (**Figure 98**). In the first report, the substitution of the two distal phenyl rings on the triazine acceptor with adamantyl units reduced the electronic conjugation of the material, leading to a wider separation between the HOMO and LUMO and thus, a bluer emission. Toluene solutions and neat films of **DMAC-TRZ** and **MA-TA** were compared, showing a blue-shifted emission of 469 nm in solution and 453 nm in neat films for **MA-TA**, compared to 494 nm in solution and 500 nm in neat films for **DMAC-TRZ**. The use of the adamantyl fragment also produces a soluble and thermally stable material and was then employed in solution-processed devices. CzSi was chosen as the host, since its amorphous nature and high glass transition temperature prevent crystallization during the spin-coating process, making it a viable host material for solution-processed devices.<sup>155</sup> The 10 wt% doped film of **MA-TA** in CzSi shows a near unity  $\Phi_{PL}$  of 99%. Efficient blue devices, with an  $EQE_{max}$  of 22.1%, at  $\lambda_{EL}$  of 475 nm, were fabricated, showing some of the highest performance metrics for blue, solution-processed OLEDs.<sup>45</sup>

The insertion of the adamantyl on the triazine blue-shifts the emission by weakening the acceptor, while the functionalization of the donor, in **a-DMAC-TRZ**, increased the rigidity of the structure. This suppressed non-radiative decays pathways, leading to a very efficient device with  $EQE_{max}$  of 28.9% and blue emission with  $\lambda_{EL}$  of 488 nm.

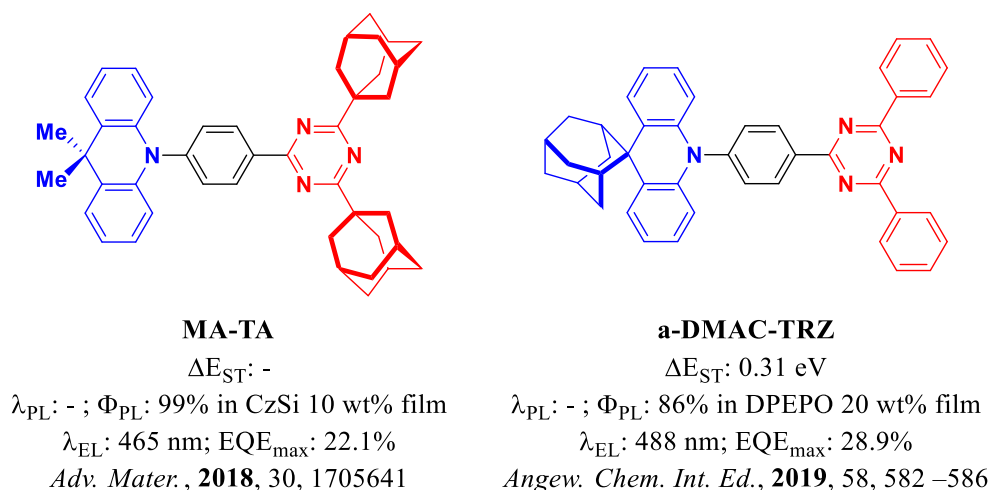


**Figure 98.** Chemical structure and properties of **MA-TA**<sup>73</sup> and **a-DMAC-TRZ**.<sup>172</sup>

Kaji and co-workers published another acceptor modification of **DMAC-TRZ**, with the emitter **DMAC-bPmT** (**Figure 99**), where the two distal phenyl rings of the triazine were replaced by pyrimidines.<sup>74</sup> An in-depth computational study was carried out and it was found that the more electronegative pyrimidines stabilize the energy of the  $S_2$  and  $T_2$  states (defined as  $CT_B$  in the paper) and bring them closer to the  $S_1$  and  $T_1$  states ( $CT_A$  in the paper), which enhanced the  $k_{RISC}$  of the material thanks to the improved SOC between  $CT_{A/B}^1$  and  $CT_{B/A}^3$ . **DMAC-bPmT** possesses a  $k_{RISC}$  of  $8.8 \times 10^5 \text{ s}^{-1}$ , which is c.a. three times faster than the  $k_{RISC}$  of **DMAC-TRZ**, at  $2.9 \times 10^5 \text{ s}^{-1}$ ; however, the  $\Phi_{PL}$  of 70% is lower ( $\Phi_{PL}$  of 93% for **DMAC-TRZ**) and there is a slight red-shift in the emission at  $\lambda_{PL}$  of 520 nm ( $\lambda_{PL}$  500 nm for **DMAC-TRZ**), measured in a toluene solution, the result of the stronger nature of the acceptor.

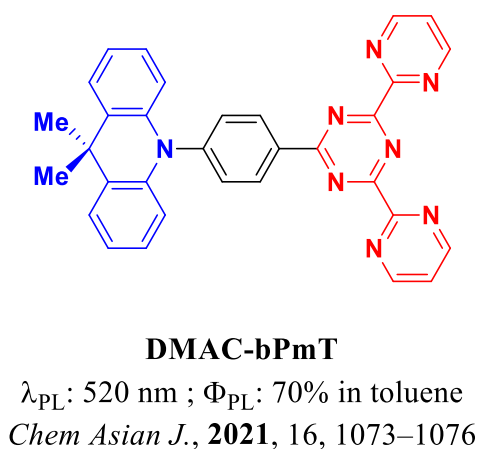


**Figure 99.** Chemical structure and properties of **DMAC-bPmT**.<sup>74</sup>

Feng *et al.*<sup>75</sup> described an arylmethylation strategy to enhance the horizontal orientation of **DMAC-TRZ** derivatives, the parent compound of which was known to present isotropic orientation.<sup>68</sup> **PFDMAC-TRZ** and **DPFDMAC-TRZ** (Figure 100) contained a **DMAC** donor that was functionalized by one and two 9-phenyl-9H-fluorene groups, respectively. These two materials possessed small  $\Delta E_{ST}$  values of 0.16 eV (vs 0.13 eV for **DMAC-TRZ**) and high  $\Phi_{PL}$  of 93%, and 97% (vs 88% for **DMAC-TRZ**) for **PFDMAC-TRZ** and **DPFDMAC-TRZ**, respectively, in a 30 wt% doped DPEPO film. These functional groups also managed to improve the horizontal orientation of the TDMs by increasing the molecular weight and length of these compounds.<sup>23</sup> **DMAC-TRZ**, **PFDMAC-TRZ**, and **DPFDMAC-TRZ** possess anisotropy factors of 0.29, 0.22, and 0.19 respectively, and the more horizontal orientation is then translated into the device performance, with increasingly higher  $EQE_{max}$  of 26.3%, 35.1%, and 37.0% for the devices with **DMAC-TRZ**, **PFDMAC-TRZ**, and **DPFDMAC-TRZ**, respectively.

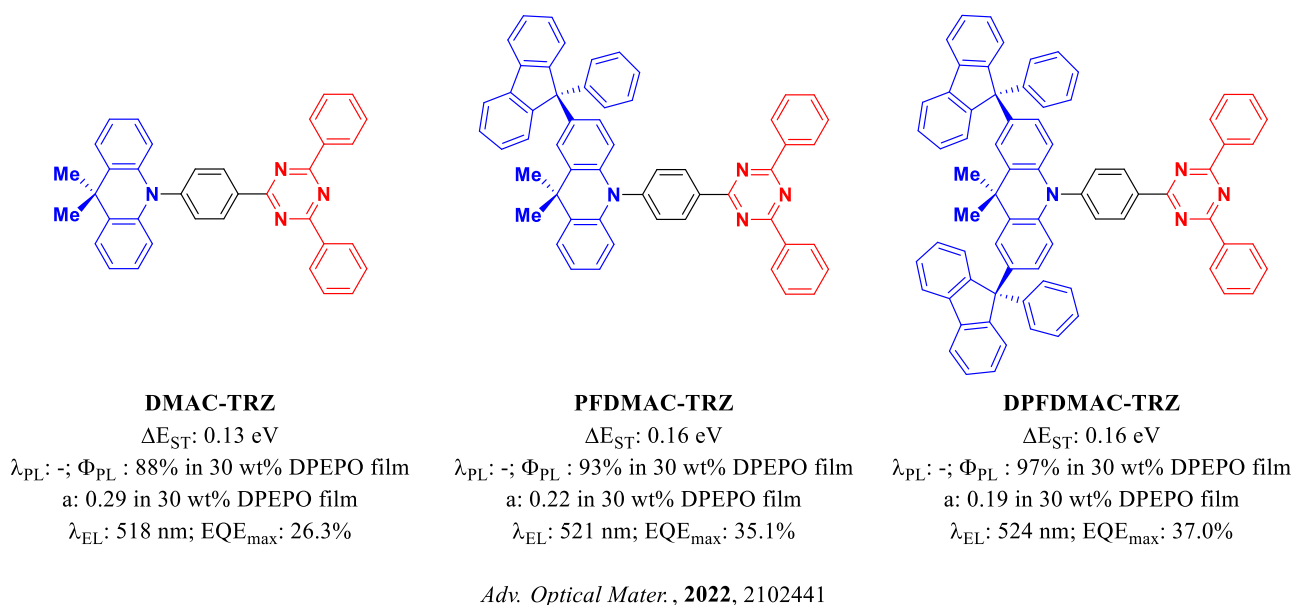
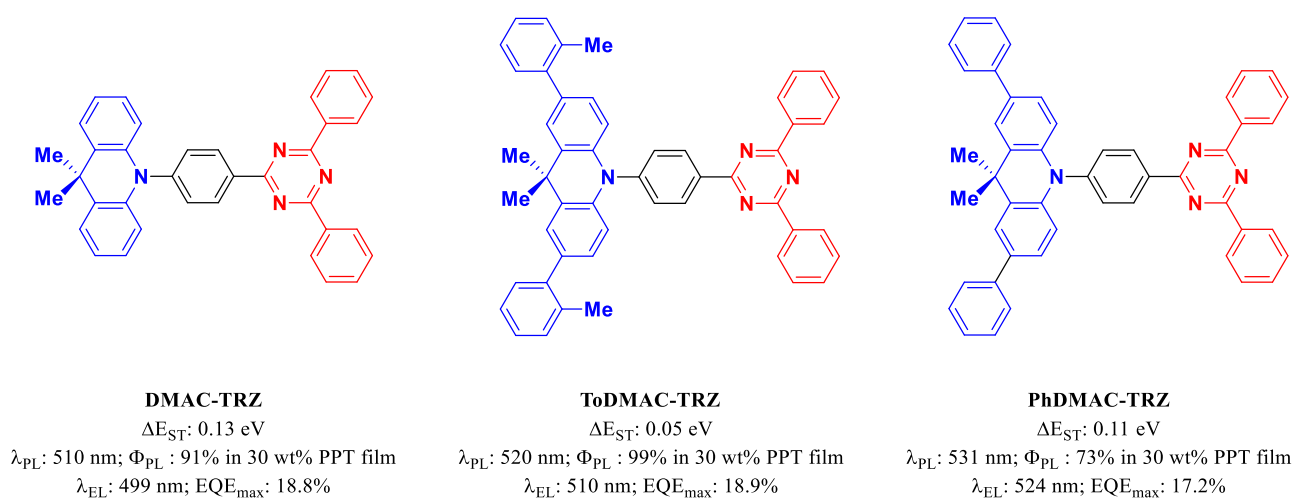


**Figure 100.** Chemical structure and properties of **DMAC-TRZ**, **PFDMAC-TRZ**, and **DPFDMAC-TRZ**.<sup>75</sup>

Other extended **DMAC-TRZ** derivatives were reported by Lie *et al.*, with the emitters **ToDMAC-TRZ** and **PhDMAC-TRZ** (Figure 101).<sup>80</sup> The functionalization of **DMAC-TRZ** with an *ortho*-tolyl unit and a phenyl unit decreases the  $\Delta E_{ST}$  from 0.13 eV for **DMAC-TRZ** to 0.05 eV for **ToDMAC-TRZ** and 0.11 eV for **PhDMAC-TRZ**. The presence of the methyl groups in the *ortho* position could explain the very low  $\Delta E_{ST}$  value of 0.05 eV as they help to ensure that the dihedral angle remains close to 90°. The emission maxima in doped film (30 wt% in PPT) are red-shifted, from 510 nm for

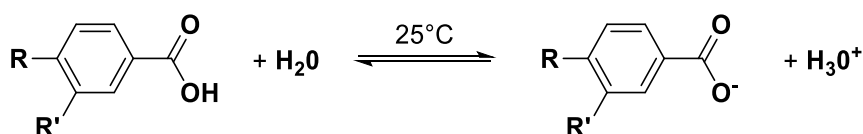
**DMAC-TRZ**, to 520 nm, and 531 nm for **ToDMAC-TRZ** and **PhDMAC-TRZ**, respectively. This is due to the conjugation of the aromatic groups with the DMAC donor core, which results in a destabilized donor-centred HOMO. The  $\Phi_{\text{PL}}$  of the material in doped films is 91%, 99%, and 73% for **DMAC-TRZ**, **ToDMAC-TRZ**, and **PhDMAC-TRZ**, respectively. Devices of these three materials showed  $\text{EQE}_{\text{max}}$  of 18.8%, 18.9%, and 17.2% at  $\lambda_{\text{EL}}$  of 499 nm, 510 nm, and 524 nm, respectively. Despite the lower efficiency, the OLED employing **PhDMAC-TRZ** possessed a lifetime ( $t_{50}$ ) much longer than that with **DMAC-TRZ**, with values of 70 h for the OLED with **DMAC-TRZ** and 1910 h for the OLED with **PhDMAC-TRZ**. The OLED with **ToDMAC-TRZ** also showed an improved lifetime, but only at 198 h.



*ACS Appl. Mater. Interfaces*, **2022**, 14, 22332–22340

**Figure 101.** Chemical structure and properties of **DMAC-TRZ**, **ToDMAC-TRZ**, and **PhDMAC-TRZ**.<sup>80</sup>

In this chapter, five novel emitters, **CNPh-DMAC-TRZ**, **CF<sub>3</sub>Ph-DMAC-TRZ**, **dPh-DMAC-TRZ**, **tBuPh-DMAC-TRZ**, **OMePh-DMAC-TRZ** (**Figure 102**) are presented. In these materials, the acridine donor has been modified to incorporate two aryl rings. The functional groups on the aryl groups ranged from EDGs such as *tert*-butyl and methoxy, to EWGs like trifluoromethyl and cyano, and finally, an extra phenyl ring, which was targeted to act to extend the conjugation length of the substituent.



**Scheme 4.** Deprotonation of benzoic acid.

A powerful tool to define the electron donating and electron withdrawing character of a substituent are the Hammett parameters.<sup>173,174</sup> The Hammett parameters are obtained from the Hammett equation (**Equation 58**), which was firstly introduced by Louis Plack Hammett in 1937.<sup>173</sup> This equation relates the equilibrium constant of the deprotonation of benzoic acid ( $K_o$ , R, R'= H), and benzoic acid derivatives ( $K$ ) (**Scheme 4**) to the substituent constant ( $\sigma$ ), and to the reaction constant ( $\rho$ ).

$$\log K = \log K_o + \sigma \rho \quad (58)$$

$\sigma$  will depend exclusively on the substituent on the benzoic acid, and  $\rho$  will depend exclusively on the reaction type (for the deprotonation of benzoic acid,  $\rho$  is arbitrarily set to 1). The position of the substituent will also matter, with different parameters,  $\sigma_p$  or  $\sigma_m$ , for para or meta substituted benzoic acid respectively. Ortho substitution is not considered as it could induce steric effect with the carboxylic acid. A positive  $\sigma$  value indicates that the acidity of benzoic acid has increased, due to the stabilization of its conjugated base. *Vice versa*, a negative  $\sigma$  value indicates that the acidity of benzoic acid had decreased. As EWG stabilize the conjugated base, they will present a positive  $\sigma$ , while EDG will have a negative  $\sigma$ .

Throughout the chapter, these materials have been ordered from the highest to the lowest Hammett substituent ( $\sigma$ ) to simplify the visualization of trends ( $\sigma$  values are CN +0.66, CF<sub>3</sub> +0.54, Ph -0.01, <sup>t</sup>Bu -0.20, OMe -0.268).<sup>174,175</sup> This order goes from the strongest EWG substituent to the stronger EDG substituent. The main goal is to study the effect that the different functional groups would have on the photophysical behavior of the parent emitter, **DMAC-TRZ**, and at the same time, increase its molecular weight and length in order to try and achieve a more horizontal orientation of the TDM, and thus improve the efficiency of the OLEDs.



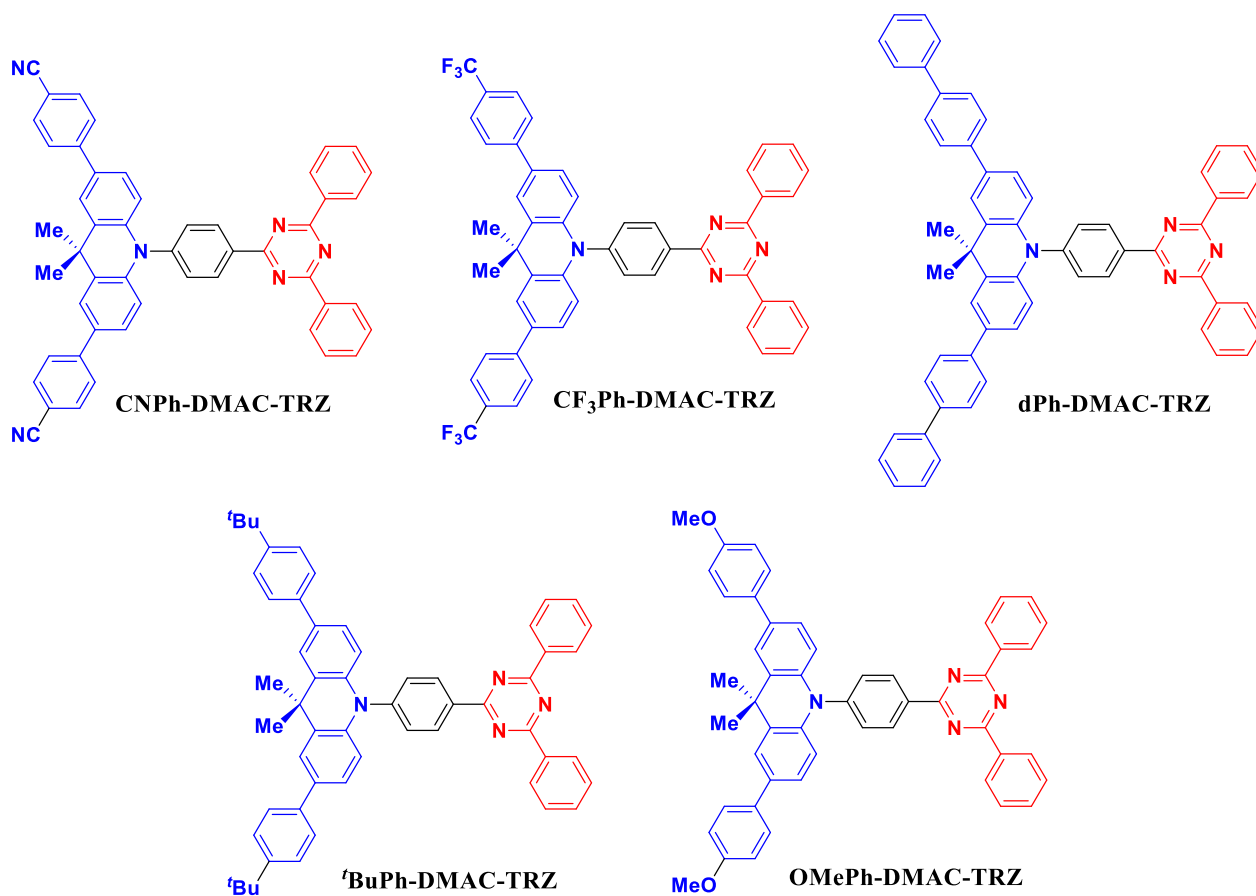
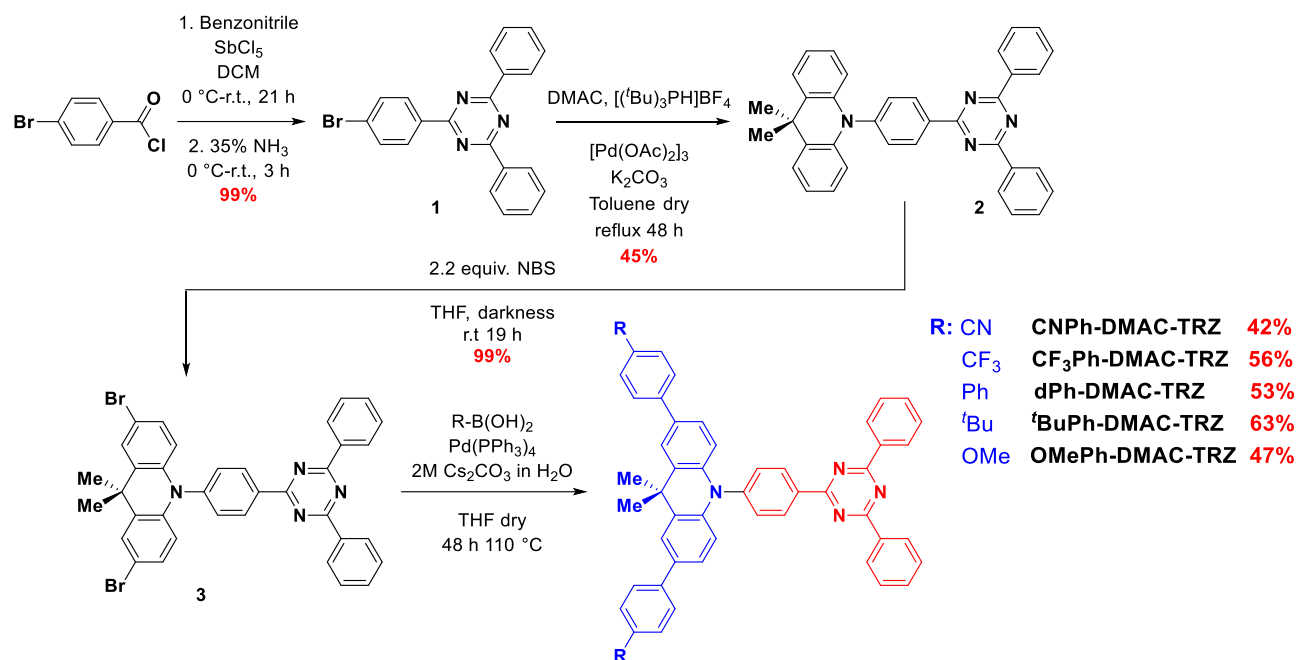


**Figure 102.** Chemical structure of CNPh-DMAC-TRZ, CF<sub>3</sub>Ph-DMAC-TRZ, dPh-DMAC-TRZ, <sup>t</sup>BuPh-DMAC-TRZ, OMePh-DMAC-TRZ.

## 5.3 - Results and discussion

### 5.3.1 - Synthesis



**Scheme 5.** Synthetic procedure for the five **DMAC-TRZ** derivatives.

The five **DMAC-TRZ** derivatives were synthesized *via* a four-step synthetic procedure (**Scheme 5**). The first step is the synthesis of the bromotriazine (**1**), which proceeds in nearly quantitative yields and involves Lewis acid-catalyzed cyclization of 4-bromobenzoyl chloride and benzonitrile using antimony pentachloride in DCM, followed by the addition of a 35% aqueous ammonia solution.<sup>176</sup> The triazine is then coupled to DMAC through a Buchwald-Hartwig coupling in 40% yield to obtain **2**. **DMAC-TRZ** is then brominated with 2.2 equivalents of N-Bromosuccinimide (NBS) in THF, shielded from light overnight, with nearly complete conversion to achieve **3**.<sup>177</sup> The final step is a Suzuki coupling with the corresponding aryl-boronic acid, with tetrakis(triphenylphosphine)palladium(0) as the catalyst, and a 2M aqueous solution of cesium carbonate as the base, in THF, carried out in a pressure vessel at 110 °C for 48 h, to obtain the final product. Yields for the final step ranged between c.a. 50% and 70%. The identity and purity of the compounds were confirmed by <sup>1</sup>H, <sup>13</sup>C, and <sup>19</sup>F spectroscopy NMR, Mp determination, HRMS, HPLC, and EA.

### 5.3.2 - Theoretical calculations

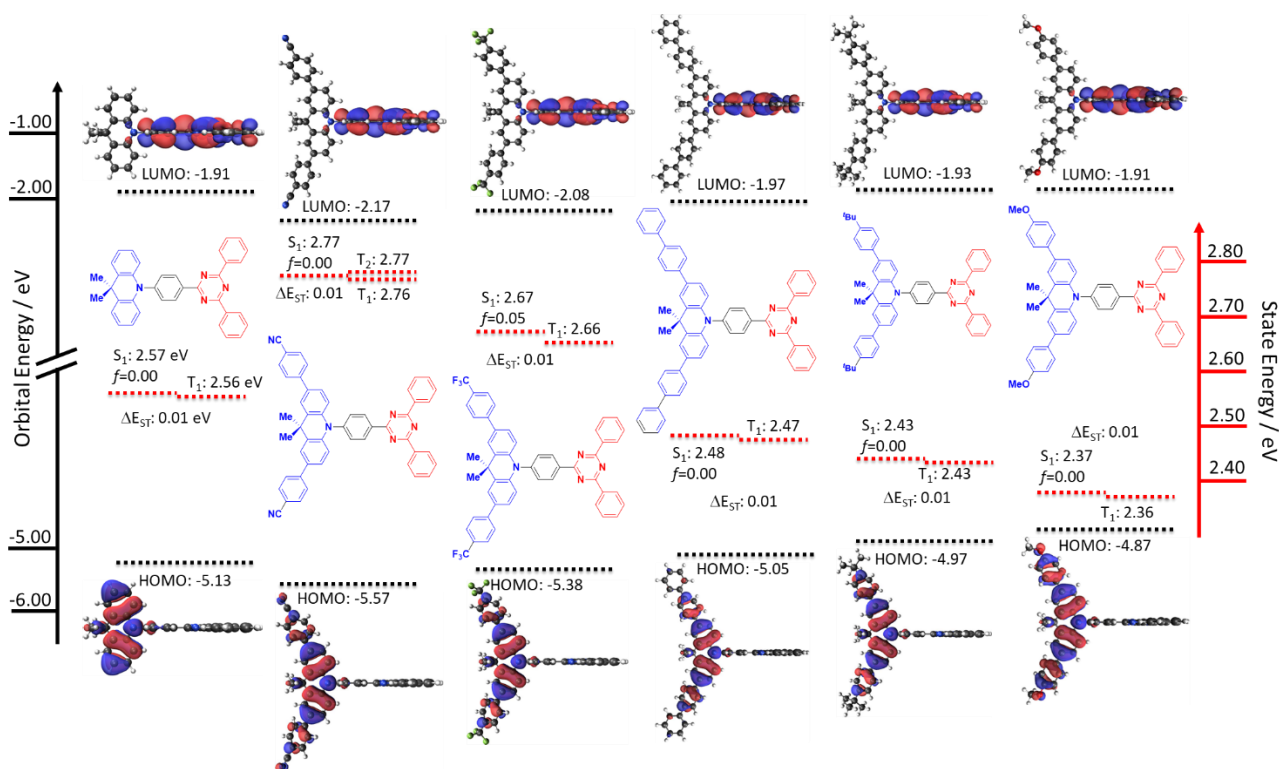


**Figure 103.** HOMO and LUMO electron density distributions and energy levels, excited state energy levels of **DMAC-TRZ** and derivatives (Obtained via DFT and TD-DFT at the PBE0/6-31G(d,p) level, Isovalue for new surfaces: MO=0.02, Density=0.0004).

The same DFT methodologies employed in the previously discussed indolocarbazole-based emitter studies were used for **DMAC-TRZ** and the five new derivatives (**Figure 103**) to first assess their properties. **DMAC-TRZ** presents HOMO and LUMO energy levels of -5.13 eV, and -1.91 eV, respectively. The ground-state optimization of the material shows a structure with a twist angle of almost 90°, as previously observed in the literature,<sup>72</sup> leading to a very low overlap between the HOMO and the LUMO, and thus an almost zero  $\Delta E_{ST}$ , with  $S_1$  and  $T_1$  levels of 2.57 eV and 2.56 eV, respectively. The small overlap between the HOMO and LUMO also leads to an oscillator strength with a value of zero.

The ground-state optimized structures of the five derivatives presented the same 90° dihedral angle conformation as that of the parent emitter **DMAC-TRZ**, and thus also very small  $\Delta E_{ST}$  values of c. a. 0.01 eV, as communication between the donor and acceptor is almost non-existent in this conformation. It can be seen that a stronger electron-donating character of the substituent leads to a

destabilization of the HOMO energy level by increasing the electron density on the acridine donor, with values of -5.57 eV, -5.38 eV, -5.05 eV, -4.97 eV, and -4.87 eV for **CNPh-DMAC-TRZ**, **CF<sub>3</sub>Ph-DMAC-TRZ**, **dPh-DMAC-TRZ**, **'BuPh-DMAC-TRZ**, **OMePh-DMAC-TRZ**, respectively. The LUMO levels are affected in the same way, with them being stabilized by more electron-withdrawing substituents, as they lower the electron density on both the acridine donor and the triazine acceptor, as they are somewhat conjugated. The LUMO values are -2.17 eV, -2.08 eV, -1.97 eV, -1.93 eV, and -1.91 eV for **CNPh-DMAC-TRZ**, **CF<sub>3</sub>Ph-DMAC-TRZ**, **dPh-DMAC-TRZ**, **'BuPh-DMAC-TRZ**, **OMePh-DMAC-TRZ**, respectively. The HOMO of **DMAC-TRZ** (-5.13 eV) falls in the middle of the series between **CF<sub>3</sub>Ph-DMAC-TRZ** and **dPh-DMAC-TRZ**, marking the changeover between EDG and EWG substituted materials. The LUMO of **DMAC-TRZ** (-1.91 eV) behaves differently than the HOMO, falling between those of **dPh-DMAC-TRZ** and **'BuPh-DMAC-TRZ**. The phenyl group is an inductively electron withdrawing group, which can then slightly stabilize the LUMO level, making it lower in energy than **DMAC-TRZ**'s.

**Table 17.** Simulated properties of **DMAC-TRZ** and derivatives (Obtained via DFT and TD-DFT at the PBE0/6-31G(d,p) level, Isovalue for new surfaces: MO=0.02, Density=0.0004).

<b>R-DMAC-TRZ</b>	<b>HOMO / eV<sup>a</sup></b>	<b>LUMO / eV<sup>a</sup></b>	<b>T<sub>1</sub> / eV<sup>a</sup></b>	<b>S<sub>1</sub> / eV<sup>a</sup></b>	<b>ΔE<sub>ST</sub> / eV<sup>a</sup></b>
<b>DMAC-TRZ</b>	-5.13	-1.91	2.56	2.57	0.01
<b>CNPh-</b>	-5.57	-2.17	2.76	2.77	0.01
<b>CF<sub>3</sub>Ph-</b>	-5.38	-2.08	2.66	2.67	0.01
<b>dPh-</b>	-5.05	-1.97	2.47	2.48	0.00
<b>'BuPh-</b>	-4.97	-1.93	2.43	2.43	0.00
<b>OMePh-</b>	-4.87	-1.91	2.36	2.37	0.00

<sup>a</sup> Obtained via DFT and TD-DFT at the PBE0/6-31G(d,p) level.

Triplet and singlet energy levels are also affected by the nature of the substituent on the DMAC donor, with the energies of the excited states becoming progressively more stabilized with stronger electron-donating substituents on the donor. The S<sub>1</sub>/T<sub>1</sub> energies are 2.77/2.76 eV, 2.67/2.66 eV, 2.48/2.47 eV, 2.37/2.36 eV, and 2.43/2.43 eV for **CNPh-DMAC-TRZ**, **CF<sub>3</sub>Ph-DMAC-TRZ**, **dPh-DMAC-TRZ**, **'BuPh-DMAC-TRZ**, **OMePh-DMAC-TRZ**, respectively. The S<sub>1</sub>/T<sub>1</sub> energies of **DMAC-TRZ** are between those of **CF<sub>3</sub>Ph-DMAC-TRZ** and **dPh-DMAC-TRZ**. All the compounds possess S<sub>1</sub> and T<sub>1</sub>

states that possess charge transfer character (HOMO→LUMO transition). **dCNPh-DMAC-TRZ** is the only molecule that possesses a degenerate T<sub>2</sub> state, which has a locally excited character, localized on the donor moiety (HOMO→LUMO+2 transition). The c. a. 90° conformation and very small ΔE<sub>ST</sub> values of ca. 0.01 eV also leads to an effective oscillator strength value of 0.00. The only exception is observed in **CF<sub>3</sub>Ph-DMAC-TRZ** with a *f* of 0.05.

**Table 18.** Excited states properties of **DMAC-TRZ** and derivatives.

Excited State <sup>a</sup>	Energy / eV	Nature <sup>b</sup>	Character of the transition
<b>DMAC-TRZ</b>			
<b>T<sub>1</sub></b>	2.56	<b>H→L (97%)</b> H→(L+2) 2%	<sup>3</sup> CT
<b>S<sub>1</sub> (f=0.00)</b>	2.57	<b>H→L (97%)</b> H→(L+2) 2%	<sup>1</sup> CT
<b>CNPh-DMAC-TRZ</b>			
<b>T<sub>1</sub></b>	2.76	<b>H→L (97%)</b>	<sup>3</sup> CT
<b>S<sub>1</sub> (f=0.00)</b>	2.77	<b>H→L (97%)</b>	<sup>1</sup> CT
<b>CF<sub>3</sub>Ph-DMAC-TRZ</b>			
<b>T<sub>1</sub></b>	2.66	<b>H→L (97%)</b>	<sup>3</sup> CT
<b>S<sub>1</sub> (f=0.05)</b>	2.67	<b>H→L (97%)</b>	<sup>1</sup> CT
<b>dPh-DMAC-TRZ</b>			
<b>T<sub>1</sub></b>	2.47	<b>H→L (97%)</b>	<sup>3</sup> CT
<b>S<sub>1</sub> (f=0.00)</b>	2.48	<b>H→L (97%)</b>	<sup>1</sup> CT
<b>OMePh-DMAC-TRZ</b>			
<b>T<sub>1</sub></b>	2.36	<b>H→L (97%)</b>	<sup>3</sup> CT
<b>S<sub>1</sub> (f=0.00)</b>	2.37	<b>H→L (97%)</b>	<sup>1</sup> CT
<b>tBuPh-DMAC-TRZ</b>			
<b>T<sub>1</sub></b>	2.43	<b>H→L (97%)</b>	<sup>3</sup> CT
<b>S<sub>1</sub> (f=0.00)</b>	2.43	<b>H→L (97%)</b>	<sup>1</sup> CT

<sup>a</sup> (PBE0/6-31G(d,p)); <sup>b</sup> the transitions highlighted in red are the main ones contributing to the excited state character.

### 5.3.3 - Optoelectronics properties

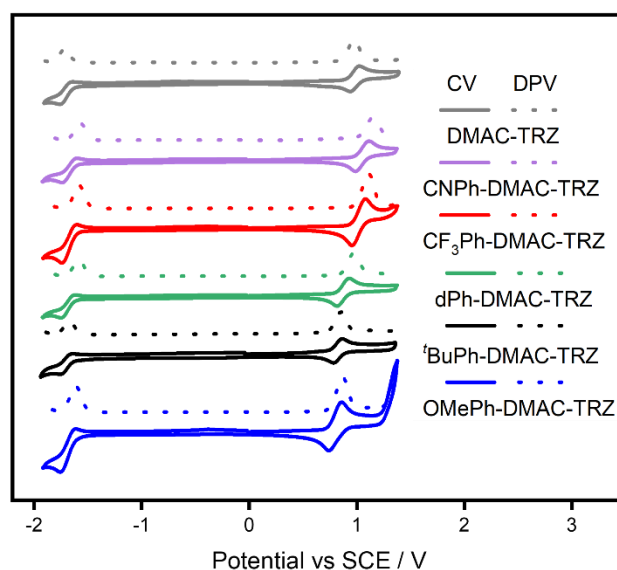


**Figure 104.** Cyclic Voltammetry (CV) and Differential Pulse Voltammetry (DPV) of **DMAC-TRZ** and derivatives in DCM (scan rate = 100 mV/s).

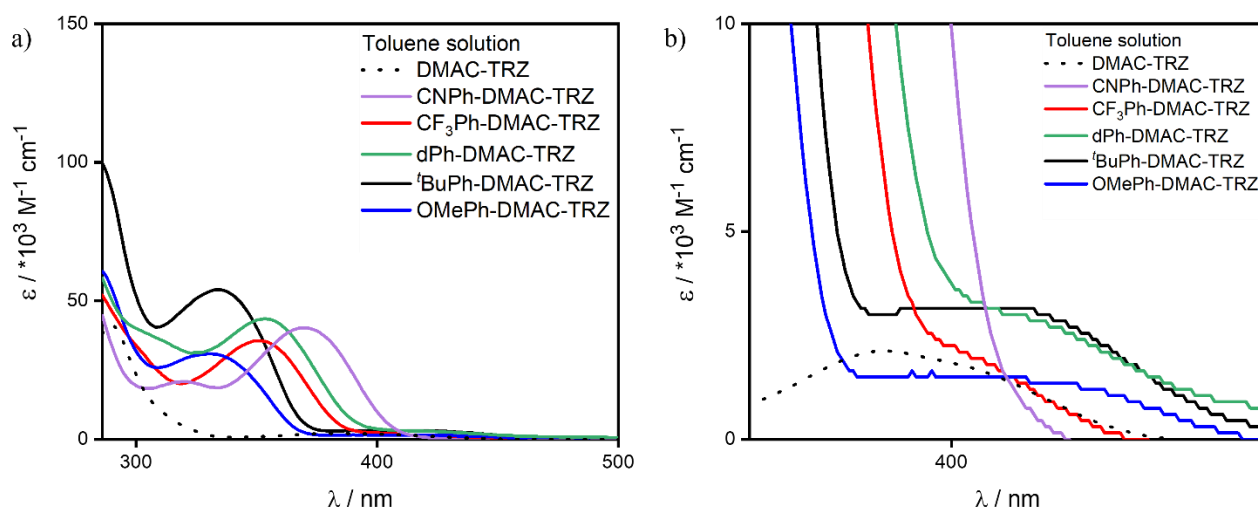
CV and DPV of **DMAC-TRZ** (for comparison) and the five novel emitters (**Figure 104**) have been carried out in DCM. The electrochemistry of **DMAC-TRZ** (oxidation attributed to the DMAC and reduction attributed to the triazine) matches the previously reported data,<sup>67,72,178</sup> with oxidation and reduction potentials of 0.97 V and -1.72 V, respectively (taken from DPV and corrected against SCE). The HOMO and LUMO energy values were obtained from the red-ox potentials measured from the DPV scan (corrected against vs Fc/Fc<sup>+</sup>) and are -5.31 V and -2.62 V, respectively.

Despite what was predicted by the DFT calculations, since the triazine acceptor is not modified, no significant change in the shape and potential of the reduction wave was observed, with values of -1.68 V, -1.68 V, -1.69 V, -1.71 V, and -1.69 V for **CNPh-DMAC-TRZ**, **CF<sub>3</sub>Ph-DMAC-TRZ**, **dPh-DMAC-TRZ**, **<sup>t</sup>BuPh-DMAC-TRZ**, **OMePh-DMAC-TRZ**, respectively, leading to almost constant LUMO values of around ~ -2.65 V, comparable to that of **DMAC-TRZ** (-2.62 V). The oxidation potentials follow the trend observed for the DFT calculations, with electron-donating groups and conjugating groups cathodically shifting the oxidation potential and thus destabilizing the HOMO energy level. The HOMO energy levels values are -5.38 V, -5.35 V, -5.21 V, -5.15 V, and -5.13 V for **CNPh-DMAC-TRZ**, **CF<sub>3</sub>Ph-DMAC-TRZ**, **dPh-DMAC-TRZ**, **<sup>t</sup>BuPh-DMAC-TRZ**, **OMePh-DMAC-TRZ**, respectively.

**Table 19.** Electrochemical properties of **DMAC-TRZ** and derivatives.

R-DMAC-TRZ	$E_{\text{ox}} / \text{V}^a$	$E_{\text{red}} / \text{V}^a$	HOMO / $\text{V}^b$	LUMO / $\text{V}^b$
DMAC-TRZ	0.97	-1.72	-5.31	-2.62
CNPh-	1.04	-1.68	-5.38	-2.66
CF <sub>3</sub> Ph-	0.80	-1.68	-5.35	-2.66
dPh-	0.86	-1.69	-5.21	-2.65
<sup>t</sup> BuPh-	0.81	-1.71	-5.15	-2.63
OMePh-	0.79	-1.69	-5.13	-2.65

<sup>a</sup> obtained from DPV; <sup>b</sup> obtained from the redox potentials from the DPV,  $E_{\text{HOMO/LUMO}} = -(E_{\text{ox/red}} + 4.8)$ , where  $E_{\text{ox/red}}$  was obtained from the DPV corrected vs Ferrocene.

**Figure 105.** a) UV-vis absorption spectra of **DMAC-TRZ**, and derivatives in toluene and b) zoom on the low intensity CT band at around 400 nm.

The UV-vis absorption of **DMAC-TRZ** and the five derivatives were carried out in a toluene solution (**Figure 105**). The absorption spectrum of **DMAC-TRZ** is reflective of the orthogonal conformation between donor and acceptor. In this conformation, the poor overlap between HOMO and LUMO would lead to an oscillator strength with zero value, making the molar absorptivity for that transition also zero. This low intensity transition is assigned to a <sup>1</sup>CT band involving the S<sub>1</sub> state, with a low  $\epsilon$  value of  $2170 \text{ M}^{-1} \text{ cm}^{-1}$ .

The absorption spectra of the five novel derivatives show the first instance of a trend that will be a staple for the series: ***t*BuPh-DMAC-TRZ** and **OMePh-DMAC-TRZ** show similar behavior, as do **CF<sub>3</sub>Ph-DMAC-TRZ**, and **dPh-DMAC-TRZ**, while **CNPh-DMAC-TRZ** displays a rather distinct behavior. The similar behavior of the two couples ***t*Bu/OMe** and **CF<sub>3</sub>/dPh** will be called “the couple trend”. Differently from **DMAC-TRZ**, a well-defined UV-vis absorption for all five emitters is present. The very low absorption band, that was previously observed in **DMAC-TRZ**, can still be observed for all materials except for **CNPh-DMAC-TRZ**. This band can be assigned to the <sup>1</sup>CT transition involving the S<sub>1</sub> state and falls around 400 nm for ***t*BuPh-DMAC-TRZ**, and **OMePh-DMAC-TRZ**, respectively with  $\epsilon$  values of 3050 M<sup>-1</sup>cm<sup>-1</sup> and 1190 M<sup>-1</sup>cm<sup>-1</sup>. The CT band is slightly redshifted for **CF<sub>3</sub>Ph-DMAC-TRZ**, and **dPh-DMAC-TRZ**, but has similar  $\epsilon$  values of 3070 M<sup>-1</sup>cm<sup>-1</sup> and 2000 M<sup>-1</sup>cm<sup>-1</sup> for **CF<sub>3</sub>Ph-DMAC-TRZ**, and **dPh-DMAC-TRZ**, respectively. **CNPh-DMAC-TRZ** behaves differently than the other compounds, with two absorption bands, at 369 nm and 318 nm, assigned to different <sup>1</sup>LE transitions on the acridine donor to the S<sub>3</sub>, and S<sub>5</sub> states, respectively, with  $\epsilon$  values of 40,100 M<sup>-1</sup> cm<sup>-1</sup> (at 369 nm) and 20,300 M<sup>-1</sup> cm<sup>-1</sup> (at 318 nm). The *tert*-butyl and methoxy derivatives then present an absorption band around 330 nm, that can be assigned with DFT calculations (**Table 20**) to a <sup>1</sup>LE transition on the acridine donor, involving the S<sub>4</sub> and S<sub>5</sub> state for ***t*BuPh-DMAC-TRZ**, and **OMePh-DMAC-TRZ**, respectively. The *tert*-butyl derivative presents the stronger absorption, with  $\epsilon$  of 53,900 M<sup>-1</sup> cm<sup>-1</sup>, against **OMePh-DMAC-TRZ** with a  $\epsilon$  of 30,900 M<sup>-1</sup> cm<sup>-1</sup> for this band. This agrees with the TD-DFT calculations, as the oscillator strength of the <sup>1</sup>LE band is much higher for ***t*BuPh-DMAC-TRZ** at 0.57, against *f* of 0.27 for **OMePh-DMAC-TRZ**. **CF<sub>3</sub>Ph-DMAC-TRZ**, and **dPh-DMAC-TRZ** present two absorption bands around 350 nm and 300 nm, that are assigned to <sup>1</sup>LE transitions on the acridine donor from the S<sub>3</sub> (c.a. 350 nm) and S<sub>5</sub> (c.a. 300 nm) states based on TDA-DFT analysis. The trifluoromethyl derivative shows the weaker absorption of the two, with  $\epsilon$  values of 35,100 M<sup>-1</sup> cm<sup>-1</sup> (at c.a. 350 nm) and 33,400 M<sup>-1</sup> cm<sup>-1</sup> (at c.a. 300 nm), while the diphenyl emitter has stronger LE transitions with  $\epsilon$  values of 43,400 M<sup>-1</sup> cm<sup>-1</sup> (at c.a. 350 nm) and 39,000 M<sup>-1</sup> cm<sup>-1</sup> (at c.a. 300 nm). The intensity of both <sup>1</sup>LE bands follows the trend predicted by DFT calculations, with the lower  $\epsilon$  value in **CF<sub>3</sub>Ph-DMAC-TRZ** being the result of the lower *f* of the material (1.00 vs 1.41 for **dPh-DMAC-TRZ** at c.a. 350 nm, and 0.15 vs 0.25 for **dPh-DMAC-TRZ** at c.a. 300 nm).



**Table 20.** Properties of the excited states involved in the UV-vis absorption transitions of **CNPh-DMAC-TRZ**, **CF<sub>3</sub>Ph-DMAC-TRZ**, **dPh-DMAC-TRZ**, ***t*BuPh-DMAC-TRZ**, **OMePh-DMAC-TRZ**.

Excited State <sup>a</sup>	Energy / eV; nm	Nature	Character of the transition
<b>CNPh-DMAC-TRZ</b>			
S <sub>3</sub> ( <i>f</i> =1.15)	3.39; 366	H→(L+2) (98%)	<sup>1</sup> LE (DMAC)
S <sub>4</sub> ( <i>f</i> =0.23)	3.78; 328	H→(L+3) (95%)	<sup>1</sup> LE (DMAC)
<b>CF<sub>3</sub>Ph-DMAC-TRZ</b>			
S <sub>3</sub> ( <i>f</i> =1.00)	3.64; 341	H→(L+2) (97%)	<sup>1</sup> LE (DMAC)
S <sub>5</sub> ( <i>f</i> =0.15)	4.09; 303	H→(L+3) (82%) H→(L+6) (9%)	<sup>1</sup> LE (DMAC)
<b>dPh-DMAC-TRZ</b>			
S <sub>3</sub> ( <i>f</i> =1.41)	3.53; 351	H→(L+2) (96%)	<sup>1</sup> LE (DMAC)
S <sub>5</sub> ( <i>f</i> =0.25)	3.93; 315	H→(L+3) (89%) H→(L+4) (4%)	
<b><i>t</i>BuPh-DMAC-TRZ</b>			
S <sub>4</sub> ( <i>f</i> =0.57)	3.74; 331	H→(L+2) (80%) H→(L+4) (16%)	<sup>1</sup> LE (DMAC)
<b>OMePh-DMAC-TRZ</b>			
S <sub>5</sub> ( <i>f</i> =0.25)	3.72; 333	H→(L+3) (77%) H→(L+4) (21%)	<sup>1</sup> LE (DMAC)

<sup>a</sup> (PBE0/6-31G(d,p)); <sup>b</sup> the transitions highlighted in red are those involved in the UV transitions.

The absorption and emission spectra of **DMAC-TRZ** (**Figure 106**) and the five derivatives were measured in different polarity solvents to assess the solvatochromism of the emitters. The absorption spectrum of **DMAC-TRZ** is unaffected by the polarity of the solvents while the emission spectra show the expected red-shift with higher polarity solvents. Toluene, THF, and DCM solutions show broad and unstructured spectra, typical of a CT-type transition, while methyl-cyclohexane shows a narrower and more structured LE-type emission.

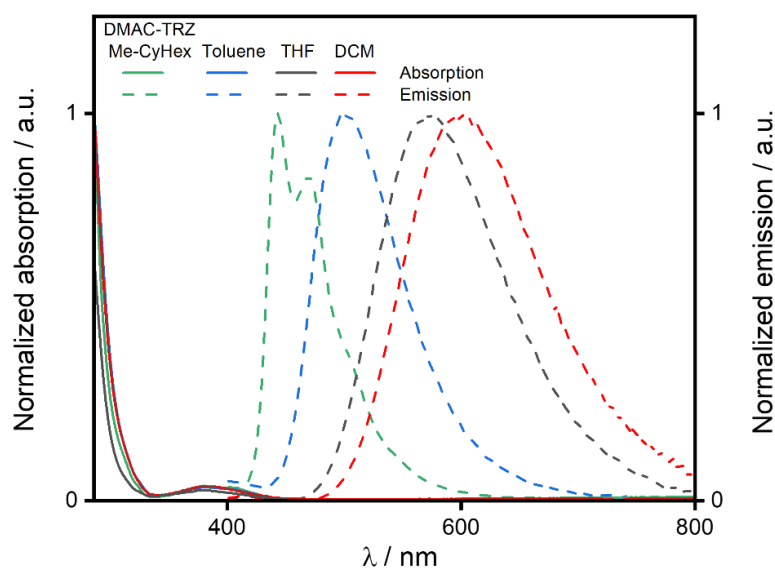


**Figure 106.** Absorption and emission spectra of **DMAC-TRZ** in different solvents ( $\lambda_{\text{exc}} = 340$  nm).

The same trend is followed by ***t*BuPh-DMAC-TRZ** and **OMePh-DMAC-TRZ** (**Figure 107**) with no solvatochromism in the absorption, and positive solvatochromism in the emission spectra. In order of increasing polarity the emission maxima in methyl-cyclohexane, Toluene, THF, and DCM, respectively, are 470/498 nm, 518 nm, 580 nm, 604 nm for ***t*BuPh-DMAC-TRZ**, and 482/504 nm, 528 nm, 594 nm, and 620 nm for **OMePh-DMAC-TRZ**. Both materials show a similar degree of red-shift, with a total difference of 134 nm and 138 nm (difference between the emission maximum in methyl-cyclohexane and the emission maximum in DCM) for ***t*BuPh-DMAC-TRZ** and **OMePh-DMAC-TRZ**, respectively. The use of the low polarity of methylcyclohexane leads once again to a LE type transition.

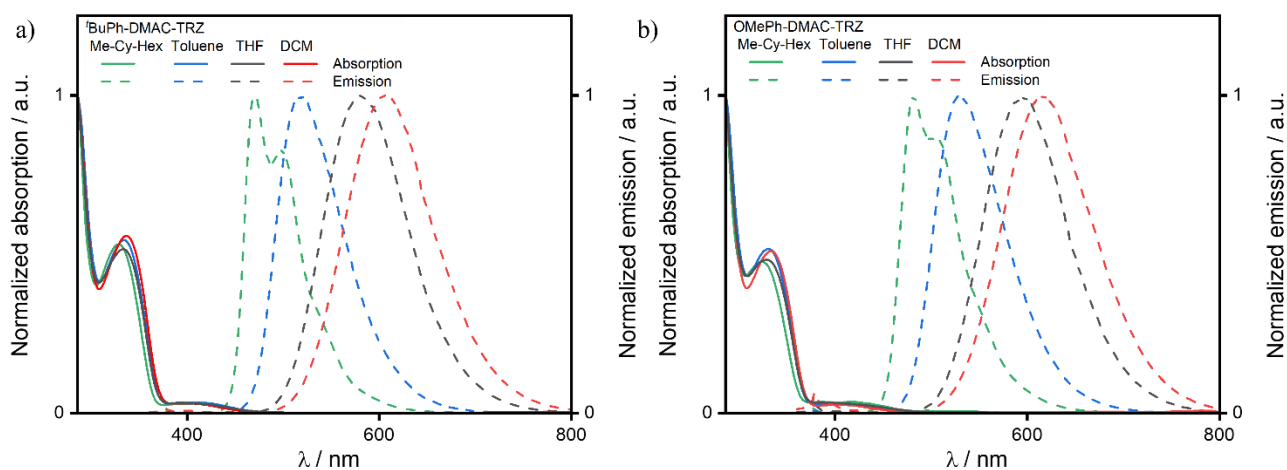


**Figure 107.** Absorption and emission spectra of **'BuPh-DMAC-TRZ** and **OMePh-DMAC-TRZ** in different solvents ( $\lambda_{exc}=340$  nm).

Some different behaviors are observed for **CF<sub>3</sub>Ph-DMAC-TRZ** and **dPh-DMAC-TRZ** (**Figure 108**). The trifluoromethyl derivative presents almost identical emission profiles in Toluene and THF solution ( $\lambda_{PL}$  of 487 nm, and 488 nm for toluene and THF, respectively), but overall, there was no solvatochromism in the absorption, and positive solvatochromism in the emission and structured emission in methylcyclohexane were seen. In order of increasing polarity, the emission maxima in methyl-cyclohexane, Toluene, THF, and DCM are, respectively, 439/498 nm, 487 nm, 488 nm, 567 nm for **CF<sub>3</sub>Ph-DMAC-TRZ**, and 465/491 nm, 511 nm, 576 nm, and 598 nm for **dPh-DMAC-TRZ**. Both materials show a similar degree of red-shift, with a total difference of 128 nm and 133 nm (difference between the emission maximum in methyl-cyclohexane and the emission maximum in DCM) for **CF<sub>3</sub>Ph-DMAC-TRZ** and **dPh-DMAC-TRZ**, respectively. **dPh-DMAC-TRZ** is the only

compound in the series where the absorption spectra present a small negative solvatochromism in DCM. The high energy transition is shifted from 350 nm (for the toluene solution) to 330 nm in DCM.

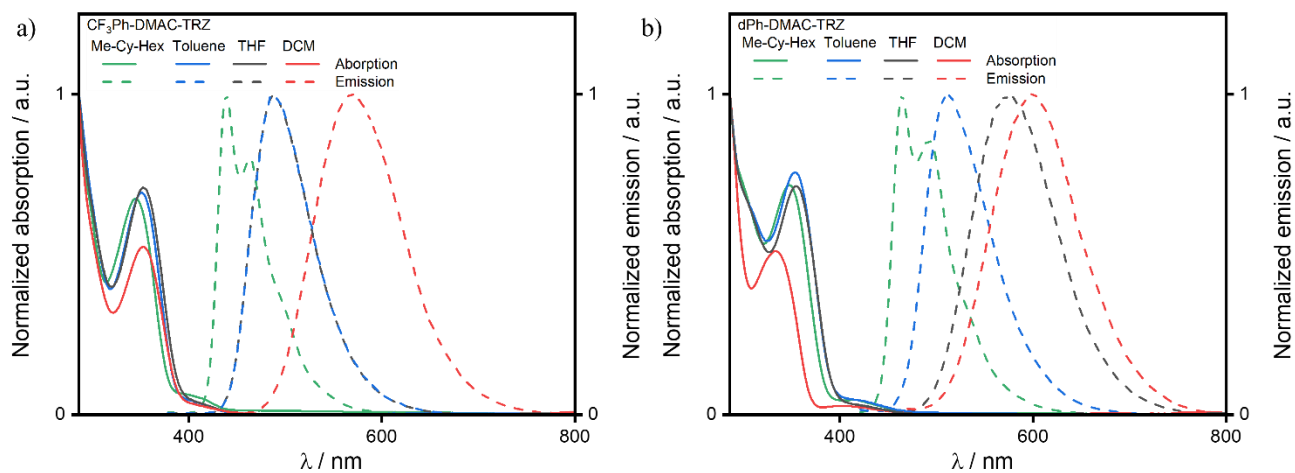


**Figure 108.** Absorption and emission spectra of **CF<sub>3</sub>Ph-DMAC-TRZ** and **dPh-DMAC-TRZ** in different solvents ( $\lambda_{exc}= 340$  nm).

**CNPh-DMAC-TRZ** possesses all the usual aforementioned trends (the lower quality of the absorption profile in methyl-cyclohexane is due to poor solubility of the material) (**Figure 109**). The emission spectra maxima are 433/457 nm, 484 nm, 544 nm, and 561 nm for methyl-cyclohexane, Toluene, THF, and DCM, respectively.

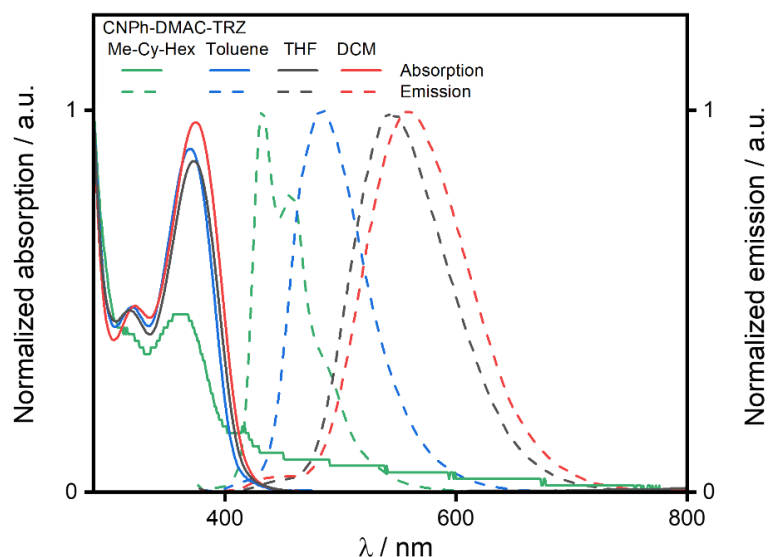


**Figure 109.** Absorption and emission spectra of **CNPh-DMAC-TRZ** in different solvents ( $\lambda_{exc}=340$  nm, Me-Cy-Hex absorption spectra is affected by the bad solubility of the material).

<b>R-DMAC-TRZ</b>	$\lambda_{em} / \text{nm}$	$\lambda_{em} / \text{nm}$	$\lambda_{em} / \text{nm}$	$\lambda_{em} / \text{nm}$
	<b>Me-Cy-Hex</b>	<b>Toluene</b>	<b>THF</b>	<b>DCM</b>
<b>DMAC-TRZ</b>	443/ 470	500	573	602
<b>CNPh-</b>	433/ 457	484	544	561
<b>CF<sub>3</sub>Ph-</b>	439/ 498	487	488	567
<b>dPh-</b>	465/ 491	511	576	598
<b><sup>t</sup>BuPh-</b>	470/ 498	518	-5.15	-1.93
<b>OMePh-</b>	482/ 504	528	594	620

**dPh-DMAC-TRZ** shows unusual solvatochromism in its absorption spectra, as the absorption wavelength should not normally change with changing solvent polarity as absorption is much faster than the solvent reorganization.<sup>136</sup> DFT and TD-DFT calculations at the PBE0/6-031G(d,p)<sup>102,103</sup> using a PCM model to emulate the toluene and DCM solvent polarity were carried out on all the emitters to try and understand the phenomena. No major difference in the predicted absorption spectra was observed between the **dPh-DMAC-TRZ** and the other materials (**Figure 110, Table 21**).

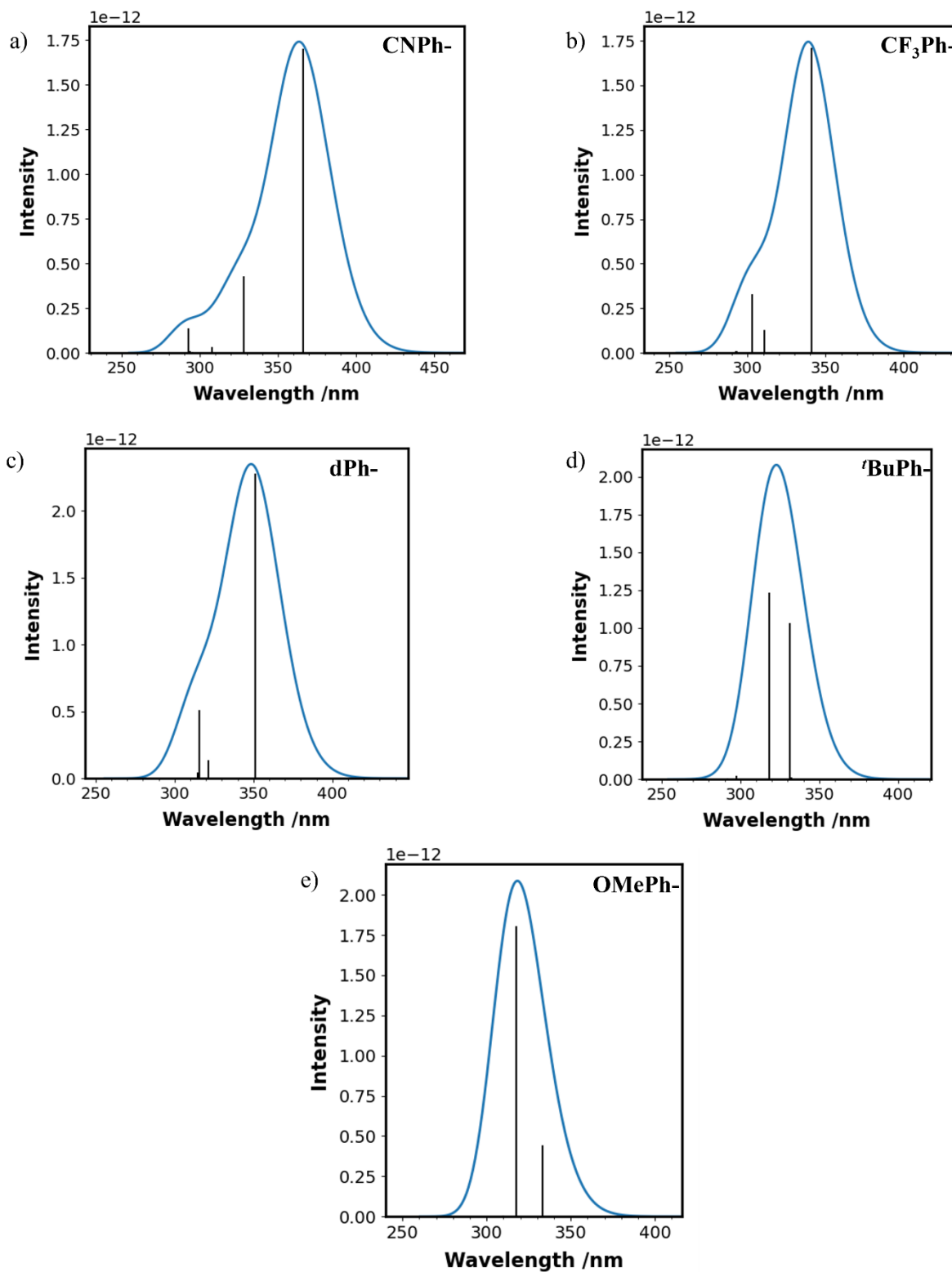


**Figure 110.** Simulated absorption spectra of DMAC-TRZ and derivatives (Obtained via DFT and TD-DFT at the PBE0/6-31G(d,p) level, Isovalue for new surfaces: MO=0.02, Density=0.0004).

**Table 21.** Properties of the excited states involved in the UV-vis absorption transitions of **CNPh-DMAC-TRZ**, **CF<sub>3</sub>Ph-DMAC-TRZ**, **dPh-DMAC-TRZ**, **<sup>t</sup>BuPh-DMAC-TRZ**, **OMePh-DMAC-TRZ**.

Excited State <sup>a</sup>	Toluene <sup>b</sup>		DCM <sup>c</sup>	
	Energy / eV	<i>f</i>	Energy / eV	<i>f</i>
<b>CNPh-DMAC-TRZ</b>				
<b>S<sub>1</sub></b>	2.78	0.00	2.76	0.00
<b>S<sub>2</sub></b>	3.11	0.01	3.08	0.05
<b>S<sub>3</sub></b>	3.24 ( <sup>1</sup> LE)	1.29	3.14 ( <sup>1</sup> LE)	1.35
<b>S<sub>4</sub></b>	3.65 ( <sup>1</sup> LE)	0.28	3.56 ( <sup>1</sup> LE)	0.30
<b>S<sub>5</sub></b>	4.05	0.01	4.06	0.010
<b>CF<sub>3</sub>Ph-DMAC-TRZ</b>				
<b>S<sub>1</sub></b>	2.69	0.00	2.70	0.00
<b>S<sub>2</sub></b>	3.02	0.00	3.01	0.00
<b>S<sub>3</sub></b>	3.53 ( <sup>1</sup> LE)	1.17	3.45 ( <sup>1</sup> LE)	1.28
<b>S<sub>4</sub></b>	4.02	0.04	3.97 ( <sup>1</sup> LE)	0.26
<b>S<sub>5</sub></b>	4.02 ( <sup>1</sup> LE)	0.22	4.03	0.04
<b>dPh-DMAC-TRZ</b>				
<b>S<sub>1</sub></b>	2.53	0.00	2.57	0.00
<b>S<sub>2</sub></b>	2.83	0.00	2.86	0.00
<b>S<sub>3</sub></b>	3.44 ( <sup>1</sup> LE)	1.60	3.38 ( <sup>1</sup> LE)	1.70
<b>S<sub>4</sub></b>	3.71	0.00	3.75	0.00
<b>S<sub>5</sub></b>	3.87 ( <sup>1</sup> LE)	0.35	3.81 ( <sup>1</sup> LE)	0.39
<b><sup>t</sup>BuPh-DMAC-TRZ</b>				
<b>S<sub>1</sub></b>	2.49	0.00	2.53	0.00
<b>S<sub>2</sub></b>	2.79	0.00	2.83	0.00
<b>S<sub>3</sub></b>	3.70 ( <sup>1</sup> LE)	1.11	3.64 ( <sup>1</sup> LE)	1.31
<b>S<sub>4</sub></b>	3.79	0.00	3.84	0.00
<b>S<sub>5</sub></b>	3.90	0.26	3.93	0.15
<b>OMePh-DMAC-TRZ</b>				
<b>S<sub>1</sub></b>	2.43	0.00	2.46	0.00

<b>S<sub>2</sub></b>	2.71	0.00	2.75	0.00
<b>S<sub>3</sub></b>	3.52	0.00	3.56	0.00
<b>S<sub>4</sub></b>	3.68	0.00	3.66 ( <sup>1</sup> LE)	1.21
<b>S<sub>5</sub></b>	3.71 ( <sup>1</sup> LE)	0.84	3.71	0.00

<sup>a</sup> the states highlighted in red are those involved in the UV transitions; <sup>b</sup> simulated in Toluene, and <sup>c</sup> DCM solutions (PBE0/6-31G(d,p)).

The photophysics of the emitters was then investigated in degassed toluene solution. **DMAC-TRZ** has an emission maximum of 479 nm. Compared to **DMAC-TRZ**, all materials have a red-shifted emission, with  $\lambda_{\text{max}}$  of 481 nm, 532 nm, 514 nm, 524 nm, and 539 nm for **CNPh-DMAC-TRZ**, **CF<sub>3</sub>Ph-DMAC-TRZ**, **dPh-DMAC-TRZ**, **<sup>t</sup>BuPh-DMAC-TRZ**, **OMePh-DMAC-TRZ**, respectively (**Figure 111**). **DMAC-TRZ** in degassed toluene solution has a  $\Phi_{\text{PL}}$  of 67%, which decreases to 21% when exposed to air. **CNPh-DMAC-TRZ**, **CF<sub>3</sub>Ph-DMAC-TRZ**, **dPh-DMAC-TRZ**, **<sup>t</sup>BuPh-DMAC-TRZ**, **OMePh-DMAC-TRZ** possess  $\Phi_{\text{PL}}$  values (degassed/aerated) of 41%/32%, 72%/28%, 70%/35%, 74%/24%, and 75%/23% respectively (**Table 24**). All materials possess an increased  $\Phi_{\text{PL}}$  compared to the parent emitter, with the exception of **CNPh-DMAC-TRZ**, which also shows a lower oxygen quenching.

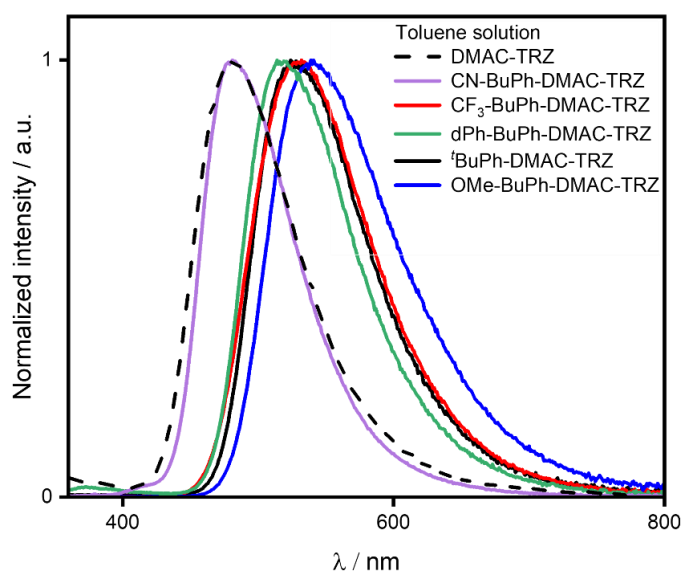


**Figure 111.** Emission spectra of **DMAC-TRZ** and derivatives in toluene ( $\lambda_{\text{exc}} = 340$  nm).



Time-resolved photoluminescence measurements were then carried out on both the degassed and aerated toluene solutions, to check for the presence of a delayed fluorescence component. The degassed solution of **DMAC-TRZ** possesses both prompt and delayed components with mono-exponential decays and lifetimes of 20.8 ns and 5.21  $\mu\text{s}$ , respectively (**Figure 112**). These lifetimes are comparable to those previously observed in the literature for the same compound by Stavrou *et al.*<sup>170</sup> ( $\tau_p$  27.4 ns and  $\tau_d$  of 5.51  $\mu\text{s}$ ). As expected, the delayed component disappears after the solution is exposed to air.

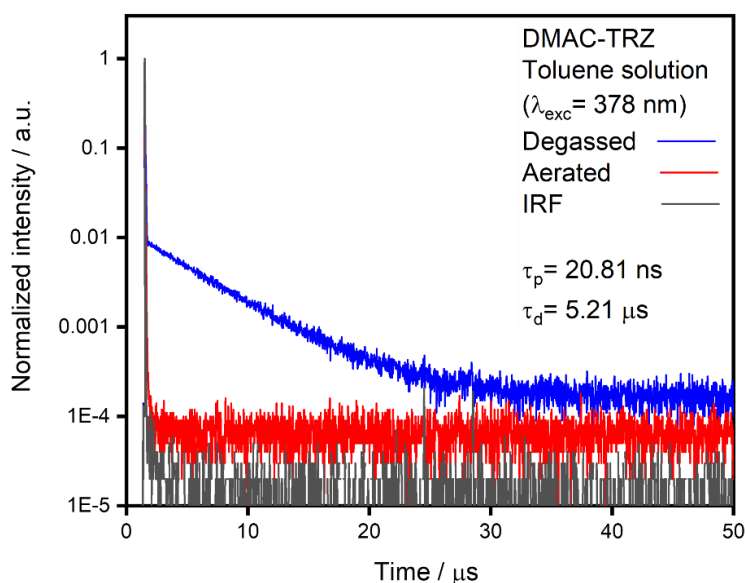


**Figure 112.** Time-resolved fluorescence decay of degassed and aerated solutions of **DMAC-TRZ** (Toluene,  $10^{-5}$  M solutions,  $\lambda_{\text{exc}}= 378$  nm, both prompt and delayed fluorescence decay were measured by TCSPC).

The derivatives decorated with electron-donating groups present slightly longer prompt lifetimes than **DMAC-TRZ**, with mono-exponential decays of 28.70 ns and 28.09 ns for ***t*BuPh-DMAC-TRZ** and **OMePh-DMAC-TRZ**, respectively (**Figure 113**). Their degassed solutions possess much shorter delayed lifetimes than **DMAC-TRZ**, with mono-exponential delayed lifetimes of 2.39  $\mu\text{s}$ , and 1.49  $\mu\text{s}$ , for ***t*BuPh-DMAC-TRZ** and **OMePh-DMAC-TRZ**, respectively, and both delayed components disappear when the solutions are exposed to air.

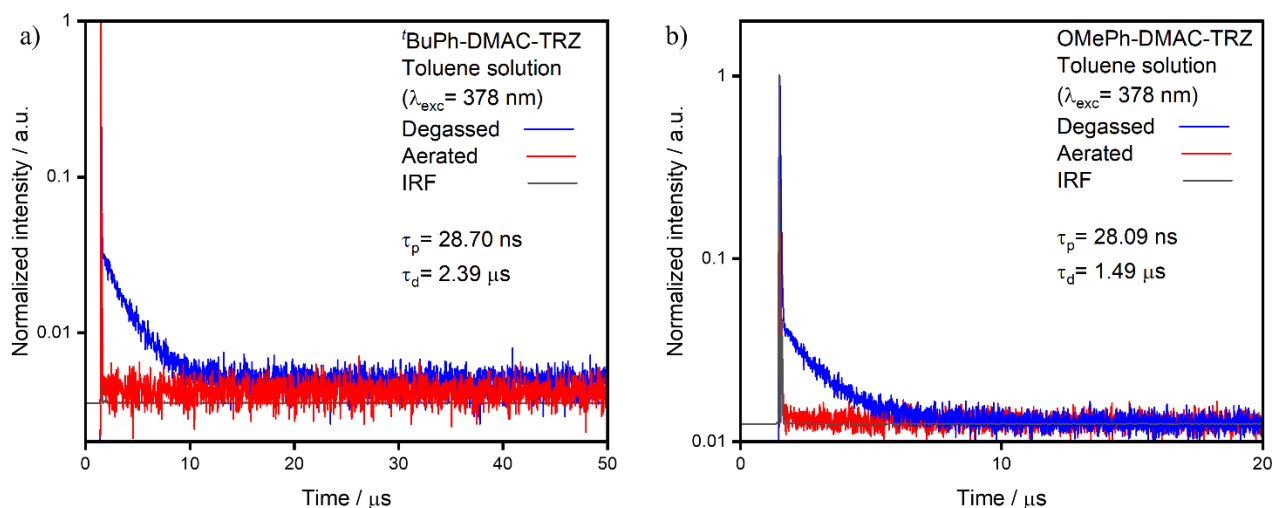


**Figure 113.** time-resolved fluorescence decay of degassed and aerated solutions of **a) 'BuPh-DMAC-TRZ** and **b) OMePh-DMAC-TRZ** (Toluene,  $10^{-5}$  M solutions,  $\lambda_{exc} = 378$  nm, both prompt and delayed fluorescence decay were measured by TCSPC).

**CF<sub>3</sub>Ph-DMAC-TRZ** and **dPh-DMAC-TRZ** present mono-exponential prompt components with lifetimes of 10.9 ns and 15.4 ns, respectively (**Figure 114**). They possess a longer-lived delayed component, with biexponential decay kinetics and average  $\tau_d$  of 20.7  $\mu$ s [ $\tau_1 = 0.939$   $\mu$ s (1.68%),  $\tau_2 = 21.0$   $\mu$ s (98.3%)] and 25.8  $\mu$ s [ $\tau_1 = 0.890$   $\mu$ s (3.99%),  $\tau_2 = 26.9$   $\mu$ s (96.0%)], respectively.

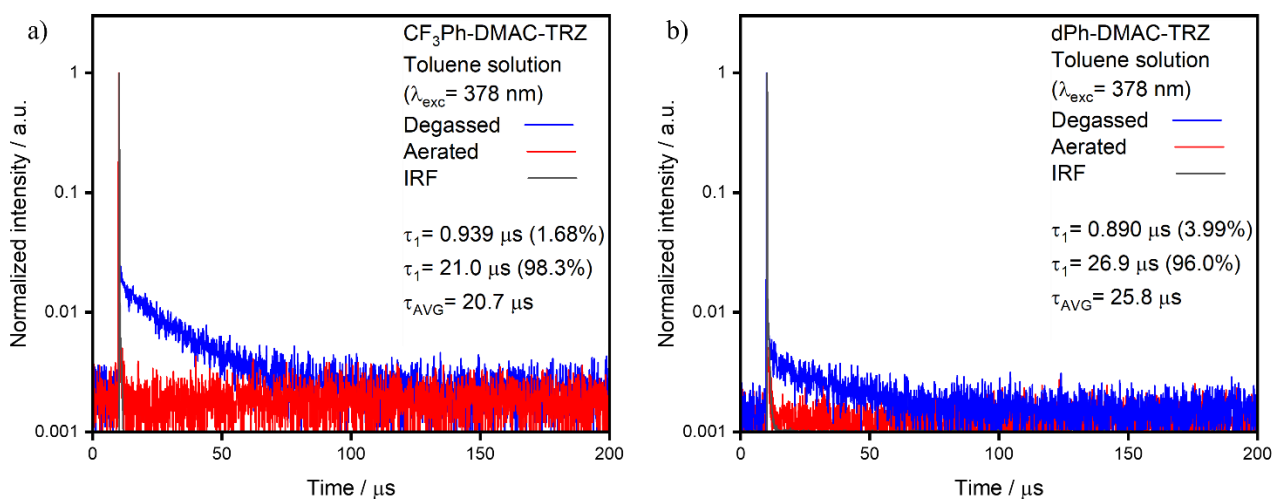


**Figure 114.** time-resolved fluorescence decay of degassed and aerated solutions of **a) CF<sub>3</sub>Ph-DMAC-TRZ** and **b) dPh-DMAC-TRZ** (Toluene,  $10^{-5}$  M solutions,  $\lambda_{exc} = 378$  nm, the delayed fluorescence decay was measured by MCS).

**CNPh-DMAC-TRZ** surprisingly doesn't present any delayed component but just a prompt decay with a lifetime of 8.24 ns, which decreases to 6.53 ns when exposed to air due to a small degree of singlet quenching caused by the presence of oxygen.<sup>179</sup>

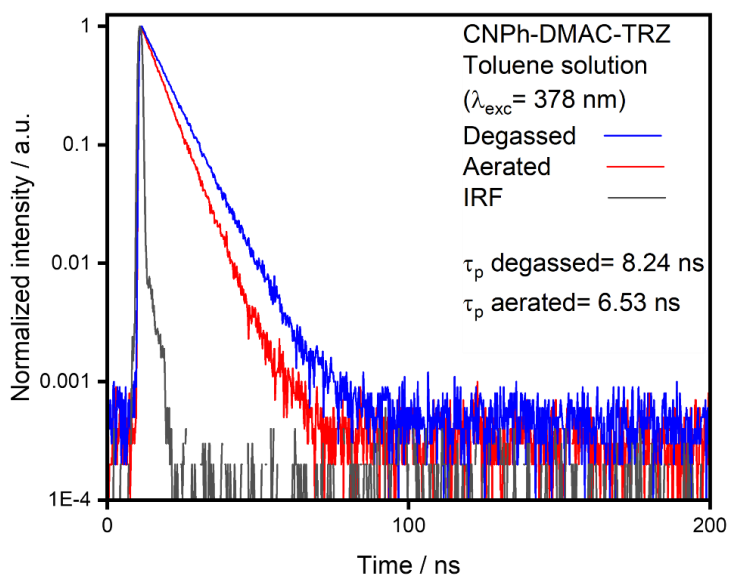


**Figure 115.** time-resolved fluorescence decay of degassed and aerated solutions of **CNPh-DMAC-TRZ** (Toluene,  $10^{-5}$  M solutions,  $\lambda_{\text{exc}} = 378$  nm, the prompt fluorescence decay was measured by TCSPC).

The analysis of these materials in solution follows the previously discussed “couple trend” where the two couples **BuPh-DMAC-TRZ**, **OMePh-DMAC-TRZ**, and **CF<sub>3</sub>Ph-DMAC-TRZ**, **dPh-DMAC-TRZ** present similar behaviour while **CNPh-DMAC-TRZ** is unique in its photophysical behaviour. Moreover, decorating **DMAC-TRZ** with EWG groups or extending its conjugation clearly leads to a shorter prompt lifetime, while EDG groups have the opposite effect. The delayed component is longer-lived for material with a weaker donor, while stronger donors lead to faster delayed fluorescence lifetimes.

**Table 22.** Concentration screen of **'BuPh-DMAC-TRZ** in mCP.

Host	Doping concentration / wt%	PLQY N <sub>2</sub> ; Air <sup>a</sup> / %
mCP	3	65; 61
	5	66; 63
	10	66; 64
	15	62; 60
	20	62; 61

<sup>a</sup>  $\lambda_{\text{exc}}=340$  nm

A concentration screen was firstly carried out in mCP as a host matrix (**Table 23**). With a view to fabricating OLEDs, this host was chosen as it has a relatively high triplet energy (2.9 eV), which makes it suitable for both green and blue devices .<sup>91</sup> When analysing the results, it needs to be considered that the integrating sphere used has an error of  $\pm 5\%$ , meaning that the  $\Phi_{\text{PL}}$  of the mCP films are nearly identical and the best results were obtained was with the 10 wt% mCP doped film, which was then used to screen the whole series of emitters. In mCP at 10 wt% doping concentration, **DMAC-TRZ** possesses a  $\Phi_{\text{PL}}$  of 47%, at  $\lambda_{\text{PL}}$  of 499 nm. As previously observed for the toluene solutions, the five derivatives show a red-shifted emission, but also an improved quantum yield, in most cases. In 10 wt% doped mCP films, **CNPh-DMAC-TRZ**, **CF<sub>3</sub>Ph-DMAC-TRZ**, **dPh-DMAC-TRZ**, **'BuPh-DMAC-TRZ**, **OMePh-DMAC-TRZ**, respectively show  $\Phi_{\text{PL}}$  values of 44%, 51%, 66%, 66%, 55%, at  $\lambda_{\text{PL}}$  of 504 nm, 505 nm, 516 nm, 515 nm, 529 nm (**Table 24**).

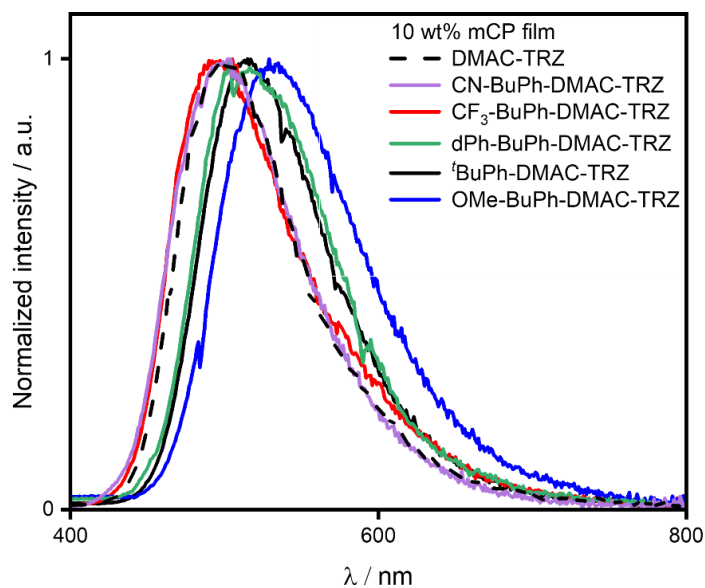


**Figure 116.** Emission spectra of **DMAC-TRZ**, and derivatives in 10 wt% doped mCP film ( $\lambda_{\text{exc}}=355$  nm).

Time-resolved measurements were also carried out on the same film (**Figure 117**), showing delayed fluorescence, even for **CNPh-DMAC-TRZ**. The prompt and delayed lifetime were extracted *via* multi-exponential fittings, with values of  $\tau_p$  of 11.8 ns, 13.8 ns, 15.1 ns, 18.3 ns, 20.0 ns, and  $\tau_d$  of 1.61  $\mu\text{s}$ , 3.32  $\mu\text{s}$ , 3.76  $\mu\text{s}$ , 2.01  $\mu\text{s}$ , 1.40  $\mu\text{s}$  for, **CNPh-DMAC-TRZ**, **CF<sub>3</sub>Ph-DMAC-TRZ**, **dPh-DMAC-TRZ**, **tBuPh-DMAC-TRZ**, **OMePh-DMAC-TRZ**, respectively. A stronger electron-donating character of the substituents on the donor led to a longer-lived prompt fluorescence, while for the delayed fluorescence lifetimes the “couple trend” in **tBu/OMe** and **CF<sub>3</sub>/dPh** can once again be observed. **tBuPh-DMAC-TRZ** and **OMePh-DMAC-TRZ** have faster delayed components than **CF<sub>3</sub>Ph-DMAC-TRZ** and **dPh-DMAC-TRZ**, which was the same behaviour observed in toluene solutions. **CNPh-DMAC-TRZ** possesses an extremely low intensity delayed component. The same measurement was carried at 80 K to assess the temperature dependence of the delayed emission. In all cases, the delayed emission decreased in intensity with decreasing temperature, demonstrating that the delayed fluorescence of the materials is temperature dependent.

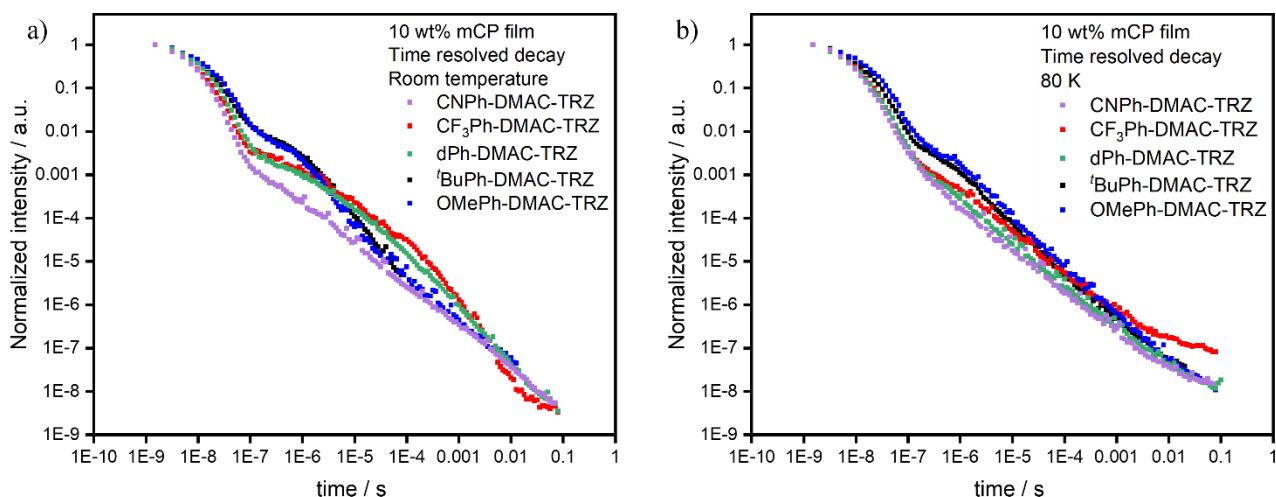


**Figure 117.** Time resolved fluorescence decay at a) room temperature; b) 80 K of **CNPh-DMAC-TRZ**, **CF<sub>3</sub>Ph-DMAC-TRZ**, **dPh-DMAC-TRZ**, **'BuPh-DMAC-TRZ**, **OMePh-DMAC-TRZ** in 10 wt% doped mCP film ( $\lambda_{exc} = 355$  nm).

**'BuPh-DMAC-TRZ**, and **OMePh-DMAC-TRZ** do not show a very large decrease in the intensity of the delayed component, when measured at low temperature (**Figure 118**). This could be indicative of a more efficient RISC process.<sup>158</sup>

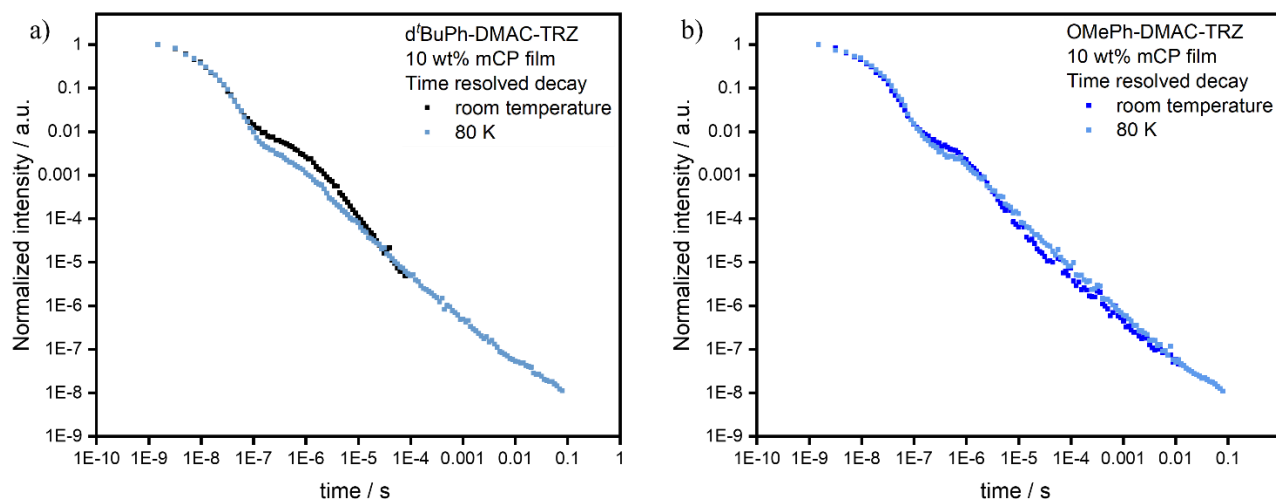


**Figure 118.** Time resolved fluorescence decay at room temperature and at 80 K of a) **'BuPh-DMAC-TRZ** and b) **OMePh-DMAC-TRZ** ( $\lambda_{exc} = 355$  nm).

**CF<sub>3</sub>Ph-DMAC-TRZ**, and **dPh-DMAC-TRZ** show a much more obvious decrease in the delayed fluorescence decay intensity, when measured at 80 K (**Figure 119**). For these materials, a complete disappearance of the delayed emission at this temperature was observed, meaning that 80 K is a sufficiently low temperature to completely suppress RISC.

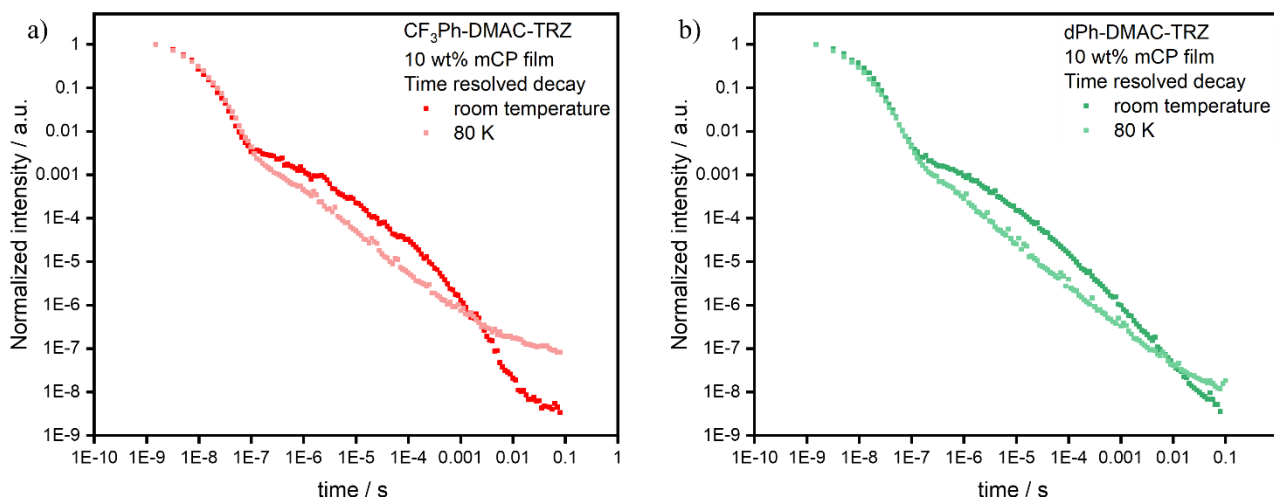


**Figure 119.** Time resolved fluorescence decay at room temperature and at 80 K of **a) CF<sub>3</sub>Ph-DMAC-TRZ** and **b) dPh-DMAC-TRZ** ( $\lambda_{\text{exc}}= 355$  nm).

**CNPh-DMAC-TRZ** shows a very weak delayed emission, which completely disappears at 80 K (**Figure 120**). These measurements are further proof of the TADF nature of these materials.

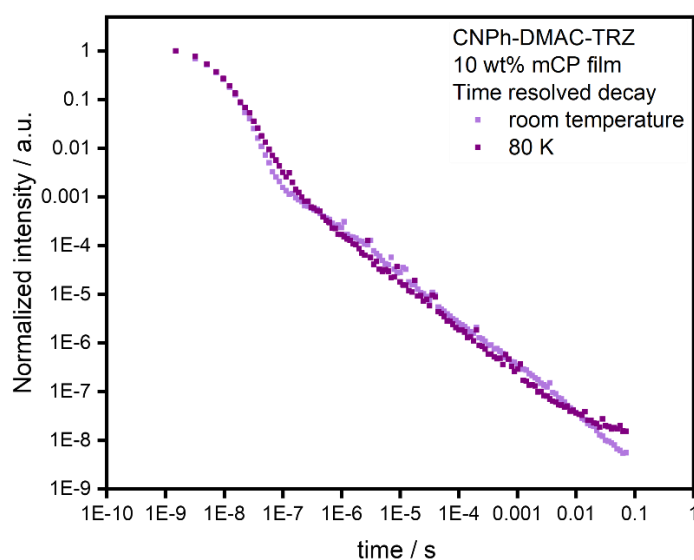


**Figure 120.** Time resolved fluorescence decay at room temperature and at 80 K of **CNPh-DMAC-TRZ** ( $\lambda_{\text{exc}}= 355$  nm).

Two more host materials were then tested, mCBPCN, and DPEPO (**Table 23**). mCBPCN was previously used as the optimal host materials for **DMAC-TRZ** as this emitter showed high  $\Phi_{\text{PL}}$  of 87% and a short lifetime of delayed fluorescence of 1.5  $\mu\text{s}$  in this host.<sup>170</sup> Moreover, both mCBPCN and DPEPO possess high MW and high  $T_g$ , which would be beneficial to influence the horizontal orientation of the TDMs of these materials. **'BuPh-DMAC-TRZ** was again used as the prototypical material for the series. mCBPCN and DPEPO films showed higher efficiencies than mCP films, with the highest value recorded in DPEPO, at a 15 wt% doping concentration, with a  $\Phi_{\text{PL}}$  of 80% that decreased to 54% when exposed to oxygen. The second best result was obtained in mCBPCN, also at a doping concentration of 15 wt%, with a  $\Phi_{\text{PL}}$  of 79% that decreased to 64% when exposed to oxygen. However, when taking the  $\pm 5\%$  error on the measurement, mCBPCN and DPEPO gave comparable results. mCBPCN was chosen as the host material to carry on the solid-state photophysical analysis as DPEPO is known to be unstable in the OLEDs and it would negatively impact the device lifetime.<sup>22</sup> As the photophysics of 10 wt%, 15 wt%, and 20 wt% films gave comparable result, a concentration of 10 wt% was chosen as the doping concentration to avoid possible quenching phenomena at higher concentrations with the other emitters.

**Table 23.** Host and concentration screen of **'BuPh-DMAC-TRZ** in mCBPCN and DPEPO.

Host	Doping concentration / wt%	PLQY N <sub>2</sub> ; Air/ %
mCBPCN <sup>a</sup>	3	62; 57
	5	65; 60
	10	72; 61
	15	79; 64
	20	70; 60
DPEPO <sup>b</sup>	3	63; 51
	5	67; 49
	10	75; 50
	15	80; 54
	20	73; 55

<sup>a</sup>  $\lambda_{\text{exc}}=340$  nm; <sup>b</sup>  $\lambda_{\text{exc}}=310$  nm



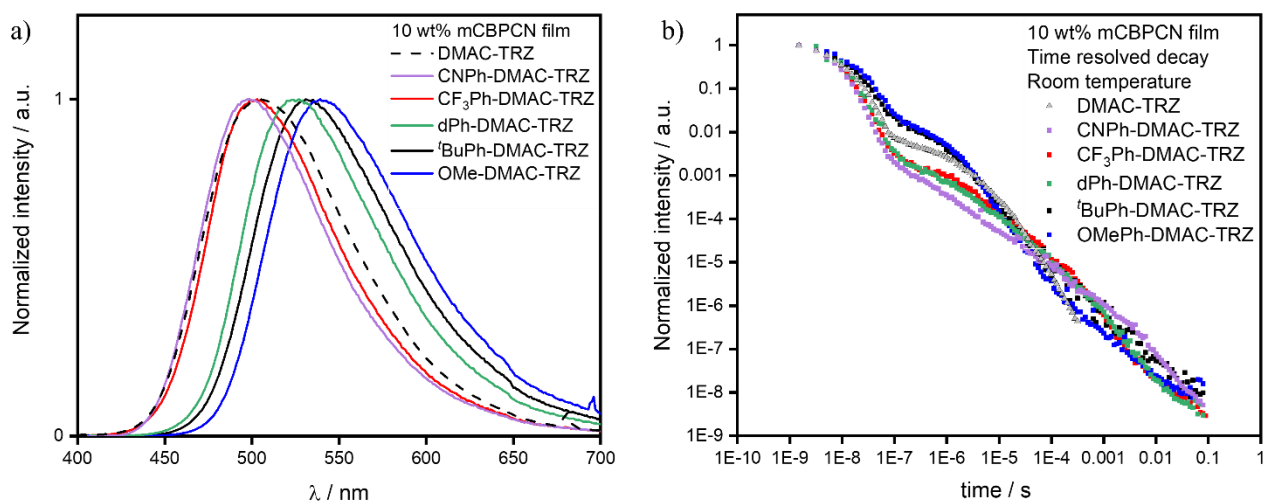


**Figure 121.** a) Emission spectra and b) Time resolved fluorescence decay at room temperature of **DMAC-TRZ**, and derivatives in 10 wt% doped mCBPCN film ( $\lambda_{\text{exc}} = 355$  nm).

In 10 wt% mCBPCN doped films the materials present emission maxima of 504 nm, 498 nm, 503 nm, 527 nm, 531 nm, 539 nm for **DMAC-TRZ**, **CNPh-DMAC-TRZ**, **CF<sub>3</sub>Ph-DMAC-TRZ**, **dPh-DMAC-TRZ**, **'BuPh-DMAC-TRZ**, **OMePh-DMAC-TRZ**, respectively, with  $\Phi_{\text{PLS}}$  of 87%, 34%, 70%, 70%, 72%, and 72%, under N<sub>2</sub>. The emissions of **'BuPh-DMAC-TRZ**, **OMePh-DMAC-TRZ** and **dPh-DMAC-TRZ** are red-shifted when compared to the values in mCP films, while **CF<sub>3</sub>Ph-DMAC-TRZ** and **CNPh-DMAC-TRZ** are slightly blue-shifted. The lifetimes of prompt fluorescence were measured at room temperature, with  $\tau_{\text{p}}$  7.68 ns, 9.39 ns, 12.8 ns, 17.7 ns, 18.9 ns for **CNPh-DMAC-TRZ**, **CF<sub>3</sub>Ph-DMAC-TRZ**, **dPh-DMAC-TRZ**, **'BuPh-DMAC-TRZ**, **OMePh-DMAC-TRZ**, respectively. As was observed in both solution and in mCP films, longer-lived prompt fluorescence is observed when the donor contains electron-donating substituents. A delayed component was observed again for all materials, with  $\tau_{\text{d}}$  5.06  $\mu\text{s}$ , 5.12  $\mu\text{s}$ , 1.92  $\mu\text{s}$ , 1.32  $\mu\text{s}$ , 1.31  $\mu\text{s}$ , **CNPh-DMAC-TRZ**, **CF<sub>3</sub>Ph-DMAC-TRZ**, **dPh-DMAC-TRZ**, **'BuPh-DMAC-TRZ**, **OMePh-DMAC-TRZ** respectively. Throughout the series, shorter delayed lifetimes are associated with more electron-rich emitters. **DMAC-TRZ** was measured in the same environment as a comparison, showing lifetimes that are between the two couples, with a  $\tau_{\text{p}}$  of 9.17 ns, and a  $\tau_{\text{d}}$  of 1.65  $\mu\text{s}$ .

**Table 24.** Photophysical properties of **DMAC-TRZ** and extended derivatives.

<b>R-DMAC-TRZ</b>	<b>Environment</b>	$\lambda_{\text{PL}} / \text{nm}^a$	<b>PLQY N<sub>2</sub>; Air<sup>b</sup>/ %</b>	$\tau_{\text{p}}, \tau_{\text{d}}^e / \text{ns}; \mu\text{s}$
<b>DMAC-TRZ</b>	Toluene ( $10^{-5}$ M)	479	67; 21 <sup>c</sup>	20.81; 5.21
	mCP 10wt%	499	47; 45 <sup>d</sup>	22.9; 15.3
	mCBPCN 10wt%	504	87; 62 <sup>d</sup>	9.17; 1.65
<b>CNPh-</b>	Toluene ( $10^{-5}$ M)	481	41; 32 <sup>c</sup>	8.24; -
	mCP 10wt%	504	44; 19 <sup>d</sup>	11.8; 1.61
	mCBPCN 10wt%	498	34; 19 <sup>d</sup>	7.68; 5.06
<b>CF<sub>3</sub>Ph-</b>	Toluene ( $10^{-5}$ M)	532	72; 28 <sup>c</sup>	10.9; 20.7
	mCP 10wt%	505	51; 38 <sup>d</sup>	13.8; 3.32
	mCBPCN 10wt%	503	70; 44 <sup>d</sup>	9.39; 5.12
<b>dPh-</b>	Toluene ( $10^{-5}$ M)	514	70; 35 <sup>c</sup>	15.4; 25.8
	mCP 10wt%	516	66; 50 <sup>d</sup>	15.1; 3.76
	mCBPCN 10wt%	527	70; 43 <sup>d</sup>	12.8; 1.92
<b><sup>t</sup>BuPh-</b>	Toluene ( $10^{-5}$ M)	524	74; 24 <sup>c</sup>	28.70; 2.39
	mCP 10wt%	515	66; 64 <sup>d</sup>	18.3; 2.01
	mCBPCN 10wt%	531	72; 61 <sup>d</sup>	17.7; 1.32
<b>OMePh-</b>	Toluene ( $10^{-5}$ M)	539	75; 23 <sup>c</sup>	28.09; 1.49
	mCP 10wt%	529	55; 51 <sup>d</sup>	20.0; 1.40
	mCBPCN 10wt%	539	72; 56 <sup>d</sup>	18.9; 1.31

<sup>a</sup> measured at room temperature; <sup>b</sup>  $\lambda_{\text{exc}} = 340$  nm; <sup>c</sup> obtained *via* the optically dilute method, <sup>138</sup> quinine sulfate (0.5 M) in H<sub>2</sub>SO<sub>4</sub> (aq) was used as the reference,  $\Phi_{\text{PL}}: 54.6\%$ ,  $\lambda_{\text{exc}} = 360$  nm; <sup>139</sup> <sup>d</sup> obtained *via* integrating sphere; <sup>e</sup>  $\tau_{\text{p}}$  (prompt lifetime) and  $\tau_{\text{d}}$  (delayed lifetime) were obtained from the transient PL decay of degassed solution/doped film,  $\lambda_{\text{exc}} = 355$  nm.

Using a kinetics modelling from Haase *et al.*,<sup>180</sup> the relative contributions of the prompt ( $\Phi_{\text{p}}$ ) and delayed fluorescence ( $\Phi_{\text{d}}$ ) to the overall photoluminescence of the material were extracted from the time-resolved fluorescence decays in mCBPCN films (**Table 25**). Once again, the “couple trend” can be observed. For both **<sup>t</sup>BuPh-DMAC-TRZ** and **OMePh-DMAC-TRZ**, the prompt and delayed fluorescence quantum yields contribute to the emission quantum yield almost equally, with a  $\Phi_{\text{p}}$  of

34% and 38% and a  $\Phi_d$  of 38% and 34%. For both **CF<sub>3</sub>Ph-DMAC-TRZ** and **dPh-DMAC-TRZ**, the main contribution to their emission comes from the prompt fluorescence, with a  $\Phi_p$  of 43% and 56% and a  $\Phi_d$  of 27% and 14%. For **CNPh-DMAC-TRZ**, it behaves similarly to **CF<sub>3</sub>-** and **dPh-**, with a much larger contribution coming from the prompt fluorescence with  $\Phi_p$  of 25% and a  $\Phi_d$  of 9%. This indicates that RISC is more efficient in the emitters decorated with EDG groups. From the same kinetics modelling in mCBPCN, the radiative decay rate from the singlet state ( $k_F$ ), intersystem crossing rate ( $k_{ISC}$ ), and reverse intersystem crossing rate ( $k_{RISC}$ ) were calculated. All materials possess  $k_F$  of the order of  $10^7 \text{ s}^{-1}$  and once again the “couple trend” can be observed. **‘BuPh-DMAC-TRZ** and **OMePh-DMAC-TRZ** possess the slowest  $k_F$  of the series at  $2.4 \times 10^7 \text{ s}^{-1}$  and  $2.0 \times 10^7 \text{ s}^{-1}$ , respectively. **CF<sub>3</sub>Ph-DMAC-TRZ** and **dPh-DMAC-TRZ** possess faster  $k_F$ , of  $5.1 \times 10^7 \text{ s}^{-1}$  and  $5.6 \times 10^7 \text{ s}^{-1}$ , respectively, which explains their faster prompt fluorescence decay. **CNPh-DMAC-TRZ** shows the highest  $k_F$  of the series at  $7.3 \times 10^7 \text{ s}^{-1}$ , in line with the very fast prompt fluorescence of the material. The  $k_{ISC}$  of all materials is also of the order of  $10^7 \text{ s}^{-1}$ , but it doesn’t give us any particular insights into the photophysical behaviour of the materials. **‘BuPh-DMAC-TRZ** and **OMePh-DMAC-TRZ** possess a  $k_{RISC}$  one order of magnitude faster than **DMAC-TRZ** ( $k_{RISC}$  of  $1.7 \times 10^5 \text{ s}^{-1}$ ) and the rest of the series, with values of  $1.8 \times 10^6 \text{ s}^{-1}$  and  $1.5 \times 10^6 \text{ s}^{-1}$  for **‘BuPh-DMAC-TRZ** and **OMePh-DMAC-TRZ**, respectively. The more efficient RISC process of these materials explains the faster delayed fluorescence decays observed in both solution and film for these two materials. **CF<sub>3</sub>Ph-DMAC-TRZ** and **dPh-DMAC-TRZ** show less efficient RISC than **‘BuPh-DMAC-TRZ** and **OMePh-DMAC-TRZ**, with rates values of  $3.7 \times 10^5 \text{ s}^{-1}$  and  $6.3 \times 10^5 \text{ s}^{-1}$ , respectively, which is again in line with the longer-lived delayed fluorescence of these materials. **CNPh-DMAC-TRZ** has a  $k_{RISC}$  of  $8.2 \times 10^5 \text{ s}^{-1}$ , putting it in the middle of the series. All the novel materials present a more efficient RISC rate than the parent, **DMAC-TRZ**.

**Table 25.** Kinetics parameter of **DMAC-TRZ** and extended derivatives in 10 wt% doped mCBPCN film.

<b>R-DMAC-TRZ</b>	$\Phi_{PL} \text{ N}_2 / \%$	$\Phi_p / \%$	$\Phi_d / \%$	$k_F / \text{s}^{-1}$	$k_{ISC} / \text{s}^{-1}$	$k_{RISC} / \text{s}^{-1}$
<b>CNPh-</b>	34	25	9	$7.3 \times 10^7$	$1.9 \times 10^7$	$8.2 \times 10^5$
<b>CF<sub>3</sub>Ph-</b>	70	43	27	$5.1 \times 10^7$	$3.6 \times 10^7$	$3.7 \times 10^5$
<b>dPh-</b>	70	56	14	$5.6 \times 10^7$	$1.7 \times 10^7$	$6.3 \times 10^5$
<b>‘BuPh-</b>	72	34	38	$2.4 \times 10^7$	$2.8 \times 10^7$	$1.8 \times 10^6$
<b>OMePh-</b>	72	38	34	$2.0 \times 10^7$	$2.1 \times 10^7$	$1.5 \times 10^6$

### 5.3.4 - Orientation measurements

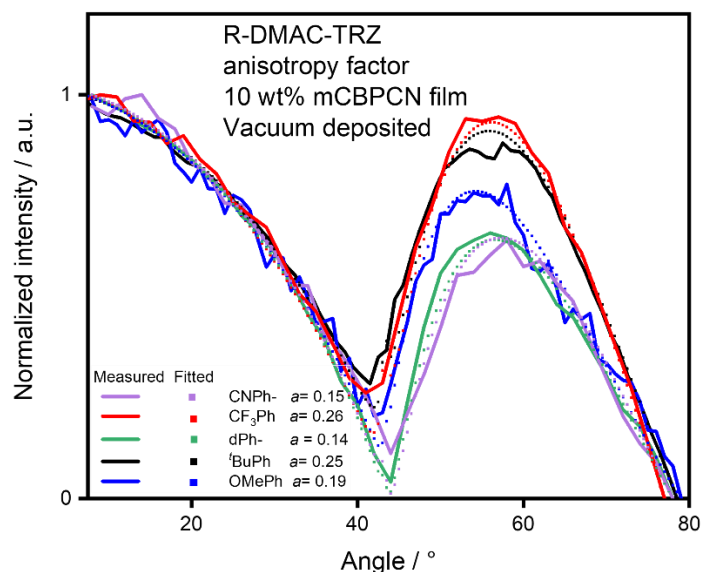


**Figure 122.** Angle-resolved photoluminescence measurement of **CNPh-DMAC-TRZ**, **CF<sub>3</sub>Ph-DMAC-TRZ**, **dPh-DMAC-TRZ**, **tBuPh-DMAC-TRZ**, **OMePh-DMAC-TRZ** in 10 wt % evaporated films in mCBPCN. The continuous line shows the measurement, and the dotted line of the matching color shows a fit using the dipole emission model, yielding the anisotropy factor,  $a$  (data taken at  $\lambda_{PL}$ = 490 nm, 500 nm, 520 nm, 521 nm, and 539 nm for **CNPh-DMAC-TRZ**, **CF<sub>3</sub>Ph-DMAC-TRZ**, **dPh-DMAC-TRZ**, **tBuPh-DMAC-TRZ**, **OMePh-DMAC-TRZ** respectively)

The orientation of the TDM of the series of derivatives was measured in evaporated 10 wt% doped mCBPCN films (**Figure 122**, **Table 5**). All materials present a preferential horizontal orientation of their TDM, with  $a$  values of 0.15, 0.26, 0.14, 0.25, and 0.19 for **CNPh-DMAC-TRZ**, **CF<sub>3</sub>Ph-DMAC-TRZ**, **dPh-DMAC-TRZ**, **tBuPh-DMAC-TRZ**, **OMePh-DMAC-TRZ**, respectively. Not every material managed to achieve an improved orientation of their TDM than **DMAC-TRZ** in the same environment ( $a= 0.21$  for 10 wt% evaporated film of **DMAC-TRZ** in mCBPCN).<sup>68</sup> To briefly repeat, we found that generally for emitters with  $MW > 600 \text{ g mol}^{-1}$ , the anisotropy factor improves with higher MW, higher  $x_E/x_H$  (ratio of emitter's and host's length), and lower  $z_E$  (thickness of the emitter)<sup>23</sup> (**Table 27**). All these derivatives present the same  $z_E$  value, thus it will not be considered in this analysis. The orthogonal conformation of the material leads the donor to be responsible for the width of the materials ( $y_E$ ) and the thickness of the materials dependent on the triazine, which is the same in all materials. The best material is **dPh-DMAC-TRZ**, which is easily explained by being the

heaviest material (MW of 821.02 g mol<sup>-1</sup>) and possessing the highest  $x_E/x_H$  value of the series ( $x_E/x_H = 1.35$ ). The second-best result is obtained by **CNPh-DMAC-TRZ**, which is the lightest material (MW of 718.84 g mol<sup>-1</sup>) and has the worst  $x_E/x_H$  value of the series (1.08). The other materials classify, in order of best  $a$ , as **OMePh-DMAC-TRZ** ( $a = 0.19$ ), ***t*BuPh-DMAC-TRZ** ( $a = 0.25$ ), and **CF<sub>3</sub>Ph-DMAC-TRZ** ( $a = 0.26$ ), and no discernable trend was identified for these materials. A study of the thermal properties and a screen of other host materials are ongoing to try and understand what controls the orientation of these emitters.

**Table 26.** Orientation data of **ICzTRZ** obtained from angle-resolved photoluminescence measurements in different host materials.

<b>R-DMAC-TRZ</b>	$a^a$	$\theta_h^b$	$S^c$
<b>CNPh-</b>	0.15	0.85	-0.275
<b>CF<sub>3</sub>Ph-</b>	0.26	0.74	-0.11
<b>dPh-</b>	0.14	0.86	-0.29
<b><i>t</i>BuPh-</b>	0.25	0.75	-0.125
<b>OMe</b>	0.19	0.81	-0.215

<sup>a</sup>anisotropy factor; <sup>b</sup> fraction of horizontal dipole ( $\theta_h = 1-a$ ); <sup>c</sup> orientation order parameter ( $S = (3a-1)/2$ ).

**Table 27.** Emitters' properties that might have influenced the orientation in evaporated films.

<b>R-DMAC-TRZ</b>	$a^a$	<b>MW</b>	$x_E/x_H$	<b><math>z_E</math></b>
<b>CNPh-</b>	0.15	718.84	1.08	11.53
<b>CF<sub>3</sub>Ph-</b>	0.26	804.82	1.09	11.53
<b>dPh-</b>	0.14	821.02	1.35	11.53
<b><i>t</i>BuPh-</b>	0.25	780.04	1.21	11.53
<b>OMe</b>	0.19	728.88	1.10	11.53

<sup>a</sup>anisotropy factor.

### 5.3.5 - OLED devices

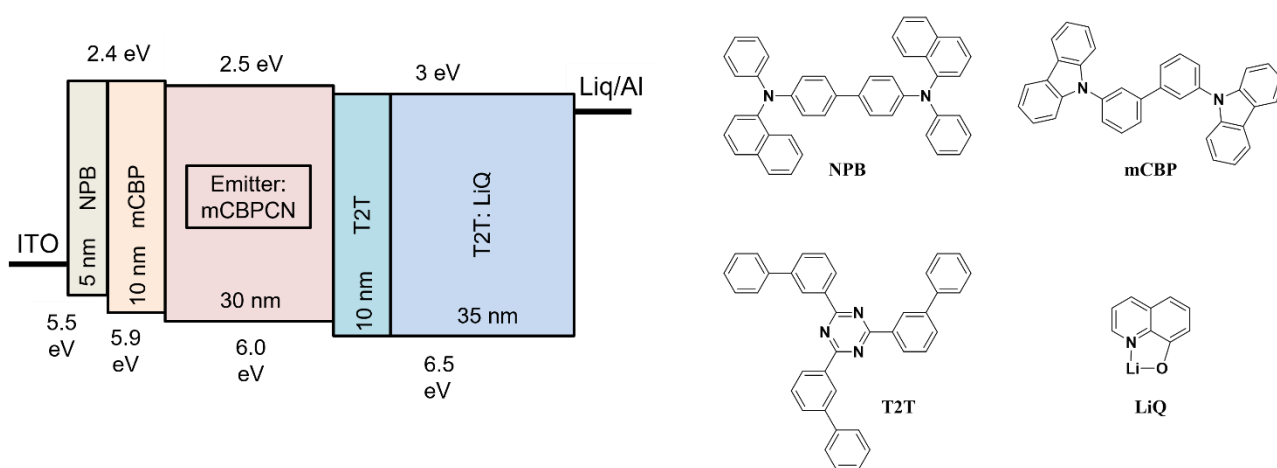


**Figure 123.** OLED device stack with extended **DMAC-TRZ** derivatives as emitters. HOMO and LUMO energy levels, and chemical structure of the different materials are provided in the figure.

An optimized device stack for **DMAC-TRZ** in mCBPCN had been previously optimized from our collaborators (this work is not published at the moment but is presented here), and this same stack was used for the five new derivatives. The stack is composed of ITO/NPB (35 nm)/NPB:mCBP (5 nm)/mCBP (10 nm)/mCBPCN:(**DMAC-TRZ** or **RPhDMAC-TRZ** x wt% (30 nm)/T2T (10 nm)/T2T:LiQ 1:1 (35 nm)/LiQ (1 nm)/Al (100 nm) (**Figure 123**). ITO is the semitransparent anode, NPB act as hole transport layer, mCBP act as electron blocking layer, mCBPCN is the host, T2T act as electron transporting layer, and LiQ modifies the work function of the aluminum cathode.

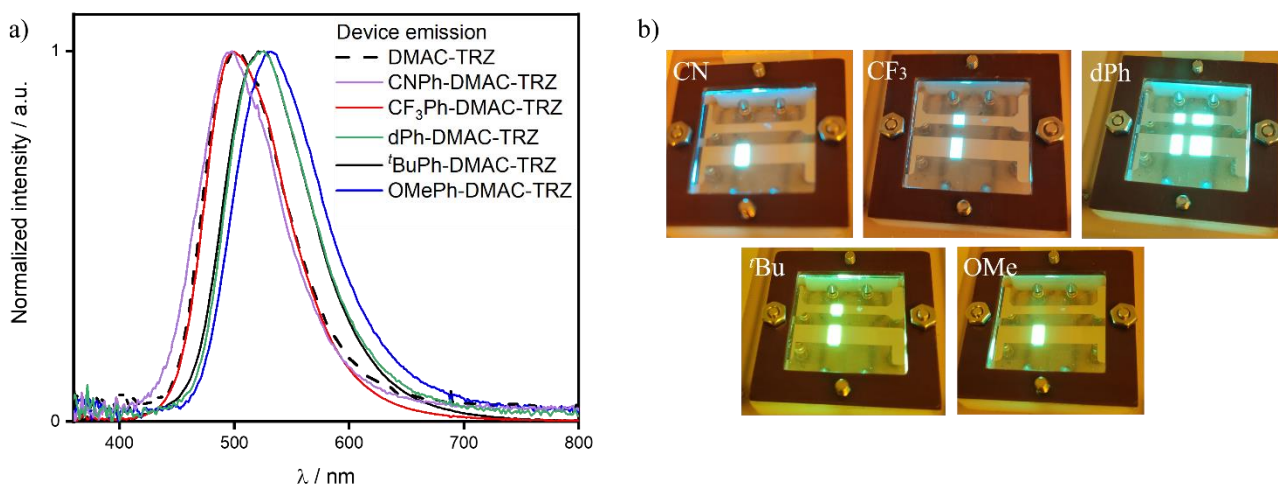


**Figure 124.** a) Emission spectra and b) pictures of  $t\text{BuPh}$ -DMAC-TRZ,  $\text{CF}_3\text{Ph}$ -DMAC-TRZ, OMePh-DMAC-TRZ, dPh-DMAC-TRZ, CNPh-DMAC-TRZ in 10 wt% doped mCBPCN devices ( $\lambda_{\text{exc}} = 355$  nm, **DMAC-TRZ**'s device emission was added for comparison).

The performances of the OLEDs are summarized in **Table 28**. All devices showed similar turn-on voltages of around 4 V, and the electroluminescence maxima followed the same trend observed in the PL of the films. The OLEDs showed  $\lambda_{EL}$  of 501 nm, 496 nm, 498 nm, 525 nm, 526 nm, and 531 nm for the devices with **DMAC-TRZ**, **CNPh-DMAC-TRZ**, **CF<sub>3</sub>Ph-DMAC-TRZ**, **dPh-DMAC-TRZ**, ***t*BuPh-DMAC-TRZ**, **OMePh-DMAC-TRZ**, respectively. The devices showed CIE coordinate of (0.20; 0.39), (0.22; 0.48), (0.29; 0.55), (0.30; 0.56), (0.34; 0.57) revealing that the only device possessing a deeper blue color than **DMAC-TRZ** (0.22; 0.48) is the one with **CNPh-DMA C-TRZ**, which sadly is the worst performing OLED of the series.

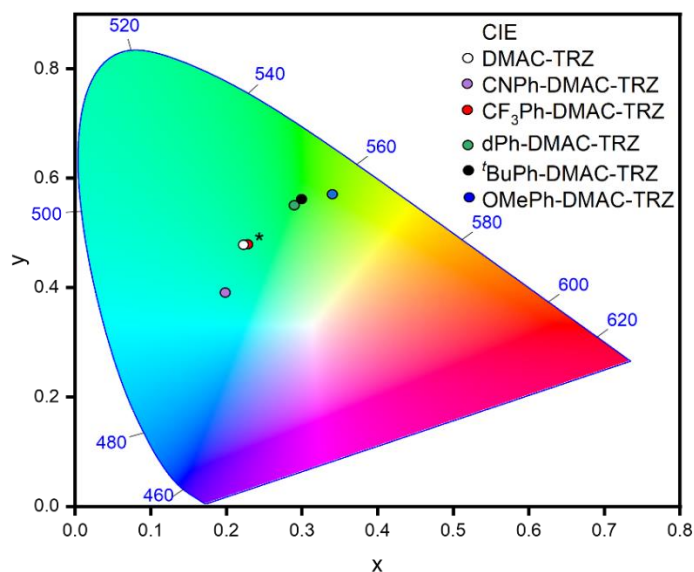


**Figure 125.** CIE coordinates of **DMAC-TRZ**, and derivatives in 10 wt% doped mCBPCN devices ( $\lambda_{exc}$ = 355 nm, \***DMAC-TRZ**'s and **CF<sub>3</sub>Ph-DMAC-TRZ** devices have identical CIE coordinates, precisely under the white dot).

The couple trend was observed in the device EQEs, with the best efficiencies (**Figure 126a**) observed in the devices with ***t*BuPh-DMAC-TRZ** and **OMePh-DMAC-TRZ**, with  $EQE_{max}$  of 23.8% and 25.5%, respectively, which is an improvement over the of 20.1% with **DMAC-TRZ**. The devices with **CF<sub>3</sub>Ph-DMAC-TRZ**, and **dPh-DMAC-TRZ** showed lower  $EQE_{max}$  of 17.8%, and 17.7%, respectively. The worst-performing device was the one with **CNPh-DMAC-TRZ**, with an  $EQE_{max}$  of 6.0%. All the devices presented very good efficiency roll-off, with  $EQE_{1000}$  of 3.2%, 12.8%, 12.0%, 20.5%, and 21.1% for **CNPh-DMAC-TRZ**, **CF<sub>3</sub>Ph-DMAC-TRZ**, **dPh-DMAC-TRZ**, ***t*BuPh-DMAC-TRZ**, and **OMePh-DMAC-TRZ** respectively, which represent a drop in efficiency of less than 5%. An excellent efficiency roll-off had already been observed for the **DMAC-TRZ** device with an  $EQE_{1000}$  of 17.7%, which is comparable in performance to the efficiency roll-off observed for the

OLEDs using the novel derivatives discussed in this chapter. Different doping concentrations were also tested for the devices with **'BuPh-DMAC-TRZ** to explore what effect it would have on the device properties (**Figure 126b**), while the roll-off seems to slightly improve at higher concentrations, the overall efficiency significantly decreases from the 10 wt% to the neat device with  $EQE_{max}$  of 20.7%, 18.6%, 11.8%, 6.1% for 20 wt%, 30 wt%, 60 wt% and non-doped device, respectively.

$$EQE = \gamma \eta_r \Phi_{PL} \eta_{out} \quad (59)$$

By using the  $EQE_{max}$  and the  $\Phi_{PL}$  values, and assuming that both the charge carrier balance  $\gamma$  and the radiative exciton fraction are 1, the outcoupling efficiency is calculated to be 18%, 25%, 25%, 33%, and 35%, for **CNPh-DMAC-TRZ**, **CF<sub>3</sub>Ph-DMAC-TRZ**, **dPh-DMAC-TRZ**, **'BuPh-DMAC-TRZ**, and **OMePh-DMAC-TRZ**, meaning that **CNPh-DMAC-TRZ** should have been the worst material, followed once again by the two “couples” **CF<sub>3</sub>/dPh** and **'Bu/OMe**. This does not follow the results obtained from the angle dependant photoluminescence measurements, which showed **dPh-DMAC-TRZ**, **CNPh-DMAC-TRZ**, and **OMePh-DMAC-TRZ** having the most horizontal orientation of their TDM and **'BuPh-DMAC-TRZ** and **CF<sub>3</sub>Ph-DMAC-TRZ** having the largest  $a$  values of the series. This is a further remark that a more in-depth analysis of the orientation behavior of these materials is needed. Nonetheless, the  $EQE_{max}$  values must have been influenced by the preferential horizontal orientation of the TDM of the materials, despite them not following the predicted trend.

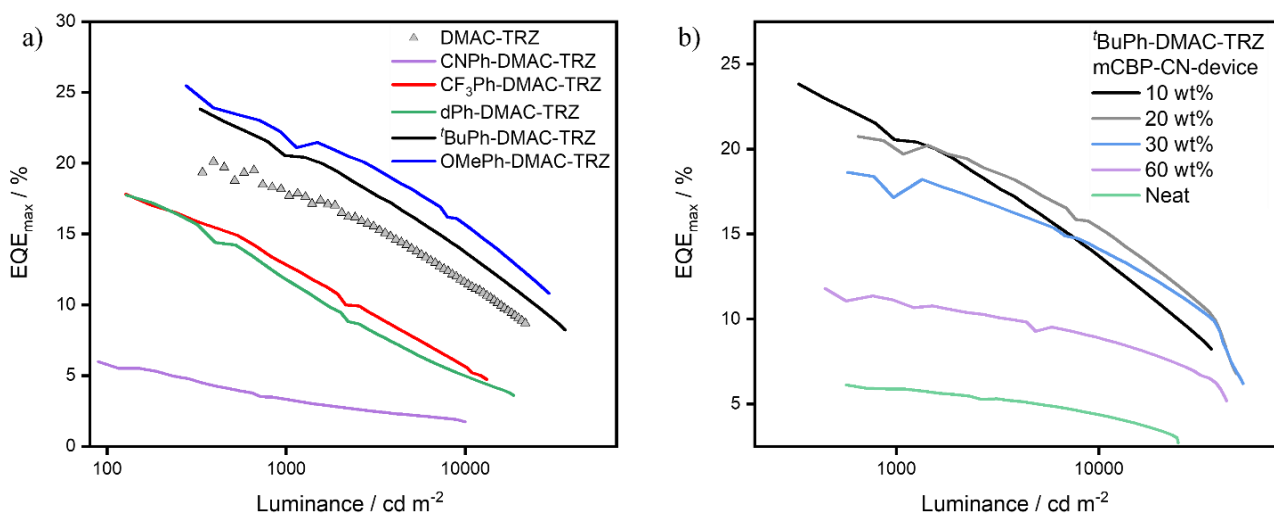


**Figure 126.** a)  $EQE_{max}$  vs Luminance curves of **DMAC-TRZ** and extended derivatives OLEDs; b)  $EQE_{max}$  vs Luminance curves of OLEDs with **'BuPh-DMAC-TRZ** at different doping concentrations.



The current density of all six devices are very similar (**Figure 127**). The devices with ***t*BuPh-DMAC-TRZ** and **OMePh-DMAC-TRZ** show the highest luminance of the series, with values of 36,000 cd/m<sup>2</sup> and 29,300 cd/m<sup>2</sup>, respectively. This represents an improvement over the device with **DMAC-TRZ**, which had a luminance of 21,600 cd/m<sup>2</sup>. The devices with **CF<sub>3</sub>Ph-DMAC-TRZ** and **dPh-DMAC-TRZ** present lower values of 13,200 cd/m<sup>2</sup>, and 16,200 cd/m<sup>2</sup>. The device with **CNPh-DMAC-TRZ** is again the worst of the series, with the lowest luminance of 10,000 cd/m<sup>2</sup>.

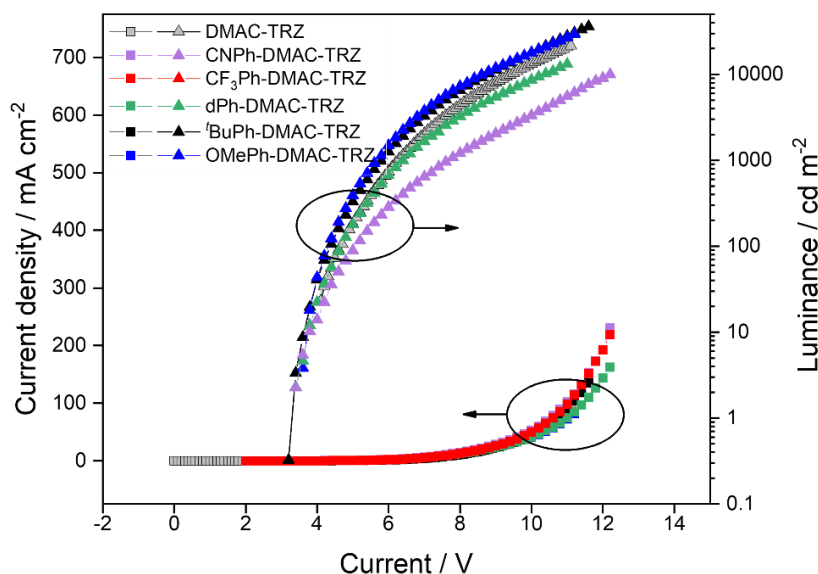


**Figure 127.** Current density vs Current vs Luminance curves of **DMAC-TRZ** and extended derivatives OLEDs.

**Table 28.** Properties and performances of the devices fabricated with the extended **DMAC-TRZ** derivatives.

<b>RPh-DMAC-TRZ</b>	$\lambda_{EL}$ / nm	$V_{on}$ / V	$EQE_{max}$ / %	$EQE_{1000}$ / %	$Ce$ / $cd A^{-1}$	$Pe$ / $lm W^{-1}$	$L$ / $cd m^{-2}$	CIE (x; y)
<b>DMAC-TRZ</b>	501	4.2	20.1	17.7	56.83	32.46	21600	0.22; 0.48
<b>CN</b>	496	3.8	6.0	3.2	17.75	11.15	10000	0.20; 0.39
<b>CF<sub>3</sub></b>	498	3.8	17.8	12.8	36.54	17.94	13200	0.22; 0.48
<b>dPh</b>	525	4	17.7	12.0	60.95	41.63	16200	0.29; 0.55
<b><i>t</i>Bu</b>	526	4	23.8	20.5	74.50	46.81	36000	0.30; 0.56
<b>OMe</b>	531	3.8	25.5	21.1	80.35	52.59	29300	0.34; 0.57

The lifetime of the devices was then measured (**Figure 128**).  $I_0$  is the luminance value taken at a current density of  $10 \text{ mA/cm}^2$ . The luminance of the devices was then normalized against these values and plotted against time.  $t_{95}$  and  $t_{85}$  were then extracted, which are the time it takes for the initial luminance to reach 95% and 85% of  $I_0$ , respectively. All devices except for that with **dPh-DMAC-TRZ** showed lower lifetimes than the device with **DMAC-TRZ**. The device with **dPh-DMAC-TRZ**, however, achieved a lifetime greatly superior to the parent emitter, with a four times longer  $t_{95}$  (0.1 h for **DMAC-TRZ** vs 0.4 h for **dPh-DMAC-TRZ**) and almost a double  $t_{85}$  (1.0 h for **DMAC-TRZ** vs 1.9 h for **dPh-DMAC-TRZ**).

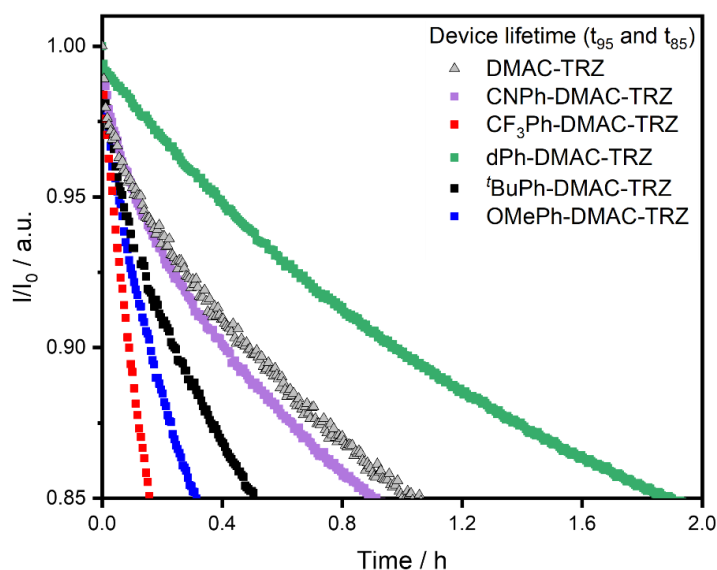


**Figure 128.** Change in luminance as a function of time.

**Table 29.** Device lifetime ( $t_{95}$  ad  $t_{85}$ ) data.

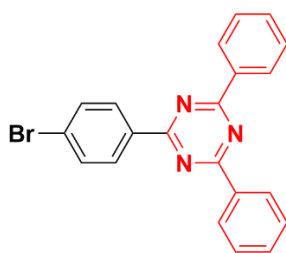
<b>RPh-DMAC-TRZ</b>	<b><math>t_{95}</math> / h</b>	<b><math>t_{85}</math> / h</b>
<b>DMAC-TRZ</b>	0.1	1.0
<b>CN</b>	0.1	0.9
<b>CF<sub>3</sub></b>	0.03	0.2
<b>dPh</b>	0.4	1.9
<b><sup>t</sup>Bu</b>	0.07	0.6
<b>OMe</b>	0.05	0.3

## 5.4 - Conclusions

In this study, the structure of the preferentially horizontally oriented emitter **DMAC-TRZ**<sup>72</sup> was modified into five novel TADF emitters, **CNPh-DMAC-TRZ**, **CF<sub>3</sub>Ph-DMAC-TRZ**, **dPh-DMAC-TRZ**, ***t*BuPh-DMAC-TRZ**, and **OMePh-DMAC-TRZ**, in order to try and achieve emitters with horizontally oriented TDM, while studying the effect that different EWG and EDG would have on their photophysics. The most noticeable effect was the change in emission color, which got red-shifted by stronger EDG substituents. This can be explained by the fact that the stronger the EDG on the donor is, the more stabilized the HOMO energy level will be, leading to a lower  $E_{\text{gap}}$ , and thus red-shifter emission. The efficiency of the materials followed a different trend, which was called the “couple trend”, where **CNPh-DMAC-TRZ** presented a unique behavior, and similar performances were observed for the two couples **CF<sub>3</sub>/dPh** and ***t*Bu/OMe**. The materials presented efficient  $\Phi_{\text{PLS}}$  of 34%, 70%, 70%, 72%, and 72% for **CNPh-DMAC-TRZ**, **CF<sub>3</sub>Ph-DMAC-TRZ**, **dPh-DMAC-TRZ**, ***t*BuPh-DMAC-TRZ**, **OMePh-DMAC-TRZ**, which led to OLEDs with  $\text{EQE}_{\text{max}}$  of 6.0%, 17.8%, 17.7%, 23.8%, and 25.5%. Unfortunately, our expectation of achieving emitters with a horizontally oriented TDM was only partially realized. While all material presented a preferential horizontal orientation, with  $a$  values below 0.3 there was no discernible correlation with either MW or  $x_{\text{E}}/x_{\text{H}}$ . A detailed host screening and a study of the thermal properties of the novel emitters are currently ongoing to try and understand what governs the TDM orientation of these materials.

## Compound characterization

### 2-(4-bromophenyl)-4,6-diphenyl-1,3,5-triazine (BrPh-dPh-TRZ)



**BrPh-dPh-TRZ** was prepared following the literature procedure.<sup>176</sup> A mixture of 4-bromobenzoyl chloride (5.0 g, 22.78 mmol, 1 equiv.) and benzonitrile (4.699 mL, 45.57 mmol, 2 equiv.), in DCM (30 mL), was cooled to 0°C in an ice bath and stirred for 30 min. Antimony pentachloride (2.924 mL, 22.78 mmol, 1 equiv.) was then added dropwise with a glass pipette. The solution immediately turned from white to canary yellow. The solution was stirred at room temperature over-night. The yellow solid was filtered and washed with dichloromethane. With an ice-bath, the yellow solid was added to a 35% ammonia solution (175 mL) and stirred in the ice bath for 30 min, and then 3h at room temperature. The white solid was then filtered and washed with cold MeOH to yield the desired product. (8.701 g). Yield: 98%; **Mp**: 200-210°C ; **R<sub>f</sub>**: 0.90 (cyclohexane/ethyl acetate = 4:1); **<sup>1</sup>H NMR** (500 MHz, CDCl<sub>3</sub>) δ: 8.78 – 8.76 (dt, *J*=6.9, 1.4, 1.1, 4H), 8.67-8.64 (dt, *J*=8.6, 2.4, 1.8, 2H), 7.73-7.70 (dt, *J*= 8.5, 2.5, 1.9, 2H), 7.64-7.57 (m, 6H); **<sup>13</sup>C NMR** (126 MHz, CDCl<sub>3</sub>) δ: 171.89, 171.00, 136.15, 135.33, 132.82, 132.06, 130.62, 129.12, 128.84, 127.63; **GC-MS retention time**: 13.529 min; **purity**: >99%; **Mass Theoretical**: (C<sub>21</sub>H<sub>14</sub>BrN<sub>3</sub>) 387.04; **Mass found**: 387.

Spectral data matches the one previously reported in the literature.<sup>181</sup>

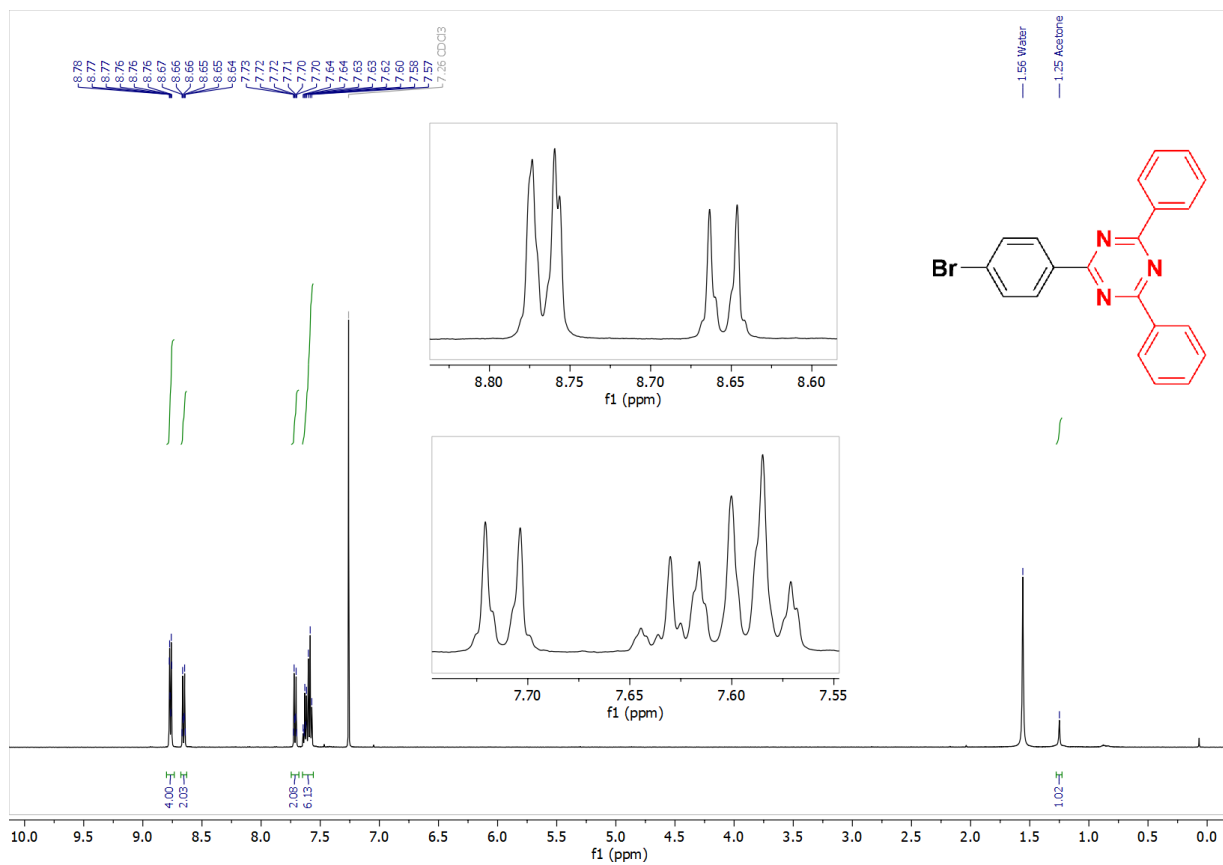


Figure 129. <sup>1</sup>H NMR of BrPh-dPh-TRZ in CDCl<sub>3</sub>.

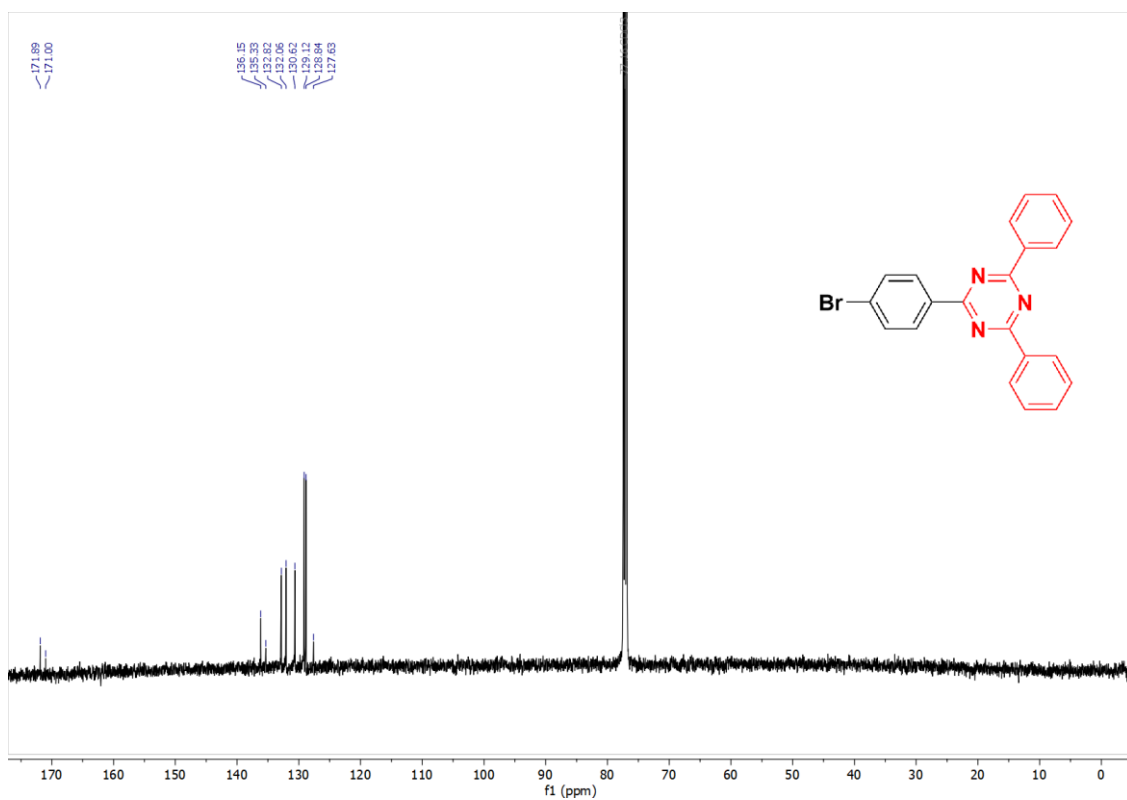
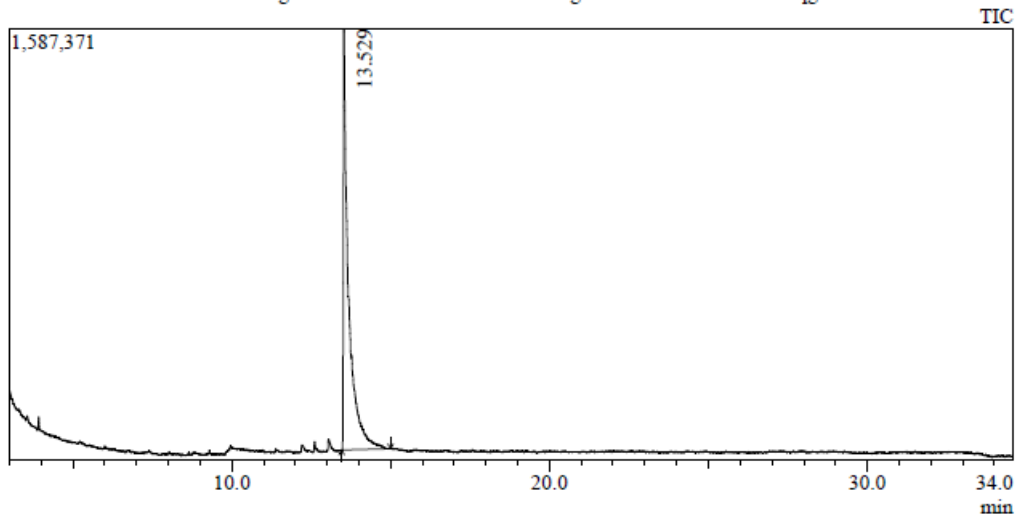


Figure 130. <sup>13</sup>C NMR of BrPh-dPh-TRZ in CDCl<sub>3</sub>.

Sample Information

Analyzed by : Admin  
 Analyzed : 30/05/2022 13:43:25  
 Sample Type : Unknown  
 Level # : 1  
 Sample Name : EC-Br-TRZ  
 Sample ID : EC-Br-TRZ  
 IS Amount : [1]=1  
 Sample Amount : 1  
 Dilution Factor : 1  
 Vial # : 127  
 Injection Volume : 1.00  
 Data File : S:\Ettore\Missing GCMS\EC-dBr-Ph-TRZ.qgd  
 Org Data File : S:\Ettore\Missing GCMS\EC-dBr-Ph-TRZ.qgd  
 Method File : S:\standard method 1 for RTX-1 column 330 injection-long.qgm  
 Org Method File : S:\standard method 1 for RTX-1 column 330 injection-long.qgm  
 Report File :  
 Tuning File : C:\GCMSsolution\System\Tune1\1 day after reinstall 09062021.qgt  
 Modified by : Admin  
 Modified : 30/05/2022 14:18:08

Chromatogram EC-Br-TRZ S:\Ettore\Missing GCMS\EC-dBr-Ph-TRZ.qgd



Peak#	R.Time	Area	Area%	Height	A/H	Base m/z	Base Int.
1	13.529	17277601	100.00	1551203	11.14	103.10	301379
		17277601	100.00	1551203			

Line#:1 R.Time:13.567(Scan#:1269)  
 MassPeaks:556  
 RawMode:Single 13.567(1269) BasePeak:103.10(254314)  
 BG Mode:None Group 1 - Event 1 Scan

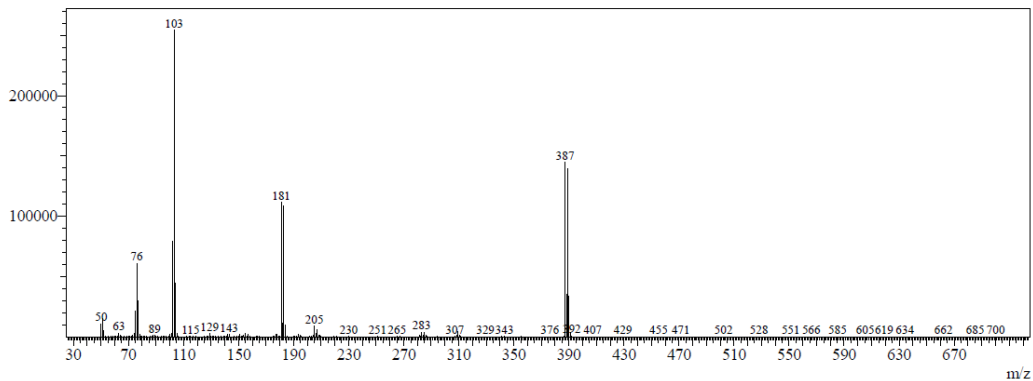
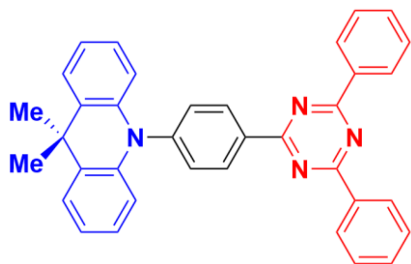


Figure 131. GC-MS trace of BrPh-dPh-TRZ.

**10-(4-(4,6-diphenyl-1,3,5-triazin-2-yl)phenyl)-9,9-dimethyl-9,10-dihydroacridine (DMAC-TRZ)**



To a schlenk flask fitted with a reflux condenser was added DMAC (2.0 g, 9.6 mmol, 1 equiv.), 2-(4-bromophenyl)-4,6-diphenyl-1,3,5-triazine (**BrPh-dPh-TRZ**) (4.1 g, 10.5 mmol, 1.1 equiv.), tribasic potassium carbonate (4.0 g, 28.8 mmol, 3 equiv.) palladium(II) acetate (214.5 mg, 0.96 mmol, 0.1 equiv.), tri-*tert*-butylphosphonium tetrafluoroborate (1.1 g, 3.8 mmol, 0.4 equiv.), and dry toluene (200 mL). The flask was connected to a Schlenk line via a reflux condenser and the mixture was heated to reflux, under N<sub>2</sub> atmosphere. After 48 h, the reaction was diluted with water, and the organic layer was extracted with DCM (50 mL × 3). The combined organic extracts were washed with brine, dried over Mg<sub>2</sub>SO<sub>4</sub> and concentrated by rotary evaporation. The crude was then washed with cold pentane (250 mL) and cold diethyl ether (250 mL) to achieve the desired product as a light brown solid (2.1 g). **Yield:** 42%; **Mp:** 250-253°C; **R<sub>f</sub>:** 0.76 (ethyl acetate/cyclohexane = 1 :4); **<sup>1</sup>H NMR** (500 MHz, CDCl<sub>3</sub>) δ: 9.04 – 9.02 (dt, *J*= 8.3, 2.3, 2.1, 2H), 8.83-8.81 (dt, *J*= 6.6, 1.4, 1.4, 4H), 7.66 – 7.56 (m, 8H), 7.50-7.48 (dd, *J*= 7.5, 1.7, 2H), 7.01-6.94 (m, 4H), 6.39-6.37 (dd, *J*= 8.0, 1.3, 2H), 1.73 (s, 6H); **<sup>13</sup>C NMR** (126 MHz, CDCl<sub>3</sub>) δ: 172.00, 171.22, 140.74, 136.23, 136.21, 132.86, 131.75, 131.68, 130.36, 129.17, 128.88, 126.60, 125.51, 121.98, 114.33, 36.19, 31.46.

Spectral data match that previously reported in the literature.<sup>72</sup>

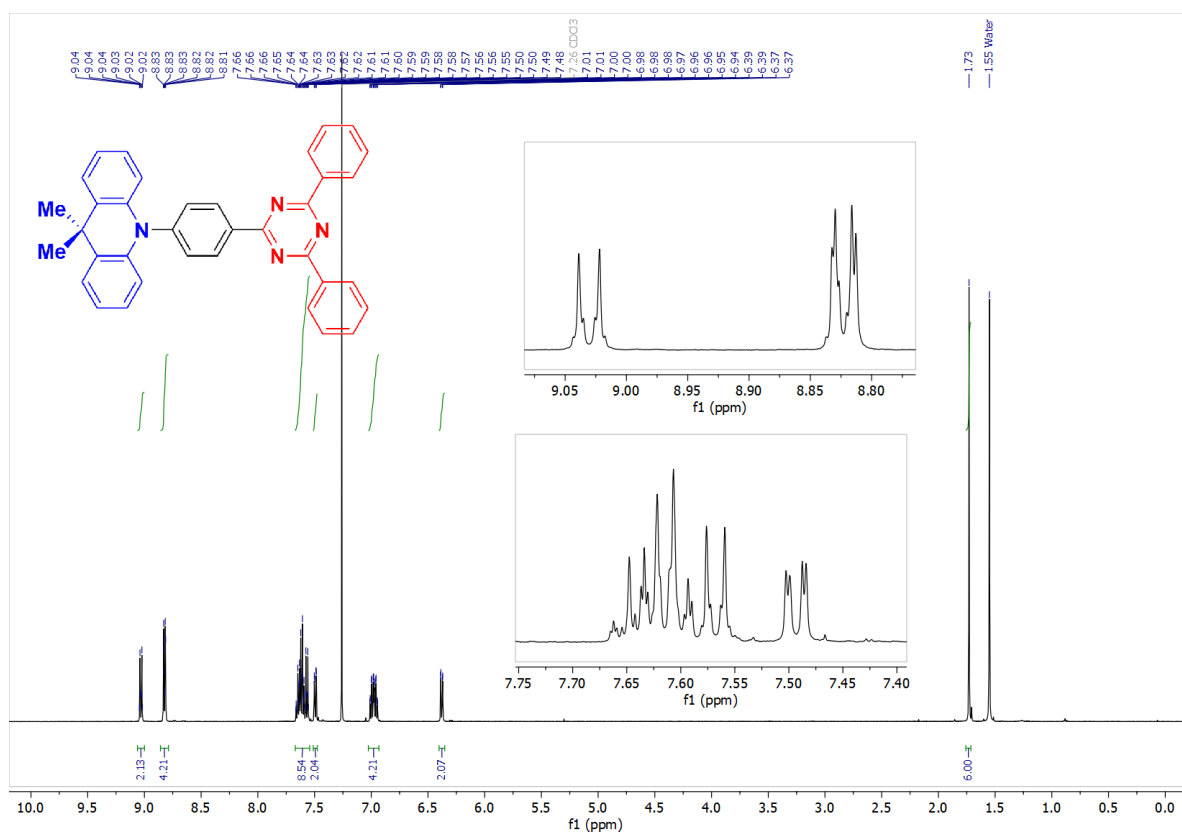


**Figure 132.  $^1\text{H}$  NMR of DMAC-TRZ in  $\text{CDCl}_3$ .**

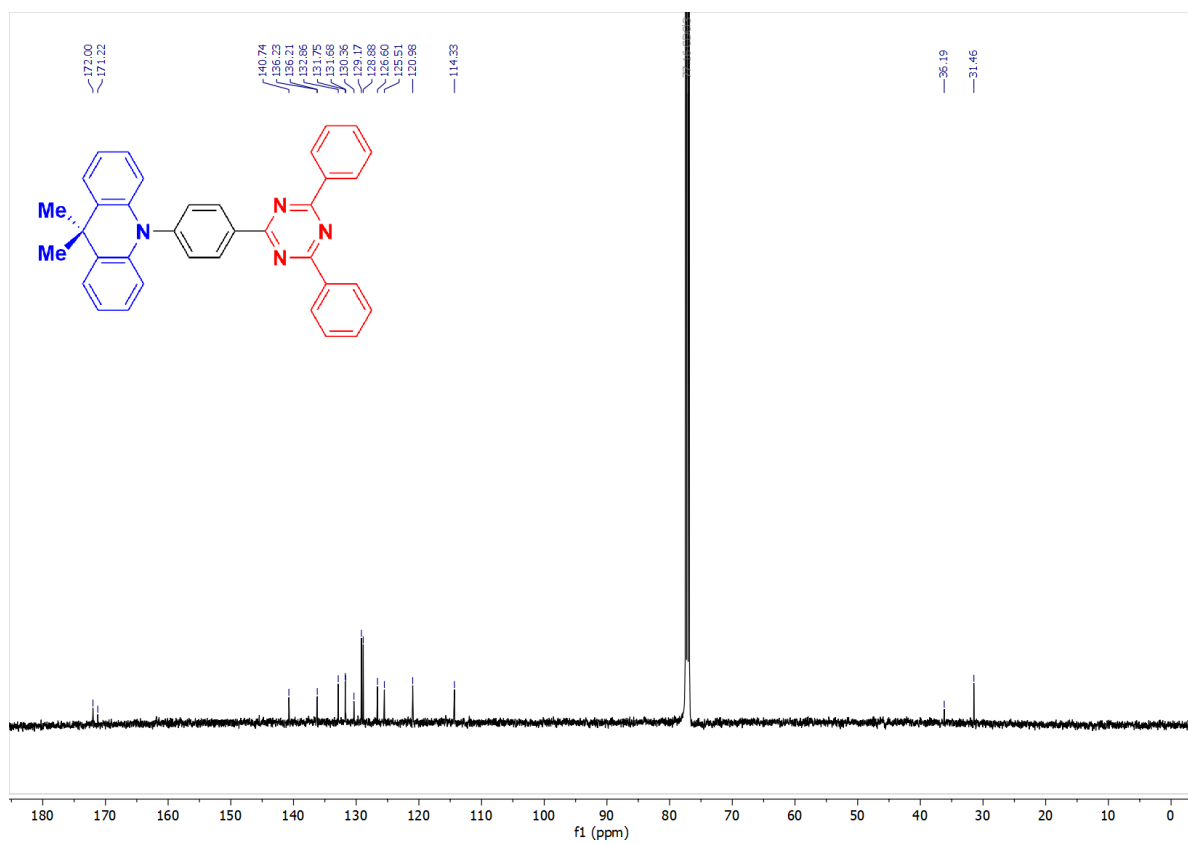
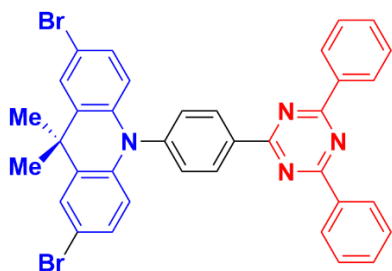


**Figure 133.  $^{13}\text{C}$  NMR of DMAC-TRZ in  $\text{CDCl}_3$ .**



**2,7-dibromo-10-(4-(4,6-diphenyl-1,3,5-triazin-2-yl)phenyl)-9,9-dimethyl-9,10-dihydroacridine (dBr-DMAC-TRZ)**



To a round bottom flask **DMAC-TRZ** (2.06 g, 3.99 mmol, 1 equiv.) and THF (90 mL) were added. The solution was cooled in an ice bath and a solution of *N*-bromosuccinimide (NBS, 1.63 g, 9.17 mmol, 2.3 equiv.) in THF (100 mL) was slowly added. The reaction mixture turned red, then yellow and then brown with the continuous addition of the NBS solution. The solution was stirred overnight, at room temperature, in darkness. The reaction was diluted with water, extracted with DCM (3 × 50 mL). The organic phase was washed with brine, dried over MgSO<sub>4</sub> and concentrated under reduced pressure. The crude was then washed with cold pentane (250 mL) and cold diethyl ether (250 mL) to achieve the desired product as a light brown solid (2.22 g). **Yield:** 75%; **Mp:** decomposition at 250 °C; **R<sub>f</sub>:** 0.83 (ethyl acetate/cyclohexane= 1:4); **<sup>1</sup>H NMR** (300 MHz, CDCl<sub>3</sub>) δ: 9.05-9.02 (dt, *J*= 8.7, 2.3, 1.9, 2H), 8.83-8.80 (dt, *J*= 6.3, 1.6, 1.3, 6H), 7.66 – 7.59 (m, 4H), 7.55-7.54 (d, *J*= 2.3, 2H), 7.52-7.49 (dt, *J*= 8.2, 2.8, 1.7, 2H), 7.10-7.06 (dd, *J*= 8.8, 2.3, 2H), 6.25-6.22 (d, *J*= 8.8, 2H), 1.68 (s, 6H). **<sup>13</sup>C NMR** (126 MHz, CDCl<sub>3</sub>) δ: 172.06, 170.99, 144.43, 139.58, 136.86, 136.10, 132.95, 131.98, 131.90, 131.31, 128.56, 128.17, 128.90, 128.36, 116.03, 113.77, 36.48, 31.17; **HR-MS** (Xevo G2-XS QTof) [M+H]<sup>+</sup> **Calculated:** (C<sub>36</sub>H<sub>26</sub>Br<sub>2</sub>N<sub>4</sub>) 674.4400 g mol<sup>-1</sup>, **Found:** 675.0595 g mol<sup>-1</sup>.

Spectral data match the ones previously reported in the literature.<sup>177</sup>

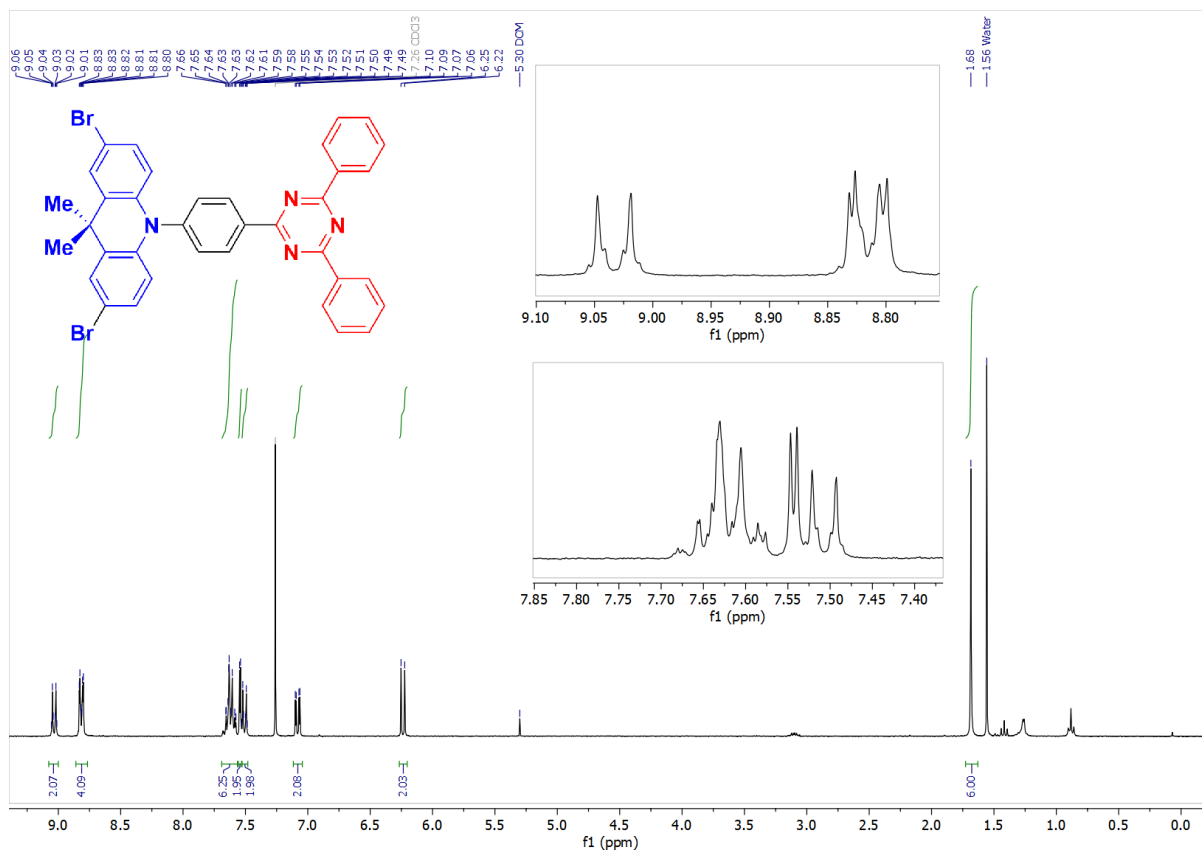


**Figure 134.  $^1\text{H}$  NMR of dBr-DMAC-TRZ in  $\text{CDCl}_3$ .**

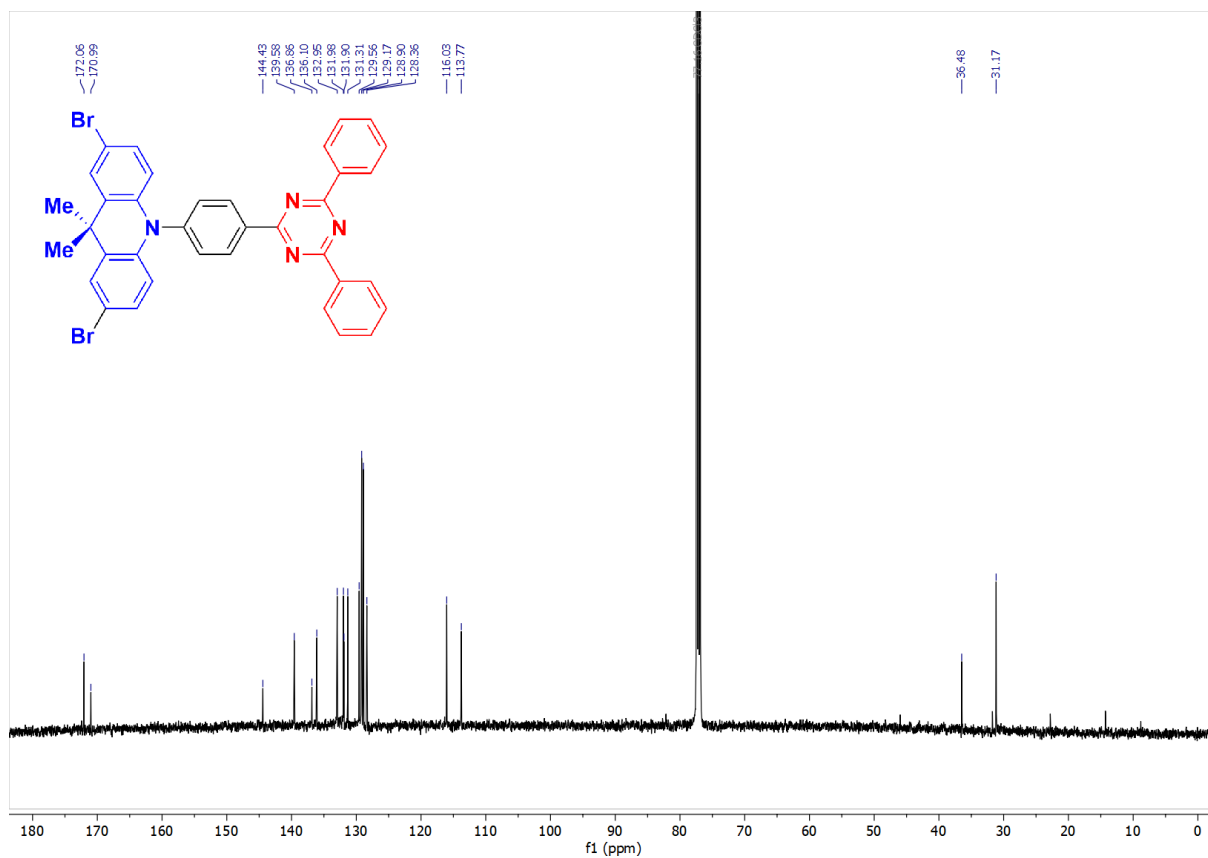


**Figure 135.  $^{13}\text{C}$  NMR of dBr-DMAC-TRZ in  $\text{CDCl}_3$ .**

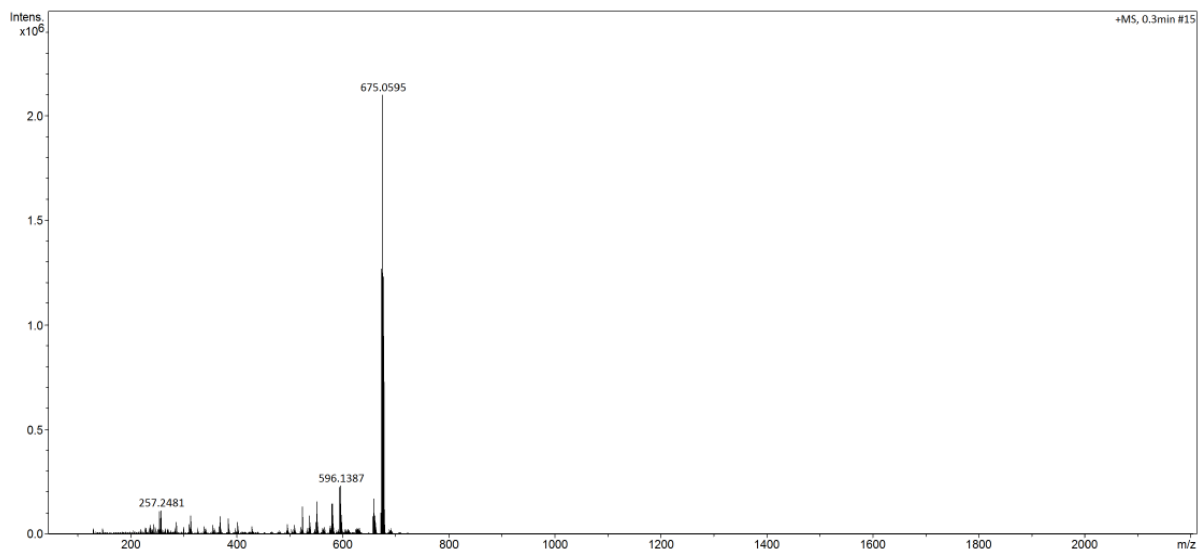
School of Chemistry Mass Spectrometry Service

SampleID  
Sample Description  
Analysis Name  
Method  
Instrument

D:\Data\stuartwarriner\manual\dBrPh\_DMAC\_TRZ\_a.d  
DIP Pos 3.m  
maXis impact  
Source Type APCI  
Ion Polarity Positive

Submitter

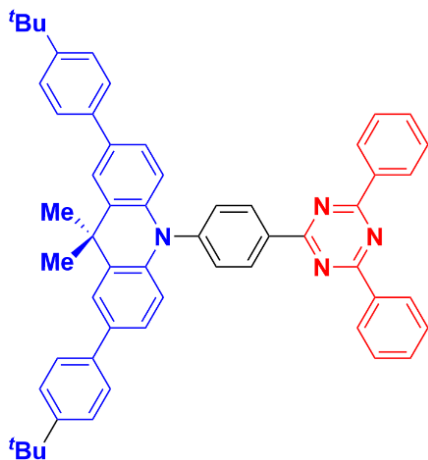
Supervisor  
Acquisition Date  
Scan Begin 50 m/z  
Scan End 2200 m/z



Bruker Compass DataAnalysis 4.3      Analysis Name      dBrPh\_DMAC\_TRZ\_a.d      12/03/2022 17:46:15      1 of 1

**Figure 136.** HRMS analysis report for **dBr-DMAC-TRZ**.

**2,7-bis(4-(tert-butyl)phenyl)-10-(4-(4,6-diphenyl-1,3,5-triazin-2-yl)phenyl)-9,9-dimethyl-9,10-dihydroacridine ('BuPh-DMAC-TRZ)**



To a pressure vessel were added 2,7-dibromo-10-(4-(4,6-diphenyl-1,3,5-triazin-2-yl)phenyl)-9,9-dimethyl-9,10-dihydroacridine (**dBr-DMAC-TRZ**) (1.0 g, 1.48 mmol, 1 equiv.) and 4-*tert*-butylphenyl-boronic acid (1.1 g, 5.93 mmol, 4 equiv.) and the vessel was degassed by alternating vacuum and nitrogen 3 times. THF (22 mL), and 16.5 mL of a 2 M Cs<sub>2</sub>CO<sub>3</sub> solution in water were added and the bi-phasic solution was degassed by bubbling N<sub>2</sub> trough for 30 min. Pd(PPh<sub>3</sub>)<sub>4</sub> was then added and the reaction was left to stir under pressure at 110°C for 72h. A yellow crystalline solid crashed out of the solution. The mixture was let to cool down and the yellow solid was filtered and washed with water (250 mL) and MeOH (250 mL) to achieve the desired product (0.73 g). The compound was further purified by gradient temperature sublimation **Yield:** 63%; **Mp:** 325-330 °C; **R<sub>f</sub>:** 0.50 (ethyl acetate/cyclohexane = 1 :9); **<sup>1</sup>H NMR** (300 MHz, CDCl<sub>3</sub>) δ: 9.08-9.06 (d, *J*= 7.1, 2H), 8.84-8.82 (d, *J*= 4.2, 4H), 7.73 (d, *J*= 2.0, 2H), 7.67-, 7.60 (m, 8H), 7.53-7.45 (dd, *J*= 22.3, 8.84, 8H), 7.24-7.22 (dd, *J*= 8.55, 2.05, 2H), 6.46-6.44 (d, *J*= 8.5, 2H), 1.83 (s, 6H), 1.36 (s, 18H); **<sup>13</sup>C NMR** (126 MHz, CDCl<sub>3</sub>) δ = 172.02, 171.20, 149.65, 145.33, 139.81, 138.54, 136.41, 136.20, 133.92, 132.88, 131.83, 131.67, 130.47, 129.18, 128.89, 126.44, 125.81, 125.28, 124.55, 114.67, 36.52, 34.63, 31.91, 31.54; **HPLC retention time:** 10.239 min; **purity:** >99%; **HR-MS** (Xevo G2-XS QTof) [M+H]<sup>+</sup> **Calculated:** (C<sub>56</sub>H<sub>52</sub>N<sub>4</sub>) 781.0600 g mol<sup>-1</sup>, **Found:** 781.4268 g mol<sup>-1</sup>; **EA** (C<sub>56</sub>H<sub>52</sub>N<sub>4</sub>) **Calculated** C: 86.12, H: 6.71, N: 7.17; **Found** C: 86.51, H: 6.76, N: 7.15.

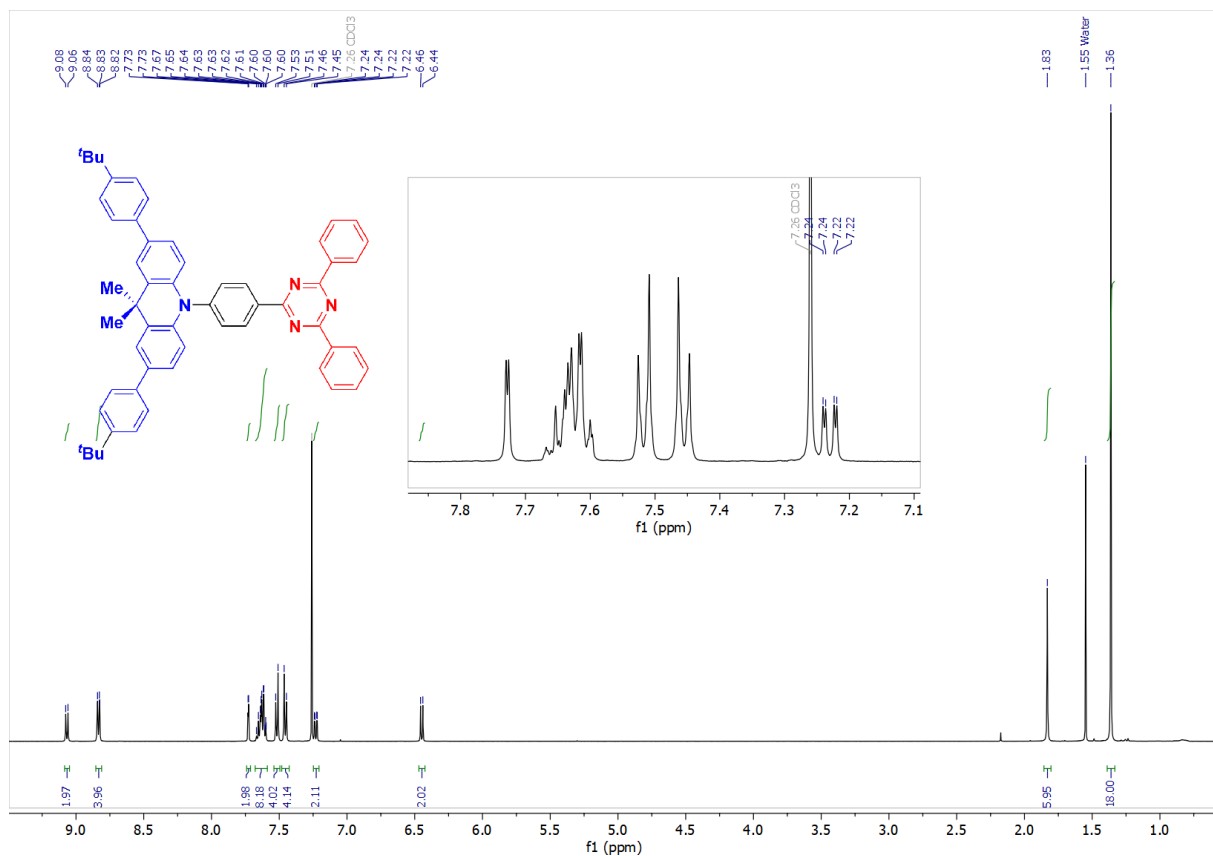


**Figure 137.  $^1\text{H}$  NMR of  $t\text{BuPh-DMAC-TRZ}$  in  $\text{CDCl}_3$ .**

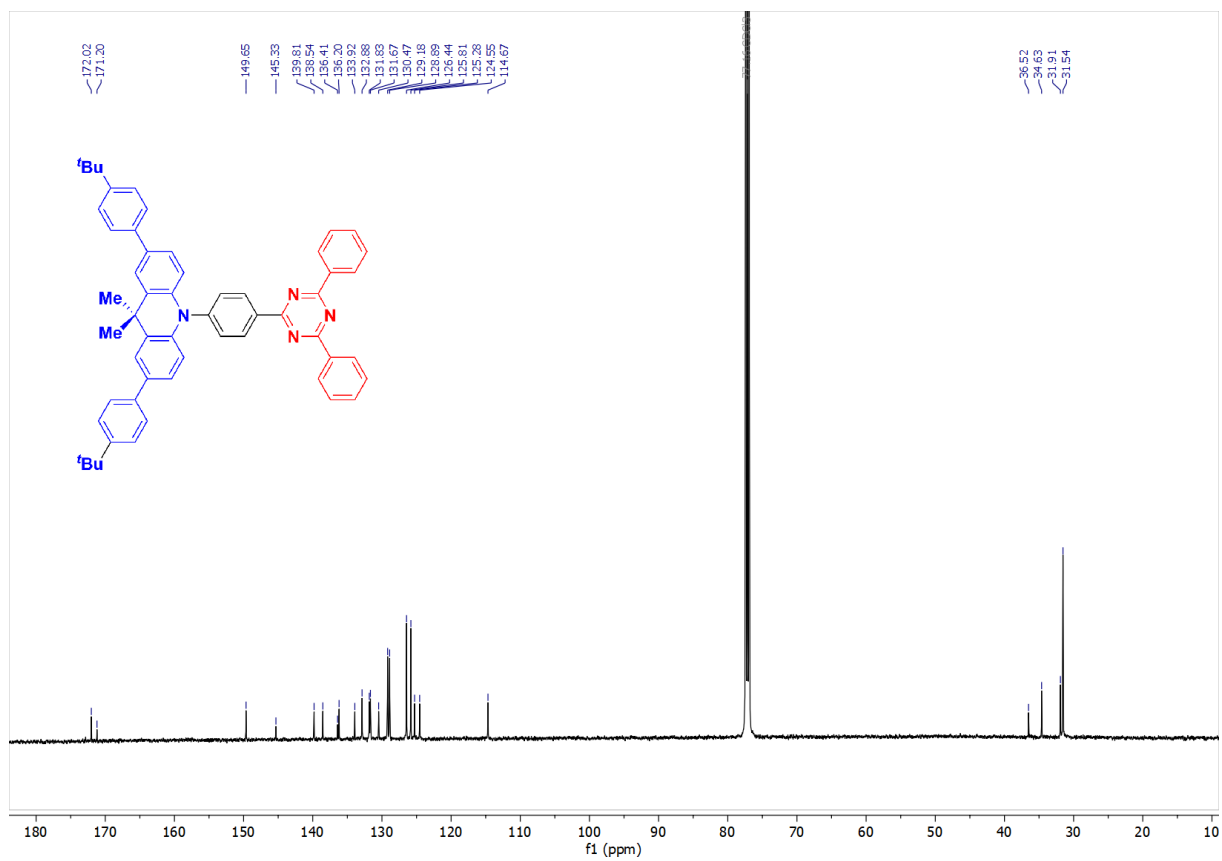


**Figure 138.  $^{13}\text{C}$  NMR of  $t\text{BuPh-DMAC-TRZ}$  in  $\text{CDCl}_3$ .**

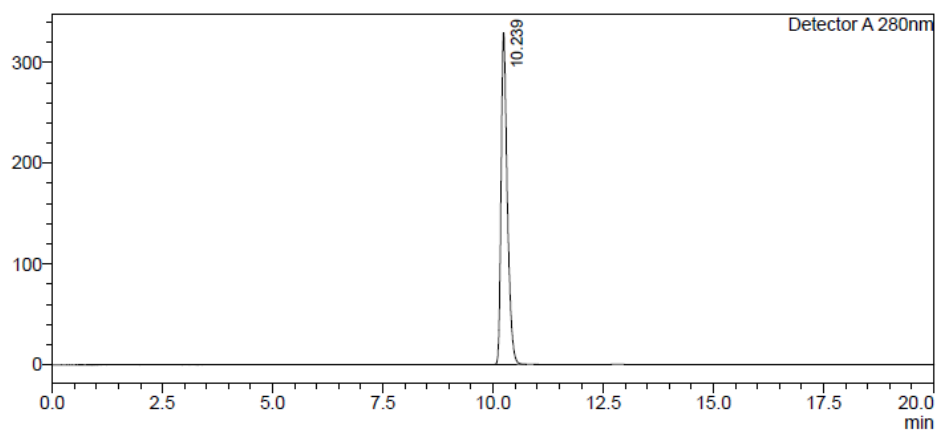
# HPLC Trace Report24Mar2022

## <Sample Information>

Sample Name : dtBuPhDMAC-TRZ-S1  
Sample ID :  
Method Filename : 100% THF 20 mins 280nm - DH.lcm  
Batch Filename : 23-03-22.lcb  
Vial # : 1-2  
Injection Volume : 10 uL  
Date Acquired : 23/03/2022 17:18:29  
Date Processed : 23/03/2022 17:38:33  
Sample Type : Unknown  
Acquired by : System Administrator  
Processed by : System Administrator

## <Chromatogram>

mV



## <Peak Table>

Detector A 280nm

Peak#	Ret. Time	Area	Height	Area%	Area/Height	Width at 5% Height
1	10.239	3232827	328784	100.000	9.833	0.349
Total		3232827	328784	100.000		

Figure 139. HPLC analysis report for 'BuPh-DMAC-TRZ.

SampleID

Sample Description

Analysis Name D:\Data\stuartwarriner\manual\dtBuPh\_DMAC\_TRZ\_b.d

Method DIP Pos 3.m

Instrument maXis impact

Source Type APCI

Ion Polarity Positive

Submitter

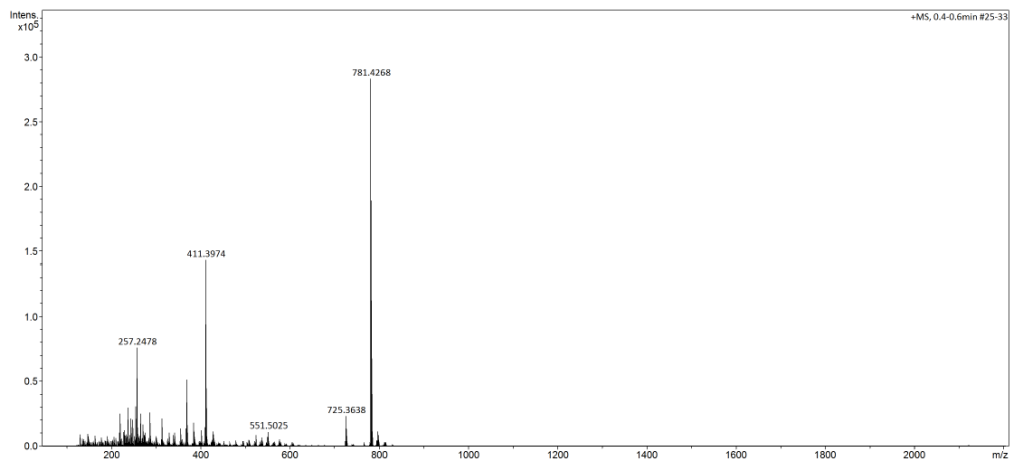
Supervisor

Acquisition Date

12/03/2022 17:48:23

Scan Begin 50 m/z

Scan End 2200 m/z



Bruker Compass DataAnalysis 4.3

Analysis Name dtBuPh\_DMAC\_TRZ\_b.d

12/03/2022 17:50:34

1 of 1

**Figure 140.** HRMS analysis report for 'BuPh-DMAC-TRZ.

## Elemental Analysis Service Request Form

Researcher name Ettore Crovini

Researcher email ec254@st-andrews.ac.uk

NOTE: Please submit ca. 10 mg of sample

Sample reference number	EC-3621
Name of Compound	d'BuPh-DMAC-TRZ
Molecular formula	C <sub>56</sub> H <sub>52</sub> N <sub>4</sub>
Stability	Air stable
Hazards	No hazards
Other Remarks	None

Analysis type: Elemental analysis

Single  Duplicate  Triplicate

Analysis Result:

Element	Expected %	Found (1)	Found (2)	Found (3)
Carbon	86.12	86.77	86.25	
Hydrogen	6.71	6.75	6.77	
Nitrogen	7.17	7.15	7.16	

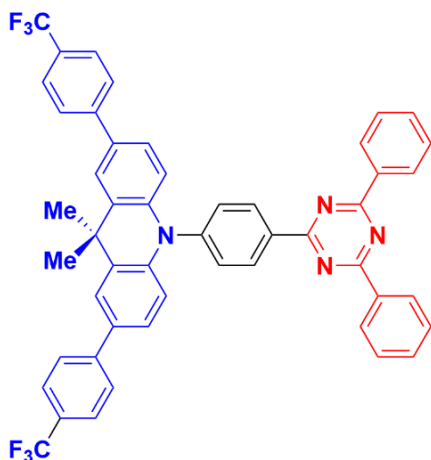
Authorising Signature:

Date completed	29.04.22
Signature	J-PL
comments	

Figure 141. EA analysis report for 'BuPh-DMAC-TRZ.



**10-(4-(4,6-diphenyl-1,3,5-triazin-2-yl)phenyl)-9,9-dimethyl-2,7-bis(4-(trifluoromethyl)phenyl)-9,10-dihydroacridine (CF<sub>3</sub>Ph-DMAC-TRZ)**



The same reaction procedure as **BuPh-DMAC-TRZ** was followed, but with a different boronic acid, 4-trifluoromethyl-phenyl-boronic acid (1.126 g, 5.931 mmol, 4 equiv.). After 72h, the reaction was diluted with THF and filtered over celite to remove any unreacted palladium. The solution was diluted with water, and the organic layer was extracted with DCM (3 × 50 mL). The organic phase was washed with brine, dried over MgSO<sub>4</sub> and concentrated under reduced pressure. The target product was isolated as yellow solid after purification by column chromatography on silica gel using 5:1 hexane/EtOAc as eluent. It was then further purified *via* recrystallization in THF/EtOH. (0.6706 g). The compound was furtherly purified by gradient temperature sublimation. **Yield:** 56%; **Mp:** 320-325 °C; **R<sub>f</sub>:** 0.49 (ethyl acetate/cyclohexane = 1:9); **<sup>1</sup>H NMR** (500 MHz, CDCl<sub>3</sub>) δ: 9.10-9.08 (d, *J*=8.5, 2H), 8.85-8.83 (dd, *J*=8.2, 1.4, 4H), 7.76-7.75 (d, *J*=2.1, 2H), 7.68 – 7.61 (m, 16H), 7.28 (d, *J*=2.1, 1H), 6.50-6.49 (d, *J*=8.6, 2H), 1.87 (s, 6H); **<sup>13</sup>C NMR** (126 MHz, CDCl<sub>3</sub>) δ: 172.08, 171.08, 144.74, 144.66, 140.50, 136.83, 136.13, 132.96, 132.66, 131.98, 131.51, 130.65, 129.18, 128.92, 126.87, 125.87, 125.84, 125.69, 125.61, 124.74, 115.01, 36.54, 32.04; **HPLC retention time:** 10.185 min; **purity:** 100.00%; **HR-MS** (Xevo G2-XS QToF) [M+H]<sup>+</sup> **Calculated:** (C<sub>50</sub>H<sub>34</sub>F<sub>6</sub>N<sub>4</sub>) 804.2700 g mol<sup>-1</sup>, **Found:** 805.2798 g mol<sup>-1</sup>; **EA** (C<sub>50</sub>H<sub>34</sub>F<sub>6</sub>N<sub>4</sub>) **Calculated** C: 74.62, H: 4.26, N: 6.96; **Found** C: 74.88, H: 4.30, N: 6.89.

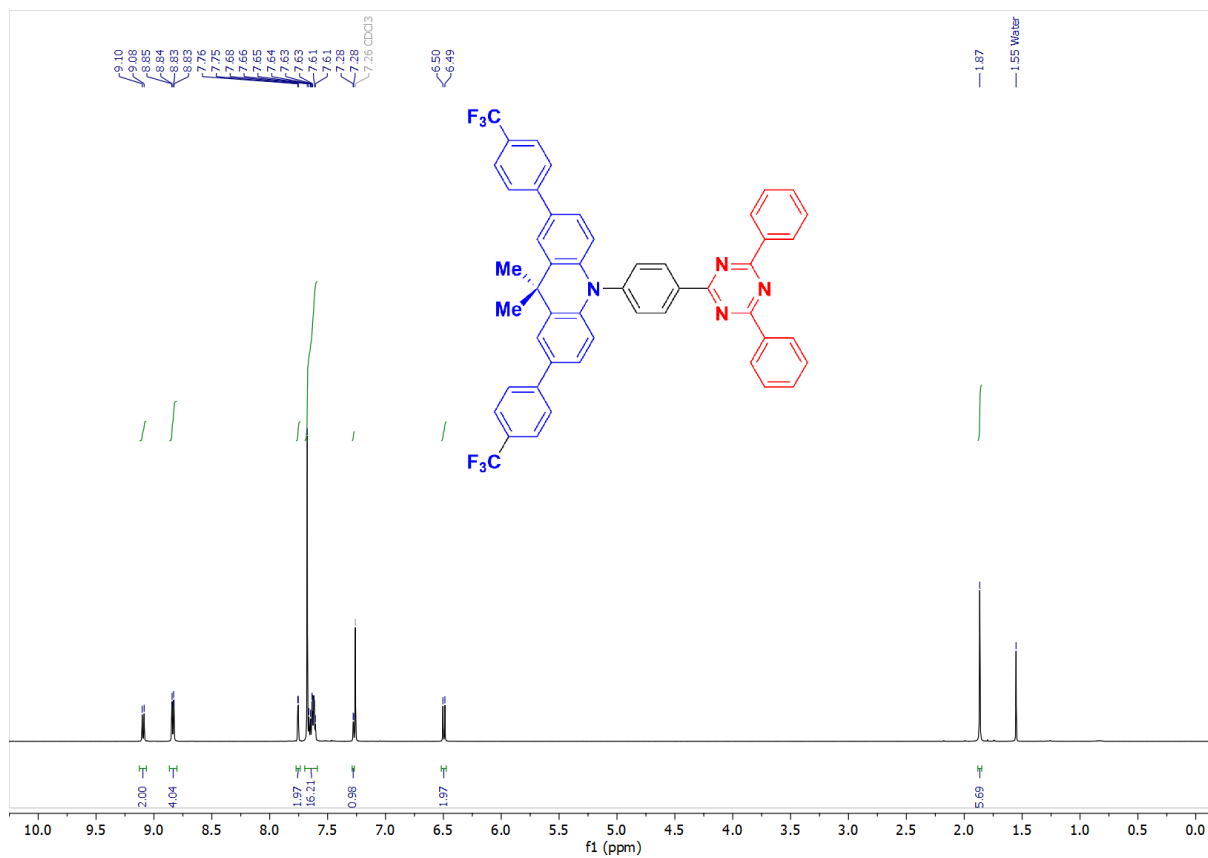


**Figure 142.  $^1\text{H}$  NMR of  $\text{CF}_3\text{Ph-DMAC-TRZ}$  in  $\text{CDCl}_3$ .**

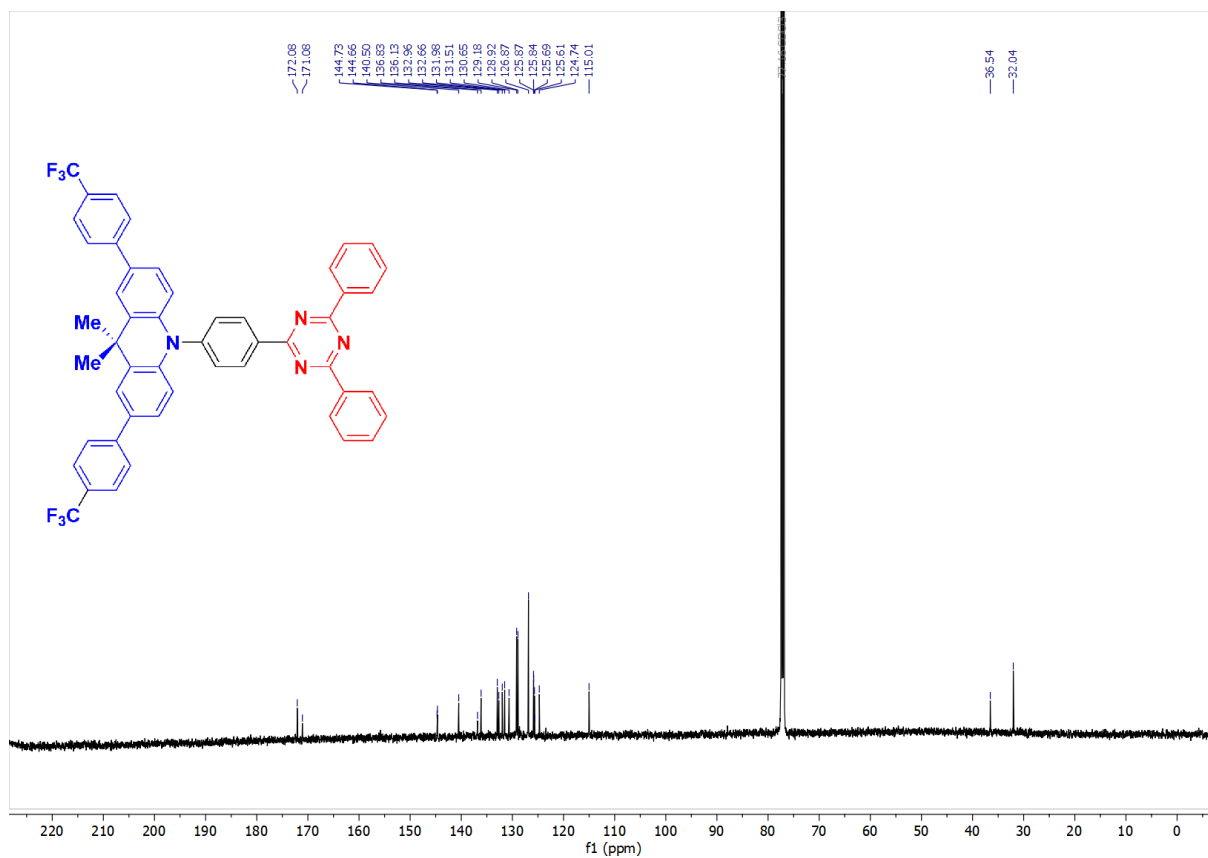


**Figure 143.  $^{13}\text{C}$  NMR of  $\text{CF}_3\text{Ph-DMAC-TRZ}$  in  $\text{CDCl}_3$ .**

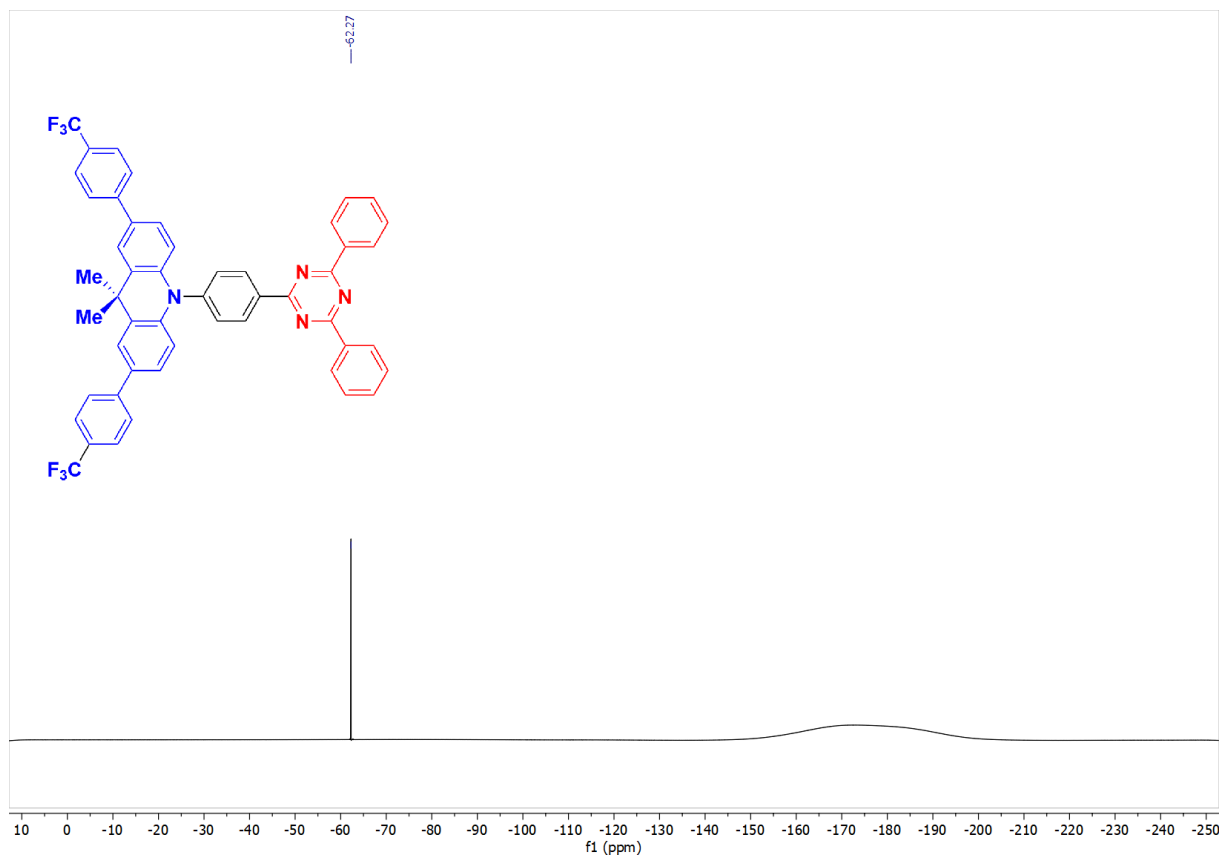


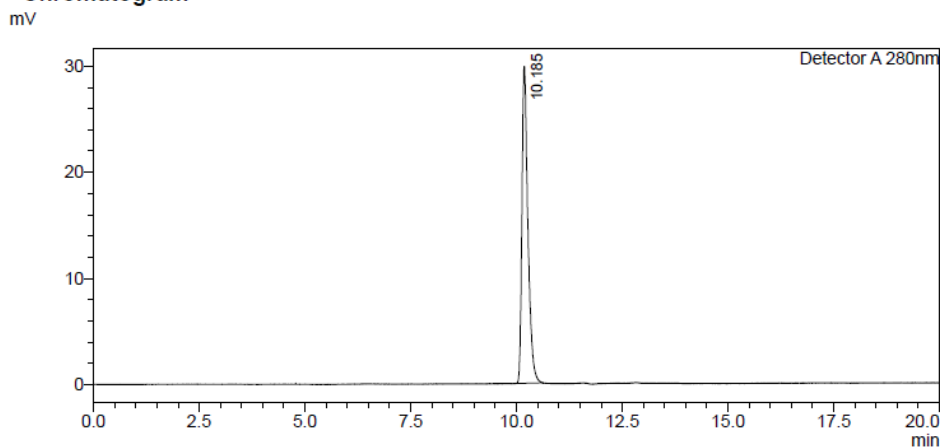
**Figure 144.** <sup>19</sup>F NMR of CF<sub>3</sub>Ph-DMAC-TRZ in CDCl<sub>3</sub>.

# HPLC Trace Report24Mar2022

## <Sample Information>

Sample Name : dCF3PhDMAC-TRZ-S2  
Sample ID :  
Method Filename : 100% THF 20 mins 280nm - DH.lcm  
Batch Filename : 23-03-22.lcb  
Vial # : 1-3  
Injection Volume : 1 uL  
Date Acquired : 23/03/2022 17:59:17  
Date Processed : 23/03/2022 18:19:19  
Sample Type : Unknown  
Acquired by : System Administrator  
Processed by : System Administrator

## <Chromatogram>



## <Peak Table>

Detector A 280nm

Peak#	Ret. Time	Area	Height	Area%	Area/Height	Width at 5% Height
1	10.185	292613	29803	100.000	9.818	0.353
Total		292613	29803	100.000		

Figure 145. HPLC analysis report for CF<sub>3</sub>Ph-DMAC-TRZ.

## School of Chemistry Mass Spectrometry Service

SampleID  
Sample Description  
Analysis Name  
Method  
Instrument

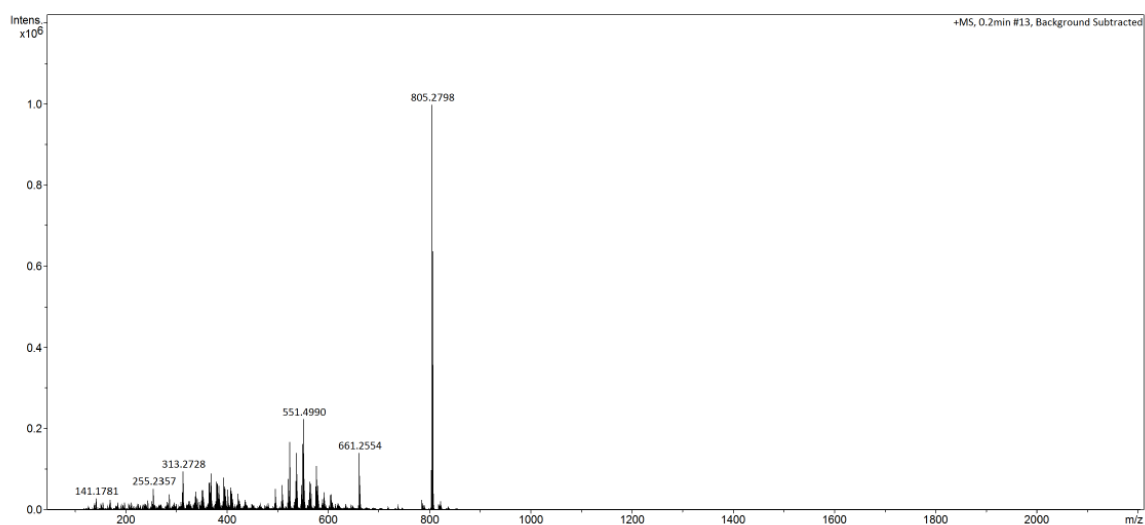
D:\Data\stuartwariner\manual\EC\_3620\_a.d  
DIP Pos 3.m  
maXis impact

Source Type APCI Ion Polarity Positive

## Submitter

Supervisor  
Acquisition Date  
Scan Begin

18/05/2022 14:06:33  
Scan End 2200 m/z



Bruker Compass DataAnalysis 4.3

Analysis Name EC\_3620\_a.d

18/05/2022 14:10:37

1 of 1

Figure 146. HRMS analysis report for CF<sub>3</sub>Ph-DMAC-TRZ.

## Elemental Analysis Service Request Form

Researcher name Ettore Crovini

Researcher email ec254@st-andrews.ac.uk

NOTE: Please submit ca. 10 mg of sample

Sample reference number	EC-3620
Name of Compound	dCF <sub>3</sub> Ph-DMAC-TRZ
Molecular formula	C <sub>50</sub> H <sub>34</sub> F <sub>6</sub> N <sub>4</sub>
Stability	Air stable
Hazards	None
Other Remarks	None

Analysis type: Elemental Analysis

Single  Duplicate  Triplicate

Analysis Result:

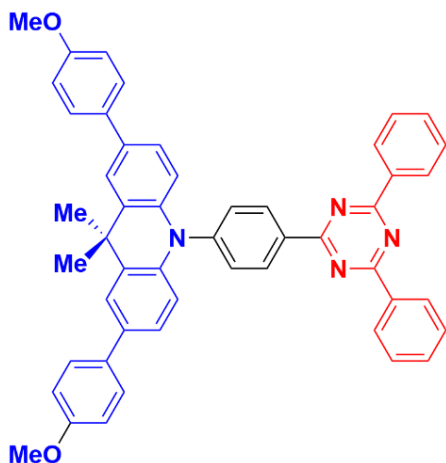
Element	Expected %	Found (1)	Found (2)	Found (3)
Carbon	74.62	74.99	74.76	
Hydrogen	4.26	4.30	4.31	
Nitrogen	6.96	6.90	6.88	
Fluorine	14.16			

Authorising Signature:

Date completed	29.04.22
Signature	S - P L
comments	

Figure 147. EA analysis report for CF<sub>3</sub>Ph-DMAC-TRZ.

**10-(4-(4,6-diphenyl-1,3,5-triazin-2-yl)phenyl)-2,7-bis(4-methoxyphenyl)-9,9-dimethyl-9,10-dihydroacridine (OMePh-DMAC-TRZ)**



The same reaction procedure as **BuPh-DMAC-TRZ** was followed, but with a different boronic acid, 4-methoxy-phenyl-boronic acid (0.901 g, 5.931 mmol, 4 equiv.). After 72 h, the reaction was diluted with THF and filtered over celite to remove any unreacted palladium. The solution was diluted with water, and the organic layer was extracted with DCM (3 × 50 mL). The organic phase was washed with brine, dried over MgSO<sub>4</sub> and concentrated under reduced pressure. The target product was isolated as yellow solid after purification by column chromatography on silica gel using 5:1 hexane/EtOAc as eluent. It was then further purified *via* recrystallization in THF/Ether. (0.502 g). The compound was furtherly purified by gradient temperature sublimation. **Yield:** 47%; **Mp:** 300-305 °C; **R<sub>f</sub>:** 0.39 (ethyl acetate/cyclohexane= 1:9); **<sup>1</sup>H NMR** (500 MHz, CDCl<sub>3</sub>) δ: 9.08-9.05 (dt, *J*= 8.4, 2.3, 1.7, 2H), 8.84 – 8.82 (dt, *J*= 7.0, 1.6, 1.6 4H), 7.69 (d, *J*= 2.1, 2H), 7.67-7.60 (m, 8H) 7.52-7.49 (dt, *J*= 8.5, 2.6, 2.0, 4H), 7.20-7.18 (dd, *J*= 8.56, 2.08, 2H), 6.99-6.96 (dt, *J*= 8.7, 3.0, 1.5, 4H), 6.45-6.43 (d, *J*= 8.5, 2H), 3.85 (s, 6H), 1.84 (s, 6H); **<sup>13</sup>C NMR** (126 MHz, CDCl<sub>3</sub>) δ: 172.02, 171.20, 158.77, 145.37, 139.56, 136.38, 136.19, 134.02, 133.68, 132.88, 131.83, 131.62, 130.53, 129.18, 128.89, 127.77, 125.02, 124.22, 114.71, 114.32, 55.52, 36.52, 31.98; **HPLC retention time:** 10.444 min; **purity:** 100.00%; **HR-MS** (Xevo G2-XS QToF) [M+H]<sup>+</sup> **Calculated:** (C<sub>50</sub>H<sub>40</sub>N<sub>4</sub>O<sub>2</sub>) 728.3200 g mol<sup>-1</sup>, **Found:** 729.3253 g mol<sup>-1</sup>; **EA** (C<sub>50</sub>H<sub>40</sub>N<sub>4</sub>O<sub>2</sub>) **Calculated** C: 82.39, H: 5.53, N: 7.69; **Found** C: 82.59, H: 5.57, N: 7.62.



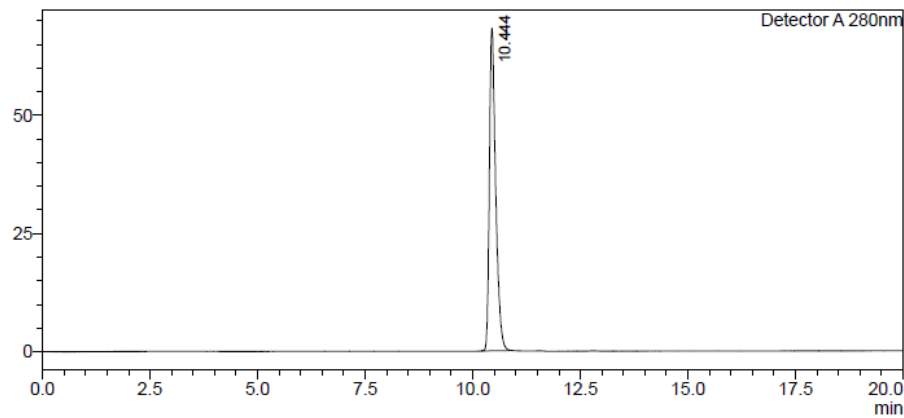
# HPLC Trace Report24Mar2022

## <Sample Information>

Sample Name : dOMePhDMAC-TRZ-S1  
Sample ID :  
Method Filename : 100% THF 20 mins 280nm - DH.lcm  
Batch Filename : 23-03-22.lcb  
Vial # : 1-4  
Injection Volume : 1 uL  
Date Acquired : 23/03/2022 18:40:01  
Date Processed : 23/03/2022 19:00:04  
Sample Type : Unknown  
Acquired by : System Administrator  
Processed by : System Administrator

## <Chromatogram>

mV



## <Peak Table>

Detector A 280nm

Peak#	Ret. Time	Area	Height	Area%	Area/Height	Width at 5% Height
1	10.444	693776	68194	100.000	10.174	0.362
Total		693776	68194	100.000		

Figure 150. HPLC analysis report for OMePh-DMAC-TRZ.

## School of Chemistry Mass Spectrometry Service

SampleID  
Sample Description  
Analysis Name  
Method  
Instrument

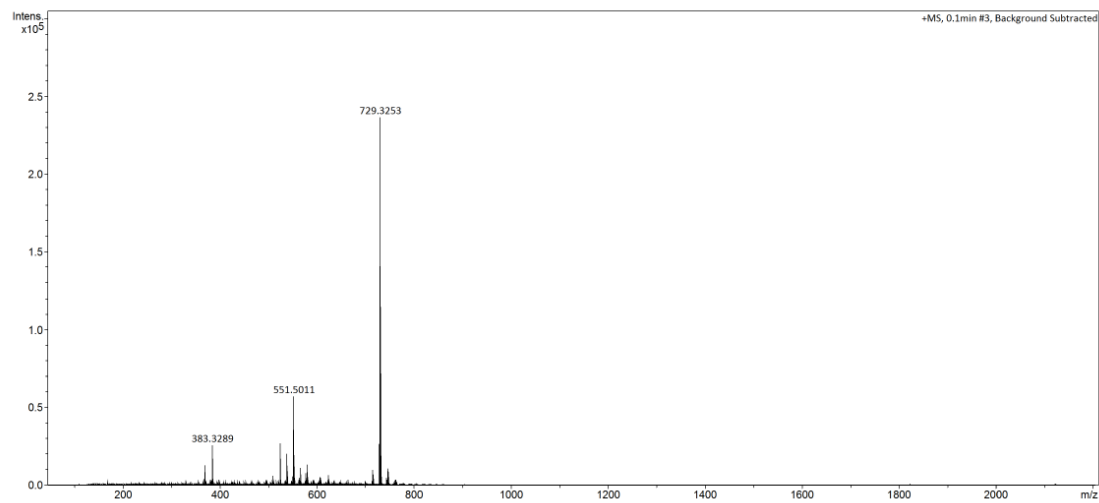
D:\Data\stuartwarriner\manual\EC\_4043\_a.d  
DIP Pos 3.m  
maXis impact

Source Type APCI Ion Polarity Positive

## Submitter

Supervisor  
Acquisition Date  
Scan Begin  
Scan End

18/05/2022 14:32:15  
50 m/z  
2200 m/z



Bruker Compass DataAnalysis 4.3

Analysis Name

EC\_4043\_a.d

18/05/2022 14:38:57

1 of 1

Figure 151. HRMS analysis report for OMePh-DMAC-TRZ.



## Elemental Analysis Service Request Form

Researcher name Ettore Crovini

Researcher email ec254@st-andrews.ac.uk

NOTE: Please submit ca. 10 mg of sample

Sample reference number	EC-4043
Name of Compound	dOMePh-DMAC-TRZ
Molecular formula	C <sub>50</sub> H <sub>40</sub> N <sub>4</sub> O <sub>2</sub>
Stability	Air stable
Hazards	None
Other Remarks	None

Analysis type: Elemental Analysis

Single  Duplicate  Triplicate

Analysis Result:

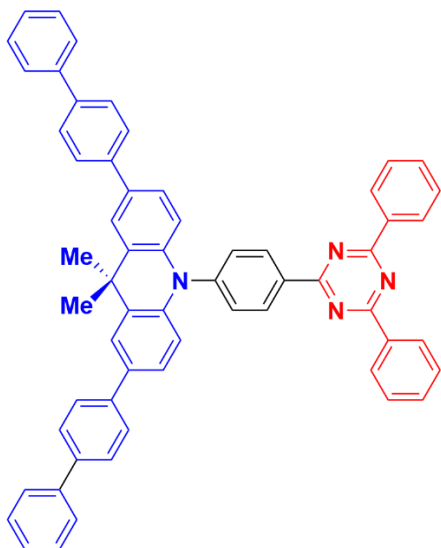
Element	Expected %	Found (1)	Found (2)	Found (3)
Carbon	82.39	82.71	82.46	
Hydrogen	5.53	5.57	5.57	
Nitrogen	7.69	7.62	7.61	
Oxygen	4.39			

Authorising Signature:

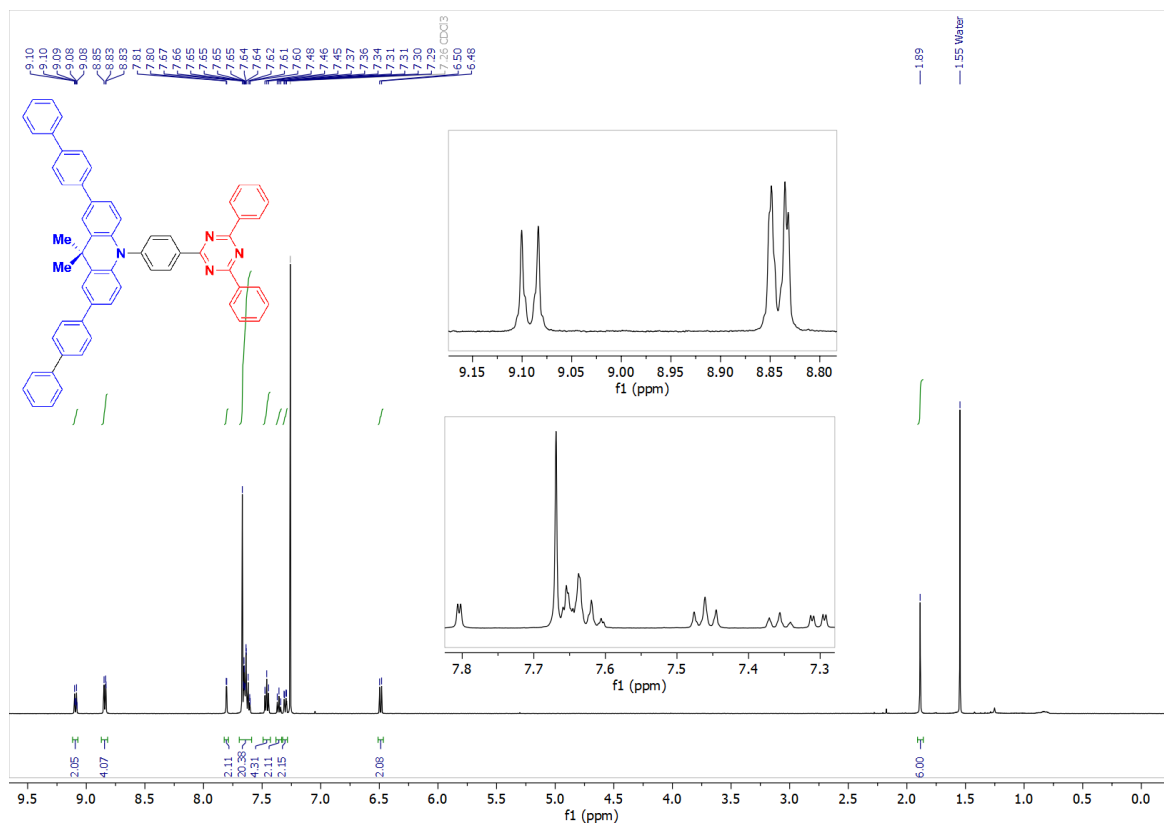
Date completed	29.04.22
Signature	J - P L
comments	

Figure 152. EA analysis report for OMePh-DMAC-TRZ.

**2,7-di([1,1'-biphenyl]-4-yl)-10-(4-(4,6-diphenyl-1,3,5-triazin-2-yl)phenyl)-9,9-dimethyl-9,10-dihydroacridine (dPh-DMAC-TRZ)**



The same reaction procedure as **'BuPh-DMAC-TRZ** was followed, but with a different boronic acid, [1,1'-biphenyl]-4-ylboronic acid (1.174 g, 5.931 mmol, 4 equiv.). After 72h, the reaction was diluted with THF and filtered over celite to remove any unreacted palladium. The solution was diluted with water, and the organic layer was extracted with DCM (3 × 50 mL). The organic phase was washed with brine, dried over MgSO<sub>4</sub> and concentrated under reduced pressure. The target product was isolated as yellow solid after purification by column chromatography on silica gel using 5:1 hexane/EtOAc as eluent. It was then further purified *via* recrystallization in THF/MeOH. (0.650 g). The compound was furtherly purified by gradient temperature sublimation. **Yield:** 53%; **Mp:** 330-335 °C ; **R<sub>f</sub>:** 0.67 (ethyl acetate/cyclohexane = 1:4); **<sup>1</sup>H NMR** (500 MHz, CDCl<sub>3</sub>) δ: 9.10-9.08 (dt, *J*= 8.4, 2.1, 1.4, 2H), 8.85-8.83 (dt, *J*= 6.7, 1.6, 1.0, 2H), 7.81-7.80 (d, *J*= 2.1, 4H), 7.67-7.70 (m, 20H), 7.48 – 7.45 (t, *J*= 7.7, 7.7, 4H), 7.37-7.34 (t, *J*= 7.4, 7.4, 2H), 7.31-7.29 (dd, *J*= 8.6, 2.1, 2H), 6.50-6.48 (d, *J*= 8.6, 2H), 1.89 (s, 6H); **<sup>13</sup>C NMR** (126 MHz, CDCl<sub>3</sub>) δ: 172.05, 171.18, 140.97, 140.24, 140.02, 139.57, 136.57, 136.19, 133.51, 132.91, 131.90, 131.65, 130.60, 129.19, 128.95, 128.90, 127.64, 127.36, 127.15, 127.08, 125.36, 124.56, 114.83, 36.57, 32.09; **HPLC retention time:** 10.326; **purity:** 100.00%; **HR-MS** (Xevo G2-XS QToF) [M+H]<sup>+</sup> **Calculated:** (C<sub>60</sub>H<sub>44</sub>N<sub>4</sub>) 820.3600 g mol<sup>-1</sup>, **Found:** 821.3653 g mol<sup>-1</sup>; **EA** (C<sub>60</sub>H<sub>44</sub>N<sub>4</sub>) **Calculated** C: 87.77, H: 5.40, N: 6.82; **Found** C: 87.36, H: 5.41, N: 6.79.



**Figure 153.**  $^1\text{H}$  NMR of dPh-DMAC-TRZ in  $\text{CDCl}_3$ .

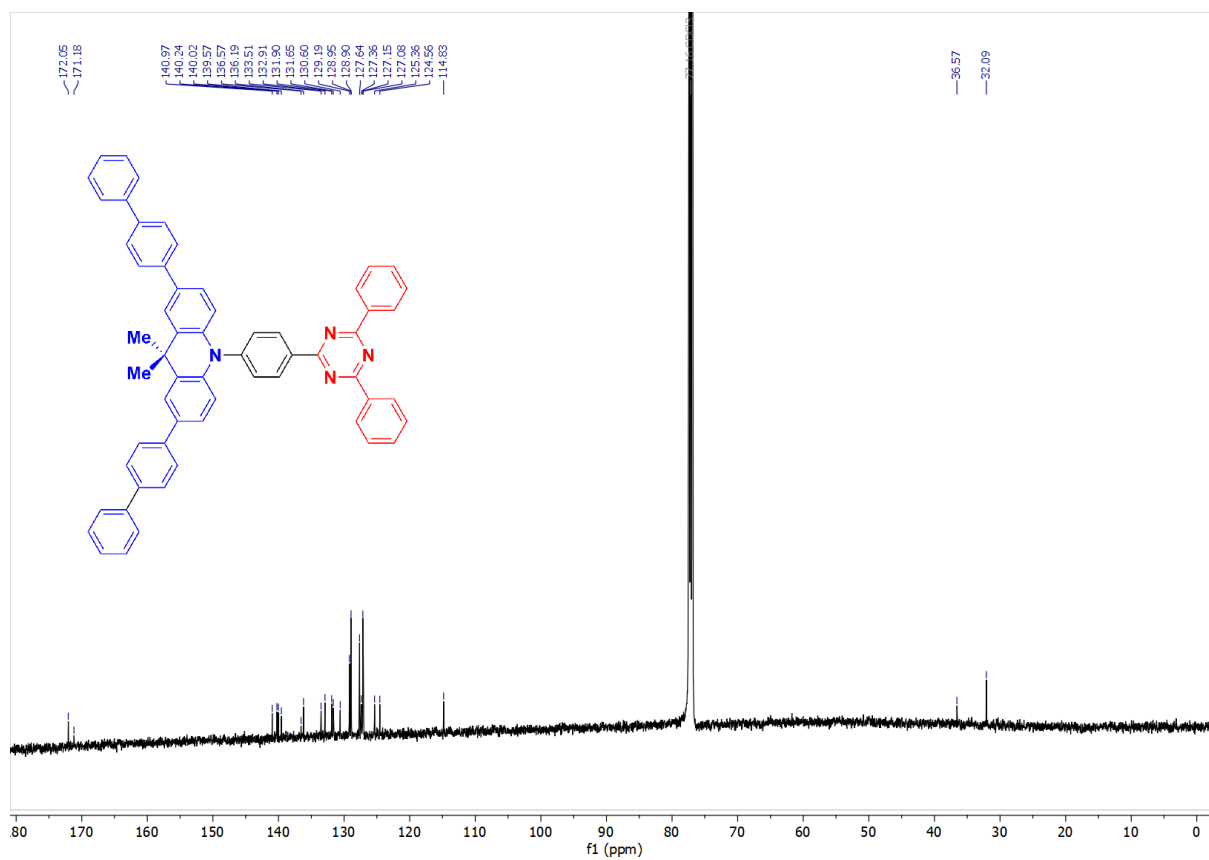


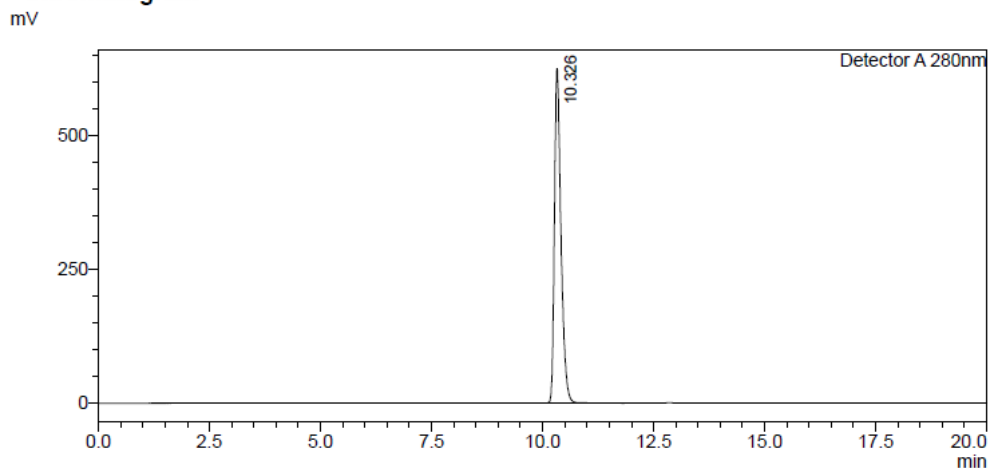
**Figure 154.**  $^{13}\text{C}$  NMR of dPh-DMAC-TRZ in  $\text{CDCl}_3$ .

# HPLC Trace Report06Apr2022

## <Sample Information>

Sample Name : EC-4044-dP-DMAC-TRZ  
Sample ID :  
Method Filename : 100% THF 20 mins 280nm - DH.lcm  
Batch Filename : 06-04-22.lcb  
Vial # : 1-47  
Injection Volume : 10 uL  
Date Acquired : 06/04/2022 11:55:36  
Date Processed : 06/04/2022 12:15:39  
Sample Type : Unknown  
Acquired by : System Administrator  
Processed by : System Administrator

## <Chromatogram>



## <Peak Table>

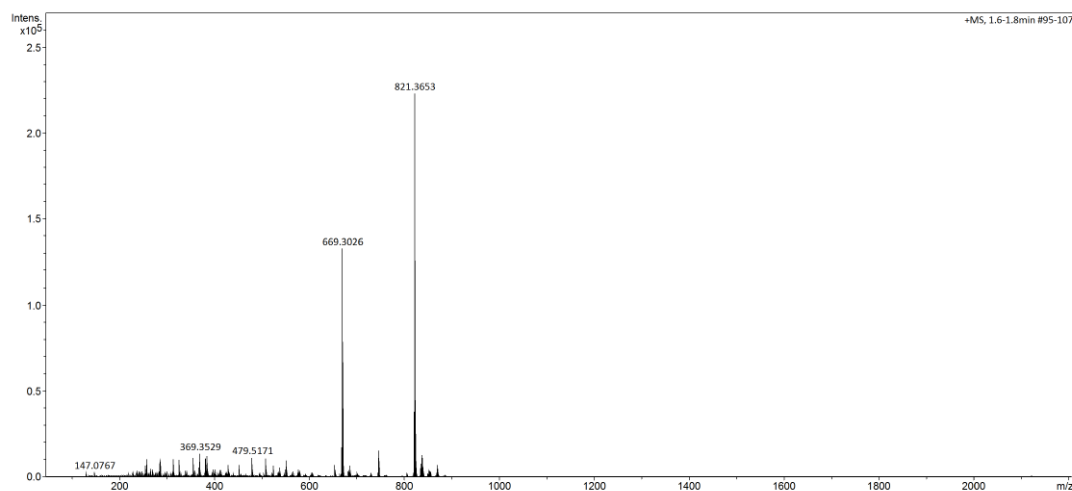
Detector A 280nm

Peak#	Ret. Time	Area	Height	Area%	Area/Height	Width at 5% Height
1	10.326	6401268	622597	100.000	10.282	0.364
Total		6401268	622597	100.000		

Figure 155. HPLC analysis report for dPh-DMAC-TRZ.

## School of Chemistry Mass Spectrometry Service

SampleID  
Sample Description  
Analysis Name D:\Data\stuartwarriner\manual\EC\_4044\_a.d  
Method DIP Pos 3.m  
Instrument maXis impact Source Type APCI Ion Polarity Positive  
Submitter  
Supervisor  
Acquisition Date 18/05/2022 15:08:34  
Scan Begin 50 m/z Scan End 2200 m/z



Bruker Compass DataAnalysis 4.3 Analysis Name EC\_4044\_a.d 18/05/2022 15:13:45 1 of 1

Figure 156. HRMS analysis report for dPh-DMAC-TRZ.

## Elemental Analysis Service Request Form

Researcher name Ettore Crovini

Researcher email ec254@st-andrews.ac.uk

NOTE: Please submit ca. 10 mg of sample

Sample reference number	EC-4044
Name of Compound	dPh-DMAC-TRZ
Molecular formula	C <sub>50</sub> H <sub>44</sub> N <sub>4</sub>
Stability	Air stable
Hazards	None
Other Remarks	None

Analysis type: Elemental analysis

Single  Duplicate  Triplicate

Analysis Result:

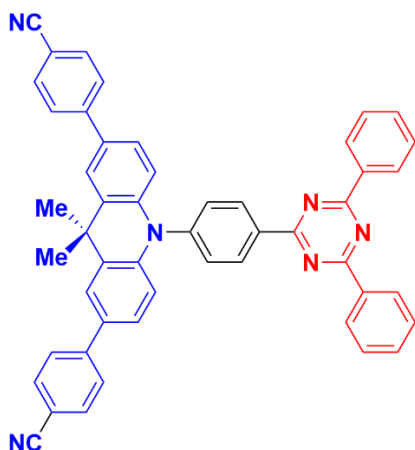
Element	Expected %	Found (1)	Found (2)	Found (3)
Carbon	87.77	87.93	86.79	
Hydrogen	5.40	5.47	5.35	
Nitrogen	6.82	6.84	6.74	

Authorising Signature:

Date completed	29.04.22
Signature	J - P C
comments	

Figure 157. EA analysis report for dPh-DMAC-TRZ.

**4,4'-(10-(4-(4,6-diphenyl-1,3,5-triazin-2-yl)phenyl)-9,9-dimethyl-9,10-dihydroacridine-2,7-diyl)dibenzonitrile (CNPh-DMAC-TRZ)**



The same reaction procedure as **BuPh-DMAC-TRZ** was followed, but with a different boronic acid, (4-cyanophenyl)boronic acid (0.872 g, 5.931 mmol, 4 equiv.). After 72h, the reaction was diluted with THF and filtered over celite to remove any unreacted palladium. The solution was diluted with water, and the organic layer was extracted with DCM (3 × 50 mL). The organic phase was washed with brine, dried over MgSO<sub>4</sub> and concentrated under reduced pressure. The target product was isolated as yellow solid after purification by column chromatography on silica gel using 5:1 hexane/EtOAc as eluent. It was then further purified *via* recrystallization in THF/MeOH. (0.448 g). The compound was furtherly purified by gradient temperature sublimation. **Yield:** 42%; **Mp:** 390-395 °C; **R<sub>f</sub>:** 0.82 (MeOH/DCM = 1:99); **<sup>1</sup>H NMR** (500 MHz, CDCl<sub>3</sub>) δ: 9.10-9.08 (d, *J*= 8.3, 2H), 8.84-8.82 (d, *J*= 7.0, 4H), 7.75 – 7.60 (m, 20H), 6.50-6.48 (d, *J*= 8.6, 2H), 1.85 (s, 6H); **<sup>13</sup>C NMR** (126 MHz, CDCl<sub>3</sub>) δ: 171.98, 170.89, 145.37, 144.31, 140.62, 136.87, 135.96, 132.87, 132.65, 131.97, 131.91, 131.28, 130.61, 129.05, 128.80, 126.96, 125.62, 124.58, 119.19, 115.05, 110.01, 36.42, 31.94; **HPLC retention time:** 10.365; **purity:** 100.00%; **HR-MS** (Xevo G2-XS QTof) [M+H]<sup>+</sup> **Calculated:** (C<sub>60</sub>H<sub>44</sub>N<sub>4</sub>) 718.2800 g mol<sup>-1</sup>, **Found:** 719.2947 g mol<sup>-1</sup>; **EA** (C<sub>50</sub>H<sub>34</sub>N<sub>6</sub>) **Calculated** C: 83.54, H: 4.77, N: 11.69; **Found** C: 82.63, H: 4.78, N: 11.55. The carbon content is not within 0.4% error; however, the remaining characterization is consistent and demonstrates the identity and purity of the compound).

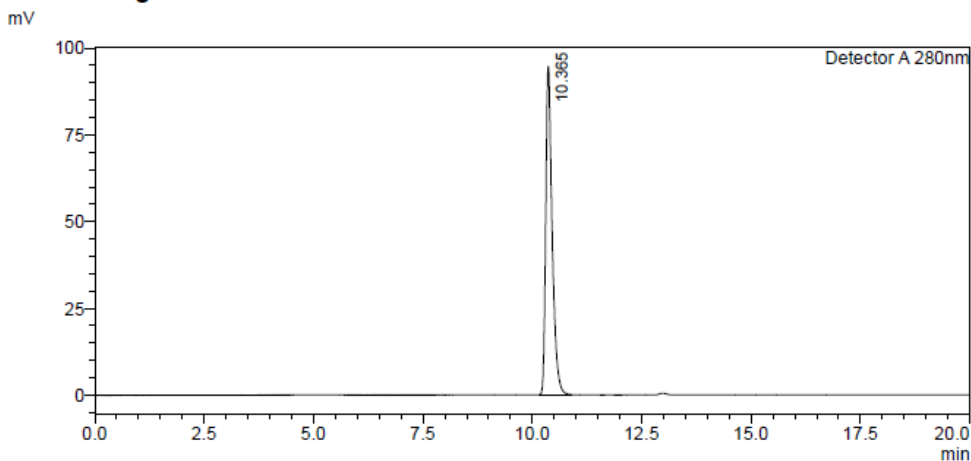


# HPLC Trace Report 31 May 2022

## <Sample Information>

Sample Name : EC-4046-dCNPh-DT  
Sample ID : EC-4046  
Method Filename : 100% THF 20 mins 280nm - DH.lcm  
Batch Filename : EC-4046-dCN.lcb  
Vial # : 1-50  
Injection Volume : 10 uL  
Date Acquired : 31/05/2022 11:12:10  
Date Processed : 31/05/2022 11:32:13  
Sample Type : Unknown  
Acquired by : System Administrator  
Processed by : System Administrator

## <Chromatogram>



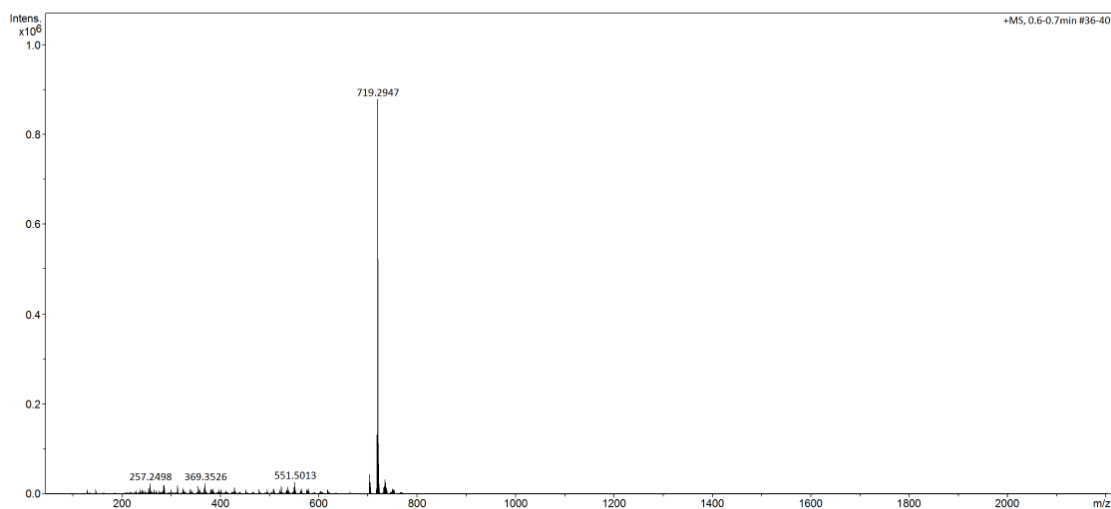
## <Peak Table>

Peak#	Ret. Time	Area	Height	Area%	Area/Height	Width at 5% Height
1	10.365	967160	94466	100.000	10.238	0.370
Total		967160	94466	100.000		

Figure 160. HPLC analysis report for CNPh-DMAC-TRZ.

## School of Chemistry Mass Spectrometry Service

Sample ID  
Sample Description  
Analysis Name  
Method  
Instrument  
D:\Data\stuartwarriner\manual\EC\_4046\_a\_d  
DIP Pos 3.m  
maXis impact  
Source Type  
APCI  
Ion Polarity  
Positive  
Submitter  
Supervisor  
Acquisition Date  
Scan Begin  
Scan End  
18/05/2022 15:17:10  
50 m/z  
2200 m/z



Bruker Compass DataAnalysis 4.3 Analysis Name EC\_4046\_a\_d 18/05/2022 15:20:28 1 of 1

Figure 161. HRMS analysis report for CNPh-DMAC-TRZ.



## Elemental Analysis Service Request Form

Researcher name Ettore Crovini

Researcher email ec254@st-andrews.ac.uk

NOTE: Please submit ca. 10 mg of sample

Sample reference number	EC-4046
Name of Compound	dCNPh-DMAC-TRZ
Molecular formula	C <sub>50</sub> H <sub>34</sub> N <sub>6</sub>
Stability	Air stable
Hazards	None
Other Remarks	None

Analysis type: Elemental Analysis

Single  Duplicate  Triplicate

Analysis Result:

Element	Expected %	Found (1)	Found (2)	Found (3)
Carbon	83.54	82.44	82.63	
Hydrogen	4.77	4.68	4.78	
Nitrogen	11.69	11.51	11.55	

Authorising Signature:


Date completed	23.05.22
Signature	
comments	

Figure 162. EA analysis report for CNPh-DMAC-TRZ.

IND.

12¢

THE INCREDIBLE

# TADF

APPROVED  
BY THE  
COMICS  
CODE  
AUTHORITY

M  
C

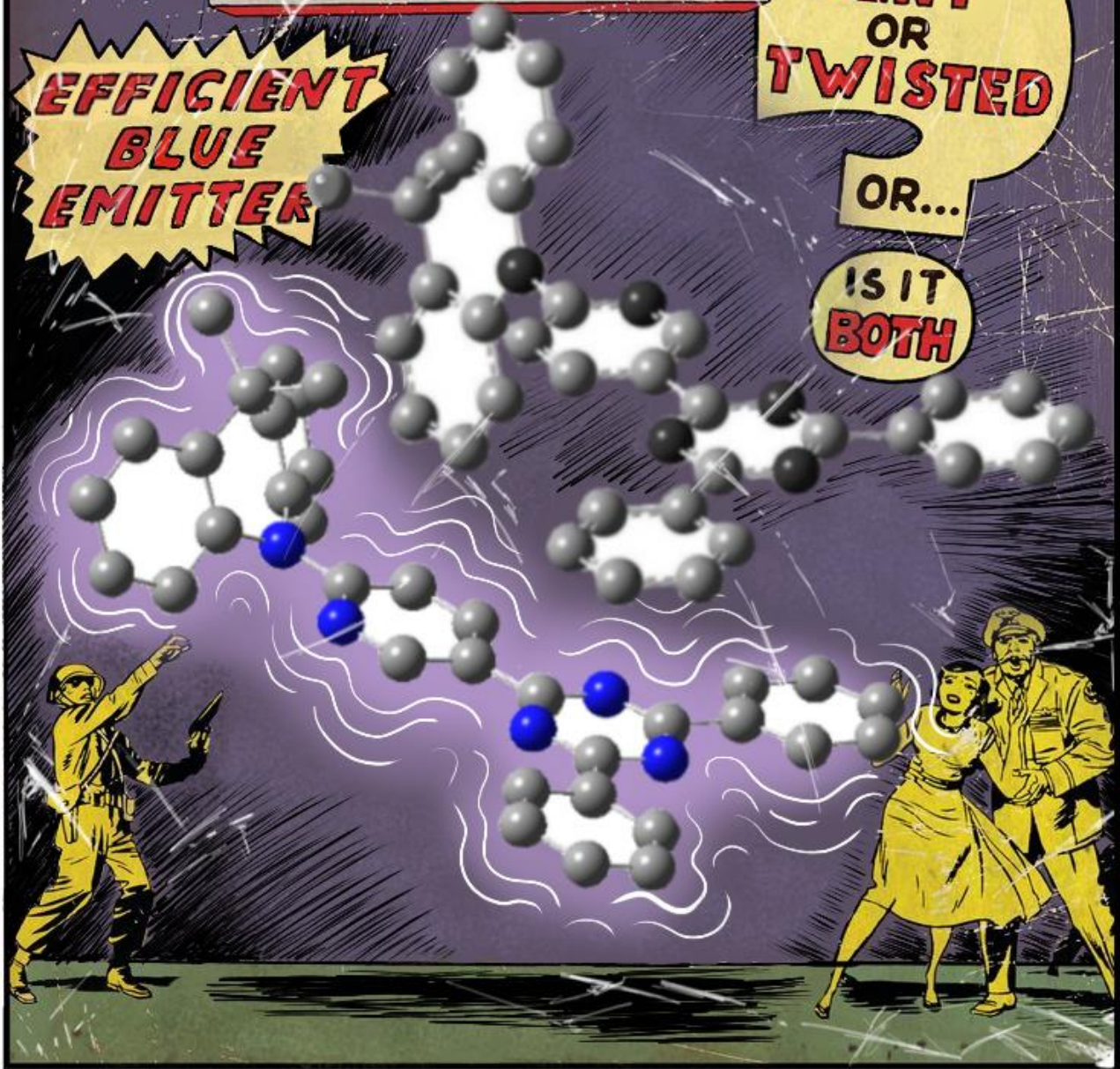
**DIHEDRAL ANGLE  
EFFECT !!**

**EFFICIENT  
BLUE  
EMITTER**

**IS IT  
BENT  
OR  
TWISTED**

**OR...**

**IS IT  
BOTH**



## Chapter 6 - The effect of an heteroaromatic bridge and the role of dihedral angle in a novel and efficient TADF emitter

### 6.1 - Attributions

I am the main author of this text. Unless otherwise stated in the text, I directly carried out the experimental work presented. The emitter presented in this chapter was originally designed and synthesised by Dr. Dianming Sun. I then remade the material on a larger scale, carried out the initial theoretical calculations and optoelectronics characterization (CV-DPV, UV-vis, solvatochromism study, and solution and solid state steady-state and time-resolved photoluminescence measurements). An in-depth computational study and some additional measurements were conducted by Dr. Rama Dhali in the group of Prof. Anna Painelli, from the University of Parma. The paper highlighting this work is currently under revision, and available at *ChemRxiv*, 2022, DOI: [10.26434/chemrxiv-2022-z8sl1](https://doi.org/10.26434/chemrxiv-2022-z8sl1).

### 6.2 - Introduction

While the extension of the DMAC donor, presented in the previous chapter, led to the fabrication of high performing devices, it also red-shifted the emission of the parent emitter, **DMAC-TRZ**. The fabrication of deep-blue emitters with good color purity is of high interest for the industry, as the currently used technologies employ TTA materials where the devices are limited to a maximum theoretical IQE of 62.5%.<sup>45,46</sup>

One of the strategies employed in the literature to achieve blue emission and good color purity is the use of heteroaromatic spacers. Rajamalli *et al.*,<sup>59</sup> and Dos Santos *et al.*,<sup>60</sup> (already discussed in **Chapter 1 - Paragraph 1.6.6 - Design of TADF emitters**) showed that the introduction of a heteroaromatic bridge in sulfone-based D-A TADF emitters can prevent structural relaxation, enhance  $\Phi_{\text{PL}}$ , improve the color purity due to a narrower emission, and improve the efficiency of the devices (**Figure 19, Figure 163**). The materials published by Rajamalli *et al.*,<sup>59</sup> **pDTCz-2DPyS**, and **pDTCz-3DPyS**, both have  $\Phi_{\text{PL}}$  of ca. 60%. The OLEDs, show blue emission, and  $\text{EQE}_{\text{max}}$  of c.a. 12-13% at  $\lambda_{\text{EL}}$  of 466 nm and 452 nm for the devices with **pDTCz-2DPyS**, and **pDTCz-3DpyS** respectively. This represents a massive improvement over the parent device with **pDTCz-DPS**, which presented  $\text{EQE}_{\text{max}}$  of 4.7%. The materials studied by Dos Santos *et al.*,<sup>60</sup> **pDTCz-DPzS** and **pDTCz-**

**DPmS**, showed that the addition of a second nitrogen atom on the bridge, enhanced the  $\text{EQE}_{\text{max}}$  to 18% and 14%, at  $\lambda_{\text{EL}}$  of 522 nm and 461 nm for the devices with **pDTCz-DPzS**, and **pDTCz-DPmS**, respectively.

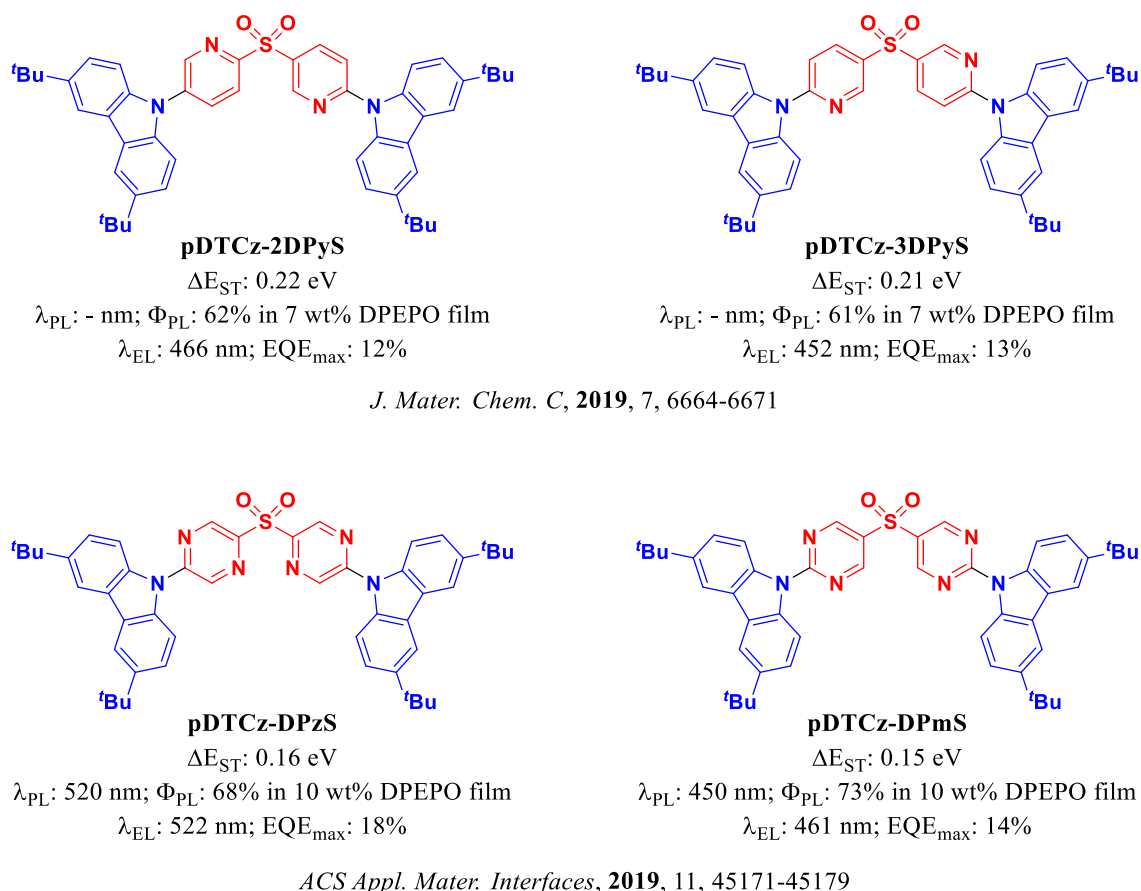
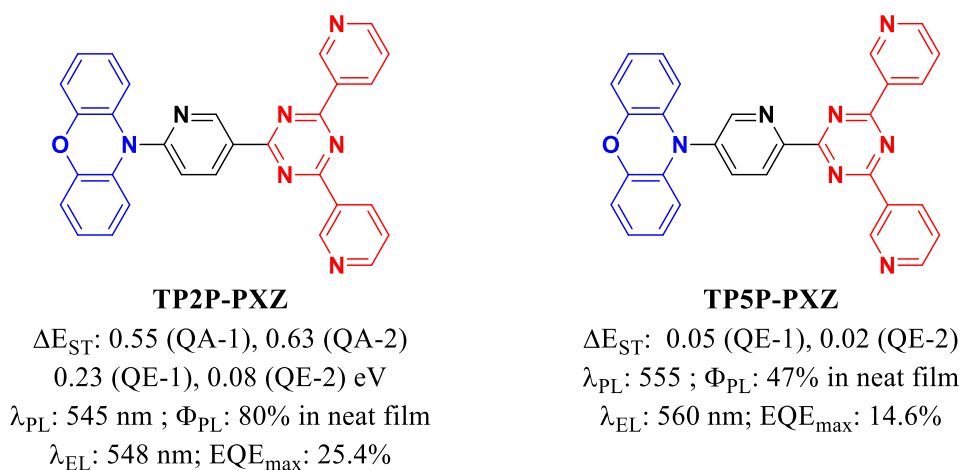


**Figure 163.** Molecular structure and properties of the **pDTCz** series of emitters.<sup>60,133</sup>

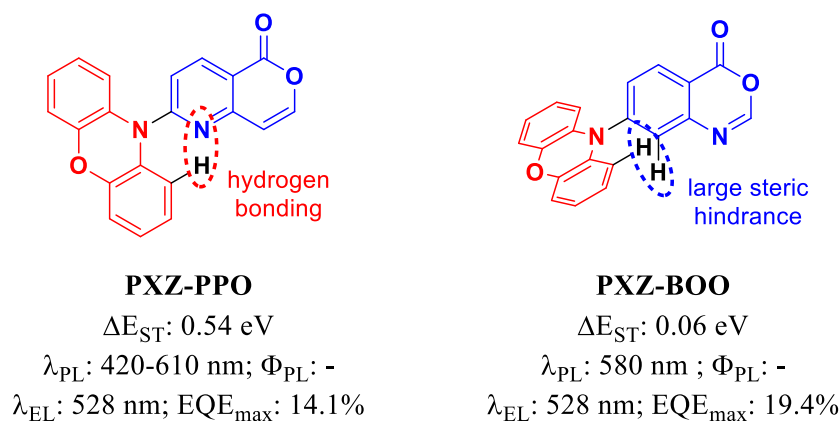
Another two emitters with a heteroaromatic ring as a spacer were documented by Shi *et al.* with TRZ derivative compounds **TP2P-PXZ** and **TP5P-PXZ** (**Figure 164**).<sup>182</sup> This led to a secondary effect, the phenoxazine and a central pyridine bridge formed an intramolecular hydrogen bond in **TP2P-PXZ**, while in the control compound **TP5P-PXZ** this interaction does not exist, due to the greater distance between the hydrogen atom of the phenoxazine and the nitrogen atom of the spacer. The intramolecular hydrogen bonding led **TP2P-PXZ** to exist as two different conformers, defined as quasi-equatorial (QE) and quasi-axial (QA) which created a self-doped system, where the QA conformer behaves as a host material. This system led to the fabrication of an efficient OLED with an  $\text{EQE}_{\text{max}}$  of 25.4% at  $\lambda_{\text{EL}}$  of 548 nm, while **TP5P-PXZ**'s device was less performing, with an  $\text{EQE}_{\text{max}}$  of 14.6% at a slightly red-shifted  $\lambda_{\text{EL}}$  of 560 nm.



*Angew. Chem. Int. Ed.*, **2021**, 133, 26082-26087

**Figure 164.** Molecular structure and properties of **TP2P-PXZ** and **TP5P-PXZ** (QA: *quasi*-axial, QE: *quasi* equatorial).<sup>182</sup>

Chen *et al.* also studied the effect of intramolecular H-bonding on the photophysical properties of TADF emitters, with the two phenoxazine based-emitters **PXZ-PPO** and **PXZ-BOO** (**Figure 165**).<sup>183</sup> The closer proximity of the nitrogen to the phenoxazine in **PXZ-PPO** led to the existence of the emitter as a mixture of two conformers in THF solution. The two conformations are a more planar structure, with N-H interaction, and a twisted structure, with no N-H interaction. The planar conformation does not have any TADF and emits deep blue light (420 nm). TADF is turned on by the more twisted conformation and emits green light (610 nm) with a very short delayed fluorescence lifetime of 170 ns. In the crystalline phase, the planar conformer dominates the photophysics, while in solution the twisted conformer is the main contributor, giving rise to TADF emission. **PXZ-PPO**'s device presented an  $EQE_{max}$  of 14.1% at  $\lambda_{EL}$  of 528 nm, which is slightly inferior to the **PXZ-BOO**'s device, which has an  $EQE_{max}$  of 19.4% at  $\lambda_{EL}$  of 528 nm.



*J. Mater. Chem. C.*, **2020**, 8, 13263-13269

**Figure 165.** Molecular structure and properties of **PXZ-PPO** and **PXZ-BOO**.<sup>183</sup>

These examples show that modification of the aromatic bridge in a TADF emitter can lead to significant changes in the molecular geometry, with the co-existence of different conformers that show distinctive photophysics. In this work, the emitter **DMAC-py-TRZ** is introduced, where the phenylene bridge in **DMAC-TRZ**<sup>72</sup> is replaced by a 2-pyridyl bridge. The novel emitter has good photophysical properties both in solution and in matrices. Its crystal structure documents a small dihedral angle between the DMAC and pyridyl bridge of 19.7° and a V-shaped or folded structure of the DMAC donor, with an associated bending angle of 45°. This behavior is in line with what was observed by Shi *et al.*<sup>182</sup>. An in-depth computational study and an extensive optoelectronic and photophysical characterization then followed, showcasing the impact that conformational changes in the excited state have on the photophysics of the compound.

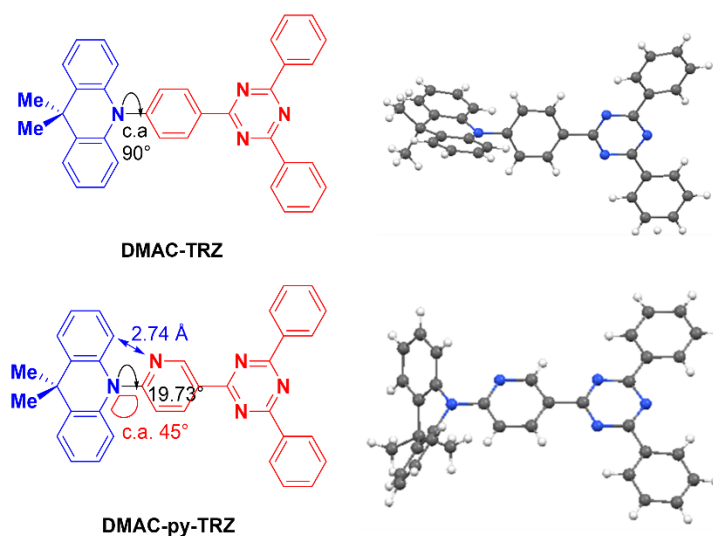


**Figure 166.** Crystal and molecular structures of **DMAC-TRZ** and **DMAC-py-TRZ**.

## 6.3 – Results and discussion

### 6.3.1 - Synthesis and crystal structure

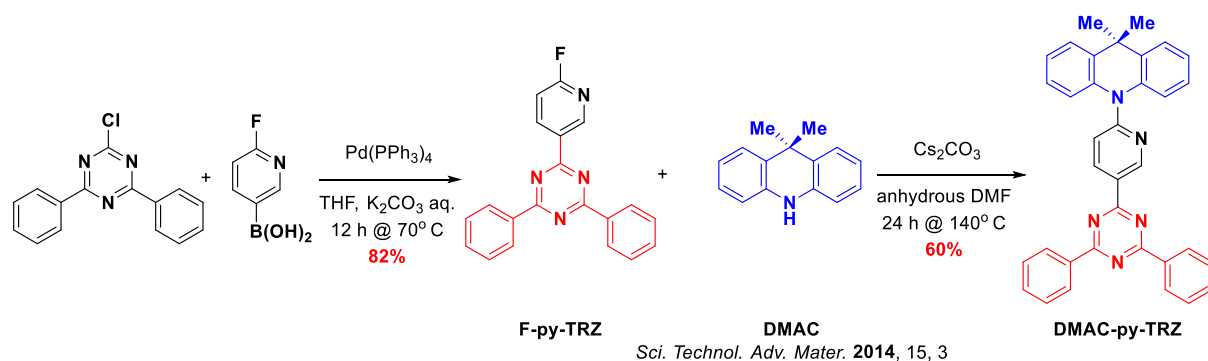


**Figure 167.** Synthetic procedure for **DMAC-py-TRZ**.

**F-py-TRZ** was synthesized via a Suzuki coupling between 2-chloro-4,6-diphenyl-1,3,5-triazine and (6-fluoropyridin-3-yl)boronic acid, with tetrakis(triphenylphosphine)palladium(0) as the catalyst, in a mixture of THF and 2M aqueous solution of  $K_3PO_4$ . The reaction was carried out for 12 hours at 70 °C to obtain the desired product with 82% yield. The modified triazine was then coupled to DMAC via a nucleophilic aromatic substitution with cesium carbonate, in anhydrous DMF, at 140 °C for 24 h, to achieve the final emitter, **DMAC-py-TRZ** with 60% yield.

The crystal structure of the material was obtained, which confirmed the structure of the molecule (**Figure 166**). Single crystals were grown by adding cold methanol to a supersaturated solution of **DMAC-py-TRZ** in boiling THF. While the structure matched the desired product, it showed an unusual geometry, with an almost planar dihedral angle between the donor and the acceptor, and with the donor folded by c.a. 45°, compared to the triazine acceptor. This is a huge difference from the orthogonal conformation of **DMAC-TRZ** (**Figure 166** *Errore. L'origine riferimento non è stata trovata.*), and an in-depth computational characterization was carried out to understand the effect of this different conformer on the properties of the material.

### 6.3.2 - Theoretical calculations

The initial theoretical study was carried out by me using the same DFT methodologies employed in the previously discussed chapters. This was followed by an in depth rotational study and excited state geometry optimization study, carried out by Dr. Rama Dhali in the group of Prof. Anna Painelli, from the University of Parma (**Chapter 6 – Paragraph 6.1 – Attributions**). For the latter study, **DMAC-TRZ** and **DMAC-py-TRZ** were studied in the gas phase using the M062X/6-31G(d) level of theory.<sup>104–106</sup> The new functional was chosen because, while more computationally demanding, it was shown to give more accurate results on **DMAC-TRZ**.<sup>171</sup> In the following analysis, the word “orthogonal” will define the structure with a dihedral angle of c.a. 90° (between the DMAC and the bridge) and the word “folded” the structure with the small dihedral angle and DMAC moiety folded in a V-shaped fashion.

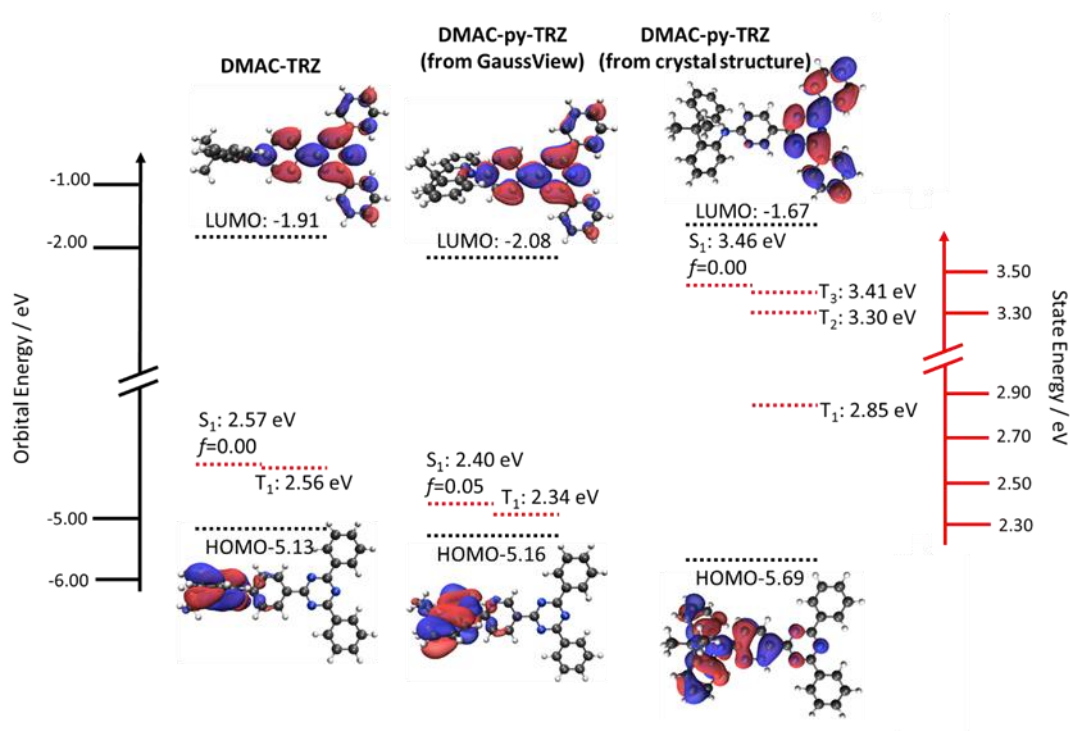


**Figure 168.** HOMO and LUMO electron density distributions and energy levels, excited state energy levels of **DMAC-TRZ** and **DMAC-py-TRZ** (Obtained via DFT and TD-DFT at the PBE0/6-31G(d,p) level, Isovalue for new surfaces: MO=0.02, Density=0.0004).

As it was reported in **Chapter 5 - Paragraph 5.3.2 - Theoretical calculations**, in the ground-state geometry of **DMAC-TRZ** the DMAC and TRZ moieties are orthogonal, in line with what is observed in its crystal structure.<sup>171</sup> In this orthogonal geometry, the HOMO and LUMO have almost no overlap,



which leads to an almost null  $\Delta E_{ST}$  of 0.01 eV. Moreover, the  $S_1$  and  $T_1$  states both have a pure charge transfer (CT) character and this same nature implies a poor SOC, due to El Sayed's rule<sup>184</sup>, leading to a poor RISC process from  $T_1$  to  $S_1$ . When the initial geometry was built in the software GaussView, **DMAC-py-TRZ**'s optimized structure assumes the orthogonal. The LUMO level was stabilized at -2.08 eV, due to the electron-withdrawing nature of the pyridine ring, which strengthens the acceptor, and a slightly stabilized HOMO level, at -5.16, due to a mild weakening of the donor. The excited states are stabilized to lower energies, at 2.40 eV and 2.34 eV for  $S_1$  and  $T_1$  respectively, showing an increased  $\Delta E_{ST}$  of 0.06 eV and a higher  $f$  of 0.05, when compared to the parent emitter. The optimization carried out starting from the crystal structure led to the folded conformer. In this geometry, the pyridine seems to have a much larger effect on the donor strength, evidenced by the decrease in energy of the HOMO (-5.69 eV vs -5.13 eV for **DMAC-TRZ**). The acceptor is also weakened leading to the higher LUMO level (-1.67 eV vs -1.91 eV for **DMAC-TRZ**). The excited states obtained from the crystal structure are destabilized to higher energies, and the  $\Delta E_{ST}$  is calculated to be 0.62 eV, and thus too large for the molecule to show TADF.

A rigid scan of the dihedral angle of **DMAC-TRZ** (**Figure 169**)<sup>171</sup> then followed, carried out by Dr. Rama Dhali in the group of Prof. Anna Painelli, from the University of Parma (**Chapter 6 – Paragraph 6.1 – Attributions**). This rigid scan was carried out by calculating the ground and excited state energies of each conformer, starting from the optimized ground-state geometry, and then adding rotation ( $+5^\circ$ ) of the D unit around the bond with the phenylene bridge, without allowing for any additional molecular relaxation. By then plotting the resulting  $S_0$ ,  $S_1$ ,  $T_2$  and  $T_3$  potential energy surfaces (PES) it can be seen that all states show a flat minimum for the orthogonal geometry, except  $T_1$  which shows a double minimum around  $(90\pm 30)^\circ$  dihedral angle.<sup>19</sup>

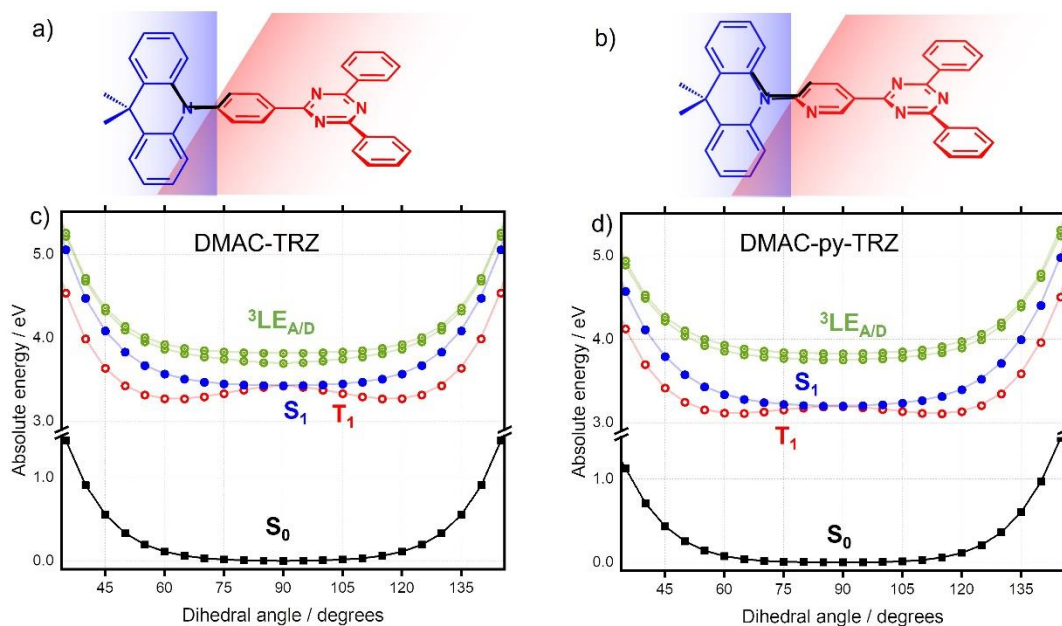


**Figure 169.** Sketch of a) **DMAC-TRZ** and b) **DMAC-py-TRZ** showing four adjacent atoms to define the dihedral angle of the dihedral rigid scan of interest. Energies of ground (black), lowest energy singlet (blue), lowest energy triplet (red) and two higher energy triplet (green) states.

The same rigid dihedral angle scan was repeated on **DMAC-py-TRZ** to better understand the structural differences with **DMAC-TRZ**. Starting from a similar orthogonal conformation to that of **DMAC-TRZ** (**Figure 169d**), the rigid scan leads to a comparable excited states energies profiles for the two compounds. The EWG strength of the acceptor is increased by the presence of the pyridine bridge, leading to a stabilized LUMO and a smaller HOMO-LUMO gap for **DMAC-py-TRZ** ( $E_{\text{gap}} = 4.78$  eV for the orthogonal structure) vs **DMAC-TRZ** ( $E_{\text{gap}} = 4.99$  eV). The  $S_1$  and  $T_1$  states are also stabilized to lower energies in **DMAC-py-TRZ** (**Figure 169** Errore. L'origine riferimento non è stata trovata. **c-d**). The rigid energy scan points to a massive increase in the ground-state energy the more the dihedral angle deviates from orthogonality, making non-orthogonal conformations not accessible.

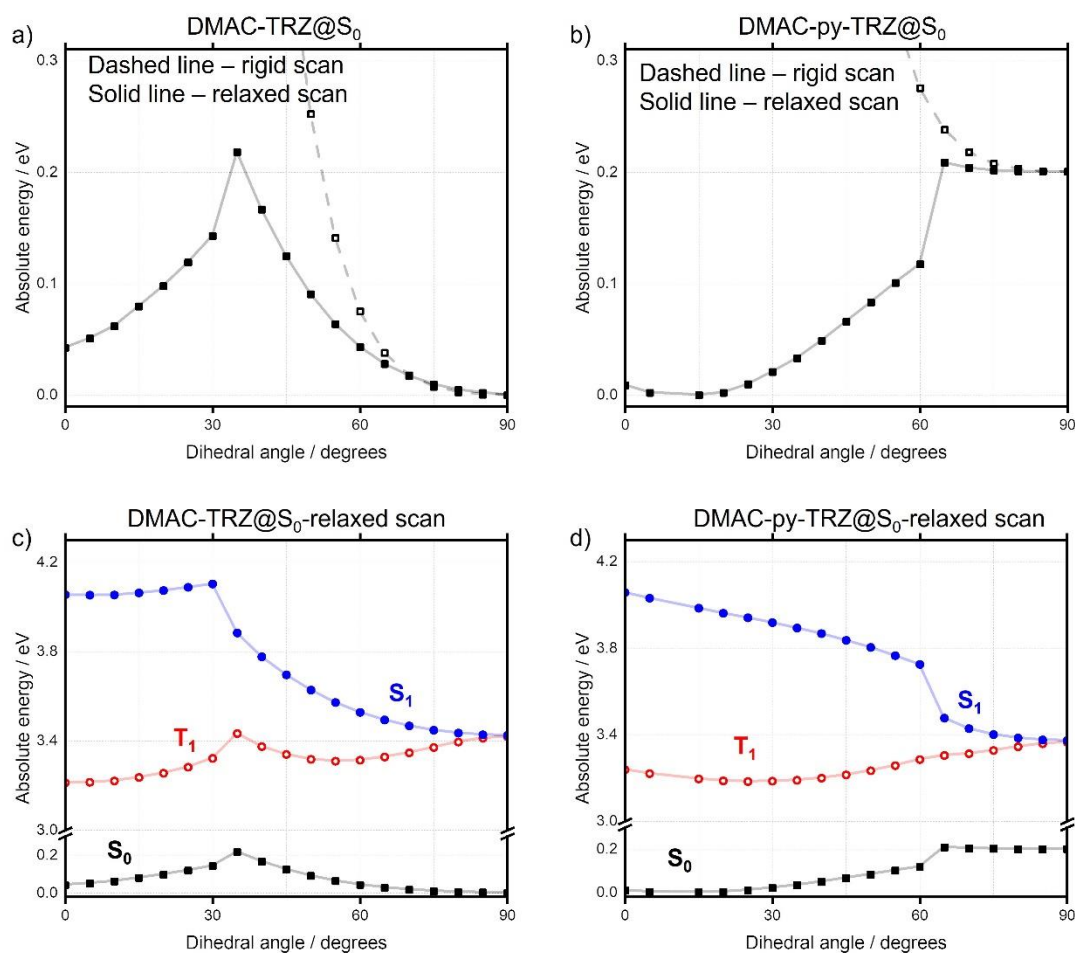


**Figure 170.** a) and b) compare the ground state ( $S_0$ ) energy calculated as a function of the dihedral angle in a rigid (dashed lines) and relaxed scan (continuous lines) for **DMAC-TRZ** and **DMAC-py-TRZ**, respectively; c) and d) show the energies of the  $S_0$ ,  $S_1$  and  $T_1$  energies as a function of dihedral angle between DMAC calculated at the relaxed  $S_0$  geometry for **DMAC-TRZ** and **DMAC-py-TRZ**, respectively.

To try and understand the folded conformer origin, a relaxed scan of the dihedral angle was then performed (**Figure 170a-b**). This means that the initial structure input in the calculation was allowed geometrical relaxation. Both emitters show two energy minima, corresponding to the orthogonal and folded structures. For **DMAC-TRZ**, the two conformers present similar energies with a difference of only 0.04 eV, slightly larger than the thermal energy at room temperature (0.038 eV or 0.885 kcal/mol). However, the energy barrier for the interconversion between the two conformers is 0.22 eV (21.2 kcal/mol), which is much larger than the thermal energy at r.t., leading us to believe only the orthogonal geometry (the lowest energy one) to be significantly populated at room temperature. The situation is significantly different for **DMAC-py-TRZ**. The folded conformer (this time at a

dihedral angle of c.a.  $10^\circ$ ) is much lower in energy than the orthogonal conformer, by 0.20 eV which is also equal to the energy barrier for the interconversion between the two conformers (19.3 kcal/mol). This means that at room temperature only the folded conformer would be populated.

Let's now compare the results from the rigid and relaxed scans (**Figure 170c-d**). **DMAC-TRZ** rigid and relaxed scans led to consistent results, where the  $S_1$  state maintained the same orthogonal conformation as the ground state, while the  $T_1$  state underwent geometrical relaxation and reached a twisted structure (dihedral angle of c.a.  $60^\circ$ ). The following optimization of the  $S_1$  and  $T_1$  excited states confirms this result,<sup>171</sup> and it shows that in the orthogonal geometry, the  $S_1$  state possesses CT character and almost null oscillator strength. Different results were obtained from the rigid and relaxed scans of **DMAC-py-TRZ**. From the relaxed scan, in the folded geometry (the energy minimum, **Figure 170b**), the  $S_1$  state energy amounts to 4.1 eV and the  $\Delta E_{ST}$  is 0.78 eV, which is far too large to achieve TADF emission. The much more significant orbital overlap in the  $S_0 \rightarrow S_1$  transition makes for a large oscillator strength ( $f = 1.27$ ) (**Figure 171c**). However, while the folded geometry was the only accessible conformation for the  $S_0$  state, it is not the equilibrium geometry for the  $S_1$  state and a huge structural deformation from the folded to the orthogonal structure was expected, when going from  $S_0$  to  $S_1$ . In conclusion, **DMAC-py-TRZ** absorption should occur from the folded geometry as this dominates in the ground state, with a high energy transition due to the large oscillator strength. The fluorescence, however, would occur from the orthogonal structure at a much lower energy (3.17 eV), with negligible oscillator strength (as per the non-overlapping orbitals, **Figure 172**). Moreover, the excitation and thus eventual change from folded to orthogonal geometry should lower the  $\Delta E_{ST}$  to only 8.2 meV, making TADF possible.

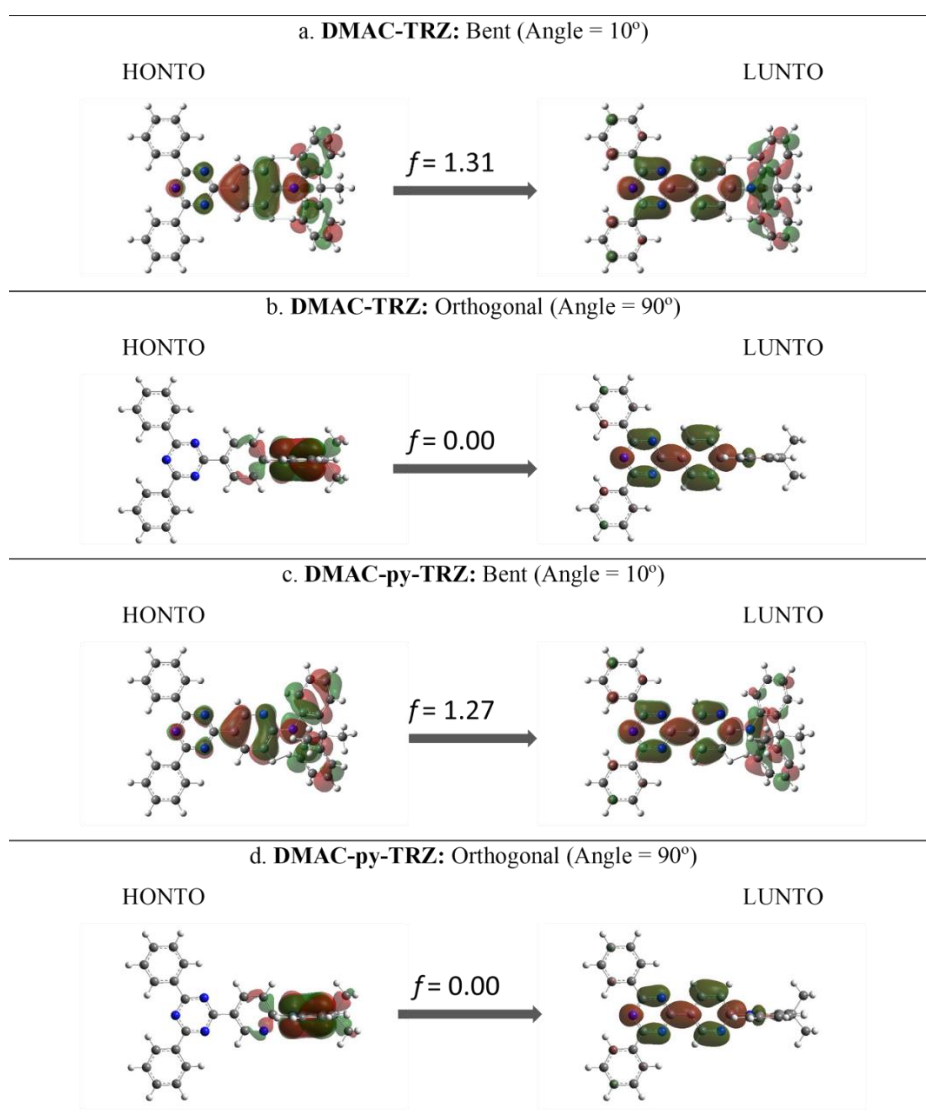


**Figure 171.** Natural transition orbitals of **DMAC-TRZ** for both **a)** folded **b)** orthogonal geometries and **DMAC-py-TRZ** for both **c)** folded **d)** orthogonal geometries shown.

The full optimization of the excited state geometry that followed further proved the  $S_1$  behavior. Starting from either the folded or the orthogonal geometry, the excited state optimization showed the geometry of the  $S_1$  always converging to the orthogonal conformation. The situation is less clear for the  $T_1$  state. Both the rigid and relaxed scans for **DMAC-py-TRZ**, predict that the  $T_1$  state will exist in a twisted conformation (**Figure 169d**). However, the full optimization of the excited state geometry of  $T_1$ , shows that two different structures are reached depending on the starting geometry. Two slightly different  $\Delta E_{S_1-T_1}$  values are obtained for the two geometries (0.93 eV for the one with dihedral angle of c.a. 30° and 0.41 eV for the one with dihedral angle of c.a. 60°), and the energies

of the two triplet conformations is similar with a difference of only  $\Delta E_{T_{160^\circ-30^\circ}} = 0.07$  eV. A firm conclusion about the equilibrium geometry for  $T_1$  cannot be reached.

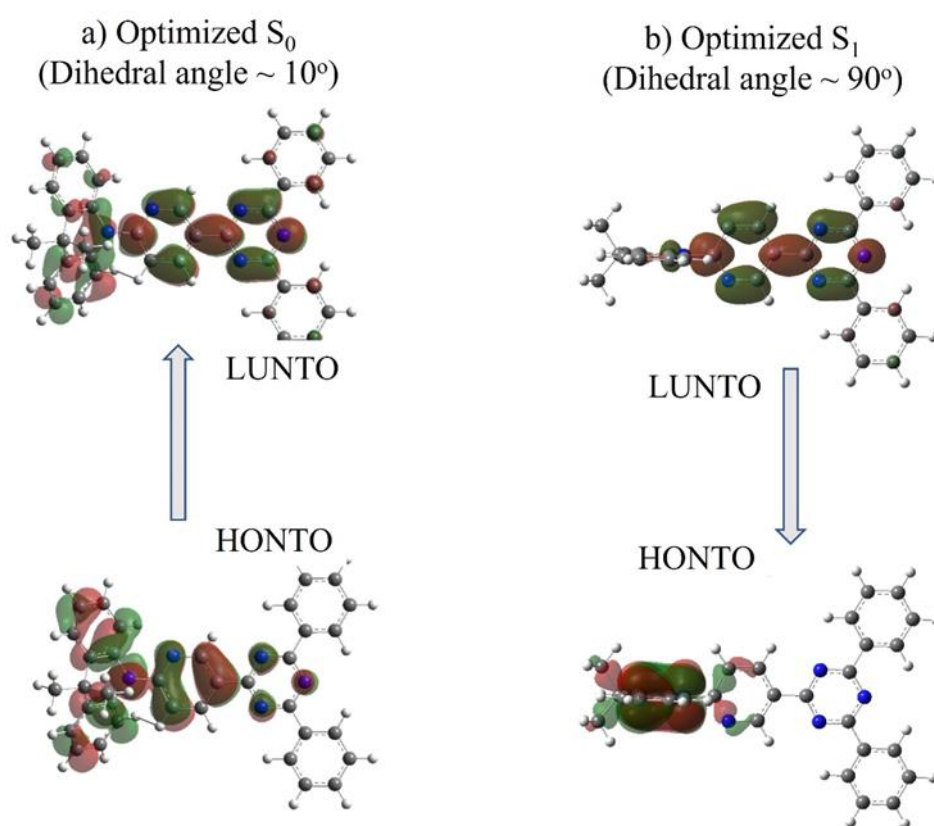


**Figure 172.** NTOs of DMAC-py-TRZ calculated for the  $S_0$ - $S_1$  transition **a)** at the  $S_0$ -optimized geometry, which is relevant to the absorption process; **b)** at the  $S_1$ -optimized geometry, which is relevant to the emission process.

### 6.3.3 - Optoelectronic characterization

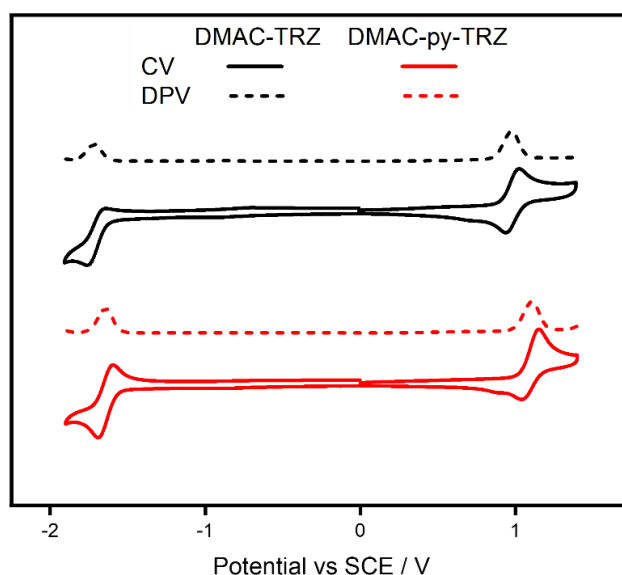


**Figure 173.** Cyclic voltammetry (CV) and differential pulse voltammetry (DPV) of **DMAC-TRZ** and **DMAC-py-TRZ** in DCM (scan rate = 100 mV/s).

Cyclic voltammetry and differential pulse voltammetry of **DMAC-py-TRZ** and **DMAC-TRZ** were measured in degassed DCM with tetra-*n*-butylammonium hexafluorophosphate as the electrolyte and Fc/Fc<sup>+</sup> as the internal reference (**Figure 173**). Both materials show *quasi* reversible reduction and oxidation waves. **DMAC-py-TRZ**'s oxidation and reduction waves ( $E_{\text{ox}}/E_{\text{red}} = 1.11 / -1.64$  V) happen at higher voltages, compared to those of **DMAC-TRZ** ( $E_{\text{ox}}/E_{\text{red}} = 0.97 / -1.72$  V). The HOMO and LUMO energies derived from these processes (measured from DPV) are -5.31 / -2.62 eV and -5.45 eV / -2.70 eV for **DMAC-TRZ** and **DMAC-py-TRZ**, respectively. The trend in the electrochemical redox gaps measured in solution does not match those calculated by DFT. Experimentally, **DMAC-py-TRZ** possesses a smaller HOMO-LUMO gap of 2.75 eV compared to that of **DMAC-TRZ** at 2.69 eV while the DFT calculated HOMO-LUMO gaps show the opposite trend at 4.78 eV for **DMAC-py-TRZ** and 4.99 eV for **DMAC-TRZ**. The HOMO stabilization in **DMAC-py-TRZ** vs **DMAC-TRZ** is ascribed to the presence of the electron-withdrawing pyridyl bridge, which reduces the electron density on the donor. Similarly, the electron density of the acceptor is reduced, resulting in a more stabilized LUMO level.

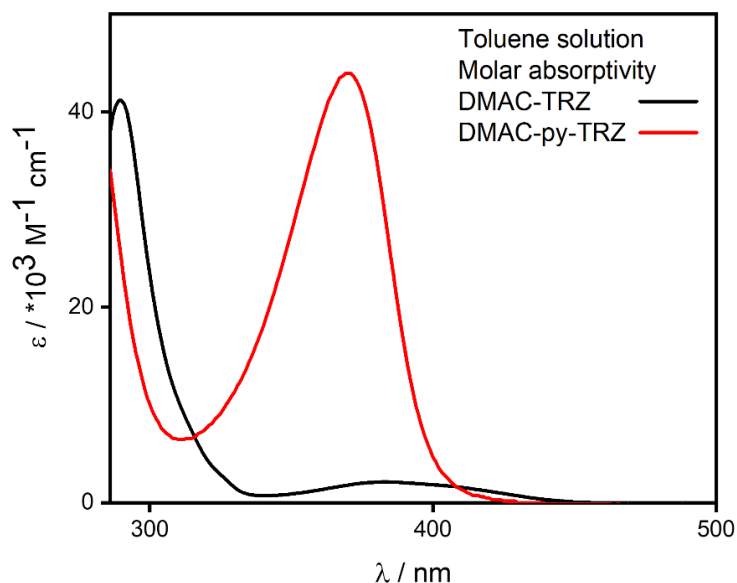


**Figure 174.** UV-vis absorption spectra of **DMAC-TRZ**, and **DMAC-py-TRZ** in toluene.

The UV-Vis absorption spectrum of **DMAC-py-TRZ** was measured in toluene and compared with the previously measured one of **DMAC-TRZ** (Figure 174). **DMAC-py-TRZ** presents a CT band at 370 nm, slightly blue-shifted when compared to **DMAC-TRZ** CT band, at 382 nm. The intensity of this band highly differs for the two compounds, with **DMAC-py-TRZ** CT band having a much higher oscillator strength ( $\epsilon = 43,800 \text{ M}^{-1} \text{ cm}^{-1}$ ) compared to **DMAC-TRZ** ( $\epsilon = 2,140 \text{ M}^{-1} \text{ cm}^{-1}$ ). This can be explained by the fact that the two materials exist in different conformations in the ground state. **DMAC-TRZ** is in an orthogonal conformation, which hinders effective communication between the orbitals involved in the  $S_0 \rightarrow S_1$  transition, thus suppressing the oscillator strength, and thus intensity, of the absorption. Opposite to this, the folded conformation of **DMAC-py-TRZ** allows a higher overlap between the orbitals involved in the  $S_0 \rightarrow S_1$  transition, allowing for a much more intense absorption transition. This is in line with the different oscillator strengths calculated with TD-DFT ( $f$  of 0.000 and 0.127 for **DMAC-TRZ** and the folded **DMAC-py-TRZ** respectively).

Both **DMAC-TRZ** and **DMAC-py-TRZ** (Figure 175) don't show solvatochromism in the absorption, while the emission spectra show a strong positive solvatochromism for both materials. The large positive PL solvatochromism shows that both materials present a large transition dipole moment for this emissive state, and confirms the CT character of both compounds.<sup>185,186</sup> As the folded conformer of **DMAC-py-TRZ** presented a more prominent LE character, the presence of a strong CT state is further proof that the photophysical behavior of the excited state is dominated by the



orthogonal conformer, (higher overlap of the HOMO and LUMO on the acridine and pyridine bridge fragments, **Figure 172a**). A well-resolved vibronic structure of the emission band in methylcyclohexane was again observed, indicating of the local nature of the relevant excitation. We also observed a large Stokes shift for **DMAC-py-TRZ** in non-polar solvents. The Stokes shift of **DMAC-py-TRZ** in methylcyclohexane is 11.8 eV (105 nm), with the absorption band falling at 370 nm, and the emission at 475 nm, while **DMAC-TRZ** only shows a Stokes shift, in methylcyclohexane, of 19.4 eV (64 nm). This large Stokes shift can be explained if the molecular structure underwent a significant change upon photoexcitation, which is what was predicted *via* TD-DFT, with **DMAC-py-TRZ** going from the folded to the orthogonal geometry when excited.

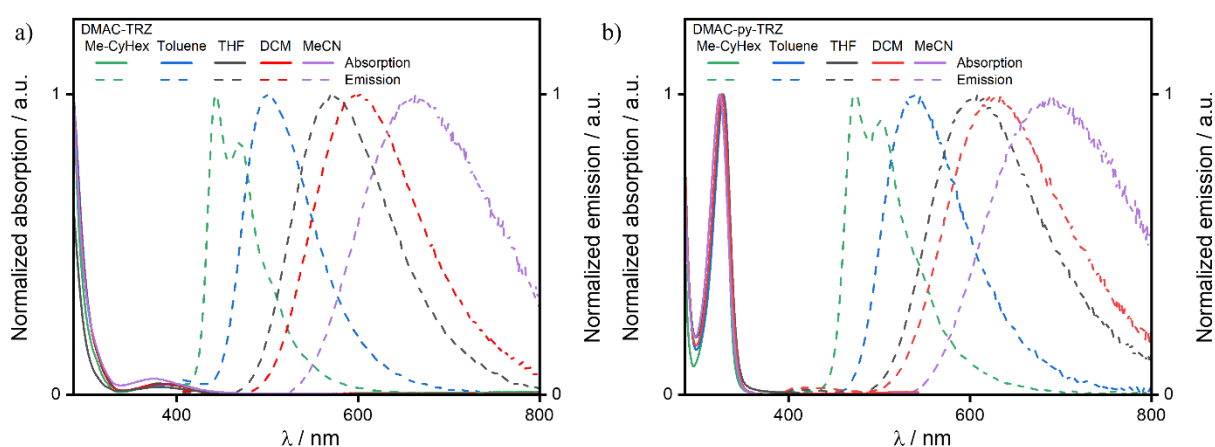


**Figure 175.** Absorption and emission spectra of **DMAC-TRZ** and **DMAC-py-TRZ** in different solvents ( $\lambda_{exc} = 340$  nm).

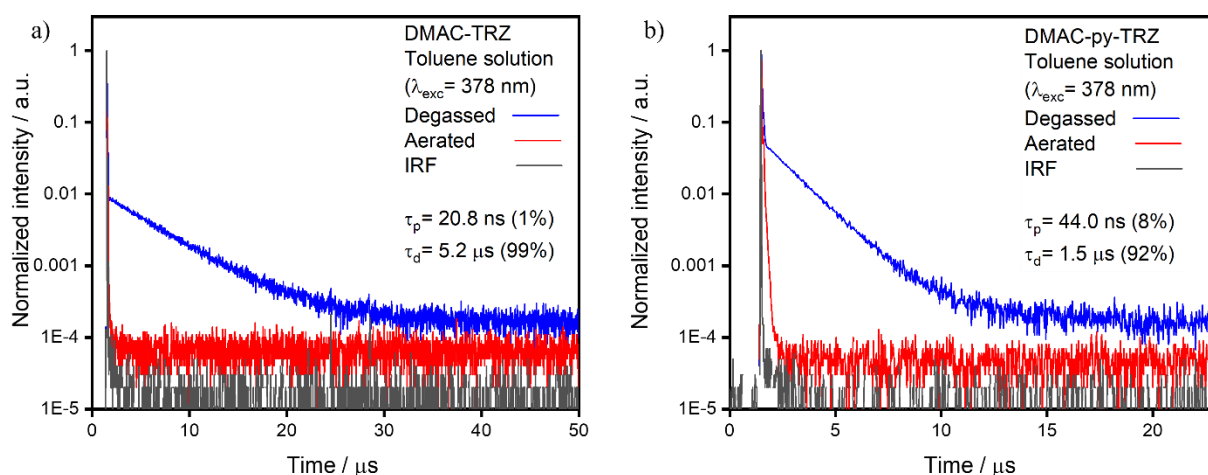


**Figure 176.** Time-resolved fluorescence decay of degassed and aerated solutions of **DMAC-TRZ** and **DMAC-py-TRZ** (Toluene,  $10^{-5}$  M solutions,  $\lambda_{exc} = 378$  nm, both prompt and delayed fluorescence decay were measured by TCSPC).

$\Phi_{\text{PL}}$  in degassed toluene are similar, at 67% and 58% for **DMAC-TRZ** and **DMAC-py-TRZ** respectively. As both materials should exist as their respective orthogonal conformers, the similarity makes perfect sense. When exposed to air, the  $\Phi_{\text{PL}}$  decreases under air for both compounds ( $\Phi_{\text{PL}} = 22\%$  and  $17\%$ , for **DMAC-TRZ** and **DMAC-py-TRZ**, respectively), meaning that triplet states are involved in the photoluminescence of the materials. Both materials present monoexponential prompt and delayed fluorescence decays, with lifetimes of 20.8 ns and 5.2  $\mu\text{s}$ , for **DMAC-TRZ** (reported again to make comparison easier) and 44.0 ns and 1.5  $\mu\text{s}$ , for **DMAC-py-TRZ** (**Figure 176**). The shorter delayed lifetime in toluene of **DMAC-py-TRZ** could signify an improved RISC rate, compared to **DMAC-TRZ**.

The measurement reported so far agree with the theory that **DMAC-TRZ** maintains the same orthogonal conformation in both the ground and the  $S_1$  states, while **DMAC-py-TRZ** undergoes a significant geometric reorganization from the folded geometry in the ground state to the orthogonal geometry in the excited state.

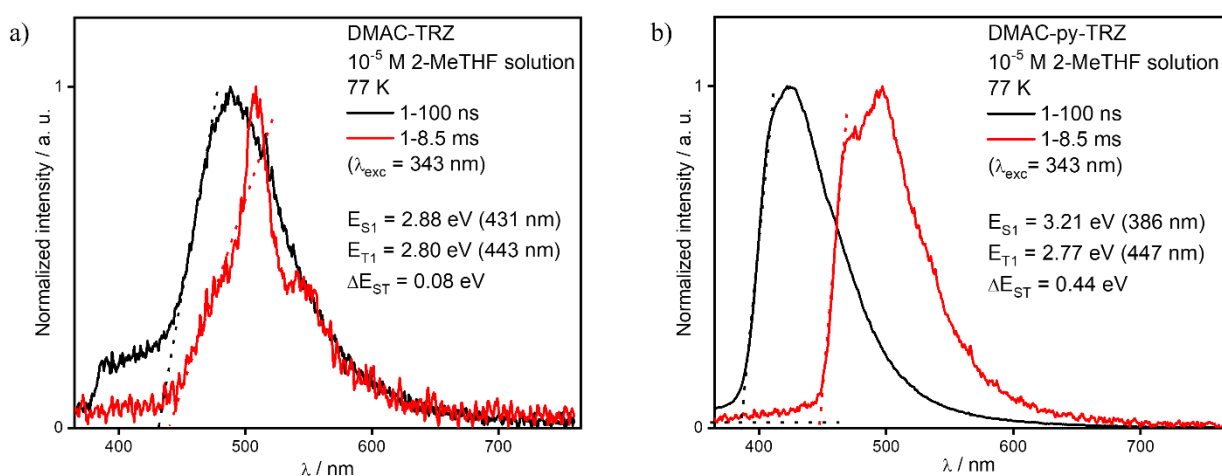


**Figure 177.** Prompt fluorescence and phosphorescence spectra of **a) DMAC-TRZ**, and **b) DMAC-py-TRZ** at 77 K in in  $10^{-5}$  M 2-MeTHF glass ( $\lambda_{\text{exc}} = 343$  nm, prompt and delayed fluorescence spectra were obtained over the 1-100 ns and 1-8.5 ms time ranges, respectively).

Collecting the fluorescence and phosphorescence spectra in 2-MeTHF glass at 77 K (**Figure 177**) gave ulterior information on the geometrical reorganization of **DMAC-py-TRZ** upon photoexcitation. In the frozen matrix, the material shows a deep blue emission at 404 nm, leading to

a very large  $\Delta E_{ST}$  of 0.44 eV. This implies that in the frozen matrix, the excited folded compound cannot convert to the orthogonal conformer so that the emission occurs from the folded conformer, which possesses a much higher  $\Delta E_{ST}$ . The  $\Delta E_{ST}$  of **DMAC-TRZ** was measured in the same environment for comparison, and it shows a very small value of 0.08 eV, meaning that the molecule is in the orthogonal conformation.

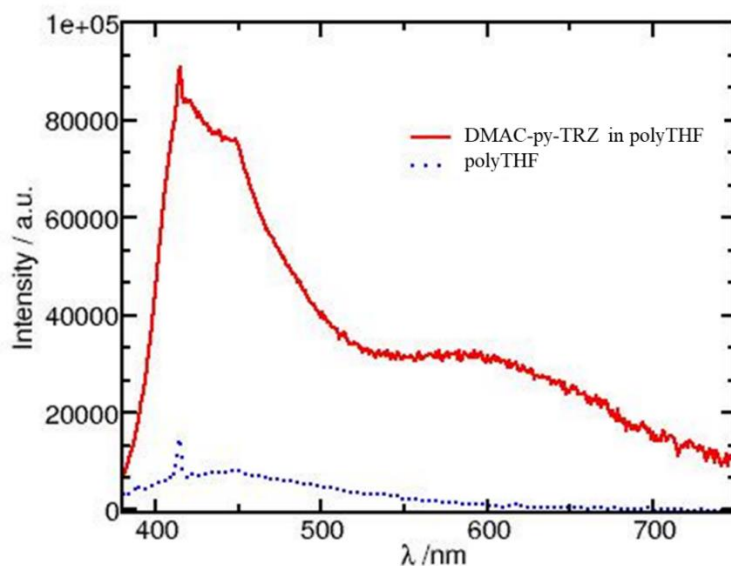


**Figure 178.** PL spectrum (red line) of **DMAC-py-TRZ** dissolved in polyTHF ( $\lambda_{exc}=370\text{nm}$ ). The blue dotted line is the emission spectrum of the pure solvent.

The spectrum of **DMAC-py-TRZ** was also obtained in the viscous solvent polyTHF, to observe if the higher viscosity environment could suppress conformational reorganization. Two emission bands are observed, the first at 410 nm and the second at 600 nm (**Figure 178**). This suggests that the viscous solvent can partially stop the geometrical reorganization, making it possible for the emission from both the orthogonal and folded conformers.

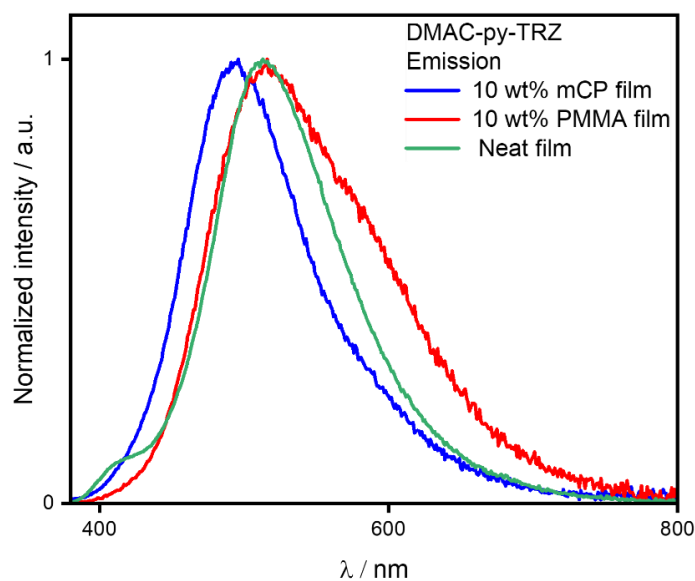


**Figure 179.** Emission spectra of **DMAC-py-TRZ** in 10 wt% mCP film, 10 wt% PMMA film, and neat film ( $\lambda_{\text{exc}}=340$ ).

The behavior of **DMAC-py-TRZ** in solid-state films was then investigated, where the large geometrical reorganization is also likely to be hindered. Spin-coated thin films of **DMAC-py-TRZ** doped into the relatively non-polar matrix PMMA at 10 wt% were prepared and showed sky-blue emission at  $\lambda_{\text{PL}}$  of 516 nm with a  $\Phi_{\text{PL}}$  of 63.8% under an  $\text{N}_2$  atmosphere, which decreased to 58.0% after exposure to air. Both prompt and delayed fluorescence, with biexponential decay kinetics, were observed, with  $\tau_{\text{p}}$  of 26.0 ns and an average  $\tau_{\text{d}}$  of 4.7  $\mu\text{s}$  [ $\tau_1=1.4$   $\mu\text{s}$  (47%),  $\tau_2=7.7$   $\mu\text{s}$  (53%)], respectively (**Figure 183a**). As the folded conformer presented a  $\Delta E_{\text{ST}}$  far too large for a TADF molecule, the presence of a delayed fluorescence means that at least some emitter molecules are in the TADF active, orthogonal conformation., **DMAC-py-TRZ** presents a shorter-lived prompt component and a slightly longer-lived delayed component, compared to the ones obtained in toluene ( $\tau_{\text{p}}$  of 44.0 ns and  $\tau_{\text{d}}$  of 1.5  $\mu\text{s}$ ). 10 wt% doped film of **DMAC-TRZ** in PMMA was also prepared as a comparison. **DMAC-py-TRZ** showed a considerable improvement in efficiency over **DMAC-TRZ** which achieved a small  $\Phi_{\text{PL}}$  of 18% under  $\text{N}_2$  atmosphere and 15% under air. The emission of **DMAC-TRZ** is slightly red-shifted, at 523 nm and the prompt and delayed lifetimes are longer, with an average  $\tau_{\text{p}}$  of 41.6 ns [ $\tau_1=18.4$  ns (66%),  $\tau_2=86.1$  ns (34%)], and  $\tau_{\text{d}}$  of 17.0  $\mu\text{s}$  [ $\tau_1=4.2$   $\mu\text{s}$  (50%),  $\tau_2=30.0$   $\mu\text{s}$  (50%)] (**Figure 180**).

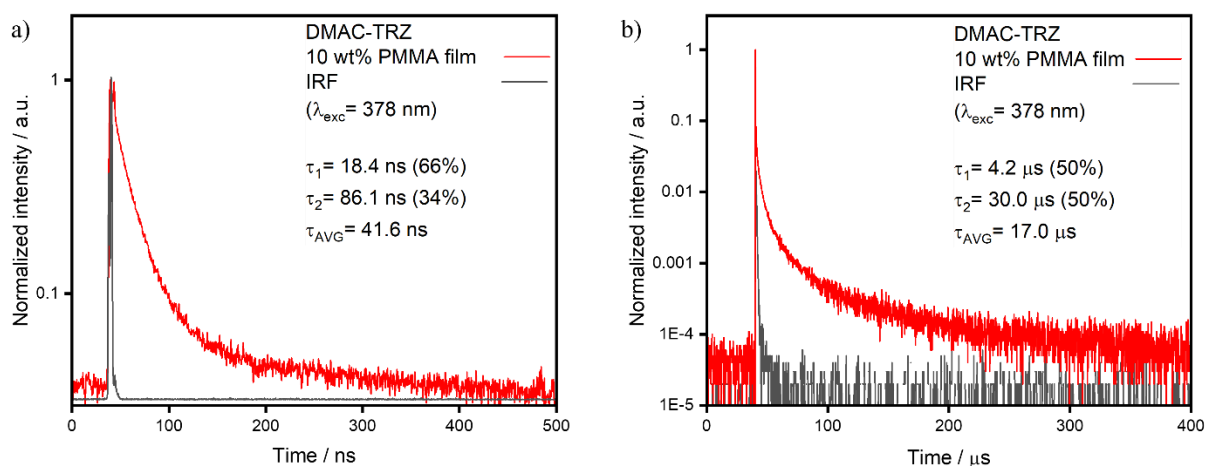


**Figure 180.** Time-resolved **a)** prompt fluorescence decay and **b)** delayed fluorescence decay of 10 wt% PMMA film of **DMAC-TRZ** and ( $\lambda_{exc} = 378$  nm, the prompt and delayed fluorescence decay were measured by TCSPC and MCS, respectively).

The  $\Delta E_{ST}$  of **DMAC-TRZ** and **DMAC-py-TRZ** was obtained by recording the spectra of the 10 wt% doped PMMA film at 77K (**Figure 181**). The singlet and triplet levels of **DMAC-TRZ** are 2.85 eV, and 2.74 eV, respectively, yielding a singlet-triple gap of 0.11 eV. Compared to the parent emitter, **DMAC-py-TRZ** has a lower energy singlet state at 2.76 eV, and an identical triplet energy of 2.74 eV, leading to a  $\Delta E_{ST}$  of 0.02 eV. This indicates that both fluorescence and phosphorescence are coming from the orthogonal conformer, meaning that in the PMMA film the material is still able to relax to the lower energy geometry. This is unlike what was observed in the 2-MeTHF glass, where the folded conformer dominated the photophysics.

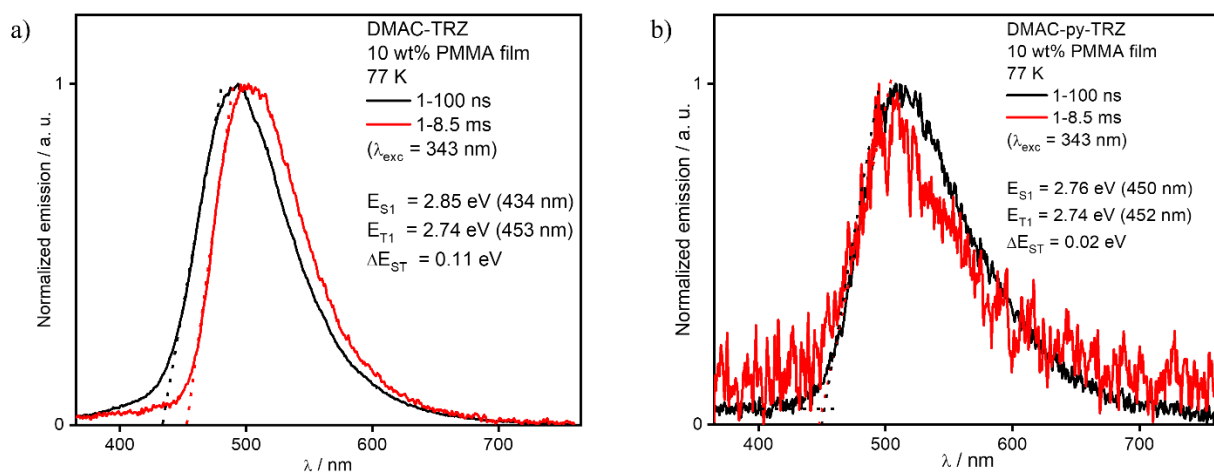


**Figure 181.** Prompt fluorescence and phosphorescence spectra of **a) DMAC-TRZ**, and **b) DMAC-py-TRZ** at 77 K in in 10 wt% PMMA film ( $\lambda_{\text{exc}} = 343$  nm, prompt and delayed fluorescence spectra were obtained over the 1-100 ns and 1-8.5 ms time ranges, respectively).

**Table 30.** Host and concentration screen of **DMAC-py-TRZ** in mCP, DPEPO, and mCBP.

Host	Doping concentration / wt%	PLQY N <sub>2</sub> ; Air/ %
<b>mCP<sup>a</sup></b>	3	49; 48
	5	55; 52
	10	57; 54
	15	55; 52
	20	49; 47
<b>DPEPO<sup>b</sup></b>	3	28; 25
	5	46; 40
	10	33; 30
	15	46; 41
	20	36; 32
<b>mCBP</b>	3	42; 39
	5	51; 48
	10	51; 49
	15	52; 49
	20	50; 48

<sup>a</sup>  $\lambda_{\text{exc}}=340$  nm; <sup>b</sup>  $\lambda_{\text{exc}}=310$  nm

Different host materials were then screened to find the optimal environment for the emitter (**Table 30**), with the best results obtained in the 10 wt% mCP film, with a  $\Phi_{\text{PL}}$  of 57% under  $\text{N}_2$ , which decreased to 54% when exposed to air. In this host, the emission is blue-shifted to  $\lambda_{\text{PL}}$  of 496 nm, compared to the PMMA film (**Figure 179**). Again, prompt and delayed fluorescence decays were observed, with lifetimes of  $\tau_{\text{p}} = 24.9$  ns and the average  $\tau_{\text{d}} = 5.3$   $\mu\text{s}$  [ $\tau_1 = 1.0$   $\mu\text{s}$  (33%),  $\tau_2 = 7.4$   $\mu\text{s}$  (67%)] (**Figure 183b**). The TADF nature of **DMAC-py-TRZ** was finally proven by observing the temperature dependence of its delayed fluorescence in both PMMA and mCP matrices (**Figure 182**).

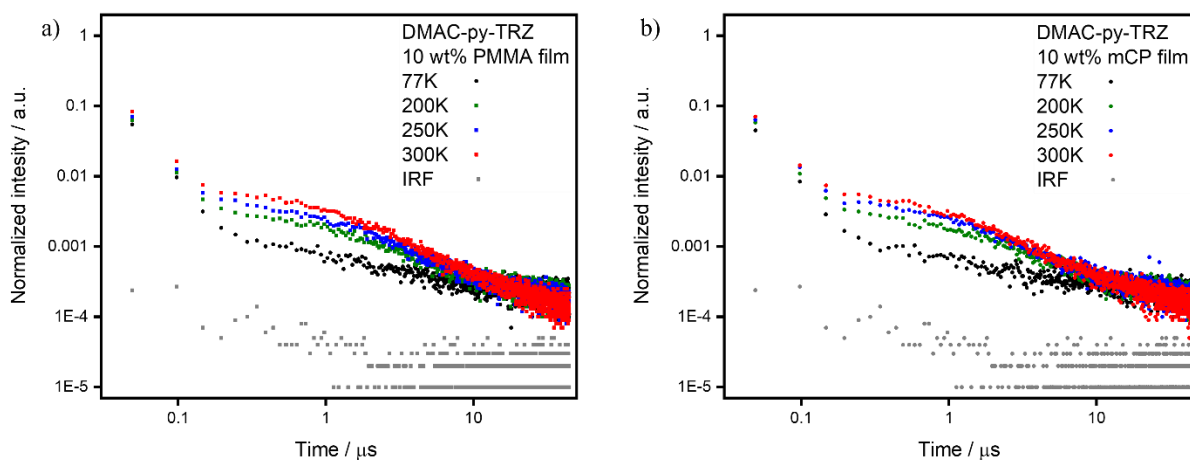


**Figure 182.** Delayed fluorescence decay data measured at different temperatures in spin-coated **a)** 10 wt% PMMA film, **b)** 10 wt% mCP film of **DMAC-py-TRZ** ( $\lambda_{\text{exc}} = 378$  nm, all the delayed fluorescence decays were measured by TCSPC).

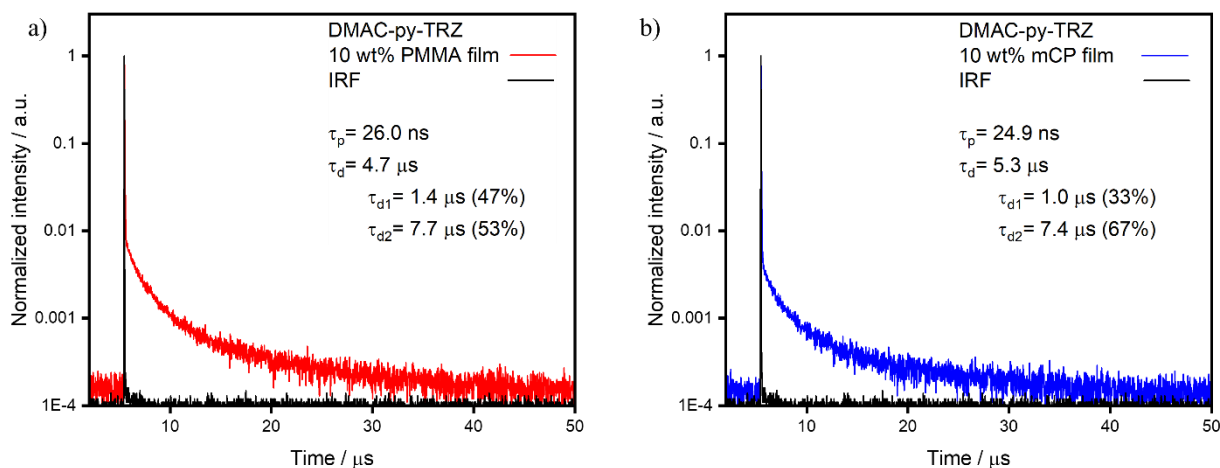


**Figure 183.** Time-resolved fluorescence decay of **a)** 10 wt% PMMA film and **b)** 10 wt% mCP film of **DMAC-py-TRZ** and ( $\lambda_{exc}=378$  nm, both prompt and delayed fluorescence decay were measured by TCSPC).

The 10 wt% doped film of **DMAC-TRZ** in mCP was also made. The  $\Phi_{PL}$  is lower than that of **DMAC-py-TRZ**, at 47% under  $N_2$ , and 45% under air, and the  $\lambda_{PL}$  is slightly red-shifted at 499 nm. The mCP film shows longer lifetimes of both the prompt and delayed fluorescence, with average lifetimes  $\tau_p$  of 23.0 ns [ $\tau_1=15.2$  ns (65%),  $\tau_2=37.3$  ns (35%)], and  $\tau_d$  of 15.3  $\mu$ s [ $\tau_1=4.1$   $\mu$ s (50%),  $\tau_2=26.5$   $\mu$ s (50%)], respectively (**Figure 184**).

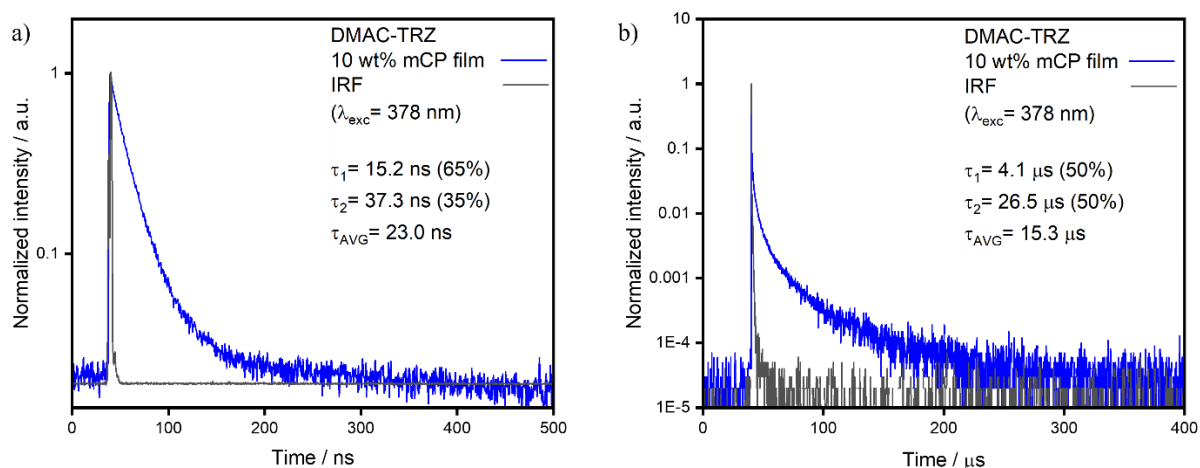


**Figure 184.** Time-resolved **a)** prompt fluorescence decay and **b)** delayed fluorescence decay of 10 wt% mCP film of **DMAC-TRZ** and ( $\lambda_{exc}=378$  nm, the prompt and delayed fluorescence decay were measured by TCSPC and MCS, respectively).



The  $\Delta E_{ST}$  of the emitters was once again measured at 77 K in the 10 wt% mCP film (**Figure 185**). **DMAC-TRZ** showed singlet and triplet energy levels of 2.83 eV and 2.81 eV, respectively, resulting in a very low  $\Delta E_{ST}$  of 0.02 eV. **DMAC-py-TRZ** has lower energy excited states, with singlet and triplet energy levels of 2.76 eV and 2.71 eV, respectively, also resulting in a very low  $\Delta E_{ST}$  of 0.05 eV. As was the case in the PMMA film, the emission originated from the orthogonal conformer of **DMAC-py-TRZ**, despite the low temperature and the solid matrix.

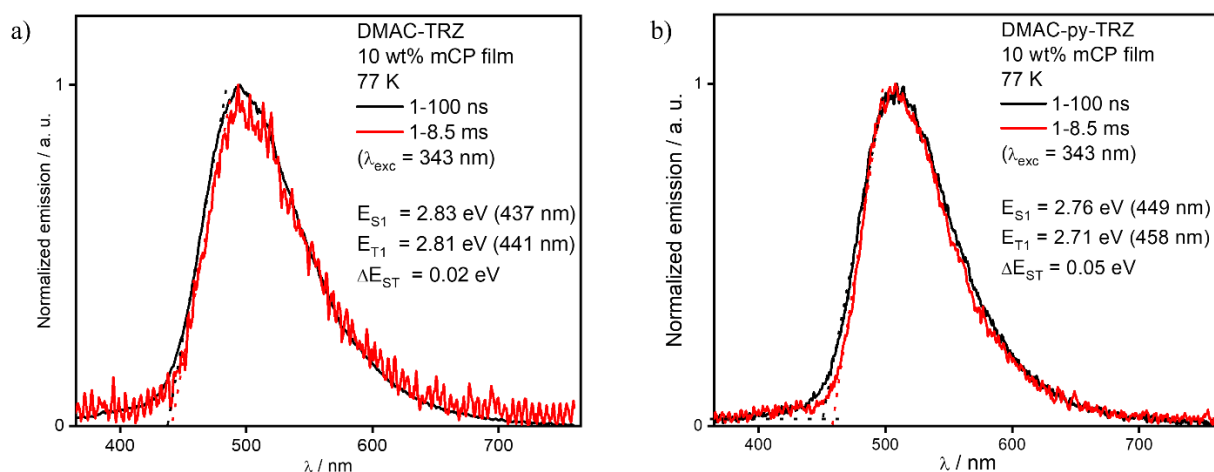


**Figure 185.** Prompt fluorescence and phosphorescence spectra of **a) DMAC-TRZ**, and **b) DMAC-py-TRZ** at 77 K in in 10 wt% mCP film ( $\lambda_{exc} = 343$  nm, prompt and delayed fluorescence spectra were obtained over the 1-100 ns and 1-8.5 ms time ranges, respectively).

Low-concentration mCP films, ranging from 1 wt% to 5 wt%, were then fabricated to see if the doping percentage of the emitter had any effect on the ratio of conformers (**Figure 186**). Both the bluer emission originating from the folded structure, and the greener emission from the orthogonal structure, were observed, suggesting that both conformers are present in all films, even if at different ratios. The folded conformer bluer emission progressively weakened with increasing concentrations, until it completely disappears at doping concentrations above 3 wt%. Two phenomena may be happening. Either self-absorption of the higher energy emission, or energy transfer from the folded to the orthogonal structure. Both phenomena are expected to become more efficient upon increasing the concentration of the emitter in the host matrix.

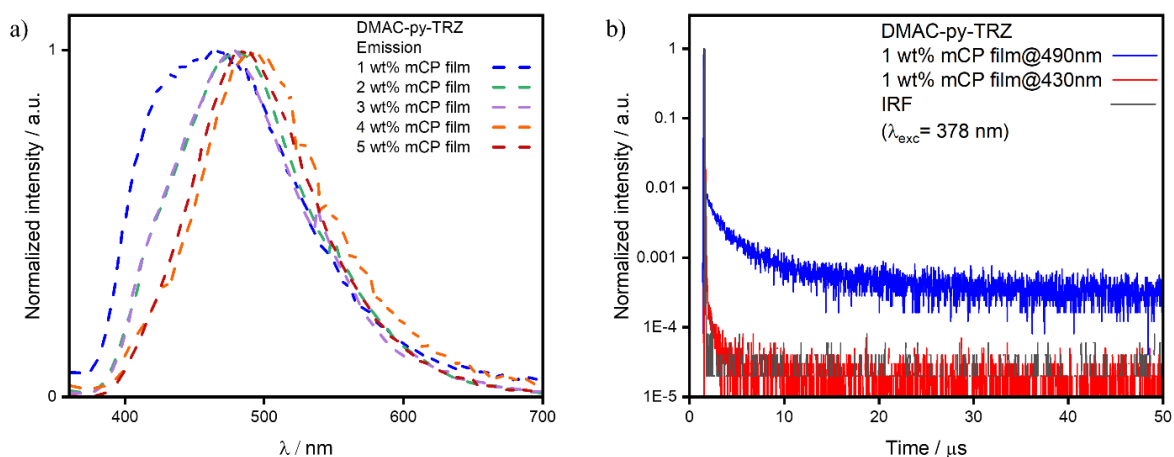


**Figure 186.** Emission spectra of **DMAC-py-TRZ** in spin-coated 1-5 wt% mCP films ( $\lambda_{\text{exc}} = 340 \text{ nm}$ ); b) time-resolved PL decay in spin-coated 1 wt% mCP film of **DMAC-py-TRZ** collected at  $\lambda_{\text{PL}} = 490 \text{ nm}$  and  $\lambda_{\text{PL}} = 430 \text{ nm}$  ( $\lambda_{\text{exc}} = 378 \text{ nm}$ , the delayed fluorescence decays were measured by TCSPC).

Finally, how the photophysical behavior of **DMAC-py-TRZ** changes in the neat film was explored. Two emission bands can be seen at  $\lambda_{\text{PL}}$  of 415 nm and 513 nm and  $\Phi_{\text{PL}}$  is 55% under  $\text{N}_2$ , which decreases to 54% when exposed to air. The two emission bands were attributed to the presence of the two conformers in the neat film. Time-resolved PL decays were recorded for both bands at 500 nm and 425 nm. At 500 nm, both prompt and delayed fluorescence were observed, with a mono-exponential  $\tau_{\text{p}}$  of 56.7 ns and a biexponential  $\tau_{\text{d}}$  of 3.2  $\mu\text{s}$  [ $\tau_1 = 1.0 \mu\text{s}$  (35%),  $\tau_2 = 4.6 \mu\text{s}$  (56%)]. At 425 nm, only prompt fluorescence was present, this permits an assignment of this band to originate from the folded conformer, in line with the predictions from the DFT calculations. The emission at 513 nm originates from the orthogonal conformer.

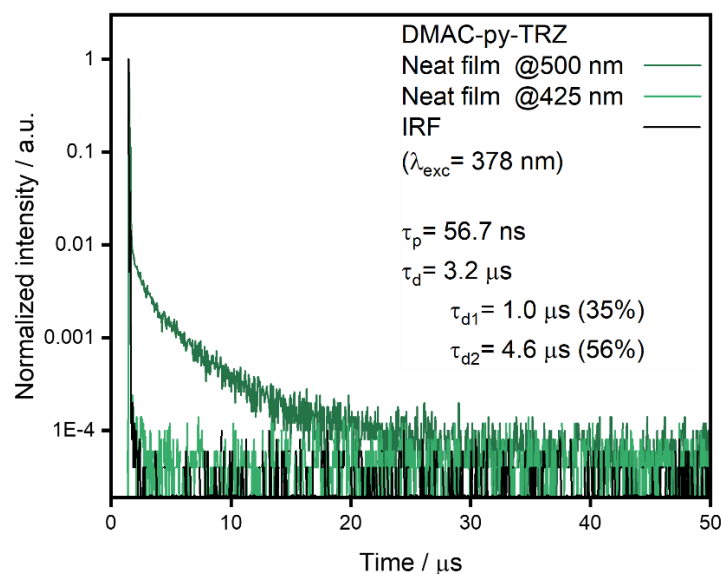


**Figure 187.** Time-resolved fluorescence decay of neat film of **DMAC-py-TRZ** and ( $\lambda_{\text{exc}} = 378 \text{ nm}$ , both prompt and delayed fluorescence decay were measured by TCSPC).

Further proof of the presence of the two conformers was obtained by comparing the fluorescence and phosphorescence spectra of the neat film, measured at room temperature and 77K (**Figure 188**). When both spectra were recorded in cryogenic conditions, the molecule is “frozen” in the folded conformation, leading to the blue-shifted fluorescence spectrum and a very large  $\Delta E_{\text{ST}}$  of 0.47 eV. The fluorescence spectrum of the twisted conformer was isolated by reducing the time range of the measurement, from 1-100 ns to 10-100 ns, and measuring it at room temperature, allowing us to observe a lower energy  $S_1$  state (2.85 eV vs 3.12 eV observed at 77 K) and obtain the  $\Delta E_{\text{ST}}$  of the twisted **DMAC-py-TRZ** in neat film, with a value of 0.20 eV. The phosphorescence spectrum measured at 77 K gave us a triplet value of 2.65 eV.

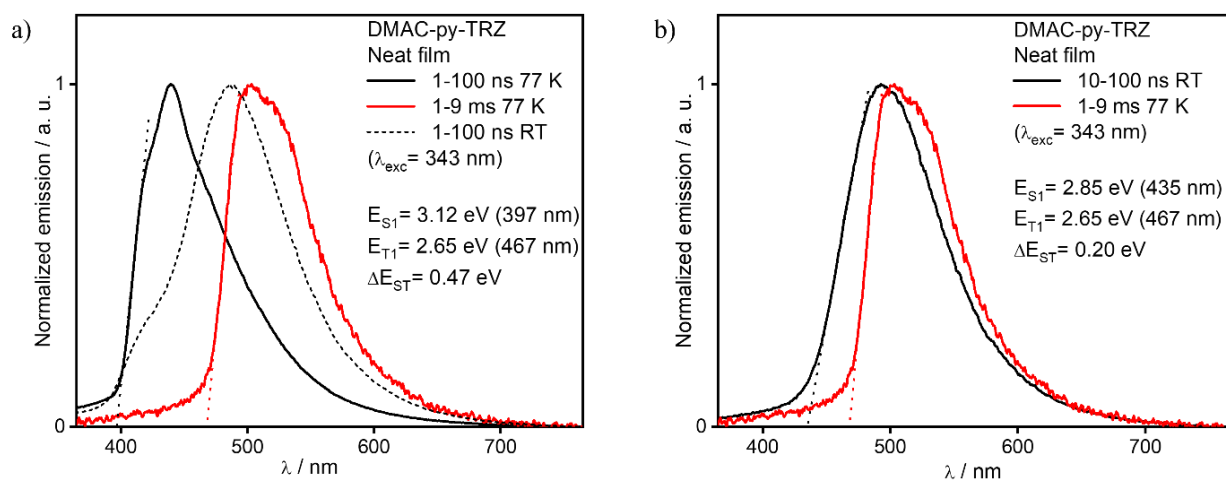


**Figure 188.** Prompt fluorescence and phosphorescence spectra at room temperature and at 77 K in drop-casted neat film ( $\lambda_{\text{exc}}=343$  nm, prompt and delayed fluorescence spectra were obtained in the 1–100 ns and 1–9 ms time range, respectively), and calculation of the of the  $\Delta E_{\text{ST}}$  from the phosphorescence spectra at 77 K and the fluorescence spectra at **a)** 77 K (corresponding to the  $\Delta E_{\text{ST}}$  of the folded conformer), and **b)** room temperature (corresponding to the  $\Delta E_{\text{ST}}$  of the twisted conformer).

**Table 31.** Photophysical properties of **DMAC-TRZ** and **DMAC-py-TRZ**.

Material	Environment	$\lambda_{\text{PL}}/$ nm <sup>a</sup>	$\Phi_{\text{PL}} N_2$ (air) <sup>b/</sup> %	$\tau_p, \tau_d$ <sup>e/</sup> ns; $\mu$ s	$S_1$ <sup>f/</sup> eV	$T_1$ <sup>g/</sup> eV	$\Delta E_{\text{ST}}$ <sup>h/</sup> eV
<b>DMAC-TRZ</b>	Toluene ( $10^{-5}$ M) <sup>67</sup>	499	67 (22) <sup>c</sup>	20.8; 5.2	2.88	2.57	0.31
	mCP 10 wt%	499	47 (45)	22.9; 15.3	2.83	2.81	0.02
	PMMA 10 wt%	523	18 (15)	41.6; 17.0	2.85	2.74	0.11
<b>DMAC-py-TRZ</b>	Toluene ( $10^{-5}$ M)	539	58 (17) <sup>c</sup>	44.0; 1.5	3.21	2.77	0.44
	mCP 10 wt%	496	57 (54) <sup>d</sup>	24.9; 5.3	2.76	2.71	0.05
	PMMA 10 wt%	516	64 (58) <sup>d</sup>	26.0; 4.7	2.76	2.74	0.02

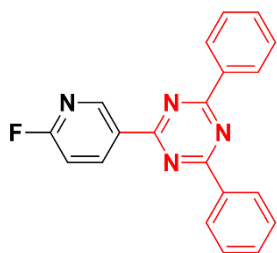
<sup>a</sup> measured at room temperature; <sup>b</sup>  $\lambda_{\text{exc}} = 340$  nm; <sup>c</sup> obtained *via* the optically dilute method<sup>138</sup>, quinine sulfate (0.5 M) in  $\text{H}_2\text{SO}_4$  (aq) was used as the reference,  $\Phi_{\text{PL}}$ : 54.6%,  $\lambda_{\text{exc}} = 360$  nm;<sup>139</sup> <sup>d</sup> obtained *via* integrating sphere; <sup>e</sup>  $\tau_p$  (prompt lifetime) and  $\tau_d$  (delayed lifetime) were obtained from the transient PL decay of degassed solution/doped film,  $\lambda_{\text{exc}} = 378$  nm; <sup>f</sup>  $S_1$  was obtained from the onset of the prompt fluorescence measured at 77 K; <sup>g</sup>  $T_1$  was obtained from the onset of the phosphorescence spectrum measured at 77 K; <sup>h</sup>  $\Delta E_{\text{ST}} = S_1 - T_1$ .

## 6.4 – Conclusions

In this Chapter, the novel TADF emitter, **DMAC-py-TRZ**, is presented, and its behavior is studied with an in-depth computational analysis and experimental characterization. **DMAC-py-TRZ** only differs from the parent emitter, **DMAC-TRZ** by having a pyridine instead of a phenyl ring as the spacer between the donor and acceptor. However, this minor change in the bridging moiety led to a significant difference. In both the ground and excited state **DMAC-TRZ** exists in an orthogonal geometry, while **DMAC-py-TRZ** assumes a folded geometry in the ground state and undergoes a significant geometrical reorganization to an orthogonal structure, upon excitation. This large reorganization is confirmed by the photophysical behavior of the material, and the very large Stokes shift measured in non-polar solvents. The blue-shifted emission of the folded conformer can be isolated by carrying out measurements in a frozen glass. In solid-state films, a distribution of conformers was observed at low concentrations, with emission bands coming from both the bluer folded conformer and the greener orthogonal conformer. The emission from the folded conformer gradually decreases with increased doping concentration. This effect can be caused by concentration-dependant phenomena like self-absorption or energy transfer from one conformer to the other. TADF is not observed in the folded structure, due to a too-large  $\Delta E_{ST}$ , while it's present at higher concentrations (10 wt%) where the orthogonal conformer dominates the photoluminescence behavior of the material.

## 6.5 - Compound characterization

### 2-(4-fluorophenyl)-4,6-diphenyl-1,3,5-triazine (F-py-TRZ)



To a mixture of 2-chloro-4,6-diphenyl-1,3,5-triazine (1.30 g, 5.00 mmol, 1 equiv.) and (6-fluoropyridin-3-yl)boronic acid (0.78 g, 5.50 mmol, 1.1 equiv.) were added 40 mL of THF and 10 mL 2 M  $K_2CO_3$  aqueous solution followed by bubbling with  $N_2$  through the solution for 10 min and heating to reflux for 12 h under a  $N_2$  atmosphere. The reaction was diluted with water, and the organic layer was extracted with DCM (DCM) ( $3 \times 50$  mL). The organic phase was washed with brine, dried over  $Na_2SO_4$  and concentrated under reduced pressure. The product was obtained as a white solid after recrystallization from THF (1.31 g). **Yield:** 80%; **Mp:** 250°C; **R<sub>f</sub>:** 0.81(cyclohexane/ethyl acetate = 4:1); **<sup>1</sup>H NMR** (500 MHz,  $CDCl_3$ )  $\delta$ : 9.59-9.58 (d,  $J=2.3$ , 1H), 9.12-9.08 (td,  $J=8.2$ , 2.4, 1H), 8.76-8.74 (dt,  $J=8.6$ , 1.9, 4H), 7.67 – 7.63 (m, 2H), 7.63 – 7.57 (m, 4H), 7.14-7.12 (dd,  $J=8.6$ , 2.8, 1H); **<sup>13</sup>C NMR** (126 MHz, Chloroform-*d*)  $\delta$ : 171.99, 169.38, 167.08, 165.13, 149.86, 149.73, 141.84, 141.77, 135.81, 133.07, 130.36, 130.32, 129.16, 128.91, 109.84, 109.54; **GC-MS retention time:** 12.024; **Mass Theoretical** ( $C_{20}H_{13}FN_4$ ): 328.35 g mol<sup>-1</sup>; **Mass Found:** 328 g mol<sup>-1</sup>.

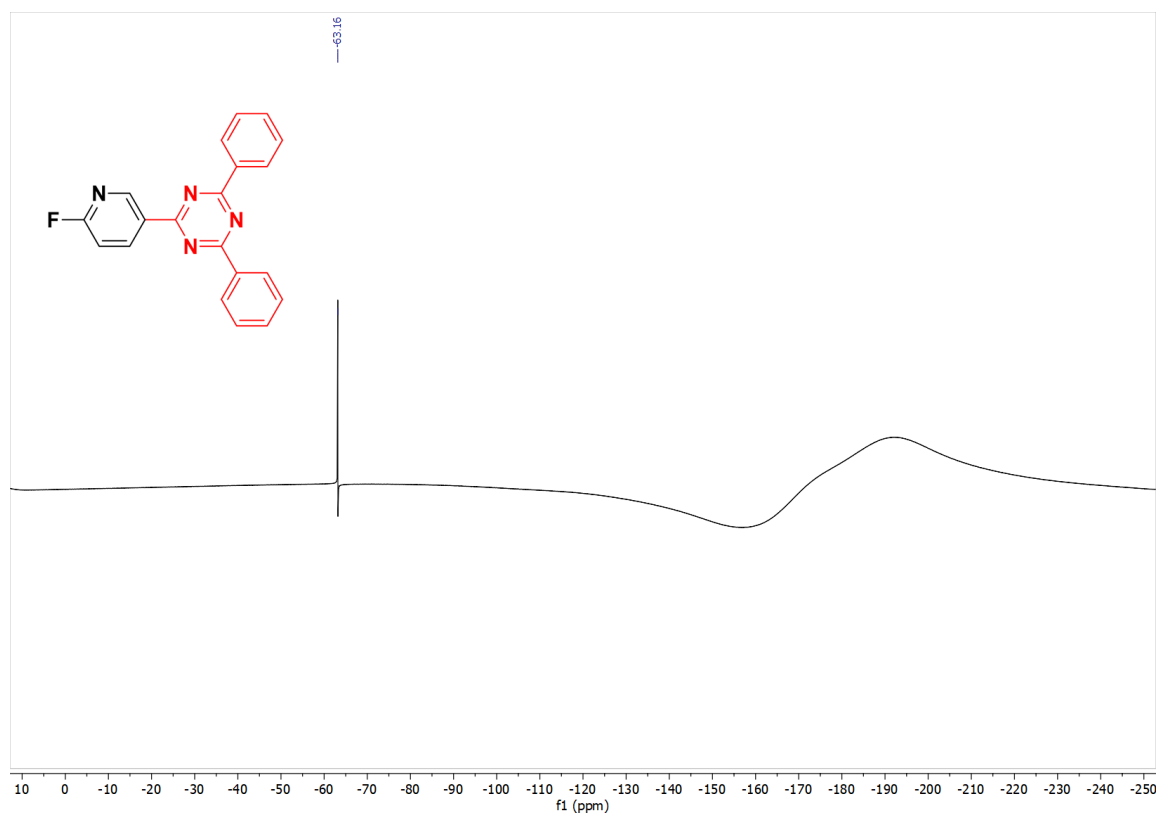
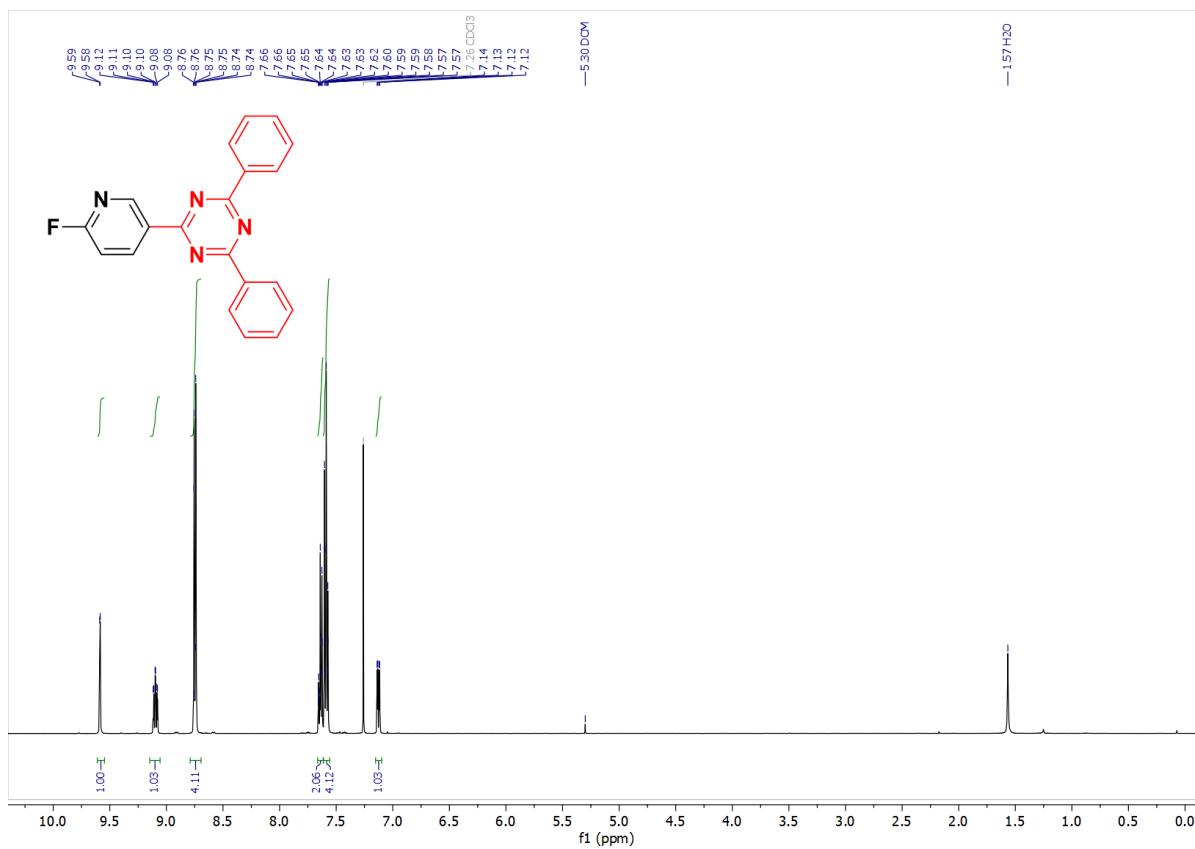


**Figure 190.**  $^{19}\text{F}$  NMR of F-py-TRZ in  $\text{CDCl}_3$ .

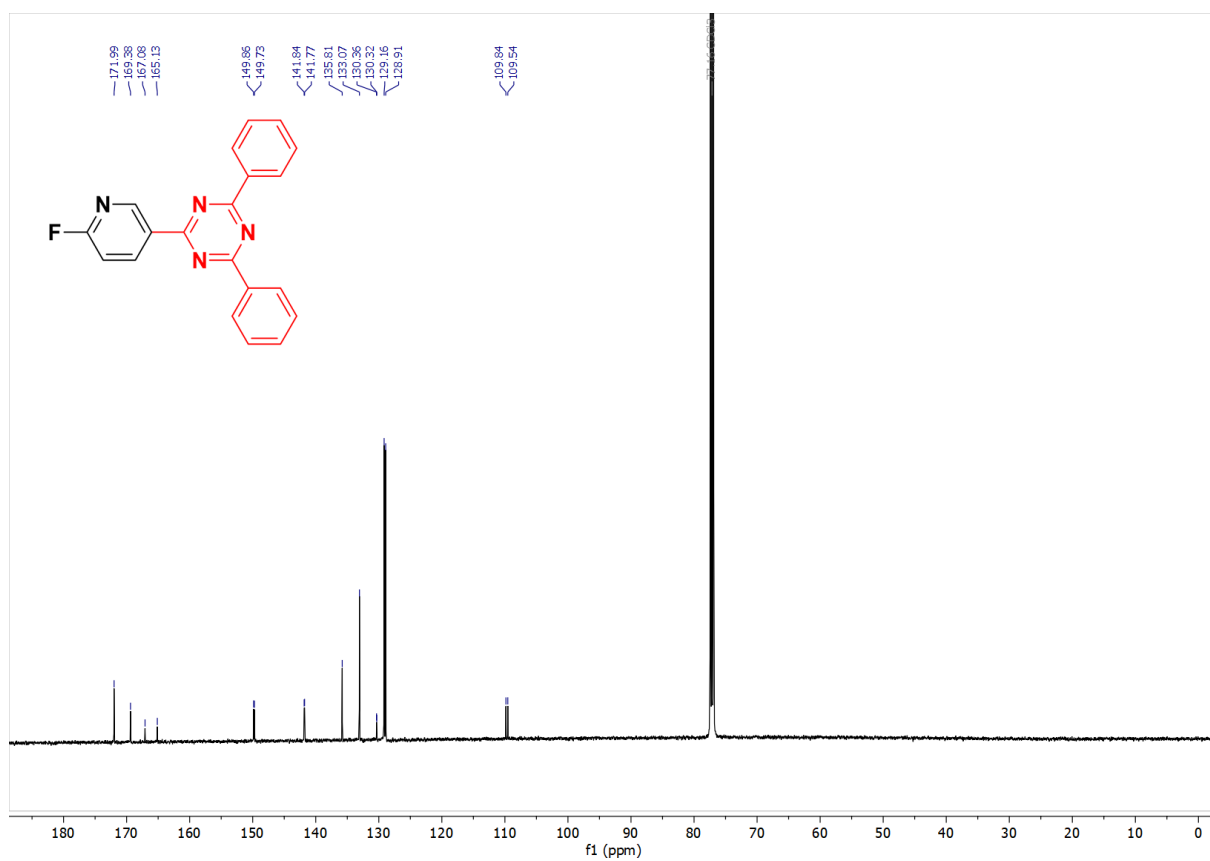


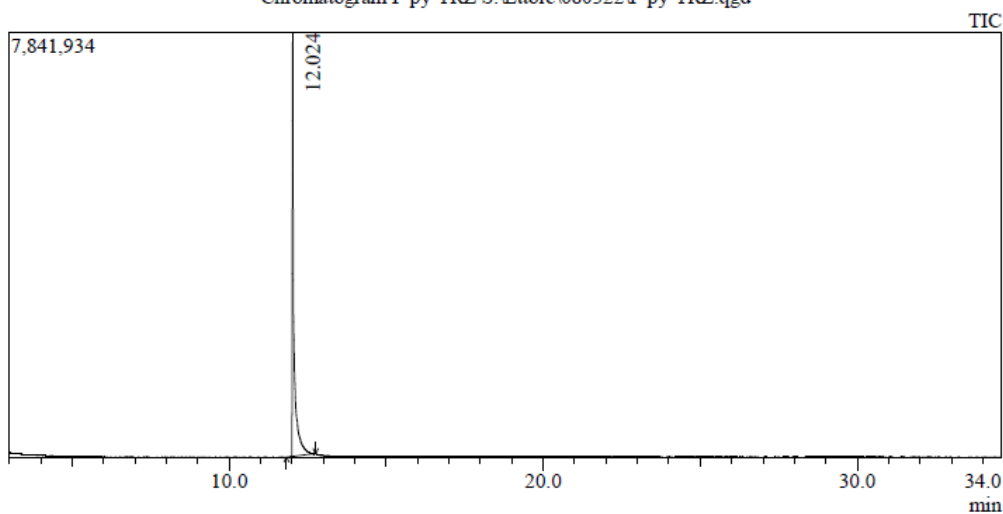
**Figure 191.**  $^{13}\text{C}$  NMR of F-py-TRZ in  $\text{CDCl}_3$ .



Sample Information

Analyzed by : Admin  
 Analyzed : 08/03/2022 15:51:06  
 Sample Type : Unknown  
 Level # : 1  
 Sample Name : F-py-TRZ  
 Sample ID :  
 IS Amount : [1]=1  
 Sample Amount : 1  
 Dilution Factor : 1  
 Vial # : 60  
 Injection Volume : 1.00  
 Data File : S:\Ettore\080322\F-py-TRZ.qgd  
 Org Data File : S:\Ettore\080322\F-py-TRZ.qgd  
 Method File : S:\standard method 1 for RTX-1 column 330 injection-long.qgm  
 Org Method File : S:\standard method 1 for RTX-1 column 330 injection-long.qgm  
 Report File :  
 Tuning File : S:\auto tuning result\03022022.qgt  
 Modified by : Admin  
 Modified : 08/03/2022 16:25:43

Chromatogram F-py-TRZ S:\Ettore\080322\F-py-TRZ.qgd



Peak#	R. Time	Area	Area%	Height	A/H	Base m/z	Base Int.
1	12.024	27141817	100.00	7807427	3.48	103.10	2762479
		27141817	100.00	7807427			

Line#:1 R. Time:12.025(Scan#:1084)  
 MassPeaks:581  
 RawMode:Single 12.025(1084) BasePeak:103.10(3337273)  
 BG Mode:None Group 1 - Event 1 Scan

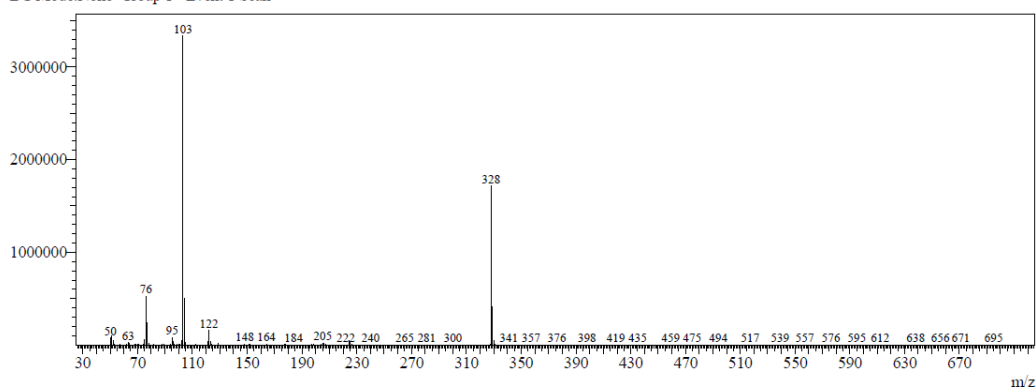
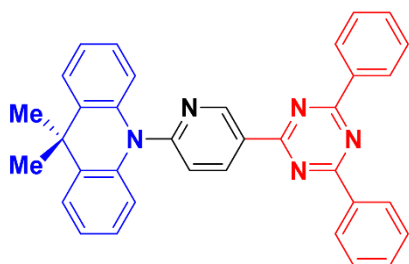
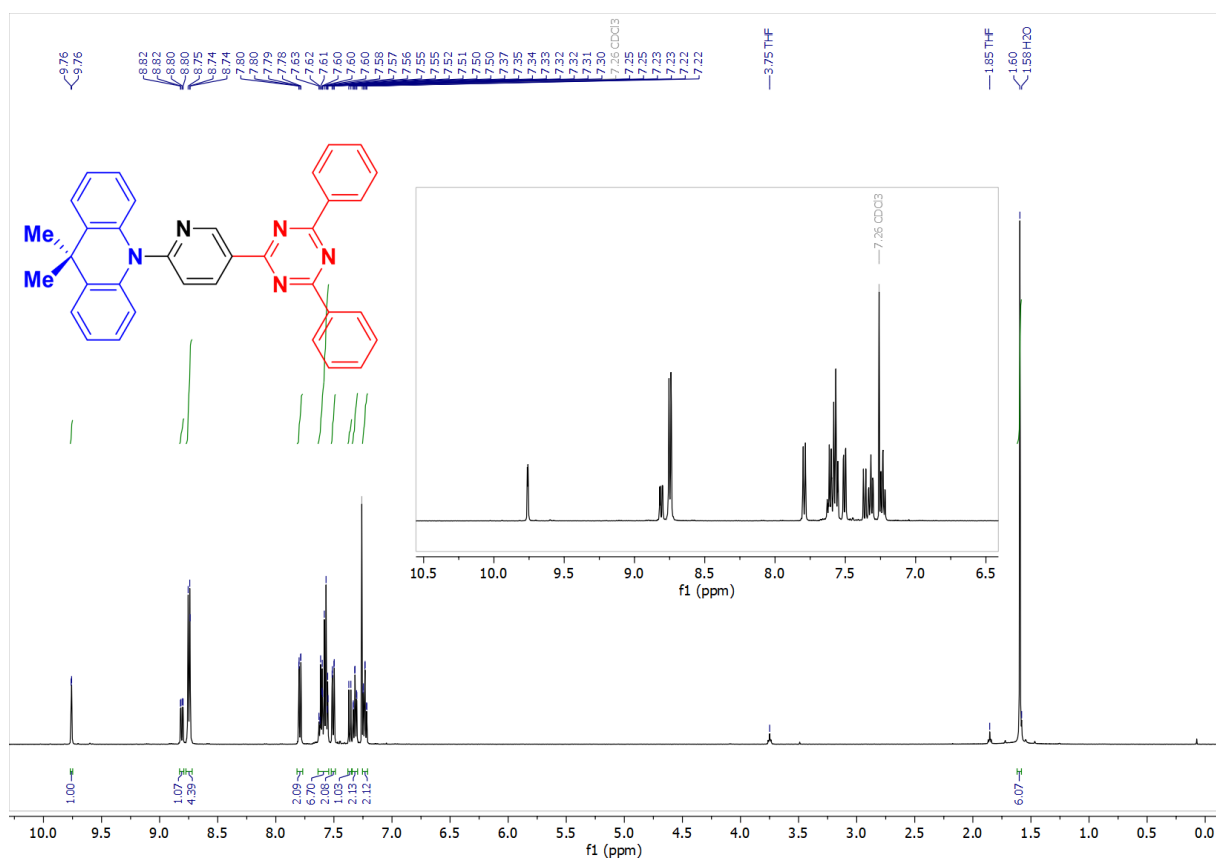


Figure 192. GC-MS trace of F-py-TRZ.

**10-(5-(4,6-diphenyl-1,3,5-triazin-2-yl)pyridin-2-yl)-9,9-dimethyl-9,10-dihydroacridine (DMAC-py-TRZ)**



To  $\text{Cs}_2\text{CO}_3$  (1.03 g, 3 mmol, 3.1 equiv.) in a Schlenk flask was added DMAC (0.24 g, 1.1 mmol, 1.1 equiv.) and 10 mL of anhydrous DMF under  $\text{N}_2$ . The suspension was stirred for 30 min at room temperature. 2-(6-fluoropyridin-3-yl)-4,6-diphenyl-1,3,5-triazine (F-py-TRZ) (0.33 g, 1.0 mmol, 1.0 equiv.) was then added and the reaction was heated to reflux for 24 h. The reaction went from white to yellow/orange to dark red with increasing temperature. The reaction was diluted with water, and the organic layer was extracted with DCM (DCM) ( $3 \times 50$  mL). The organic phase was washed with brine, dried over  $\text{Na}_2\text{SO}_4$  and concentrated under reduced pressure. The target product was obtained as a yellow solid after purification by column chromatography on silica gel using 5:1 hexane/DCM as eluent followed by recrystallization in THF/MeOH. (0.30 g). **Yield:** 60%; **Mp:** 260-270°C; **R<sub>f</sub>:** 0.81(cyclohexane/ethyl acetate = 4:1); **<sup>1</sup>H NMR** (500 MHz,  $\text{CDCl}_3$ )  $\delta$ : 9.76 (d,  $J=2.1$ , 1H), 8.82-8.74 (m, 4H), 7.80-7.78 (dd,  $J=7.9$ , 1.0, 2H), 7.63 – 7.55 (m, 5H), 7.52-7.50 (dd,  $J=7.8$ , 1.2, 2H), 7.37-7.30 (m, 1H), 7.25 – 7.22 (m, 1H), 1.60 (s, 4H); **<sup>13</sup>C NMR** (126 MHz,  $\text{CDCl}_3$ )  $\delta$ : 171.58, 170.22, 158.42, 150.44, 141.43, 140.13, 138.30, 136.30, 132.69, 129.06, 128.79, 126.18, 125.21, 125.06, 124.62, 124.05, 110.63, 37.94, 27.51; **HPLC retention time:** 5.039 min; **purity:** 99.98%; **HR-MS** (Xevo G2-XS QTof)  $[\text{M}+\text{H}]^+$  **Calculated:** ( $\text{C}_{35}\text{H}_{27}\text{N}_5$ ) 517.64; **Found:** 518.23.



**Figure 193.  $^1\text{H}$  NMR of DMAC-py-TRZ in  $\text{CDCl}_3$ .**

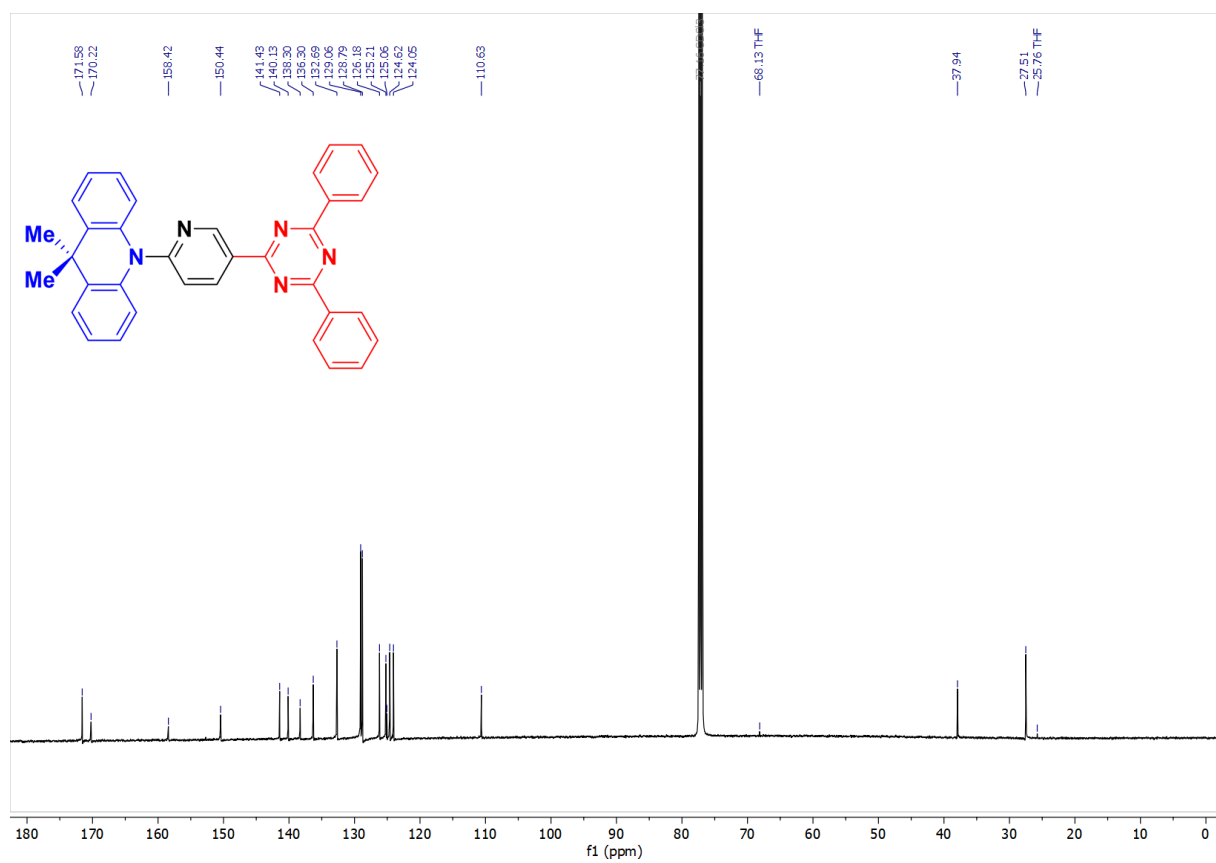


**Figure 194.  $^{13}\text{C}$  NMR of DMAC-py-TRZ in  $\text{CDCl}_3$ .**

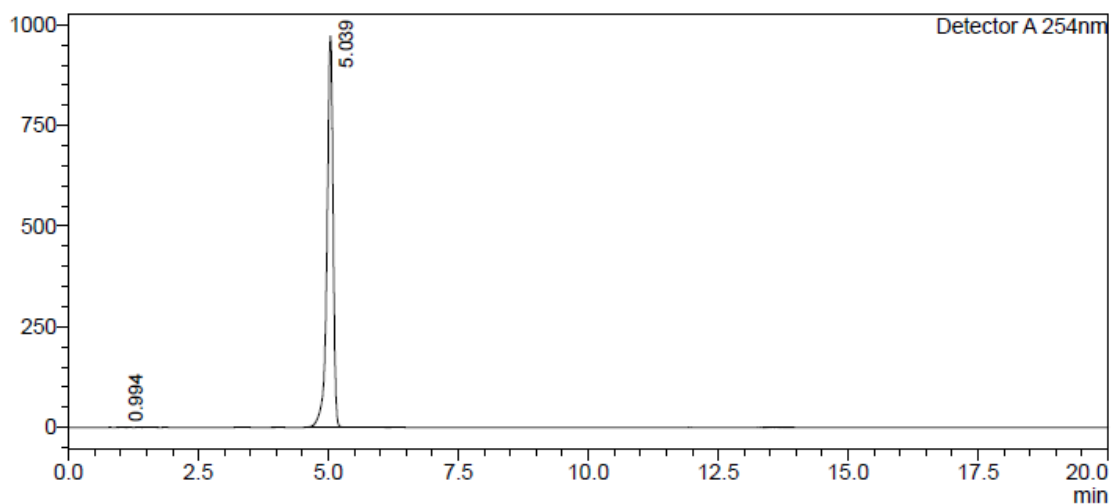
# HPLC Trace Report31Aug2021

## <Sample Information>

Sample Name : EC-2894-DMAC-py-TRZ  
Sample ID :  
Method Filename : 95% Acetonitrile 5 Water 20 mins.lcm  
Batch Filename : EC-2591-2713-2894-DMAC-py-TRZ-recryst-MeCN-95-try2.lcb  
Vial # : 1-5 Sample Type : Unknown  
Injection Volume : 10 uL  
Date Acquired : 31/08/2021 12:13:23 Acquired by : System Administrator  
Date Processed : 31/08/2021 12:33:26 Processed by : System Administrator

## <Chromatogram>

mV



## <Peak Table>

Detector A 254nm

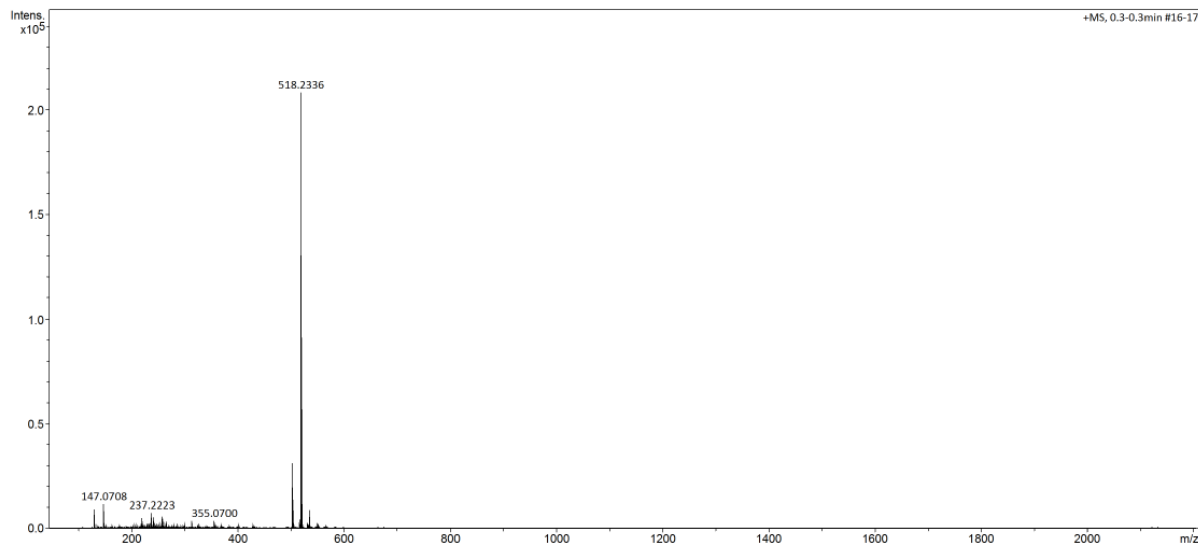
Peak#	Ret. Time	Area	Height	Area%	Area/Height	Width at 5% Height
1	0.994	1528	485	0.019	3.152	--
2	5.039	7924891	970451	99.981	8.166	0.305
Total		7926419	970936	100.000		

Figure 195. HPLC analysis report for DMAC-py-TRZ.

School of Chemistry Mass Spectrometry Service

SampleID  
Sample Description  
Analysis Name D:\Data\stuartwarner\manual\DMAC\_py\_TRZ\_a.d  
Method DIP Pos 3.m  
Instrument maXis impact Source Type APCI Ion Polarity Positive

Submitter  
Supervisor  
Acquisition Date 12/03/2022 17:38:44  
Scan Begin 50 m/z Scan End 2200 m/z



Bruker Compass DataAnalysis 4.3 Analysis Name DMAC\_py\_TRZ\_a.d 12/03/2022 17:41:00 1 of 1

**Figure 196.** HRMS analysis report for **DMAC-py-TRZ**.

## Chapter 7 - Conclusions and future outlooks

The work presented in this thesis focused on the study of novel blue and oriented TADF emitters to achieve high-performing OLEDs. Starting with **ICzTRZ** (Chapter 2), this emitter was the first reported di-functionalized indolocarbazole-based compound and showed an almost-completely horizontal orientation of its TDM in all the host materials that were tested. The strong horizontal orientation was attributed to a combination of the high MW and low molecular thickness of the emitter, and the ability of the host materials to prevent diffusion phenomena during film deposition. The favorable orientation, together with its high  $\Phi_{\text{PL}}$  of 70%, and a short delayed lifetime of 121.1  $\mu\text{s}$  resulted in a highly efficient device with an  $\text{EQE}_{\text{max}}$  of 22.1%, a sky-blue emission at  $\lambda_{\text{EL}}$  of 483 nm (CIE coordinates of 0.17, 0.32), and a high luminance value of 7800  $\text{cd}/\text{m}^2$ .

Literally building upon the **ICzTRZ** structure, a twin-emitter design strategy was used to obtain the novel TADF emitter, **DICzTRZ** (Chapter 3). The main reason behind this design choice was to try and achieve a horizontal orientation of the emitter TDM in solution-processed films. Sadly, this was not the case, as **DICzTRZ** high MW wasn't sufficient to achieve a low  $a$ , and resulted in a non-desirable vertical orientation. Despite this unfortunate result, the twin-emitter design led to an improved RISC rate and thus a shorter-lived delayed fluorescence lifetime, thanks to a much higher density of triplets states. The molar extinction coefficient of the emitter increased compared to its precursor, **ICzTRZ**, together with a slight red-shift in the emission, but it was accompanied by a decrease in the  $\Phi_{\text{PL}}$  of the material (from 63% for **ICzTRZ** to 57% for **DICzTRZ** in 20 wt% doped CzSi film). The combination of the vertical orientation and lower  $\Phi_{\text{PL}}$  resulted in an underperforming solution-processed device with an  $\text{EQE}_{\text{max}}$  of only 8.4%.

Starting again from **ICzTRZ**, three novel TADF emitters were reported, **ICzTRZ-0**, **d'Bu-ICzTRZ-0**, and **d'Bu-ICzTRZ** (Chapter 4). The focus of the project was to understand the effect that the different number and position of *tert*-butyl groups have on the horizontal orientation of the materials. The analysis was based on the review by Teonopala *et al.*<sup>23</sup> and all materials (including the previously reported **ICzTRZ**) followed the trends identified in the review article. All the emitters presented horizontal orientation, and  $a$  being mainly influenced by the MW and the thickness of the emitter.

In the framework of this thesis, **Chapter 4** is the conclusion of our analysis of the **ICzTRZ** family of emitters. However, a few points can be addressed in future research. By looking at the crystal structure of **ICzTRZ** (**Figure 197**)  $\pi$ - $\pi$  interaction between the electron-rich indolocarbazole of one molecule and the electron-poor triazine of a second molecule can be observed. The presence of this interaction could lead to the formation of an exciplex-type system. Concentration-dependent measurements and PL in the crystal need to be done to investigate this phenomenon.

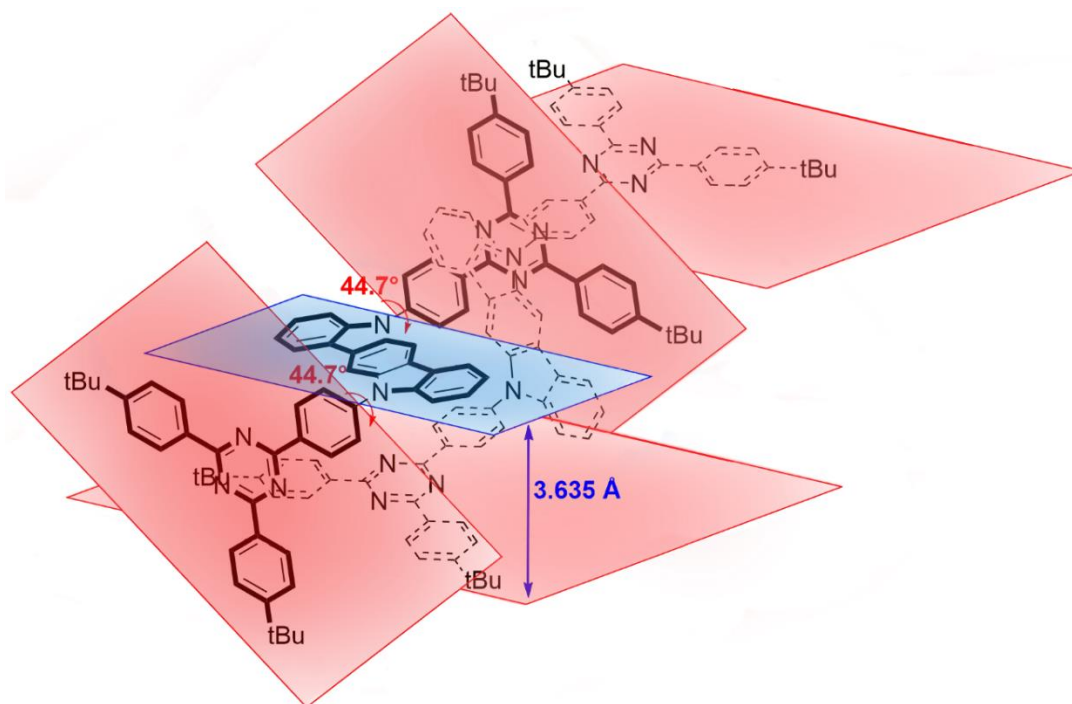


**Figure 197.** Schematic representation of the crystal packing of **ICzTRZ** obtained from X-Ray diffraction.

Moreover, while **ICzTRZ** possesses very good photophysical properties, the emission color doesn't reach the deep-blue coordinate needed for display application. A possible solution would be to replace the distal phenyl rings on the triazine acceptor with adamantyl groups. This strategy was used by Kaji *et al.*,<sup>73</sup> where they were able to synthesize a deep-blue solution-processable material by using di-adamantyl-triazine as an acceptor unit (**Figure 198**). When compared with the diphenyl-triazine counterpart, **DMAC-TRZ**, the lower degree of conjugation of the adamantyl led to a much deeper color of the emission, from  $\lambda_{EL}$  of 495 nm to 450 nm.

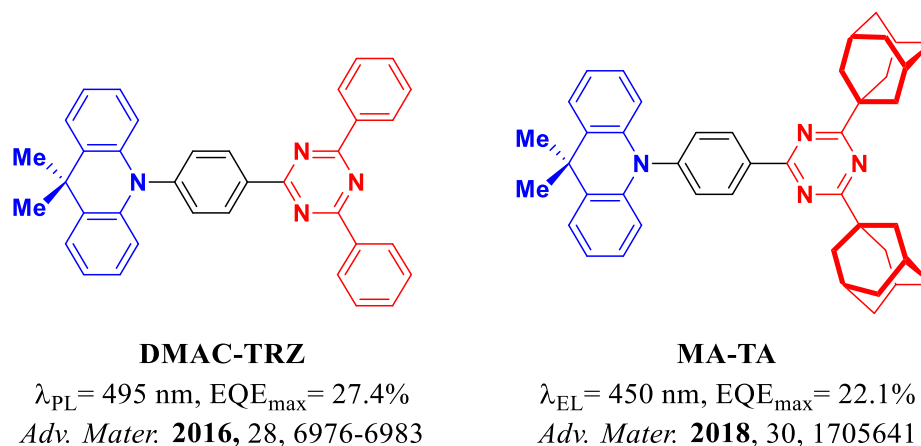


**Figure 198.** Chemical structure and properties of **DMAC-TRZ** and **MA-TA**.

**ICz-TA (Figure 199)** was designed, and future work on this material will ideally lead to a deep-blue and well-oriented TADF emitter. Density functional theory (DFT) and time-dependent DFT (TD-DFT) calculations at the PBE0/6-031G(d,p)<sup>102,103</sup> were carried out to assess the properties of **ICzTA (Figure 200)**. The desired widening of the  $E_{\text{gap}}$  was seen (from 3.44 eV for **ICzTRZ** to 3.52 eV for **ICzTA**), which should lead to a deeper-blue emission color. The excited state profiles are fairly similar between the two materials, with a slight increase in the  $\Delta E_{\text{ST}}$ , from 0.22 eV for **ICzTRZ** to 0.25 eV for **ICz-TA**, and a slight decrease in oscillator strength (from 0.72 for **ICzTRZ** to 0.66 for **ICzTA**), which would most likely indicate that the emitter would not be as bright. Moreover, the new target molecule also possesses intermediate triplet states, as was the case for **ICzTRZ**. The combination of a small  $\Delta E_{\text{ST}}$  and the presence of intermediate triplet states, both beneficial to the RISC process,<sup>128-131</sup> and high oscillator strength makes **ICz-TA** a promising molecule for TADF applications. The main concern for this material is that the removal of the terminal *tert*-butyl groups could lead to a completely insoluble compound, as was the case for **ICzTRZ-0** and **d'Bu-ICzTRZ-0**, which would create problems for some of the optoelectronics characterization.



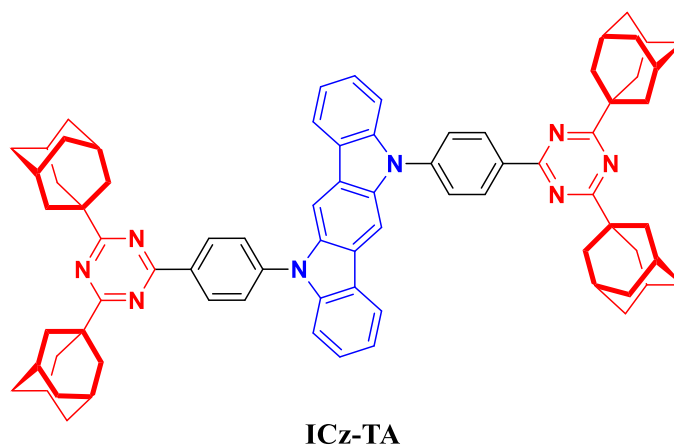


**Figure 199.** Chemical structure of ICzTA.

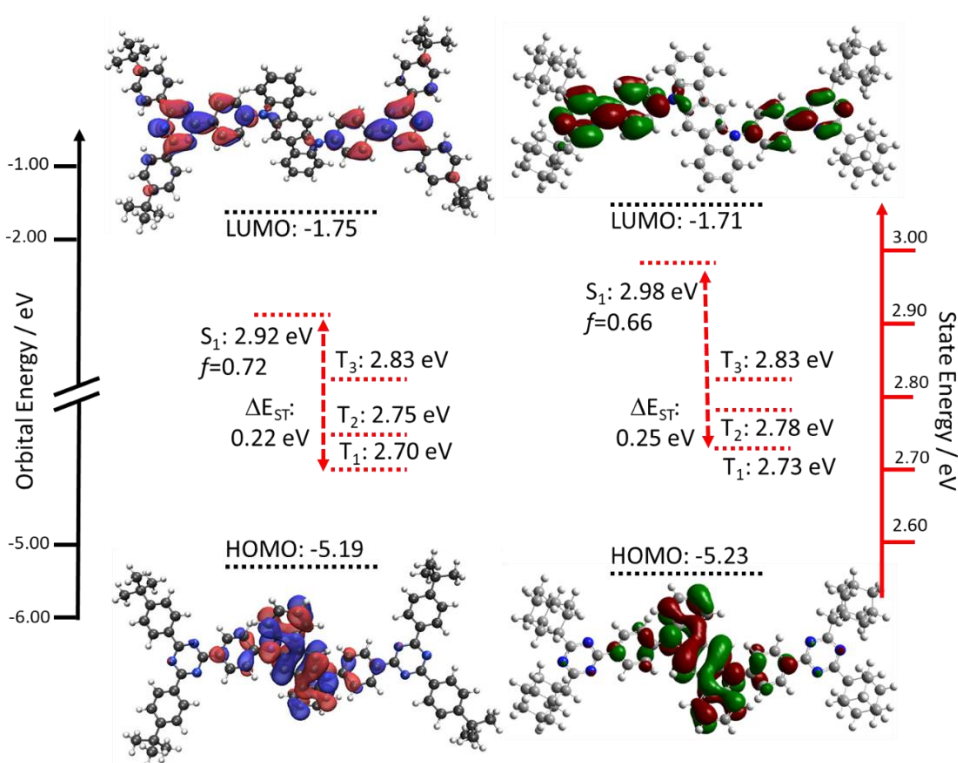


**Figure 200.** HOMO and LUMO electron density distributions and energy levels, excited state energy levels of **ICzTRZ** (left) and **ICzTA** (right). (Obtained via DFT and TD-DFT at the PBE0/6-31G(d,p) level, Isovalue for new surfaces: MO=0.02, Density=0.0004).

The subsequent chapters focused on dimethyl acridine-triazine systems. Using the knowledge obtained from **Chapter 4** and the review article, the previously published emitter **DMAC-TRZ**<sup>72</sup> was modified into five novel TADF emitters, **CNPh-DMAC-TRZ**, **CF<sub>3</sub>Ph-DMAC-TRZ**, **dPh-DMAC-TRZ**, **'BuPh-DMAC-TRZ**, and **OMePh-DMAC-TRZ** (**Chapter 5**). The main reason for these modifications was that the increased molecular weight of the materials could lead to an improved

horizontal orientation; **DMAC-TRZ** has a  $MW < 600 \text{ g mol}^{-1}$  and isotropic orientation, having to rely on higher  $T_g$  hosts to achieve better  $a$  values.<sup>122</sup> The addition of the functionalized phenyl groups would push the MW above  $600 \text{ g mol}^{-1}$ , which should make the orientation dependent on the MW and length of the molecule, as was the case for the functionalized indolocarbazole emitters of **Chapter 4**. Moreover, using phenyl rings functionalized with different EWG and EDG groups produced a Hammett series of materials ( $\sigma$  values are CN +0.66,  $\text{CF}_3$  +0.54, Ph -0.01,  $t\text{Bu}$  -0.20, OMe -0.27),<sup>175</sup> allowing us to study the effect of the different substituents on the photophysics of the materials. In the optimized conditions of 10 wt% doped mCBPCN film, the compounds showed  $\Phi_{\text{PL}}$  of 34%, 70%, 70%, 72%, and 72% for **CNPh-DMAC-TRZ**, **CF<sub>3</sub>Ph-DMAC-TRZ**, **dPh-DMAC-TRZ**, ***t*BuPh-DMAC-TRZ**, **OMePh-DMAC-TRZ**, respectively, revealing an increase in efficiency for the more electron-rich congeners. Angle-dependant luminescence spectroscopy was used to measure the anisotropy factor of 10 wt% evaporated film of the emitters in mCBPCN. All materials presented a preferential horizontal orientation in their TDM, but to our surprise, we couldn't find any discernible trend in their behaviour. OLEDs were then fabricated, with  $\text{EQE}_{\text{max}}$  of 6.0%, 17.8%, 17.7%, 23.8%, and 25.5% at  $\lambda_{\text{EL}}$  of 496 nm, 498 nm, 525 nm, 526 nm, and 531 nm for the devices with **CNPh-DMAC-TRZ**, **CF<sub>3</sub>Ph-DMAC-TRZ**, **dPh-DMAC-TRZ**, ***t*BuPh-DMAC-TRZ**, **OMePh-DMAC-TRZ**, respectively. These results are in line with what was observed in the thin film with the “couple trend” associated with the efficiency of the devices and the Hammett values impacting the emission color. The big remaining open question in this study is to understand whether there is a correlation between TDM orientation of the materials and any specific physical factor. An in-depth host screening and a study of the thermal properties of these materials are currently being carried out to try and find an answer.

The devices with ***t*BuPh-DMAC-TRZ** and **OMePh-DMAC-TRZ** managed to surpass in  $\text{EQE}_{\text{max}}$  the OLED with **DMAC-TRZ**, ( $\text{EQE}_{\text{max}}$  of 20.1%) but showed a red-shifted emission due to the more electron-rich nature of the donor. In **Chapter 6** this point was addressed by introducing a heteroaromatic bridge in the novel emitter **DMAC-py-TRZ**, which has been shown to be a valuable strategy to achieve blue emission, good color purity, and high efficiencies in devices.<sup>59,187</sup> The pyridine bridge led to an unusual crystal structure, which prompted an in-depth computational study. From the theoretical study, **DMAC-py-TRZ** was assumed to exist in a folded geometry in the ground state and then to undergo a large geometrical relaxation to an orthogonal conformation when the molecule was excited. These calculations were then experimentally confirmed. A large Stokes shift was measured in non-polar solvents, and when the material was frozen in a glass, only the blue-shifted

emission of the folded conformer was observed, meaning that the relaxation process was hindered. High  $\Phi_{\text{PL}}$  of 57% and 64% were obtained in 10 wt% film in mCP and PMMA, respectively, at  $\lambda_{\text{PL}}$  of 496 nm and 516 nm. A concentration study in mCP film was carried out and a distribution of conformers at low concentrations was observed, with dual emission originating from both the folded and orthogonal structures. The emission from the orthogonal conformer took over at higher concentrations, which can be caused by an efficient energy transfer from one conformer to the other. In conclusion, the emission was slightly blue-shifted, compared to **DMAC-TRZ**, and the  $\Phi_{\text{PL}}$  was increased by introducing a heteroaromatic spacer between the donor and the acceptor ( $\Phi_{\text{PL}}$  of 47% at  $\lambda_{\text{PL}}$  499 for **DMAC-TRZ** vs  $\Phi_{\text{PL}}$  of 57% at  $\lambda_{\text{PL}}$  496 for **DMAC-py-TRZ** in 10 wt% mCP film), while understanding the conformational effects that such spacer caused.

**Chapter 6** represents the end of my study on the **DMAC-TRZ** derivatives and the end of the work presented in this thesis. With the work on these acridine-triazine systems, the  $\Phi_{\text{PL}}$  of the parent emitter was improved by functionalizing the donor and introducing a heteroaromatic bridge between the D and A units, and carry out an in-depth photophysical study of all the novel material. Efficient devices in terms of  $\text{EQE}_{\text{max}}$  were produced for the 5 extended **DMAC-TRZ** derivatives, and device fabrication will be the immediate next step for **DMAC-py-TRZ**. The anisotropy factor of the material will be measured, as it would be of strong interest to see how the presence of dual conformers would impact the anisotropy factor of the material.

The five different projects presented in this thesis showed the full life cycle of a TADF emitter, starting from the design and synthesis of the material, to both the theoretical and the experimental study of its properties, and its final inclusion in an OLED device, with a particular emphasis on highly horizontally oriented TADF emitters. Hopefully, the results showcased in my thesis will reinforce the importance of controlling orientation to achieve highly efficient OLEDs.

## Experimental section

**General Synthetic Procedures.** All reagents and solvents were obtained from commercial sources and used as received. Air-sensitive reactions were performed under a nitrogen atmosphere using Schlenk techniques, no special precautions were taken to exclude air or moisture during work-up and crystallisation. Flash column chromatography was carried out using silica gel (Silia-P from Silicycle, 60 Å, 40-63 µm). Analytical thin-layer-chromatography (TLC) was performed with silica plates with aluminum backings (250 µm with F-254 indicator). TLC visualization was accomplished by 254/365 nm UV lamp. HPLC analysis was conducted on a Shimadzu LC-40 HPLC system. HPLC traces were performed using a Shim-pack GIST 3µm C18 reverse phase analytical column. GCMS analysis was conducted using a Shimadzu QP2010SE GC-MS equipped with a Shimadzu SH-Rtx-1 column (30 m × 0.25 mm). <sup>1</sup>H, <sup>13</sup>C and <sup>19</sup>F NMR spectra were recorded on a Bruker Advance spectrometer (500 MHz for <sup>1</sup>H, 125 MHz for <sup>13</sup>C, 471 MHz for <sup>19</sup>F). The following abbreviations have been used for multiplicity assignments: “s” for singlet, “d” for doublet, “t” for triplet, “q” for quartet, “m” for multiplet, and “br” for broad. <sup>19</sup>F spectra were recorded with proton decoupling. <sup>1</sup>H and <sup>13</sup>C NMR spectra were referenced residual solvent peaks with respect to TMS (δ = 0 ppm). Melting points were measured using open-ended capillaries on an Electrothermal 1101D Mel-Temp apparatus and are uncorrected.

Concerning specific characterization of the materials discussed in **Chapter 2-4 (ICzTRZ and derivatives)**. The infrared spectra of solid samples were recorded on Bruker IFS 88 and measured by attenuated total reflection (ATR method). Absorption is given in wavenumbers  $\bar{\nu}$  [cm<sup>-1</sup>]. Elemental analysis (EA) was done with an Elementar vario MICRO instrument. The weight scale used was a Sartorius M2P. Electron ionization (EI) and fast atom bombardment (FAB) mass spectrometry were conducted using a Finnigan MAT 90 spectrometer (70 eV). 3-Nitrobenzyl alcohol (3-NBA) was used as the matrix and reference for high resolution mass spectrometry measurements. For the interpretation of the spectra, molecular ions [M]<sup>+</sup>, peaks of pseudo molecules [M+H]<sup>+</sup> and characteristic fragment peaks are indicated with their mass to charge ratio ( $m/z$ ) and in the case of EI MS their intensity in percent, relative to the base peak (100%) is given. In the case of high-resolution measurements, the tolerated error is 0.0005  $m/z$ .

Concerning specific characterization of the materials discussed in **Chapter 5 and 6 (DMAC-TRZ derivatives)**. High-resolution mass spectrometry (HRMS) was performed by the university of Leeds.

Elemental analyses were performed at the School of Geosciences at the University of Edinburgh, using a Thermo Fisher Scientific Flash SMART 2000 instrument. Electron Spray Ionization (ESI) experiments were recorded on a Q-Exactive (Orbitrap) mass spectrometer equipped with a HESI II probe.

***Electrochemistry measurements.*** Cyclic Voltammetry (CV) and Differential Pulse Voltammetry analyses were performed on an Electrochemical Analyzer potentiostat model 620D from CH Instruments. Sample of the different materials were prepared in DCM and MeCN that were degassed by sparging with DCM or MeCN-saturated nitrogen gas for 10 minutes before measurements. All measurements were performed in 0.1 M DCM or MeCN solution of tetrabutylammonium hexafluorophosphate, which was used as the supporting electrolyte. An Ag/Ag<sup>+</sup> electrode was used as the reference electrode while a glassy carbon electrode and a platinum wire were used as the working electrode and counter electrode, respectively. The redox potentials are reported relative to a saturated calomel electrode (SCE) with a ferrocene/ferrocenium (Fc/Fc<sup>+</sup>) redox couple as the internal standard (0.38 V vs SCE for MeCN<sup>188</sup> and 0.46 V vs SCE for DCM<sup>189</sup>). Unless stated otherwise, CV was performed with a scan rate of 100 mV/s and sensitivity of 1e<sup>-5</sup> A/V. Unless stated otherwise, DPV was performed with an increment of potential of 0.01 V, amplitude of 0.05 V, pulse width of 0.06 sec, sample width of 0.02 sec, pulse period 0.05 sec, quiet time of 2 sec, and sensitivity of of 1e<sup>-5</sup> A/V.

***Photophysical measurements.*** Optically dilute solutions of concentrations on the order of 10<sup>-5</sup> M were prepared in HPLC grade methyl-cyclohexane, toluene, DCM, THF and MeCN for absorption and emission analysis. Absorption spectra were recorded at room temperature on a Shimadzu UV-1800 double beam spectrophotometer with a 1 cm quartz cuvette. Molar absorptivity determination was verified by linear least-squares fit of values obtained from at least five independent solutions at varying concentrations from 1×10<sup>-5</sup> M to 3.34×10<sup>-6</sup> M.

Aerated solutions for emission studies were prepared by bubbling with compressed air for 5 minutes and spectra were taken using the same cuvette as for the absorption analysis. Degassed solutions were prepared via three freeze-pump-thaw cycles and spectra were taken using a home-made Schlenk quartz cuvette. Steady-state emission, excitation spectra and time-resolved emission spectra were recorded at 298 K using an Edinburgh Instruments FLS980 and FS5. Samples were excited at 340 nm for both steady-state measurements and time-resolved measurements, unless stated otherwise.

Photoluminescence quantum yields for solutions were determined using the optically dilute method<sup>138</sup> in which four sample solutions with absorbances of ca. 0.09, 0.07, 0.05 and 0.03 at 360 nm were used. The Beer-Lambert law was found to remain linear at the concentrations of the solutions. For each sample, linearity between absorption and emission intensity was verified through linear regression analysis with the Pearson regression factor ( $R^2$ ) for the linear fit of the data set surpassing 0.9. Individual relative quantum yield values were calculated for each solution and the values reported represent the slope obtained from the linear fit of these results. The equation  $\Phi_s = \Phi_r(A_r/A_s)(I_s/I_r)(n_s/n_r)^2$  was used to calculate the relative quantum yield of the sample, where ( $\Phi_r$ ) is the absolute quantum yield of the external reference quinine sulfate ( $\Phi_r = 54.6\%$  in 0.5 M  $H_2SO_4$ ).<sup>190</sup> A stands for the absorbance at the excitation wavelength of 360 nm, I is the integrated area under the corrected emission curve and n is the refractive index of the solvent. The subscripts “s” and “r” representing sample and reference, respectively. The experimental uncertainty in the emission quantum yields is conservatively estimated to be 10%, though we have found that statistically we can reproduce  $\Phi_{PL}$  measurements to 3% relative error. Thin film  $\Phi_{PL}$  measurements were performed using an integrating sphere in a Hamamatsu C9920-02 system. A xenon lamp coupled to a monochromator enabled excitation selectivity, chosen here to be 340 nm. The output was then fed into the integrating sphere via a fibre, exciting the sample. PL spectra were collected with a multimode fibre and detected with a back-thinned CCD. Doped thin films were prepared by mixing sample and host material in solution, followed by spin-casting on a quartz substrate, for measurements carried out at room temperature, or sapphire substrate, for measurements carried out at 77 K. The  $\Phi_{PL}$  of the films were then measured in air and by purging the integrating sphere with flowing  $N_2$  gas. Time-resolved PL measurements of the thin films were carried out using the time-correlated single-photon counting technique. The samples were excited at 378 nm by a pulsed laser diode (Picoquant, model PLS 370) and were kept in a vacuum of  $< 8 \times 10^{-4}$  mbar.

The singlet-triplet splitting energy,  $\Delta E_{ST}$ , was estimated by recording the prompt fluorescence spectra and phosphorescence emission at 77 K. The films were excited either by a Q-switched Nd:YAG laser emitting at 343 nm (Laser-export) or by a femtosecond optical parametric amplifier emitting at 320 nm (Orpheus-N, Light Conversion). Emission from the samples was focused onto a spectrograph (Chromex imaging, 250is spectrograph) and detected on a sensitive gated iCCD camera (Stanford Computer Optics, 4Picos) having subnanosecond resolution. Phosphorescence spectra were measured 1 ms after the 343 nm excitation with iCCD exposure time of 9 ms. Prompt fluorescence spectra were measured 1 ns after the 343 nm excitation with iCCD exposure time of 100 ns.

Time-resolved measurements of the materials discussed in **Chapter 5** (extended **DMAC-TRZ** derivatives) were performed using a spectrograph and a gated iCCD camera (Stanford Computer Optics), where samples were excited with a Nd:YAG laser (EKSPLA), 10 Hz, 355 nm or using a nitrogen laser, 10 Hz, 337 nm, for power dependence measurement.

**Fitting time-resolved luminescence measurements.** Time-resolved PL measurements were fitted to a sum of exponentials decay model with chi-squared ( $\chi^2$ ) values between 1 and 2, using the EI FLS980 software. Each component of the decay is assigned a weight, ( $w_i$ ), which is the contribution of the emission from each component to the total emission.

The average lifetime was then calculated using the following:

Two exponential decay model:

$$\tau_{AVG} = \tau_1 w_1 + \tau_2 w_2 \quad (60)$$

with weight defined as  $w_1 = \frac{A_1 \tau_1}{A_1 \tau_1 + A_2 \tau_2}$  and  $w_2 = \frac{A_2 \tau_2}{A_1 \tau_1 + A_2 \tau_2}$  where  $A_1$  and  $A_2$  are the preexponential-factors of each component.

**Angular dependent photoluminescence spectroscopy.** Thin films of emitter and host were co-evaporated in high vacuum on a pre-cleaned glass substrate. This substrate was then glued with an index matching fluid on a fused-silica prism which was mounted on the rotating stage. The organic film was then irradiated with a UV laser (Kimmon, HeCd laser,  $\lambda=325$  nm) under vertical incidence and was rotated from  $-90^\circ$  to  $+90^\circ$  with respect to the substrate normal. The luminescence was recorded with a grating spectrograph coupled to a liquid-nitrogen cooled charge-coupled device (Princeton Instruments Acton 2300i with PyLoN detector) in s and p polarization mode. P-polarized signal was then subjected to numerical simulation to calculate the anisotropy factor ( $a$ ):

$$a = \frac{\Sigma p_z^2}{\Sigma p^2} \quad (61)$$

Where  $\Sigma p_z^2$  is the sum of the power emitted by vertically oriented dipoles and  $\Sigma p^2$  is the sum of the power emitted by all emitting dipoles.<sup>191</sup> The parameter  $a$  (or synonymously  $\Theta_v = \langle \cos^2 \vartheta \rangle$ ) denotes the second moment of the TDM's angular distribution around the surface normal of the film, where  $\vartheta$  is the angle between the molecule's TDM vector and the said direction. The details about the method can be further found in the reference.<sup>122,191</sup>

**OLED fabrication and testing.** OLED devices of **ICzTRZ** were fabricated using pre-cleaned indium-tin-oxide (ITO) coated glass substrates with ITO thickness of 90 nm. The OLED devices had a pixel size of 2 mm × 1 mm. The small molecules and cathode layers were thermally evaporated using an angstrom deposition chamber at 10<sup>-7</sup> mbar at 0.3 A/s or 0.6 A/s for organic layers and 3 A/s for cathode. OLED testing was performed using a Keithley 2400 sourcemeter and photodiode, assuming that the OLEDs show Lambertian emission. Electroluminescence spectra were collected using an Oriel MS125 spectrograph coupled to an Andor DV420-BU CCD camera.

OLED devices of **DICzTRZ** were fabricated according to following procedure. Before fabrication, the ITO patterned glass substrates were cleaned by sonication in detergent and H<sub>2</sub>O (twice) for 10 minutes, then by hot steam of *isopropanol* for 5 minutes followed by UV-O<sub>3</sub> irradiation for 30 minutes. Subsequently, 50 wt% PEDOT:PSS (CLEVIOUS<sup>TM</sup> P VP CH 8000, Heraeus) : ultrapure H<sub>2</sub>O was spin-coated on cleaned ITO glass substrates at 4000 rpm for 12 s, dried at 150 °C for 10 minutes and cooled at room temperature (RT) with N<sub>2</sub> flow for 5 minutes. 10 mg mL<sup>-1</sup> of PVK (Mw ~ 1,100,000) in 1,2-dichlorobenzene solution was spin-coated onto the PEDOT:PSS layer at 2000 rpm for 30 s, dried at 120 °C for 10 minutes and cooled for at RT with N<sub>2</sub> flow for 5 minutes. 10 mg mL<sup>-1</sup> of emitter in toluene solution was spin-coated on the PVK layer at 2200 rpm for 30 s, dried at 100 °C for 10 minutes and cooled at RT with N<sub>2</sub> flow for 5 minutes. Subsequent layers were vacuum-deposited using deposition apparatus (SE-4260, ALS Technology, Japan) at ~10<sup>-4</sup> Pa. To remove both oxygen and moisture, OLEDs were sealed with glass caps containing getter films in a glove box. Device characterization was performed by an integrating sphere (Hamamatsu Photonics, C9920-12) with Keithley 2400 Source Meter. During this characterization, voltages incremented by 400 mV were applied to devices.



OLEDs devices of the materials discussed in **Chapter 5** (extended **DMAC-TRZ** derivatives) were fabricated on patterned indium tin oxide (ITO)-coated glass (VisionTek Systems) with a sheet resistance of 15  $\Omega$ /sq. Oxygen-plasma cleaned substrates were loaded into a Kurt J. Lesker Super Spectros deposition chamber, and both the small molecule and cathode layers were thermally evaporated at pressure below  $10^{-7}$  mbar. Devices tested in a calibrated 10-inch integrating sphere (Labsphere), and their electrical properties were measured using a source meter (Keithley 2400). Emission spectra were simultaneously measured using a calibrated fiber coupled spectrometer (Ocean optics USB4000). All devices were evaluated at RT (298 K) and under an air atmosphere.

**Theoretical calculations.** For all materials, with the exception of **DMAC-py-TRZ**, all calculations were submitted and processed using in-house developed software, *Silico*, which incorporates a number of publicly available software libraries, including: cclib<sup>192</sup> for parsing of result files, VMD<sup>193</sup>/Tachyon<sup>194</sup> for 3D rendering, Open Babel<sup>195</sup>/Pybel<sup>196</sup> for file interconversion. All ground state optimizations have been carried out at the density functional theory (DFT) level with Gaussian 16<sup>197</sup> in the gas phase. Excited state calculation with TD-DFT calculation (Tamm-Dancoff approximation)<sup>116</sup> used the PBE0<sup>198</sup> functional and the 6-31G(d,p) basis set<sup>103</sup> for all materials with the exception of **DMAC-py-TRZ**, where the M062X<sup>104</sup> functional and the 6-31G(d) basis set were used.<sup>103</sup> Excited-state calculations were performed using time-dependent DFT (TD-DFT) within the Tamm-Dancoff approximation (TDA)<sup>115,116</sup> using the same functional and basis set as for ground state geometry optimization. This methodology has been demonstrated to show quantitative estimate of  $\Delta E_{ST}$  in comparison to experiment.<sup>199</sup>

## Appendix

### Molecular structures

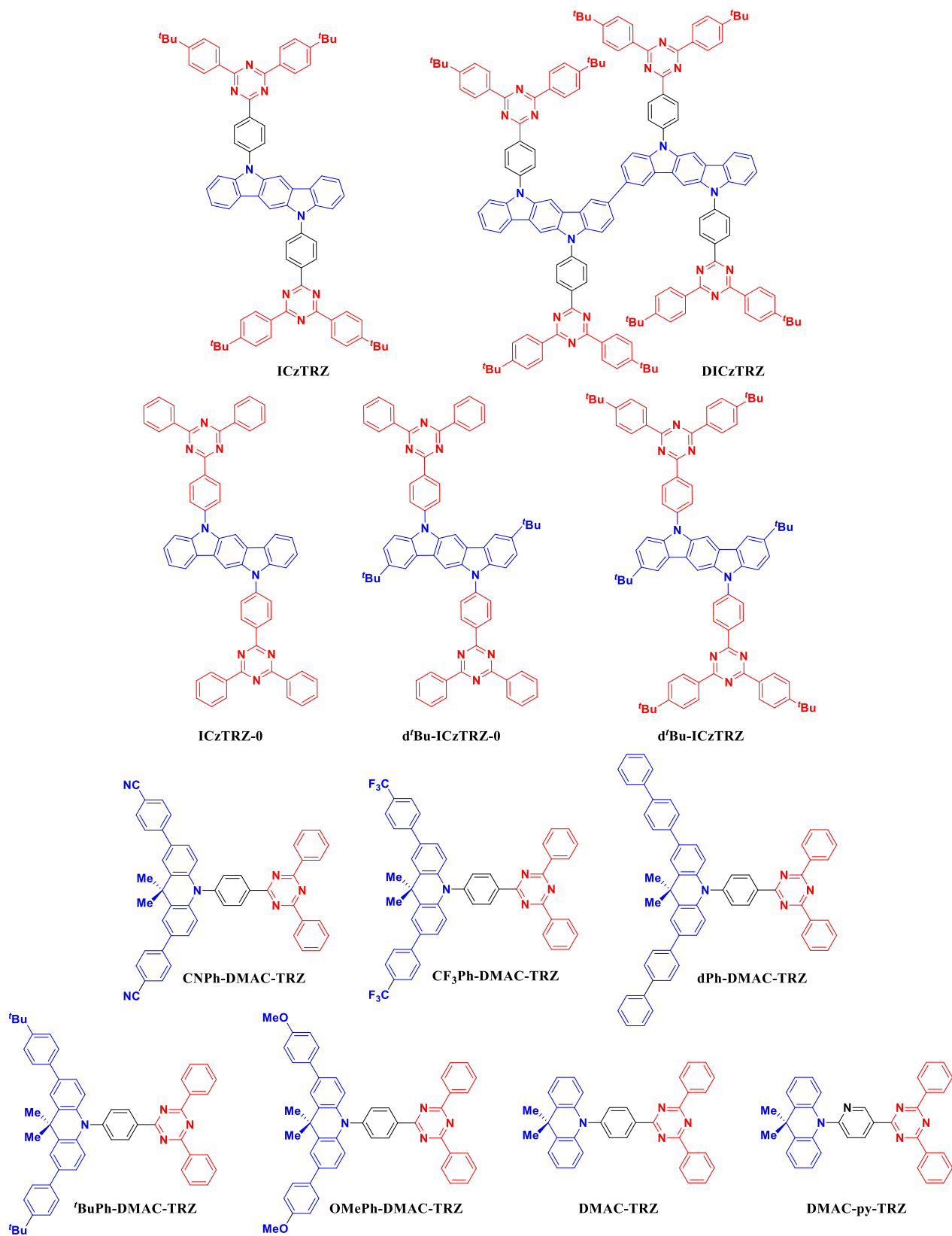


**Figure 201.** Molecular structure of the emitters studied in this thesis.

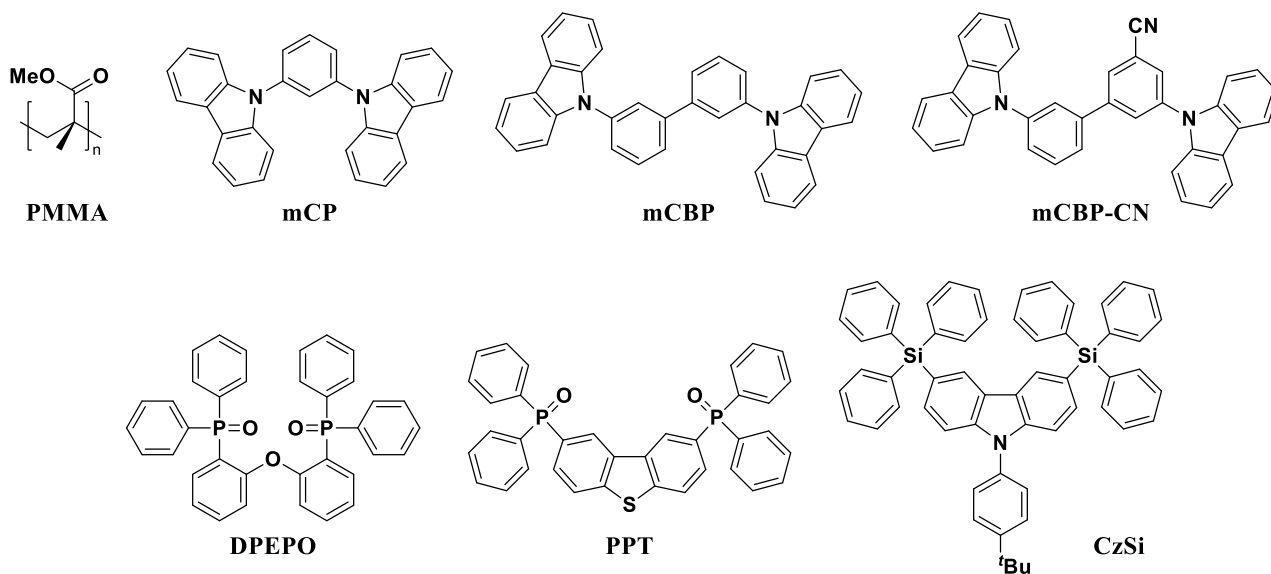


**Figure 202.** Molecular structure of the host materials utilized in this thesis.

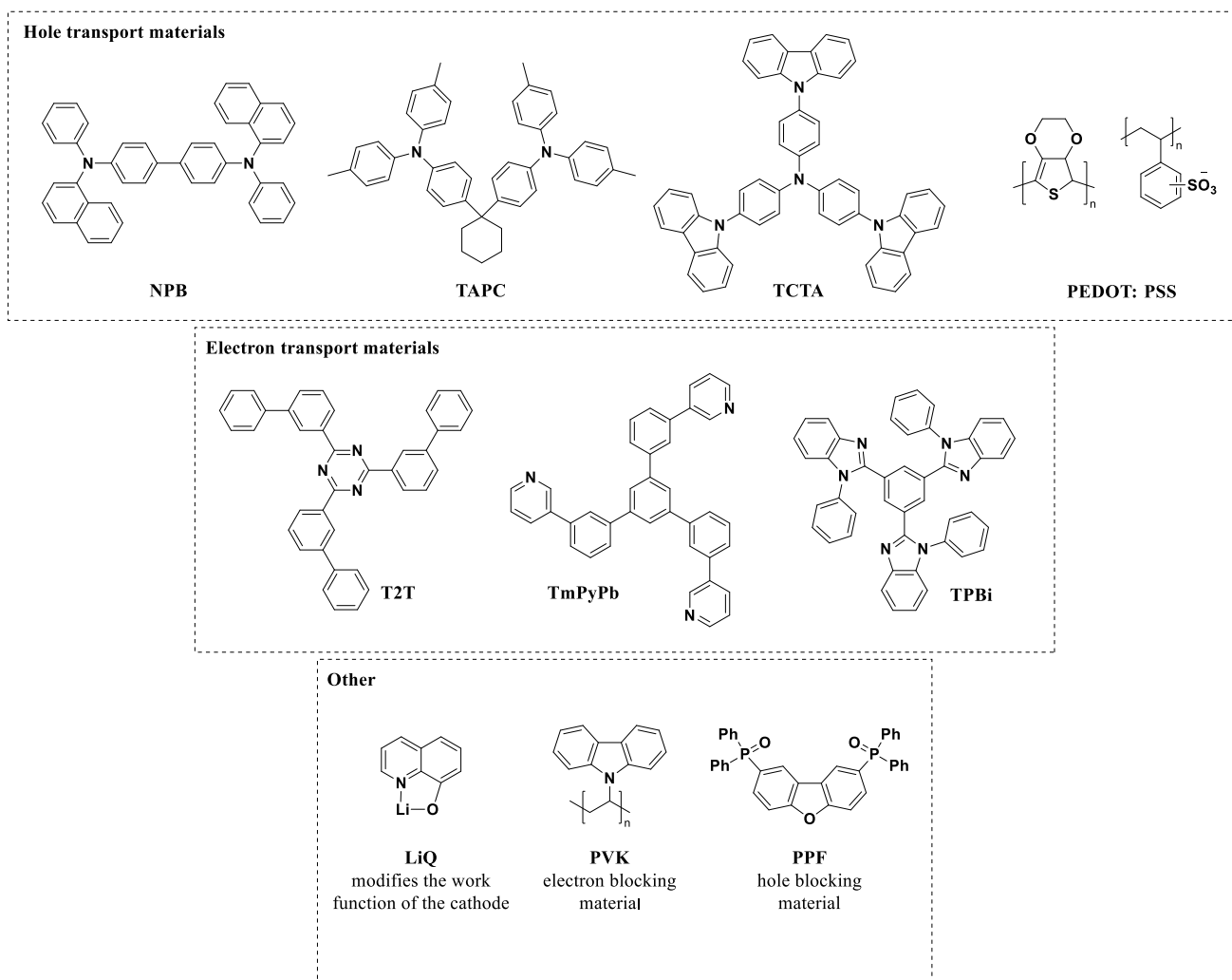


**Figure 203.** Molecular structure of the materials used for device fabrication.

## References

- (1) Wong, M. Y.; Zysman-Colman, E. Purely Organic Thermally Activated Delayed Fluorescence Materials for Organic Light-Emitting Diodes. *Adv. Mater.* **2017**, *29*, 1605444. <https://doi.org/10.1002/adma.201605444>.
- (2) Salehi, A.; Fu, X.; Shin, D. H.; So, F. Recent Advances in OLED Optical Design. *Adv. Funct. Mater.* **2019**, *29* (15), 1–21. <https://doi.org/10.1002/adfm.201808803>.
- (3) Tang, C. W.; Vanslyke, S. A. Organic Electroluminescent Diodes. *Appl. Phys. Lett.* **1987**, *51* (12), 913–915. <https://doi.org/10.1063/1.98799>.
- (4) Baldo, M. A.; O'Brien, D. F.; You, Y.; Shoustikov, A.; Sibley, S.; Thompson, M. E.; Forrest, S. R. Highly Efficient Phosphorescent Emission from Organic Electroluminescent Devices. *Nature* **1998**, *395* (6698), 151–154. <https://doi.org/10.1038/25954>.
- (5) Liu, H.; Cheng, G.; Hu, D.; Shen, F.; Lv, Y.; Sun, G.; Yang, B.; Lu, P.; Ma, Y. A Highly Efficient, Blue-Phosphorescent Device Based on a Wide-Bandgap Host/FIrpic: Rational Design of the Carbazole and Phosphine Oxide Moieties on Tetraphenylsilane. *Adv. Funct. Mater.* **2012**, *22* (13), 2830–2836. <https://doi.org/10.1002/adfm.201103126>.
- (6) Lee, C. W.; Lee, J. Y. Above 30% External Quantum Efficiency in Blue Phosphorescent Organic Light-Emitting Diodes Using Pyrido[2,3-b]Indole Derivatives as Host Materials. *Adv. Mater.* **2013**, *25* (38), 5450–5454. <https://doi.org/10.1002/adma.201301091>.
- (7) Wang, Q.; Oswald, I. W. H.; Yang, X.; Zhou, G.; Jia, H.; Qiao, Q.; Chen, Y.; Hoshikawa-Halbert, J.; Gnade, B. E. A Non-Doped Phosphorescent Organic Light-Emitting Device with above 31% External Quantum Efficiency. *Adv. Mater.* **2014**, *26* (48), 8107–8113. <https://doi.org/10.1002/adma.201402947>.
- (8) El-Sayed, M. A. The Triplet State: Its Radiative and Nonradiative Properties. *Acc. Chem. Res.* **1968**, *1* (1), 8–16. <https://doi.org/10.1021/ar50001a002>.
- (9) Zhang, Y.; Lee, J.; Forrest, S. R. Tenfold Increase in the Lifetime of Blue Phosphorescent Organic Light-Emitting Diodes. *Nat. Commun.* **2014**, *5*, 1–7. <https://doi.org/10.1038/ncomms6008>.
- (10) Henwood, A. F.; Zysman-Colman, E. Lessons Learned in Tuning the Optoelectronic Properties of Phosphorescent Iridium(III) Complexes. *Chem. Commun.* **2017**, *53* (5), 807–826. <https://doi.org/10.1039/c6cc06729h>.
- (11) Mackenzie, C. F. R.; Zhang, L.; Cordes, D. B.; Alexandra, M. Z.; Samuel, I. D. W.; Zysman-colman, E. Bulky Iridium NHC Complexes for Bright, Efficient Deep-Blue OLEDs. *Adv. Opt. Mater.* **2022**, *001*, 2201495. <https://doi.org/10.1002/adom.202201495>.
- (12) Wong, M. Y.; Zysman-Colman, E. Purely Organic Thermally Activated Delayed Fluorescence Materials for Organic Light-Emitting Diodes. *Adv. Mater.* **2017**, *29* (22), 1605444. <https://doi.org/10.1002/adma.201605444>.
- (13) Parker, C. A.; Hatchard, C. G. Delayed Fluorescence of Pyrene in Ethanol. *Trans. Faraday Soc.* **1963**, *59*, 284–295. <https://doi.org/10.1039/TF9635900284>.
- (14) Parker, C. A.; Hatchard, C. G. Triplet-Singlet Emission in Fluid Solutions. Phosphorescence of Eosin. *Trans. Faraday Soc.* **1961**, *57*, 1894–1904. <https://doi.org/10.1039/TF9615701894>.
- (15) Lewis, G. N.; Lipkin, D. Reversible Photochemical Processes in Rigid Media. a Study of the Phosphorescent State. *J. Am. Chem. Soc.* **1941**, *63* (11), 3005–3018.

<https://doi.org/10.1021/ja01856a043>.

- (16) Salazar, F. A.; Fedorov, A.; Berberan-Santos, M. N. A Study of Thermally Activated Delayed Fluorescence in C60. *Chem. Phys. Lett.* **1997**, *271* (4–6), 361–366. [https://doi.org/10.1016/S0009-2614\(97\)00469-7](https://doi.org/10.1016/S0009-2614(97)00469-7).
- (17) Endo, A.; Sato, K.; Yoshimura, K.; Kai, T.; Kawada, A.; Miyazaki, H.; Adachi, C. Efficient Up-Conversion of Triplet Excitons into a Singlet State and Its Application for Organic Light Emitting Diodes. *Appl. Phys. Lett.* **2011**, *98* (8), 118–121. <https://doi.org/10.1063/1.3558906>.
- (18) Uoyama, H.; Goushi, K.; Shizu, K.; Nomura, H.; Adachi, C. Highly Efficient Organic Light-Emitting Diodes from Delayed Fluorescence. *Nature* **2012**, *492* (7428), 234–238. <https://doi.org/10.1038/nature11687>.
- (19) Zhang, Q.; Li, B.; Huang, S.; Nomura, H.; Tanaka, H.; Adachi, C. Efficient Blue Organic Light-Emitting Diodes Employing Thermally Activated Delayed Fluorescence. *Nat. Photonics* **2014**, *8* (4), 326–332. <https://doi.org/10.1038/nphoton.2014.12>.
- (20) Monkman, A. Why Do We Still Need a Stable Long Lifetime Deep Blue OLED Emitter? *ACS Appl. Mater. Interfaces* **2021**, 20463–20467. <https://doi.org/10.1021/acsami.1c09189>.
- (21) Sharma, N. “Through Space Interactions in Thermally Activated Delayed Fluorescent Emitters - Novel Materials and Organic Light Emitting Diodes,” 2019.
- (22) Chatterjee, T.; Wong, K. T. Perspective on Host Materials for Thermally Activated Delayed Fluorescence Organic Light Emitting Diodes. *Adv. Opt. Mater.* **2019**, *7* (1), 1–34. <https://doi.org/10.1002/adom.201800565>.
- (23) Tenopala-Carmona, F.; Lee, O. S.; Crovini, E.; Neferu, A. M.; Murawski, C.; Olivier, Y.; Zysman-Colman, E.; Gather, M. C. Identification of the Key Parameters for Horizontal Transition Dipole Orientation in Fluorescent and TADF Organic Light-Emitting Diodes. *Adv. Mater.* **2021**, *33* (2100677). <https://doi.org/10.1002/adma.202100677>.
- (24) Mills, I.; Cvita, T.; Homann, K.; Kallay, N.; Kozokuchitsu, K. *IUPAC Gren Book*; 1993.
- (25) Verhoeven, J. W. Glossary of Terms Used in Photochemistry (IUPAC Recommendations 1996). *Pure Appl. Chem.* **1996**, *68* (12), 2223–2286. <https://doi.org/10.1351/pac199668122223>.
- (26) Union, I.; Pure, O. F.; Chemistry, A. Glossary of Terms in Quantities and Units in Clinical Chemistry (IUPAC-IFCC Recommendations 1996). *Pure Appl. Chem.* **1996**, *68* (4), 957–1000. <https://doi.org/10.1351/pac199668040957>.
- (27) *Encyclopedia Britannica*; 2022.
- (28) Demchenko, A. P.; Heldt, J.; Waluk, J.; Chou, P.-T.; Sengupta, P. K.; Brizhik, L.; del Valle, J. C. Michael Kasha: From Photochemistry and Flowers to Spectroscopy and Music. *Angew. Chemie Int. Ed.* **2014**, *53* (52), 14316–14324. <https://doi.org/10.1002/anie.201405222>.
- (29) Köhler, A.; Bäessler, H. Triplet States in Organic Semiconductors. *Mater. Sci. Eng. R Reports* **2009**, *66* (4–6), 71–109. <https://doi.org/10.1016/j.mser.2009.09.001>.
- (30) Alfvén, H.; Neel, L. The Energy Gap Law for Radiationless Transitions in Large Molecules. *Physics*, **1970**, *18* (2), 301–343. <https://doi.org/10.1016/b978-0-444-40993-5.50013-9>.
- (31) Fetter, S.; Mozley, R. Emission And Absorption Of Radiation. *Sci. Glob. Secur.* **1990**, *1* (3–4), 265–285. <https://doi.org/10.1080/08929889008426335>.

- (32) Gather M. C., Köhnen A., and M. K. White Organic Light-Emitting Diodes. *Adv. Mater.* **2011**, *23*, 233–248. <https://doi.org/10.1002/adma.201002636>.
- (33) Murawski C. , Leo K., and G. M. C. Efficiency Roll-Off in Organic Light-Emitting Diodes. *Adv. Mater.* **2013**, *25*, 6801–6827. <https://doi.org/10.1002/adma.201301603>.
- (34) Fröbel, M.; Fries, F.; Schwab, T.; Lenk, S.; Leo, K.; Gather, M. C.; Reineke, S. Three-Terminal RGB Full-Color OLED Pixels for Ultrahigh Density Displays. *Sci. Rep.* **2018**, *8* (1), 1–7. <https://doi.org/10.1038/s41598-018-27976-z>.
- (35) Xin, J.; Li, Z.; Liu, Y.; Liu, D.; Zhu, F.; Wang, Y.; Yan, D. High-Efficiency Non-Doped Deep-Blue Fluorescent Organic Light-Emitting Diodes Based on Carbazole/Phenanthroimidazole Derivatives. *J. Mater. Chem. C* **2020**, *8* (30), 10185–10190. <https://doi.org/10.1039/d0tc02594a>.
- (36) Lee, C. W. L. and J. Y. Above 30 External Quantum Efficiency in Blue Phosphorescent Organic Light-Emitting. *Adv. Mater.* **2013**, *25*, 5450–5454. <https://doi.org/10.1002/adma.201301091>.
- (37) Kim, S. Y.; Kim, J. J. Outcoupling Efficiency of Organic Light Emitting Diodes and the Effect of ITO Thickness. *Org. Electron. physics, Mater. Appl.* **2010**, *11* (6), 1010–1015. <https://doi.org/10.1016/j.orgel.2010.03.023>.
- (38) Sei-Yong Kim, Won-Ik Jeong, Christian Mayr, Young-Seo Park, K.-H. K.; Jeong-Hwan Lee, Chang-Ki Moon, Brütting W., and K. J.-J. Organic Light-Emitting Diodes with 30% External Quantum Efficiency Based on a Horizontally Oriented Emitter. *Adv. Funct. Mater.* **2013**, *23*, 3896–3900. <https://doi.org/10.1002/adfm.201300104>.
- (39) Shin, H.; Ha, Y. H.; Kim, H. G.; Kim, R.; Kwon, S. K.; Kim, Y. H.; Kim, J. J. Controlling Horizontal Dipole Orientation and Emission Spectrum of Ir Complexes by Chemical Design of Ancillary Ligands for Efficient Deep-Blue Organic Light-Emitting Diodes. *Adv. Mater.* **2019**, *31* (21), 1–6. <https://doi.org/10.1002/adma.201808102>.
- (40) Dongdong Zhang, Juan Qiao, Deqiang Zhang, and L. D. Ultrahigh-Efficiency Green PHOLEDs with a Voltage under 3 V and a Power Efficiency of Nearly 110 Lm W<sup>-1</sup> at Luminance of 10 000 Cd M<sup>-2</sup>. *Adv. Mater.* **2017**, No. 1702847. <https://doi.org/10.1002/adma.201702847>.
- (41) Lu, G. Z.; Zhu, Q.; Liu, L.; Wu, Z. G.; Zheng, Y. X.; Zhou, L.; Zuo, J. L.; Zhang, H. Pure Red Iridium(III) Complexes Possessing Good Electron Mobility with 1,5-Naphthyridin-4-Ol Derivatives for High-Performance OLEDs with an EQE over 31%. *ACS Appl. Mater. Interfaces* **2019**, *11* (22), 20192–20199. <https://doi.org/10.1021/acsami.9b02558>.
- (42) Jian-Yong Hu, Yong-Jin Pu, Satoh F. , Kawata S. , Katagiri H. , Sasabe H., and K. J. Bisanthracene-Based Donor Acceptor-type Light-Emitting Dopants Highly Efficient. *Adv. Funct. Mater.* **2014**, *24*, 2064–2071. <https://doi.org/10.1002/adfm.201302907>.
- (43) Chou, P. Y.; Chou, H. H.; Chen, Y. H.; Su, T. H.; Liao, C. Y.; Lin, H. W.; Lin, W. C.; Yen, H. Y.; Chen, I. C.; Cheng, C. H. Efficient Delayed Fluorescence via Triplet–Triplet Annihilation for Deep-Blue Electroluminescence. *Chem. Commun.* **2014**, *50* (52), 6869–6871. <https://doi.org/10.1039/c4cc01851f>.
- (44) Kukhta, N. A.; Matulaitis, T.; Volyniuk, D.; Ivaniuk, K.; Turyk, P.; Stakhira, P.; Grazulevicius, J. V.; Monkman, A. P. Deep-Blue High-Efficiency TTA OLED Using Para- and Meta-Conjugated Cyanotriphenylbenzene and Carbazole Derivatives as Emitter and Host. *J. Phys. Chem. Lett.* **2017**, *8* (24), 6199–6205.

<https://doi.org/10.1021/acs.jpcclett.7b02867>.

- (45) Chen, W. C.; Lee, C. S.; Tong, Q. X. Blue-Emitting Organic Electrofluorescence Materials: Progress and Prospective. *J. Mater. Chem. C* **2015**, *3* (42), 10957–10963. <https://doi.org/10.1039/c5tc02420j>.
- (46) Lee, J. H.; Chen, C. H.; Lee, P. H.; Lin, H. Y.; Leung, M. K.; Chiu, T. L.; Lin, C. F. Blue Organic Light-Emitting Diodes: Current Status, Challenges, and Future Outlook. *J. Mater. Chem. C* **2019**, *7* (20), 5874–5888. <https://doi.org/10.1039/c9tc00204a>.
- (47) Cai, X.; Su, S. J. Marching Toward Highly Efficient, Pure-Blue, and Stable Thermally Activated Delayed Fluorescent Organic Light-Emitting Diodes. *Adv. Funct. Mater.* **2018**, *28* (43), 1–33. <https://doi.org/10.1002/adfm.201802558>.
- (48) Bui, T.-T.; Goubard, F.; Ibrahim-Ouali, M.; Gigmes, D.; Dumur, F. Thermally Activated Delayed Fluorescence Emitters for Deep Blue Organic Light Emitting Diodes: A Review of Recent Advances. *Appl. Sci.* **2018**, *8* (4), 494. <https://doi.org/10.3390/app8040494>.
- (49) Dias, F. B.; Penfold, T. J.; Monkman, A. P. Photophysics of Thermally Activated Delayed Fluorescence Molecules. *Methods Appl. Fluoresc.* **2017**, *5* (1), 012001. <https://doi.org/10.1088/2050-6120/aa537e>.
- (50) Zhang, Q.; Li, J.; Shizu, K.; Huang, S.; Hirata, S.; Miyazaki, H.; Adachi, C. Design of Efficient Thermally Activated Delayed Fluorescence Materials for Pure Blue Organic Light Emitting Diodes. *J. Am. Chem. Soc.* **2012**, *134* (36), 14706–14709. <https://doi.org/10.1021/ja306538w>.
- (51) Etherington, M. K.; Gibson, J.; Higginbotham, H. F.; Penfold, T. J.; Monkman, A. P. Revealing the Spin-Vibronic Coupling Mechanism of Thermally Activated Delayed Fluorescence. *Nat. Commun.* **2016**, *7*, 1–7. <https://doi.org/10.1038/ncomms13680>.
- (52) Zysman-Colman, E. Molecular Designs Offer Fast Exciton Conversion. *Nat. Photonics* **2020**, *14* (10), 593–594. <https://doi.org/10.1038/s41566-020-0696-8>.
- (53) Liu, Y.; Li, C.; Ren, Z.; Yan, S.; Bryce, M. R. All-Organic Thermally Activated Delayed Fluorescence Materials for Organic Light-Emitting Diodes. *Nat. Rev. Mater.* **2018**, *3*, 18020. <https://doi.org/10.1038/natrevmats.2018.20>.
- (54) Milián-Medina, B.; Gierschner, J. Computational Design of Low Singlet-Triplet Gap All-Organic Molecules for OLED Application. *Org. Electron.* **2012**, *13* (6), 985–991. <https://doi.org/10.1016/j.orgel.2012.02.010>.
- (55) Zhang, Q.; Kuwabara, H.; Potscavage, W. J.; Huang, S.; Hatae, Y.; Shibata, T.; Adachi, C. Anthraquinone-Based Intramolecular Charge-Transfer Compounds: Computational Molecular Design, Thermally Activated Delayed Fluorescence, and Highly Efficient Red Electroluminescence. *J. Am. Chem. Soc.* **2014**, *136* (52), 18070–18081. <https://doi.org/10.1021/ja510144h>.
- (56) Cui, L. S.; Nomura, H.; Geng, Y.; Kim, J. U. k.; Nakanotani, H.; Adachi, C. Controlling Singlet-Triplet Energy Splitting for Deep-Blue Thermally Activated Delayed Fluorescence Emitters. *Angew. Chemie - Int. Ed.* **2017**, *56* (6), 1571–1575. <https://doi.org/10.1002/anie.201609459>.
- (57) Huang, W.; Einzinger, M.; Zhu, T.; Chae, H. S.; Jeon, S.; Ihn, S. G.; Sim, M.; Kim, S.; Su, M.; Teverovskiy, G.; Wu, T.; Van Voorhis, T.; Swager, T. M.; Baldo, M. A.; Buchwald, S. L. Molecular Design of Deep Blue Thermally Activated Delayed Fluorescence Materials

Employing a Homoconjugative Triptycene Scaffold and Dihedral Angle Tuning. *Chem. Mater.* **2018**, *30* (5), 1462–1466. <https://doi.org/10.1021/acs.chemmater.7b03490>.

- (58) Wang, Y. K.; Huang, C. C.; Ye, H.; Zhong, C.; Khan, A.; Yang, S. Y.; Fung, M. K.; Jiang, Z. Q.; Adachi, C.; Liao, L. S. Through Space Charge Transfer for Efficient Sky-Blue Thermally Activated Delayed Fluorescence (TADF) Emitter with Unconjugated Connection. *Adv. Opt. Mater.* **2019**, *1901150*, 1–7. <https://doi.org/10.1002/adom.201901150>.
- (59) Rajamalli, P.; Chen, D.; Li, W.; Samuel, I. D. W.; Cordes, D. B.; Slawin, A. M. Z.; Zysman-Colman, E. Enhanced Thermally Activated Delayed Fluorescence through Bridge Modification in Sulfone-Based Emitters Employed in Deep Blue Organic Light-Emitting Diodes. *J. Mater. Chem. C* **2019**, *7* (22), 6664–6671. <https://doi.org/10.1039/c9tc01498e>.
- (60) Dos Santos, P. L.; Chen, D.; Rajamalli, P.; Matulaitis, T.; Cordes, D. B.; Slawin, A. M. Z.; Jacquemin, D.; Zysman-Colman, E.; Samuel, I. D. W. Use of Pyrimidine and Pyrazine Bridges as a Design Strategy to Improve the Performance of Thermally Activated Delayed Fluorescence Organic Light Emitting Diodes. *ACS Appl. Mater. Interfaces* **2019**, *11* (48), 45171–45179. <https://doi.org/10.1021/acsami.9b16952>.
- (61) Liu, M.; Komatsu, R.; Cai, X.; Hotta, K.; Sato, S.; Liu, K.; Chen, D.; Kato, Y.; Sasabe, H.; Ohisa, S.; Suzuri, Y.; Yokoyama, D.; Su, S. J.; Kido, J. Horizontally Orientated Sticklike Emitters: Enhancement of Intrinsic Out-Coupling Factor and Electroluminescence Performance. *Chem. Mater.* **2017**, *29* (20), 8630–8636. <https://doi.org/10.1021/acs.chemmater.7b02403>.
- (62) Yokoyama, D.; Sakaguchi, A.; Suzuki, M.; Adachi, C. Horizontal Orientation of Linear-Shaped Organic Molecules Having Bulky Substituents in Neat and Doped Vacuum-Deposited Amorphous Films. *Org. Electron.* **2009**, *10* (1), 127–137. <https://doi.org/10.1016/j.orgel.2008.10.010>.
- (63) Lai, C. C.; Huang, M. J.; Chou, H. H.; Liao, C. Y.; Rajamalli, P.; Cheng, C. H. M-Indolocarbazole Derivative as a Universal Host Material for RGB and White Phosphorescent OLEDs. *Adv. Funct. Mater.* **2015**, *25* (34), 5548–5556. <https://doi.org/10.1002/adfm.201502079>.
- (64) Hall, D.; Stavrou, K.; Duda, E.; Danos, A.; Bagnich, S.; Warriner, S.; Slawin, A. M. Z.; Beljonne, D.; Köhler, A.; Monkman, A.; Olivier, Y.; Zysman-Colman, E. Diindolocarbazole - Achieving Multi-resonant Thermally Activated Delayed Fluorescence without the Need for Acceptor Units. *Mater. Horizons* **2022**, *9* (3), 1068–1080. <https://doi.org/10.1039/d1mh01383a>.
- (65) Xiang, S.; Lv, X.; Sun, S.; Zhang, Q.; Huang, Z.; Guo, R.; Gu, H.; Liu, S.; Wang, L. To Improve the Efficiency of Thermally Activated Delayed Fluorescence OLEDs by Controlling the Horizontal Orientation through Optimizing Stereoscopic and Linear Structures of Indolocarbazole Isomers. *J. Mater. Chem. C* **2018**, *6* (21), 5812–5820. <https://doi.org/10.1039/c8tc01419a>.
- (66) Maeng, J. H.; Ahn, D. H.; Lee, H.; Jung, Y. H.; Karthik, D.; Lee, J. Y.; Kwon, J. H. Rigid Indolocarbazole Donor Moiety for Highly Efficient Thermally Activated Delayed Fluorescent Device. *Dye. Pigment.* **2020**, *180* (March), 108485. <https://doi.org/10.1016/j.dyepig.2020.108485>.
- (67) Zhang, Z.; Crovini, E.; dos Santos, P. L.; Naqvi, B. A.; Cordes, D. B.; Slawin, A. M. Z.; Sahay, P.; Brütting, W.; Samuel, I. D. W.; Bräse, S.; Zysman-Colman, E. Efficient Sky-Blue Organic Light-Emitting Diodes Using a Highly Horizontally Oriented Thermally Activated



Delayed Fluorescence Emitter. *Adv. Opt. Mater.* **2020**.  
<https://doi.org/10.1002/adom.202001354>.

- (68) Naqvi, B. A.; Schmid, M.; Crovini, E.; Sahay, P.; Naujoks, T.; Rodella, F.; Zhang, Z.; Strohriegl, P.; Bräse, S.; Zysman-Colman, E.; Brütting, W. What Controls the Orientation of TADF Emitters? *Front. Chem.* **2020**, *8*, 750. <https://doi.org/10.3389/fchem.2020.00750>.
- (69) Meerwein, H. “Über Den Reaktionsmechanismus Der Umwandlung von Borneol in Camphen; [Dritte Mitteilung Über Pinakolinumlagerungen.]” *Justus Liebig’s Ann. der Chemie.* **1914**, *405*, 129–175.
- (70) Vagner, G. “In ‘Protokol Zasedaniya Otdeleniya Khimii R. F. Khimicheskago Obshestva. 9-Go Sentyabrya 1899 Goda [Minutes of the Meeting of the Chemistry Section of the Russian Physical-Chemical Society. 9th September 1899].”” *J. Russ. Phys. Chem. Soc.* **1899**, *31*, 680–684.
- (71) Zhu, C.; Ji, X.; You, D.; Chen, T. L.; Mu, A. U.; Barker, K. P.; Klivansky, L. M.; Liu, Y.; Fang, L. Extraordinary Redox Activities in Ladder-Type Conjugated Molecules Enabled by B ← N Coordination-Promoted Delocalization and Hyperconjugation. *J. Am. Chem. Soc.* **2018**, *140* (51), 18173–18182. <https://doi.org/10.1021/jacs.8b11337>.
- (72) Tsai, W. L.; Huang, M. H.; Lee, W. K.; Hsu, Y. J.; Pan, K. C.; Huang, Y. H.; Ting, H. C.; Sarma, M.; Ho, Y. Y.; Hu, H. C.; Chen, C. C.; Lee, M. T.; Wong, K. T.; Wu, C. C. A Versatile Thermally Activated Delayed Fluorescence Emitter for Both Highly Efficient Doped and Non-Doped Organic Light Emitting Devices. *Chem. Commun.* **2015**, *51* (71), 13662–13665. <https://doi.org/10.1039/c5cc05022g>.
- (73) Wada, Y.; Kubo, S.; Kaji, H. Adamantyl Substitution Strategy for Realizing Solution-Processable Thermally Stable Deep-Blue Thermally Activated Delayed Fluorescence Materials. *Adv. Mater.* **2018**, *30* (8), 1705641. <https://doi.org/10.1002/adma.201705641>.
- (74) Wada, Y.; Nakagawa, H.; Kaji, H. Acceleration of Reverse Intersystem Crossing Using Different Types of Charge Transfer States. *Chem. - An Asian J.* **2021**, *16* (9), 1073–1076. <https://doi.org/10.1002/asia.202100091>.
- (75) Feng, Q.; Qian, Y.; Wang, H.; Hou, W.; Peng, X.; Xie, S.; Wang, S.; Xie, L. Donor Arylmethylation toward Horizontally Oriented TADF Emitters for Efficient Electroluminescence with 37% External Quantum Efficiency. *Adv. Opt. Mater.* **2022**, *10* (10), 1–9. <https://doi.org/10.1002/adom.202102441>.
- (76) Ito, H.; Shimizu, T.; Wada, Y.; Kaji, H.; Fukagawa, H. Comprehensive Study on Operational Lifetime of Organic Light-Emitting Diodes: Effects of Molecular Structure and Energy Transfer. *Jpn. J. Appl. Phys.* **2021**, *60* (4). <https://doi.org/10.35848/1347-4065/abec51>.
- (77) Takahashi, T.; Shizu, K.; Yasuda, T.; Togashi, K.; Adachi, C. Donor–Acceptor-Structured 1,4-Diazatriphenylene Derivatives Exhibiting Thermally Activated Delayed Fluorescence: Design and Synthesis, Photophysical Properties and OLED Characteristics. *Sci. Technol. Adv. Mater.* **2014**, *15* (3), 034202.
- (78) Lin, T. A.; Chatterjee, T.; Tsai, W. L.; Lee, W. K.; Wu, M. J.; Jiao, M.; Pan, K. C.; Yi, C. L.; Chung, C. L.; Wong, K. T.; Wu, C. C. Sky-Blue Organic Light Emitting Diode with 37% External Quantum Efficiency Using Thermally Activated Delayed Fluorescence from Spiroacridine-Triazine Hybrid. *Adv. Mater.* **2016**, *28* (32), 6976–6983. <https://doi.org/10.1002/adma.201601675>.
- (79) Maeng, J. H.; Ahn, D. H.; Lee, H.; Jung, Y. H.; Karthik, D. Rigid Indolocarbazole Donor

Moiety for Highly Efficient Thermally Activated Delayed Fluorescent Device. *Dye. Pigment.* **2020**, 108485. <https://doi.org/10.1016/j.dyepig.2020.108485>.

- (80) Liu, T.; Deng, C.; Duan, K.; Tsuboi, T.; Niu, S.; Wang, D.; Zhang, Q. Zero-Zero Energy-Dominated Degradation in Blue Organic Light-Emitting Diodes Employing Thermally Activated Delayed Fluorescence. *ACS Appl. Mater. Interfaces* **2022**, *14* (19), 22332–22340. <https://doi.org/10.1021/acsami.2c02623>.
- (81) Rodella, F.; Saxena, R.; Bagnich, S.; Banevičius, D.; Kreiza, G.; Athanasopoulos, S.; Juršėnas, S.; Kazlauskas, K.; Köhler, A.; Strohmriegl, P. Low Efficiency Roll-off Blue TADF OLEDs Employing a Novel Acridine-Pyrimidine Based High Triplet Energy Host. *J. Mater. Chem. C* **2021**, *9* (48), 17471–17482. <https://doi.org/10.1039/d1tc03598c>.
- (82) Rodella, F.; Bagnich, S.; Duda, E.; Meier, T.; Kahle, J.; Athanasopoulos, S.; Köhler, A.; Strohmriegl, P. High Triplet Energy Host Materials for Blue TADF OLEDs—A Tool Box Approach. *Front. Chem.* **2020**, *8*, 1–16. <https://doi.org/10.3389/fchem.2020.00657>.
- (83) Sun, D.; Si, C.; Wang, T.; Zysman-colman, E. 1,3,5-Triazine-Functionalized Thermally Activated Delayed Fluorescence Emitters for Organic Light-Emitting Diodes. *Adv. Photonics Res.* **2022**, 2200203. <https://doi.org/10.1002/adpr.202200203>.
- (84) An, Z. F.; Chen, R. F.; Yin, J.; Xie, G. H.; Shi, H. F.; Tsuboi, T.; Huang, W. Conjugated Asymmetric Donor-Substituted 1,3,5-Triazines: New Host Materials for Blue Phosphorescent Organic Light-Emitting Diodes. *Chem. - A Eur. J.* **2011**, *17* (39), 10871–10878. <https://doi.org/10.1002/chem.201101118>.
- (85) Dong, S. C.; Zhang, L.; Liang, J.; Cui, L. S.; Li, Q.; Jiang, Z. Q.; Liao, L. S. Rational Design of Dibenzothiophene-Based Host Materials for PHOLEDs. *J. Phys. Chem. C* **2014**, *118* (5), 2375–2384. <https://doi.org/10.1021/jp412107g>.
- (86) Wang, H.; Xie, L.; Peng, Q.; Meng, L.; Wang, Y.; Yi, Y.; Wang, P. Novel Thermally Activated Delayed Fluorescence Materials-Thioxanthone Derivatives and Their Applications for Highly Efficient OLEDs. *Adv. Mater.* **2014**, *26* (30), 5198–5204. <https://doi.org/10.1002/adma.201401393>.
- (87) Kitamoto, Y.; Namikawa, T.; Ikemizu, D.; Miyata, Y.; Suzuki, T.; Kita, H.; Sato, T.; Oi, S. Light Blue and Green Thermally Activated Delayed Fluorescence from 10H-Phenoxaborin-Derivatives and Their Application to Organic Light-Emitting Diodes. *J. Mater. Chem. C* **2015**, *3* (35), 9122–9130. <https://doi.org/10.1039/c5tc01380a>.
- (88) Sagara, Y.; Shizu, K.; Tanaka, H.; Miyazaki, H.; Goushi, K.; Kaji, H.; Adachi, C. Highly Efficient Thermally Activated Delayed Fluorescence Emitters with a Small Singlet-triplet Energy Gap and Large Oscillator Strength. *Chem. Lett.* **2015**, *44* (3), 360–362. <https://doi.org/10.1246/cl.141054>.
- (89) Tanaka, H.; Shizu, K.; Nakanotani, H.; Adachi, C. Dual Intramolecular Charge-Transfer Fluorescence Derived from a Phenothiazine-Triphenyltriazine Derivative. *J. Phys. Chem. C* **2014**, *118* (29), 15985–15994. <https://doi.org/10.1021/jp501017f>.
- (90) Lee, S. Y.; Yasuda, T.; Park, I. S.; Adachi, C. X-Shaped Benzoylbenzophenone Derivatives with Crossed Donors and Acceptors for Highly Efficient Thermally Activated Delayed Fluorescence. *Dalt. Trans.* **2015**, *44* (18), 8356–8359. <https://doi.org/10.1039/c4dt03608e>.
- (91) Mei, L.; Hu, J.; Cao, X.; Wang, F.; Zheng, C.; Tao, Y.; Zhang, X.; Huang, W. The Inductive-Effect of Electron Withdrawing Trifluoromethyl for Thermally Activated Delayed Fluorescence: Tunable Emission from Tetra- to Penta-Carbazole in Solution Processed Blue

- OLEDs. *Chem. Commun.* **2015**, 51 (65), 13024–13027. <https://doi.org/10.1039/c5cc04126k>.
- (92) Tao, Y.; Yang, C.; Qin, J. Organic Host Materials for Phosphorescent Organic Light-Emitting Diodes. *Chem. Soc. Rev.* **2011**, 40 (5), 2943–2970. <https://doi.org/10.1039/c0cs00160k>.
- (93) Han, C.; Zhao, Y.; Xu, H.; Chen, J.; Deng, Z.; Ma, D.; Li, Q.; Yan, P. A Simple Phosphine-Oxide Host with a Multi-Insulating Structure: High Triplet Energy Level for Efficient Blue Electrophosphorescence. *Chem. - A Eur. J.* **2011**, 17 (21), 5800–5803. <https://doi.org/10.1002/chem.201100254>.
- (94) Dos Santos, P. L.; Ward, J. S.; Bryce, M. R.; Monkman, A. P. Using Guest-Host Interactions to Optimize the Efficiency of TADF OLEDs. *J. Phys. Chem. Lett.* **2016**, 7 (17), 3341–3346. <https://doi.org/10.1021/acs.jpcclett.6b01542>.
- (95) Lee, S. Y.; Yasuda, T.; Yang, Y. S.; Zhang, Q.; Adachi, C. Luminous Butterflies: Efficient Exciton Harvesting by Benzophenone Derivatives for Full-Color Delayed Fluorescence OLEDs. *Angew. Chemie - Int. Ed.* **2014**, 53 (25), 6402–6406. <https://doi.org/10.1002/anie.201402992>.
- (96) Cho, Y. J.; Chin, B. D.; Jeon, S. K.; Lee, J. Y. 20% External Quantum Efficiency in Solution-Processed Blue Thermally Activated Delayed Fluorescent Devices. *Adv. Funct. Mater.* **2015**, 25 (43), 6786–6792. <https://doi.org/10.1002/adfm.201502995>.
- (97) Elementary Quantum Chemistry. In *A Chemist's Guide to Density Functional Theory*; John Wiley & Sons, Ltd, 2001; pp 3–18. <https://doi.org/https://doi.org/10.1002/3527600043.ch1>.
- (98) Density functional theory. (2023, January 30). [https://en.wikipedia.org/wiki/Density\\_functional\\_theory](https://en.wikipedia.org/wiki/Density_functional_theory).
- (99) The Hohenberg-Kohn Theorems. In *A Chemist's Guide to Density Functional Theory*; John Wiley & Sons, Ltd, 2001; pp 33–40. <https://doi.org/https://doi.org/10.1002/3527600043.ch4>.
- (100) The Kohn-Sham Approach. In *A Chemist's Guide to Density Functional Theory*; John Wiley & Sons, Ltd, 2001; pp 41–64. <https://doi.org/https://doi.org/10.1002/3527600043.ch5>.
- (101) Beck, A. D. Density-Functional Thermochemistry. III. The Role of Exact Exchange. *J. Chem. Phys.* **1993**, 98 (7), 5648–5656.
- (102) Adamo, C.; Barone, V. Toward Reliable Density Functional Methods without Adjustable Parameters: The PBE0 Model. *J. Chem. Phys.* **1999**, 110 (13), 6158–6170. <https://doi.org/10.1063/1.478522>.
- (103) Dunning, T. H. Gaussian Basis Sets for Use in Correlated Molecular Calculations. I. The Atoms Boron through Neon and Hydrogen. *J. Chem. Phys.* **1989**, 90 (2), 1007–1023. <https://doi.org/10.1063/1.456153>.
- (104) Zhao, Y.; Truhlar, D. G. The M06 Suite of Density Functionals for Main Group Thermochemistry, Thermochemical Kinetics, Noncovalent Interactions, Excited States, and Transition Elements: Two New Functionals and Systematic Testing of Four M06-Class Functionals and 12 Other Function. *Theor. Chem. Acc.* **2008**, 120 (1–3), 215–241. <https://doi.org/10.1007/s00214-007-0310-x>.
- (105) Petersson, G. A.; Bennett, A.; Tensfeldt, T. G.; Al-Laham, M. A.; Shirley, W. A.; Mantzaris, J. A Complete Basis Set Model Chemistry. I. The Total Energies of Closed-Shell Atoms and Hydrides of the First-Row Elements. *J. Chem. Phys.* **1988**, 89 (4), 2193–2218. <https://doi.org/10.1063/1.455064>.

- (106) Al-Laham, G. A. P. and M. A. A Complete Basis Set Model Chemistry. II. Open-Shell Systems and the Total Energies of the First-Row Atoms. *J. Chem. Phys.* **1988**, *94* (4), 6081–6090. <https://doi.org/10.1063/1.455064>.
- (107) Basis Set (Chemistry). (2023, January 2).
- (108) Density Functional Theory. In *Computational Chemistry*; John Wiley & Sons, Ltd, 2001; pp 42–48. <https://doi.org/https://doi.org/10.1002/0471220655.ch5>.
- (109) Using Existing Basis Sets. In *Computational Chemistry*; John Wiley & Sons, Ltd, 2001; pp 78–91. <https://doi.org/https://doi.org/10.1002/0471220655.ch10>.
- (110) Hall, D. L. S. Computational Design, Synthesis and Optoelectronic Characterisation of Thermally Activated Delayed Fluorescent Materials - Donor-Acceptor and Multi-Resonance Designs, 2022.
- (111) Time-dependent density functional theory. (2022, December 20). [https://en.wikipedia.org/wiki/Time-dependent\\_density\\_functional\\_theory](https://en.wikipedia.org/wiki/Time-dependent_density_functional_theory).
- (112) Dreuw, A.; Head-Gordon, M. Single-Reference Ab Initio Methods for the Calculation of Excited States of Large Molecules. *Chem. Rev.* **2005**, *105* (11), 4009–4037. <https://doi.org/10.1021/cr0505627>.
- (113) Marques, M. A. L.; Maitra, N. T.; Nogueira, F. M. S.; Gross, E. K. U.; Rubio, A. *Fundamentals of Time-Dependent DFT*; 2012; Vol. 837.
- (114) Bauernschmitt, R.; Ahlrichs, R. Treatment of Electronic Excitations within the Adiabatic Approximation of Time Dependent Density Functional Theory. *Chem. Phys. Lett.* **1996**, *256* (4–5), 454–464. [https://doi.org/10.1016/0009-2614\(96\)00440-X](https://doi.org/10.1016/0009-2614(96)00440-X).
- (115) Grimme, S. Density Functional Calculations with Configuration Interaction for the Excited States of Molecules. *Chem. Phys. Lett.* **1996**, *259*, 128–137. [https://doi.org/10.1016/0009-2614\(96\)00722-1](https://doi.org/10.1016/0009-2614(96)00722-1).
- (116) Hirata, S.; Head-Gordon, M. Time-Dependent Density Functional Theory within the Tamm-Dancoff Approximation. *Chem. Phys. Lett.* **1999**, *314* (3–4), 291–299. [https://doi.org/10.1016/S0009-2614\(99\)01149-5](https://doi.org/10.1016/S0009-2614(99)01149-5).
- (117) Muccioli, L.; Son, W.-J.; Olivier, Y.; Sancho-García, J. C.; Moral, M. Theoretical Rationalization of the Singlet–Triplet Gap in OLEDs Materials: Impact of Charge-Transfer Character. *J. Chem. Theory Comput.* **2014**, *11* (1), 168–177. <https://doi.org/10.1021/ct500957s>.
- (118) Barnes, W. L. Fluorescence near Interfaces: The Role of Photonic Mode Density. *J. Mod. Opt.* **1998**, *45* (4), 661–699. <https://doi.org/10.1080/09500349808230614>.
- (119) Wasey, J. A. E.; Barnes, W. L. Efficiency of Spontaneous Emission from Planar Microcavities. *J. Mod. Opt.* **2000**, *47* (4), 725–741. <https://doi.org/10.1080/09500340008233393>.
- (120) Neyts, K. A. Simulation of Light Emission from Thin-Film Microcavities. *J. Opt. Soc. Am. A* **1998**, *15* (4), 962. <https://doi.org/10.1364/JOSAA.15.000962>.
- (121) Furno, M.; Meerheim, R.; Thomschke, M.; Hofmann, S.; Lüssem, B.; Leo, K. Outcoupling Efficiency in Small-Molecule OLEDs: From Theory to Experiment. *Light. Diodes Mater. Devices, Appl. Solid State Light. XIV* **2010**, 7617, 761716. <https://doi.org/10.1117/12.840043>.
- (122) Schmidt, T. D.; Lampe, T.; Daniel Sylvinson, M. R.; Djurovich, P. I.; Thompson, M. E.;

- Brütting, W. Emitter Orientation as a Key Parameter in Organic Light-Emitting Diodes. *Phys. Rev. Appl.* **2017**, *8* (3), 37001. <https://doi.org/10.1103/PhysRevApplied.8.037001>.
- (123) Komino, T.; Sagara, Y.; Tanaka, H.; Oki, Y.; Nakamura, N.; Fujimoto, H.; Adachi, C. Electroluminescence from Completely Horizontally Oriented Dye Molecules. *Appl. Phys. Lett.* **2016**, *108* (24), 8–13. <https://doi.org/10.1063/1.4954163>.
- (124) Mayr, C.; Brütting, W. Control of Molecular Dye Orientation in Organic Luminescent Films by the Glass Transition Temperature of the Host Material. *Chem. Mater.* **2015**, *27* (8), 2759–2762. <https://doi.org/10.1021/acs.chemmater.5b00062>.
- (125) Tanaka, M.; Noda, H.; Nakanotani, H.; Adachi, C. Molecular Orientation of Disk-Shaped Small Molecules Exhibiting Thermally Activated Delayed Fluorescence in Host-Guest Films. *Appl. Phys. Lett.* **2020**, *116* (2), 023302. <https://doi.org/10.1063/1.5140210>.
- (126) Byeon, S. Y.; Kim, J.; Lee, D. R.; Han, S. H.; Forrest, S. R.; Lee, J. Y. Nearly 100% Horizontal Dipole Orientation and Upconversion Efficiency in Blue Thermally Activated Delayed Fluorescent Emitters. *Adv. Opt. Mater.* **2018**, *6* (15), 1701340. <https://doi.org/10.1002/adom.201701340>.
- (127) Kaji, H.; Suzuki, H.; Fukushima, T.; Shizu, K.; Suzuki, K.; Kubo, S.; Komino, T.; Oiwa, H.; Suzuki, F.; Wakamiya, A.; Murata, Y.; Adachi, C. Purely Organic Electroluminescent Material Realizing 100% Conversion from Electricity to Light. *Nat. Commun.* **2015**, *6*, 8476. <https://doi.org/10.1038/ncomms9476>.
- (128) Santos, P. L.; Ward, J. S.; Data, P.; Batsanov, A. S.; Bryce, M. R.; Dias, F. B.; Monkman, A. P. Engineering the Singlet-Triplet Energy Splitting in a TADF Molecule. *J. Mater. Chem. C* **2016**, *4* (17), 3815–3824. <https://doi.org/10.1039/c5tc03849a>.
- (129) Hosokai, T.; Matsuzaki, H.; Nakanotani, H.; Tokumaru, K.; Tsutsui, T.; Furube, A.; Nasu, K.; Nomura, H.; Yahiro, M.; Adachi, C. By Delocalized Excited States. *Sci. Adv.* **2017**, *3*, 1603282. <https://doi.org/10.1126/sciadv.1603282>.
- (130) Noda, H.; Nakanotani, H.; Adachi, C. Excited State Engineering for Efficient Reverse Intersystem Crossing. *Sci. Adv.* **2018**, *4* (6), eaao6910. <https://doi.org/10.1126/sciadv.aao6910>.
- (131) Samanta, P. K.; Kim, D.; Coropceanu, V.; Brédas, J. L. Up-Conversion Intersystem Crossing Rates in Organic Emitters for Thermally Activated Delayed Fluorescence: Impact of the Nature of Singlet vs Triplet Excited States. *J. Am. Chem. Soc.* **2017**, *139* (11), 4042–4051. <https://doi.org/10.1021/jacs.6b12124>.
- (132) Sharma, N.; Spuling, E.; Mattern, C. M.; Li, W.; Fuhr, O.; Tsuchiya, Y.; Adachi, C.; Bräse, S.; Samuel, I. D. W.; Zysman-Colman, E. Turn on of Sky-Blue Thermally Activated Delayed Fluorescence and Circularly Polarized Luminescence (CPL): Via Increased Torsion by a Bulky Carbazolophane Donor. *Chem. Sci.* **2019**, *10* (27), 6689–6696. <https://doi.org/10.1039/c9sc01821b>.
- (133) Chen, D.; Rajamalli, P.; Tenopala-Carmona, F.; Carpenter-Warren, C. L.; Cordes, D. B.; Keum, C. M.; Slawin, A. M. Z.; Gather, M. C.; Zysman-Colman, E. Bipyridine-Containing Host Materials for High Performance Yellow Thermally Activated Delayed Fluorescence-Based Organic Light Emitting Diodes with Very Low Efficiency Roll-Off. *Adv. Opt. Mater.* **2020**, *8* (1), 1901283. <https://doi.org/10.1002/adom.201901283>.
- (134) Li, Z.; Li, W.; Keum, C.; Archer, E.; Zhao, B.; Slawin, A. M. Z.; Huang, W.; Gather, M. C.; Samuel, I. D. W.; Zysman-Colman, E. 1,3,4-Oxadiazole-Based Deep Blue Thermally

Activated Delayed Fluorescence Emitters for Organic Light Emitting Diodes. *J. Phys. Chem. C* **2019**, *123* (40), 24772–24785. <https://doi.org/10.1021/acs.jpcc.9b08479>.

- (135) Wong, M. Y.; Krotkus, S.; Copley, G.; Li, W.; Murawski, C.; Hall, D.; Hedley, G. J.; Jaricot, M.; Cordes, D. B.; Slawin, A. M. Z.; Olivier, Y.; Beljonne, D.; Muccioli, L.; Moral, M.; Sancho-Garcia, J. C.; Gather, M. C.; Samuel, I. D. W.; Zysman-Colman, E. Deep-Blue Oxadiazole-Containing Thermally Activated Delayed Fluorescence Emitters for Organic Light-Emitting Diodes. *ACS Appl. Mater. Interfaces* **2018**, *10* (39), 33360–33372. <https://doi.org/10.1021/acsami.8b11136>.
- (136) Liptay, W. Electrochromism and Solvatochromism. *Angew. Chem. Int. Ed.* **1969**, *8* (3). <https://doi.org/10.1002/anie.196901771>.
- (137) Serevičius, T.; Skaisgiris, R.; Fiodorova, I.; Kreiza, G.; Banevičius, D.; Kazlauskas, K.; Tumkevičius, S.; Juršėnas, S. Single-Exponential Solid-State Delayed Fluorescence Decay in TADF Compounds with Minimized Conformational Disorder. *J. Mater. Chem. C* **2021**, *9* (3), 836–841. <https://doi.org/10.1039/d0tc05503d>.
- (138) Crosby, G. A.; Demas, J. N. Measurement of Photoluminescence Quantum Yields. Review. *J. Phys. Chem.* **1971**, *75* (8), 991–1024. <https://doi.org/10.1021/j100678a001>.
- (139) Song, F.; Xu, Z.; Zhang, Q.; Zhao, Z.; Zhang, H.; Zhao, W.; Qiu, Z.; Qi, C.; Zhang, H.; Sung, H. H. Y.; Williams, I. D.; Lam, J. W. Y.; Zhao, Z.; Qin, A.; Ma, D.; Tang, B. Z. Highly Efficient Circularly Polarized Electroluminescence from Aggregation-Induced Emission Luminogens with Amplified Chirality and Delayed Fluorescence. *Adv. Funct. Mater.* **2018**, *28* (17), 1800051. <https://doi.org/10.1002/adfm.201800051>.
- (140) Lee, Y. H.; Lee, W.; Lee, T.; Jung, J.; Yoo, S.; Lee, M. H. Achieving over 36% EQE in Blue OLEDs Using Rigid TADF Emitters Based on Spiro-Donor and Spiro-B-Heterotriangulene Acceptors. *Chem. Eng. J.* **2023**, *452* (P2), 139387. <https://doi.org/10.1016/j.cej.2022.139387>.
- (141) Cha, J. R.; Lee, C. W.; Lee, J. Y.; Gong, M. S. Design of Ortho-Linkage Carbazole-Triazine Structure for High-Efficiency Blue Thermally Activated Delayed Fluorescent Emitters. *Dye. Pigment.* **2016**, *134*, 562–568. <https://doi.org/10.1016/j.dyepig.2016.08.023>.
- (142) Park, H. J.; Han, S. H.; Lee, J. Y. A Directly Coupled Dual Emitting Core Based Molecular Design of Thermally Activated Delayed Fluorescent Emitters. *J. Mater. Chem. C* **2017**, *5* (46), 12143–12150. <https://doi.org/10.1039/c7tc03133e>.
- (143) Cho Y. J, Jeon S. K., Lee S., Yu E., and L. J. Y. Donor Interlocked Molecular Design for Fluorescence-like Narrow Emission in Deep Blue Thermally Activated Delayed Fluorescent Emitters. *Chem. Mater* **2016**, *28*, 5400–5405. <https://doi.org/10.1021/acs.chemmater.6b01484>.
- (144) Cho, Y. J.; Jeon, S. K.; Chin, B. D.; Yu, E.; Lee, J. Y. The Design of Dual Emitting Cores for Green Thermally Activated Delayed Fluorescent Materials. *Angew. Chemie - Int. Ed.* **2015**, *54* (17), 5201–5204. <https://doi.org/10.1002/anie.201412107>.
- (145) Kim, M.; Jeon, S. K.; Hwang, S. H.; Lee, S. S.; Yu, E.; Lee, J. Y. Highly Efficient and Color Tunable Thermally Activated Delayed Fluorescent Emitters Using a “Twin Emitter” Molecular Design. *Chem. Commun.* **2016**, *52* (2), 339–342. <https://doi.org/10.1039/c5cc07999c>.
- (146) Wei, D.; Ni, F.; Wu, Z.; Zhu, Z.; Zou, Y.; Zheng, K.; Chen, Z.; Ma, D.; Yang, C. Designing Dual Emitting Cores for Highly Efficient Thermally Activated Delayed Fluorescent Emitters. *J. Mater. Chem. C* **2018**, *6* (43), 11615–11621. <https://doi.org/10.1039/c8tc02849d>.

- (147) Kim, M.; Jeon, S. K.; Hwang, S. H.; Lee, S. S.; Yu, E.; Lee, J. Y. Correlation of Molecular Structure with Photophysical Properties and Device Performances of Thermally Activated Delayed Fluorescent Emitters. *J. Phys. Chem. C* **2016**, *120* (5), 2485–2493. <https://doi.org/10.1021/acs.jpcc.5b09114>.
- (148) Senes, A.; Meskers, S. C. J.; Dijkstra, W. M.; Van Franeker, J. J.; Altazin, S.; Wilson, J. S.; Janssen, R. A. J. Transition Dipole Moment Orientation in Films of Solution Processed Fluorescent Oligomers: Investigating the Influence of Molecular Anisotropy. *J. Mater. Chem. C* **2016**, *4* (26), 6302–6308. <https://doi.org/10.1039/c5tc03481g>.
- (149) Senes, A.; Meskers, S. C. J.; Greiner, H.; Suzuki, K.; Kaji, H.; Adachi, C.; Wilson, J. S.; Janssen, R. A. J. Increasing the Horizontal Orientation of Transition Dipole Moments in Solution Processed Small Molecular Emitters. *J. Mater. Chem. C* **2017**, *5* (26), 6555–6562. <https://doi.org/10.1039/C7TC01568B>.
- (150) Duan, L.; Hou, L.; Lee, T. W.; Qiao, J.; Zhang, D.; Dong, G.; Wang, L.; Qiu, Y. Solution Processable Small Molecules for Organic Light-Emitting Diodes. *J. Mater. Chem.* **2010**, *20* (31), 6392–6407. <https://doi.org/10.1039/b926348a>.
- (151) Huang, T.; Jiang, W.; Duan, L. Recent Progress in Solution Processable TADF Materials for Organic Light-Emitting Diodes. *J. Mater. Chem. C* **2018**, *6* (21), 5577–5596. <https://doi.org/10.1039/C8TC01139G>.
- (152) Zou, Y.; Gong, S.; Xie, G.; Yang, C. Design Strategy for Solution-Processable Thermally Activated Delayed Fluorescence Emitters and Their Applications in Organic Light-Emitting Diodes. *Adv. Opt. Mater.* **2018**, *6* (23), 1–25. <https://doi.org/10.1002/adom.201800568>.
- (153) Wu, J. L.; Lee, Y. T.; Chen, C. T.; Chen, C. T. Solution-Processed Small Molecular Materials: Bulk Heterojunction Organic Photovoltaic Materials, Host Materials for Phosphorescence Organic Light-Emitting Diodes, and Nondopant Thermally Activated Delayed Fluorescence Materials. *J. Chinese Chem. Soc.* **2018**, *65* (1), 87–106. <https://doi.org/10.1002/jccs.201700244>.
- (154) Cho, Y. J.; Yook, K. S.; Lee, J. Y. High Efficiency in a Solution-Processed Thermally Activated Delayed-Fluorescence Device Using a Delayed-Fluorescence Emitting Material with Improved Solubility. *Adv. Mater.* **2014**, *26* (38), 6642–6646. <https://doi.org/10.1002/adma.201402188>.
- (155) Tsai, M. H.; Ke, T. H.; Lin, H. W.; Wu, C. C.; Chiu, S. F.; Fang, F. C.; Liao, Y. L.; Wong, K. T.; Chen, Y. H.; Wu, C. I. Triphenylsilyl- and Trityl-Substituted Carbazole-Based Host Materials for Blue Electrophosphorescence. *ACS Appl. Mater. Interfaces* **2009**, *1* (3), 567–574. <https://doi.org/10.1021/am800124q>.
- (156) Chen, X. L.; Jia, J. H.; Yu, R.; Liao, J. Z.; Yang, M. X.; Lu, C. Z. Combining Charge-Transfer Pathways to Achieve Unique Thermally Activated Delayed Fluorescence Emitters for High-Performance Solution-Processed, Non-Doped Blue OLEDs. *Angew. Chemie Int. Ed.* **2017**, *56* (47), 15006–15009. <https://doi.org/10.1002/anie.201709125>.
- (157) Wada, Y.; Shizu, K.; Kubo, S.; Suzuki, K.; Tanaka, H.; Adachi, C.; Kaji, H. Highly Efficient Electroluminescence from a Solution-Processable Thermally Activated Delayed Fluorescence Emitter. *Appl. Phys. Lett.* **2015**, *107*, 183303. <https://doi.org/10.1063/1.4935237>.
- (158) Dianming Sun, Eimantas Duda, Xiaochun Fan, Rishabh Saxena, Ming Zhang, Sergey Bagnich, Xiaohong Zhang, Anna Köhler, and E. Z.-C. Thermally Activated Delayed

Fluorescent Dendrimers That Underpin High-Efficiency Host-Free Solution-Processed Organic Light-Emitting Diodes. *Adv. Mater.* **2022**, *34*, 2110344. <https://doi.org/10.1002/adma.202110344>.

- (159) Maeda, C.; Takata, M.; Honsho, A.; Ema, T. Intramolecular Electronic Coupling in the Thiophene-Bridged Carbazole-Based Diporphyrin. *Org. Lett.* **2016**, *18* (23), 6070–6073. <https://doi.org/10.1021/acs.orglett.6b03054>.
- (160) Ediger, M. D.; De Pablo, J.; Yu, L. Anisotropic Vapor-Deposited Glasses: Hybrid Organic Solids. *Acc. Chem. Res.* **2019**, *52* (2), 407–414. <https://doi.org/10.1021/acs.accounts.8b00513>.
- (161) Kumar, M.; Pereira, L. Mixed-Host Systems with a Simple Device Structure for Efficient Solution-Processed Organic Light-Emitting Diodes of a Red-Orange TADF Emitter. *ACS Omega* **2020**, *5* (5), 2196–2204. <https://doi.org/10.1021/acsomega.9b03253>.
- (162) Vecchi, P. A.; Padmaperuma, A. B.; Qiao, H.; Sapochak, L. S.; Burrows, P. E. A Dibenzofuran-Based Host Material for Blue Electrophosphorescence. *Org. Lett.* **2006**, *8* (19), 4211–4214. <https://doi.org/10.1021/ol0614121>.
- (163) Crovini, E.; Zhang, Z.; Kusakabe, Y.; Ren, Y.; Wada, Y.; Naqvi, B. A.; Sahay, P.; Matulaitis, T.; Diesing, S.; Samuel, I. D. W.; Brütting, W.; Suzuki, K.; Kaji, H.; Bräse, S.; Zysman-Colman, E. Effect of a Twin-Emitter Design Strategy on a Previously Reported Thermally Activated Delayed Fluorescence Organic Light-Emitting Diode. *Beilstein J. Org. Chem.* **2021**, *17*, 2894–2905. <https://doi.org/10.3762/bjoc.17.197>.
- (164) Kim, K.-H.; Baek, J. Y.; Cheon, C. W.; Moon, C.-K.; Sim, B.; Choi, M. Y.; Kim, J.-J.; Kim, Y.-H. Highly Efficient Non-Doped Deep Blue Fluorescent Emitters with Horizontal Emitting Dipoles Using Interconnecting Units between Chromophores. *Chem. Commun.* **2016**, *52* (73), 10956–10959. <https://doi.org/10.1039/c6cc05076j>.
- (165) Li, W.; Li, B.; Cai, X.; Gan, L.; Xu, Z.; Li, W.; Liu, K.; Chen, D.; Su, S. J. Tri-Spiral Donor for High Efficiency and Versatile Blue Thermally Activated Delayed Fluorescence Materials. *Angew. Chemie - Int. Ed.* **2019**, *58* (33), 11301–11305. <https://doi.org/10.1002/anie.201904272>.
- (166) Lee, Y.; Woo, S.-J.; Kim, J.-J.; Hong, J.-I. Blue Thermally Activated Delayed Fluorescence Emitter Using Modulated Triazines as Electron Acceptors. *Dye. Pigment.* **2020**, *172*, 107864. <https://doi.org/10.1016/j.dyepig.2019.107864>.
- (167) Liu, M.; Komatsu, R.; Cai, X.; Hotta, K.; Sato, S.; Liu, K.; Chen, D.; Kato, Y.; Sasabe, H.; Ohisa, S.; Suzuri, Y.; Yokoyama, D.; Su, S.-J.; Kido, J. Horizontally Orientated Sticklike Emitters: Enhancement of Intrinsic Out-Coupling Factor and Electroluminescence Performance. *Chem. Mater.* **2017**, *29*, 8630–8636. <https://doi.org/10.1021/acs.chemmater.7b02403>.
- (168) Zeng, X.; Pan, K.-C.; Lee, W.-K.; Gong, S.; Ni, F.; Xiao, X.; Zeng, W.; Xiang, Y.; Zhan, L.; Zhang, Y.; Wu, C.-C.; Yang, C. High-Efficiency Pure Blue Thermally Activated Delayed Fluorescence Emitters with a Preferentially Horizontal Emitting Dipole Orientation via a Spiro-Linked Double D-A Molecular Architecture. *J. Mater. Chem. C* **2019**, *7* (35), 10851–10859. <https://doi.org/10.1039/c9tc03582f>.
- (169) Lee, Y.-T.; Tseng, P.-C.; Komino, T.; Mamada, M.; Ortiz, R.-J.; Leung, M.; Chiu, T.-L.; Lin, C.-F.; Lee, J.-H.; Adachi, C.; Chen, C.-T.; Chen, C.-T. Simple Molecular-Engineering Approach for Enhancing Orientation and Outcoupling Efficiency of Thermally Activated



- Delayed Fluorescent Emitters without Red-Shifting Emission. *ACS Appl. Mater. Interfaces* **2018**, *10* (50), 43842–43849. <https://doi.org/10.1021/acsami.8b16199>.
- (170) Stavrou, K.; Franca, L. G.; Monkman, A. P. Photophysics of TADF Guest-Host Systems: Introducing the Idea of Hosting Potential. *ACS Appl. Electron. Mater.* **2020**, *2* (9), 2868–2881. <https://doi.org/10.1021/acsaelm.0c00514>.
- (171) Dhali, R.; Phan Huu, D. K. A.; Bertocchi, F.; Sissa, C.; Terenziani, F.; Painelli, A. Understanding TADF: A Joint Experimental and Theoretical Study of DMAC-TRZ. *Phys. Chem. Chem. Phys.* **2021**, *23* (1), 378–387. <https://doi.org/10.1039/d0cp05982j>.
- (172) Li, W.; Cai, X.; Li, B.; Gan, L.; He, Y.; Liu, K.; Chen, D.; Wu, Y. C.; Su, S. J. Adamantane-Substituted Acridine Donor for Blue Dual Fluorescence and Efficient Organic Light-Emitting Diodes. *Angew. Chemie - Int. Ed.* **2019**, *58* (2), 582–586. <https://doi.org/10.1002/anie.201811703>.
- (173) Hammett, L. P. The Effect of Structure upon the Reactions of Organic Compounds. Temperature and Solvent Influences. *J. Chem. Phys.* **1936**, *4* (9), 613–617. <https://doi.org/10.1063/1.1749914>.
- (174) Yadav, V. K. *Steric and Stereoelectronic Effects in Organic Chemistry*; 2016. <https://doi.org/10.1007/978-981-10-1139-9>.
- (175) Hansch Corwin.; Leo Albert. *Substituent Constants for Correlation Analysis in Chemistry and Biology*; Wiley-Interscience, NY, 1979.
- (176) Furue, R.; Nishimoto, T.; Park, I. S.; Lee, J.; Yasuda, T. Aggregation-Induced Delayed Fluorescence Based on Donor/Acceptor-Tethered Janus Carborane Triads: Unique Photophysical Properties of Nondoped OLEDs. *Angew. Chemie - Int. Ed.* **2016**, *55* (25), 7171–7175. <https://doi.org/10.1002/anie.201603232>.
- (177) Hsieh, Y. Y.; Sánchez, R. S.; Raffy, G.; Shyue, J. J.; Hirsch, L.; Del Guerso, A.; Wong, K. T.; Bassani, D. M. Supramolecular Gating of TADF Process in Self-Assembled Nano-Spheres for High-Resolution OLED Applications. *Chem. Commun.* **2022**, *58* (8), 1163–1166. <https://doi.org/10.1039/d1cc06120h>.
- (178) Hundemer, F.; Crovini, E.; Wada, Y.; Kaji, H.; Bräse, S.; Zysman-Colman, E. Tris(Triazolo)Triazine-Based Emitters for Solution-Processed Blue Thermally Activated Delayed Fluorescence Organic Light-Emitting Diodes. *Mater. Adv.* **2020**, *1* (8), 2862–2871. <https://doi.org/10.1039/d0ma00659a>.
- (179) Tsuchiya, Y.; Diesing, S.; Bencheikh, F.; Wada, Y.; dos Santos, P. L.; Kaji, H.; Zysman-Colman, E.; Samuel, I. D. W.; Adachi, C. Exact Solution of Kinetic Analysis for Thermally Activated Delayed Fluorescence Materials. *J. Phys. Chem. A* **2021**, *125* (36), 8074–8089. <https://doi.org/10.1021/acs.jpca.1c04056>.
- (180) Haase, N.; Danos, A.; Pflumm, C.; Morherr, A.; Stachelek, P.; Mekic, A.; Brütting, W.; Monkman, A. P. Kinetic Modeling of Transient Photoluminescence from Thermally Activated Delayed Fluorescence. *J. Phys. Chem. C* **2018**, *122* (51), 29173–29179. <https://doi.org/10.1021/acs.jpcc.8b11020>.
- (181) Wu, Z. C.; Boger, D. L. Synthesis, Characterization, and Cycloaddition Reactivity of a Monocyclic Aromatic 1,2,3,5-Tetrazine. *J. Am. Chem. Soc.* **2019**, *141* (41), 16388–16397. <https://doi.org/10.1021/jacs.9b07744>.
- (182) Shi, Y.; Wang, K.; Zhang, S.; Fan, X.; Tsuchiya, Y.; Lee, Y.; Dai, G.; Chen, J.; Zheng, C.;

- Xiong, S.; Ou, X.; Yu, J.; Jie, J.; Lee, C.; Adachi, C.; Zhang, X. Characterizing the Conformational Distribution in an Amorphous Film of an Organic Emitter and Its Application in a “Self-Doping” Organic Light-Emitting Diode. *Angew. Chemie* **2021**, *133* (49), 26082–26087. <https://doi.org/10.1002/ange.202108943>.
- (183) Chen, J. X.; Xiao, Y. F.; Wang, K.; Fan, X. C.; Cao, C.; Chen, W. C.; Zhang, X.; Shi, Y. Z.; Yu, J.; Geng, F. X.; Zhang, X. H.; Lee, C. S. Origin of Thermally Activated Delayed Fluorescence in a Donor-Acceptor Type Emitter with an Optimized Nearly Planar Geometry. *J. Mater. Chem. C* **2020**, *8* (38), 13263–13269. <https://doi.org/10.1039/d0tc03747h>.
- (184) M. A. El-Sayed. Spin — Orbit Coupling and the Radiationless Processes in Nitrogen. *J. Chem. Phys.* **1963**, *38*, 2834–2838. <https://doi.org/10.1063/1.1733610>.
- (185) Painelli, A.; Terenziani, F. A Non-Perturbative Approach to Solvatochromic Shifts of Push-Pull Chromophores. *Chem. Phys. Lett.* **1999**, *312* (2–4), 211–220. [https://doi.org/10.1016/S0009-2614\(99\)00960-4](https://doi.org/10.1016/S0009-2614(99)00960-4).
- (186) Boldrini, B.; Cavalli, E.; Painelli, A.; Terenziani, F. Polar Dyes in Solution: A Joint Experimental and Theoretical Study of Absorption and Emission Band Shapes. *J. Phys. Chem. A* **2002**, *106* (26), 6286–6294. <https://doi.org/10.1021/jp020031b>.
- (187) Patrycja Stachelek, Jonathan S. Ward, Paloma L. dos Santos, Andrew Danos, Marco Colella, Nils Haase, Samuel J. Raynes, Andrei S. Batsanov, Martin R. Bryce, and Andrew P. Monkman, Patrycja Stachelek, Jonathan S. Ward, Paloma L. dos Santos, Andrew Danos, Ma, and A. P. M. Molecular Design Strategies for Color Tuning of Blue TADF Emitters. *ACS Appl. Mater. Interfaces* **2019**, *11*, 27125–27133.
- (188) Pavlishchuk, V. V.; Addison, A. W. Conversion Constants for Redox Potentials Measured versus Different Reference Electrodes in Acetonitrile Solutions at 25°C. *Inorg. Chim. Acta* **2000**, *298*, 97. [https://doi.org/10.1016/S0020-1693\(99\)00407-7](https://doi.org/10.1016/S0020-1693(99)00407-7).
- (189) Connelly, N. G., and Geiger, W. E. Chemical Redox Agents for Organometallic Chemistry. *Chem. Rev.* **1996**, *96* (2), 877–910. <https://doi.org/10.1021/cr940053x>.
- (190) Melhuish, W. H. Quantum Efficiencies Of Fluorescence Of Organic Substances: Effect Of Solvent And Concentration Of The Fluorescent Solute. *J. Phys. Chem.* **1961**, *65* (2), 229–235. <https://doi.org/10.1021/j100820a009>.
- (191) Frischeisen, J.; Yokoyama, D.; Adachi, C. and; Brütting, W. Determination of Molecular Dipole Orientation in Doped Fluorescent Organic Thin Films by Photoluminescence Measurements. *Appl. Phys. Lett.* **2010**, *96* (7), 1–4. <https://doi.org/10.1063/1.3309705>.
- (192) O’Boyle, N. M.; Tenderholt, A. L.; Langner, K. M. Cclib A Library for Package-independent Computational Chemistry Algorithms.Pdf. *Journal of Computational Chemistry*. 2007, pp 839–845.
- (193) Humphrey, W.; Dalke, A.; Schulten, K. VMD: Visual Molecular Dynamics. *J. Mol. Graph.* **1996**, *14* (October 1995), 33–38.
- (194) Stone, J. TACHYON: An Efficient Library for Parallel Ray Tracing and Animation. Master’s thesis, Computer Science Department, University of Missouri-Rolla ... 1998.
- (195) O’Boyle, N. M.; Banck, M.; James, C. A.; Morley, C.; Vandermeersch, T.; Hutchison, G. R. Open Babel. *J. Cheminform.* **2011**, *3* (33), 1–14.
- (196) O’Boyle, N. M.; Hutchison, G. R. Cinfony - Combining Open Source Cheminformatics Toolkits behind a Common Interface. *Chem. Cent. J.* **2008**, *2* (1), 1–10.

<https://doi.org/10.1186/1752-153X-2-24>.

- (197) Frisch, M. J.; Trucks, G. W.; Schlegel, H. B.; Scuseria, G. E.; Robb, M. a.; Cheeseman, J. R.; Scalmani, G.; Barone, V.; Petersson, G. a.; Nakatsuji, H.; Li, X.; Caricato, M.; Marenich, a. V.; Bloino, J.; Janesko, B. G.; Gomperts, R.; Mennucci, B.; Hratchian, H. P.; Ortiz, J. V.; Izmaylov, a. F.; Sonnenberg, J. L.; Williams; Ding, F.; Lipparini, F.; Egidi, F.; Goings, J.; Peng, B.; Petrone, A.; Henderson, T.; Ranasinghe, D.; Zakrzewski, V. G.; Gao, J.; Rega, N.; Zheng, G.; Liang, W.; Hada, M.; Ehara, M.; Toyota, K.; Fukuda, R.; Hasegawa, J.; Ishida, M.; Nakajima, T.; Honda, Y.; Kitao, O.; Nakai, H.; Vreven, T.; Throssell, K.; Montgomery Jr., J. a.; Peralta, J. E.; Ogliaro, F.; Bearpark, M. J.; Heyd, J. J.; Brothers, E. N.; Kudin, K. N.; Staroverov, V. N.; Keith, T. a.; Kobayashi, R.; Normand, J.; Raghavachari, K.; Rendell, a. P.; Burant, J. C.; Iyengar, S. S.; Tomasi, J.; Cossi, M.; Millam, J. M.; Klene, M.; Adamo, C.; Cammi, R.; Ochterski, J. W.; Martin, R. L.; Morokuma, K.; Farkas, O.; Foresman, J. B.; Fox, D. J. G16\_C01. 2016, p Gaussian 16, Revision C.01, Gaussian, Inc., Wallin.
- (198) Adamo, C.; Barone, V. Toward Reliable Density Functional Methods without Adjustable Parameters: The PBE0 Model. *J. Chem. Phys.* **1999**, *110* (13), 6158–6170.  
<https://doi.org/10.1063/1.478522>.
- (199) Moral, M.; Muccioli, L.; Son, W. J.; Olivier, Y.; Sancho-Garcia, J. C. Theoretical Rationalization of the Singlet-Triplet Gap in Oleds Materials: Impact of Charge-Transfer Character. *J. Chem. Theory Comput.* **2015**, *11* (1), 168–177.  
<https://doi.org/10.1021/ct500957s>.